EVALUATION OF VERTICAL AND LATERAL LOAD CAPACITY OF RECYCLED PLASTIC PIN

By

SEHNEELA SARA AURPA

DISSERTATION

Presented to the Faculty of the Graduate School of

The University of Texas at Arlington

In Partial Fulfillment for the

Requirements of the Degree of

DOCTOR OF PHILOSOPHY

THE UNIVERSITY OF TEXAS AT ARLINGTON

December 2023

ACKNOWLEDGEMENT

ABSTRACT

EVALUATION OF VERTICAL AND LATERAL LOAD CAPACITY OF RECYCLED
PLASTIC PIN

Sehneela Sara Aurpa

The University of Texas at Arlington, 2023

Supervising Professor: MD Sahadat Hossain

RPPs have been in use as a sustainable and effective technique to stabilize and reinforce weak ground for geotechnical purposes. Application of RPP in stabilization of slopes and improvement of load carrying capacity of foundation soil has yielded tremendous results. However, to facilitate the seamless integration of RPPs in design of foundation requires the load carrying capacity of RPP to be known. As RPP has been in use for both its vertical and lateral load carrying capacity, exploration of the load capacity of this material is essential. The objective of the study is to determine the load carrying capacity of RPPs in order to develop design charts that can be used towards designing foundation for improving the vertical and lateral load carrying capacity of soil. This endeavor involved an extensive field-testing program, which encompassed the determination of the vertical and lateral load capacities of RPPs in various sizes and arrangements. A total of 16 full scale vertical load tests were conducted of four different sizes (10 cm x 10 cm, 15 cm x 15 cm, 25 cm x 25 cm and 30 cm x 30 cm) of single RPPs and groups 10 cm x 10 cm and 15 cm x 15 cm RPPs arranged in two different spacings of 0.6 m and 0.9 m. 16 lateral load tests were conducted on RPPs of 10 cm x 10 cm, 15 cm x 15 cm and 25 cm x 25 cm sizes embedded in three depths of 2.7 m, 2.4 m and 2.1 m into the ground. Based on the load test data, an empirical and analytical approach was undertaken for determining the vertical load capacity of the single and group RPPs, whereas p-y analysis was undertaken for determination of ultimate lateral load capacity of RPPs. The average vertical load capacity ranged from 50 kN to 207 kN for the single RPPs whereas for RPPs arranged in a group had load capacity ranging from 193 kN to 477 kN. The lateral load capacity of RPP was found much less than its vertical load capacity and ranged from 16 kN to 125 kN for varying sizes and embedment depths.

Furthermore, the load settlement response was assessed through numerical modeling using finite element software PLAXIS 3D for the vertical load tests, and the LPILE software was employed for the lateral load test response. A parametric study was conducted using the calibrated model to evaluate the influence of foundation soil strength, RPP size, spacing and embedment depth on settlement due to application of load. In total, 540 different scenarios involving various sets of data were investigated using numerical models to develop design charts for predicting settlement or deformation responses to applied load. Moreover, a prediction model was established using MATLAB to forecast the settlement or deformation responses of different RPPs under different site-specific soil conditions.

TABLE OF CONTENT

LIST OF FIGURES

xix

LIST OF TABLES

CHAPTER 1

INTRODUCTION

1.1 Background

Construction of civil engineering infrastructures, for example, retaining structures, embankments for highways, roadways, dams, levees etc. is preferred in the sites having suitable foundation soil with good geotechnical characteristics. However, rapid growth of civilization forced the use of weak unsuitable sub-grade soil for the construction and development of various transportation related projects (Rao, 2006). Weak foundation soil exhibits poor strength and high compressibility (Nazir and Azzam, 2010). Major concerns associated with weak foundation soil type under large structural loads include bearing capacity failure, total as well as differential settlement of the footing, lateral pressure, and instability. Structures (e.g. embankments, retaining walls etc.) constructed on such foundation soil are prone to large deformations, resulting in construction delays as well as premature failure of infrastructures. In addition to the bearing capacity failure, sliding or shear capacity failure of the retaining structures, especially mechanically stabilized retaining walls (MSEWs) constructed on stiff soil is another major concern. Most of the time, instead of a complete failure, a lateral shift at the base of the wall is noticed due to excessive lateral pressure generated from the backfill soil in the slope side of the wall. Which is mainly due to lack of support resulting from insufficient shear resistance between the foundation and the base of the wall (Khan et al., 2014).

According to TxDOT (Texas Department of Transportation) memorandum (2013), for sites with problematic soils, sometimes a ground (foundation) improvement plan is more economical to allow the safe use of structure rather than changing the structure type. The general and conventional approach to the construction of any highway or runway on weak sub-grade soil is remove and replacement method. However, the excessive material replacement cost causes the related administrations to evaluate alternative methods of construction on soils with low bearing capacity (Ozdemir, 2016). To support the load from the structures, installation of piles up to the bearing stratum below the unsuitable soil layer proved to be very effective (Barchard, 1999) and has been used for decades. The use of piles is an effective improvement technique for unsuitable foundation. Among the available methods, RPPs can be viable alternative to conventional piles as compared to other piles, e.g., concrete or steel piles, drilled shafts, timber or other structural

materials, RPP weighs much less and is more resistant to chemical and biological degradation. Additionally, it will be a very good application of recycling plastic products, reducing the waste volume entering the landfill. Therefore, use of recycled plastic pin (RPP) can be a sustainable and cost-effective solution for ground improvement compared to conventional techniques (Loehr & Bowders, 2007; Khan et al., 2015).

Typically, RPP is composed of 55 - 70% high-density polyethylene (HDPE), 5 - 10% low-density polyethylene, and a small percentage of polystyrene and polypropylene (McLaren 1995). Moreover, additives, including fiberglass and wood fibers, are added during the manufacturing process to improve the modulus of elasticity of RPP (Breslin et al. 1998). Approximately 600 mineral water/soda bottles are used for one 3 m long (10 cm × 10 cm) RPP (Hossain et al. 2017). Compressive strengths of recycled plastic members ranged from 11 MPa to 21 MPa with no cross-sectional area correction, tested at a nominal strain rate of 0.006 mm/mm/min (Bowders et al. 2003). Compression moduli determined at one percent strain ranged from 552 MPa to 1310 MPa (Bowders et al. 2003).

A preliminary investigation conducted by Zaman (2019) found that RPPs significantly reduce foundation settlement of an MSE wall base. Now a days, RPP is being utilized in many other states of the USA as a cost-effective solution for slope stabilization (Khan et al. 2016; Hossain et al. 2017). It can also be used as soil reinforcement beneath the foundation to improve the bearing capacity by transferring the load from the flexible foundation to the stiffer layer (Badhon,2021). Shearing resistance provided by RPP has also been used in improving the lateral movement of MSE wall base (Bhandari,2021). However, vertical and lateral load carrying capacity of individual RPP or RPP group has not been evaluated.

Despite the difficulties in obtaining the ultimate capacity of the piles using the in situ loading test, this method is the most recommended by several codes and design standards. To investigate the vertical load bearing behavior of manually excavated large diameter belled concrete piles (LDBCPs), Gao et al (2019) performed field loading tests on a total of 16 LDBCPs, ranging from 0.8 to 3.5 m in base diameter from 6.1 to 18.0 m in embedment length. Yi et al (2017) employed full-scale field loading tests to investigate the vertical bearing capacity behavior of a single T-shaped column in soft ground.

Xiang et al (2015) carried out field lateral loading tests on one 2×5 and two 3×5 grouted steel-pipe pile groups at a highway slope-stabilization site. The tests simulated the performance of slope-stabilization pile groups subject to lateral soil movements caused by surcharge fill loading behind the pile groups. Feagin (1937) conducted tests to determine the resistance under lateral loads of timber and concrete piles, driven in Mississippi River sand. The work includes descriptions of tests on single piles with heads not fixed, and on groups of four, twelve, and twenty piles with heads fixed in concrete test monoliths. Wu et al (1995) conducted a series of lateral load tests involving instrumented single piles in Shanghai, PRC with the diameter of the piles varying from 0.09 m to 0.60 m. The lateral deflections and the moment distribution and the p-y curves from the lateral load tests in the laterally loaded piles have been estimated.

1.2   Problem Statement

High compressibility and inadequate strength are characteristics of weak foundation soil. Total and differential settlement of footing, lateral pressure, and instability are the main issues with foundation with weak soil when subjected to heavy structural loads. Buildings (such dams, retaining walls, etc.) built on unsuitable foundation soil are vulnerable to significant deformations, which can delay construction and hasten infrastructure breakdown.

RPP has been successfully incorporated with various geotechnical structures in improving structural stability. Previously, RPP has been used to stabilize slopes for increasing lateral resistance of slopes (Khan et al., 2014), in the foundations of embankments (Zaman, 2019) in the foundation of an embankment over soft soils (Islam, 2021), in the MSE wall foundation for increasing bearing capacity (Badhon, 2021), in the MSE wall base as shear keys (Bhandari 2021); and the tremendous results of performance monitoring of these studies have made RPP a viable alternative to other ground improvement techniques. However, the studies are based on the performance monitoring results and no study attempted to evaluate the load capacity of RPPs. Even though RPP has proven to be effective in increasing the bearing capacity and lateral resistance of foundation soil, one of the largest obstacles preventing its widespread application, is the lack of knowledge regarding the load carrying capacity of individual and group RPP in the design process. Therefore, it is necessary to determine the vertical and lateral load capacity of RPP under field conditions in order to facilitate future design considering various site and loading situations.

1.3 Research Objectives

The objective of the study is to determine the load carrying capacity of Recycled Plastic Pins (RPP) by doing load tests. Based on the load test results, design charts were developed for improving vertical and lateral load carrying capacity of soil foundation systems. The specific tasks to achieve the objective of the study include:

1.   Site investigation and selection for field load test location.

2.   Development of preliminary design for the load tests.

3.   Instrumentation of the RPPs for performance evaluation.

4.   Field installation of RPPs and construction of test sections.

5.   Conducting vertical load tests on individual and group RPP for vertical load capacity.

6.   Conducting lateral load test on individual RPP for lateral capacity.

7.   Analysis of the field data for evaluating the load capacity of RPP.

8.   Numerical modeling for the simulation of foundation soil improvement, incorporating various sizes of RPPs, cross-sectional areas, and site soil profile.

9.   Development of design charts to enhance the vertical and lateral capacity of foundation soil using RPPs in the design process.

1.4 Dissertation Organization

Chapter 1 provides an overview of the research by presenting the background, problem statement, and objectives. Essentially, it encapsulates the essence of the entire dissertation. Following Chapter 1, Chapter 2 delves into an in-depth literature review. The subsequent sections of the dissertation are structured into four distinct papers. The initial paper outlines a field-scale study, focusing on the vertical load capacity evaluation of both single and group RPPs. This study involves real-time data of field load test incorporation with ultimate vertical load capacity analysis. The second paper elaborates on the in-situ observations of vertical load tests within a numerical framework, illustrating the impact of diverse design parameters through an extensive parametric study. The third paper concentrates on lateral load deflection behavior of RPPs. The final paper provides valuable insights into the load capacity of RPP in comparison with traditional timber piles. Chapter

7 addresses the development of design charts for enhancing the bearing capacity of foundation soil through the utilization of RPP. In the subsequent chapter, Chapter 8, a comprehensive overview is provided of the statistical analysis carried out on the numerical study's outcomes. The analysis entailed the use of multiple regression techniques to formulate predictive models for settlement concerning RPP under both vertical and lateral loading conditions. Lastly in Chapter 9, the primary findings from field tests, numerical investigations, statistical analyses, and design methodologies are summarized and presented as significant conclusions.

CHAPTER 2

LITERATURE REVIEW

2.1   Introduction

Geotechnical structures constructed on weak or unsuitable soil pose problems like instability. This instability results from the insufficient bearing capacity and shearing resistance of the unsuitable foundation soil and the structure eventually experiences excessive settlement or other modes of failure associated with the structure. Unfortunately, rapid growth of population and urbanization demands the use of land with weak foundation soil for the construction of massive geotechnical structures. Different technics of stabilization methods are available and are used in recent years to stabilize and reinforce the weak foundation soil for construction. Some of the conventional methods for strengthening the foundation soils include removal, compacting, and replacement of existing ground soil, cement, or lime stabilization, using stone columns, and piers. Drilled shafts and piles made of concrete and steel have also been in use as ground improvement technic. However, these conventional methods are expensive and time-consuming. In this respect, utilization of Recycled Plastic Pins or RPP can offer a sustainable and economic alternative to the conventional ground improving technics for weak foundation soil. Nevertheless, in order to ensure the smooth incorporation of RPPs into foundation design, it is crucial to have a clear understanding of their load-bearing capabilities. Given that RPP has been utilized for both its ability to support vertical and lateral loads, it is imperative to investigate and understand the load-bearing potential.

2.2   Bearing Capacity of Foundation

Ultimate bearing capacity of foundation soil is the maximum load that the soil can carry before undergoing excessive settlement. After passing the maximum allowable settlement, which is typically taken as 1 inch, the structure supported by the underlying soil leads towards failure. There are three possible types of failure occurring in foundation on weak soil such as-

1.   General Shear Failure,

2.   Local Shear Failure; and

3.   Punching Shear Failure.

Figure 2-1 presents types bearing capacity failure of soil for a strip footing of width B. General shear failure is the most common one and it generally occurs when the foundation soil consists of dense sand or stiff clay. Local shear failure occurs if the soil type is medium dense or medium stiff clay. Where the soil beneath the foundation is weak and foundation width is not enough to resist the punching force, punching shear failure occurs.
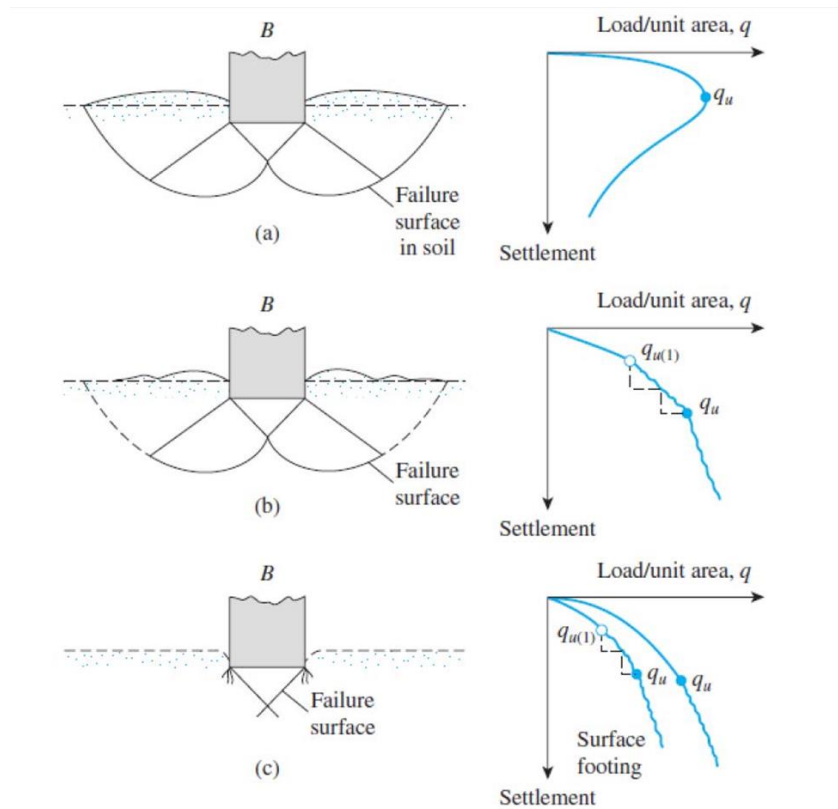
Figure 2-1 Bearing Capacity failure of soil (a) general shear failure; (b) local shear failure; and

(c) punching shear failure (Das, 2011)

Terzaghi's solution for bearing capacity

Terzaghi in 1943 first presented a theory to evaluate the ultimate bearing capacity of shallow foundations based on drained strength parameter. The solution is based on drained strength parameter of soil. Terzaghi proposed a failure surface for a continuous, or strip foundation in soil subjected to ultimate load to be assumed as the case presented in Figure 2-2. Figure 2-3 shows the forces acting on a wedge of soil.
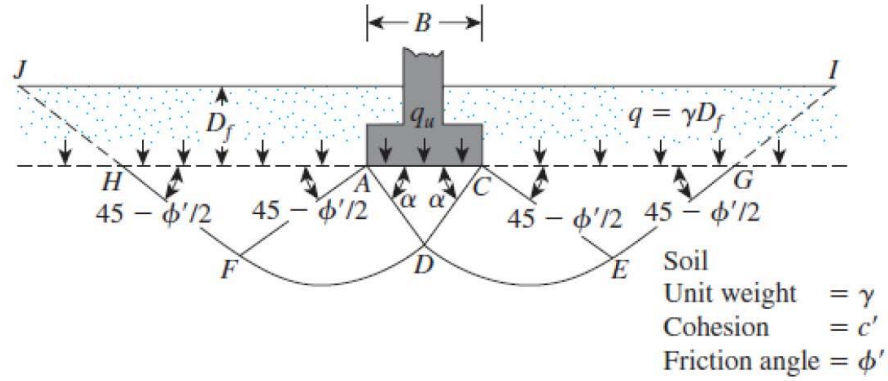
Figure 2-2 Ultimate bearing capacity for strip footing (Das, 2011)
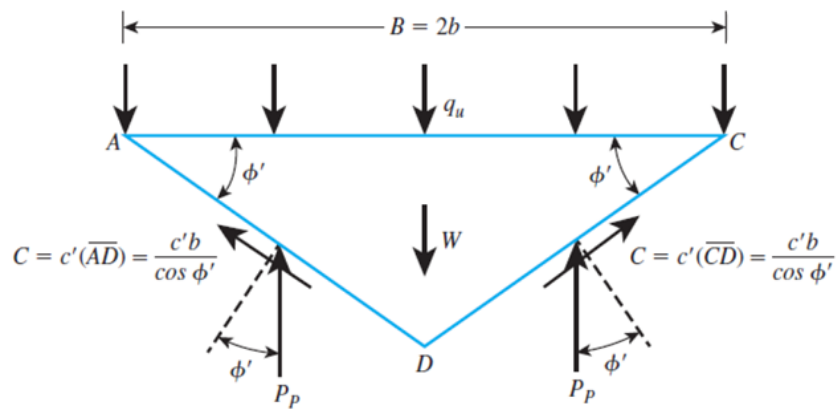
Figure 2-3 Free body diagram showing the force equilibrium (Das, 2011)

For determining the ultimate bearing capacity of different foundations, Terzaghi suggested the following equation:

For strip footing:

$$q_u = c\,N_c + q\,N_q + \tfrac{1}{2}\gamma\,B\,N_\gamma \tag{2.1}$$

For square footing:

$$q_u = 1.3\,c\,N_c + q\,N_q + 0.4\,\gamma\,B\,N_\gamma \tag{2.2}$$

For circular footing:

$$q_u = 1.3\,c\,N_c + q\,N_q + 0.3\,\gamma\,B\,N_\gamma \tag{2.3}$$

Where,

c = drained cohesion of soil

N_c, N_q and N_γ are bearing capacity factors proposed by Terzaghi

B = width of footing/ diameter of footing

Skempton's solution for undrained bearing capacity

Terzaghi's bearing capacity equation was modified by Skempton to determine the undrained bearing capacity of cohesive soil. He suggested a modified bearing capacity factor N_{cu} instead of N_c in Terzaghi's equation which tends to increase with the depth in case of cohesive soil. The modified equation uses the undrained bearing capacity factor (N_{cu}) which depends on size and depth of the foundation. However, the N_{cu} value will be equal to N_c in case of square footing. Skempton's equation for undrained clay soils is as follows:

$$q_u = s_u N_{cu} + q_0 \qquad (2.4)$$

Here,

N_{cu} = Skempton's bearing capacity factor = N_c. s_c. d_c

Where, s_c is a shape factor and d_c is a depth factor.

$N_q = 1$, $N_\gamma = 0$, $N_c = 5.14$

$s_c = 1 + 0.2$ (B/L) for $B \leq L$; $d_c = 1 + Ö$ (0.053 D/B) for D/B < 4

When the foundation is on ground surface, $q_o = 0$

Shape factor, $s_c = 1$; Depth factor, $d_c = 1$

As the friction angle is considered as zero for cohesive soil, the undrained bearing capacity will be the multiplication of undrained shear strength and Nc and the simplified equation becomes as follows.

$$q_u = 5.14 \, s_u \; or \; (2 + \pi)s_u \qquad (2.5)$$

2.2.1 Weak Soil

Soil with insufficient strength and excessive compressibility are generally characterized as weak soil. Change in climatic conditions results in consequential variation of the physical and

engineering properties such as grain size distribution, void ratio, water content, strength, permeability, and compressibility of this soil.

Construction on weak foundation soil results in various problems during and after construction. Excessive settlement of the foundation, and lateral and vertical deformation of the structure are common consequences of construction on weak soil which eventually fails the structure. Figure 2-4 shows the problems faced during construction over weak soil.

(a) (b)

Figure 2-4 (a) Weather variation consequence of weak soil; (b) Construction equipment sinking in weak soil

TxDOT defines the consistency of a predominantly clay and/or silt by unconfined compressive strength (UCS) of soil. According to TEX-142-E, the consistency is tested in the laboratory under the natural moisture content in an undisturbed condition. Lower strength resulted from higher water content whereas lower water content yields higher strength. Consistency of soil based on unconfined compressive strength is shown in Table 2-1.

Table 2-1 Soil consistency based on UCS.

Unconfined Compressive Strength (tsf)	Consistency
Less than 0.25	Very Soft
0.25 to 0.50	Soft
0.50 to 1.0	Medium Stiff
1.0 to 2.0	Stiff
2.0 to 4.0	Very Stiff

Unconfined Compressive Strength (tsf)	Consistency
Greater than 4	Hard

2.2.2 Fully Soften Clay of High Plastic Clay Soil

A moderate to steep slope built on highly plastic clay is prone to the top soil weakening due to the wet-dry cycle. The shear strength of high plastic clay that corresponds to totally softened shear strength appears to increase over time as a result of the cycle of soaking and drying (Wright, S. G., 2005). Skempton first put up the idea of totally softened strength. in 1977 for naturally occurring and excavated slopes in the London Clays. According to Skempton (1977), the resilience of slopes in the highly plastic London Clay gradually lost strength until it was "fully softened," as Skempton put it. Strength shown in Figure 2-5 that is midway between peak and residual strength. According to Skempton (1977), the totally softened strength is like the shear strength in a typically consolidated state.
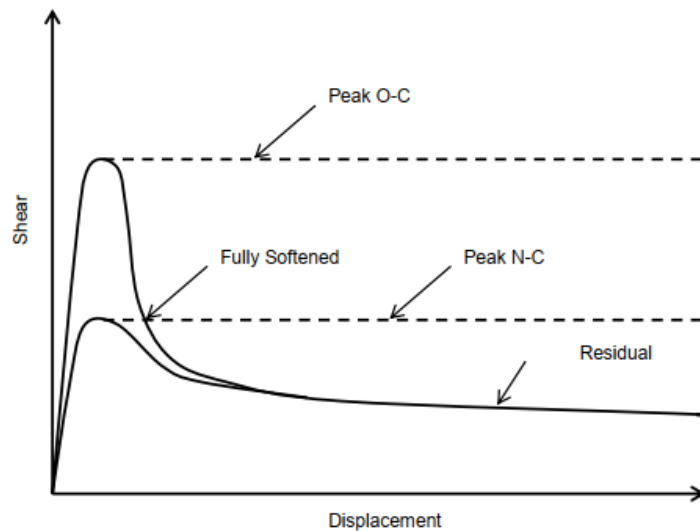
Figure 2-5 Comparisons of peak, residual and fully softened shear strength (Khan, 2014)

Rogers and Wright (1986) investigated the impact of cyclic wetting and drying on highly plastic clay soil in Texas. They performed direct shear tests on clay specimens from Houston, exposed to 1, 3, 9, and 30 wetting and drying cycles, which indicated a significant loss of shear strength, especially in terms of effective cohesion intercept (c'). The initial cycles caused the most substantial strength reduction. While the laboratory wetting and drying was more intense than field

conditions, the effects were deemed comparable. Kayyal and Wright (1991) developed a technique for triaxial specimens exposed to repeated wetting and drying cycles, focusing on highly plastic clay from Houston and Paris. Their consolidated undrained compression tests showed that the strength envelope for specimens subjected to wetting and drying had a nonlinear character, with lower strength under the as-compacted condition, particularly at lower normal stress levels. The intercept of the strength envelope for wetted and dried specimens was modest. Table 2-2 provides a summary of the study's shear strength parameters.

Table 2-2 Summary of Shear Strength Parameters from drained direct shear tests on specimens subjected to wetting and drying cycles (Rogers and Wright, 1986)

Number of Wet-Dry Cycles	Cohesion, c (psf)	Friction Angle, φ
1	29	23°
3	77	26 °
9	33	25 °
30	0	27 °

.
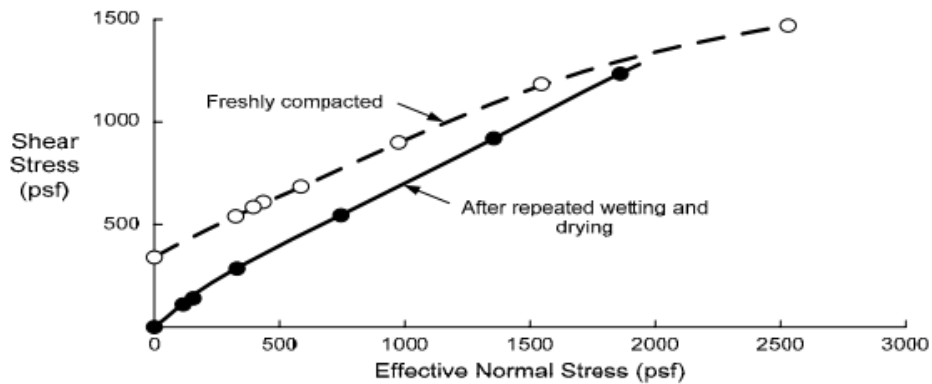
(a)
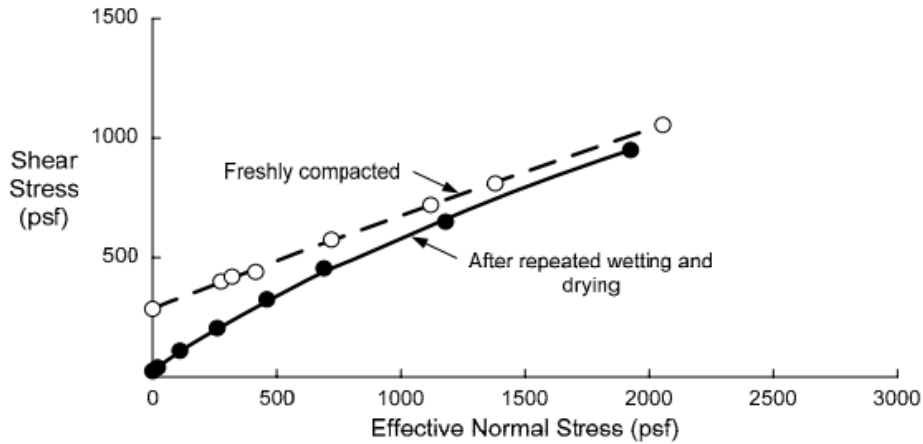
(b)

Figure 2-6 Shear strength envelopes in terms of effective stress a. Beaumont clay, b.

Paris clay (Kayyal and Wright, 1991)

Wright et al. (2007) investigated the shear strength of Eagle Ford clay exposed to seasonal wetting and drying in the field using triaxial compression tests. They compared samples prepared in compacted slurry to those subjected to 20 wetting and drying cycles. The results showed that compacted samples experienced more softening after reaching peak strength due to higher consolidation pressure. The modified Mohr failure envelope was nearly linear. In contrast, the stress-strain curves for regularly consolidated slurry samples displayed a reduction in stress after the peak, with some scatter in the data. The study noted that typically consolidated clay might have a zero-cohesion intercept until it's cemented. Samples subjected to wetting and drying cycles displayed less brittle stress-strain curves compared to compacted specimens. Their stress trajectories resembled those of slurry-formed samples, with a curved modified Mohr failure envelope and minimal cohesiveness.

In 2005, Wright S. G. conducted a study on slopes and embankments in Texas constructed on highly plastic clay soil. These compacted fillings are initially strong, with factors of safety often exceeding 2 at the end of construction. However, over time, these soils tend to weaken, and safety factors drop to around 1, approaching failure. The soil's softening is likely attributed to the seasonal wetting and drying cycles causing expansion and contraction. A curved Mohr failure envelope best represents the fully softened strength of the soil, which is located below the envelope for freshly

13

compacted soil. The literature reviews various slope ground improvement techniques used in different US states.

2.3   Bearing Capacity Improvement Methods

Different methods are in use at present for improving the bearing capacity of foundation soil or the ground where the structure is situated over. Numerous studies have been conducted by scholars for over decades to improve the bearing capacity of problematic foundation soil. Some of the technics are compaction, drainage, grouting, soil replacement, and piling (Jones et al., 1990). These methods work by improving the shear strength and thus reducing settlement of soft foundation soils.

2.3.1   Soil Nailing

Soil nailing is generally used as a soil retention technic. In this method, tension-resisting steel elements are grouted into the ground that can be used for either permanent or temporary support (Jadid et al., 2019). It is a common practice to construct the wall from the top down. With planned excavation of 3 to 6 feet of earth layer on topsoil nails are implemented. The exposed face is drilled in near-horizontal holes typically spaced 3 to 6 feet apart. Soil nailing along with vegetation increases factor of safety up to 61% for sandy soils (Elahi et al., 2019).

2.3.2   Stone Columns

Stone columns are a cost-effective method to improve soft soils, including silts, clays, and silty sands. They involve mixing crushed aggregates of different sizes to strengthen the ground. Two methods, top-feed and bottom-feed are used for this purpose. Water jetting may be used in the top-feed method to ensure proper stone column placement, while the bottom-feed method involves no water.

Guetif et al. (2007) utilized vibro-compacted stone columns to increase the Young's modulus of soft clay through a numerical study. They found that effective stress decreases radially from the center of the stone column and that the radial stress increases with the vertical mean stress. This led to an improvement in the Young's modulus of the soft clay after consolidation.

The load capacity of stone columns relies on the lateral confinement provided by the surrounding soil. In very soft soils, this confinement may be inadequate, raising questions about the effectiveness of stone columns (Murugesan and Rajagopal, 2009). Using geosynthetics to encase

individual columns, known as Encased Stone Columns (ESC), has shown significant improvements in load-bearing capacity compared to Ordinary Stone Columns (OSC). Load tests were conducted on stone columns in a clay bed, showing the enhanced performance of ESC compared to OSC, particularly with varying sizes.

2.3.3   Sand Compaction Pile

The Sand Compaction Pile (SCP) is a cost-effective method for improving ground stability and reducing settlement in soft foundation soils. SCPs, with or without confinement, enhance foundation soil properties by driving a hollow mandrel into the ground and compacting sand poured from the top. They are typically 0.46 to 0.76 m (1.5 to 2.5 ft.) in diameter and spaced about 1.5 to 3.0 m (5 to 10 ft.) apart.

In a case history by Basore and Boitano (1969), 356 mm (14 in.) diameter sand compaction piles were used to densify a 9 m (30 ft) thick subsoil in San Francisco, California. Standard penetration resistance, N_{60}, was used to assess their effectiveness, showing negligible improvement when the spacing-to-pile diameter ratio exceeded about 4 to 5.
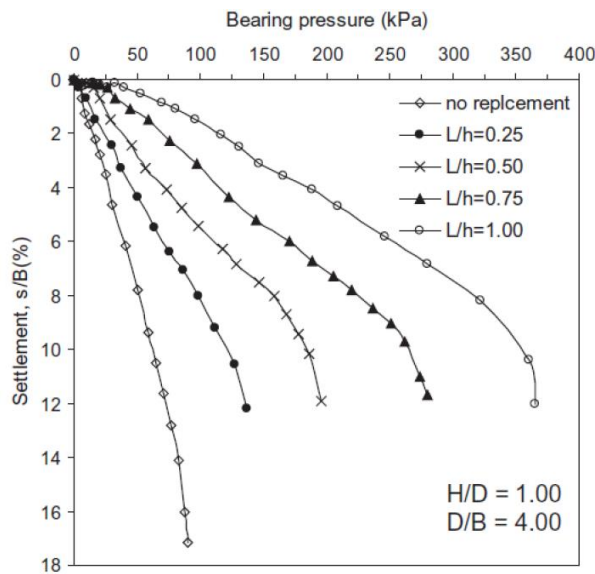
Figure 2-7 Variation of bearing stress, q versus normalized settlement for different replaced depth for footing with skirts (Nazir and Azzam, 2010).

Nazir and Azzam (2010) conducted laboratory model tests on soft clay layers, using partially replaced sand piles with or without confinement to increase bearing capacity and control settlement. Increasing the L/h ratio (L/h = 0 for no replacement and L/h = 1 for full replacement

with sand) led to a significant improvement in bearing capacity, with full replacement resulting in a nearly sevenfold increase.

2.3.4 Micropiles

Micropiles, also known as minipiles, are slender foundation elements made of high-strength steel casing and threaded bars, offering structural support with minimal disruption in confined spaces. Jenck et al. (2009) found that micropiles effectively reduce embankment settlement and seismic response, using a 3D finite difference model with FLAC 3D. Esmaeili (2012) conducted lab-scale tests to enhance railway embankment bearing capacity and prevent subgrade sliding with micropiles. Results are presented in Figure 2-8, and verification using the Plaxis 3D code is summarized in Table 2-3.
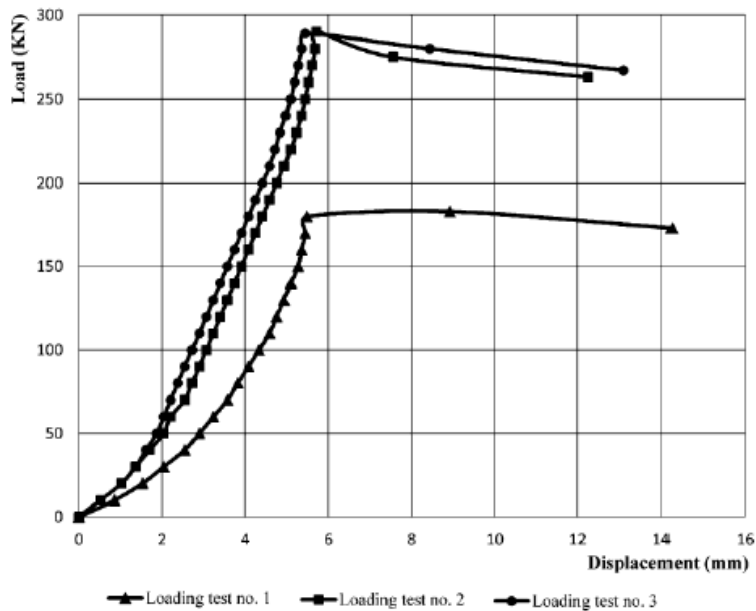
Figure 2-8 Load displacement of embankment crest (Loading test no 1: no micropile; Loading test no.2: 1 row of micropile; Loading test no. 3: 2 rows of micropile) (Esmaeili et al., 2012).

16

Table 2-3 Load bearing capacity of test embankment obtained from numerical and experimental results.

Test Number	Numerical load bearing capacity	Experimental load bearing capacity
1	258.30	254.16
2	404.17	402.78
3	404.17	401.39

2.3.5 Slender Piles

Slender piles, flexible or rigid, are increasingly used for slope stabilization, bearing lateral loads from soil movements in slope stability. They transfer loads to the foundation while resisting lateral soil movement, employing two design approaches: pressure-based and displacement-based methods.

In the pressure-based approach, ultimate soil pressures are estimated directly or as an equivalent loading condition applied to the piles. However, this method's assumptions may not hold for free-headed slender piles subjected to significant deformation or plastic flow. In such cases, soil-pile interaction is assessed based on relative displacement between the soil and piles.
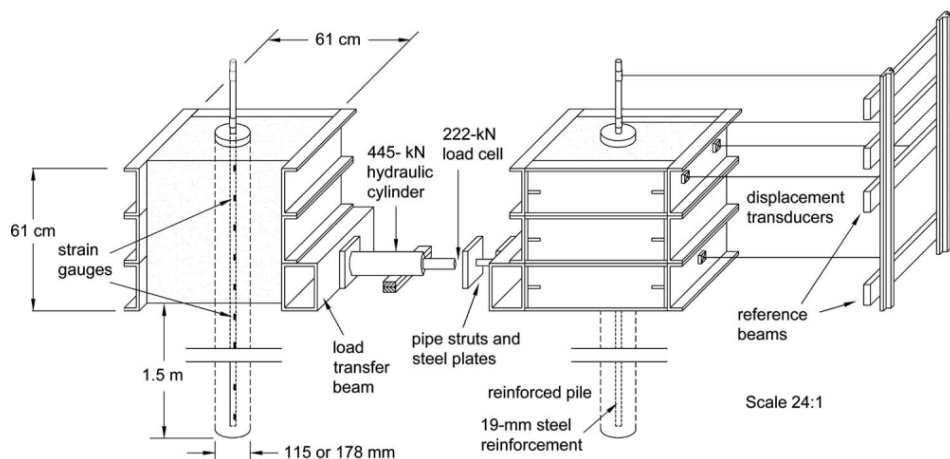
Figure 2-9 Load Test Set up (White et al., 2008)

White et al. (2008) conducted a large-scale lateral load test to assess the applicability of Reese and Wang's (2000) finite difference approach for slender piles. Lateral loading tests were performed in Iowa on a short concrete pile (7 ft) with two diameters, on three different soil types (Loess, Glacial till, and worn shale), as depicted in Figure 2-9. A full-scale direct shear test was also carried out to evaluate the impact of reinforcement placement along the displacement plane compared to no reinforcement, and the results are illustrated in Figure 2-10.
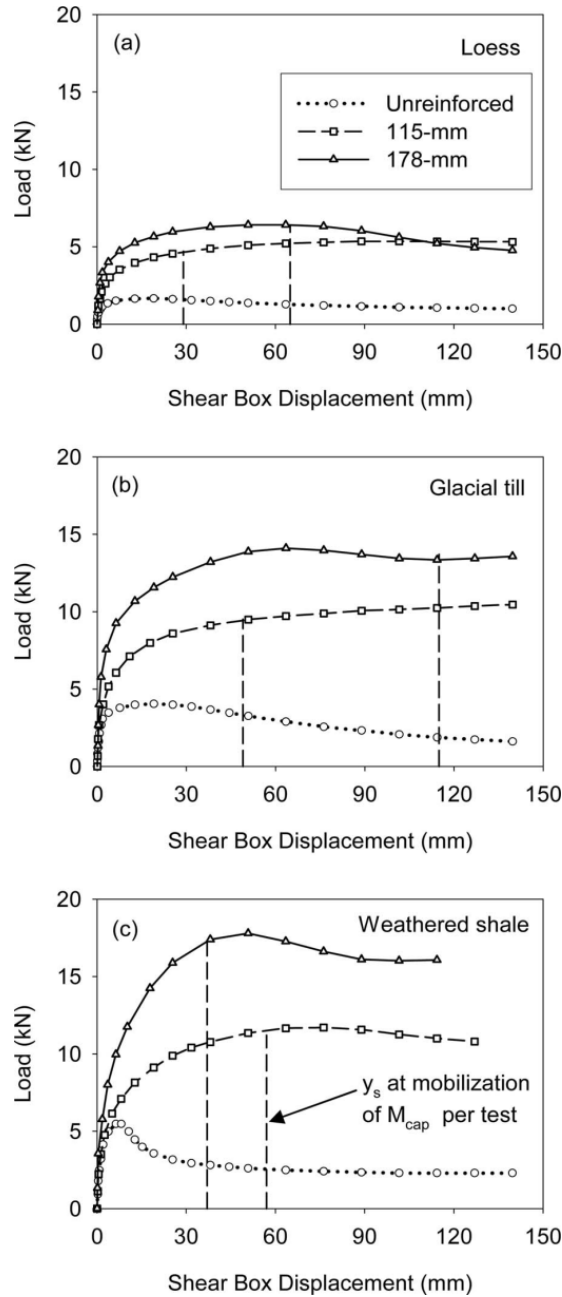
Figure 2-10 Load vs Shear Displacement from Lateral Load test (White et al., 2008)

18

The experiments indicated that slender piles could provide significant resistance to lateral soil movement in unstable soils, with an improvement factor ranging from 2.1 to 3.9. The depth of maximum moment varied from 2.7 to 5.4 pile diameters below the shear box's bottom. The piles exhibited the flexible or long pile failure mode and effectively mobilized their moment capacity.

2.3.6 Pile Supported System

For appropriate design of civil engineering infrastructures over soft foundation soils, it is necessary to consider cost, construction time and availability of fill or replacement materials. Due to the various disadvantages associated with other ground improvement techniques, pile foundation system is a popular choice to support structure on soft soils. Pile refers to traditional piles like-steel, concrete, timber piles and soil improvement columnar systems, like- vibro-compacted granular columns, jet grout columns, soil-cement mixing columns, stone columns, etc. Most of the load coming from the structure is arched down to firm stratum by piled embankment system (Hewlett & Randolph, 1988; Jones et al., 1990; Low et al., 1994; Islam et al. 2021; Islam et al. 2022). This system minimizes the settlement problem as the soft foundation soils do not receive any or very little direct loading. However, for ensuring the effectiveness of soil arching the piles to be placed closely together or the pile caps should be adequately large.

2.4 Soil Arching of Pile Supported System

Geotechnical engineering often encounters the phenomenon of soil arching. Soil arching results from variations in movement between the subsoil and supports. Soil arching—in which piles act as supports—is frequently used in the design of pile embankments. Loads are transmitted from the soil to the piles during deformation of a piled embankment, which causes soil arching.

As shown in Figure 2-11, the interactions between the pile (caps), foundation soil, fill, and geosynthetic can be depicted schematically. Due to the existence of soft foundation soil, the embankment fill mass between pile caps has a propensity to slide downward under the impact of fill weight, W_1. Shear resistance, τ, from the fill above the pile caps is preventing some of this movement. The shear resistance increases the weight placed on the pile caps while decreasing the pressure on the geosynthetic. Terzaghi referred to this load-transfer mechanism as the "soil arching action." According to Han & Gabr (2002), the amount of soil arching was characterized as follows:

$$\rho = \frac{\rho_b}{\gamma H + q_0} \tag{2.12}$$

Where ρ = soil arching ratio; $\rho = 0$ represents the complete soil arching while $\rho = 1$ represents no soil arching; ρ_b=applied pressure on the top of the trapdoor in Terzaghi or McNulty's studies (geosynthetic for this study); γ = unit weight of the embankment fill; H = height of embankment; and q_0 = uniform surcharge on the embankment.
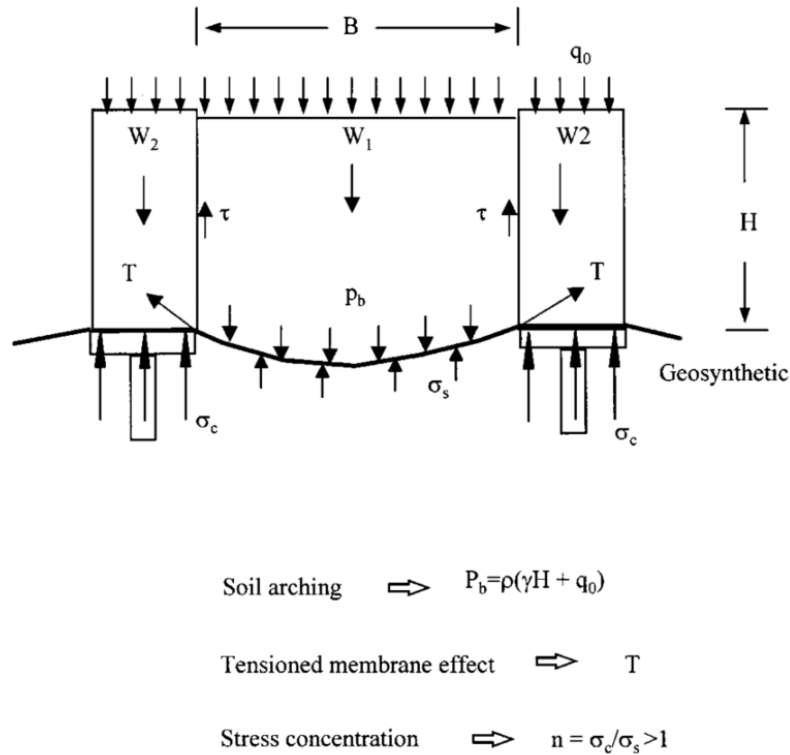
Figure 2-11 Load transfer mechanisms of geosynthetic-reinforced pile supported earth platforms (Han & Gabr, 2002)

Low et al. (1994) conducted model tests and theoretical calculations to study embankment arching with piles, cap beams, geotextiles, and soft soil. They applied loads to a model with cap beams and soft ground, both with and without geotextiles. Their analysis involved semicircular arches to assess equilibrium between the cap beams and soft ground. Results indicated that increased area ratio improved effectiveness. Competency also rose with cap-beam spacing but reached a plateau at larger distances. The stress reduction ratio began at 1, reflecting no initial fill arching, and decreased as H/s' increased. Closer cap-beam spacing reduced stress on soft ground, while geotextiles were 1.15–1.3 times more effective than when not used.

The embankments with beam foundations supported by floating and end bearing piles were tested by Hong et al. in 2014. Geosynthetics were not used to reinforce the embankments. The soft soil, which is primarily made up of silty clay and silty sand, was used to build the embankments. Seven settlement plates, four earth-pressure gauges, and four load cells were used to monitor the performance on-site (Figure 2-12). The vertical load transferred to the beam when the embankment is filled to a height of 8 m is 60% more than the vertical load sent to the soil. Corner beams prevented the full mobilization of the soil arching.

(a)   (b)
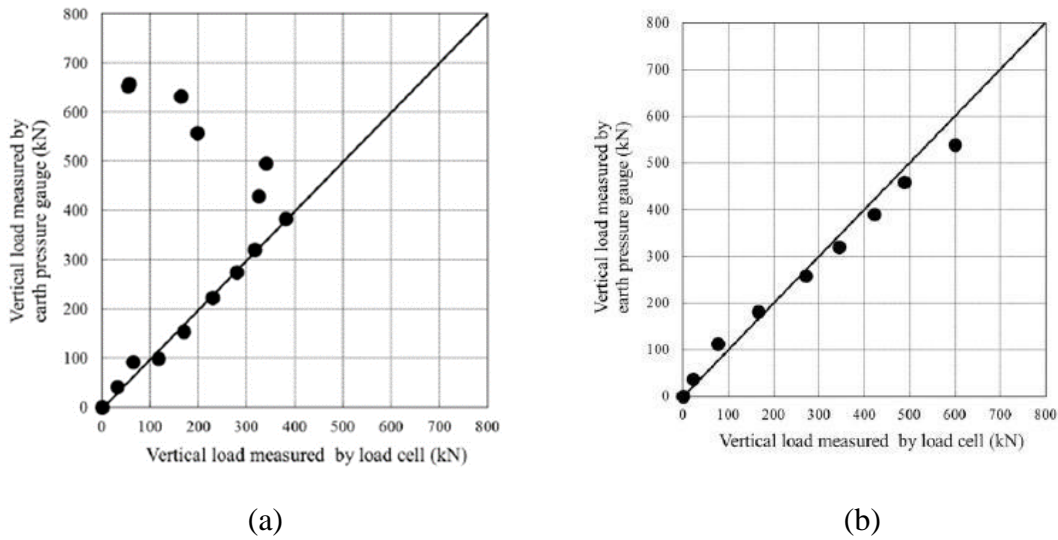
Figure 2-12 (a) Vertical load transfer to the middle beam; (b) Vertical load transfer to the corner beam (Hong et al., 2014)

Several techniques have been used to simulate the soil arching phenomenon. Terzaghi (1936) (quoted in Han & Gabr, 2002) thought about shear strength along the soil prism up to a particular height, when there is a plane of equal settlement. McNulty's model was used by (Han & Gabr, 2002) to provide a study of soil layer-geosynthetic systems. Hewlett and Randolph believed the sand between two piles to be in limit equilibrium. Most of the load above the crown was transferred to the support through the crown. Schmertmann (1991) asserts that all loads contained within conical or triangular prisms (axisymmetric or planar strain, respectively) are passed to the nearby support.

In this context, geosynthetics are assumed to support all the pressure in a void beneath them. They form a rigid platform when bonded with embankment fill, promoting load transfer and interaction with piles. High-quality fill enhances this interaction. The fill's weight descends due to soft soil

below the geosynthetics, resisted by pile tops' shear resistance. Reduced shear resistance minimizes soil arching's load-carrying capacity and lowers pressure on the geosynthetics but increases pressure on the caps. Differential settlement of pile caps is thus reduced. Single geosynthetic sheets serve as tension membranes, while multiple layers can act as reinforced beams. The reinforced mass's shear resistance is described as apparent cohesiveness. Under a perfectly rigid geosynthetic-reinforced platform, there's no differential settlement, reinforcement stress, or relative movement between soil and reinforcement, eliminating processes like soil arching, tensioned membranes, or apparent cohesiveness. Tension is concentrated on the pile caps due to differing stiffness between soil and pile caps.

2.4.1 Stress Concentration Ratio

The stress concentration ratio can be used to calculate the amount of load transfer. The force on the pile (caps) divided by the soil between the piles is how it is calculated. A global index called stress concentration takes into account the mechanisms of soil arching, tension membranes, and pile-soil stiffness variations.

Ooi and Carter (1987) discovered that the value of n for standard pile embankments ranged from 1.0 to 8.0. As the ratio of embankment height to net spacing between the two near ends of the piles grew, the ratio also increased. Reid et al. (1993) investigated GRPS systems on vibro-concrete columns and concrete piles, whose n values were much larger than those of piled embankments (8 to 25). The addition of the geosynthetic layer causes n to increase. The stiffness or rigidity of the foundation affects the value of n. The stress concentration is taken to be one in the scenario of a totally flexible foundation resting on a pile-soil composite foundation without soil arching. Strong concentration ratios are present in rigid foundations. A GRPS system exists in between a flexible and a rigid foundation.

2.4.2 Stress Reduction Factor

The stress reduction ratio (S_{3D}) has been developed as a tool for contrasting various approaches. According to its definition, this is the ratio between the typical vertical load exerted on the reinforcement and the pressure imposed by the embankment fill overburden.

2.4.2.1 BS8006 (1995)

The British Standard technique BS8006 (given in British Standard 8006, 1995) is used for embankments with reinforced soil foundations on poor ground. It is the most popular and

conservative approach. The reinforcement between the pile cap is subject to a distributed vertical load of W_T.

$$For\ H > 1.4 \times (s - a)$$

$$W_T = \frac{1.4\ s\ f_{fs}\gamma(s - a)}{s^2 - a^2} \times \left(s^2 - a^2 \left(\frac{p_c}{\sigma_v}\right)\right)$$ (2.13)

$$For\ 0.7(s - a) \leq H \leq 1.4\ (s - a)$$

$$W_T = \frac{s \times (f_{fs}\gamma H + f_q\ ws)}{s^2 - a^2} \times \left(s^2 - a^2 \left(\frac{p_c}{\sigma_v}\right)\right)$$ (2.14)

$$but\ W_T = 0 \quad if\ \frac{s^2}{a^2} \leq \frac{p_c}{\sigma_v}$$

Where,

s is the spacing between the piles

a is the size of the pile caps

w_s is the uniformly distributed surcharge loading

p'_c is the vertical stress on pile caps

σ'_v is the factored average vertical stress at the base of the embankment

$$\sigma'_v = f_{fs}\gamma H + f_q Ws$$ (2.15)

f_{fs} is the partial load factor for soil unit weight

f_q is the partial load factor for applied external loads

γ is the unit weight of the soil

H is the height of the embankment fill

Piles are considered rigid conduits buried in the ground by this method. According to Marston's formula, vertical stress is determined by positive projecting conduits.

$$p_c = \sigma_v \left(C_c \times \frac{a}{H}\right)^2$$ (2.16)

BS8006 gives empirical equations for arching coefficient as follows,

$$C_c = 1.95 \frac{H}{a} - 0.18 \quad for\ end$$

$$- bearing\ piles\ (unyielding) \qquad (2.17)$$

$$C_c = 1.5 \frac{H}{a} - 0.07 \quad for\ friction\ and\ other\ piles \qquad (2.18)$$

Based on the above equations the stress reduction ratio is given by

$$S_{3D} = \frac{2.8s}{(s+a)^2\, H}\left(s^2 - a^2 \left(\frac{p_c}{\gamma H}\right)\right) \qquad (2.19)$$

2.4.2.2 Terzaghi Method

In order to develop his methodology, Terzaghi (1943) used trap door tests with enormous displacements. Terzaghi thought of the issue as having three dimensions. A soil prism that has been mobilized to a specific height, where a plane of equal settling occurs, was taken into consideration for determining the shear strength. The given stress reduction ratio is

$$S_{3D} = \frac{(s^2 - a^2)}{4HaK\tan(\phi')} \times \left(1 - e^{\frac{-4aHK\tan(\phi')}{s^2 - a^2}}\right) \qquad (2.20)$$

K is the ratio of the horizontal to vertical pressure. Terzaghi has taken K=1.
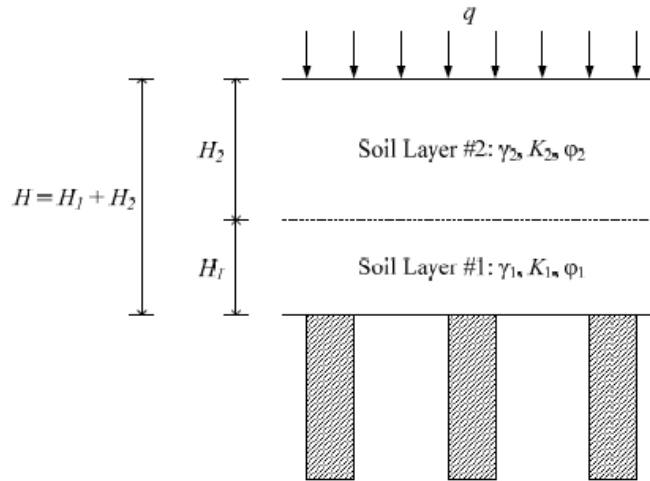
Figure 2-13 Cross-sectional geometry for generalized Adapted Terzaghi Method (Sloan et al., 2011)

A generalized Adapted Terzaghi method of arching in column supported embankments is suggested by Sloan et al. (2011). It applies to any column layout and column cross-section based on the unit cell area and column perimeter distance (Figure 2-13). It also applies to two layers of embankment fill, allowing it to account for higher quality fill material in a load transfer platform or bridging layer by increasing this layer's friction angle as well as to account for compaction-induced lateral earth pressures and the lateral confining effect of the geogrid in a load transfer platform or bridging layer by increasing this layer's lateral earth pressure coefficient.

The proposed SRR is

$$SRR = \frac{\frac{\gamma_1}{\alpha_1}(1 - e^{-\alpha_1 H_1}) + \frac{\gamma_2}{\alpha_2}e^{-\alpha_1 H_1}(1 - e^{-\alpha_2 H_2}) + qe^{-\alpha_1 H_1}e^{-\alpha_2 H_2}}{\gamma_1 H_1 + \gamma_2 H_2 + q} \quad (2.21)$$

A good agreement was discovered when an instrumented case history was compared with SRRs from the generalized Adapted Terzaghi Method.

2.4.2.3 Hewlett and Randolph Theory

Hewlett and Randolph (1988) developed a theoretical solution for a free-draining granular soil based on test models. The notion of soil arching is a succession of hemispherical domes supported by pile caps. In this scenario, the pile caps or the crown of the domes would be the critical failure places. A stress reduction factor can be determined using the limiting plastic equilibrium theory.
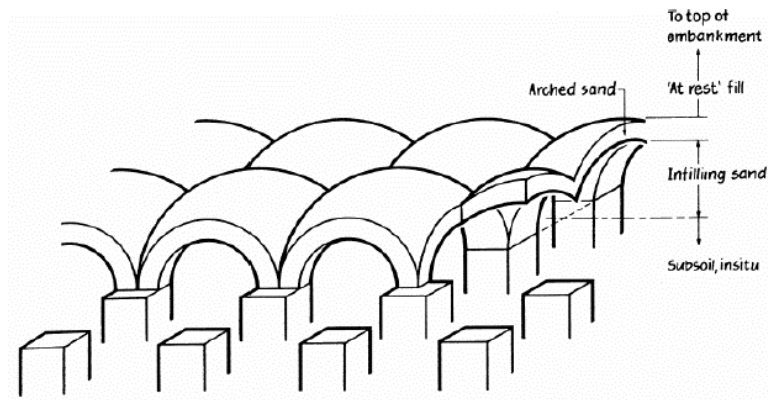
Figure 2-14 Hemispherical domes model (Hewlett and Randolph, 1988)

The stress reduction ratio at crown is given by

25

$$S_{3D} = \left(1 - \frac{a}{s}\right)^{2(K_p - 1)} \left(1 - \frac{s}{2\sqrt{H}} \times \frac{2(K_p - 1)}{(2K_p - 3)}\right) + \frac{(s - a)}{2\sqrt{H}} \times \frac{2(K_p - 1)}{(2K_p - 3)} \qquad (2.22)$$

The stress reduction ratio on the pile caps is given by

$$S_{3D} = \frac{1}{\left(\frac{2K_p}{K_p + 1}\right)\left(\left(1 - \frac{a}{s}\right)^{(1 - K_p)} - \left(1 - \frac{a}{s}\right)\left(1 + \frac{a}{s}K_p\right)\right) + \left(1 - \frac{a^2}{s^2}\right)} \qquad (2.23)$$

The passive earth pressure is denoted here by K_p. The larger of the two ratios of stress reduction is used in the calculations. The worst-case situation is taken into account in this way.

The intricate interactions between piles, pile tops, foundation soils, and embankment fills are noted by Chen et al. (2008). The embankment fills between piles often move downward because loose foundation soil settles more easily between piles due to fill weight. The shear resistance produced within the embankment fills regulates the movement of the fills. These shear resistances cause the pile caps to be under higher pressure while the foundation soil is under less pressure. Numerous scholars have investigated the piled embankments using various model experiments (Hewlett & Randolph 1988; Low et al., 1994; Chen et al., 2010). The model testing was concentrated on the soil arching in the embankment. In truth, load transfer is influenced by a number of other factors besides soil arching. Understanding the interactions between piles, soils, and embankments is crucial to create the extended applications of pile embankments. Numerical techniques have been used to study the mechanisms of load transmission (Han & Gabr, 2002; Pham et al., 2004). Numerical analyses are sometimes helpful for examining interactions in pile-supported embankments, although they are typically time-consuming and challenging to implement for everyday use in reality. There are a fairly limited number of standards and methods for the design of piled embankments. Marston's formula is used to determine vertical tension at the top of piles in accordance with British Standard BS8006 (British Standard 1995). Additionally, the impact of material characteristics on the vertical stress of embankment fill is not considered. The Nordic handbook (NGG 2002) uses a soil wedge model with a top angle of 30° to forecast soil arching. According to Hewlett and Randolph's definition, soil arching is supported by a succession of hemispherical domes supported by piles. The field test is regarded as an efficient method to research pile-supported embankment systems because of their complexity (Liu et al., 2007).

2.5 Recycled Plastic Pins (RPP)

Recycle Plastic Pins (RPP), sometimes referred to as plastic lumber in the marketplace, are made from recycled plastic as well as other waste products such as polymers, fly ash, and sawdust (Chen et al., 2007). Geotechnical operations can benefit from the practical, environmentally sustainable use of RPP. According to life cycle cost analysis (LCCA) and environmental considerations, recycled plastic pins (RPP) are being seriously considered as structural materials for maritime and application of the waterfront (Khan, 2014). RPP is a sustainable material which requires almost no maintenance and is resistant to insects, rotting, rust, and moisture. Typically, high density polyethylene (HDPE), low density polyethylene (LDPE) and polypropylene (PP) makes up more than 50% of the feedstock used to make plastic lumber (Khan, 2014). When high melted polymers and additives like fiberglass and wood fibers are combined, a rigid structure is made possible because of the adhesive action of the polyolefin utilized in the combination.

2.5.1 RPP: A Sustainable Engineering Solution

Recycled Plastic Pins (RPP) offer an eco-friendly alternative for geotechnical projects, helping reduce landfill waste. With a growing population, the production of municipal solid waste (MSW) is increasing, particularly plastic waste, which comprises around 10% of the 1.3 billion tons of MSW generated annually. This non-biodegradable plastic waste accounts for approximately 13% of all waste volume, increasing to 30% during the COVID-19 pandemic (Aurpa, 2021). Proper utilization of non-degradable waste, such as RPP made from recycled plastic bottles, can save valuable landfill space and extend landfill lifespan, while also reducing overall project repair costs (Gupta 2023). RPP proves to be a sustainable engineering solution with various applications, including soil improvement and slope stabilization (Hossain et al., 2017).

2.5.2 Engineering Properties of RPP

Researchers from Columbia University, Carroll et al. (2001), discovered that the modulus of plastic lumber is lower than that of wooden lumber regardless of whether the modulus is evaluated in compression, flexure, or tension. It is an unsuitable material when acting as a tensile member since it has a low tensile strength. Plastic lumber is more resilient to shear than timber lumber and is probably less prone to crack and break. Overall, plastic lumber is more environmentally friendly than timber lumber and has sufficient structural qualities for a wide range of applications.

Bowders et al. (2003) carried out a study on the various engineering features of RPP to assess a variety of manufacturing standards. Uniaxial compression testing and four-point flexure testing were done as part of the study; the findings are shown in Table 2-4 and Table 2-5, respectively.

Table 2-4 Uniaxial compression test results of different RPP samples (Bowders et al., 2003)

Specimen Batch	No. of Specimen tested	Nom. Strain Rate (%/min)	Uniaxial Compressive Strength (ksi)		Young's Modulus, E1% (ksi)		Young's Modulus E5% (ksi)	
			Avg.	Std. Dev.	Avg.	Std. Dev.	Avg.	Std. Dev.
A1	10	-	2.76	0.13	133.7	7.7	56.6	3.9
A2	7	0.005	2.9	0.12	186.4	10	54.8	2.2
A3	6	0.006	2.9	0.13	176.9	15.7	52.6	3.9
A4	3	0.004	2.9	0.13	199.7	23.9	52.6	3.6
A5	4	0.006	1.74	0.15	93.5	23.1	32.6	2.5
A6	4	0.006	1.89	0.13	114	15.4	34.5	4.9
B7	2	0.007	2.03	0.07	78.5	5.2	38.9	0.4
B8	2	0.006	2.32	0.06	93.3	0.1	44.7	0.1
C9	3	0.0085	2.47	0.16	77.3	12.2	56.1	5.8

Table 2-5 Four-point bending test results of various RPP samples (Bowders et al., 2003).

Specimen Batch	No of Specimens Tested	Nom. Def. Rate (in/min)	Flexural Strength (ksi)	Secant Flexural Modulus $E_{1\%}$ (ksi)	Secant Flexural Modulus $E_{5\%}$ (ksi)
A1	13	-	1.6	113.0	96.0
A4	3	0.168	2.6	201.3	-
A5	3	0.226	1.6	103.1	73.1
A6	4	0.143	1.5	92.0	64.3
B7	1	4.05	1.3	78.9	61.6
B8	1	5.67	-	118.4	-
C9	2	3.21	1.7	100.2	80.2

Lampo and Nosker (1997) conducted experimental research on the compressive strength of recycled plastic lumber using 10 plastic samples from eight manufacturers with varying compositions. They followed ASTM 695-85 standards, testing samples approximately 12 inches tall. Compressive strength, modulus, ultimate strength at 10% strain, and yield strength at 2% offset were determined from the load-displacement data. Specific modulus and specific strength,

normalized by specific gravity, were calculated to account for void effects. Table 2-6 summarizes the compressive strength results, while Figure 2-15 and Figure 2-16 compare compressive strength among different samples. The research found that RPP lumber has a compressive strength range of 1.74 to 3.5 ksi and a tensile strength range of 1.25 to 3.5 ksi, noting that RPP reaches its maximum strength at a different strain level than softwood.

Table 2-6 Average values of specific gravity, modulus, specific modulus, yield stress, ultimate stress, ultimate strength and specific strength for each sample type of RPP (Lampo and Nosker, 1997)

Sample	Specific Gravity	Modulus (ksi)	Specific Modulus (ksi)	Yield Stress (ksi)	Ultimate Strength (ksi)	Specific Strength (ksi)
51A	0.2789	38.00	121.83	0.71	0.78	2.80
1B	0.7012	61.93	88.33	1.38	1.89	2.70
2D (BR)	0.8630	85.28	98.92	1.67	2.32	2.69
2D (G)	0.8098	116.03	143.30	2.10	2.86	3.53
1E	0.862	80.79	93.84	1.77	2.42	2.81
1F	0.7888	108.20	137.06	2.19	2.81	3.56
1J(B)	0.7534	93.26	123.86	1.90	2.36	3.13
1J(W)	0.9087	110.08	121.25	2.16	2.83	3.11
23L	0.7856	191.45	243.66	1.71	1.93	2.46
1M	0.5652	57.87	102.25	0.96	1.23	2.18
1S	0.9090	80.50	88.47	1.67	2.05	2.26
1T	0.8804	117.92	133.58	2.25	3.12	3.54
9U	0.774	86.73	111.53	1.83	2.41	3.11
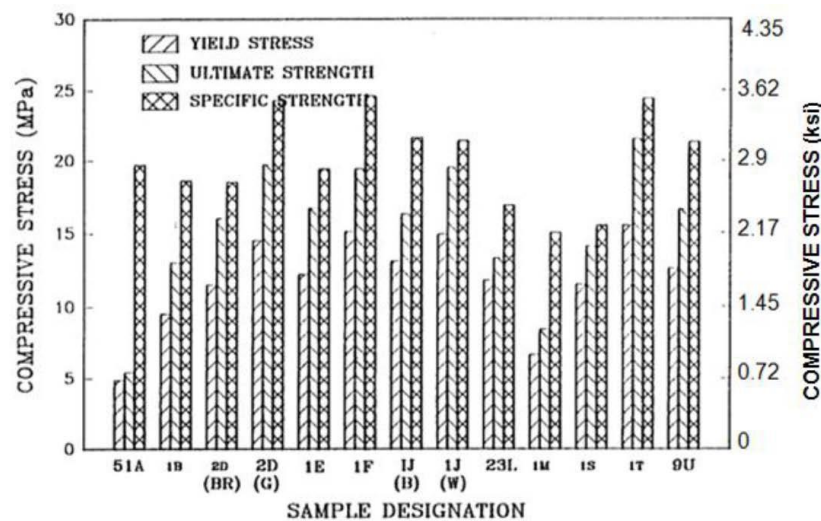
Figure 2-15 Comparison between compressive strength of RPP (Lampo and Nosker, 1997)
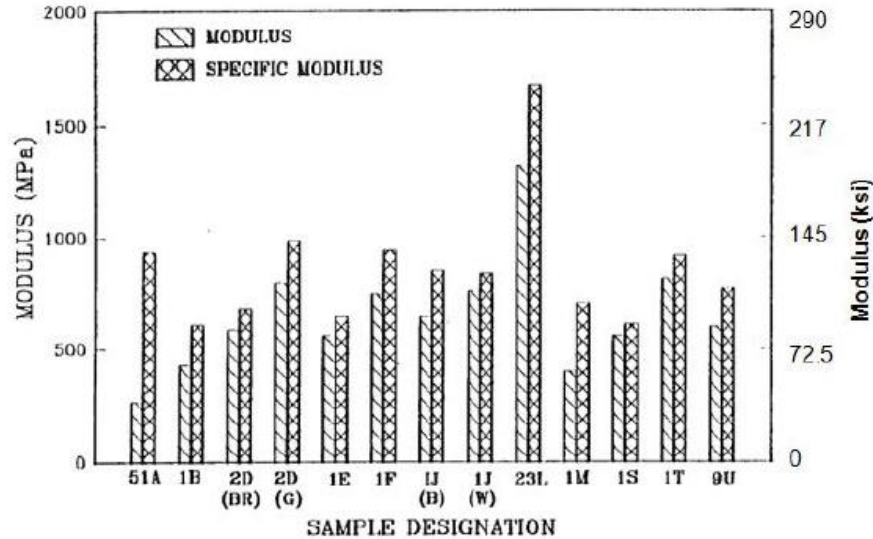
Figure 2-16 Comparison between Compressive modulus of RPP (Lampo and Nosker, 1997)

As shown in Table 2-7 from research by Breslin et al. (1998), various test results from literature were compared. The rigidity of the finished product is increased, according to the authors, by adding various additives such fibers, glass, polystyrene, etc. to plastic lumber.

Table 2-7 Engineering properties of recycled plastic pins (Breslin et. al, 1998).

Product	Composition	Compressive Strength (psi)	Modulus of Elasticity (psi)	Tensile Strength (psi)	Source
TRIMAX	HDPE / Glass Fiber	1740	450 000	1250	TRIMAX literature SUNY at Stony Brook
TRIMAX	HDPE / Glass Fiber			1189	www.lumberlast.com
Lumber Last	Commingled recycled plastic	3755 (ultimate) (D198)	140 000 (D790)	1453 (ultimate) (D198)	www.ecpl.com
Earthcare recycled maid	Post-consumer milk jugs	0.79 (Density)	3205 (D695)	93 000– 102 500 (D790)	Zarillo and Lockert (1993)
Hammer's plastic	80%HDPE/20%LDPE	2708	89 814		Zarillo and Lockert (1993)
	HDPE/LDPE (20PSGF)	4247	527 000		

30

Product	Composition	Compressive Strength (psi)	Modulus of Elasticity (psi)	Tensile Strength (psi)	Source
	HDPE/LDPE (40PS20GF)	3514 (D695)	653 000 (D790)	1793 (D638)	
Superwood Selma, Alabama	33%HDPE/33%LDPE/33%PP	3468 (D695)	146 171 (D790)	1793 (D638)	Beck, R. (1993)
California recycling company	100% Commingled	81 717			Beck, R. (1993)
	10% Polypropylene	79 319			
	50% HDPE	92 636 (D790)			
		92 636 (D790)			
RPL-A	HDPE/Glass fibers	2000			Smith and Kyanka (1994
RPL-B	49% HDPE/51% wood fiber				Smith and Kyanka (1994)
Rutgers University	100% Curb tailings	3049	89 500		Renfee et al. (1989)
	60% Milk bottles, 15% Detergent bottles, 15% Curb tailings, 10% LDPE	3921	114 800		Renfee et al. (1989)
	50% Milk bottles, 50% Densified PS	4120 (D695)	164 000 (D790)		
Earth care products	HDPE		173 439 (D790)		www.ecpl.com
BTW recycled plastic lumber	Post-consumer	1840–2801	162 000		BTW/Hammers Brochure

Plastic is temperature sensitive. In contrast to its weak and ductile characteristics at higher temperatures, plastic is considerably stronger and brittle at lower temperatures. The impact of temperature variation on HDPE's tensile strength is shown in Figure 2-17.
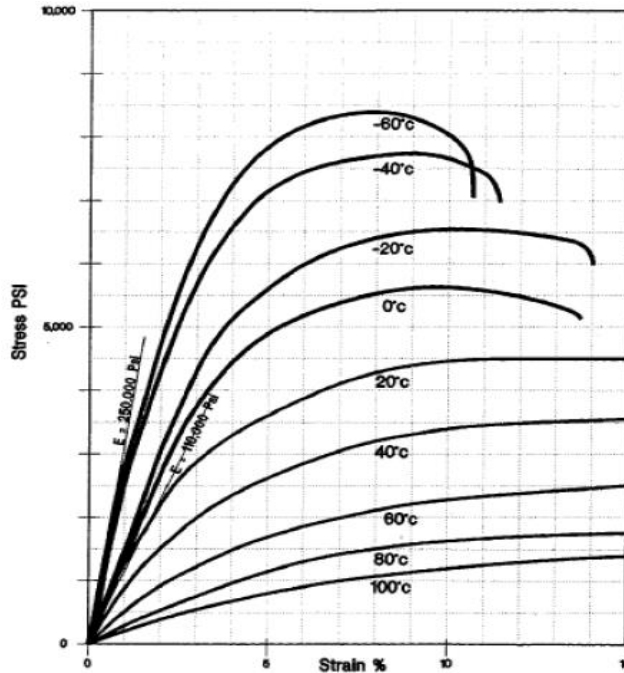
Figure 2-17 Tensile strength of HDPE for different temperature (Malcolm, 1995)

Ahmed (2013) compared RPP, wood, and bamboo piles, finding that wood had the highest compressive and flexural strengths, while RPP allowed for greater soil movement, up to 19%. RPP's adaptability to various chemical and climatic conditions made it the preferred choice, with only an 8% reduction in strength under different climates, compared to approximately 50% for wood and 65% for bamboo. RPP's strength, longevity, and minimal strength reduction in various conditions make it a cost-effective alternative. Additionally, Ahmed presented the Modulus of Elasticity variation of RPP under different environmental conditions and loading rates (Figure

2-16).
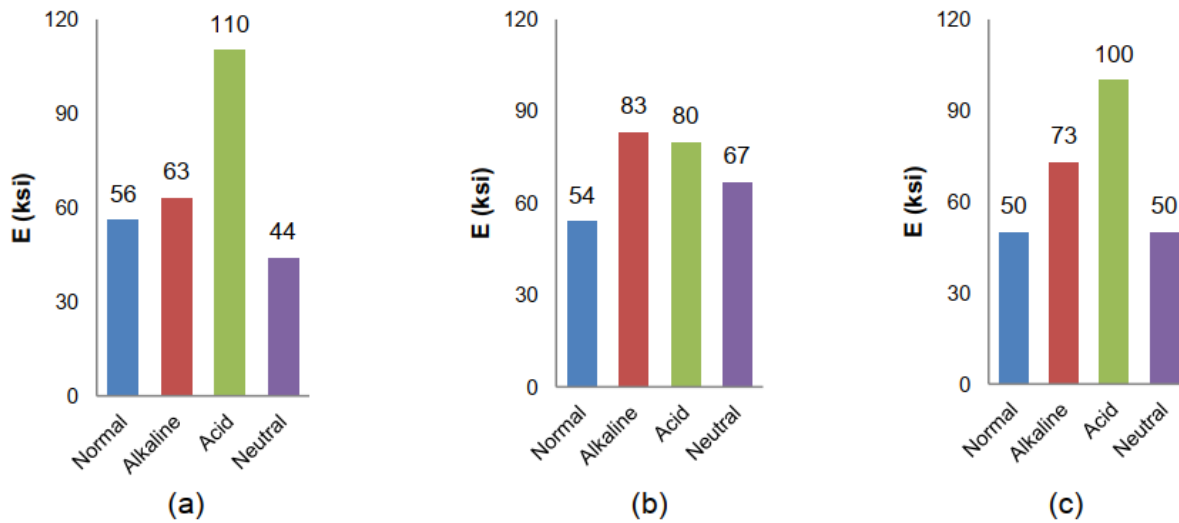
Figure 2-18 Modulus of Elasticity variation of RPP with environment conditions at (a) 2.5 kips/min. (b) 3.1 kips/min. (c) 3.75 kips/min (Ahmed, 2013).

2.5.3 Skin Friction of RPP

Friction between the soil and the pile material is one of the most significant elements that geotechnical engineers take into account when designing piles. Friction between the parts of structures like diaphragm walls, retaining walls, sheet piles, and piles is taken into consideration when building them. Particularly in loose sandy soils, the effect of pile point tip resistance on bearing capacity is typically disregarded, and the bearing capacity is solely based on skin friction. It follows that it is crucial to establish the skin friction angle for use in engineering calculations.

If one or more test piles that are sufficiently instrumented with strain gauges, then the difference in measured load (or stress) between any two points is taken as the load transferred to the soil by skin resistance and is assumed constant in the segment length (Bowles, 1988). Since the pile perimeter and segment length are known, the shear resistance can be calculated with ease.

According to Wada (2004), the skin friction of pile is found as a parameter of pile shaft displacement. From the interpretation result of the monitoring data obtained from instrumentation, it shows that stress distribution, friction and deformation/displacement of pile shaft can be obtained at each depth of pile. The behavior of pile under surcharge load is showed in Figure 2-19. The pile shaft displacement increases the skin friction, which reaches its maximum at a displacement of 5

to 15 mm. Eventually, when the displacement increases, it diminishes to residual strength. According to Table 2-8, which confirms that the maximal skin friction is a measure of soil shear strength.
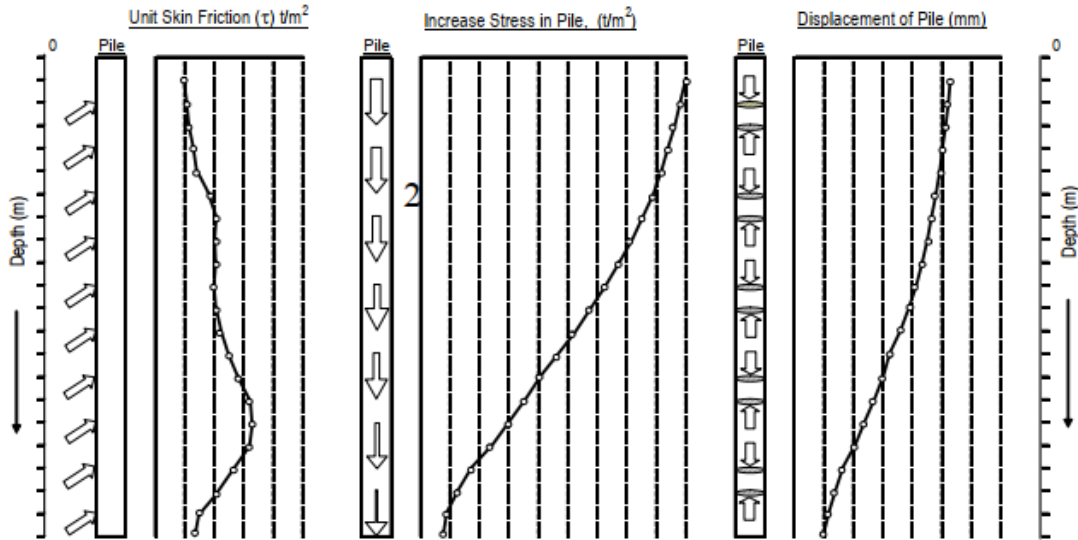
Figure 2-19 Unit skin friction, stress distribution, and deformation/displacement of pile shaft at each depth of pile (Wada,2004)

Surfaces between construction materials and pure sands (free of clay and silt) were compared for friction (Pando et al., 2002; Sakr et al., 2005; Tiwari & Al-Adhadh, 2014). Large-scale direct shear box tests were conducted by several researchers to measure the skin friction of soil and different structural materials (Liu et al., 2009; Laskar & Dey, 2011; Khan et al., 2014).

Aksoy et al. (2016) evaluated clayey sand soils with varying ratios (0%, 20%, 30%, 40%, and 45%) using laboratory research. Different skin friction angles between the soils and the FRP, steel, and wood were identified during the examination of the soils. A graph (Figure 2-20) was suggested based on the findings of these experiments and depicts the relationship between the internal and skin friction angles. This chart can be used to calculate the skin friction angles between pile materials (FRP, steel, and wood) based solely on the internal friction angles of the soils.

Table 2-8 Skin friction of pile in various soil and weathered rock (Wada,2004)

Ground Material		Skin Friction						Soil Parameters	
		Max. Skin Friction		Residual Skin Friction		Ratio			
Formation	Soil / Rock Weathered Grade	Displacement	Strength	Displacement	Strength	$\dfrac{\tau_{res}}{\tau_{max}}$		N	C_u
		(mm)	τ_{max} (KN/m²)	(mm)	τ_{res} (KN/m²)				(KN/m²)
Top Soil / Fill	Sandy Clay / Sandy Silt	10.0	44	19.7	31	0.68		7	20
	Silty Sand / Reclaimed Sand	8.8	110	14.0	25	0.21		14	24
Alluvium	Marine Clay	7.5	60	16.0	52	0.85		14	24
	Silty Clay	4.0	64	-	-	-		10	29
	Organic Clay/ Organic sand / Peat	7.8	40	16.0	31	0.77		2	11
	Sandy Clay / Clayey Sand / Silty Sand	13.8	90	24.4	32	0.45		17	30
Jurong Formation	Residual Soil of Limestone (VI)	9.3	117*	-	-	-		12	99
	Compl. Weathered Mudstone (V)	7.5	195	-	-	-		28	210
	Highly Weathered Mudstone (IV)	8.0	400*	-	-	-		>100	2100
	Moderately Weathered Limestone (III)	5.7	1520*	-	-	-		>100	-
Bukit Timah Granite	Residual Soil of Granite (VI)	7.1	77	16.6	59	0.69		19	50
	Completely Weath. Granite (V)	7.2	135	8.3	108	0.77		46	203
	Completely Weath. Granite (V)	8.1	287	12.8	253	0.94		72	-
	Highly Weathered Granite (IV)	5.0	690*	10.0	430	0.91		>100	2643
	Moderately Weathered Granite (III)	5.0	2600*	-	-	-		>100	-
Boulder Clay	Residual Soil of Boulder Clay	5.1	60	9.5	52	0.79		19	45
	Residual Soil of Boulder Sandstone	5.9	86	-	-	-		25	-
	Weathered Zone of Boulder Clay	8.0	144	12.0	58	0.52		37	98
	Cemented Zone of Boulder Clay	7.1	398	11.0	253	0.87		>100	175
Old Alluvium	Weathered Zone of Old Alluvium	14.0	98	16.3	62	0.63		32	60
	Cemented Zone (I) of Old Alluvium	14.5	258*	-	-	-		>100	-
	Cemented Zone (II) of Old Alluvium	9.8	820	14.5	790	0.96		>100	-

Note : (*) - Under Progress
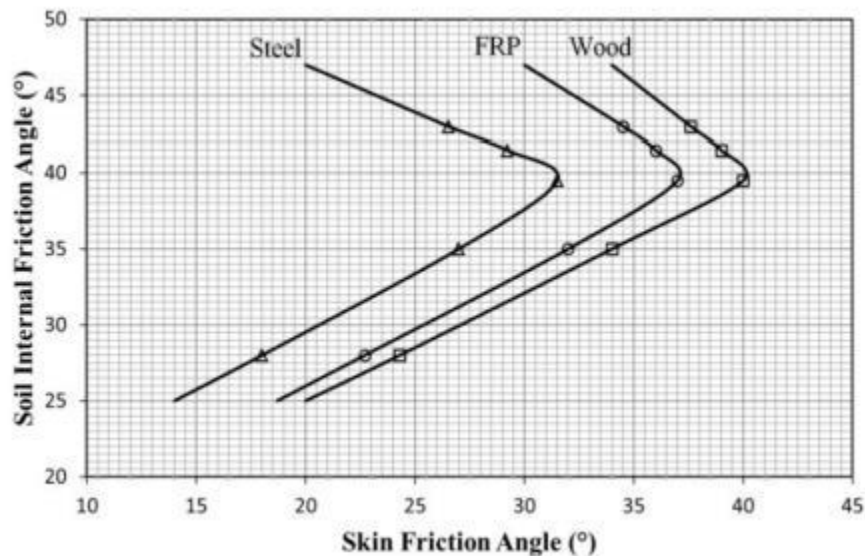
Figure 2-20 Skin friction chart for FRP, steel, and wood (Aksoy et al., 2016)

A series of interface shear experiments were performed by Pando et al. (2002) on a prestressed concrete pile and two commercially available FRP composite piles. Density sand ($D_{50} = 0.5$ mm, sub-rounded to rounded particle shape) and Model sand ($D_{50} = 0.18$ mm, sub-angular to angular particle shape) were the two types of sand evaluated. The relative spacing (S_m/D_{50}) and relative height (R_t/D_{50}) have an impact on the interface friction angles of FRP composite piles. The friction angles have been observed to increase as the height increases and decrease as the spacing increases.

The constructability of FRP-concrete composite piles is examined by Sakr et al. (2005) as part of an experimental study on the FRP/dense sand interface properties. Installing the empty FRP shells in the ground before filling them with self-consolidating concrete requires the development of a new toe driving technique. Both large-scale models and a variety of FRP samples were being tested for interface shear and uplift load. In line with ASTM Standard D5321-97, interface shear tests were carried out. As illustrated in Figure 2-21, the FRP composite sections were positioned in the bottom half of a direct shear box with 88 dimensions of 60 mm 60 mm and a height of 9.5 mm. Two varieties of FRP piles with various degrees of roughness are contrasted with a steel pile. Different piles are tested in the pressure chamber under various confining pressures. FRP materials excelled traditional steel materials when it came to interface friction. FRP piles can be installed in dense soils using toe drive.
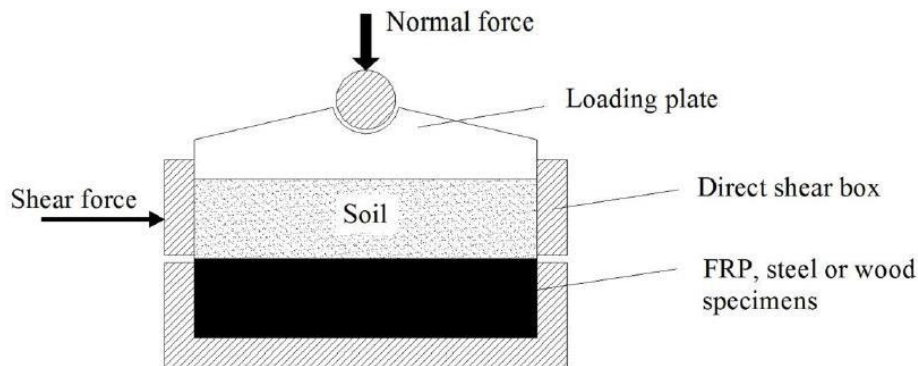
Figure 2-21 Test set up for interface shear test (Sakr et al., 2005)

Tiwari and Al-Adhadh (2014) proposed a novel method to predict the friction between construction materials and sands, taking into account compaction conditions (relative density), moisture content, and effective external pressures. They conducted tests with well-graded sand at various relative densities and moisture levels, following the USCS classification system, to assess

frictional resistance. Similar tests were also carried out between the soils and wooden, concrete, and steel building blocks. The findings revealed that the frictional resistance between soil and materials is influenced by soil type, relative density, and moisture content. The shear envelopes for soil-soil and soil-structure frictional resistance were observed to be curved, and it was found that certain geotechnical textbooks' soil-structure frictional resistance figures were overly conservative.

2.6   Vertical Load Carrying Capacity of RPP

RPP has been suggested as a sustainable substitution to conventional piles in pile supported system considering the economic and environmental aspects (Badhon,2021). Application of RPP ranges from slope stabilization, reinforcement of embankment foundation soil to MSE wall base reinforcement and much more. RPP has been successfully used in both vertical and lateral loading conditions.

Piles or RPPs serve as structural elements in order to transfer surface loads to lower levels in the soil mass. This transfer may take the form of distributing the weight vertically along the pile shaft or applying the load directly through the pile point to a lower stratum. A friction (or floating) pile distributes the load vertically, whereas a point (or end-bearing) pile applies the load directly. Since all piles transport load through a mix of side resistance and point bearing, this distinction is only used for convenience unless the pile is through extremely soft soil to a strong base.

In most cases, a long period of time (a few months to years) passes before the full design loads are applied. Excessive pore pressures dissipate at this time, and conditions are drained (or consolidated-undrained if below GWT). These tend to have soil behavior that is best described by remolded (or residual) soil characteristics. According to Flaate and Seines (1977) and Orrje and Broms (1967), soft clay heaps can hold more weight over time, with the majority of that strength returning during the first three months.

2.6.1   Load Transfer Mechanism of Piles

The load-transfer method involves using load-transfer data from instrumented test piles to back-calculate the static capacity and settlement of a pile. Strain gauges and telltales can provide stress information along the pile, assuming constant load transfer via skin resistance. Segment deformation can be calculated based on point displacement and average axial load. This information helps create a slip vs shear resistance curve for estimating the static capacity of nearby

piles. Multiple load-transfer curves may be required, and strain gauges or telltales define segments for this purpose. A composite curve can be used for similar segment curves, while distinct curves are applied when variations are significant. This method is illustrated in Figure 2-22.

(a)   (b)
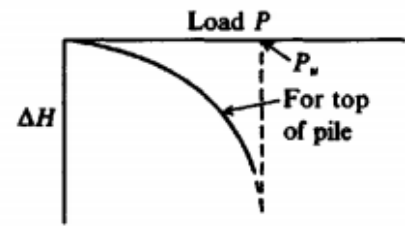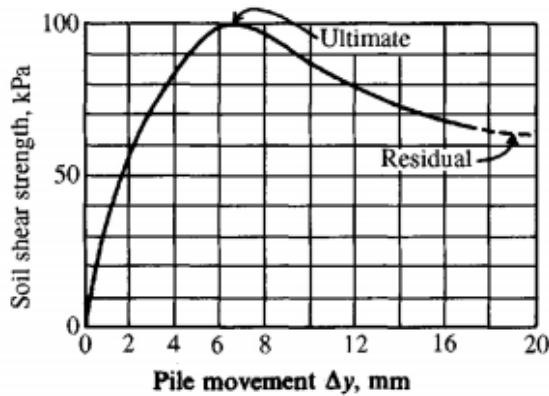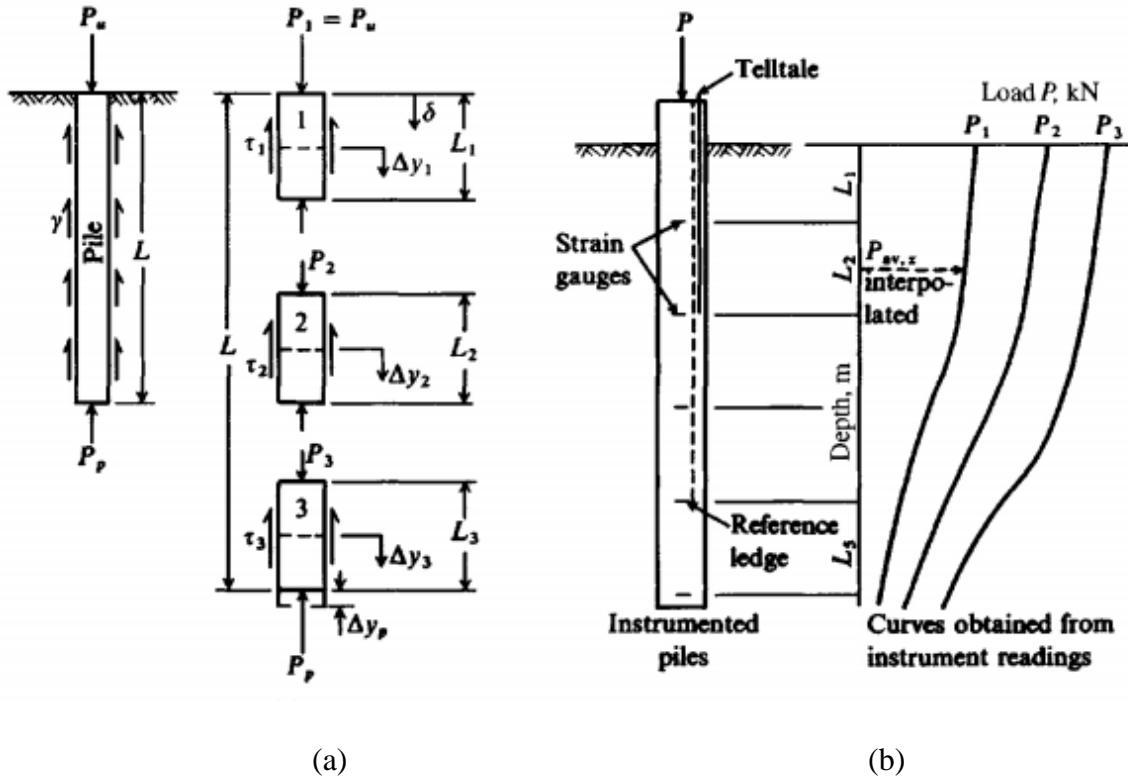
(c)   (d)

Figure 2-22 Method of computing load-settlement relationships for an axially loaded pile in clay. (Bowles, 1996)

The slip required for maximum skin resistance falls between 5 and 10 mm based on load tests [Whitaker and Cooke (1966), Coyle and Reese (1966), AISI (1975)]. It depends on soil parameters like φ and c but is less influenced by shaft diameter and embedment length. Various factors, including soil properties, pile length and stiffness, and the actual load, affect the load carried by the point under butt loading. Soft-soil end-bearing piles may see increased point load over time due to load duration and time since application. The point displacement for mobilizing ultimate point resistance in soils is approximately 10% of the tip diameter. For piles in non-rock materials, there could be added point displacement due to soil settlement from skin resistance stresses. In most cases, skin resistance is the primary load-bearing mechanism within typical working load ranges.

Load transfer can be nearly linear in cohesionless soils, and the shape is significantly influenced by embedding depth. Short piles tend to have more nearly linear load-transfer curves than long piles, although there's limited data for very long piles due to cost and instrumentation challenges.

(a)   (b)
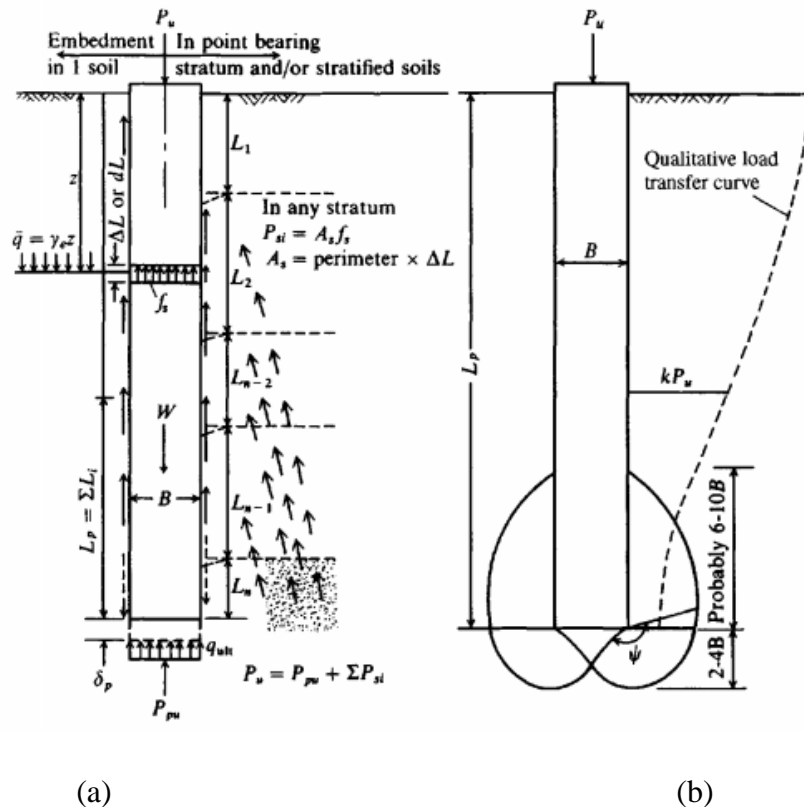
Figure 2-23 Piles in soil. Pile-to-soil friction tan δ defined for pile perimeters shown (Bowles, 1996)

Both manual calculations and computer programs can be used to determine the pile capacity (Coyle and Reese, 1966) and (Bowles, 1974a). For no more than three to five pile parts, hand computations are practical. If there are enough load-transfer curves and the data are of high quality, better results may be obtained by employing more segments. For hand calculation, the following .equation is employed for each segment.

$$P_p \ = \ A_p \, k_s \, \varDelta y_p \qquad\qquad (2.25)$$

Where,

P_p = Point resistance

k_s = The modulus of subgrade reaction

$\varDelta y_p$ = Slip movement

2.6.2   Theoretical Solution

In general practice, RPPs are driven into the soil using hammer blows. As a result, they can be considered as driven piles in terms of installation process. There are several different approaches in determining vertical loading capacity of piles which can be useful in terms of determining load capacity of RPP.

The soil's cohesion c and the angle of internal friction are required for static pile (and group) capacity calculations. Since some designers employ undrained (or total) stress parameters and others, especially more lately, utilize effective stress values, there is an instant dispute. The following formulae can be used to determine all static pile capacities.

$$P_u \ = \ P_{pu} + \ \varSigma P_{si} \qquad\qquad (2.26)$$

Where, P_u = ultimate (maximum) pile capacity—usually defined as that load producing a large settlement rate in a load test

P_{pu} = ultimate pile tip capacity

$\varSigma P_{si}$ = skin resistance developing with ultimate tip resistance P_{pu};

2.6.2.1   Ultimate Static Pile Point Capacity

The point capacity is typically calculated as

$$P_{pu} = A_p\left(cN_c'd_cs_c + \eta qN_q'd_qs_q + \tfrac{1}{2}\gamma'^{B_p N_\gamma s_\gamma}\right) \qquad (2.27)$$

Where,

A_p = area of pile point effective in bearing,

c = cohesion of soil beneath pile point (or su)

B_p = width of pile point

N'_c = bearing capacity factor for cohesion; $d_c = 1 + 0.4 \tan^{-1}(L/B)$

when $\varphi = 0$; c = su; $N'_c = 9$.

N'_q = bearing capacity factor for depth; $d_q = 1 + 2\tan\varphi\,(1 - \sin\varphi)^2 \tan^{-1} L/B$

N_γ = bearing capacity factor for base width

$q = \gamma L$ = effective vertical (or overburden) pressure at pile point

$\eta = 1.0$ for all except the Vesic (1975a) N_i factors where

$$\eta = \frac{1 + 2k_o}{3} \qquad (2.28)$$

K_0 = at rest earth pressure coefficient

The point capacity Eqn can be rewrite by ignoring the N_γ part and accounting for pile weight as follows:

$$P_{Pu} = A_p\left[cN_c'd_c + \eta q(N_q' - l)d_q\right] \qquad (2.29)$$

For c = su and $\varphi = 0$, the value of Nq = 1 and
$$P_{Pu} = A_p(9s_u) \qquad (2.30)$$

For the purpose of design, a Safety Factor on the order of 1.5 to 3 is used to divide the ultimate point capacity.

The Hansen bearing-capacity factors can be used in conjunction with the shape and depth factors with a reliability that is comparable to that of any other method, according to results from Coyle and Castello (1981), who back-calculated the point capacities of many piles in sand. Although they are strictly true only for L< B, the Terzaghi bearing-capacity equation and factors are frequently

utilized. They appear to provide roughly the same point capacity as the Hansen equation at pile depths of between 10 and 20 m, which is likely due to the bigger Terzaghi N_q factor that the Hansen $N_q d_q$ term equates to.

The bearing-capacity factors N'$_q$ of Eq. (16-6) can be calculated using the following, according to Vesic (1975a):

$$N_q' = \frac{3}{3 - \sin\phi}\left\{exp\left[\left(\frac{\pi}{2} - \phi\right)\tan\phi\right]\tan^2\left(45° + \frac{\phi}{2}\right)I_{rr}^{\frac{1.333\sin\phi}{1+\sin\phi}}\right\} \qquad (2.31)$$

The reduced rigidity index I_{rr} in this equation is computed using the volumetric strain ε_v as

$$I_{rr} = \frac{I_r}{1 + \epsilon_v I_r} \qquad (2.32)$$

The rigidity index I_r is computed using the shear modulus G' and soil cohesion and shear strength s (or τ) as

$$I_r = \frac{G'}{c + \overline{q}\tan\phi} = \frac{G'}{s} \qquad (2.33)$$

Use $\varepsilon_v = 0.0$ to make $I_{rr} = I_r$ when the soil is dense or has an undrained condition. With lower I_{rr} values in sand when ηq is low, the value of I_{rr} depends on the soil state (loose, dense; low, medium, or high plasticity) and the mean normal stress indicated by ηq. When clay has a high water content and/or a high r) q, greater I_r values are employed. The clay with the lowest values of I_r 10 is one with a high OCR and low ηq. I_r estimates can be made using the Table 2-9 below:

Table 2-9 Estimates of I_r based on soil type

Soil	I_r
Sand (D$_r$ = 0.5-0.8)	75-150
Silt	50-75
Clay	150-250

It is possible to calculate the Vesic bearing-capacity factor N'$_c$ term using one of the following equation:

$$N_c' = \left(N_q' - 1\right)\cot\phi \qquad (2.34)$$

When φ = 0 (undrained conditions)

$$N_c' = \frac{4}{3}(\ln I_{rr} + 1) + \frac{\pi}{2} + 1 \tag{2.35}$$

Janbu (1976) computes N'$_q$ as follows: ηq (with angle ψ in radians)

$$N_q' = \left(\tan\phi + \sqrt{1 + \tan^2\phi}\right)^2 \exp(2\psi\tan\phi) \tag{2.36}$$

N'$_c$ term in Janbu method follows the same equation as Veic's method. Fig. 16-116 shows the value of ψ for the Janbu equation, which ranges from 60° for light compressible soils to 105° for dense soils.

Meyerhof (1956, 1976) offered the following for standard penetration test (SPT) data:

$$P_{pu} = A_p(40N)\frac{L_b}{B} \le A_p(380N) \qquad (kN) \tag{2.37}$$

Where,

N = statistical average of the SPT N$_{55}$ numbers in a zone of about 8B above to 3B below the pile point

B = width or diameter of pile point

L$_b$ = pile penetration depth into point-bearing stratum

L$_b$/B = average depth ratio of point into point-bearing corrections given in

Shioi and Fukui (1982) state that pile tip resistance is calculated in Japan as

$$P_{pu} = q_{ult}\, A_p \tag{2.38}$$

with the ultimate tip bearing pressure q$_{ult}$ computed from the SPT based on the embedment depth ratio L$_b$/D into the point-bearing stratum and where this SPT N should be taken as N$_{55}$.

For Driven piles,

$$q_{ult}/N = 6L_b/D < 30\ (open-end\ pipe\ piles) \tag{2.39}$$

$$q_{ult}/N = 10 + 4L_b/D < 30\ (closed-end\ pipe) \tag{2.40}$$

2.6.2.2 Pile Skin Resistance Capacity

Nordlund method

Skin friction angle (δ) is frequently regarded as being equal to 2/3 of the internal friction angle (ϕ) of soil (Terzaghi and Peck 1948). However, it is understood that when the same soil and various materials come into contact, skin friction angle δ can change. It is unknown what the skin friction angle (δ) is between soil and the recycled plastic pins (RPP) materials. The Nordlund method can be used to determine the total skin friction provided by Recycled Plastic Pins (RPP) if the skin friction angle (δ) between soil and RPP can be measured. The following is the Nordlund equation for a uniform cross-section pile embedded for a length of D in a uniform cohesionless soil deposit.

$$Q_s = K_\delta . C_F . p_d . \sin \delta . C_d . D \qquad (2.41)$$

Where,

K_δ = coefficient of lateral earth pressure

C_F = Correction factor for K_δ

p_d = Effective overburden pressure at the center of the pile

δ = Interface friction angle between pile and soil

C_d = Pile perimeter

Commonly, there are three methods to compute the skin resistance of piles in cohesive soils. These methods are called α, λ and β methods for the factors used in the skin resistance capacity. The β method can also be used for cohesionless soil. These methods can be applied towards determining the total skin friction provided by Recycled Plastic Pins (RPP). In all cases the skin resistance capacity is computed in unit of f_s as

$$\sum_{1}^{n} A_s f_s \qquad (2.42)$$

Where,

A_s = effective pile surface area on which f_s acts.

f_s = skin resistance

α method, that was initially proposed by Tomlinson (1986) provided some empirical correlations for evaluating α in the following equation for different types of soil conditions and L/d ratios to determine skin friction.

$$Q_u = c_b N_c A_b + \sum_0^L \alpha \overline{c_u} A_s \qquad (2.43)$$

The correlation required a great deal of judgement and often resulted into different interpretations. As a result, Dennis and Olson (1983b) made a simplified approach by making use of the information provided by Tomlinson and developed a single curve giving the relationship between α and the undrained shear strength c_u of clay as shown in Figure 2-24.
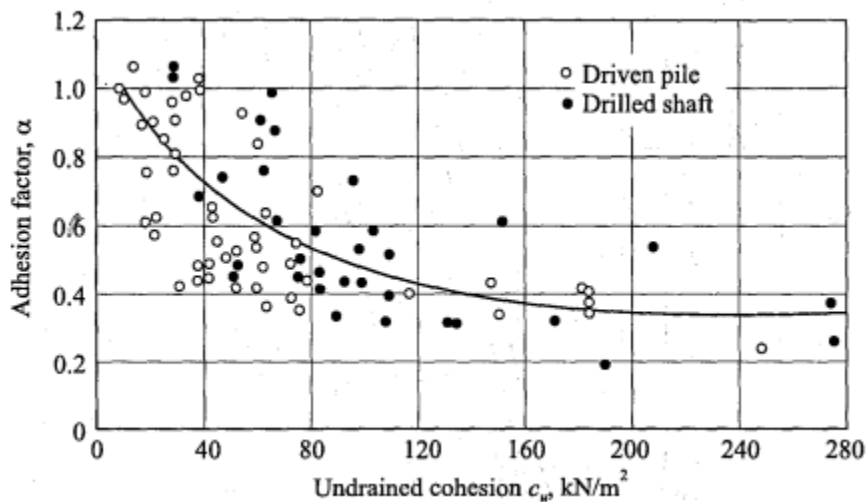
Figure 2-24 Relationship between the adhesion factor α and undrained cohesion c_u with penetration length less than 50 m in clay (Murthy, 2007)

λ- Method

In their approach for determining a pile's skin resistance in over consolidated clays, Vijayvergiya and Focht (1972) asserted a connection between design and load testing of about 10% which is well known as λ method. The initial development was mainly based on studies of pile loads. The equation is of the form

$$f_s = \lambda(\overline{q} + 2s_u) \qquad (2.44)$$

Where,

s_u = undrained shear strength of soil previously defined (kPa, ksf)

q = γ_{sZi} effective overburden pressure to the average depth of pile segment or full depth

λ = coefficient, which can be obtained from Figure 2-25
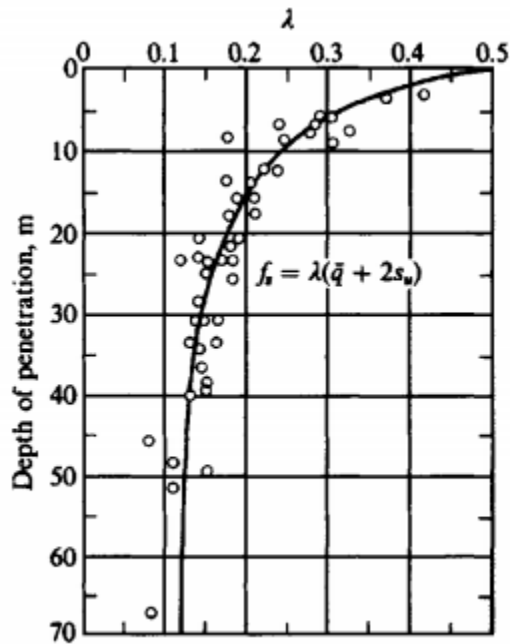
Figure 2-25 The dependence of λ coefficients on pile penetration (Vijayvergiya and Focht ,1972).

A plot containing numerous pile-load tests was subjected to a graphical regression (best-fit) analysis to get the λ coefficient. It is clear from comparing Equations of α and λ method that the λ term takes into account both the α and the K tan δ effects.

β -Method

The long-term drained shear strength conditions of piles may be effectively modeled using effective stress methods. Effective stress-based methods were developed to model long term drained shear strength conditions. Therefore, the effective soil friction angle, φ' should be used. The β -Method, developed by Burland (1973) is a simple design equation written as

$$f_s = K_s \tan \delta \ q \qquad (2.45)$$

46

$$\beta = the\ skin\ factor = K_s \tan\delta \qquad (2.46)$$

Where,

K_s = Lateral earth pressure coefficient,

δ = angle of wall friction

q = average effective overburden pressures

As per Jaky (1944)

$$K_o = (1 - \sin\varphi') \qquad (2.47)$$

Therefore,

$$\beta = (1 - \sin\varphi') \tan\varphi' \qquad (2.48)$$

For driven piles in stiff overconsolidated clay, K_s is roughly 1.5 times greater than K_o. In this case,

$$K_o = (1 - \sin\varphi')\sqrt{R_{oc}} \qquad (2.49)$$

Where,

R_{oc} = Overconsolidation ration of clay

A particularly attractive feature of the β method is that the range of β is from about 0.27 to 0.30 in the practical range of φ' (range of 25° to 45°). That is, almost any reasonable estimate for φ' gives the same computed skin resistance. However, it remains to be seen from a load test whether it is correct.

Meyerhof's method

Meyerhof (1976) has suggested a semi-empirical relationship for estimating skin friction in clays. For driven piles,

$$f_s = 1.5\ c_u\ \tan\varphi° \qquad (2.50)$$

For bored piles,

$$f_s = c_u\ \tan\varphi' \qquad (2.51)$$

Considering a value of 20° for φ' for the stiff to very stiff clays, the expression reduces to
For driven piles,

$$f_s = 0.55\ c_u \qquad (2.52)$$

For bored piles,

$$f_s = 0.36\ c_u \qquad (2.53)$$

There are a few other computational procedures for obtaining *fs* for the skin resistance contribution. One of the ways is to use SPT value for obtaining skin resistance. For SPT data, Meyerhof (1956, 1976) suggested obtaining *fs* as

$$f_s = X_m N_{55} \ (kPa) \hspace{3cm} (2.54)$$

Where,

Xm = 2.0 for piles with large-volume displacement

= 1.0 for small-volume piles

N_{55} = statistical average of the blow count in the stratum (and with corrections)

Shioi and Fukui (1982) suggest the following:

For driven piles:

$$f_s = 2N_{S,55} \ for \ sand; \ = 10N_{c,55} \ for \ clay \hspace{1cm} (kPa) \hspace{2cm} (2.55)$$

For bored piles:

$$f_s = 1N_{S,55} \ for \ sand; \ = 5N_{c,55} \ for \ clay \hspace{1cm} (kPa) \hspace{2cm} (2.56)$$

Where, $N_{i,55}$ = average blow count in the material indicated for the pile or pile segment length

Although all of the pile capacity calculations are for a single pile, it is important to note that groups of two, three, or even more piles are more frequently utilized. Furthermore, it is to keep in mind that the soil characteristics utilized in the design are those from the original soil investigation program, and that the soil values that exist after the foundation is in operation may fluctuate significantly depending on the installation method and the quantity of piles employed. The soil immediately surrounding a pile that is driven into the soil mass is always remolded. Undrained soil-strength parameters are subsequently created, and if the degree of saturation S is low or the coefficient of permeability k is sufficiently high, the parameters may resemble remolded drained values.

2.6.2.3 Vertical Bearing Capacity of Pile Group

For group bearing capacity, no appropriate efficiency formula exists. Engineers occasionally utilize a few formulae like the Field rule and Converse-Labarre formula. These empirical formulas produce efficiency factors that are less than one. However, Vesic's experimental study on groups of piles in sand shown that an efficiency factor greater than unity can be achieved when piles are

erected in the sand. For piles buried in clay soils, there is insufficient experimental data to assess group efficiency.

Pile Group Embedded in Sands and Gravels

The soil surrounding the piles to a radius of at least three times the pile diameter is estimated if they are driven into loose sands and gravel. Soil surrounding and between piles becomes heavily compacted when piles are driven in a group at close spacing. The piles and the soil between them move collectively when the group is loaded. As a result, the pile group functions as a pier foundation with a base area equal to the piles' combined gross plan area. According to the prior explanation, the efficiency of the pile group will be higher than unity. It is typically believed that when the separation is raised to five or six diameters, the efficiency equals one. It is quite conservative to assume an efficiency factor of one for all practical purposes because the available knowledge is insufficient to evaluate the efficiency for varied pile spacings. Therefore, we may write

$$Q_{gn} = n \, Q_u \qquad\qquad (2.57)$$

Where,

n = the number of piles in the group

If pile tops are resting on clays or silts, which are compressible soils, the approach described above is not relevant. The pressures that are imparted when the pile tips rest on compressible soils may cause excessive stress or severe consolidation in the pile group's compressible soils. In these circumstances, the shear strength and compressibility of the soil, not the effectiveness of the pile group within the sand or gravel structure, determine the carrying capacity of pile groups.

Pile Group in Cohesive Soils

Driving piles into cohesive soils, such as clays and silts, has a drastically different result than doing it in cohesionless soils. There will be significant soil remolding when piles are driven into clay soils, especially when the soil is soft and sensitive. Additionally, because driving cannot compact soils with such limited permeability, the soil between the piles would heave. During this process of soil heaving, there is a strong chance that the pile will also lift. According to experimental findings, a pile group built in cohesive soils may fail in one of the following ways when loaded:

1.May fail as a block called as block failure

2. Individual piles within a group could collapse.

When piles are placed farther apart, the soil between them moves downward along with the piles, and when a pile fails, soil and piles move together to cause the typical block failure. This kind of failure typically happens when piles are located within two to three pile diameters. The piles, however, fail on their own for broader spacing. At narrower spacings, the efficiency ratio is less than one and may become one at a spacing of roughly 8 diameters.

The block failure equation can be expressed as

$$Q_{gu} = cN_cA_g + P_gL\bar{c} \qquad (2.58)$$

Where,

c = cohesive strength of clay beneath the pile group,

$\bar{c}$ = average cohesive strength of clay around the group

L = length of pile

P_g = perimeter of pile group

A_g = sectional Area of group

N_c = Bearing capacity factor which may be assumed as 9 for deep foundation

Based on individual pile failure, the bearing capacity of a pile group may be expressed as

$$Q_{gu} = n\,Q_u \qquad (2.59)$$

Where,

n = the number of piles in the group,

Q_u = bearing capacity of an individual pile

Terzaghi and Peck advise using the lesser of the two supplied equations to represent the bearing capacity of the piles group.

2.6.3 Field Load Test

The field load test, also known as the plate load test, is a highly reliable method for predicting the ultimate load-bearing capacity and allowable load-bearing capacity of a foundation. This testing method involves driving the pile to its design depth and applying a series of loads. Typically, several piles are driven together, and the load is applied using neighboring piles as reactions. A rigid beam crosses the test pile and is anchored to the reaction piles. Load increments are created using a high-capacity jack between the reaction beam and the top of the test pile. The configuration resembles the plate load test, and the testing process follows ASTM D 1143 standards. The plates used in field tests come in various sizes and are typically round with a thickness of 25 mm (1 in). The test involves incrementally applying load to the pile until failure occurs, with dial gauges used to monitor plate settlement. The test continues until failure, defined as when rapid, progressive movement occurs or when the total axial movement exceeds 15% of the pile diameter or width. Comparing the load-settlement curve from these tests helps determine the ultimate load per unit area.
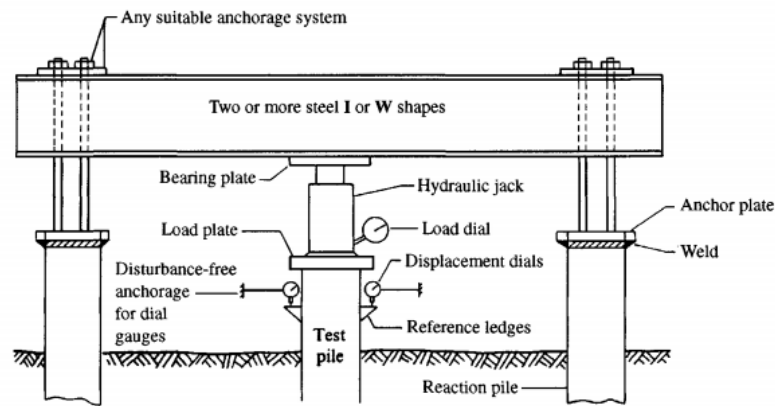
Figure 2-26 Typical pile load test setup using adjacent piles in group for reaction (Bowles, 1996)

2.6.3.1 Load- movement Diagram

Fellenius (1980) distinguished between the movement of the pile tip and the measured compression of the pile using the findings of a Quick ML test on a 130ft long (40m) 12in (300mm) precast concrete pile in Figure 2-27. The pile's overall cross section was 124 in^2 (800 cm^2), its steel reinforcing area was 1.9 in^2 (12 cm^2) in size, and its circumference was 41in (107 cm). A load cell was used to measure the test load, which was applied to the pile in pauses of 22.4 tons. In the test, a center pipe had been cast in the pile, enabling a tell-tale to be inserted all the way to the pile tip

to track the pile's movement and compression. The observed compression plots in a straight line after a load of 70–50 tons, suggesting that the proportion of the additional load utilized to overcome shaft resistance is constant. It would be extremely unlikely for the constant value to be anything other than zero. Because of this, the additional force imparted does not decrease due to shaft friction all the way to the tip of the pile, and the slope of the compression line is therefore identical to the slope of the elastic line.

In accordance with an analytical technique put forth by Trow (1967), the pile tip begins to move after the elastic line turns tangential to the pile head's load movement curve, and any additional loads are delivered directly to the pile tip. The Trow analysis is applicable to a linear distribution of shaft resistance, such as a triangular or rectangular shape. The test findings shown in Figure 2-27 demonstrate that the elastic line derived from the observed compression becomes parallel to the load-movement curve at a load of approximately 70–50 tons. The shaft friction must therefore roughly follow a linear distribution, and its value cannot be larger than 70–50 tons, according to Trow's technique of study.
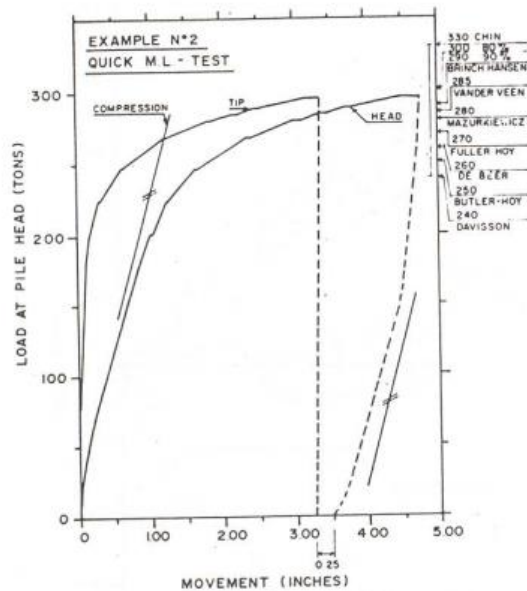
Figure 2-27 Load-movement diagram from Quick M.L. test with measurement of pile tip movement (Fellenius, 1980).

The relationships could be established between the load at the pile end and the total shaft resistance, as shown in Figure 2-28. The observed compressions were 0.96, 1.07, and 1.24 inches

with pile head loads of 224, 240, and 280 tons, respectively. Calculated pile tip loads as a result of the values are 160, 182, and 216 tons, respectively. For all three pile loads, the corresponding predicted pile shaft resistance was 64 tons. Distribution of load in the pile becomes linear under the assumption of constant unit shaft friction, or rectangular shaft resistance, and Fellenius (1969) demonstrated that as straightforward.

The unit shaft friction is probably not consistent for a variety of reasons. A method of analysis employing measured pile compression was recently proposed by Leonards and Lovell (1978), allowing the analysis of test data to examine different distributions of shaft resistance. The equation that Leonards and Lovell developed is as follows:

$$x = \frac{C' - C}{1 - C} \qquad\qquad (2.60)$$

Where,

x = ratio between the pile tip load and the load applied to the pile head ($P_{tip} = x \times P$)

C'= ratio of measured compression to column compression, the latter being the compression of a free column subjected to the same load as the pile

C= the ratio of elastic compression of the pile at a load P supported totally by shaft friction to the column compression for the same load

53
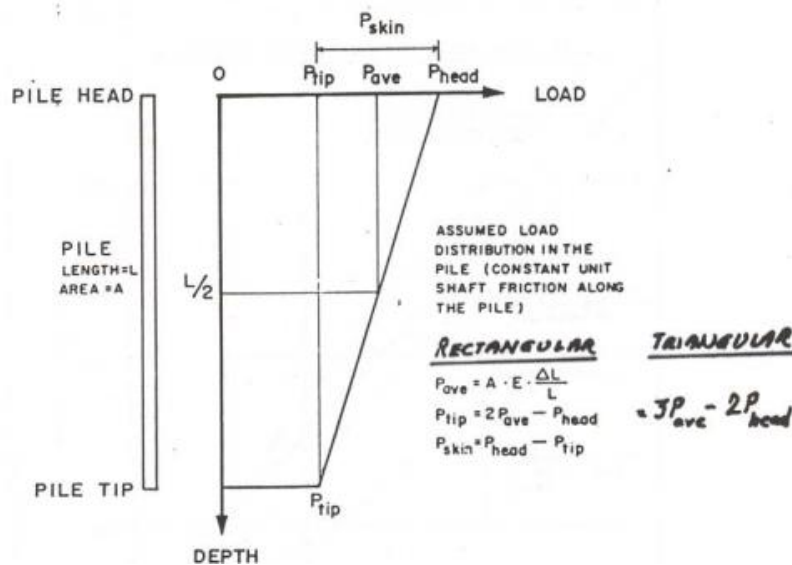
Figure 2-28 Shaft and tip load calculation from measurement of pile compression (tip movement when assuming constant unit shaft friction (Fellenius, 1980)

The measured data allow us to determine the ratio C'. The goal of the study is to either determine C, or the relative distribution of shaft resistance, from knowledge of x, or tip load, or to derive tip load, in reverse, from knowledge of relative distribution of shaft resistance.

The equations for measuring C are presented in Figure 2-29.
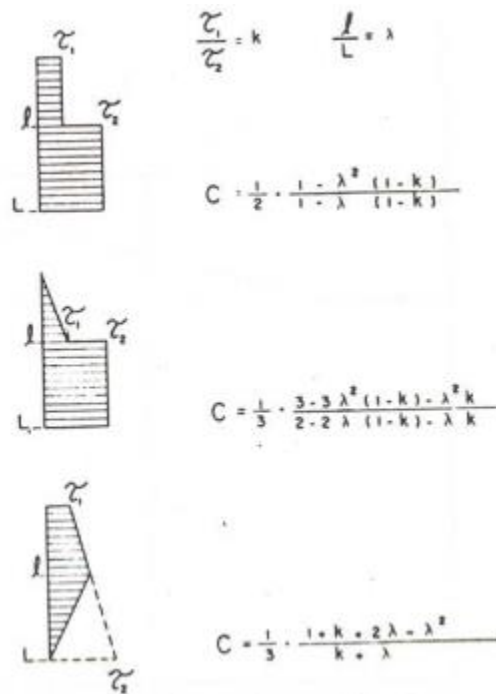
Figure 2-29 Mathematical expressions for co-efficient C for various distribution of unit shaft friction

The actual tip and shaft loads cannot be established in the absence of sufficient soil data. They fall somewhere in the middle, though. Fellenius (1980) presented the findings of the comprehensive study in Figure 2-30, which depicts the load-movement curves for the tip and shaft (as head movement) for the two extreme distributions of the shaft resistance.

54
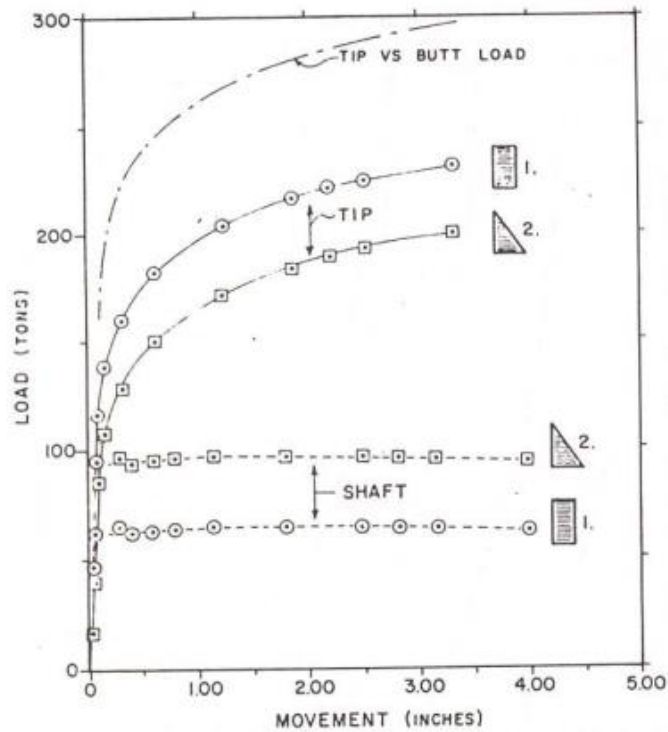
Figure 2-30 Load -movement diagram for shaft and tip loads (Fellenius, 1980)

Bica et al. (2014) conducted a load test program to investigate various aspects of the design and behavior of driven steel piles. The study focused on instrumented axial stress testing of an H pile and a closed-ended pipe pile in a multilayered soil profile composed of transitional soils. The primary objectives of these axial load tests were to establish load-settlement and load-transfer correlations and to compare measured data with design values. The study detailed the steps required for successful pile instrumentation and data collection, presenting the findings of four instrumented pile load tests on steel piles in a mixed soil profile.

The results of the axial stress experiments indicated both the ultimate and limit loads for the H pile and the closed-ended pipe pile, according to Chin's criterion. These loads were determined as 1839 kN and 1345 kN for the H pile and 2282 kN and 1678 kN for the closed-ended pipe pile in the first loading test. The measured shaft capacities of both piles were fairly similar, with the closed-ended pipe pile having a slightly higher shaft capacity. The results are illustrated in Figure 2-31.

Measured load-transfer curves showed that a significant amount of QsL was mobilized in the lower third of each pile. However, the H pile exhibited a base capacity approximately twice as high as

the closed-ended pipe pile. This difference was attributed to variations in the influence zones beneath the pile bases and the thinner bearing layer under the pipe pile, which limited the buildup of base resistance at that location. Load-transfer curves for the first and second static load tests on the H pile and the closed-ended pipe pile are depicted in Figure 2-32.
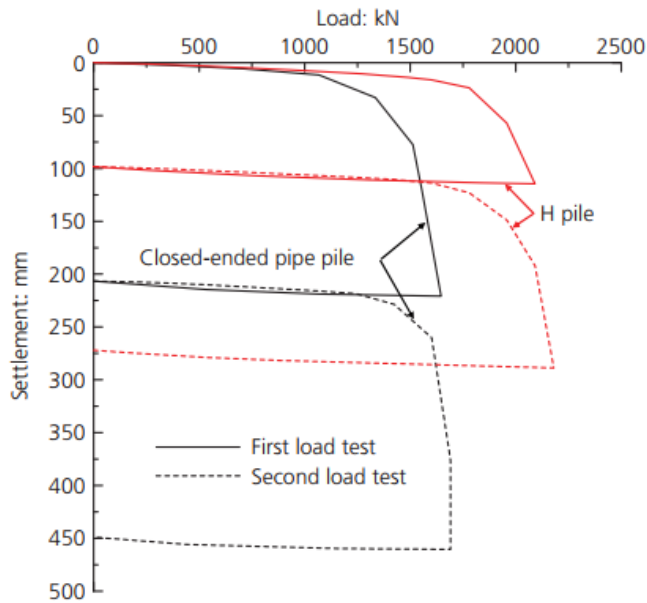
Figure 2-31 Load–settlement curves at the pile head (Bica et. al., 2014)

(a)

(b)
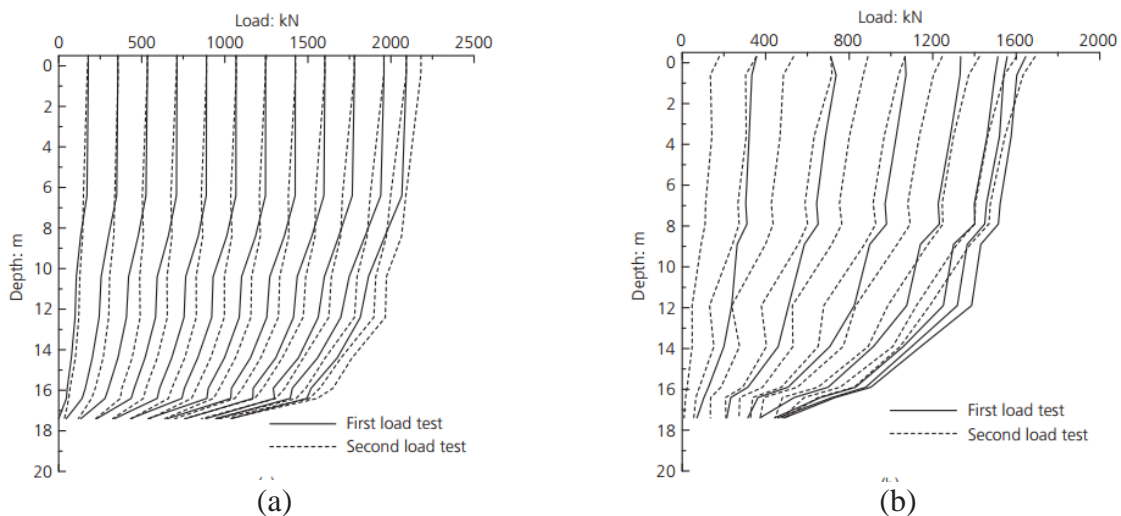
Figure 2-32 Load–transfer curves: (a) H pile; (b) closed-ended pipe pile (Bica et. al., 2014)

Despite the difficulties in obtaining the ultimate capacity of the piles using the in situ loading test, this method is the most recommended by several codes and design standards. To investigate the vertical load bearing behavior of manually excavated large diameter belled concrete piles (LDBCPs), Gao et al (2019) performed field loading tests on a total of 16 LDBCPs, ranging from 0.8 to 3.5 m in base diameter from 6.1 to 18.0 m in embedment length. Yi et al (2017) employed full-scale field loading tests to investigate the vertical bearing capacity behavior of a single T-shaped column in soft ground. Aurpa et al (2024) conduced field load test on various sizes of RPPs and analyzed the ultimate vertical load capacity following six different method.

2.6.3.2   Ultimate Failure Load

The ultimate load capacity of pile can be obtained from the analysis of load settlement curve after axial load testing of vertical piles. There are several analysis methods suggested by different authors with the view of finding the ultimate load capacity of piles. If pile groups are loaded to failure, the ultimate load of the group may be found by any of the methods mentioned in this subsection. The following section discusses different analysis procedures.

<u>Davisson's Limit Method</u>

The load corresponding to the movement that exceeds the pile's elastic compression by a value of 0.15 inches (4 millimeters) plus a factor equal to the pile's diameter divided by 120 is known as Davisson's limit value. The Davisson limit (1972) was created in tandem with the wave equation analysis of driven piles and has become increasingly common as the adoption of this form of analysis has grown. Its main use is for test results from driven piles examined using the quick methods detailed in ASTM D 1143. Figure 2-33 shows ultimate failure load determination according to Davisson's Method.
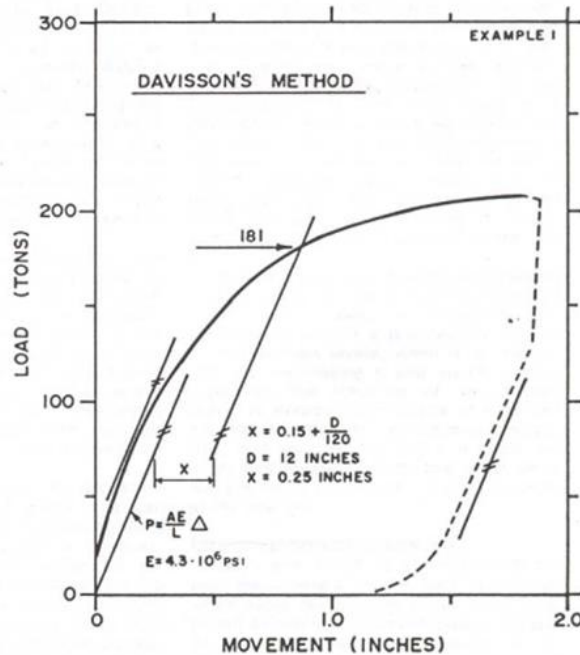
Figure 2-33 Ultimate Failure according to Davisson's Method (Fellenius, 1975)

Chin's Method

The Chin method (1970 and 1971) makes the assumption that the load-movement curve has a hyperbolic shape as it approaches the failure point. The method involves dividing each load value by its associated movement value, then plotting the resultant value against the movement. The values plotted descend, with some early variation, on a straight line, as seen in Figure 2-34. The Chin failure load is the inverse slope of this line. Both quick and slow tests can be conducted using the Chin approach. if consistent time intervals are employed. Therefore, the "standard approach" of ASTM is typically not relevant. Additionally, the "standard test" has too few monitored data; an interesting development could very easily occur between load increments number seven and eight and go undetected.

In general, a line is formed by two points, and a third point along the same line validates the line. However, while employing Chin's technique, it is to be noted that, if administered too early in the test, it is quite simple to obtain a false Chin value. The right straight line typically does not begin to appear until the test load has gone beyond the Davisson limit. Typically, the Chin failure load is between 20% to 40% higher than the Davisson limit. When this isn't the case, it's a decent idea to look more closely at all the test results.
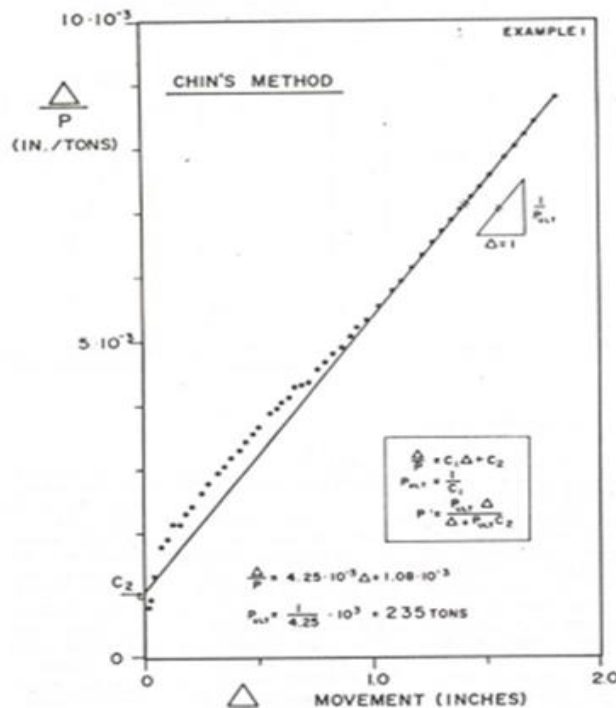
Figure 2-34 Ultimate Failure according to Chin's Method (Fellenius, 1975)

Brinch Hansen Method

Brinch Hansen (1963) defined failure as the load that causes the pile head to move twice as much as it did for 90% of that load. Figure 2-35 illustrates this concept. In Scandinavia, this approach, sometimes known as the 50% criterion, has become widely used (Swedish Pile Commission, 1970). In addition, Brinch Hansen (1963) suggests an 80% criterion that defines the ultimate load as the load that causes the pile head to move four times as much as it does for 80% of that load. Extrapolating from the curve yields an estimate of the 80% criterion failure load of around 210 tons in Figure 2-35.
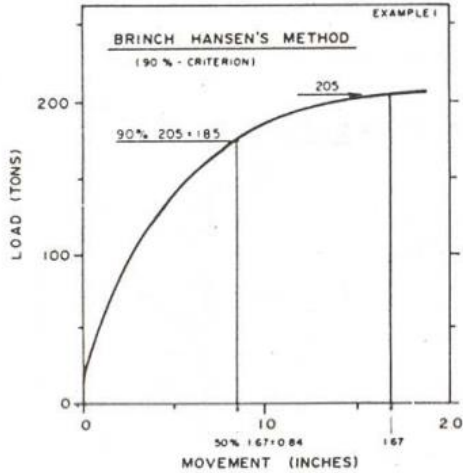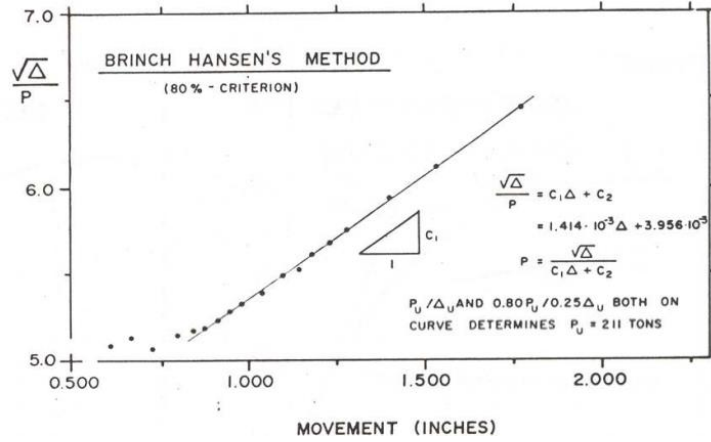
Figure 2-35 Ultimate Failure according to (a) 90% criterion by Brinch Hansen; (b)) 80% criterion by Brinch Hansen (Fellenius, 1975)

Brinch Hansan's 80% criterion is depicted on a plot in Figure 2-35(b). The criterion that a point represents determines the eventual failing value. When the point, co-ordinates $(0.80P_u, 0.25\Delta_u)$, also, lies on the load-movement curve, that point, co-ordinates (P_u, Δ_u) on the curve, is the point of ultimate failure. The criterion provides the straightforward correlations listed below for use in determining the ultimate failure, P_u:

$$P_u = \frac{1}{2\sqrt{C_1 C_2}} \qquad\qquad (2.61)$$

$$\Delta_u = \frac{C_2}{C_1} \qquad\qquad (2.62)$$

Where,

C_1 is the slope of the straight line

and C_2- is the y-intercept in the $\sqrt{\Delta}/P$ plot.

It is crucial to confirm that the point $(0.80P_u, 0.25\Delta_u)$ indeed lies on the recorded load-movement curve when employing the Brinch Hansen 80% criterion. In the illustration. P_u is 211 tons, which is directly in agreement with the extrapolated rate from the load-movement curve.

According to Brinch Hansen's 80% criteria, the load movement curve is roughly parabolic. Chin asserts that it is roughly exaggerated. It is clear that the actual curve's shape is sufficiently similar

60

to both mathematical curves to support both approximations. However, the failure value for Brinch Hansen's 80% criterion is around 10% lower than Chin's figure.

Fuller & Hoy Method

A straightforward definition suggested by Fuller & Hoy (1970) is presented in Figure 2-36 Where the load movement curve slopes by 0.05 inches per ton (0.14 millimeters per kilogram), the failure load is equal to the test load. The Fuller and Hoy technique penalizes the long pile since the slope of 0.05in/ton occurs sooner for a long pile as opposed to a "short pile" due to the bigger elastic movements that occur for a long pile.

Butler & Hoy Method

Butler & Hoy (1977) defined the failure load as the load at the intersection of the tangent sloping 0.05in/ton and the tangent to the initial straight segment of the curve. Figure 2-36 also illustrates a development of this definition or to a line that is perpendicular to the curve's rebound region. The author advises that the intersection be that of a tangent parallel to the elastic line instead because the latter component is more or less parallel to the elastic line. The Butler and Hoy development significantly reduces the length impact by accounting for elastic deformations.
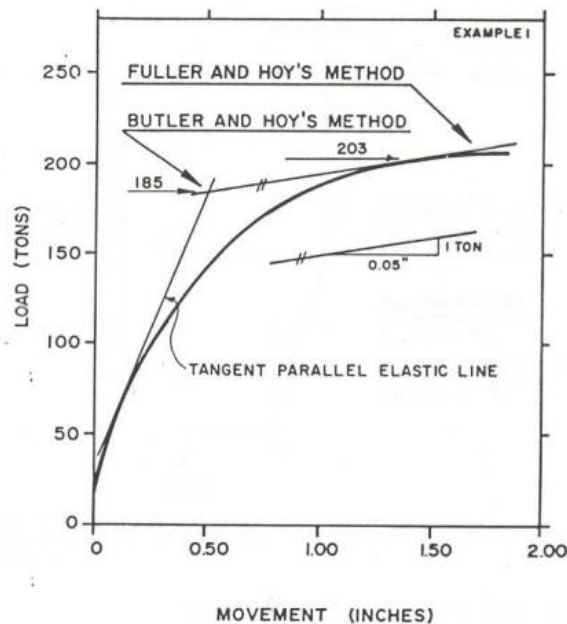
Figure 2-36 Ultimate failure according to Fuller and Hoy and Butler and Hoy (Fellenius, 1980)

Fellenius (1975) compared different analysis methods used for obtaining failure load utilizing pile load test data. Nine potential criteria of failure were presented using the test data presented as a load-movement curve in Figure 2-37(a). The example pile was a 12-inch (305-mm) concrete pile that was inserted 60 feet (18.3 meters) into delicate clay. 10 feet (3 meters) of clayey silt and 6 feet (1.8 meters) of silt. After driving for six weeks, the pile was tested. The CRP technique was used for testing.
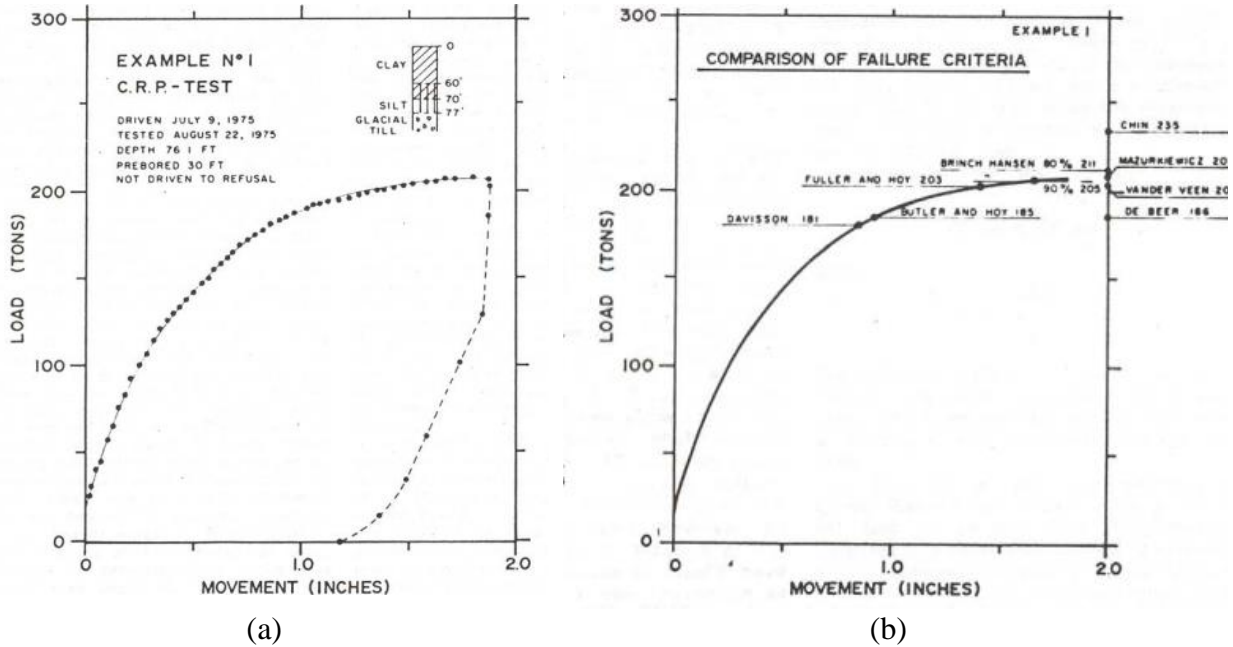
Figure 2-37 (a) Load-movement diagram from CRP test; (b) Comparison of nine failure criteria (Fellenius, 1980)

Figure 2-37(b) shows that Davisson's limit (180 tons) gave the lowest value in comparison with other methods and Chin's method suggested the highest value of 235 tons. Other values suggested values around an average of 200 tons. Fellenius (1980) advised considering three to four criteria in determining ultimate load capacity preferably, Davisson's limit load, Chin's failure load, Brinch Hansen 80% criterion, and the Butler and Hoy failure load.

Van Weele

Van Weele proposed a concept in 1957 that the load at which the load-settlement curve approaches a vertical asymptote is typically considered to be the ultimate pile load. Van Weele asserts that the load-bearing elements of the pile are as illustrated on Figure 2-38. If the dashed line 0 to c is drawn

through the origin and parallel to the point capacity region from a to b. In this picture, the weight carried at settlement δ= 42.5 mm is shown as follows:

Point Load = 350 kN

Skin Resistance = 1650 kN
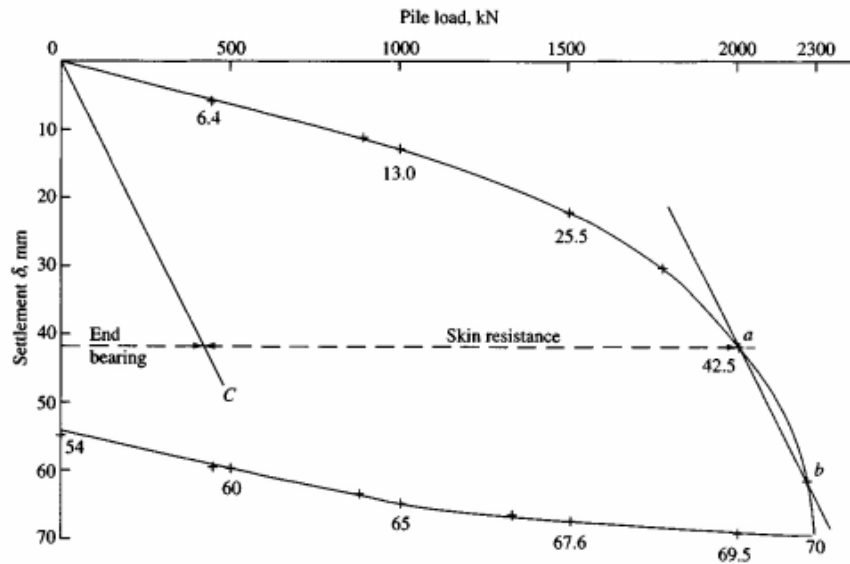
Figure 2-38 Ultimate pile load according to Van Weele (Bowles, 1996)

2.7   Lateral Load Carrying Capacity of RPP

RPP used in slope stabilization and MSE wall base experience lateral loads. Based on the design procedure and failure mechanism, in these cases, RPPs work as partially embedded piles and are subjected to lateral loading. For successful application, it is necessary to determine lateral load capacity of RPP. Vertical piles can transport lateral loads via shear, bending, and lateral soil resistance rather than as axially loaded elements, as completely proven by a vast number of load tests. When there are both axial and lateral loads, superposition is frequently used to calculate pile stresses. When both lateral and axial loads were present, Bowles (1974a) created a computer program to calculate pile stresses, which includes the P - Δ effect and in the typical case of a battered, totally or partially embedded pile.

In deep foundations, lateral stresses induce shear and moment, causing the foundation to deflect sideways and affecting the adjacent soil's lateral resistances. The magnitude of these lateral

deflections and resistances, as well as the foundation's load-bearing capacity, depends on the stiffness of both the soil and the foundation.

Deep foundations are categorized into short and long based on how well the toe is anchored. A long foundation effectively anchors the toe, while a short foundation lacks sufficient embedment for toe stabilization. The classification depends on factors like foundation rigidity and soil lateral resistance, with flexible foundations considered long with a D/B ratio over 20, and stiffer foundations typically requiring a D/B ratio of at least 35.
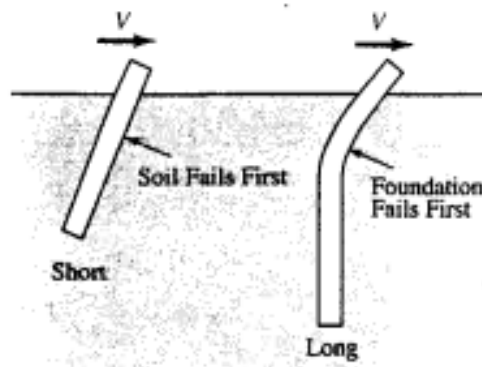
Figure 2-39 Short vs Long Foundation (Coduto, 2001)

Short foundations' ultimate lateral capacity is mostly determined by the soil. In other words, the foundation's flexural capacity is exceeded before the soil fails. On the other hand, in long piles, as the foundation will break structurally before the soil fails, its flexural strength governs the eventual lateral capacity of long foundations.

2.7.1   Load Transfer Mechanism

The transmission of lateral loads from deep foundations to the ground is a problem involving soil-structure interaction between foundations and the underlying soil. In other words, whereas the soil resistance depends on the foundation's movements and flexural stresses, the foundation's movements depend on the soil resistance. Therefore, it is not possible to arbitrarily divide the analyses' structural and geotechnical components. Both must be assessed simultaneously.

One of the most important aspects of solving the problem of a lateral loaded pile is likely the prediction of the soil resistance at any point along the pile as a function of pile deflection. Figure 2-40(a) displays the distribution of stresses against a cylindrical pile prior to installation. When

mounted vertically and without causing bending, the stresses will be homogenous and normal to the pile wall at a given depth (Reese and Van Impe 2001). Following lateral loading, the pile will deflect and the distribution of the soil stresses acting on the pile will be similar to that in Figure 2-40(b). It is vital to note that some strains will arise at the interface between the pile and the earth and won't be perpendicular to the pile wall. Integrating the stresses near the pile cross section yields the net soil reaction, $p(x)$. $p(x)$ is expressed in terms of force per unit length.
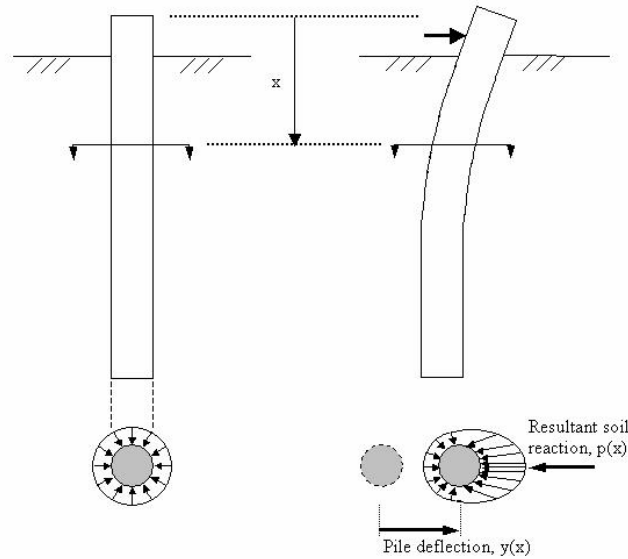
Figure 2-40 Distribution of stresses against a pile before and after lateral loading (adapted from Reese and Van Impe 2001) (FHWA, 2006)

Diagrams of lateral deflection, slope, moment, and shear in a long foundation, as well as the lateral soil reaction, are all shown in Figure 2-41 as functions of depth. At the top of the foundation, the applied shear and/or moment loads cause a lateral displacement. According to Figure 2-42, which is known as a p-y curve, this deflection causes the soil to exhibit lateral resistance, which is a function of the deflection. Since the applied stresses are opposed by the soil resistance close to the ground surface, the deflection gradually decreases with depth until it eventually reaches zero deflection. The foundation deflects in the opposite direction and causes soil reactions that are also in the opposite direction since the shear and moment at this depth are not zero.

(a) Loading M, V
(b) Deflection y
(c) Slope S
(d) Moment M
(e) Shear V
(f) Soil Reaction p
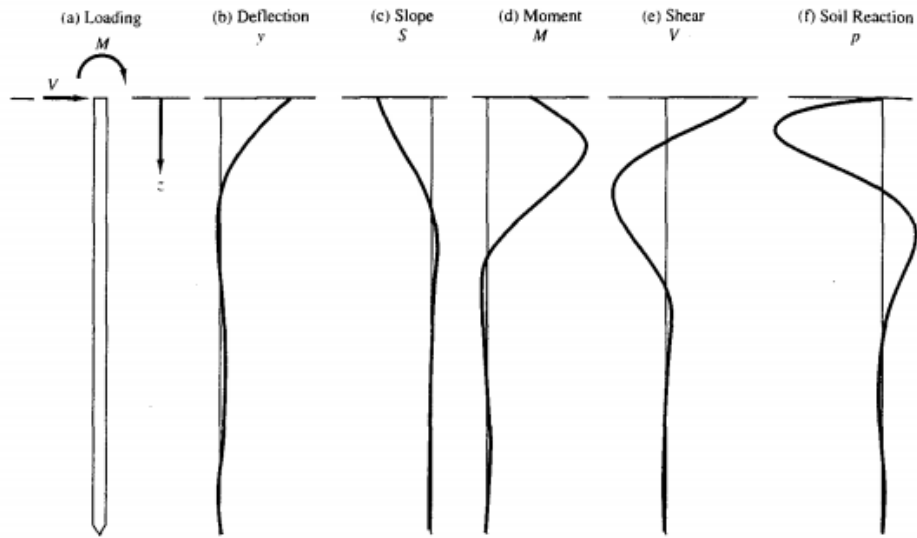
Figure 2-41 Forces and deflections in a long deep foundation subjected to lateral loads (Coduto, 2001; Adapted from Matlock and Reese, 1960).
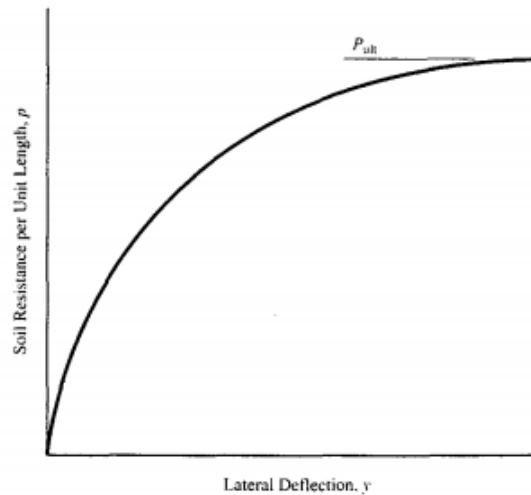
Figure 2-42 Soil resistance per unit length, P as a function of lateral deflection, y

The shapes and magnitudes of these plots depend on many factors. Including the type (shear and/or moment) and magnitude of the applied loads, resistance-deflection relationship in the soil (known as the p-y curve) and flexural rigidity of the foundation, which is the product of its modulus of elasticity, E, and moment of inertia, I. The following are the definitions provided by the principles of structural mechanics for how each of these parameters changes with depth:

$$S = \frac{dy}{dz} \tag{2.63}$$

$$M = EI\frac{dS}{dz} = EI\frac{d^2y}{dz^2} \tag{2.64}$$

$$V = \frac{dM}{dz} = EI\frac{d^3y}{dz^3} \tag{2.65}$$

$$P = \frac{dV}{dz} = EI\frac{d^4y}{dz^4} \tag{2.66}$$

Where,

S = slope of foundation

M = bending moment in foundation

V= shear force in foundation

p = lateral soil resistance per unit length of the foundation

E = modulus of elasticity of foundation

I = moment of inertia of foundation in the direction of bending

y = lateral deflection

z = depth below ground surface

If one of these curves has a known form either from computation or field observations, the others can be calculated using progressive integration or differentiation with the proper boundary conditions.

2.7.2 Field Load Test

Full-scale lateral load tests, while less common than axial load tests, are occasionally conducted for large projects or in unique soil conditions. Typically, both foundations are tested in these setups since they move equally during the test, making it a practical choice for field testing.
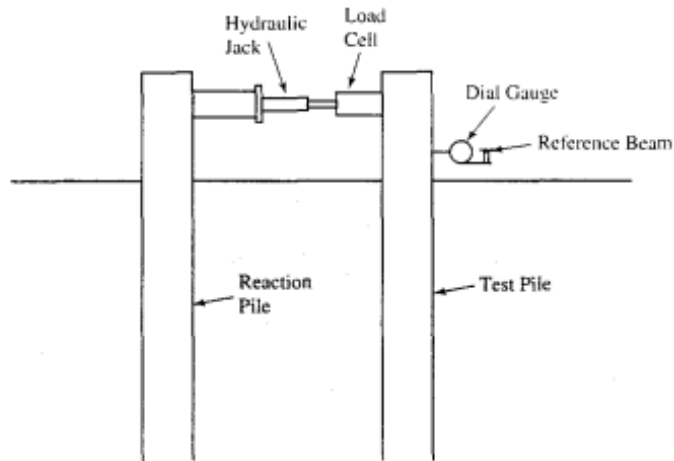
Figure 2-43 Typical full-scale lateral load test on a prototype deep foundation. (Coduto, 2001)

In full-scale load tests, prototype foundations are installed at the project site, lateral loads are applied, and the resulting lateral deformation and slope at the foundation's top are measured. This approach allows for a direct determination of load deformation properties. Shears and moments within the foundation can also be calculated if strain gauges are installed or deformations are recorded at various depths.

Data from lateral load tests can be applied directly to design production foundations or used to derive unique p-y curves specific to a particular location when combined with p-y studies. However, the high cost of full-scale load tests limits their economic feasibility to large projects.

To reduce testing costs, scale model foundations tested in a laboratory environment are an option. Model lateral load tests are particularly useful when assessing undrained loading conditions in clay since undrained shear strength (SU') is independent of effective stress and remains unaffected by scaling. Nevertheless, extrapolating model test results to full-scale foundations can be challenging due to varying scaling ratios for different parameters. Some engineers have explored centrifuge testing to address scalability issues, as the added "gravity" in a centrifuge model helps align the scaling ratios for mass and stress with linear dimensions. However, centrifuge tests are only applicable to very small-scale models and come with additional challenges.

Wu et al (1995) conducted a series of lateral load tests involving instrumented single piles in Shanghai, PRC with the diameter of the piles varying from 0.09 m to 0.60 m. The lateral

deflections and the moment distribution in the laterally loaded piles have been estimated using the hyperbolic stress-strain curves from the triaxial tests (UU-, ACU-tests) and the p-y curves from the lateral load tests. A coefficient, which was discovered to be independent of pile diameter, could be used to connect the findings from the field load testing and the laboratory triaxial experiments. Up to a depth of 4D to 5D, this coefficient grew linearly from the surface of the earth. A was constant below this critical depth. When the clay was over consolidated, value of the coefficient, A, decreased by about 20% to 25%. The author found the following equation that was able to fit the test results.

$$\frac{P}{P_u} = \frac{y/y_{50}}{\frac{\beta'}{\beta' - 1} + \frac{\beta' - 2}{\beta' - 1} y/y_{50}}$$

(2.67)

Where,

β is equal to $y_{100}/y_{50} = (2 - R_f)/(1 - R_f)$ and y_{50} and y_{100} are the lateral displacements of the pile at $0.5P_u$ and P_u respectively. P_u is the ultimate lateral resistance of the soil.

It should be noted that the failure strength of the soil $(\sigma_1 - \sigma_3)_f$ as measured by triaxial tests (UU- and ACU-tests) and the strain ε_{50} at half of the failure load might be used to define the hyperbolic stress-strain relationship of the soil. When the clay is overconsolidated, a lower shear strength had to be employed in the calculations. As the soil's overconsolidation ratio increased, the reduction increased.

For the laterally loaded piles in Shanghai, PRC, the author compared the calculated moment distribution and the deflection at the ground surface with the observed moment distribution and deflection. The consistency between the measured and calculated moment distributions for the pile with a 0.16 m diameter is very acceptable, as can be shown in Figure 2-44. Other piles tested in the USA in Austin, Sabine Pass, and Manor have also had their moment distribution and deflection at the ground surface examined. The agreement between measured and estimated bending moments is excellent for these tests as well.
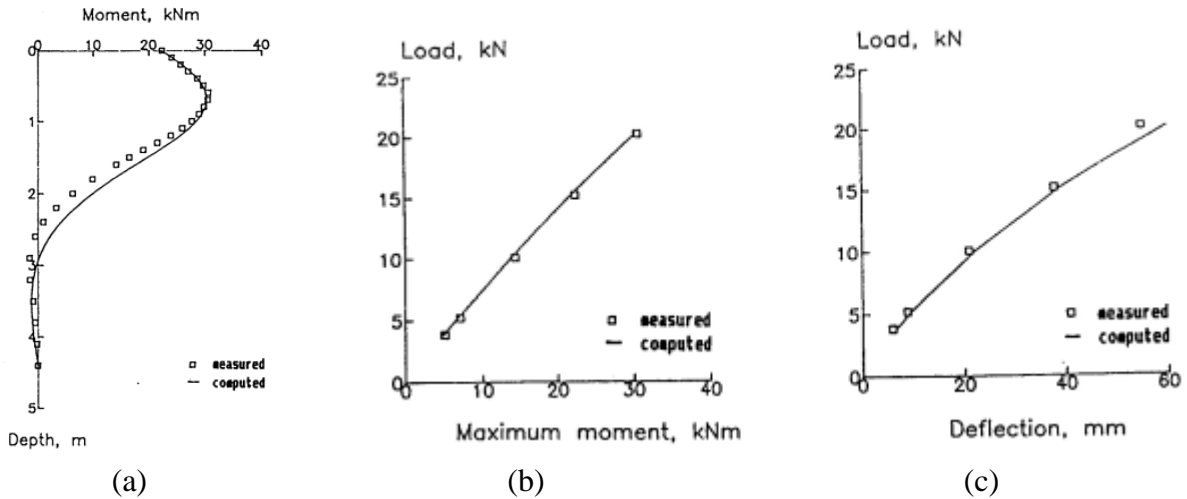
Figure 2-44 Comparisons between measured and computed (a) moment curves on 0.16-m diameter pile, (b) maximum moments, and (c) deflections for the Shanghai tests

Xiang et al (2015) carried out field lateral loading tests on one 2×5 and two 3×5 grouted steel-pipe pile groups at a highway slope-stabilization site. The tests simulated the performance of slope-stabilization pile groups subject to lateral soil movements caused by surcharge fill loading behind the pile groups. Feagin (1937) conducted tests to determine the resistance under lateral loads of timber and concrete piles, driven in Mississippi River sand. The work includes descriptions of tests on single piles with heads not fixed, and on groups of four, twelve, and twenty piles with heads fixed in concrete test monoliths. Aurpa et al (2024) used the p-y method for investigating the lateral load capacity of RPP from field load tests performed in the field.

2.7.3 Methods of Analysis

2.7.3.1 Finite-difference method

Finite-difference method (FDM) was initially utilized to study a laterally loaded pile, as explained by Howe (1955), Matlock and Reese (1960), and Bowles (1968). In order to predict the ground-line deflection and maximum bending moment in the pile shaft, Matlock and Reese (about 1956) employed the FDM to create a series of nondimensional curves. Users may then enter the appropriate curve with the specified lateral load. The preceding curves were then extended by Matlock and Reese (1960) to accommodate a few variations in soil modulus with depth.

Users of this method started referring to it as the "p-y method" because the early work on the FDM lateral pile solution (McClelland and Focht (1958)) used node springs p and lateral node

displacements y. The information needed to create a p-y curve is often derived from empirical equations created from lateral load experiments conducted along the Gulf Coast in the southwest of the United States. Theoretically, a p-y curve can be obtained for each node along the pile shaft. Since the only known deflections are at or above the ground line unless a hollow-pipe pile is employed with telltale devices installed, a single curve is about all that can be developed in practice when a lateral load test is back-computed to acquire these curves.

Since the end and interior difference equations are different, the FDM is complex to program; however, by employing 1-ft components, the ends can be accurately modeled using interior equations. Whether the pile head is free or is constrained in translation, rotation, or both will also affect the equations for the pile head. If the pile section is not constant, additional issues arise, and soil stratification or other factors point to the usage of segments of varying length. Of course, one can take into account each of these factors. The FDM matrix is NxN in size, with N equaling the number of nodes and all nodes having a uniform spacing.

Reese and Wang's (2000) finite difference method was utilized by White et al. in 2008 to analyze the behavior of slender piles subject to lateral soil movement in a free field. The isolated piles subject to free-field lateral soil movement were studied, and the displacement-based analysis approach was able to approximate the deflection, bending moment, shear, and soil reaction. In general, the predictions made using the p-y curves created from the peak undrained shear strengths measured in the lab agreed with the results of the experimental tests, especially at small relative displacements. Figure 2-45 shows the comparison between measured and predicted pile behavior.
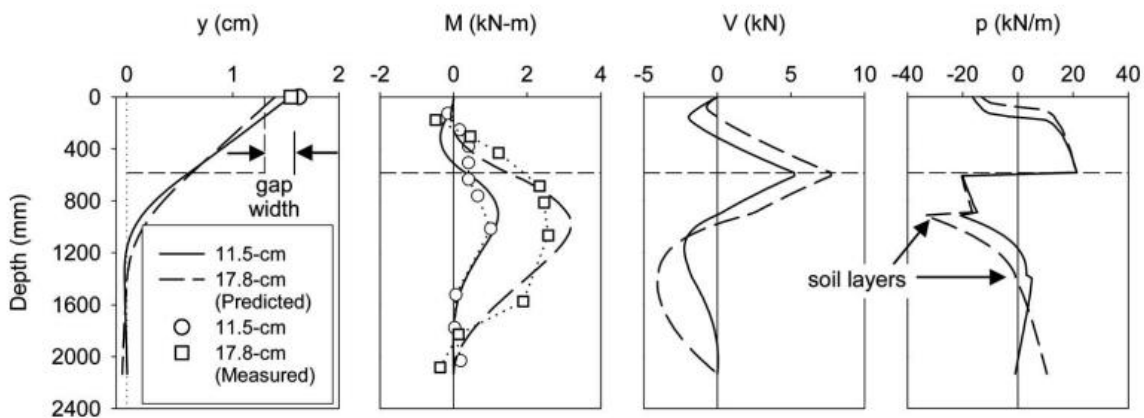
Figure 2-45 Measured and predicted pile behavior characteristics and correlation with

71

experimental data at 13 mm lateral soil movement: Piles 5 and 6 glacial till (White et al., 2008).

2.7.3.2 Finite Element Method

The Finite Element Method (FEM) has the advantage over the FDM in that it has node rotation in addition to translation, whereas the FDM just has node translation. Both translation and rotation help to define the elastic curve more precisely. Boundary cases (nodes with either zero rotation or translation) and lateral loads can be specified using FEM. Any node can be utilized as a load point or have known translation or rotation with the use of FEM.

In a finite element method (FEM) analysis, the soil and the foundation are each broken down into a number of small elements and given the proper stress-strain properties. The study then takes into account how these components respond to applied loads and analyzes this response to gauge the foundation's shears, moments, and lateral deflections. Either two-dimensional or three-dimensional elements can be used for finite element studies.

The accuracy of finite element analysis relies on our ability to provide the elements with the appropriate engineering qualities. As a result of the well-defined qualities of structural materials, this can be done with ease for the foundation, but because the soil is more complex, it is extremely challenging to execute. For instance, the soil's stress-strain characteristics are unquestionably nonlinear. Additionally, the more precise three-dimensional FEM analyses demand more intensive computer resources.

2.7.3.3 Broms Method

Brom's theory of laterally loaded piles is based on articles he wrote and published in 1964. He addresses the following in his theory:

1. Lateral deflections of ground-level piles under working loads

2. Ultimate resistance of soil

The author has studied both short and long piles buried in soils with and without cohesiveness. The following topics are covered in relation to his theory:

1.   Lateral deflections at working loads in saturated cohesive soils (1964a).

2.   Ultimate lateral resistance of piles in cohesive soils (1964a).

3. Lateral deflections at working loads in cohesionless soils (1964b).

4. Ultimate lateral resistance of piles in cohesionless soils (1964b).

Lateral deflections at working loads in saturated cohesive soils

For calculating the deflections of laterally loaded piles inserted into saturated cohesive soils, Broms has developed methods. He has thought about both short and long piles with either a fixed or free rotating head. The idea of subgrade reaction action has been used to determine lateral deflections under working loads. When the applied loads are less than one-half to one-third the pile's ultimate lateral resistance, it is expected that the deflections grow roughly linearly with the applied loads.

The dimensionless length is the main determinant of the deflections, bending moments, and soil reactions where,

$$\beta = \sqrt[4]{\frac{kd}{4\,EI}} \qquad\qquad (2.71)$$

EI = stiffness of the pile section,

k = coefficient of subgrade reaction,

d = width or diameter of pile,

L = length of pile.

A pile is considered long or short on the following conditions:

Free-head pile

For long piles, $\beta L > 2.50$

For short piles, $\beta L < 2.50$

Fixed-head pile

For long pile, $\beta L > 1.5$

For short pile, $\beta L < 1.5$

Deflection y_o for infinitely stiff pile when $\beta L < 1.5$ - free head,

$$y_0 = \frac{4\,P_t(1 + 1.5\ e/L)}{kdL} \qquad (2.72)$$

where, e is the height above the ground level where the lateral load P_t is applied

Deflection y_o for retrained pile with $\beta L < 0.5$,

$$y_0 = \frac{P_t}{kdL} \qquad (2.73)$$

The deflection of restrained piles is theoretically one-fourth or less than that of corresponding free-head piles.

y_o for long piles,

Free head:

$$y_0 = \frac{2P_t\beta(e\beta + 1)}{k_\infty d} \qquad (2.74)$$

Fixed head:

$$y_0 = \frac{P_t\beta}{k_\infty d} \qquad (2.75)$$

where, $k\infty$ = coefficient of subgrade reaction for long piles.

The method Broms suggests for calculating k, coefficient of subgrade reaction for short piles, is fairly complex. Tomlinson contends that for the situation of soil with constant modulus, it is precise enough to use k as k_1 (the modulus for 300 mm plate).

Ultimate lateral resistance of piles in cohesive soils

In cohesive soils, the ultimate soil resistance for piles rises with depth, from 2 c_u (c_u = undrained shear strength) at the surface to 8–12 c_u at a depth of around three pile diameters (3d) below the surface. According to Broms, the soil resistance is zero from the ground surface to a depth of 1.5d and constant at $9c_u$ below this depth. For the following types of piles, the mechanism of soil failure under ultimate lateral load P_u is explored.

1.   Short piles, free head and restrained

2.   Long piles, free head and restrained

Short Free-head Pile

Figure 2-46 (a) displays the distribution of soil responses and bending moments. Failure occurs when the pile rotates as a unit and the soil yields throughout the entire length of the pile. At a depth of (f + 1.5d) below the ground's surface, the maximum moment M_{max} occurs, and at this level, the shear force is equal to zero. *f* and M_{max} are expressed as:

$$f = \frac{P_u}{9c_u d} \qquad\qquad (2.76)$$

$$M_{max} = P_u(e + l.5d + 0.5f) \qquad\qquad (2.77)$$

Integration of the lower part of the shear diagram yields,

$$M_{max} = 2.25\ c_u\ dg^2 \qquad\qquad (2.78)$$

Since *L = (1.5d + f + g),* Eqs (2.77) and (2.78) can be solved for the ultimate load P_u that will produce a soil failure.

Short Fixed Head Pile

For fixed-head situations, Broms takes into account two categories of short piles.

1. Very short pile.

2. Intermediate length of pile.

Figure 2-46 (b) and (c) depict the failure processes for both types of piles. Failure occurs when the applied lateral load P_u equals the ultimate lateral resistance of the soil in the case of a very short pile, or when

$$P_u = 9c_u d(L - 1.5d) \qquad\qquad (2.79)$$
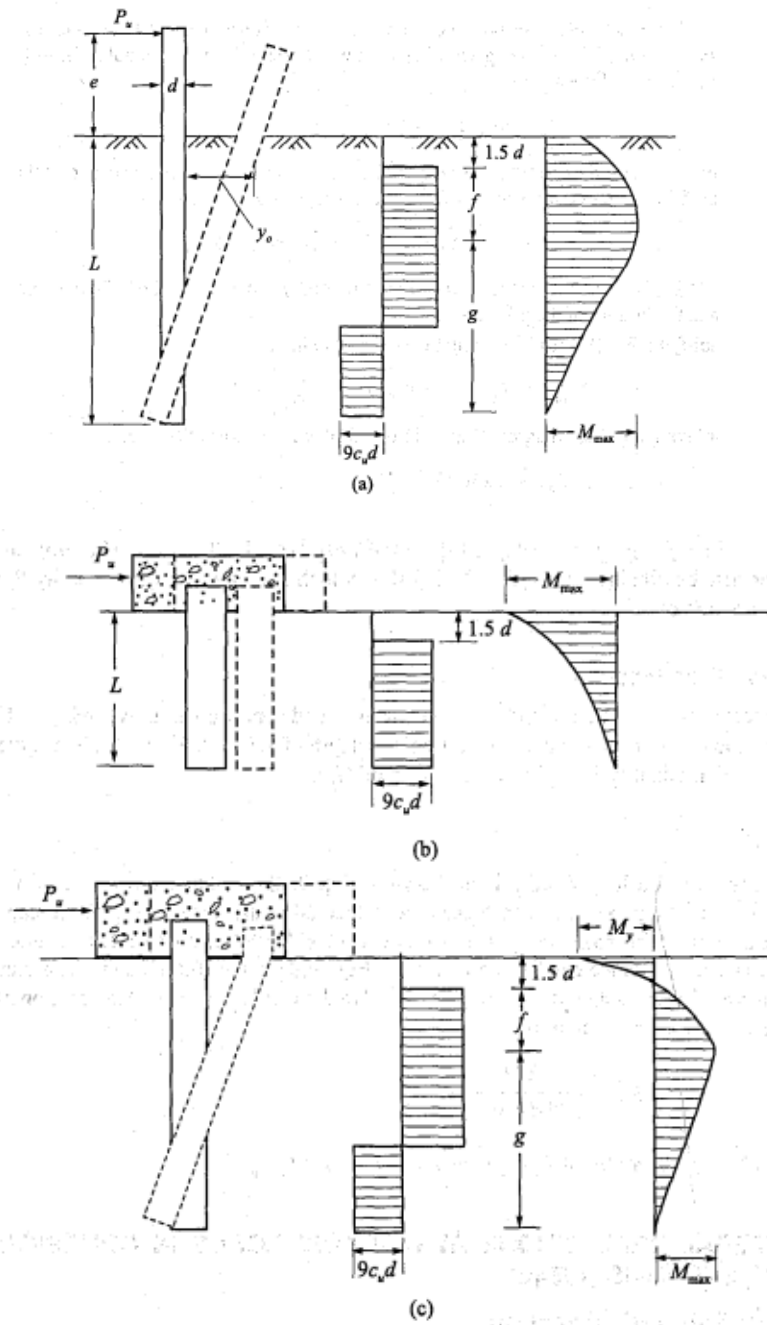
Figure 2-46 Deflection, soil reaction and bending moment distribution along short piles in cohesive. soils: (a) Short pile-free-head, (b) very short pile-fixed head, (c) intermediate length-fixed pile (Broms, 1964)

The first yield of a pile takes place near the head in the case of an intermediate pile. When the shear is zero, the equation for moment equilibrium is

$$M_{max}^+ = P_u(1.5d + 0.5f) - M_{max}^- \tag{2.80}$$

Since $L = 1.5d + f + g$, $f = P_u/9c_ud$, Eq. (2.80) can be solved for Pu.

Long Free Head Piles

Figure 2-47 illustrates the long pile's failure mechanism under the maximum lateral load condition (a). In this instance, at a depth of $(1.5d + f)$, a plastic hinge develops in the pile portion. A plot of the non-dimensional quantity P_u/c_ud^2 as a function of M_y/c_ud^3 is shown in Figure 2-48.

Long Fixed head Pile

Figure 2-47 (b) depicts the method of failure of a lengthy fixed pile. Failure occurs when two plastic hinges start to form along the stack. The first hinge is at the base of the pile cap, and the second is at the part with the greatest positive moment, which is $(1.5d+f)$ below the ground. The final lateral resistance equals

$$P_u = \frac{2M_y}{(1.5d + 0.5f)} \tag{2.81}$$

Deflection   Soil reaction   Bending moment

(a)
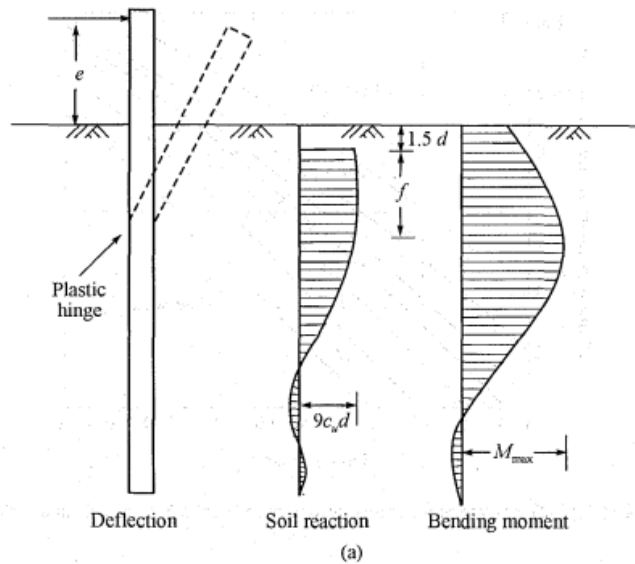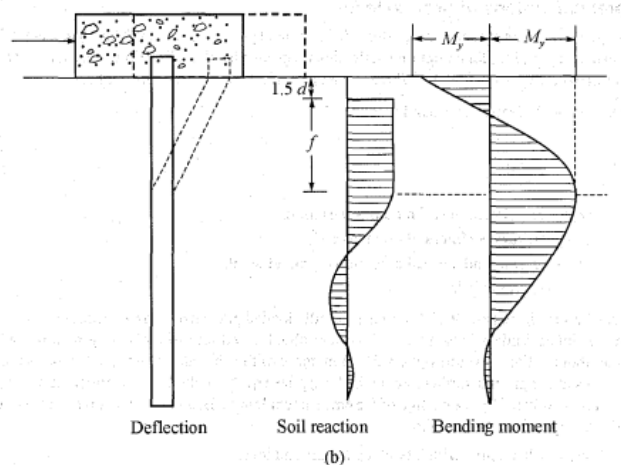
Figure 2-47 Deflection, soil reaction and bending moment distribution along piles in cohesive soils (a) Long pile-free head, (b) long piles-fixed head (Broms, 1964)
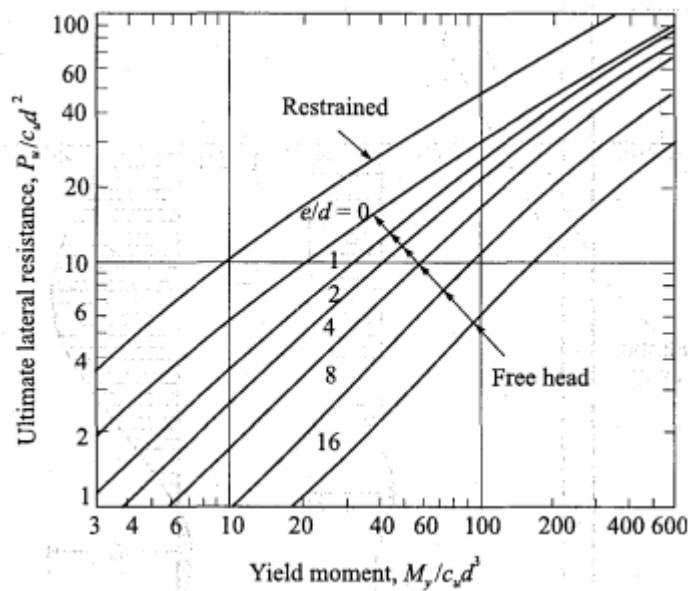
Figure 2-48 Ultimate lateral resistance of long plies in cohesive soils (Broms, 1964)

2.7.3.4 p-y Method

In the p-y technique, the soil-structure interaction is modeled using a set of nonlinear "springs". Compared to the finite element method, this is significantly easier. Although the p-y approach is less exacting than the finite element method, it has undergone considerable calibration using full scale load test results and is simpler to use because commercial software is so widely available.

Therefore, for most real-world design issues, especially those involving "long" foundations, this approach is favored.
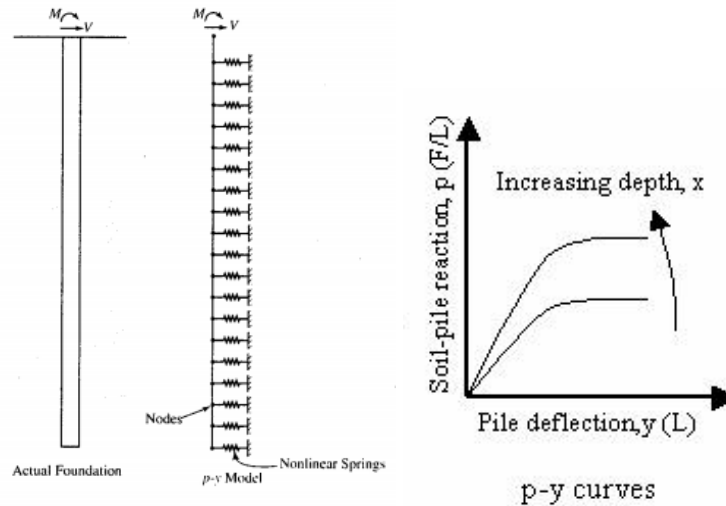
Figure 2-49 Analytical model used in the p-y method (Coduto, 2001)

With the help of a two-dimensional finite difference analysis, the p-y method models the foundation. As depicted in Figure 2-49, it divides the foundation into n intervals with a node at the end of each interval and the soil acting as a series of nonlinear "springs" situated at each node. Each interval's flexural stiffness is determined by the suitable EI, and each spring's load-deformation characteristics are determined by a p-y curve similar to those shown in Figure 2-49. Applying adequate boundary conditions is also required, as previously mentioned. The software determines a state of static equilibrium using this data and incrementally adding structural stresses. It then calculates the shear, moment, and lateral displacement at each interval.

The definition of the lateral load-deflection relationships between the foundation and the soil forms the basis of the p-y approach. These are presented as p-y curves, where p represents the lateral soil resistance per unit length of the foundation (expressed in units of force per length) and y represents the lateral deflection. The Winkler bear-on-elastic-foundation concept might initially seem to be extended nonlinearly by the p-y relationship. But there is a significant distinction between the two: The lateral soil load operating on a deep foundation is caused by compression on the leading side, shear friction on the two adjacent sides, and potentially a tiny amount of compression on the back side. The Winkler model only takes compressive forces between the foundation and the soil into

account. Therefore, even though the numerical model appears to interpret the p-y curve as a compression phenomenon only, doing so is erroneous (Smith, 1989). The ultimate side shear resistance is most likely significantly less than the ultimate compression resistance. However, since mobilizing the side shear needs much less deflection, it might contribute significantly to the total resistance at the modest deflections typically associated with working loads.

The p-y curve for a particular point on a foundation depends on factors such as soil and loading type, foundation size and shape, coefficient of friction between foundation and soil depth below the ground surface, foundation construction method and effects of group interaction. The impact of some of these parameters on p-y curves was studied analytically by Ashour and Norris (2000) using the strain wedge model. They discovered that stiffer piles produce stiffer p-y curves for homogeneous sand deposition. They also discovered that the p-y curves will differ if two piles have the same dimension but one has a circular cross section and the other a square cross section. In sand, the square pile demonstrated greater soil-pile resistance than the circular pile. Analytical research served as the foundation for Ashour and Norris' conclusions.

It has been required to create p-y curves empirically by back calculating them from full-scale load tests because the influence of these parameters is not well understood. Many of the tests carried out thus far are summarized by Reese (1984,1986), who also offers suggested p-y curves for analysis and design for different soil (Table 2-10).

Table 2-10 Recommended criteria for p-y curves in different soils (adapted from Reese, et al., 1997) (FHWA)

Soil Type and Condition	Reference
Soft clay below the water table	Matlock (1970)
Stiff clay below the water table	Reese, et al. (1975)
Stiff clay above the water table	Welch and Reese (1972), Reese and Welch (1975)
Sands	Reese, et al. (1974)
Sands	API (1993)
Soils with cohesion and friction	Evans and Duncan (1982)
Weak rock	Reese (1997)
Strong rock	Nyman (1980)

These curves and relationships are included in the p-y program. Some curves were found ductile whereas some were found brittle as shown as Curve A and Curve B in Figure 2-50 In some clays, especially those that are stiff or when loading is recurrent or dynamic, brittle curves can develop. Sands and soft clays appear to have ductile curves under static loading. Because they have the potential to produce significant foundation shifts, brittle curves may be more problematic.
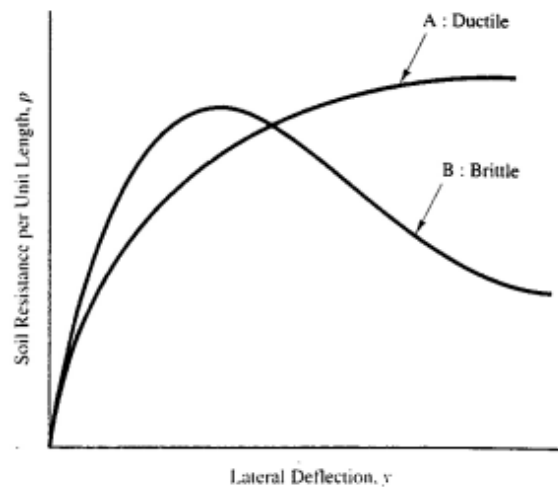
Figure 2-50 Typical p-y curves. (Coduto, 2001)

CLAY

The following stages can be used to describe the p-y curves technique for cohesive soils:

1. obtaining the most accurate estimation of the change of the shear strength (c), submerged unit weight (γ'), and strain equal to half of the highest primary stress difference (ε_{50}). In the absence of stress-strain curves, typical values of ε_{50} are provided in Table 2-11 for comparison.
2. calculating the pile's length in terms of the ultimate soil resistance (P_u).
3. calculating the deflection at other locations on the curve, such as y_{50}, the point where the soil resistance is half its maximum.

Table 2-11 Typical values for ε_{50} related to the undrained shear strength

Undrained Shear strength, c_u [kN/m2]	ε_{50} [-]
<12	0.02
12-24	0.02
24-48	0.01
48-96	0.006
96-192	0.005
>192	0.004

Matlock et al. (1970)

Full-scale lateral tests were performed by Matlock (1970) on steel piles with a diameter of 0.3 m that were buried in a soft clay deposit at Lake Austin, Texas. A parabolic p-y curve shape with an initial theoretical tangent modulus that is infinite at zero deflection was proposed by Matlock in 1970. Soil strain, ε, was employed to generate the initial tangent p-y stiffness. The depth and diameter have a significant impact on the p-y curve's maximum capacity, p_u. The proposed formulation for soft clays in the presence of free water is as follows:

$$p = 0.5 p_u \left(\frac{y}{y_{50}} \right)^{\frac{1}{3}}, y < 8 y_{50} \qquad (2.94)$$

$$p = p_u, y > 8 y_{50} \qquad (2.95)$$

$$with \quad p_{uz} = min \left[\left(3 + \frac{\gamma'}{c_{uz}} + \frac{J}{b} z \right) c_z b, 9 c_{uz} b \right]$$

$$with \quad y_{50} = 2.5 \varepsilon_{50} b$$
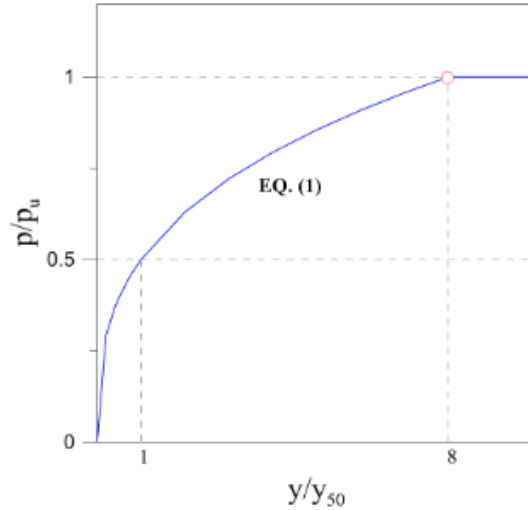
Figure 2-51 P-y curves for clay: Matlock et al. (1970).

Reese et al. (1975)

In order to depict the behavior of stiff clays in the presence of free water, Reese et al. (1975) suggested a p-y curve formulation. After performing lateral load testing on two 0.6 m diameter steel piles embedded in hard clay below the water table near Manor, Texas, this methodology was created. The proposed curves are divided into five parts (Eq. 2.97), and Figure 2-52 shows their shape. Kpy, the starting stiffness of the initial straight line (Eq. 2.98), is determined by the coefficient of variation in the subgrade modulus with depth (FL^{-3}). The initial stiffness can be assumed to be independent of pile diameter, b once it has been multiplied by depth z. This presumption is only true for deflections smaller than 0.02 inches. The secant stiffness will rely on the initial tangent modulus and both p_u and diameter for all non-zero deflection values (Eq. 2.96).

Eqs. 2.97 and Eqs. 2.98 provide the final soil resistance p_u and y_{50}:

$$p_u = min[(2c_a b + \gamma' bz + 2.83 c_a z), 11cb] \tag{2.96}$$

$$y_{50} = \varepsilon_{50} b \tag{2.97}$$

Reese et al.'s p-y curve is composed by five parts, given by the following equations. The initial straight line is given by:

$$p = (k_{py} z) y \tag{2.98}$$

with the initial stiffness, K_{py}, depending on c_{uz} (Table 2-12).

83

Table 2-12 Initial stiffness, K_{py}, according to Reese et al. (1975).

	Average undrained shear strength, ca [kPa]		
	50-100	**200-300**	**300-400**
Kpy(static) [MN/m3]	135	270	540
Kpy(static) [MN/m3]	55	110	540

The straight line is followed by two parabolic portions, given by:

$$p = 0.5p_u \left(\frac{y}{y_{50}}\right)^{\frac{1}{2}} \qquad (2.99)$$

$$p = 0.5p_u \left(\frac{y}{y_{50}}\right)^{\frac{1}{2}} - 0.055p_u \left(\frac{y - A_s y_{50}}{A_s y_{50}}\right)^{\frac{5}{4}} \qquad (2.100)$$

The two final straight lines are given by:

$$p = 0.5p_u (6A_s)^{\frac{1}{2}} - 0.411p_u - \frac{0.0625}{y_{50}} p_u (y - 6A_s y_{50}) \qquad (2.101)$$

$$p = p_u [1.225(A_s)^{\frac{1}{2}} - 0.75A_s - 0.411] \qquad (2.102)$$

As is dimensionless parameter used in static loading and function of the depth and pile diameter.
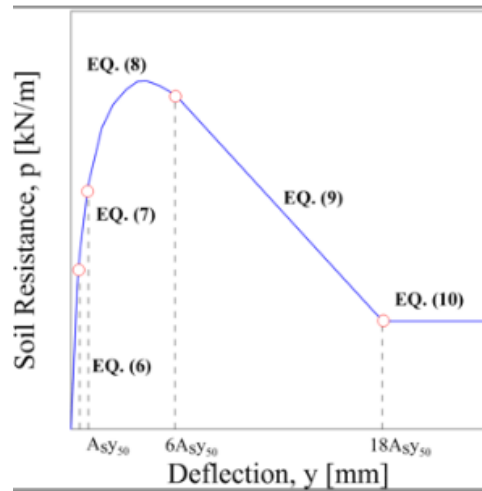
Figure 2-52 P-y curves for clay: Reese et al. (1975).

<u>Reese & Welch (1972)</u>

After performing lateral load experiments on a 0.76-m diameter bored pile in Houston, Texas, Reese and Welch (1972) developed a p-y curve formulation for stiff clays with no free water. Due to the usage of the fourth degree of the parabolic relationship between p and y, which is as follows, the curves in Figure 2-53 have the same shape as those in Matlock (1970) but are stiffer:

$$p = 0.5p_u \left(\frac{y}{y_{50}}\right)^{\frac{1}{4}} \hspace{3cm} (2.103)$$

Beyond y = 16y_{50}, the value of p/p_u remains constant.
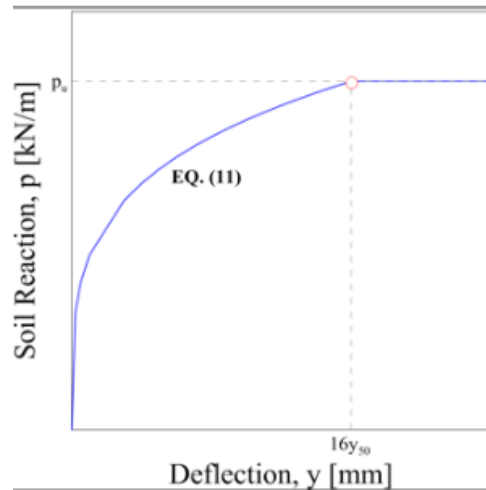
Figure 2-53 P-y curves for clay: Reese and Welch (1972).

SAND

<u>Reese, Cox and Koop (1974)</u>

After conducting tests at Mustang Island on two 0.6-m diameter piles embedded in a deposit of submerged, dense, fine sand, Reese, Cox, and Koop (1974) developed the sand p-y curve method. As shown in Figure 2-54, the p-y curve's distinctive shape can be described by three sections of straight lines and a parabolic curve.

The process is for both cyclic and short-term static loads. The smallest answers to the two following equations provide the ultimate soil resistance:

$$p_{u1} = \gamma z \left[\frac{K_0 z \tan \varphi \sin \beta}{\tan(\beta - \varphi) \cos \alpha_s} + \frac{\tan \beta}{\tan(\beta - \varphi)} (b + z \tan \beta \tan \alpha_s) + K_0 z \tan \beta (\tan \varphi \sin \beta - \tan \alpha_s) - K_a b \right] \qquad (2.104)$$

$$p_{u2} = K_a b \gamma z \tan^3(\beta - 1) + K_0 b \gamma z \tan \varphi \tan^4 \beta \qquad (2.105)$$

The p-y curve is composed by four parts: an initial straight line (13), a parabolic portion (14), and a final straight line (15):

$$p = K_{py} z y \qquad (2.106)$$

A$_s$ and B$_s$ are dimensionless parameters that depend on the pile diameter and depth when static loading is applied.

Table 2-13 Initial stiffness, Kpy, according to Reese, Cox and Koop 1974.

	Loose (f<30°)	Medium (30≤f<36°)	Dense (f≥36°)
K$_{py}$ (below water table) [MN/m³]	5.4	16.3	34
K$_{py}$ (above water table) [MN/m³]	6.8	24.4	61

$$p = C y^{1/n} \qquad (2.107)$$

$$m = \frac{p_u - p_m}{y_u - y_m}; \quad n = \frac{p_m}{m y_m}; \quad C = \frac{p_m}{y_m^{1/n}} \qquad (2.108)$$

With

$$p_{ms} = B_s p_u \qquad (2.109)$$

$$p_{us} = A_s p_u \qquad (2.110)$$

The value of p remains constant after $y = \frac{3b}{80}$
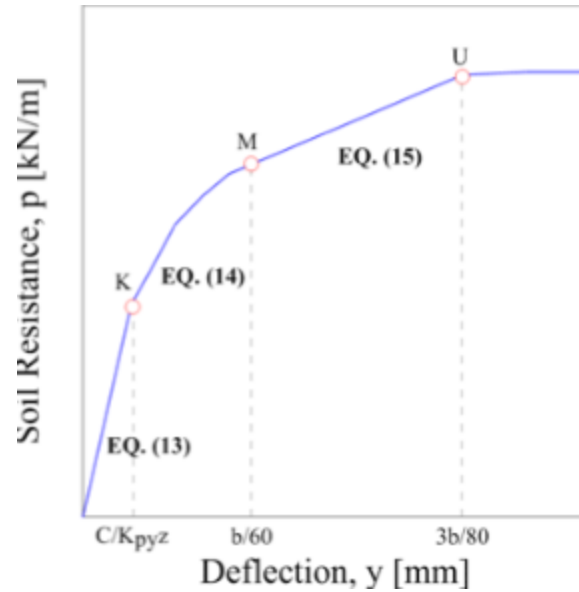
Figure 2-54 P-y curves for sand: Reese, Koop and Cox (1974).

O'Neill and Murchinson (1983)

To simplify the original Reese's approach without making significant changes, O'Neill and Murchinson (1983) conducted a study for sand in tandem to the study of O'Neill and Gazioglu (1984) in clay (Lam, 2009). The initial parabolic curve's shape was changed to a hyperbolic one as the single modification. The initial tangent stiffness and the eventual capacity in the hyperbolic curve are the only other differences between the two approaches. The use of three coefficients C1, C2, and C3 as a function of the friction angle further reduced the complex equations for calculating the final soil pressure (Eq. 2.111).

The proposed p-y curve parameterization is as follows:

$$p = Ap_u \tanh\left(\frac{k_{py\,max}\,z}{Ap_u}y\right) \qquad (2.111)$$

$$p_u = \min[(C_1 z + C_2 b)\gamma z, C_1 c\gamma z] \qquad (2.112)$$

With C_1, C_2, C_3 = dimensionless coefficients related to f; kpy is determined as function of f.

SILT

There are no generally accepted advice on how to build p-y curves for soil with cohesion and friction angle. In design, earth is typically divided into one of two categories: cohesive or

cohesionless. In reality, this simplification results in a very conservative design for silt or cemented soil that never takes into account the soil resistance from the cohesiveness component (Juirnarongrit et al. 2005).

The method outlined below was suggested by Evans and Duncan (1982) for creating p-y curves in silty soils. What determines the ultimate soil resistance is:

$$p_u = A_s p_{u\varphi} + p_{uc} \qquad (2.113)$$

The smallest of (12) is with puf, while the smallest of is with $p_{u}c$ (1). Reese, Koop, and Cox are the authors of the dimensionless parameter, As (1974). An initial straight line (21), a parabolic section (14), and two straight lines make up this p-y curve.

Beyond $y = \frac{3b}{80}$ the value of p doesn't change.

$$p = K_{py} z y \qquad (2.114)$$

With: $K_{py} = k_c + k_\varphi$ where K_c and K_f are respectively functions of c_{uz} and f.
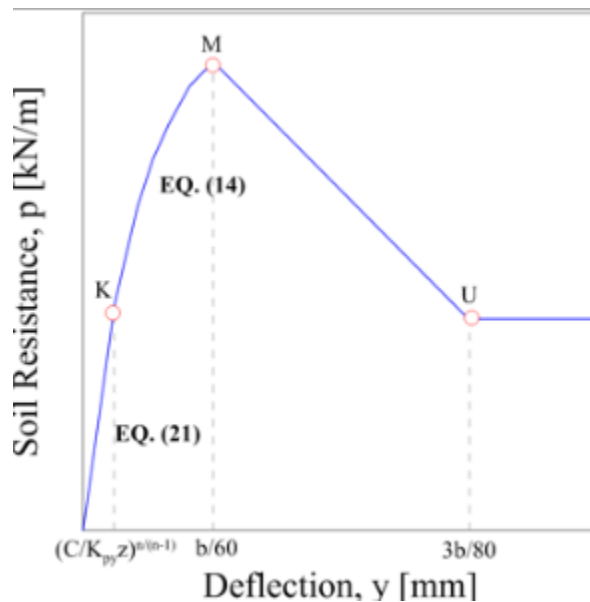
Figure 2-55. C-f model's p-y curve.

2.8   Instrumentation for Load Test

To evaluate the strain distribution within the foundation element, strain gauges are frequently employed in deep foundation load tests. In order to evaluate the resistance of distinct soil strata,

data from gauges installed at discrete depths, frequently an average of many gauges positioned around the reinforcing steel cage perimeter, are converted to force. Several gauges are often placed at each of several distinct depths. To calculate force dissipation into the soil, the gauges at each depth are averaged, the average is transformed into a force, and the forces at different depths are distinguished.

Sinnreich (2020) explains how the horizontal arrangement of gauges can be improved to obtain high statistical reliability while ensuring the findings reflect the average axial strain through a simple error analysis. This outcome enables the vertical arrangement to be optimized, lowering the number of redundant gauge levels in any given soil stratum while preserving the accuracy of the data collection required for design. The author emphasized in maintaining gauges in the lowest level, levels closest to the interfaces between soil strata, and a few intermediate levels.
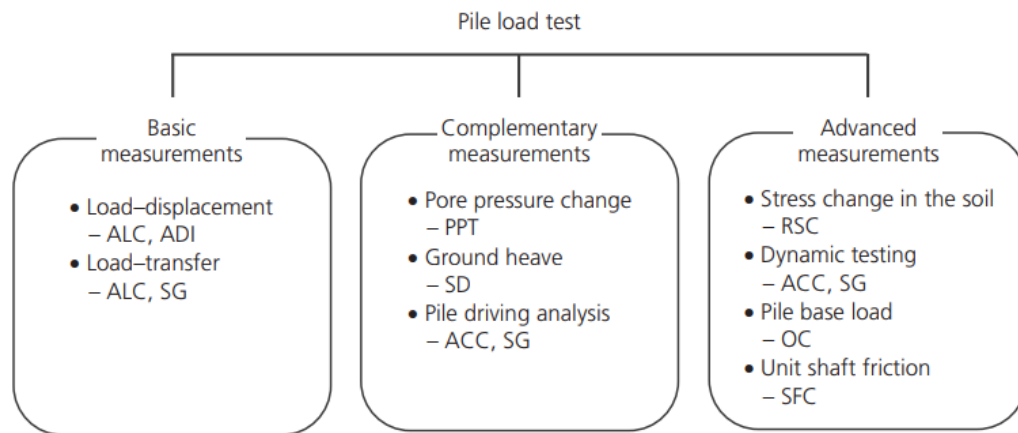
Figure 2-56 Measurements and instruments in pile load test programs (ALC: axial load cell; ADI: axial displacement instrument; SG: strain gauge; PPT: pore pressure transducer; SD: surveying device; ACC: accelerometer; RSC: radial stress cell; OC: Osterberg cell; SFC: shaft friction cell)

An effort was made by Bica et al. (2014) to record instrumentation procedures that may be utilized to plan a load testing program. On instrumented full-scale piles, axial load experiments have been carried out primarily to establish the correlations between loads and settlement and loads and transfer, as well as to compare measured data with equivalent values anticipated by pile design methods. The steps necessary for successful pile instrumentation and data collection are described in detail in this study, together with the findings of four top-notch instrumented pile load tests

carried out on steel piles driven in a mixed soil profile. The measures and tools frequently employed in pile load test procedures are summarized in Figure 2-56.

Twenty-four vibrating-wire strain gauges (Geokon Model 4150) were attached to the outside of the two flanges of the H pile, at 12 levels. Thirty-two vibrating-wire strain gauges (also Geokon Model 4150) were attached to the outer surface of the pipe pile, at 16 levels. All gauges were spot-welded to the pile surface, covered with a semicircular plate, and sealed with silicone rubber. Both test piles were fabricated in two segments for ease of instrument attachment, transportation, and lifting. After the lower pile segment was driven into the ground, the strain gauge cables were identified and rewired at the pile junction, then inserted into the angle channel of the upper pile segment. The upper pile segment was lifted, aligned with the lower segment, and butt-welded to its top before being driven to its final depth. All gauge cables were connected to a field data logger (Geokon Micro-10, model 8020) through three multiplexers (Geokon model 8032). The measurement and data acquisition system were protected against environmental conditions and lightning damage. The pile instrumentation layout provided a dense array of strain gauges, offering redundancy for potential gauge losses during pile driving. Driving and load testing did not damage four strain gauges.

(a)   (b)
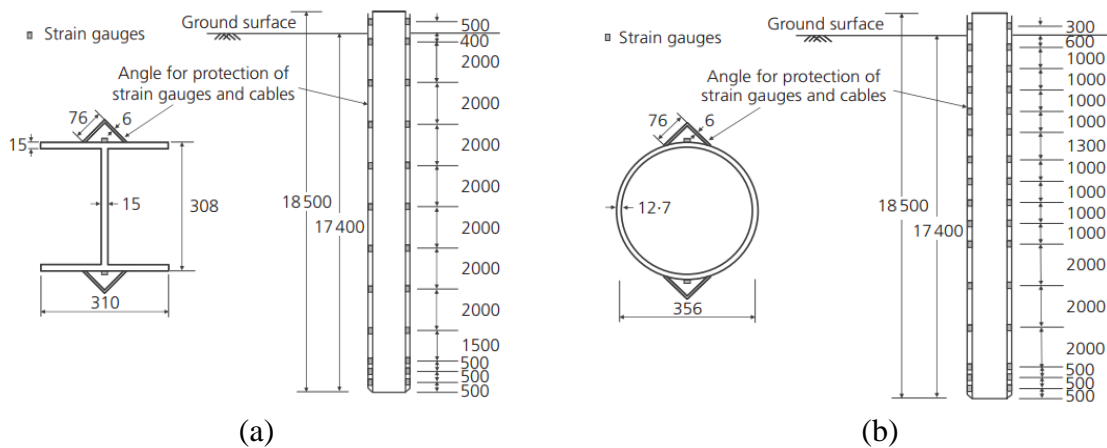
Figure 2-57 . Instrumentation details: (a) H pile; (b) closed-ended pipe pile (dimensions in mm) (Bica et al., 2014)

2.9   Numerical Study Using Finite Element Modeling

Researchers have used numerical analysis with Finite Element Modeling (FEM) to assess the field behavior of a number of geotechnical structures. It offers a foundation for assessing the

90

performance of structures using stringent and complex numerical calculations. Calibration of the model to match the field behavior in terms of deformation is typically the initial step in such studies. The field performance is then assessed in further detail through additional analysis and parametric analyses. The geotechnical engineering sector frequently uses the finite element method (FEM) program like PLAXIS 2D, PLAXIS 3D, ABAQUS to numerically analyze deformation, stability, and groundwater flow (Gupta 2023; Gupta et al. 2023; Islam et al. 2022).

2.9.1 Single Pile Response

In the experimental study presented by Anagnostopoulos and Georgiadis, the authors investigated the interaction of axial and lateral responses of piles in clay. In the study, a soft laboratory-prepared clay bed was tested six times with closed-ended aluminum piles (19 mm outer diameter, 1.5 mm wall thickness). The aim was to investigate interactions between axial and lateral loads and their effects on pile displacements and stresses. Displacement transducers and strain gauges were used to measure vertical, horizontal, and rotational displacements as well as axial forces and bending moments along the pile's length. The research found that lateral loads significantly increased pile settlement, and the magnitude of the lateral force determined pile head settlement. Axial loading had a negligible impact on lateral pile displacements. Additionally, the study conducted a 2D finite-element analysis, which confirmed that increased load inclination led to greater pile settling due to the same vertical load. At low vertical load levels with linearly elastic soil behavior, the presence of a lateral load had no effect on axial displacements.

| (a) | (b) |
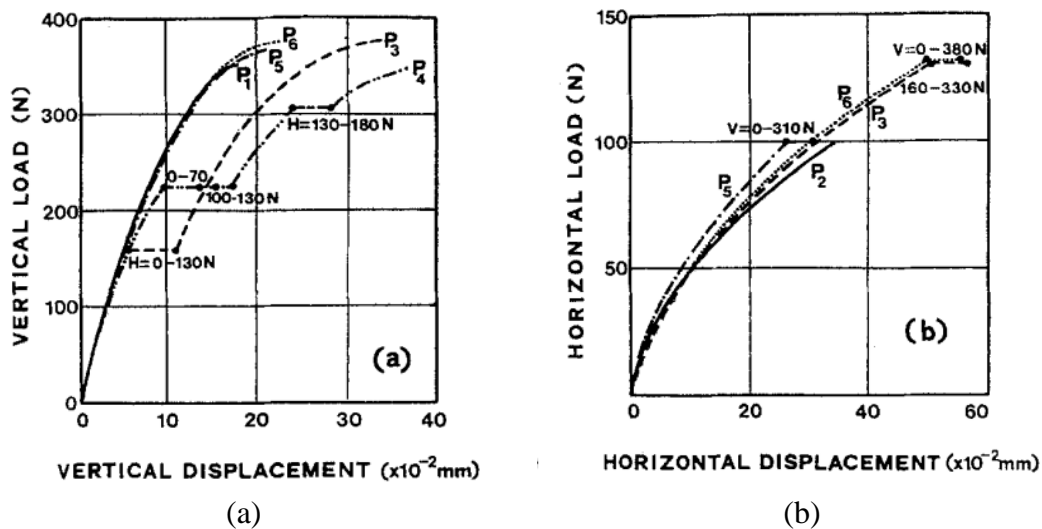
Figure 2-58 Experimental axial and lateral pile head displacements
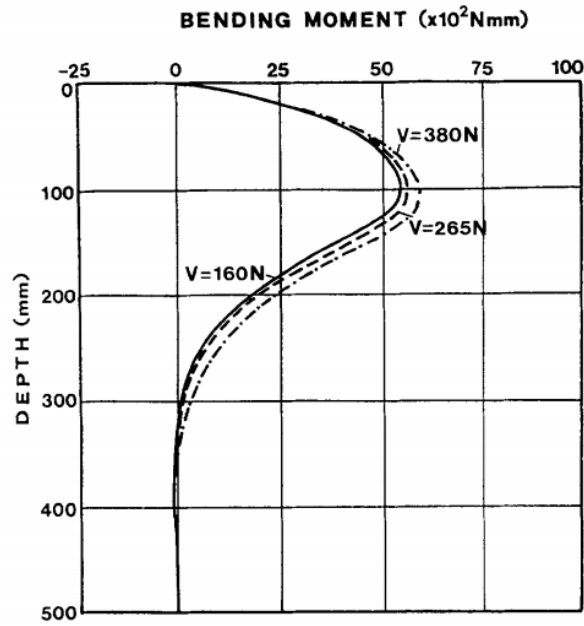
Figure 2-59 Variation of bending moment along pile for H = 130 N
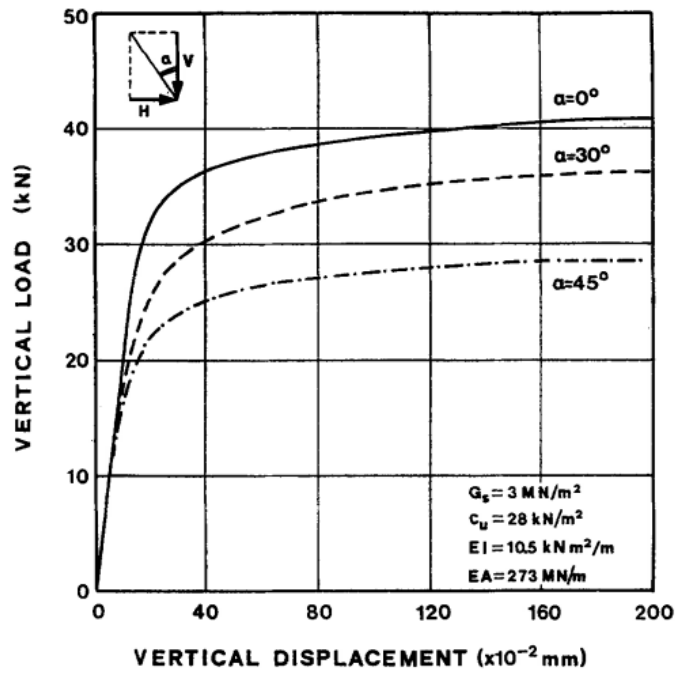
Figure 2-60 Axial load versus settlement relationships from 2D FE analysis

2.9.2 Analyses of Group Efficiency of Pile

In granular soils, Tuan (2016) introduced a novel technique for group efficiency analysis of frictional piles. This approach is based on taking into account both the bearing capacity of the

92

block dimension at the points and the shear around the perimeter of the group indicated by the plan dimensions. The newly developed theoretical analysis, which is comparable to the analysis put forth by Sayed and Bakeer for the examination of group efficiency of granular soil, particularly sand soil, has been provided. The suggested formula has an advantage over Sayed and Bakeer's (1992) method in that it is straightforward to find the solution to the equations that have been developed and does not require the use of experimental values to find the solution to an unknown parameter. The equation demonstrates how much frictional resistance and pile point resistance affect group efficiency. The equation also demonstrates that group effectiveness is increased by pile cap rigidity. The group-reduction factor proposed by the author is as follows:

$$\eta = \frac{\eta_f + \eta_p}{2} = \frac{1}{2}\left[\frac{2(n_1 + n_2 - 2)s + 4D}{pn_1 n_2} + \eta_p\right] \tag{2.115}$$

Hence,

$$Q_{g(u)} = \eta \sum Q_u = \frac{1}{2}\left[\frac{2(n_1 + n_2 - 2)s + 4D}{pn_1 n_2} + \eta_p\right]\sum Q_u \tag{2.116}$$

Where,

η_p = group efficiency at point pile

η_f = group efficiency as block pile
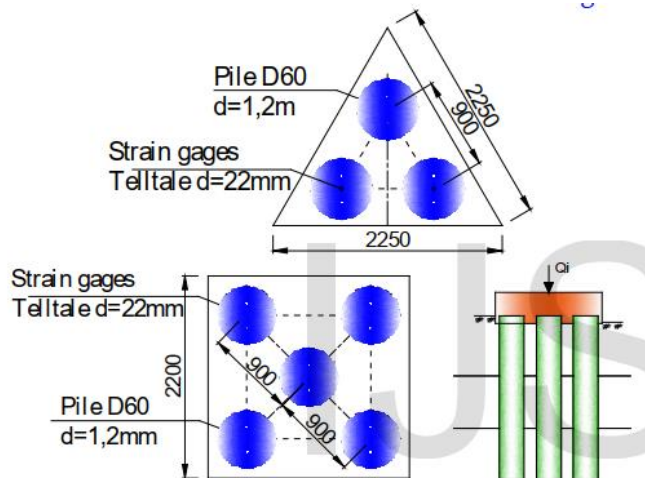
Figure 2-61 Model of pile group for full-scale field test and numerical model

This investigation used the quick Lagrangian analysis continue (PLAXIS 3D) version 2.1 using a 3D finite difference approach. A single model, a model of group 3 piles, and a model of group 5 piles are chosen in the project to investigate in the study to be evaluated and calibrated for the numerical model in Figure 2-61. Upon the completion of large-scale field tests for three models to check and assess if the numerical analytical technique agreed with the practical outcomes, it was also put to use. Figure 2-62 depicts the comparison of the calibration numerical model's findings with full-scale field experiments. For all three models, there is an excellent match between the measured and computed values; the differences are only about 5%−7% for single piles, 8%−11% for group 3 piles, and 6%−9% for group 5 piles. Additionally, the measured and calculated values practically cross at the same location at the position of 5%D=30mm (D is the diameter of the pile).
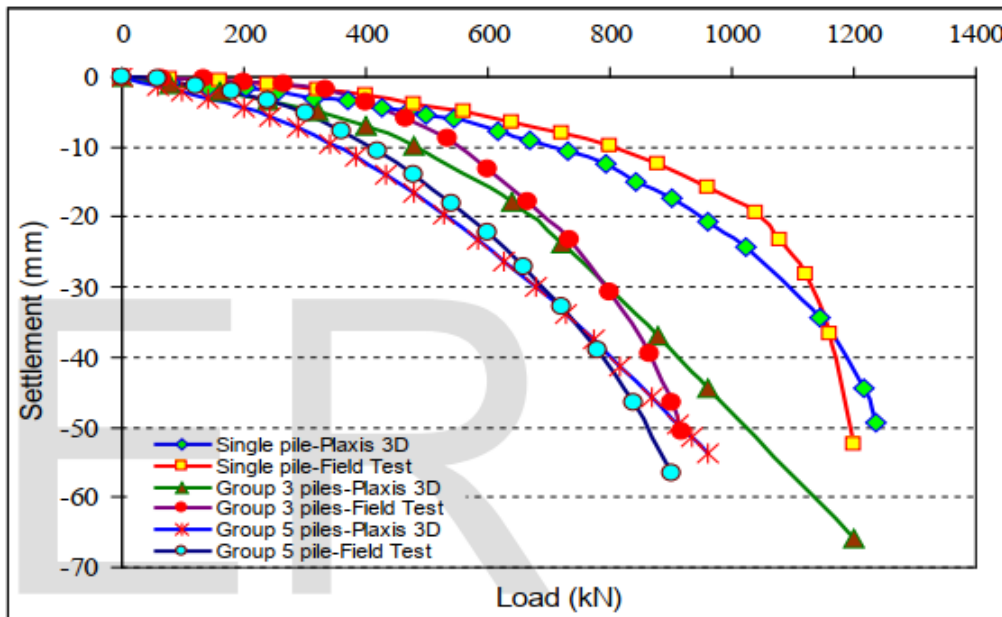
Figure 2-62 The results of calibration numerical model with full scale field test

This demonstrated that the numerical calibration model had produced a good match, and from this, an analysis for the model of group 9 piles with variable pile spacing from 1.5D to 8D was developed. Figure 2-63 (a) and (b) show the outcomes of the numerical analysis for group 9 piles. The settlement of pile groups, as can be shown, is significantly smaller than the settlement of a single pile. This can be explained by how group effectiveness plays a role. Equation (2.117), which

$$\eta = \frac{Q_{g(u)}}{\sum Q_u} = \frac{Q_{g(u)}}{n(Q_{s(u)})} \qquad (2.117)$$

was used in this study to determine group efficiency. $Q_g(u)$ and $Q_s(u)$ are found at the positions where the settlement reaches a value of 5%D and 5%D, respectively. Figure 2-63 also show that the value of settlement in model without pile cap is significantly higher than the model with pile cap (by about 14 to 20%). This demonstrated how the structural loads will be distributed among the different piles depending on how stiff the pile cap is. To significantly affect the stiffness of the foundation, the thickness of the pile cap must be at least four times the width of each individual pile. As is typically the case for enormous concrete caps, a rigid cap can be assumed if the cap's stiffness is 10 or more times greater than the stiffness of the individual piles.

(a)   (b)
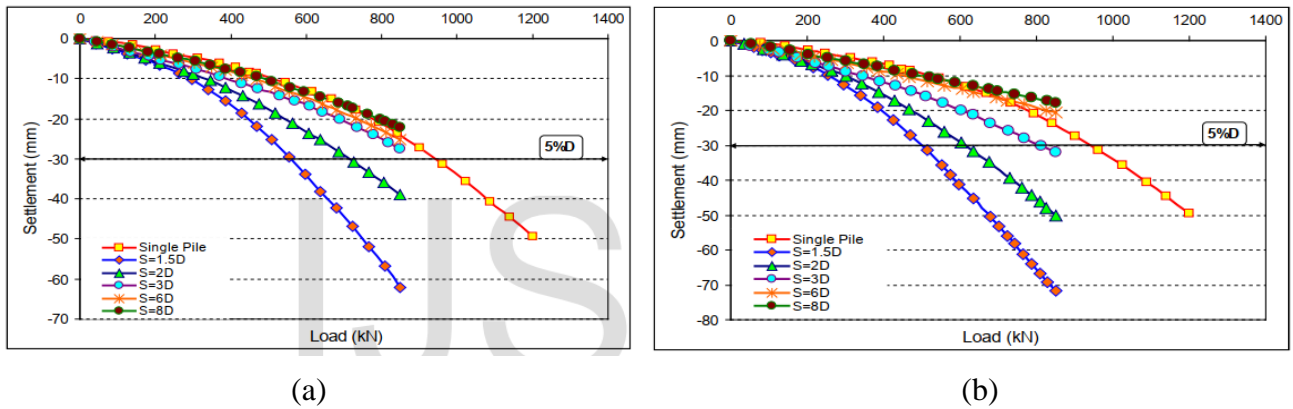
Figure 2-63 The results of analysis for group of 9 piles with different ratio s/D (a) with pile cap;

(b) without pile cap

The group's geometry and the design criteria used for comparison of group efficiency are the same as those previously utilized. The piles are spaced 3D apart from one another for ease of calculation, and groups of 9 piles are used. In Table 2-14, the outcomes from a number of existing design equations are compared to the outcomes of the current approach.

Table 2-14 Comparison of results from theoretical solution, numerical analysis, and other

formulae

	Group size	s/D=1.5	s/D=2.0	s/D=3.0	s/D=5.0	s/D=6.0	s/D=8.0
Present method	3x3	0.570	0.654		**0.875**	1.0	1.0
Numerical analysis	3x3	0.585	0.747	**0.82**	0.913	0.982	1.0

95

	Group size	s/D=1.5	s/D=2.0	s/D=3.0	s/D=5.0	s/D=6.0	s/D=8.0
Converse-Labarre formula	3x3	0.50	0.606	0.727	0.832	0.86	0.894
Sayed and Bakeer formula	3x3	0.582	0.662	**0.816**	**0.889**	0.964	1.0
Zhong Zhao, H.K. Stolar ski	3x3	0.60	0.72	**0.85**	1.0	1.0	1.0
Brown and Reese	3x3	-	-	0.75	-	-	-
Morrison and Reese	3x3	-	-	0.77	-	-	-
Shibata et.al	3x3	-	-	**0.818**	1.0	-	-
Ruesta and Townsend	3x3	-	-	**0.80**	-	-	-

The results of the current formula are in good accordance with those of Sayed and Bakeer and Shibata et al. when compared to current design formulae. It appears that the Converse-Labarre formula undervalues the effectiveness of the group. As a result, the Converse-Labarre calculation understates the pile groups' ability to support loads.

2.9.3 Behavior of Pile Under Lateral Loadings

The study by Abbas et al. (2008) presents the findings of the 3D finite element analysis on the behavior of a single pile under lateral loadings. The study included full-scale pile load tests to validate a finite element model of the geotechnical structure. It investigated the effects of pile shape, cross-section (circular and square), and the slenderness ratio (L/D). The piles were modeled with linear elastic theory, and the soil was simulated using the Mohr-Coulomb model, with pile-soil interaction components. Eight main models were tested, divided equally between square and circular cross-sections, with loads ranging from 50 kN to 400 kN. The results showed a strong correlation between experiments and analyses, as depicted in Figure 2-64.
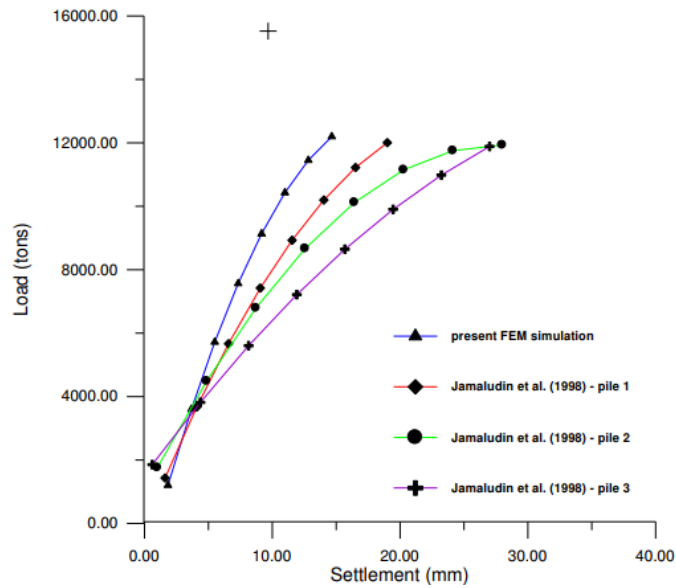
Figure 2-64 Comparison of finite element results with field test data of Jamaludin, 1998 (Abbas et al., 2008)
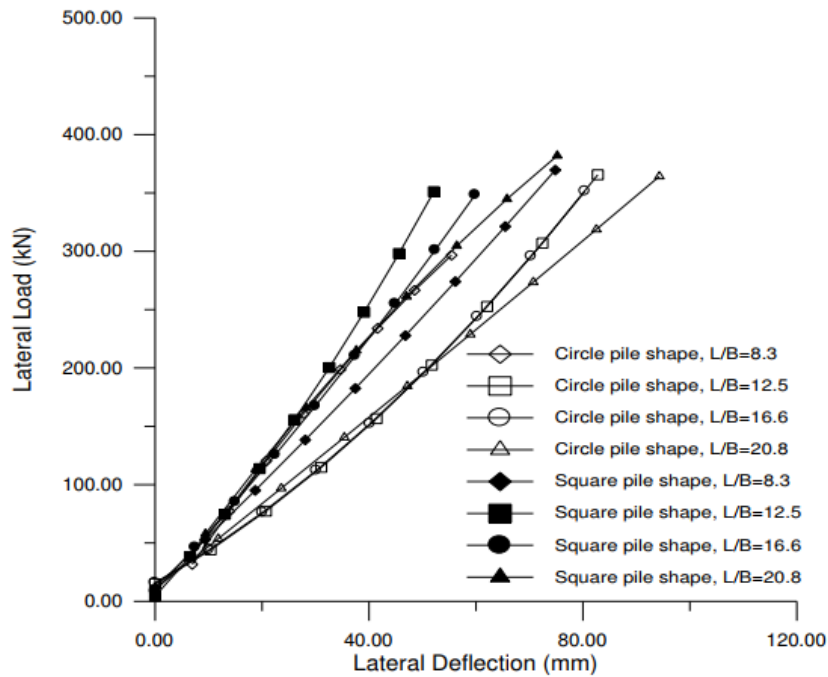
Figure 2-65 Comparison of square and circle pile shape in the lateral load – deflection curve (Abbas et al)

The study found that the pile's response was influenced by the load magnitude, pile cross-section shape, and slenderness ratio. For both square and circular piles, a 50% increase in load led to nearly 60% more pile deflection. Figure 2-65 compared the lateral load-deflection curve for circular and square piles, demonstrating that square piles exhibited less tip deflection than circular ones under the same load intensity.

The impact of the pile slenderness ratio (L/D) on pile deformation due to lateral load is shown in Figure 2-66. Short piles (L/D = 8.3) exhibited less lateral tip deflection for the same load compared to piles with higher slenderness ratios. In the case of short piles, the point of inflection was located 1/5 from the base, while in long piles (L/D = 16.7, 20.8), it was positioned 3/5 from the base. The pile body also tended to rotate around the inflection point and produce slight negative deflection near the pile base, depending on the load and slenderness ratio.
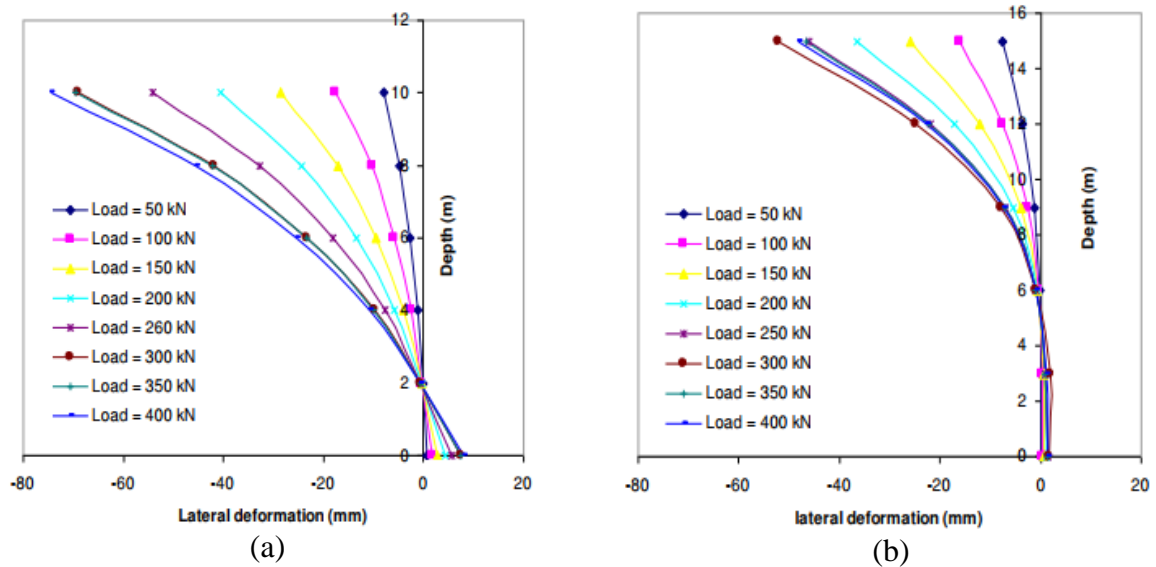
Figure 2-66 Lateral deformation of single pile along the depth of square cross section: (a) L/D=8.3, (b) L/D=12.5 (Abbas et al., 2008)

A study by the Federal Highway Administration examined the findings of the three test piles' lateral load tests at the Route 351 Bridge project and compared them to the measured responses. This study utilized the p-y technique and the computer tool LPILE Plus 4.0M (2000) for its analyses. LPILE Plus 4.0M employs nonlinear p-y curves to model the soil and a finite difference approach to solve the differential problem. The program allows for the computation of pile

response while considering user-specified nonlinear pile flexural stiffness, Ep Ip. It provides default p-y curves for various soil types, or users can input p-y curves generated using different formulations. In this study, the piles were divided into 300 elements for analysis, which is the maximum number of increments permitted by the LPILE 4.0M program.

At the test site, silty sands made up the majority of the soil types. In order to represent these soils, the default p-y curves suggested by Reese et al. (1974) were chosen. At the test site's north and south ends, manufactured infill was present, with average thicknesses of about 1 meter (3.3 feet) and 1.8 meters (5.9 feet), respectively, forming the topmost soil layer. As most of the fill materials were situated in pits approximately 1.0 meter (3.3 feet) deep for all three test piles (pre-stressed concrete, FRP, and plastic), it was assumed they had been removed. Therefore, the p-y analyses were conducted using a soil model primarily consisting of silty sands. It should be noted that the clayey fill layer at the southern end extended about 0.9 meters (2.9 feet) beyond the bottom of the pit for the pre-stressed concrete pile. In the LPILE model for the south-side test pile, this remaining fill was not explicitly included; instead, it was considered to be part of the underlying silty sand deposit. Given the limited thickness of the polymeric clay fill layer, sand and silt content, and other factors, this approximation was deemed credible.

Table 2-15 Parameters used to define default p-y curves in LPILE for the piles.

Parameter	Loose Sand	Medium-Dense Sand
Default p-y curve	Reese, et al., 1974	Reese, et al., 1974
γ'**, Submerged unit weight (kN/m³)**	10	11
c, Cohesion (kPa)	0	0
σ**, Friction angle (degrees)**	33	35

The two layers of sand utilized to build the LPILE model for the piles were an upper layer of loose to medium-dense sand and a lower layer of medium to dense sand. The initial p-y modulus and the sand's friction angle serve as the key input data points for defining these curves. It seemed appropriate to model the initial p-y modulus for sands as growing linearly with depth (Reese, et al., 1974). After obtaining the best fit between the LPILE results and the field measurements, the

rate of growth of the p-y modulus was chosen. Table 2-15 lists the p-y parameters that produced the best match.

The estimated pile lateral deflections and head rotations at the ground surface using the LPILE soil model align well with the field observations. When assuming constant pile flexural stiffness, the predicted values for pile head rotation and lateral deflection are generally close to the measurements. However, under large lateral loads (> 200 kN or 45,000 lbf), the projected deflections with constant pile flexural stiffness are approximately 7% lower than the measured deflections at the pile. This can be attributed to the prestressed pile's flexural stiffness being roughly constant up to a moment of about 400 kN-m (295,028 lbf-ft), after which the flexural stiffness decreases linearly with increasing moment. The pile head rotations exhibit a similar trend.

For the FRP pile, lateral deflections and pile head rotations were calculated at the ground surface using the provided p-y curves to simulate the soil, and the results are shown in Figure 2-67. The predicted values for lateral deflection and pile head rotation are in good agreement with the field measurements at the ground surface. However, when considering constant pile flexural stiffness, under large lateral loads (> 150 kN or 33,750 lbf), the projected deflections are about 30% lower than the actual deflections, although they are closer at lower lateral loads. This is due to the FRP pile's flexural stiffness remaining roughly constant up to a moment of approximately 200 kN-m (147,514 lbf-ft), beyond which the flexural stiffness decreases linearly with the applied moment. The pile head rotations exhibit a similar pattern of behavior.

The computed lateral deflections and plastic pile head rotations at the ground surface using the LPILE soil model, as shown in Figure 2-68, are in good agreement with field measurements. The results for this pile are consistent whether considering variable or constant flexural stiffness, which is reasonable because the majority of the plastic pile's flexural stiffness is contributed by the steel rebar cage. As a result, the flexural stiffness for this pile remains roughly constant up to a moment of about 650 kN-m (479,421 lbf-ft), which was not exceeded during the field load testing.
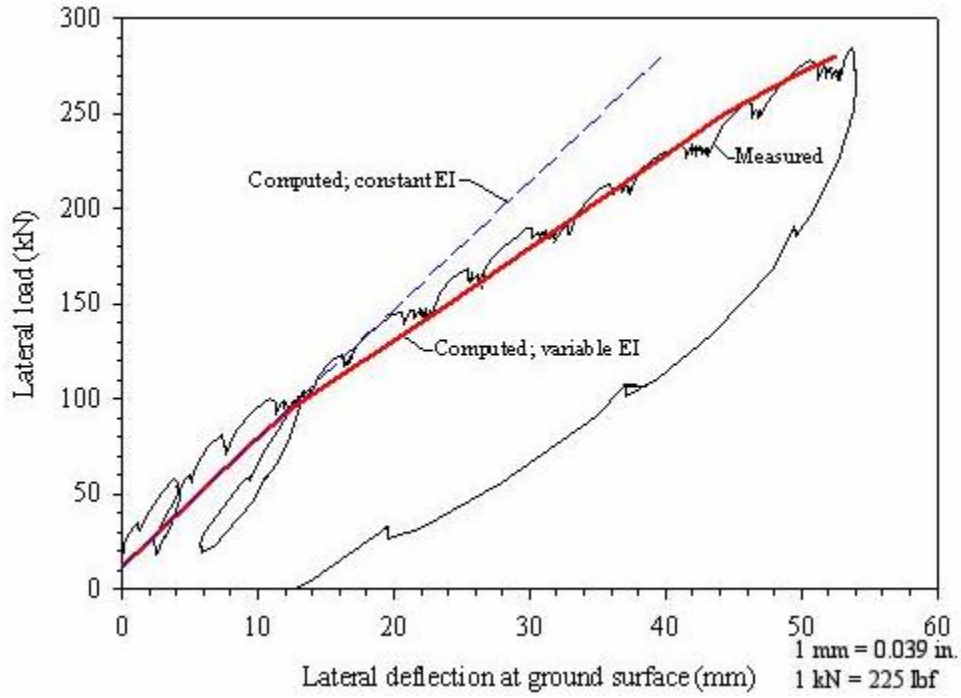
Figure 2-67 Calculated load-deflection curve for the FRP pile.
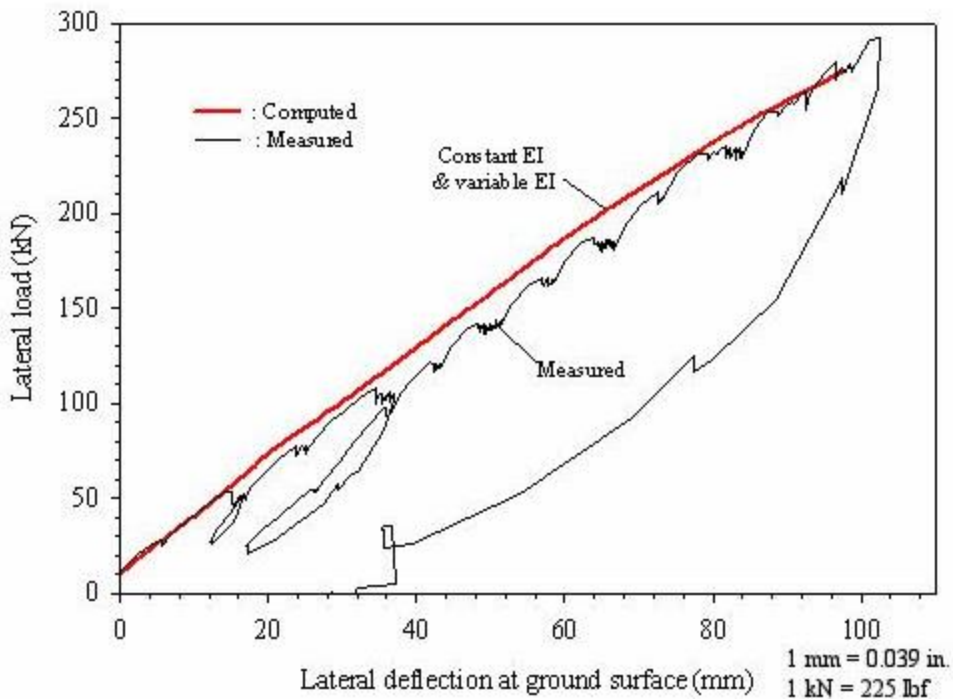
Figure 2-68 Calculated load-deflection curve for the plastic pile.

Initially, it was assumed that the p-y modulus would increase linearly with depth for the three test piles. This assumption was based on the characteristics of sand deposits at the test site. However, to achieve the best alignment between analytical predictions and field observations, the rate of modulus increase with depth was determined. This analysis revealed that the prestressed, FRP, and plastic piles had rates of modulus increase with depth of 1.7, 5.5, and 2.2 MN/m³ (10,831, 35,041, and 14,016 lbf/ft³, respectively).

Interestingly, these variations in the p-y modulus's rate of increase with depth did not align with the anticipated trend based on the findings of the axial load tests. The average unit shaft capacities for the prestressed concrete pile, the FRP pile, and the plastic pile were 61.8, 46.9, and 48.9 kPa (8.96, 6.80, and 7.09 lbf/in², respectively). The differences in the rate of modulus increase with depth may be attributed to variations in soil stratigraphy at each test pile's site and disparities in pile characteristics such as cross-sectional shape, pile width, pile stiffness, surface roughness, and friction at interfaces.

Amirmojahedi et al. (2022) conducted a study in which the authors investigated the lateral behavior of piles driven in sand soils. To determine the lateral capacity of piles in sandy soils and construct p-y curves, a 3-D Finite Element model was created using the ABAQUS program. This model considered the pile (a circle with diameter D) and the surrounding soil. The lateral behavior of piles is significantly influenced by the soil's characteristics in a zone extending from the ground surface down to 8D to 10D below the surface, as demonstrated by Duncan et al. (1994) and Christensen (2006). In this study, p-y curves for soil to a depth at x=15D were obtained and analyzed. To minimize the impact of boundary conditions on the pile reaction, a depth of 18D and a radius of 40D were chosen for the FE model based on sensitivity analysis. The lateral boundaries were constrained by roller supports to prevent horizontal soil movement, and roller supports were used to stabilize the soil domain's bottom and prevent vertical soil movement. Because of symmetry, only half of the pile and soil were modeled, significantly reducing the solution time.

For the soil components, the C3D8R element type was selected, offering linear interpolation of displacements in each direction. It is an eight-node linear brick element with reduced integration. The elastic-perfectly plastic Mohr-Coulomb (M-C) model with no cohesion was used to simulate soil composition. The elastic modulus of the pile material, E_p, was modeled using elastic

characteristics with a Poisson's ratio of 0.15 and Ep = 2,000 GPa. A high value of Ep was chosen to prevent pile deflection when simultaneously moving the top and bottom of the pile laterally.

The simulation involved two steps: in the first step, global stress equilibrium was achieved by applying a gravity load (g=9.81 m/s²) to establish the geostatic stress in the soil. In the second step, the entire pile was pushed laterally to obtain a complete p-y curve shape. In this study, a simple equation form for p-y curves in sands was assumed by introducing a power function inside the hyperbolic tangent function, as shown below:

$$p = p_u \tanh\left[\left(\frac{ay}{y_{ref}}\right)^n\right] \qquad (2.118)$$

where p is the soil reaction, y is the displacement, p_u is the ultimate soil resistance, and y_{ref} is the reference deflection. In the above equation, when $y = y_{ref}$, the value of p becomes equal to $p_u \tanh(\alpha n)$. When the value of $\alpha = 2$ and $n = 1$, the soil resistance reaches to $0.96 p_u$ at $y = y_{ref}$.
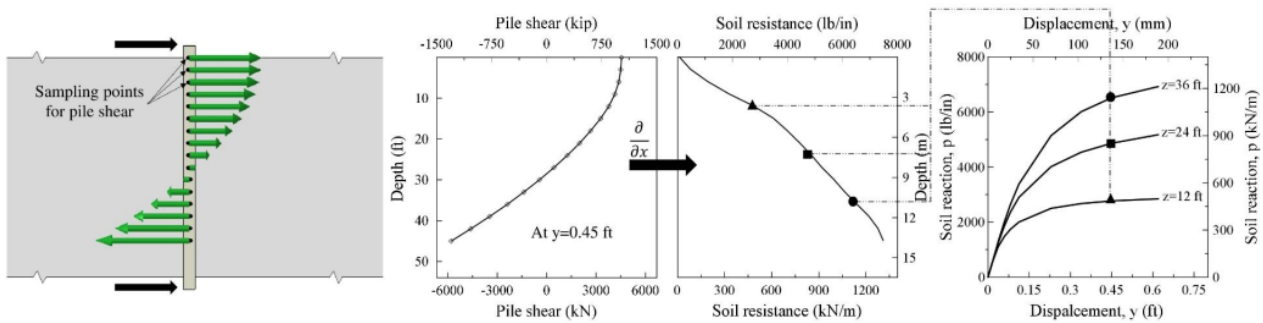
Figure 2-69 Procedure of obtaining soil resistance from results of finite element at a specific displacement for calculating p-y curves

The impacts of various soil and pile parameters on the p-y curves were then studied parametrically using the FE model. According to a parametric analysis of the pile finite element results, the value of ultimate soil resistance, p_u, is unaffected by the soil elastic modulus, while the value of reference deflection, y_{ref}, is changed in the opposite direction. In this study, y_{ref} is defined as a displacement where the soil resistance almost equals p_u. The effects of the soil Poisson's ratio and soil-pile friction coefficient on the values of p_u and y_{ref} were negligible, however the friction angle, effective

103

soil weight, coefficient of lateral earth pressure, and pile diameter had a direct correlation with p_u and y_{ref}.

2.10 Statistical Modeling

Effective investigational techniques include field testing, experimental testing, centrifuge modeling, and numerical analysis. However, there are occasions when they cannot be accomplished because of time and financial limitations. In these circumstances, statistical prediction models have shown to be helpful in analyzing or understanding the behavior of geotechnical structures.

The pile literature is full of contradictory conclusions drawn from both accurate and inaccurate interpretations of the results of measured load tests and naturally occurring soil anomalies. Statistical correlations are therefore highly valuable, but only with accurate data.

Table 2-16 Developed model for p-y curves in sands for different pile shapes (Amirmojahedi et al., 2022)

Pile shape	p-y curve function	ultimate resistance, p_u, and y_{ref}
circular	$p = p_u \tanh\left[\left(\dfrac{2y}{y_{ref}}\right)^{0.8}\right]$	$p_u = 21299 \times (x/L_0)^{0.9} \times \tan^{1.2}\varphi' \times (\gamma'/\gamma_w)^{0.5} \times K^{0.8} \times (D/L_0)$
		$y_{ref} = 44.9 \times (x/L_0)^{0.8} \times (P_0/E_s) \times \tan^{1.4}\varphi' \times (\gamma'/\gamma_w)^{0.6} \times K^{0.9} \times (D/L_0)^{0.9}$
square	$p = p_u \tanh\left[\left(\dfrac{2y}{y_{ref}}\right)^{0.66}\right]$	$p_u = 24044 \times (x/L_0)^{0.8} \times \tan^{1.2}\varphi' \times (\gamma'/\gamma_w)^{0.5} \times K^{0.8} \times (D/L_0)$
		$y_{ref} = 117.6 \times (x/L_0)^{0.5} \times (P_0/E_s) \times \tan^{1.4}\varphi' \times (\gamma'/\gamma_w)^{0.6} \times K^{0.9} \times (D/L_0)^{0.9}$
rhombus	$p = p_u \tanh\left[\left(\dfrac{2y}{y_{ref}}\right)^{0.8}\right]$	$p_u = 20814 \times (x/L_0)^{0.8} \times \tan^{1.2}\varphi' \times (\gamma'/\gamma_w)^{0.5} \times K^{0.8} \times (D/L_0)$
		$y_{ref} = 60.6 \times (x/L_0)^{0.5} \times (P_0/E_s) \times \tan^{1.4}\varphi' \times (\gamma'/\gamma_w)^{0.6} \times K^{0.9} \times (D/L_0)^{0.9}$

Amirmojahedi et al. (2022) created models made up of p_u and y_{ref} terms inside a composition of power and hyperbolic tangent functions for the distinct pile shapes of circular, square, and rhombus, using the obtained p-y curves in various depths for lateral piles. The developed model for p-y curves in sands for various pile shapes is summarized in Table 2-16. In the scenarios of multidirectional lateral loading on square piles, soils with increasing elasticity with depth, soil

layers with varied elasticity and unit weight, and overburden pressure, it was demonstrated that the created model can predict p-y curves.

The model was validated through a full-scale lateral pile test at Mustang Island, where the measured values for p_u and the initial slope at different depths aligned with the coefficient of lateral earth pressure, K, as projected by the model. Reese's method, widely used for predicting p-y curves in sand, was modified based on findings from the Mustang Island test. It was noted that the factor A, used to match the model with measured values, can vary under different conditions, even for open-ended piles driven in sand.

The installation of piles can alter soil properties due to soil disturbance, expansion, friction between the pile and soil during driving, and gap formation. To account for these uncertainties in soil attributes, it was recommended that the values of K in the proposed model for non-displacement and displacement-driven piles be adjusted to 0.5-1.0 and 1.0-2.0, respectively. This approach results in various p-y curves for different depths, enabling a range of pile behaviors under lateral loads in sands to be predicted.

Duncan et al. (1994) introduced the characteristic load method (CLM), a less complex alternative to p-y analyses that produces results similar to p-y studies. CLM uses dimensional analysis to describe the nonlinear behavior of laterally loaded piles and drilled shafts by examining correlations between dimensionless variables. It provides good agreement between calculated lateral deflections and maximum bending moments and values obtained from field load tests.

Dimensionless relationships are used to represent real-world conditions, normalizing loads with a characteristic load Pc, moments with a characteristic Mc, and deflections with the pile width D. Increasing Pc values signify higher lateral load capacity and lower deflection, while increasing Mc values indicate greater moment resistance and reduced deflection under a fixed moment. Dimensionless charts depict nonlinear behavior for fixed-head and free-head deep foundations in sand and clay, allowing for the calculation of ground-line deflections and the size and location of maximum moments in piles or drilled shafts under various loading conditions. These charts are versatile and can be used manually or with basic spreadsheets and computer applications.
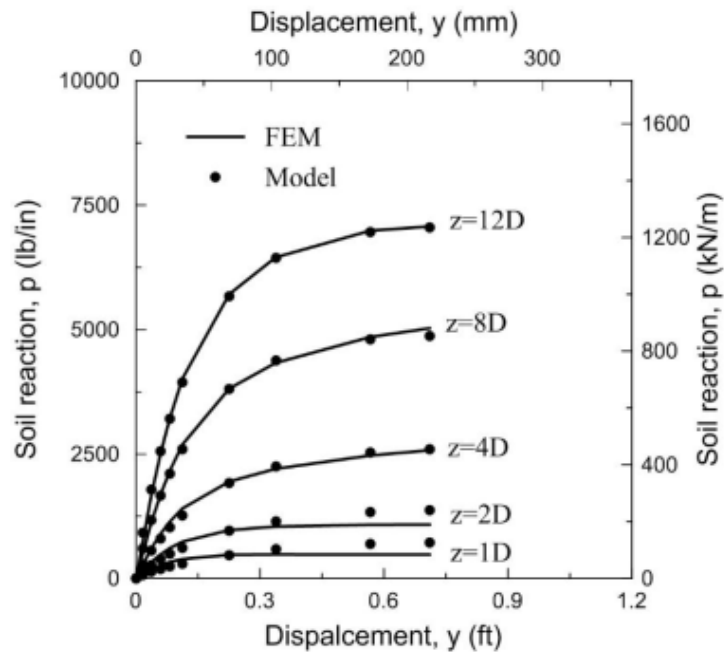
Figure 2-70 Comparison between p-y curves of Finite Element and model
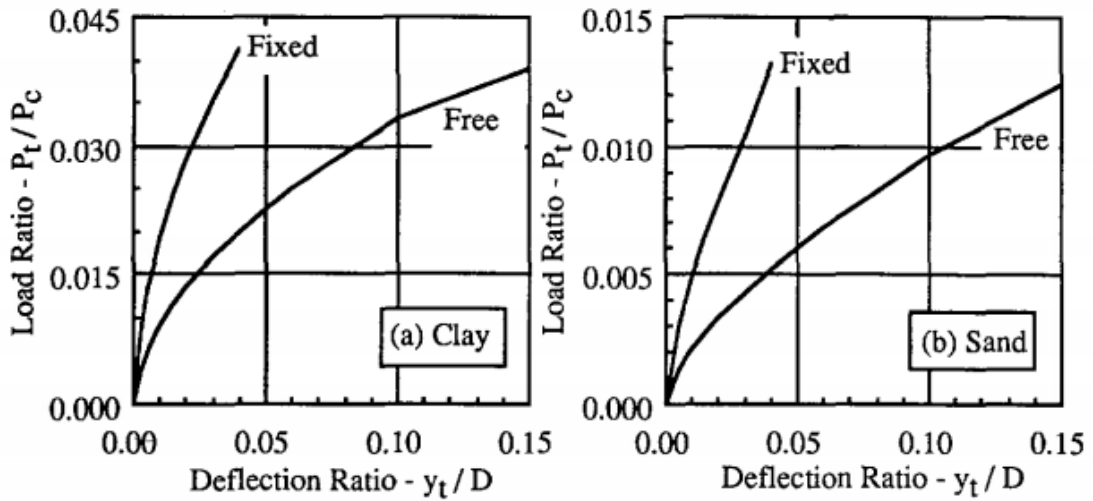
Figure 2-71 Load-Deflection Curves: (a) Clay; (b) Sand
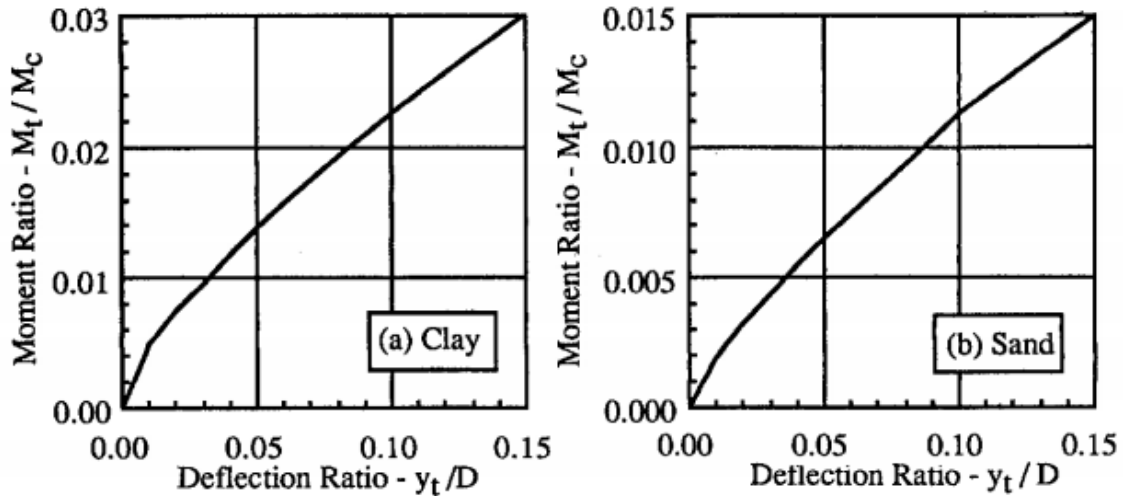
Figure 2-72 Moment-Deflection Curves: (a) Clay; (b) Sand

The characteristic load method (CLM) provides estimates of moments and deflections that are slightly higher than those obtained through p-y analyses for deep foundations in stiff clay under static load conditions. However, it closely approximates the results of p-y analyses for piles and drilled shafts in soft clay and sand, as shown in Figure 2-73 and Figure 2-74. When it comes to deflection and moment values for piles and drilled shafts in soft clay and sand under cyclic load conditions, the CLM aligns closely with the outcomes of p-y studies.

In the case of stiff clay below the water table, where clay erosion around the pile or shaft can lead to significant deflections and progressive failure, piles and drilled shafts subjected to cyclic loading experience larger deflections and bending moments compared to what is calculated by the CLM. Therefore, for deep foundations in stiff clay exposed to cyclic loads, it is not advisable to rely on the CLM for estimating their behavior. Comparisons with the results of single-pile load testing in clay and sand demonstrate that the conclusions drawn from these methods are reasonably consistent with observed field behavior.
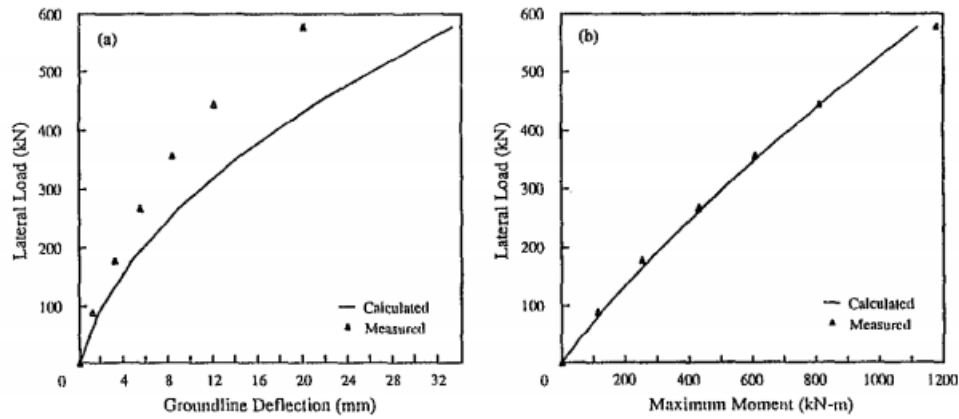
Figure 2-73 Comparison of Measured and Calculated Deflections and Moments for Pipe Pile in Stiff Clay [Measured Values from Reese et al (1975)]: (a) Deflection; (b) Moment (Duncan et. al, 1994)
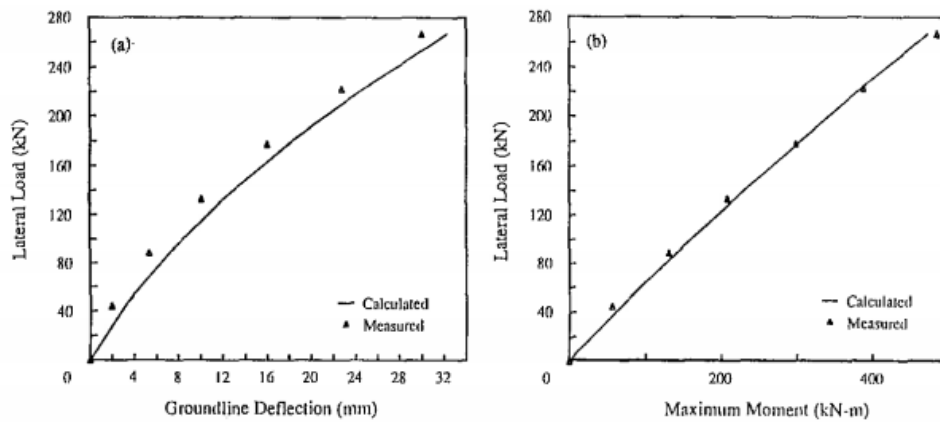
Figure 2-74 Comparison of Measured and Calculated Deflections and Moments for Pipe Pile in Sand [Measured Values from Cox et al. (1974): (a) Deflection; (b) Moment (Duncan et. al, 1994)

The estimated deflection and moment values in the studied scenarios were found to be in good agreement with the measured values, or somewhat higher. The method offered a straightforward, practical basis for designing laterally loaded deep foundations, and seemed to be as accurate as the data on soil conditions and qualities.

2.11 Limitations of Previous Studies

RPP has been successfully incorporated with various geotechnical structures in improving its structural stability. RPP has been used to stabilize slopes for increasing lateral resistance of slopes, in foundation soil of embankment and MSE wall for increasing bearing capacity, in MSE wall base as shear keys; and the tremendous results of performance monitoring of these studies have made RPP a viable alternative to other ground improvement techniques. However, very few studies are available on the load capacity of RPPs alone in actual field condition. Therefore, Vertical and Lateral load capacity of RPP in actual field conditions are required to be determined in order to facilitate future design involving different site and loading conditions.

CHAPTER 3

VERTICAL LOAD TEST OF RECYCLED PLASTIC PINS

ABSTRACT

Construction of geotechnical structures over soft foundation soils is an incredibly challenging task due to the risk of bearing failure and excessive settlement of foundation soil. Recycled Plastic Pin (RPP) has been used as a noble approach to improve the problematic foundation soil by increasing the bearing capacity of the foundation. The objective of the study was to evaluate the vertical load capacity of RPPs by conducting field load tests using plate load tester. In this study, vertical pile load tests were conducted on both cases of single and group RPPs. Four different sizes of single RPPs and four different combination of sizes and spacings arranged in a group were tested in the field. Six empirical methods were followed to investigate the ultimate load bearing capacity of RPPs. Finally, an analytical approach was undertaken to determine the bearing capacity of the RPP reinforced foundation system.

Key words: Single RPP; Group RPP; Vertical Load Capacity; Field Load Test; Load Settlement Behavior.

3.1 Introduction

RPP has been successfully incorporated with various geotechnical structures as a ground improvement technic to enhance structural stability. Previously, RPP has been used to stabilize slopes for increasing lateral resistance of slopes (Khan et al., 2014), in the foundations of embankments (Zaman, 2019), even over soft soils (Islam, 2021), in the MSE wall foundation for increasing bearing capacity (Badhon, 2021) and shearing resistance (Bhandari 2021); and the tremendous results of performance monitoring of these studies have made RPP a viable alternative to other ground improvement techniques. However, vertical load carrying capacity of RPPs has not been evaluated, which is one of the critical design parameters.

Despite the difficulties in obtaining the ultimate capacity of the piles using the in situ static loading test, this method is the most recommended by several codes and design standards. Static load tests involve applying a gradually increasing load to a pile and measuring its strain response. Based on these measurements, the pile's load-displacement behavior can be determined, and its ultimate capacity is estimated. Numerous authors (Bica et. al., 2014), (Gao et. al., 2019), (Yi et. al., 2017)

110

used field load tests for determining load capacity of various types of piles in different soil and loading conditions. The ultimate load capacity of pile can be obtained from the analysis of load settlement curve after axial load testing of vertical piles. There are several analysis methods among which Davisson's limit method, Brinch Hansen's method, Chin's Method, Van Weele's method, Fuller and Hoy's method and Butler and Hoy's method are the most suggested ones with the view of finding the ultimate load capacity of piles. Fellenius (1980) applied eight load increments up to a maximum load. The maximum load was twice the predetermined allowable load. Application of loading was maintained until zero settlement was reached. The ultimate failure mode was determined when the pile plunged into the soil. However, settlement is a very inadequate interpretation of failure. Adib et al (2001) used wave analysis to find the driving stresses during installing concrete piles and predicted the vertical behavior of piles adequately.

Yi et al (2017) employed full-scale field loading tests to investigate the vertical bearing capacity behavior of a single T-shaped column in soft ground. To investigate the vertical load bearing behavior of manually excavated large diameter belled concrete piles (LDBCPs), Gao et al (2019) performed field loading tests on a total of 16 LDBCPs, ranging from 0.8 to 3.5 m in base diameter from 6.1 to 18.0 m in embedment length. Yousif et al (2021) investigated the bearing capacity of six concrete piles, where bearing capacity was calculated using three empirical methods (Brinch-Hansen, Chin-Kondner, and Decourt) and compared with the results obtained from numerical modeling in AllPile. Wang et al (2006) illustrated the applicability of plate load test (PLT) in designing foundation.

Therefore, it is necessary to determine the vertical load capacity of RPP under field conditions in order to facilitate future design considering various site and loading situations utilizing PLT. This study presents the ultimate capacity of RPP obtained by following six methods (Davisson's Limit Method, Brinch Hansen Method, Chin's Method, Van Weele's Method, Fuller and Hoy's Method and Butler and Hoy's Method). For the current study, the ultimate capacity was determined by analyzing the field load test data of four various sizes of single RPPs and four different combinations of group RPPs.

3.2   Methodology

3.2.1   Project Background and Site Soil Conditions

A location inside Hunter Ferrell Landfill in the City of Irving, Texas was selected for the study. Geotechnical drilling and resistivity imaging were conducted for the sub-soil investigation. Two locations were selected for soil investigation and drillings were conducted for these locations with a drilling depth of about 6 m to investigate the soil properties.

Figure 3-1 Location of field load testing on RPP in the Hunter Ferrell Landfill Site in Irving

The average blow count of the foundation soil was found to be 5 at a depth of 1.2 m. Disturbed and undisturbed soil samples were collected during boring. A detailed laboratory investigation was carried out to determine the index properties and shear strength parameters of collected soil samples. The results indicated the presence of medium to high plastic clay throughout the borehole depth and classified as Fat clay (CH) according to the Unified Soil Classification System (USCS). No groundwater was detected during the drilling. The moisture content varied from 10% to 28%. The plasticity index varied from 36 to 48, and the range of liquid limit was between 51 to 66.
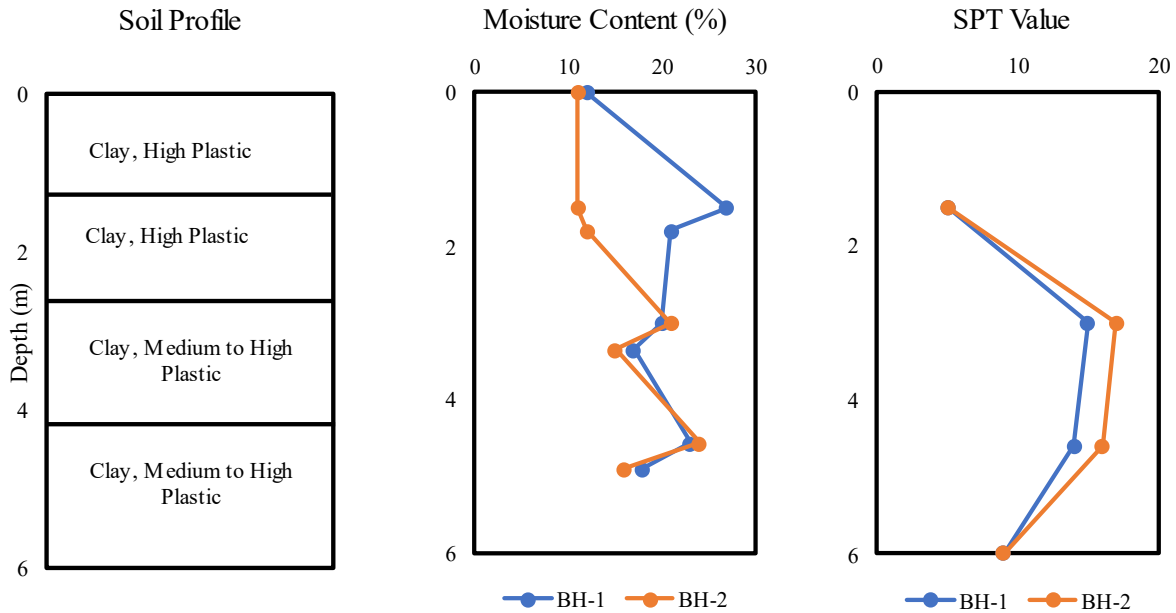
Figure 3-2 Variation of moisture content and SPT value in different layers of soil

UCS tests were conducted on undisturbed soil samples collected in thin-walled Shelby tubes at two different depths of 1.5 m. and 4.6 m. respectively. The undrained shear strength at 1.5 m depth was found to be 6.7 kN/m^2 and the ultimate bearing capacity was calculated to be 34.5 kN/m^2. Based on the field SPT data, N value for the top layer (From BH1_S4) of soil was 5, which indicates that the compressive strength will be in between 23.9 to 47.9 kN/m^2. For the sample collected from 4.6 m depth, undrained shear strength was found as high as 114.9 kN/m^2 and the ultimate bearing capacity was calculated to be 590 kN/m^2, indicating an extremely stiff soil layer. Based on undrained shear strength parameter as well as field SPT value, it was confirmed that topsoil within this zone was weak and thus, was selected for conducting the tests.

3.2.2 Design and Construction Details

The field experiments were designed to incorporate 8 vertical load tests on single RPPs and 8 vertical load tests on RPPs arranged in groups of four. Finite element modeling was conducted using PLAXIS 2D with the in-situ soil properties. A parametric study was performed with available RPP properties to investigate the effect of different RPP sizes, length, and spacing. The Mohr-Coulomb soil model with elastic perfectly plastic behavior, was used for deformation calculations using 15 node triangular elements. The FEM analysis employed 9 stress points for

113

producing high quality stress results. The FEM analysis was covered in detail under the study by Zaman (2019). The Engineering properties of RPPs used in this context are listed in Table 3-1.

Table 3-1 Engineering properties of Recycled Plastic Pin (Chen, 2003 and Bowders et al. 2003)

Parameter	Value
Modulus of Elasticity (MPa)	1170
Compressive Strength (kPa)	31,026.4
Tensile Strength (kPa)	24,821.1
Specific Gravity (g/cc)	0.93

It was observed from the study that RPP length has insignificant effect. The size of RPP plays a significant role in increasing the bearing capacity of the foundation soil. For a larger RPP size, the ground settlement is lower, as larger RPP has a higher load-carrying capacity. Based on the finite element modeling results, four different sizes of RPP 10 cm × 10 cm, 15 cm × 15 cm, 25 cm x 25 cm and 30 cm x 30 cm were selected for vertical load test in field. The typical plan and layout of the load test is shown in Table 3-2 and Figure 3-3.

Table 3-2 Summary of Field Installation of RPPs for Vertical Load Tests

RPP size	Combination	Spacing, s (m)	Number of tests	Number of RPPs	Number of Instrumented RPPs	Total Number of RPPs
10 cm x 10 cm	Single	-	2	1*2 =2	1*1=1	18
	Group	0.6	2	4*2 =8	1*2=2	
		0.9	2	4*2 =8	1*2=2	
15 cm x 15 cm	Single	-	2	1*2 =2	1*1=1	18
	Group	0.6	2	4*2 =8	1*2=2	
		0.9	2	4*2 =8	1*2=2	
25 cm x 25 cm	Single	-	2	1*2 =2	1*1=1	2
30 cm x 30 cm	Single	-	2	1*2 =2	1*1=1	2
Total Number of Test =			16	Total installed RPPs =		40
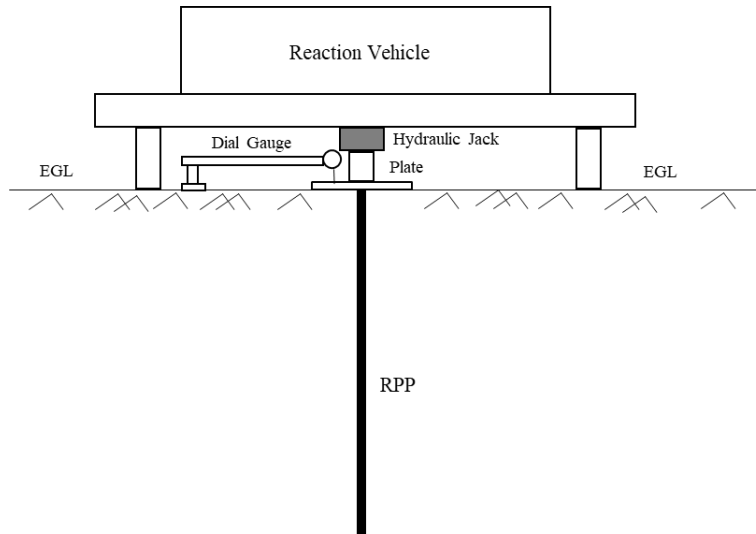
Figure 3-3 Schematic diagram of test setup for Vertical Load Test

3.2.3 Instrumentation Plan

The RPPs were instrumented with electrical resistance type strain gauges with a view of obtaining unit skin friction while conducting the load tests. For this purpose, 90°2- element Rosette Plane type strain gauges modeled GFCAB-3-70-5LJB-F were used. One out of the two RPPs of each size, total 12 RPPs, were instrumented to ensure at least one set of all the combination of RPPs were instrumented. All the RPPs were 3 m long and strain gauges were installed in 3 different depths of 0.3 m, 1.5 m and 2.7 m. At each depth 2 strain gauges were installed on opposite sides totalling to 6 strain gauges per RPP. System 8000 data acquisition (DAQ) system with 8 channels was used to collect the data from the strain gauges during load testing. Figure 3-4 (a) and (b) show the schematic diagram and instrumented RPP in field.

Earth pressure cells, also called total pressure cells, are installed to measure the stresses experienced by the soil. In this study, Model 4800 Earth Pressure Cell (produced by GEOKON PTE. LTD.) was used to measure vertical earth pressure acting on the ground in between the RPPs. The diameter and the thickness of the pressure cell is 230 mm and 6 mm, respectively. To measure the pressure coming on the top of soil, pressure plates were installed on top of soil in between RPPs. Then the pressure plates were connected to a data logger (LC–2 x 4) for continuous data collection. Before the commencement of installation, the initial no-load zero reading was taken and compared with the supplied calibration report. The installation of the pressure plate is shown in Figure 3-4 (c).

115
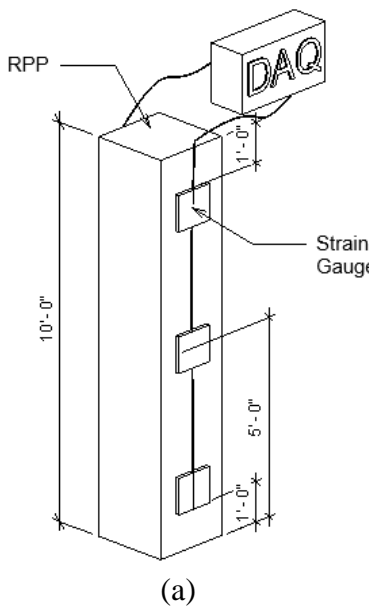
Figure 3-4 (a) Schematic Diagram of Instrumented RPPs; (b) Instrumented RPP; (c) Pressure plate

Installation of strain gauges was a rigorous process and required several steps to be followed. The steps are described in detail as follows:

At first two long grooves were created along the length of the RPPs on two opposite sides using Ryobi Router. The bottom surface of the grooves was cleaned off the plastic dust and fibers after cutting the groove. The surface where strain gauges will be attached were sanded properly to ensure a smooth surface to stick on pin surface. Strain Gauge was then installed on the smooth surface of the RPP with the use of CN type adhesive and a protective layer of epoxy resin was used to cover the gauges. Wires of the strain gauges were then placed and secured inside the groove. Sealant was used to cover the wires and to fill up the gap created for cutting the groove. The gauges were further protected with plastic films and duct tapes to minimize damage during installation. After installation of strain gauges, a circuit was created with the wire ends using RJ 45 connector to facilitate connection with the data acquisition system. The process followed is illustrated in following Figure 3-5.

(a) Cutting Groove

(b) Sanding for a
smooth surface

(c) Grooved and
sanded surface
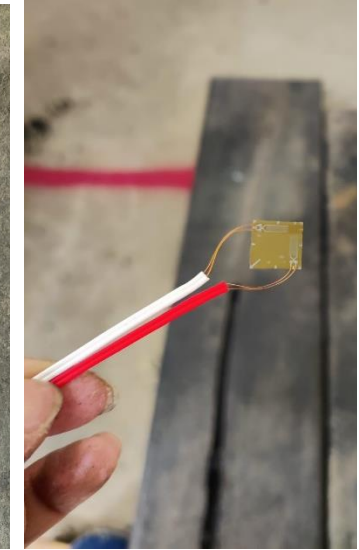
(d) Strain Gauge

(e) Strain Gauge
attached on RPP's

(f) Putting protective
layer on the gauges

(g) Placement of
wire inside the
groove
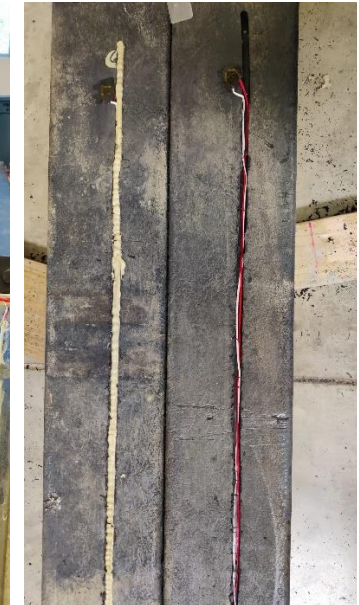
(h) Protected wires with
sealant

| (i) Plastic films used to minimize the effect of drag force | (j) Covered strain Gauges | (k) Creating circuit with RJ 45 connector |
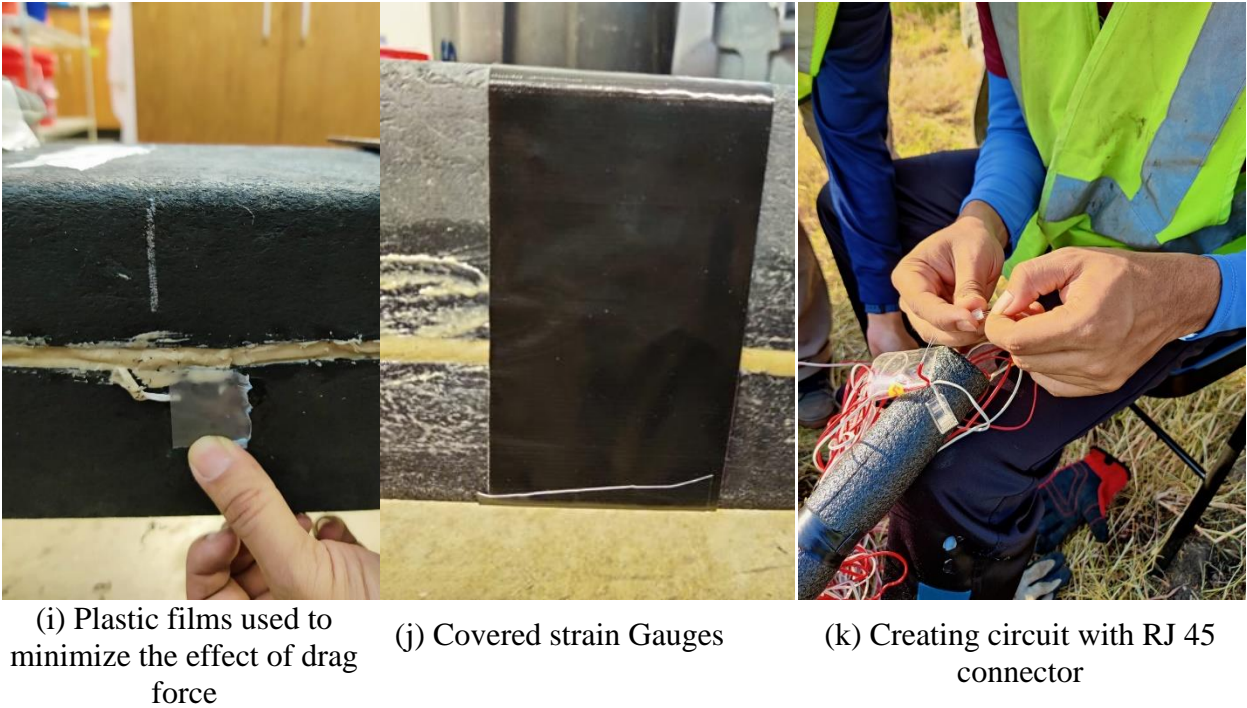
Figure 3-5 Instrumentation of RPP

3.2.4 Installation of the RPPs

The installation of RPP took place on two occasions (May 19, 2022, and May 25, 2022; March 14, 2023). An excavator equipped with a hydraulic breaker hammer was utilized to install the smaller RPPs (10 cm × 10 cm, and 15 cm × 15 cm). Flags were used to mark the locations where the RPPs would be installed. A steel pin was used to create a hole at each marked location and the RPPs were then placed in the holes and driven into the ground with the help of a conventional hydraulic excavator (KOBELCO model: SK210LC), which was equipped with two different Hydraulic Breaker hammers NPK GH-3 and NPK GH-6 for 10 cm × 10 cm, and 15 cm × 15 cm RPPs respectively. Stroimatic Pile Driver was used to install the larger RPPs with the dimensions of 25 cm × 25 cm, and 30 cm × 30 cm. A total of 40 RPPs were flushed into the ground for vertical load tests as shown in Figure 3-6 and Figure 3-7.

Figure 3-6 Field Installation of 10 cm × 10 cm, and 15 cm × 15 cm RPPs

Figure 3-7 Field Installation of 25 cm × 25 cm, and 30 cm × 30 cm RPPs

3.2.5   Construction of Load Transfer Platform (LTP)

A load transferring platform (LTP) made of reinforced cement concrete was constructed on top of the RPPs in the groups. After installing all the RPPs, one layer of Tensar® TriAx® Geogrid with a tensile stiffness of 215.46 kN/m^2 at the strain level of 0.5% was laid above the RPPs and soil in between RPPs. The purpose of placing geogrid layer was to distribute the load from the soil to the RPP by arching action (Han & Akins, 2002). The whole load transfer platform will act as a rigid platform that will maximize the transfer of the load into the RPPs. A level surface was achieved with sand and then concrete mix of 27,579 kN/m^2 average compressive concrete strength was poured on the rebar cage to act as a load transferring platform. The slab thickness was designed to be 19 cm and LTP was reinforced with #4 rebars with 2.54 cm clear distance at the bottom of the platform to provide tensile strength, to prevent the concrete from cracking and to ensure uniform

distribution of the load. Figure 3-8 shows the construction of load transferring platform on top of RPP groups.

(a)   (b)   (c)   (d)
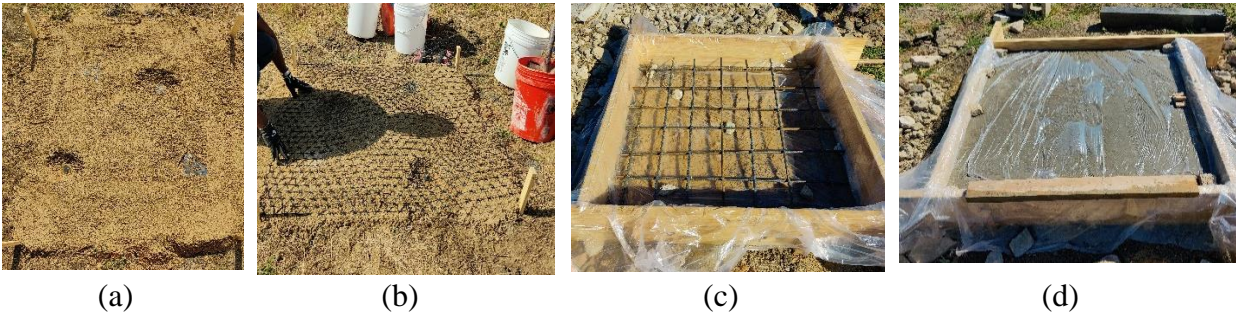
Figure 3-8 Construction of load transferring platform on top of RPP groups (a) leveled surface with sand (b) Geo-grid placement (c) Rebar cage placed in the formwork with 2.54 mm cover, and (d) Completed LTP

3.2.6 Load Test on RPP

The vertical load test was performed according to ASTM- D1143 (Quick test) standard. To assess the vertical load capacity in the field, a total of 8 tests on individual RPP and 8 tests on groups of four RPPs were conducted. Vertical load tests were conducted using a plate bearing load tester. The load tester comprises of a hydraulic jack, a reference beam, a hydraulic pump, plate set of varying size and three dial gauges. Heavy weight dump truck was used as reaction vehicle and load was applied against the rear axle.

(a)   (b)   (c)   (d)
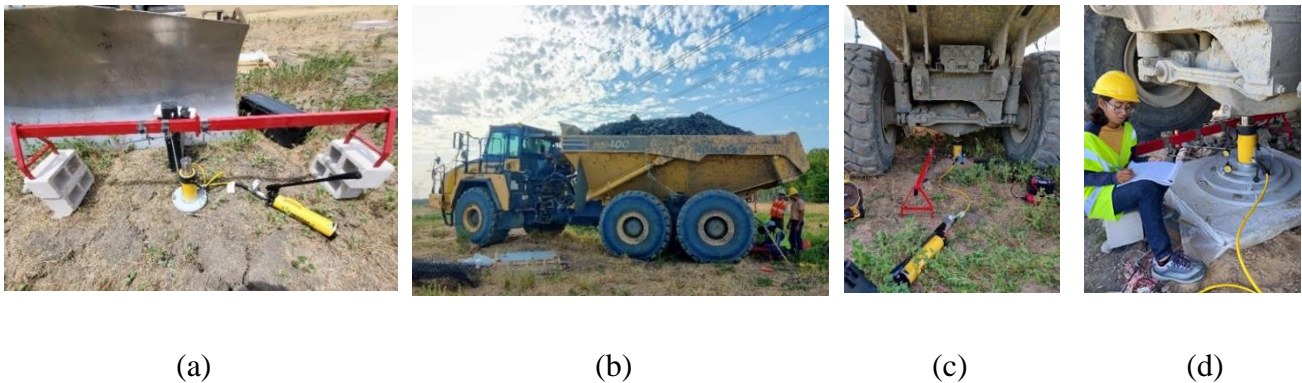
Figure 3-9 (a) Load Testing Equipment; (b) Reaction vehicle; Vertical load test set up in field (c) for Single RPP and (d) Group RPP

Axial compressive load was continuously applied until failure was initiated, that means the test load caused rapid continuing, progressive movement, or the total axial movement exceeds 15 %

of the pile diameter or width. Three dial gauges were used to report the settlement resulting from the application of load. Figure 3-9 (a) shows the plate load test equipment. Figure 3-9 (b) shows the reaction vehicle used and Figure 3-9 (c) and (d) the vertical load test set up.

3.3 Results and Analysis

3.3.1 Ultimate Load Capacity

Based on the field test results, 10 cm x 10cm single and 15 cm x 15 cm single RPP experienced rapid movement after reaching 45 kN and 116 kN with corresponding settlement of 15.75 mm and 12.5 mm respectively. RPPs with larger cross sections, 25 cm x 25cm and 30 cm x 30 cm RPP, displayed failure at the load of 155 kN and 196 kN with corresponding settlement of 9.0 mm and 4.0 mm respectively. Figure 3-10 shows one load-displacement graph of four different sizes of RPPs tested for vertical load capacity.
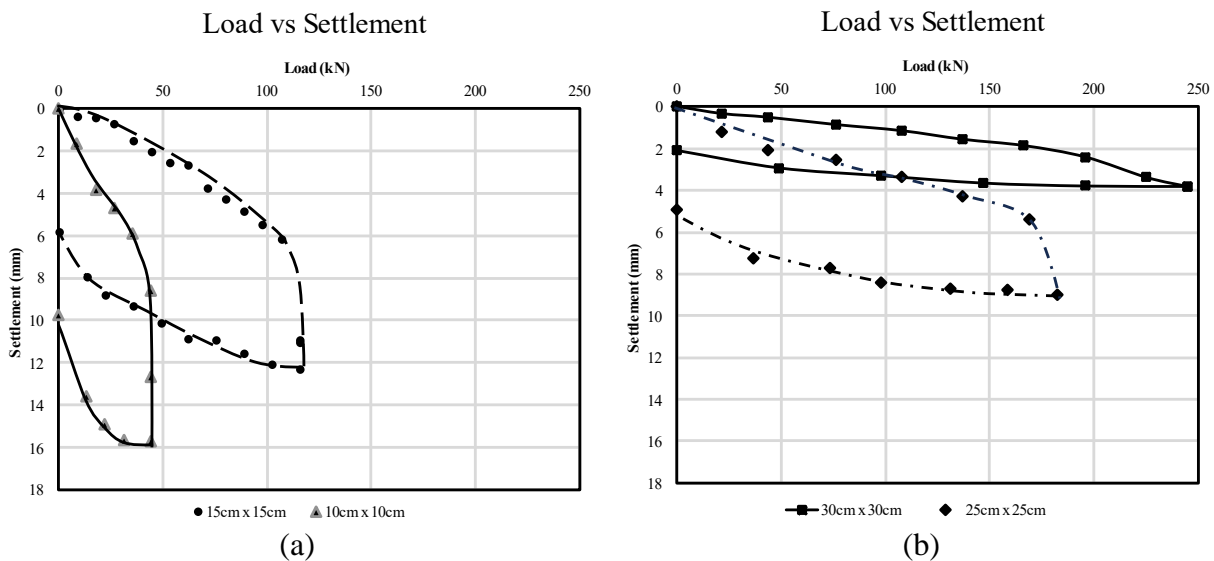
Figure 3-10 Load vs Displacement Curve (a) 10 cm × 10 cm, and 15 cm × 15 cm RPP (b) 25 cm × 25 cm, and 30 cm × 30 cm

25 cm x 25 cm RPPs, with 2.78 to 6.25 times larger cross section in comparison with 15 cm x 15 cm and 10 cm x 10 cm RPP performed better than the smaller sized RPP and failed at 32% - 74% higher load and settled 42% - 56% less. On the other hand, 30 cm by 30 cm RPP having 20% larger dimension had 26% higher load at failure and experienced 38% less settlement than 25 cm by 25 cm RPPs. In comparison with 15 cm x 15 cm and 10 cm x 10 cm RPP which are 4 to 9 times smaller than the 30 cm by 30 cm RPP, failed at 41% to 77% less load and experienced 212% to

295% more settlement. The 15 cm x 15 cm RPPs performed better by withstanding about 63% more load and about 24% less settlement at failure than 10 cm x 10 cm RPPs because of having larger cross-sectional area. 10 cm x 10 cm RPP experienced almost similar settlement as 15 cm x 15 cm RPP corresponding to failure load with application of only one third of the load experienced by the later RPP. Figure 3-11 depicts how load capacity improves as RPP cross sectional area increases. The data points follow an exponential relationship which can be expressed as $y = 19.463e^{0.0029x}$. The data points were fitted by the curve with an R-squared value of 0.9253, indicating good agreement.

Relationship between RPP size vs Load Capacity
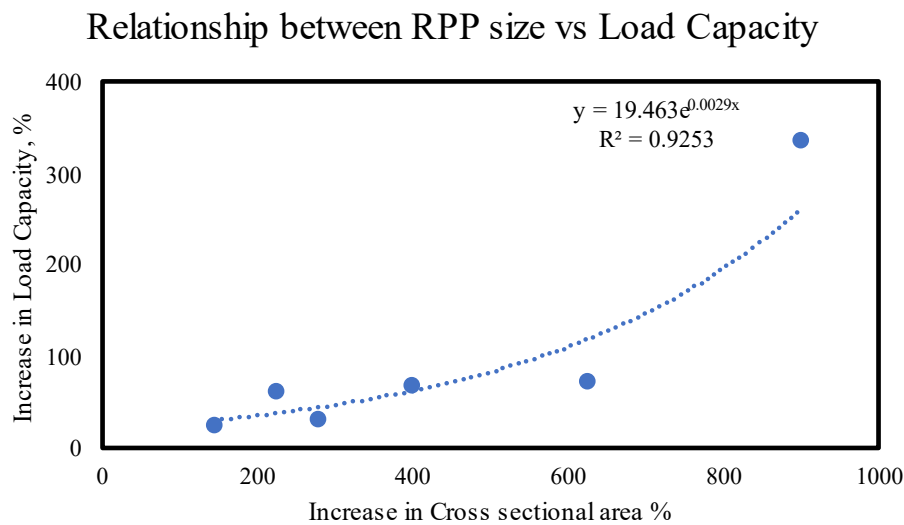
Figure 3-11 Relationship between RPP size and Load Capacity

For simpler representation, 10 cm by 10 cm RPPs, spaced at 0.9 m and 0.6 m are referred to as 10 x 0.9 and 10 x 0.6 and 15 cm by 15 cm RPPs, spaced at 0.9 m and 0.6 m are referred to as 15 x 0.9 and 15 x 0.6. Based on the field test results, groups 10 x 0.9 and 10 x 0.6 were observed to undergo rapid movement after reaching 203 kN and 235 kN respectively with corresponding settlement of 34 mm and 32 mm respectively. Experienced permanent settlement was 17.5 mm and 17.8 mm respectively after withdrawal of load. Groups 15 x 0.9 and 15 x 0.6 experienced failure load at 525 kN and 543 kN with corresponding settlement of 27.5 mm and 22.5 mm respectively. After unloading operation, permanent settlement of 16.5 mm and 12.5 mm were observed. As allowable settlement in foundation system is 25 mm, the graphs were further studied to obtain the load withstood by the RPP groups corresponding to 25 mm settlement. 15 x 0.6 encountered settlement

of less than 25 mm during the field load test, implying that the ultimate load is the same as the failure load of field load tests. 15 x 0.9, 10 x 0.9 and 10 x 0.6 all settled 25 mm, equating to 520 kN, 445 kN and 489 kN, respectively. The field test results of vertical load capacity and settlement corresponding to failure load of group RPPs are presented in Figure 3-12.
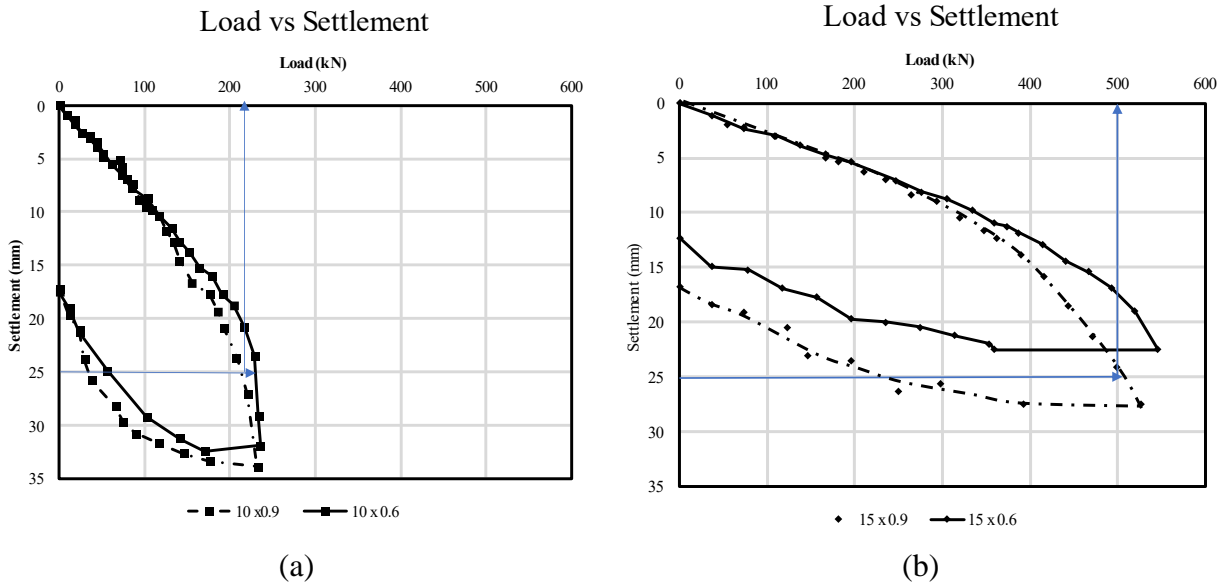
Figure 3-12 Load vs Displacement Curve (a) 10 cm by 10 cm RPPs spaced at 0.9 m and 0.6 m
(b) 15 cm by 15 cm RPPs spaced at 0.9 m and 0.6 m

Ultimate vertical load capacity for individual RPPs were analyzed using six different methods and results are described in the following section. Load vs settlement curves of 15 cm x 15 cm RPP and 15 x 0.9 RPP group are used to explain different methods of analysis.

Davisson's Limit Method. Davisson's method (1972) is based on an offset called Davisson's limit value that defines the failure load. The offset is defined as the load corresponding to the movement which exceeds the elastic compression of the pile by a value of 4 mm plus a factor equal to the dimension of the pile divided by 120. The offset value was found 5 mm for 15 cm by 15 cm RPPs. The Davisson limit was developed in conjunction with the wave equation analysis of driven piles and has gained widespread use in phase with the increasing popularity of this method of analysis. It is primarily intended for test results from driven piles tested in accordance with quick methods. Figure 3-13 applied Davisson's method to identify ultimate load capacity of RPP.
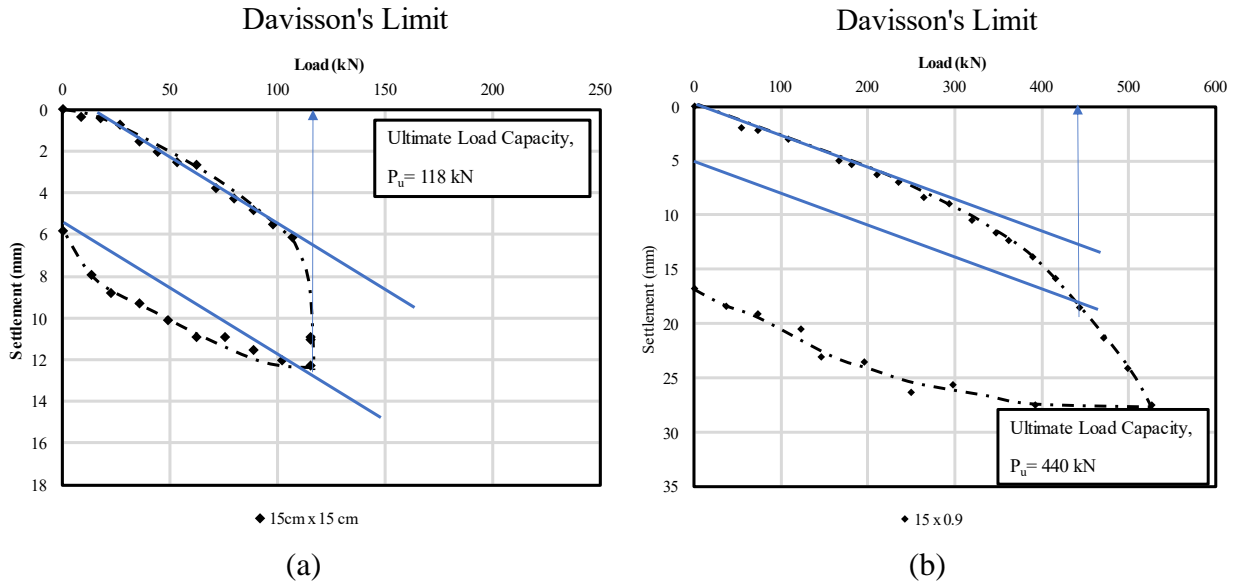
Figure 3-13 Ultimate load capacity according to the Davisson's Method (a) 15 cm by 15 cm Single RPP; (b) 15 cm by 15 cm RPPs at 0.9 m Spacing

Brinch Hansen Method. Brinch Hansen (1963) defines failure as the load that gives twice the movement of the pile head as obtained for 90% of that load. Figure 3-14 shows the ultimate failure load according to Brinch Hansen method.
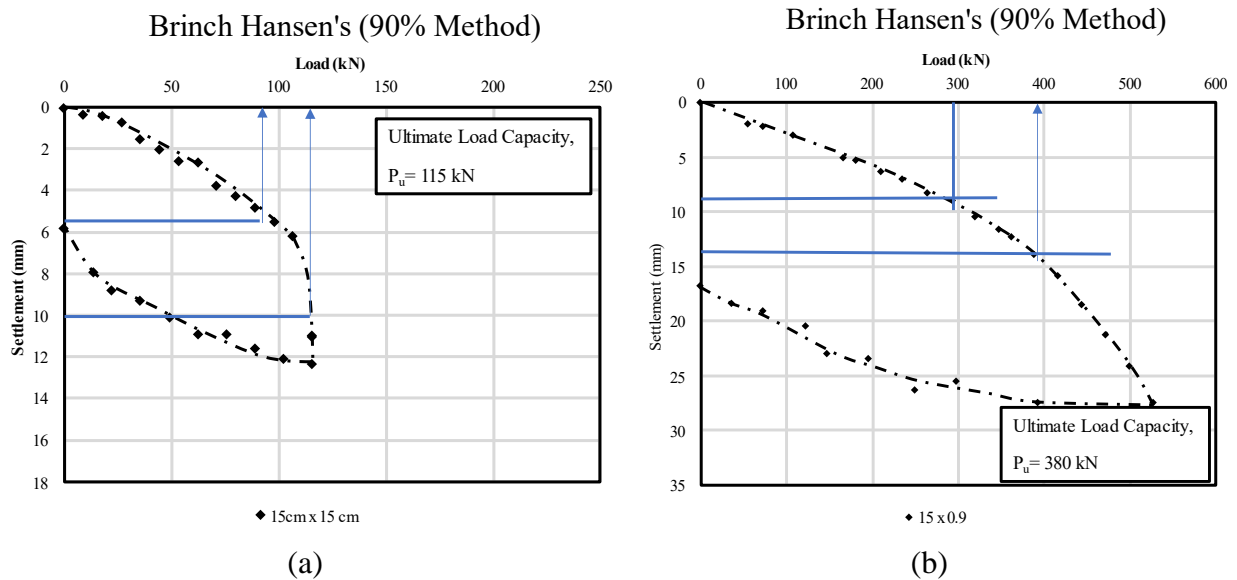
Figure 3-14 Ultimate load capacity according to the Brinch Hansen Method (a) 15 cm x 15 cm Single RPP; (b) 15 cm x 15 cm RPPs at 0.9 m Spacing

Chin's Method. The method assumes that the load-settlement curve when the load approaches the failure load is of hyperbolic shape. By the Chin's method, each load value is divided with its corresponding movement value and the resulting value is plotted against the settlement. As shown in Figure 3-15, after some initial variation, the plotted values fall on a straight line. The inverse slope of this line is the Chin's failure load.
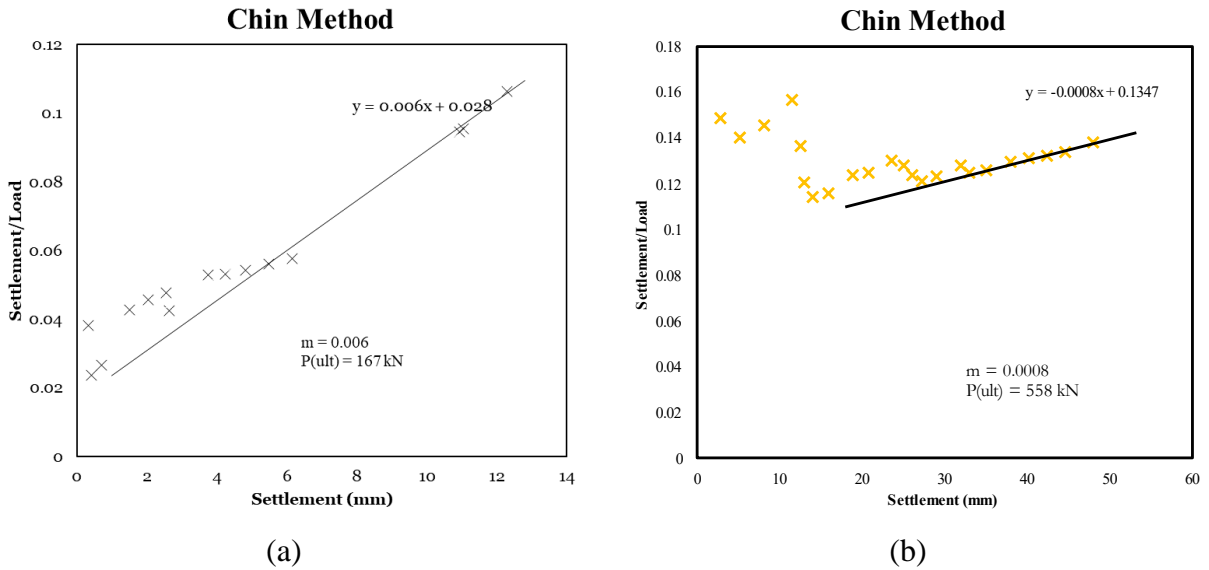
Figure 3-15 Ultimate load capacity according to the Chin's Method (a) 15 cm x 15 cm Single RPP; (b) 15 cm x 15 cm RPPs at 0.9 m Spacing

Van Weele. Van Weele's Method is based on the concept that the load is carried mostly by skin resistance until the shaft slip is sufficient to mobilize the limiting value. When the limiting skin resistance is mobilized, the point load increases nearly linearly until the ultimate point capacity is reached. At this point further applied load results in direct settlement (load curve becomes vertical). Figure 3-16 shows ultimate vertical load capacity of RPP according to the Van Weele's Method.
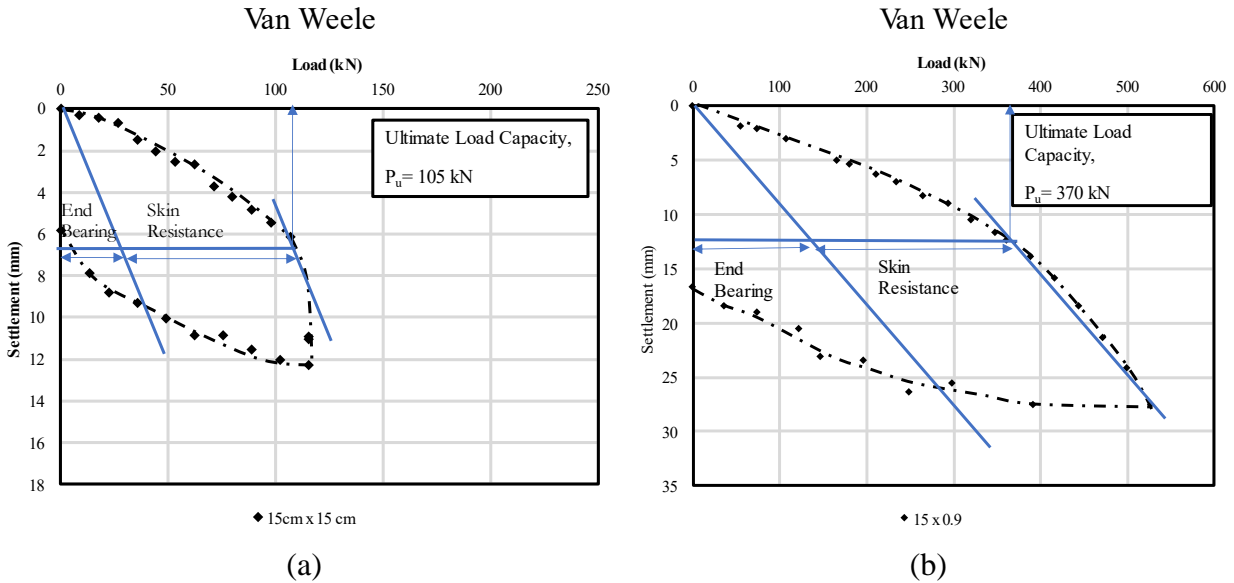
Figure 3-16 Ultimate load capacity according to the Van Weele's Method (a) 15 cm x 15 cm Single RPP; (b) 15 cm x 15 cm RPPs at 0.9 m Spacing

Fuller and Hoy. In Figure 3-17 a simple definition proposed by Fuller & Hoy (1970) is shown. The failure load is equal to the test load for where the load settlement curve is sloping 0.14 mm/kN.
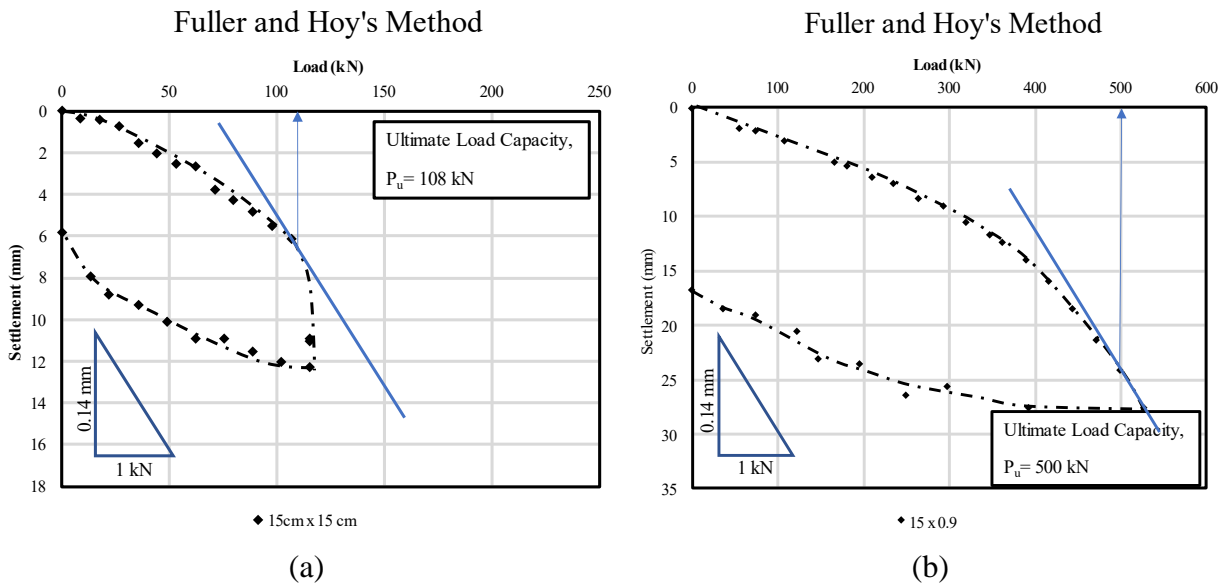
Figure 3-17 Ultimate load capacity according to the Fuller and Hoy's Method (a) 15 cm x 15 cm Single RPP; (b) 15 cm x 15 cm RPPs at 0.9 m Spacing

Butler and Hoy. Figure 3-18 shows a development of the above definition proposed by Butler & Hoy (1977) defining the failure load as the load at the intersection of the tangent sloping 0.14 mm/kN and the tangent to the initial straight portion of the curve or to a line that is parallel to the rebound portion of the curve. As the latter portion is more or less parallel to the elastic line.
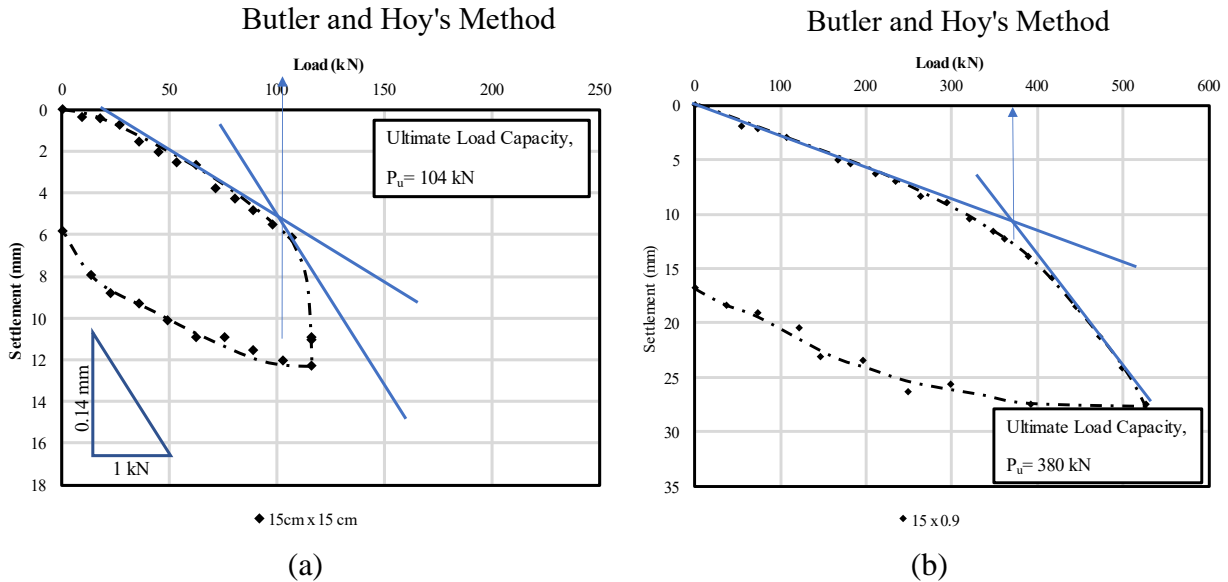
Figure 3-18 Ultimate Failure according to the Butler and Hoy's Method (a) 15 cm x 15 cm Single RPP; (b) 15 cm x 15 cm RPPs at 0.9 m Spacing

The ultimate load and the settlement derived from different methods for the four different sizes of single RPPs are shown in Table 3-3. The maximum ultimate load for 15 cm x 15 cm RPP was found 167 kN utilizing Chin's method and the minimum load was found 104 kN from Butler and Hoy's Method. In the case of 10 cm x 10 cm RPP, a similar pattern was observed. As the load increased, the settlement due to the loading also increased.

RPP with larger cross-section showed higher ultimate load carrying capacity. 50% increase in the section increases the capacity by 200% (most conservative in Butler and Hoy's Method) to 335% (Chin's Method). However, the change in settlement is similar in RPP with different cross-sections. The maximum settlement was found to be 13.5 mm which is a little more than half an inch for 10 cm x 10 cm RPP. RPPs with smaller cross-section experienced higher settlement. A possible explanation of this phenomenon lies in the installation process of RPPs. As RPPs were pushed into the soil and flushed to the ground, the soil surrounding the RPP was heavily compacted which eventually resulted in the increase of skin friction. 15 cm x 15 cm RPP having larger cross-

section, the surrounding soil was more compacted and resulted in higher load capacity and less settlement.

Table 3-3 Summary of Average Ultimate Vertical Load Capacity Result of Single RPPs

CODES/ METHODS	10 cm x 10 cm		15 cm x 15 cm		25 cm x 25 cm		30 cm x 30 cm	
	Ultimate Load (kN)	Settlement at Ultimate Load (mm)	Ultimate Load (kN)	Settlement at Ultimate Load (mm)	Ultimate Load (kN)	Settlement at Ultimate Load (mm)	Ultimate Load (kN)	Settlement at Ultimate Load (mm)
Field Test	45	15.75	116	12.5	155	5.5	196	4
Davisson (1972) Method	45	13	118	10	178	7.5	----	----
Brinch Hansen's (1963)	45	13.5	115	9	160	5.5	200	3.5
Chin's Method (1971)	83	----	167	----	222	----	280	----
Van Weele (1957)	40	7	105	6.2	135	3.4	178	2
Fuller and Hoy's (1970)	43	8	108	6.3	148	4	200	3.8
Butler and Hoy's Method (1977)	42	5	104	5.5	135	3	187	2.1

A comparative graphical representation of ultimate vertical laod capacity of RPPs of four different sizes are presented in Figure 3-19. Furthermore, the average load capacity found from different methods are presented. For single RPPs of 10 cm x 10 cm, 15 cm x 15 cm, 25 cm x 25 cm and 30 cm x 30 cm, the average load carrying capacity were found 50 kN, 119 kN, 162 kN and 207 kN respectively.
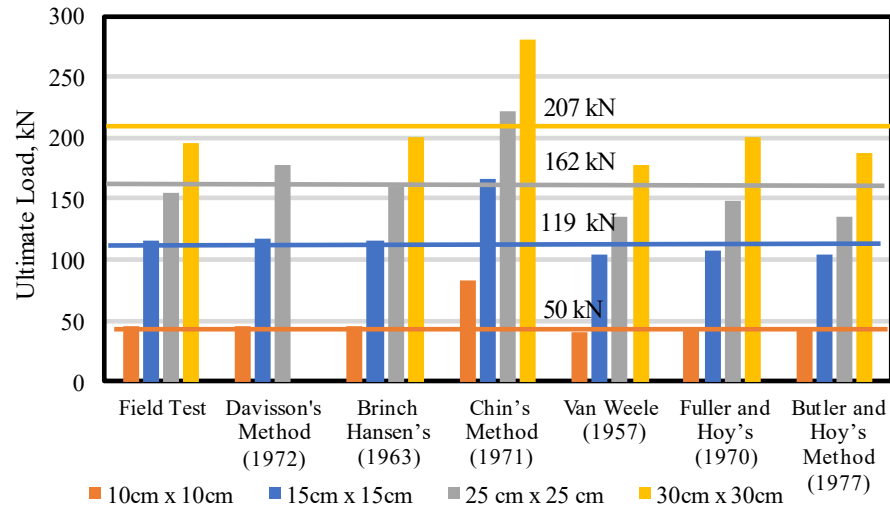
Figure 3-19 Ultimate Vertical load capacity of Single RPPs following different methods

From the analysis, the average of ultimate vertical load capacity for group RPPs in different methods was found to be 193 kN for 10 x 0.9 and 225 kN for 10 x 0.6. For the groups 15 x 0.9 and 15 x 0.6, the average ultimate vertical load capacity was found to be 450 kN and 477 kN respectively. Figure 3-20 shows average ultimate load capacity of the RPP groups. Ultimate load capacity of 10 cm by 10 cm, 15 cm by 15 cm RPP groups were analyzed by following listed methods in Table 3-4. Increasing the RPP size from 10 cm x 10 cm to 15 cm x 15 cm reduced the vertical displacement to 19% and 34% for 0.3 m center to center arrangement and 0.6 m center to center arrangement respectively. Due to a 0.3 m increment in spacing from 0.6 m to 0.9 m the settlement increase was not significant (only 6%) in the case of 10 cm by 10 cm RPP. However, in the case of 15 cm by 15 cm RPP the settlement was 18% more. For increasing the spacing 50%, the load capacity reduced 6% to 16% for 15 cm by 15 cm and 10 cm by 10 cm RPP respectively.

Table 3-4: Summary of Average Ultimate Vertical Load Capacity Result of Single RPPs

CODES/ METHODS	10 cm x 10 cm at 0.9 Spacing		10 cm x 10 cm at 0.6 Spacing		15 cm x 15 cm at 0.9 Spacing		15 cm x 15 cm at 0.6 Spacing	
	Ultimate Load (kN)	Settlement at Ultimate Load (mm)	Ultimate Load (kN)	Settlement at Ultimate Load (mm)	Ultimate Load (kN)	Settlement at Ultimate Load (mm)	Ultimate Load (kN)	Settlement at Ultimate Load (mm)
Field Test	203	34	235	32	525	27.5	543	22.5
Davisson (1973) Method	190	21	225	25	440	18.5	525	18.5
Brinch Hansen's (1963)	220	33	230	28	380	13.5	499	17.5
Chin's Method (1978)	230	----	285	----	558	----	556	----
Van Weele (1957)	180	17	205	18.5	370	12.5	378	11.5
Fuller and Hoy's (1970)	190	19	210	18	500	24	445	14.5
Butler and Hoy's Method	150	13	200	18	380	11	391	12.5
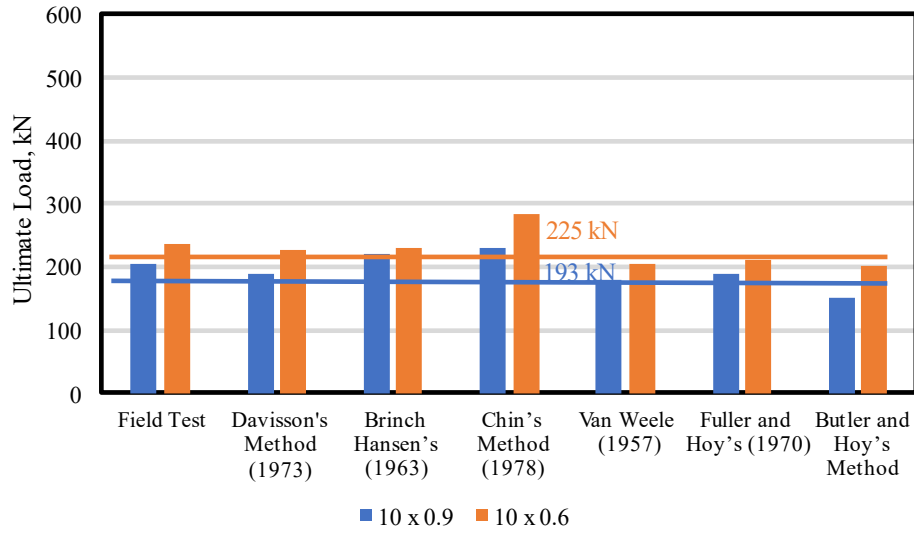
(a)
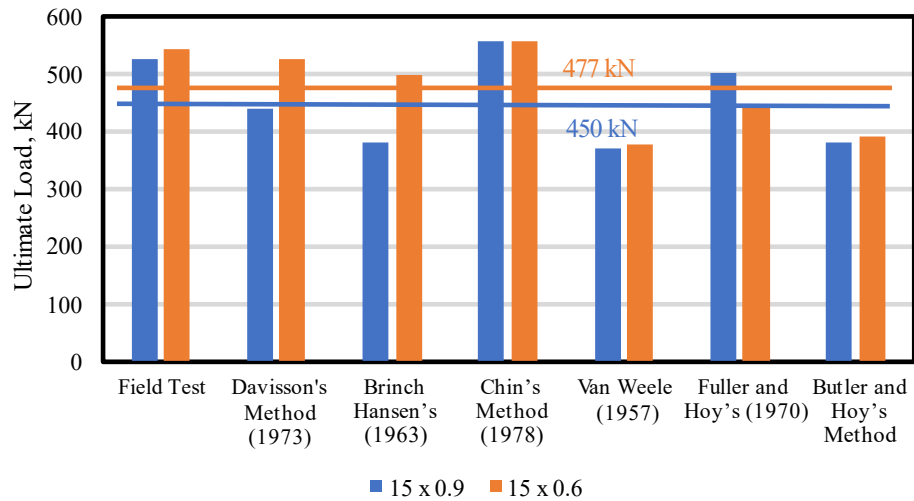
(b)

Figure 3-20 Ultimate Vertical load capacity of (a) 10 cm x 10 cm RPP at 0.9 m c/c spacing and 0.6 m c/c spacing , (b) 15 cm x 15 cm RPP at 0.9 m c/c spacing and 0.6 m c/c spacing following different methods

The Chin's method provides higher load capacity values compared to the Butler & Hoy method because it allows for continuous monitoring, is less sensitive to data inaccuracies, and may predict higher load capacities even when the Butler & Hoy criteria are not met. Engineers may choose one

method over the other based on the specific project requirements, site conditions, and their preferred approach to pile load testing and interpretation.

3.3.2   Skin Resistance and End Bearing

The load testing and strain gauge data analysis of various sizes and configurations of RPP reveal significant trends and findings. These investigations help in understanding the behavior of RPPs under vertical loads, providing insights into unit skin friction and displacement at different depths. Unit skin resistance and displacement along the length of single and group RPPs are shown in Figure 3-21. The unit skin friction and deformation of the RPP were calculated from measurements of strain gauges using the following two formula:

$$P = \bar{\varepsilon} E_p A \qquad (3.1)$$

$$\Delta l = \frac{Pl}{AE} \qquad (3.2)$$

In the individual RPP tests, the 10 cm x 10 cm RPP experienced a significant increase in unit skin friction as depth increased, ranging from 0.95 kPa at 0.3 m to 2.43 kPa at 1.5 meters. At 2.7 meters, the highest skin friction of 25.75 kPa was observed at the bottom, representing a 27-fold increase compared to the 1.5-meter depth. Settlement exhibited the opposite trend, with the highest settlement of 8.73 mm at the top and the lowest of 1.83 mm at the bottom, resulting in an 80% reduction from top to bottom. Similar trends were observed for the 15 cm x 15 cm and 25 cm x 25 cm RPPs, albeit with variations in values and reductions in settlement (83% and 92%, respectively).

A consistent pattern in all these RPP tests is the direct relationship between unit skin friction and depth. As depth increases, the surrounding soil becomes more compacted, leading to higher values of skin friction at the bottom. This compaction is intensified by the installation process, which involves using a 2.13 m steel pin to create a hole and then pushing the RPPs into the soil, effectively anchoring them and further increasing skin friction. Additionally, the larger cross-sectional area of the 15 cm x 15 cm and 25 cm x 25 cm RPPs intensifies the compaction of the surrounding soil at the bottom, resulting in higher unit skin friction.
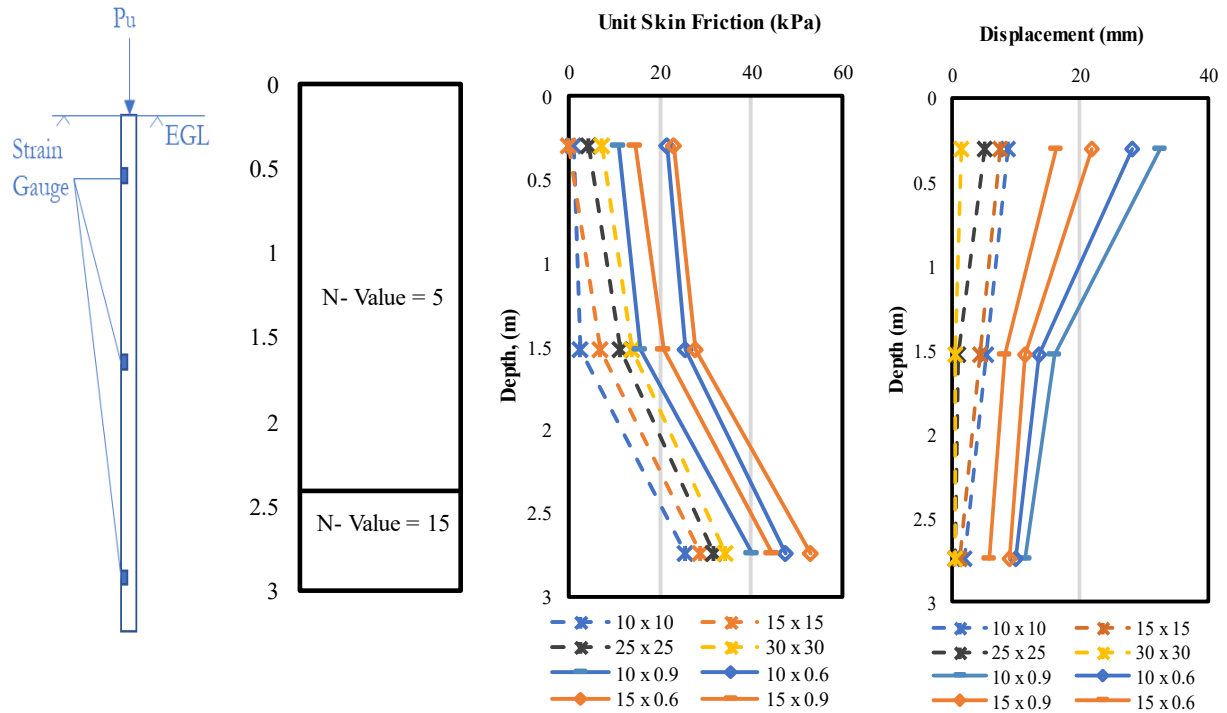
Figure 3-21 Unit Skin Friction and Displacement along the depth

Expanding the analysis to group configurations, such as 15 x 0.6 and 15 x 0.9 groups, and 10 x 0.6 and 10 x 0.9 RPP groups, reveals consistent trends. In 15 x 0.6 group, for example, unit friction ranged from 14.82 kPa at 0.3 meters to 44.79 kPa at 2.7 meters, with a 65% reduction in displacement from top to bottom. 10 x 0.6 and 10 x 0.9 similarly displayed increasing unit skin friction with depth, along with reductions in displacement (65% and 61%, respectively). These findings emphasize the importance of considering both depth-related behaviors and the installation process in the design and evaluation of RPP systems.

The unit skin friction could be used towards calculating the ultimate skin resistance and ultimate tip resistance of the RPPs. The following formulae can be used to determine all static pile capacities.

$$Q_u = Q_{pu} + \Sigma Q_{si} \qquad (3.3)$$

Where, Q_u = ultimate (maximum) pile capacity

Q_{pu} = ultimate pile tip capacity

ΣQ_{si} = skin resistance developing with ultimate tip resistance Q_{pu};

Ultimate skin resistance was calculated based on the unit skin friction obtained from the strain gauge data and was assumed to be the same along the distributed length of the RPP. Figure 3-22 shows the distribution of length along the RPP.
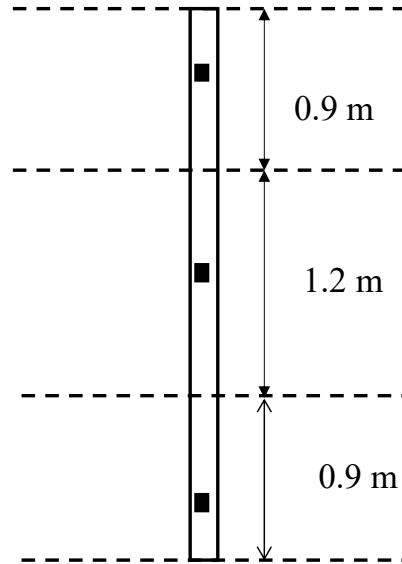
Figure 3-22 Distribution of length along the RPP

Ultimate skin resistance of RPP can is written as:

$$Q_{si} = \sum_{1}^{n} A_s f_s \qquad (3.4)$$

Where,

A_s = effective pile surface area on which f_s acts.

f_s = skin resistance

For 10 cm x 10 cm RPP, unit skin friction along the strain gauges were found to be 0.95 kPa, 2.43 kPa and 25.75 kPa at the depth of 0.3 m, 0.6 m and 0.9 m. Therefore,

$$Q_{si} = 0.95 * 4 * 0.10 * 0.9 + 2.43 * 4 * 0.10 * 1.2 + 25.75 * 4 * 0.10 * 0.9$$

$$= 10.78 \ kN$$

We can find ultimate tip resistance from the ultimate load capacity and the ultimate skin friction by rearranging equation (3.3) as:

$$Q_{pu} = Q_u - \Sigma Q_{si} \qquad\qquad (3.5)$$

$$= 45\ kN - 10.78\ kN$$

$$= 34.22\ kN$$

Similarly, ultimate skin friction and ultimate tip resistance was calculated for the 15 cm x 15 cm and 25 cm x 25 cm RPPs. The results are tabulated in Table 3-5.

Table 3-5 Ultimate skin friction and ultimate tip resistance of RPPs of different sizes

RPP Size	Ultimate Skin Friction (kN)	Ultimate Tip Resistance (kN)
10 x 10	10.78	34.22
15 x 15	24.35	91.6
25 x 25	58.37	96.6

3.3.3 Pressure Distribution on Soil and RPPs

Earth Pressure plate has been installed on top of soil in between RPPs to measure the stresses of applied load on the soil. The section being reinforced with RPP, a major portion of surcharge load is carried by RPP and thus stress on soil has been reduced. Figure 3-23 shows the pressure plate data for the RPP groups during vertical load tests. The decrease of the earth pressures on the soil was due to the differential settlement of the soil and pins, and the soil arching is developed. When the load reached failure, the additional load was mostly carried by the RPPs.
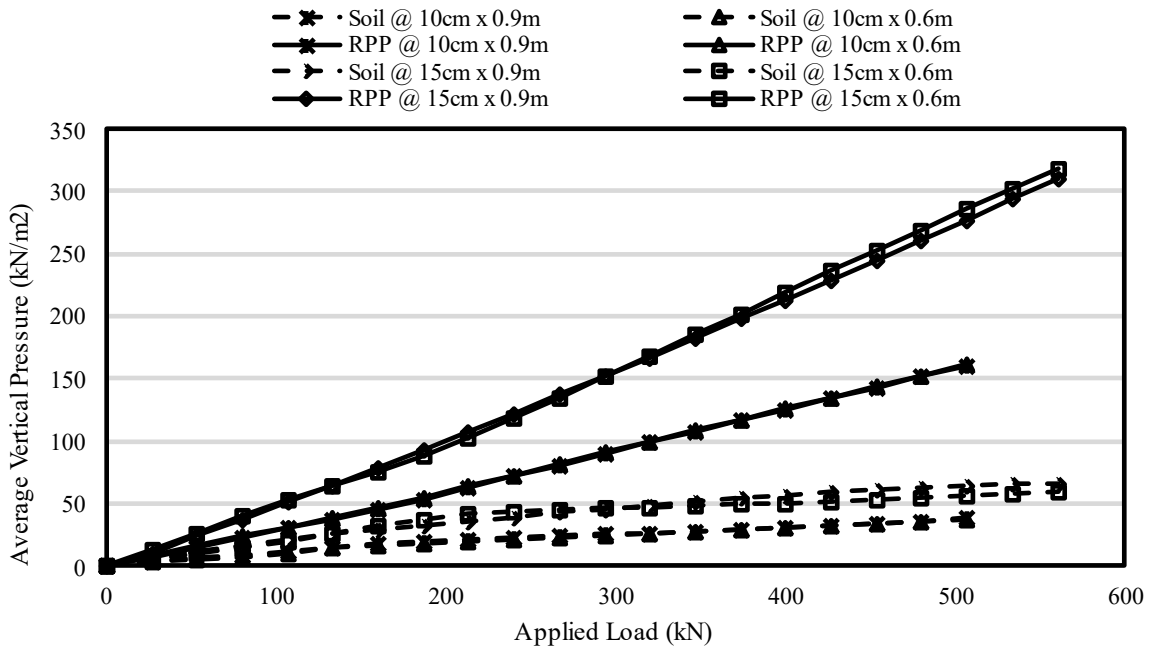
Figure 3-23 Average pressure on top of RPPs and soil with increasing load

The stress reduction ratio (SRR) is a measure used to describe the decrease of load on soft subsoil. It is defined as the ratio of average vertical load on the top of soil between piles to total surcharge load. SRR values can range from 0 to 1. A lower SRR number reflects the extent of load transfer. An SRR of 0 indicates complete soil arching, while a ratio of 1 indicates no soil arching. A lower SRR value indicated less pressure on the soil of the strengthened portion.

The SCR is defined as the vertical stress acting on the top of the RPP (σ_p) divided by the vertical stress acting at the ground surface between the RPPs (σ_s). In order to understand the load transfer effectiveness on RPP, the stress concentration ratio was estimated for various combinations.

If there was no RPP, the maximum pressure on soil was supposed to be 353 kPa and 365 kPa at the failure of 15 cm x 15 cm RPP at 0.9 m c/c spacing 15 cm x 15 cm RPP at 0.6 m c/c spacing groups; and 137 kPa and 158 kPa at the failure of 10 cm x 10 cm RPP at 0.9 m c/c spacing 10 cm x 10 cm RPP at 0.6 m c/c spacing groups. At the failure, the pressure on soil was recorded to be 75% to 84% less than that carried by the RPPs. This means that the RPPs carried most of the applied loads, and so relatively, the weak soil beneath the geogrid was subjected to less compressive stress. The pressures on the soils between the pins were far smaller than those

136

measured on the RPPs. SRR and SCR were calculated for each RPP group, and the results are tabulated below in Table 3-6.

Table 3-6 Summary of SRR and SCR for different RPP groups

	Pressure on Soil (kPa)	Pressure on RPP (kPa)	SRR	SCR
10 cm x 0.9	26.99	108.36	0.22	4.02
10 cm x 0.6	30.89	125.29	0.20	4.10
15 cm x 0.9	62.02	291.00	0.19	4.69
15 cm x 0.6	52.59	312.38	0.16	5.43

3.4   Analytical Study

3.4.1   Bearing Capacity and Settlement

When driven into the foundation, recycled plastic pins aid in densifying the soil. Additionally, depending on the size and spacing of the RPPs, it produces a composite of soil and RPPs whose stiffness is significantly improved. The new composite foundation can withstand the load from the structure with less settlement owing to the RPP reinforcement. Analytical methods can be used to assess RPP's capability for strengthening deficient foundation soil.

The settlement of the foundation soil can be classified into two types: elastic settlement (load dependent) and consolidation settlement (time dependent). However, there is no consolidation settlement in the absence of a water table. No water table was discovered during the field research in the site location for the current study. According to Das (2011), the theoretical statement of elastic settlement is, if the foundation is fully flexible:

$$S_e = q_o(\alpha B') * \frac{1 - \mu_s^2}{E_s} * I_s I_f \qquad (3.6)$$

where,

q_0 = net pressure applied on the foundation

μ_s = Poisson's ratio of the soil

E_s = average modulus of elasticity of the soil under the foundation

B' = B/2 for center of the foundation; or B for the corner of the foundation

I_s = Shape factor

I_f = depth factor

α = a factor that depends on the location on the foundation where settlement is to be calculated

= 4 (for center of the foundation); 1 (for corner of the foundation)

For the current study, a section was considered having a square foundation of width, B = 1.22 m. The net pressure due to applied load during load test on the foundation was, q_0 = 300 kPa. The average modulus of elasticity of the soil under the foundation was calculated to be, E_s = 5973.64 kN/m^2. and poisons ratio, μ_s = 0.25. For a square foundation on the ground surface, shape factor (I_s) and depth factor (I_f) are considered to be 1.0. For a foundation under uniform load, the maximum stress is usually experienced at the center of the foundation, therefore, maximum settlement will take place at the center of the foundation. Hence, the maximum settlement of the foundation can be calculated using equation 3.6.

$$S_e = q_o(\alpha B') * \frac{1 - \mu_s^2}{E_s} * I_s I_f$$
$$= 300 * \left(4 * \frac{1.22}{2}\right) * \frac{1 - 0.25^2}{5973.64} * 1$$
$$= 0.115 \, m$$
$$= 11.50 \, cm > 2.54 \, cm$$

Which is excessive considering the allowable settlement to be 2.54 cm which is generally considered as a permissible settlement in foundation. The bearing capacity of the foundation for 2.54 cm settlement can be back calculated using equation 3.7.

$$q_u = \frac{S_e}{(\alpha B') * \frac{1 - \mu_s^2}{E_s}} \qquad (3.7)$$
$$= \frac{0.0254}{\left(4 * \frac{1.22}{2}\right) * \frac{1 - 0.25^2}{5973.64}}$$

$$= 66.33 \ kN/m^2$$

RPPs driven into the foundation soil are expected to improve the support capability of the existing foundation soil. Without replacing the soft foundation soil, driving RPP into it ensures that the soil matrix will become denser, resulting in a composite foundation with increased rigidity. $E_{RPP} = 13.8 \times 10^5 \ kN/m^2$ is the RPP's elasticity modulus. The equivalent average modulus of elasticity of the RPP-soil composite is $E_{eqs} = 13382.58 \ kN/m^2$ if 10 cm by 10 cm RPPs are embedded into the foundation soil at 0.9 m c/c spacing in a square configuration (Zaman, 2019).

Using equation 3.4 to get the settlement for the new reinforced foundation:

$$S_e = 300 * 4 * \frac{1.22}{2} * \frac{1 = 0.25^2}{13382.58}$$

$$= 0.051 \ m$$

$$= 5.13 \ cm$$

Reduction in settlement = 55%

The usage of 10 cm x 10 cm RPP at 0.9 m c/c spacing can result in a 55% reduction in settling. Equation 3.5 can be used to compute the bearing capacity of the upgraded foundation for 2.54 cm settlement.

$$q_u = \frac{S_e}{(\alpha B') * \frac{1 - \mu_s^2}{E_s}}$$

$$= \frac{0.0254}{\left(4 * \frac{1.22}{2}\right) * \frac{1 - 0.25^2}{13382.58}}$$

$$= 148.60 \ kN/m^2$$

This demonstrates that the implementation of 10 cm x 10 cm RPP at 0.9 m c/c can result in a bearing capacity improvement of approximately 2.24 times over the unreinforced section.

Settlement and bearing capacity for foundation reinforced with varied sizes and spacing of RPP can be estimated using the same analytical approach. The computed anticipated settlement for the foundation soil reinforced with 10 cm by 10 cm, 15 cm by 15 cm, and 25 cm by 25 cm RPP at 0.6 m, 0.9 m, and 1.2 m spacing is shown in Table 3-7. Table 3-8 shows the bearing capacity of various RPP reinforced sections for 2.54 cm settlement.

Table 3-7 Settlement calculated for RPP reinforced foundation soil due to applied load of 300 kPa

Settlement Reduction (%)			
RPP size Spacing (m)	10 cm by 10 cm RPP	15 cm by 15 cm RPP	25 cm by 25 cm RPP
0.6	70	83	94
0.9	55	74	89
1.2	40	60	81

Table 3-8 Bearing capacity of the reinforced foundation (for 2.54 cm settlement)

Bearing Capacity (kN/m^2)			
RPP size Spacing (m)	10 cm by 10 cm RPP	15 cm by 15 cm RPP	25 cm by 25 cm RPP
0.6	225	387	1032
0.9	148	253	590
1.2	112	167	344

Based on the calculations, it was discovered that the implementation of RPP can increase bearing capacity by up to 16 times when compared to the unreinforced section. Based on the analytical solution, a considerable reduction in settlement was discovered for each of the reinforced portions. Figure 3-24 depicts a bar chart comparing bearing capacity of foundation between various RPP reinforced sections and a control section (without RPP reinforcement).
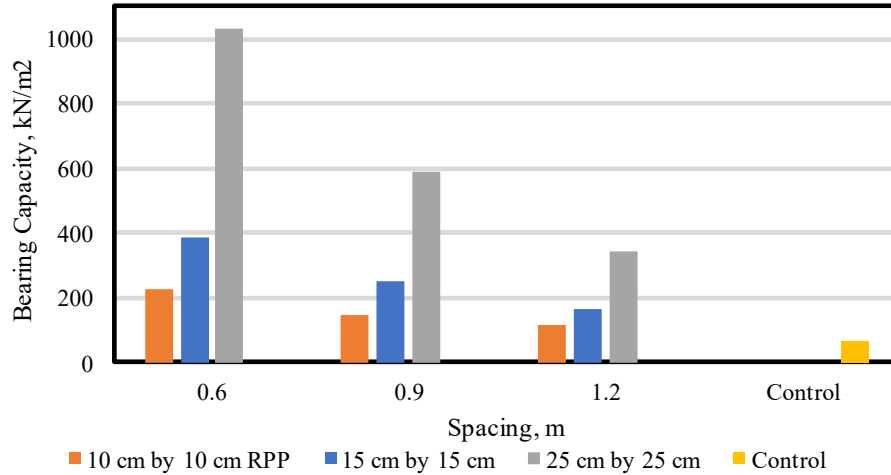
Figure 3-24 Comparison of bearing capacity of foundation between control and RPP reinforced.

The predicted bearing capacity of reinforced foundation's (for 2.54 cm settlement) was plotted against RPP spacing and RPP size, as shown in Figure 3-25 and Figure 3-26, respectively. The plot shows that for the same RPP size, bearing capacity increases with decreasing RPP spacing. Furthermore, for RPPs with fixed spacing, bearing capacity improves with RPP size. The rate of increase in bearing capacity was observed to increase with increasing RPP size, which is due to the larger size having the benefit of replacing more void space in the soil matrix, which better densifies the soil, improves stiffness, has much higher load carrying capacity, and thus improves the bearing capacity of the foundation soil.
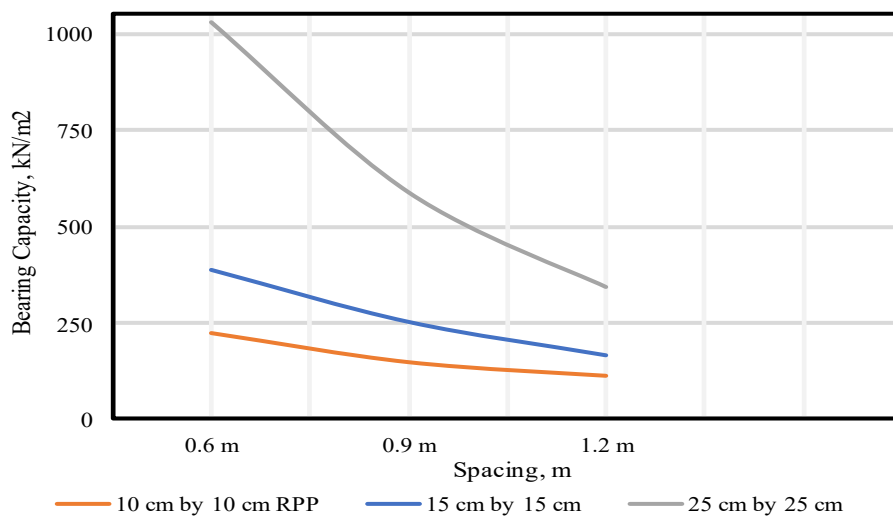
Figure 3-25 Relation between bearing capacity and RPP spacing for different sizes of RPPs based on analytical study.
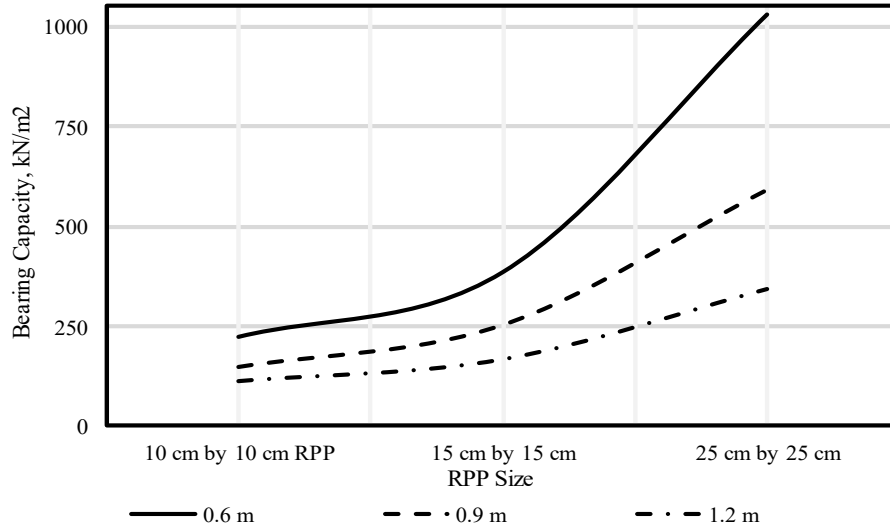
Figure 3-26 Relation between bearing capacity and size of RPP for fixed spacing based on analytical study.

Under varied bearing pressures, elastic settlement was computed for the foundation soil reinforced with RPP of various sizes and spacing. Figure 3-27 depicts a plot of settlement versus bearing pressure. The graphic shows that bearing pressure increases significantly for each configuration of RPP reinforcement when compared to the control section (no RPP reinforcement). It was also discovered that in some circumstances, the performance of the test section reinforced with larger RPP with wider spacing was relatively better than the smaller sized RPP with narrower spacing.
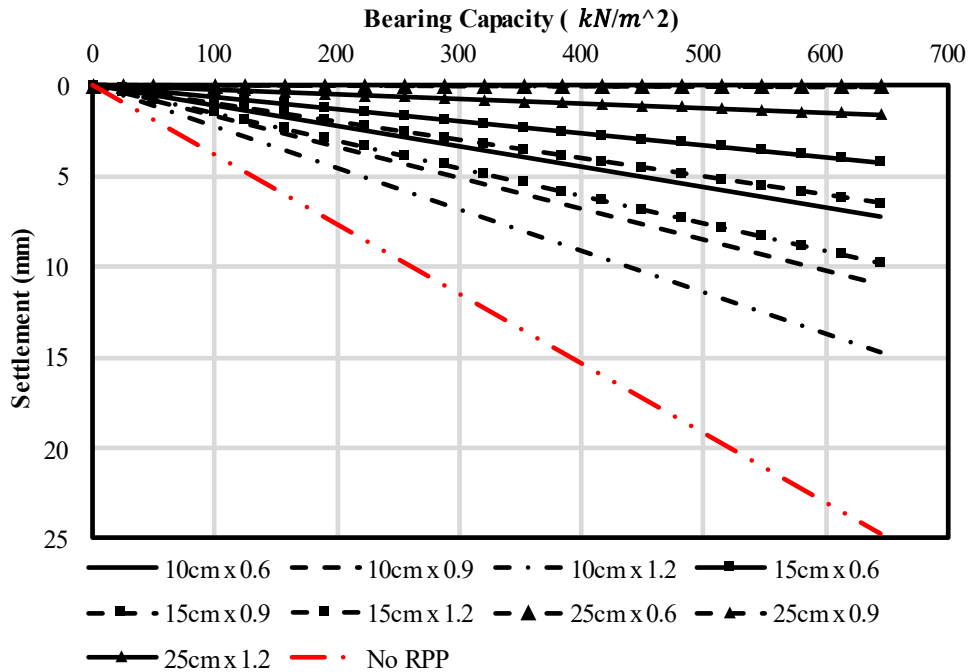
Figure 3-27 Comparison of bearing capacity between control section and different RPP reinforced section based on analytical calculation.

3.4.2 Ultimate Load Capacity of RPPs in a Group

Typically, piles in geosynthetic reinforced pile-supported embankments are constructed in a square or triangular configuration. In the absence of ground water, elastic settlement occurs in the subsoil with the application of load, resulting in differential settlement between the RPP and the foundation soil. The tension on the subsoil reduces while it increases on the RPPs. Soil arching is a phenomenon that can be intensified by utilizing geosynthetic reinforced LTP. SCR and SRR can be used to assess the efficiency of soil arching.

Following assumptions are used to develop the analytical framework for the geosynthetic reinforced and RPP supported foundation:

a) The applied load is uniform, and the load transfer platform are homogenous, isotropic, and elastic perfectly plastic materials.

b) The subsoil is assumed to be in a plane-strain condition.

c) The compression of foundation soil is one-dimensional. The stresses and strains of the subsoil are evenly distributed.

d) The weight of the geosynthetics is assumed negligible.

e) The vertical deformation of geosynthetic at the top of RPP is negligible.

f) The deformation of geosynthetic is elastic.

For a single RPP, the point load capacity will be the result of skin friction and end bearing. As the friction angle is considered as zero for cohesive soil, the undrained bearing capacity will be the multiplication of undrained shear strength and N_c and the simplified equation becomes as follows.

$$q_{soil} = 5.14 \, s_u \; or \; (2 + \pi)s_u \qquad (3.8)$$

$$= 5.14 * 6.7$$

$$= 34.4 \, kN/m2$$

Since the applied load is distributed both on RPP and soft soil, the bearing capacity of the RPP reinforced foundation will be contributed by both RPP and foundation soil. The ultimate bearing capacity, Q_u can be expressed as

$$Q_u = Q_{RPP} * \text{SCR} * \eta + q_{soil} * A_s * \text{SRR} \qquad (3.9)$$

Here, η is the group efficiency; and the total load carried by the RPP will be ultimate load of RPP (Q_{RPP}) times SCR, or

$$Ultimate \; Load \; Capcity \; of \; RPP \; in \; Group, Q_{uRPP} = Q_{RPP} * \text{SCR} * \eta \qquad (3.10)$$

On the other hand, total load carried by the soil will be ultimate load of soil (q_{usoil}) times SRR, or

$$Ultimate \; Load \; Capcity \; of \; soil, q_{usoil} = q_{soil} * \text{SRR} \qquad (3.11)$$

Simplifying and rearranging equation 3.9 yields:

$$Q_{uRPP} = Q_u - q_{usoil} * A_s \qquad (3.12)$$

Where, As is the area of soft foundation soil except RPP $= A - Ap$.

By substituting equation (3.10) and (3.11) into equation (3.12), the Q_{uRPP} can be determined. The substitution of equations (3.10), (3.11) and (3.12) into (3.9) yields the bearing capacity of RPP in group, Q_{RPP}.

3.4.2.1 Determination of Ultimate Load Capacity of RPP in Group

Both RPPs and the foundation soil contribute to the total load capacity of the group RPP. A field load test was conducted on top of soil without any RPP to determine the bearing capacity of soil under load testing conditions. The load was applied employing the RCC slab to ensure consistent load distribution over a total area of 1.2 m by 1.2 m. To duplicate the load testing of group RPPs, the RCC slab was underlain by geogrid. The soil bearing capacity test is depicted in Figure 3-28. The soil failed at 41 kN exhibiting drastic movement with load application while conducting the test indicating the ultimate bearing capacity of soil in the field, q_{usoil}.
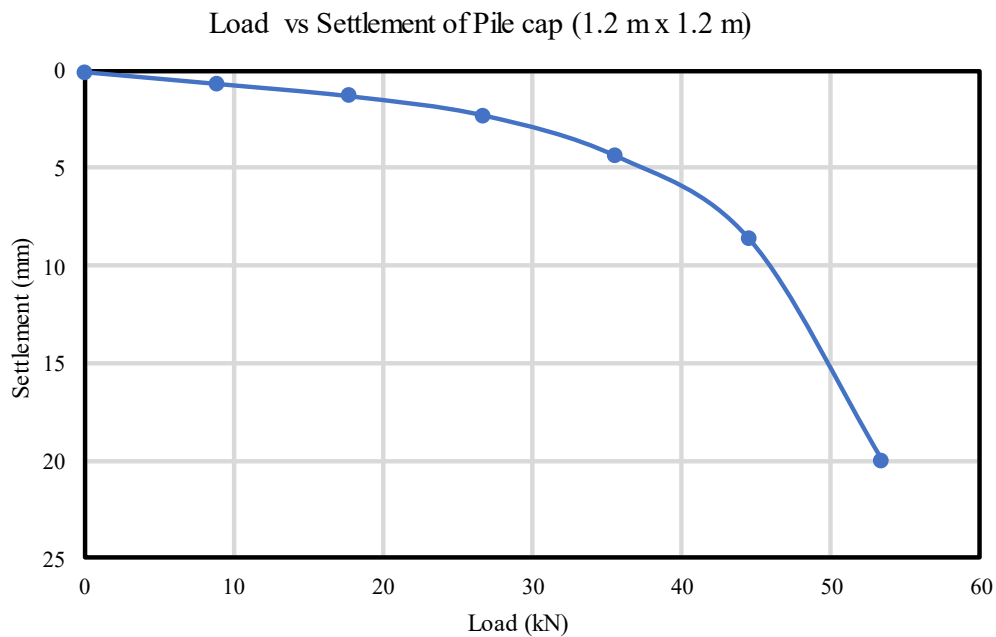
Figure 3-28 Soil bearing capacity test results

In group RPPs, the soil and the RPPs receive load together as a system. The LTP works as a device to uniformly distribute the applied load and the geogrid helps in activating soil arching within the system. Group Efficiency of the four 10 cm by 10 cm RPPs arranged at 0.9 m c/c spacing, was calculated using following equation:

$$\eta = \frac{Q_{g(u)}}{\Sigma Q_u} \qquad (3.13)$$

145

The efficiency for this RPP group was found 1.0, which depicts, the maximum load capacity of the RPPs will be four times of that of the individual RPPs. Similarly, group efficiency for other groups was calculated and in all cases of the current study, group efficiency was found to be 1.0.

By substituting equation (3.10) and (3.11) into equation (3.12), the Q_{uRPP} was determined. For 15 x 0.9 RPP group,

$$Ultimate\ Load\ Capcity\ of\ soil, q_{usoil} = q_{soil} * \text{SRR}$$

$$= 41 * 0.19$$

$$= 7.79\ \text{kN/m}^2$$

$$Q_{uRPP} = Q_u - q_{usoil} * A_s$$

$$= 477 - 7.79 * 1.35$$

$$= 439\ \text{kN}$$

The results for ultimate load capacity of the RPP in a group arrangement are tabulated in Table 3-9.

Table 3-9 Ultimate load capacity of RPPs in group arrangement

RPP Group	Q_u (kN)	As (m²)	SRR	Q_{uRPP} (kN)
10 x 0.9	193	1.4	0.22	168
10 x 0.6	225	1.4	0.20	180
15 x 0.9	450	1.35	0.19	439
15 x 0.6	477	1.35	0.16	462

3.5   Conclusion

Plate Load Test was performed in field scale to evaluate the vertical load carrying capacity of RPP in high plastic clay. The study provided a detailed testament about the field tests and analytical studies related to the use of Recycled Plastic Pins (RPPs) for ground reinforcement and load-bearing capacity. Ultimate load carrying capacity of 8 single RPPs of four different sizes and 8 RPP groups of two different sizes and spacing totaling to four different combinations were found out from the load settlement behaviour of RPPs. Six different methods have been utilized for

analysing the field data obtained from the field load tests. The significant observations can be summarised as follows.

- The ultimate load capacity of single RPPs from the field load test was 45 kN, 116 kN, 155 kN, and 196 kN for 10 cm x 10 cm, 15 cm x 15 cm, 25 cm x 25 cm, and 30 cm x 30 cm RPPs, respectively, with corresponding settlement of 15.45 mm, 12.5 mm, 9.0 mm and 4.0 mm.

- The ultimate load carrying capacity is higher in the RPP with larger cross-section. The increase of load capacity of RPP has an exponential relationship with the increase of RPP size. The relationship can be expressed as $y = 19.463e^{0.0029x}$ providing a significant correlation with the data.

- Average ultimate vertical load capacity of the single RPPs were found to be 50 kN, 119 kN, 162 kN and 207 kN for 10 cm x 10 cm, 15 cm x 15 cm, 25 cm x 25 cm, and 30 cm x 30 cm RPPs, respectively.

- The field load capacity of group RPPs acting as a system was determined to be 203 kN, 235 kN, 525 kN, and 543 kN for 10 x 0.9, 10 x 0.6, 15 x 0.9, and 15 x 0.6 RPP groups, with corresponding settlement of 34 mm, 32 mm, 27.5 mm, and 22.5 mm.

- The average ultimate vertical load capacity of the RPP groups 10 x 0.9, 10 x 0.6, 15 x 0.9, and 15 x 0.6 was determined to be 193 kN, 225 kN, 450 kN, and 477 kN, respectively.

- Chin's Method shows higher ultimate load carrying capacity of the RPPs both in single and group arrangement, however, Butler and Hoy's Method show the most conservative values in both load capacity and settlement criteria.

- The direct relationship between unit skin friction and RPP depth is a consistent trend in all of these RPP studies. Settlement followed the reverse pattern, with the highest settlement at the top and the lowest at the bottom, resulting in a decline of 80% to 92% from top to bottom.

- The ultimate skin resistance and ultimate tip resistance were derived from the field load capacity using the unit skin friction acting on the RPPs measured with the strain gauges.

- According to the pressure plate data, the pressure on the soil at the failure was 75% to 84% lower than that carried by the RPPs. This suggests that the RPPs carried the majority of the applied loads, exposing the weak soil beneath the geogrid to less compressive stress.

- The ultimate load capacity of the RPPs alone in the group arrangement was computed analytically. The study also presented a straightforward analytical method for determining the

bearing capacity of an RPP reinforced foundation system. With increasing RPP size, the rate of increase in bearing capacity was observed to rise.

CHAPTER 4

NUMERICAL ANALYSIS OF VERTICAL LOAD CAPACITY OF RECYCLED PLASTIC PIN

ABSTRACT

Recycled Plastic Pins (RPP) is a noble approach to improve the problematic foundation soil by increasing the bearing capacity of the foundation. Despite its success in strengthening the foundation soil in numerous geotechnical projects, the load capacity of RPP yet needs to be evaluated. The objective of the study is to assess vertical load capacity of RPPs in terms of load-settlement behavior using finite element analysis. In this paper, field measurements of axially loaded to failure RPP driven in high plastic clay have been used to assess numerical models established to simulate the behavior of RPPs in varying soil conditions. Utilizing the finite element program PLAXIS 3D, a numerical model was established against the field measured data in the context of settlement. After calibration, a comprehensive parametric analysis was carried out to evaluate the effect of shear strength of foundation soil and RPP size, length and spacing on the results.

Key words: RPP; Vertical Load Capacity; Field Load Test; Load Settlement Behavior; Numerical Modeling.

4.1 Introduction

Recycled Plastic Pin (RPP) is a recent innovation in ground improving technologies. RPP could be an effective substitute for piles for enhancing the soil's bearing capacity by making it more rigid. At a minimal strain rate of 0.006%/min, RPP's compressive strengths ranged from 230 ksf (11MPa) to 439 ksf (21 MPa) whereas compression moduli measured at one percent strain ranged from 11529 ksf (552 MPa) to 27360 ksf (1310 MPa) (Bowders et al. 2003; Chen et al. 2007). RPPs are lighter and less prone to chemical deterioration than concrete or steel piles. According to Bowders et al. (2003) and Chen et al. (2007), RPPs are mostly made of polymeric materials made from recycled plastics and other waste materials. According to Hossain et al. (2017), a 3 m x 100 cm^2 (Length x Area) RPP uses about 600 recycled water/soda bottles. As a result, using RPP lowers

the amount of waste going to landfills and creates a new market for recycled plastic (Loehr et al. 2000).

As a sustainable solution for stabilizing roadway slopes, RPP was initially applied in the states of Missouri and Iowa (Hossain et al. 2017). Today, RPP is used in many other US states as a practical means of stabilizing slopes (Khan et al. 2016; Hossain et al. 2017; Bhandari et al. 2020). Recycled Plastic Pins (RPP) are increasingly being used in slope stabilization projects, but the lack of a clearly defined design framework remains a major barrier to their wider acceptance, particularly in the context of improving the load carrying capacity of soft soils. Engineers must have a thorough understanding of the performance parameters related to RPP-supported geotechnical structures to facilitate effective and economical design and construction initiatives. A mathematical analysis of the engineering behavior of Recycled Plastic Pins (RPP) is instrumental in establishing a standardized design framework.

The development of a mathematical model that can simulate responses to certain activities is needed to ensure that projected outcomes align reasonably with empirical observations (Meyer, 1987; Rao, 2006). There are various ways to standardize, change, and verify a mathematical model. Numerical analysis is a powerful tool that can be used to evaluate the vertical load capacity of driven piles. In this context, finite element analysis (FEA) is a widely used numerical technique that can provide accurate predictions of the pile behavior under different loading conditions. The common engineering practice is to build a mathematical model and predict from the results. The accuracy of the mathematical model and the physical test are both confirmed by a satisfactory match between projected results and physical experiments. Consequently, model calibration is essential for numerical analysis.

A study conducted by AlKhafaji et al. (2022) evaluated the vertical load capacity of driven piles using Finite Element Analysis (FEA). The study involved modeling single and group RPPs using the software PLAXIS 3D and analyzing its behavior under different loading conditions. The results of the study showed that FEA can provide accurate predictions of pile behavior and can be used to optimize the design of pile foundations. Another study conducted by Wu et al. (2022) evaluated the vertical load capacity of driven piles in sand using FEA. The study involved modeling a single pile using the software ABAQUS and analyzing its behavior under different loading conditions.

The results of the study showed that FEA can provide accurate predictions of pile behavior and can be used to optimize the design of pile foundations.

Badhon (2021) evaluated the effectiveness of RPP in improving the bearing capacity of foundation soil. Four identical test sections of 4.6 m x 4.6 m. were constructed; one as a control section (without RPP reinforcement) while the others were reinforced with RPP having different sizes and spacings. The performance of the test sections was evaluated in numerical modeling using finite element software PLAXIS 2D. The field and numerical results have proven the effectiveness of this innovative technique in improving the bearing capacity of unsuitable foundation soil. Another study conducted by Islam et al. (2021) evaluated the effectiveness of RPP in improving the bearing capacity of soft foundation soil using finite element analysis. An extensive parametric study was performed to evaluate the effect of RPP and LTP on settlement reduction.

One of the main advantages of FEA is its ability to model complex geometries and loading conditions. This makes it an ideal tool for evaluating the vertical load capacity of driven recycled plastic pins, which can be influenced by a wide range of factors such as soil type, pile length, and pile diameter. FEA can also be used to evaluate the effect of different design parameters on pile behavior, such as pile spacing and pile arrangement Babu et al. (2022).

The primary aim of the present study is to establish a design methodology for the implementation of recycled plastic pins (RPP) to enhance the vertical load-bearing capacity of foundations. As a part of the study, full-scale field load tests were conducted to evaluate the load capacity of RPP in improving the condition of unsuitable soil. The field scale study was divided into two major parts. The first part included field load testing on single RPPs, whereas the second part included field load testing on group RPPs in association with a load-transferring platform constructed with reinforced cement concrete. The performance of the RPP under field load tests was recalibrated using numerical analysis (PLAXIS 3D), and the calibrated model was then used to examine the impact of increasing loading and varying the length, size, and spacing of the RPP.

The main objective of this chapter is to numerically simulate the field load test behavior of single and group RPP using PLAXIS 3D. The calibrated model was used to study the effects of various RPP parameters and soil conditions on the performance of the vertical load capacity of RPP. The details of the model calibration, parametric study, and other relevant modeling results are presented herein.

4.2 Model Development

PLAXIS 3D developed by PLAXIS BV was used for numerical analysis of the study. It is a three-dimensional finite element (FE) package which can perform deformation and stability analyses for geotechnical applications. The foundation soil was modeled using an elastic-perfectly plastic Mohr-Coulomb (MC) yield function with a non-associated flow rule (Kibria et al., 2014). The Mohr-Coulomb model is regarded as most comparable to the behavior of real soil. This elastic perfectly plastic model needs five fundamental soil input parameters: unit weight (γ), young's modulus (E), poisons ratio (υ), cohesion (c), and friction angle (φ). Mohr-Coulomb model is highly recommended if the soil characteristics are not known with great accuracy (Zaman, 2019).

Material models for soil and rock are typically expressed as a relationship between infinitesimal increments of effective stress rates and infinitesimal increments of strain rates. RPP acts as a stiff foundation element. A linear elastic model of materials is followed to model the material properties of RPP. This material model in PLAXIS is based on Hooke's law for isotropic linear elastic behavior. The effective Young's modulus (E'), and the effective Poisson's ratio (v'), are two parameters used in this model. The effective Young's modulus (E'), is a measure of the stiffness of the material, while the effective Poisson's ratio (v'), is a measure of the material's ability to deform in response to stress.

In order to do a finite element analysis with PLAXIS, a finite element mesh must be created, and boundary conditions and material properties must be specified. A 3D geometry model in the XYZ plane is used for developing a finite element model. The PLAXIS mesh generator automatically generates properties, boundary conditions, and the appropriate mesh based on input from the geometry model. It is necessary to produce water pressure and set the initial state of the initial effective stresses at the final stage.

The model has been developed to simulate the vertical load test for field scale study of both single RPP and RPPs in groups of four. The model is calibrated to reflect field scenario using field test results. For variable parameters, the calibrated model is utilized to anticipate the load settlement results of RPP more accurately in the field. Initial properties of the foundation soil were as per the laboratory results. Standard fixities were applied as boundary conditions. The soil was modeled to have undrained behavior with no generation of excess pore water pressure. The properties of the structural elements were in accordance with the manufacturer's specification.

152

The soil reinforcement or RPPs were modeled as linear elastic volume element. Table 4-1 Table 4-1 Properties of the Structural Elements in the FE Modeland

Table 4-2 show the properties of the structural elements and geogrid, respectively. The analyses were performed using 15 node triangular elements which furnished high-quality stress results. The geometry of the test section and corresponding mesh connectivity are shown in Figure 4-1 and Figure 4-2, respectively. The RPPs are modeled as 3 m long flushed to the ground elastic volume element. Steel plate and RCC slab used for uniform load application during load tests were modeled as elastic plate element. The geogrid length is 1.5 m to cover the reinforced area in the case of RPP groups. In order to simulate the bi-axial geogrid utilized for the group RPP sections, linear elastic sheet components were used.

Table 4-1 Properties of the Structural Elements in the FE Model

Parameter	Unit Wt. (kN/m³)	Stiffness, E (kN/m²) x10⁶	Poison's Ratio	Interfaces
RPP	18.85	1.38	0.1	0.7
Steel Plate	76.97	200	-	-
RCC slab	24.35	25	.15	-

Table 4-2 Properties of the Geogrid in the FE Model

Geogrid	Axial Stiffness, EA (kN/m)
TX5 Geogrid	51.08

(a)   (b)
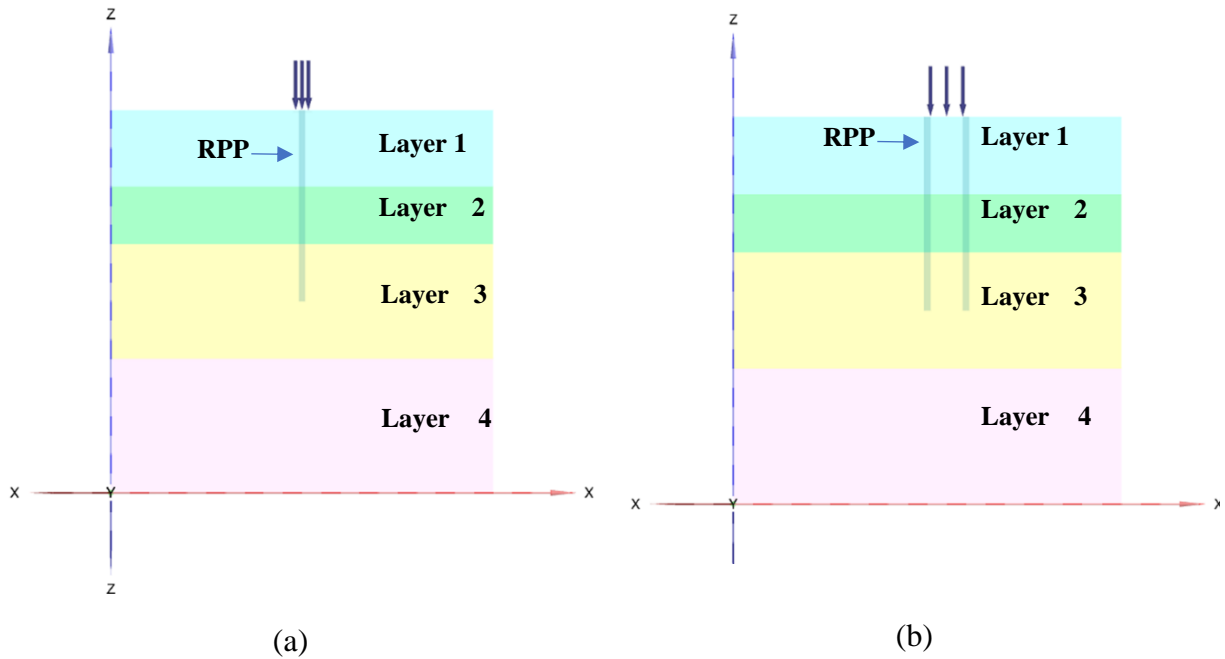
Figure 4-1 Geometry of the field load test section in the FE Model for (a) Single RPP (b) Four RPPs in Group

(a)   (b)
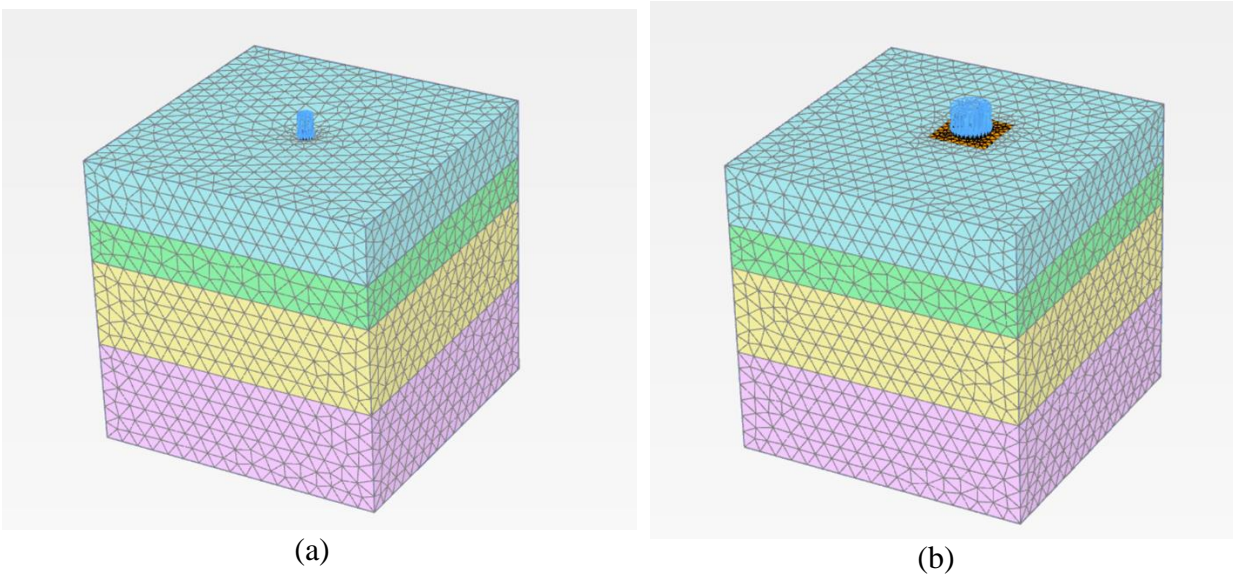
Figure 4-2 Mesh Connectivity in the FE Model for (a) Individual RPP (b) RPP Group

4.3   Model Calibration and Validation

The deformations as seen in the field during the load tests were used to calibrate the FE model. Laboratory test results were employed to establish calibration parameters, which encompass soil

unit weights and the strength properties of cohesion and friction angle. Typical Poisson's ratios were applied, while the elastic modulus of the soil layers was derived using empirical equations reliant on the SPT number. The calibration was performed by back analysis of the foundation soil properties. Several iterations were performed by changing the soil parameters within a certain range as obtained from the laboratory tests. Table 4-3 shows the back-calculated soil properties along with all the soil parameters used in the calibrated FE model. Various interface friction angles were chosen for the soil blocks as shown in Table 4-3.

Four layers of native soil profile are used to simulate the finite element model, together with an applied load. The foundation of the soil profile is made up of 2.13 m of fat clay (soil layer 4), which is covered by 1.83 m of lean clay (soil layer 3) and 0.90 m of sandy fat clay (soil layer 2). The top layer, or soil layer 1, is composed of a soft clay layer that is 1.22 m thick. According to the Mohr-Coulomb failure criterion, all the soil layers were modeled as linear elastic, perfectly plastic materials. For short-term or quick construction, undrained behavior was taken into consideration for all soil layers, where effective properties define the stiffness and strength of the soil layers.

The calibrated model was reinforced with individual RPPs to match the load settlement results as recorded in the field test. Different size and combinations of individual and group RPP reinforced sections were modeled with the respective RPP parameters. Due to load application limitation in the field, maximum applied load during vertical load test for the RPP groups was limited to 500 kN. However, in the model load was applied up to 850 kN to encounter load settlement behavior for the application of greater size of RPP. The model held good for both sizes of individual RPPs and different combinations of group RPPs. The magnitude and resulting settlement of the failure load predicted from PLAXIS 3D was fairly similar to the actual movement measured during field testing. It is to be noted that the FE model could successfully simulate the behavior RPP reinforcing the foundation soil.

Table 4-3 Properties of the Soil in the FE Model

Parameter	Layer 1	Layer 2	Layer 3	Layer 4
Unsat. Unit Wt. (kN/m^3)	16	16	16.5	16.7
Sat. Unit Wt. (kN/m^3)	19.1	19.4	19.6	19.3

Parameter	Layer 1	Layer 2	Layer 3	Layer 4
Stiffness x 10^3 (kN/m^2)	9.6	9.6	16.8	16.8
Angel of Internal Friction (degree)	24	22	19	17
Poison's Ratio	0.3	0.3	0.3	0.3
Cohesion (kN/m^2)	6.2	7.2	23.9	57.5
Interface	0.7	0.7	0.7	0.7

RPPs are intended to carry a significant percentage of the vertical load and transfer it to the stronger strata when weak soil is reinforced with them. As a result, the weak foundation soil's bearing capacity rises, and foundation settlement reduces. Figure 4-3 depicts the stress distribution in the FE model of the RPP reinforced soil, illustrating how the stress is centered on the RPPs and how they are carrying greater load than the soil between them.
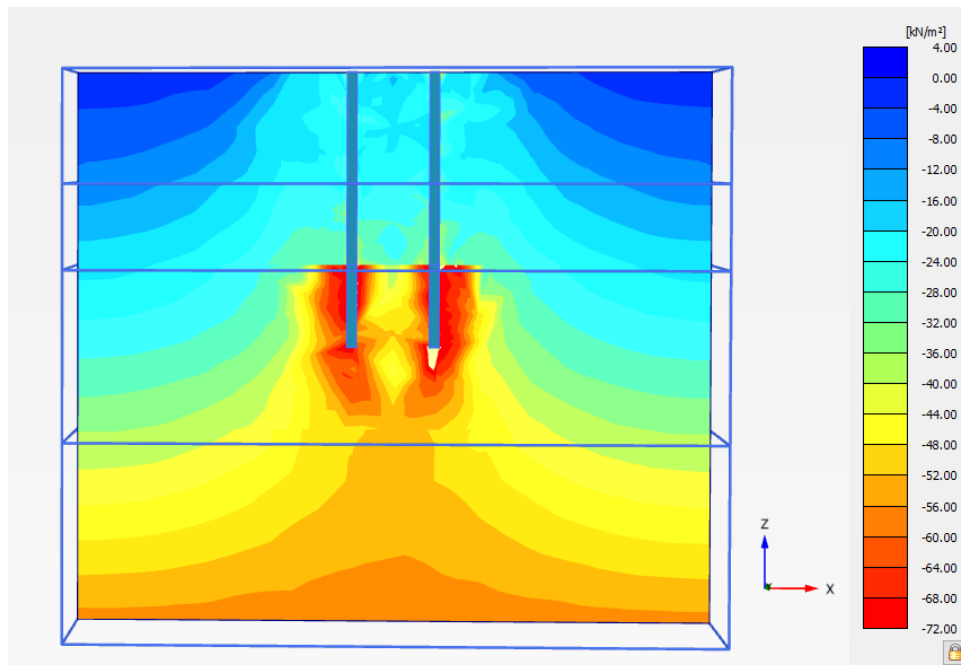

Figure 4-3 Contour diagram of stress distribution in reinforced section with Group RPP in the FE model.

4.3.1 Maximum Settlement

The load settlement profiles comparing the field and FE model outputs for the vertical load test are presented in Figure 4-4, Figure 4-5 and Figure 4-6. Figure 4-4, Figure 4-5 and Figure 4-6 also show the comparison between the field results and numerical model results. A very close match between the displacements measured in the field and the FE model was found with a maximum variation of 12.1%. The trend or pattern of the foundation soil settlement with the application of vertical load for different arrangement and combinations of RPP size and spacing were also similar with Badhon 2021. The charts presented validate the FE model since the load settlement behavior predicted by the numerical model were very close to the actual measurements recorded in the field. The slight variations encountered can be attributed to the soil heterogeneity in the real field condition. So, the resistance provided by RPPs with varying size and spacing could be effectively simulated by the FE model. 25 cm by 25 cm single RPP,15 cm by 15 cm single RPP, 15 cm by 15 cm RPPs arranged in 0.6 m and 0.9 m are represented as 25 x 25, 15 x 15, Grp_15 x 0.6 and Grp_15 x 0.9 respectively; and 10 cm by 10 cm single RPP, 10 cm by 10 cm RPPs arranged in 0.6 m and 0.9 m are represented as 10 x 10, Grp_10 x 0.6 and Grp_10 x 0.9 respectively.
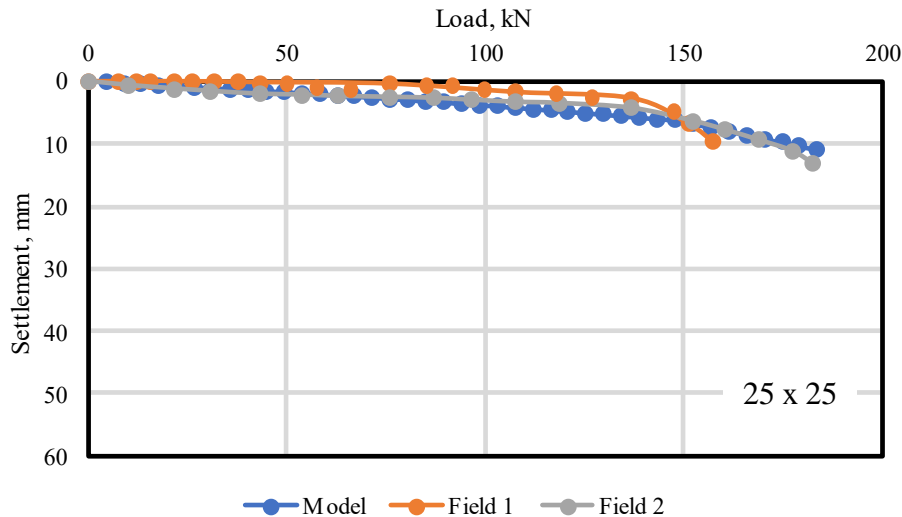

Figure 4-4 Comparison of Field and Model Settlement of 25 cm x 25 cm Single RPP
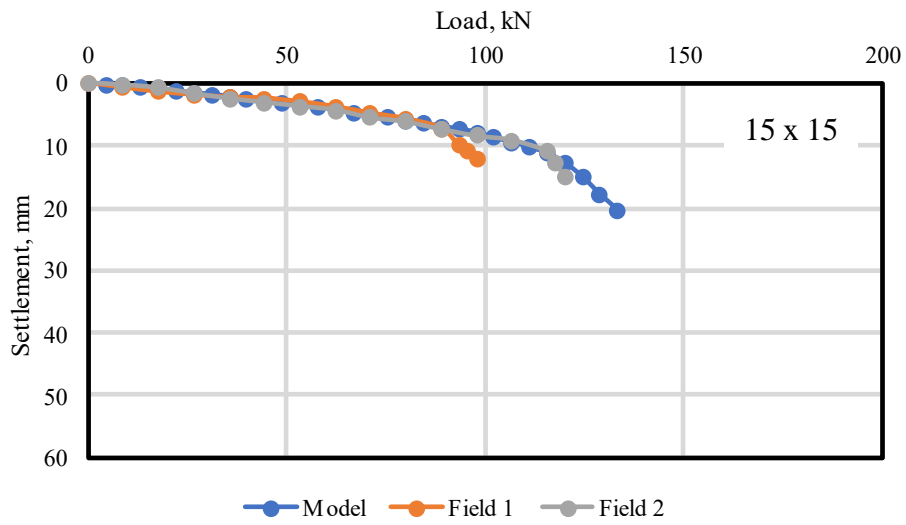
(a)
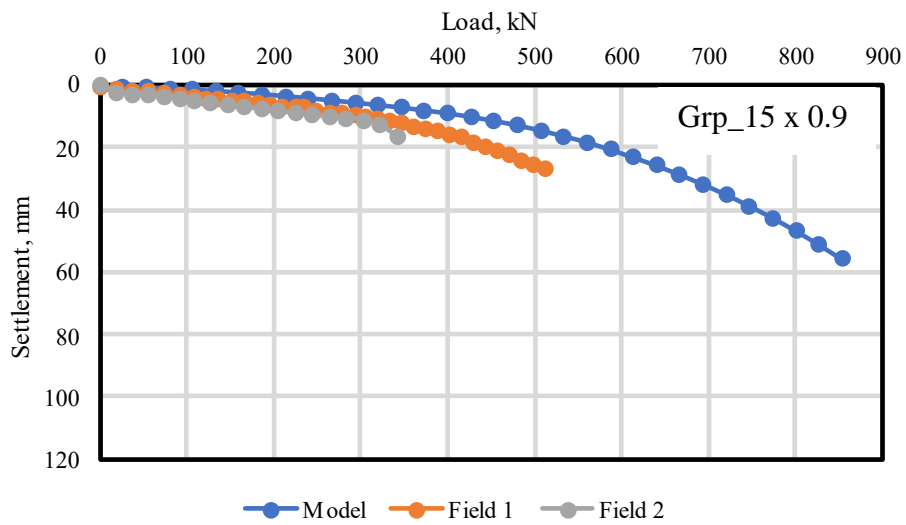
(b)
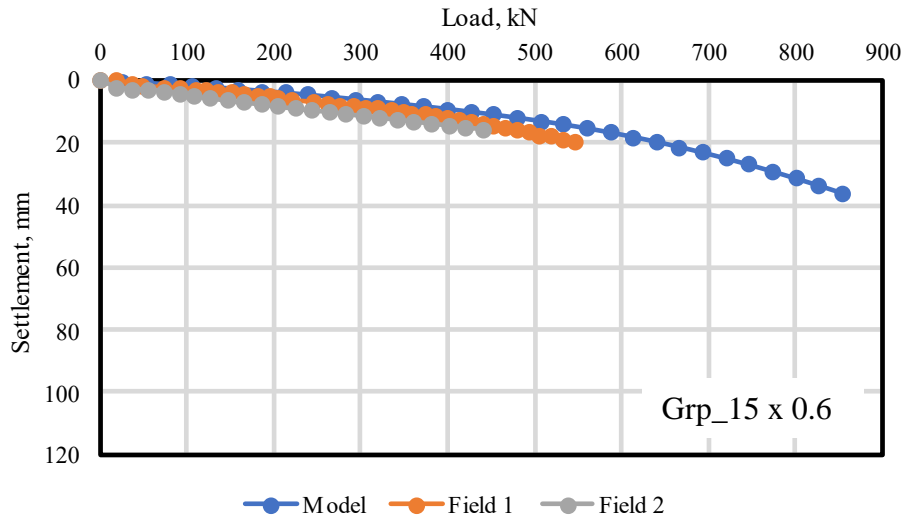
(c)

Figure 4-5 Comparison of Field and Model Settlement of 15 cm x 15 cm Single and Group RPPs
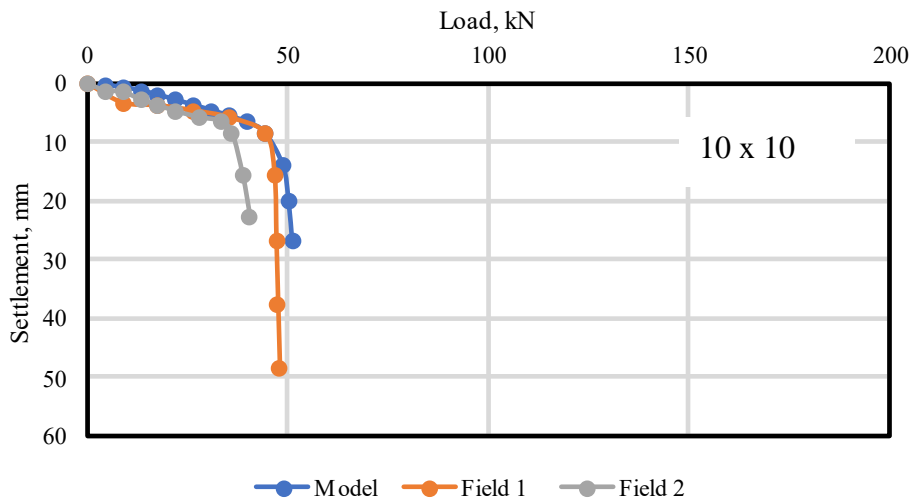
(a)
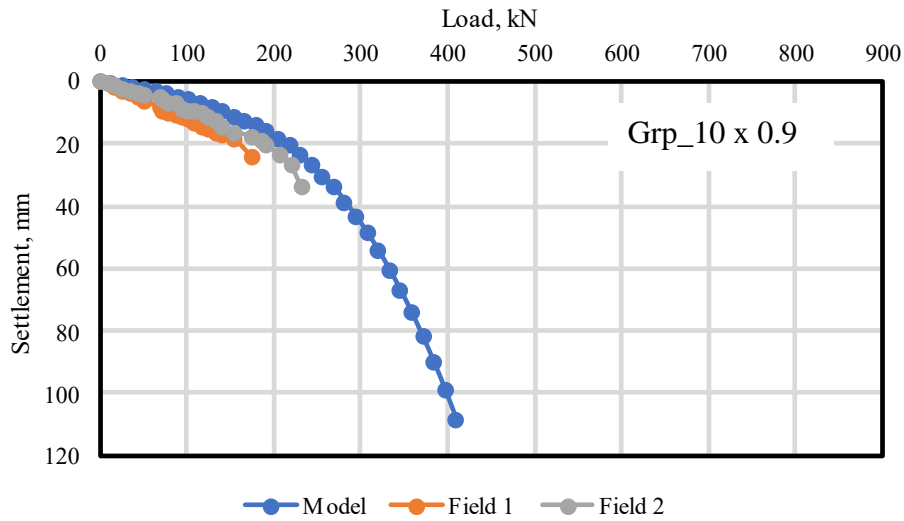
(b)
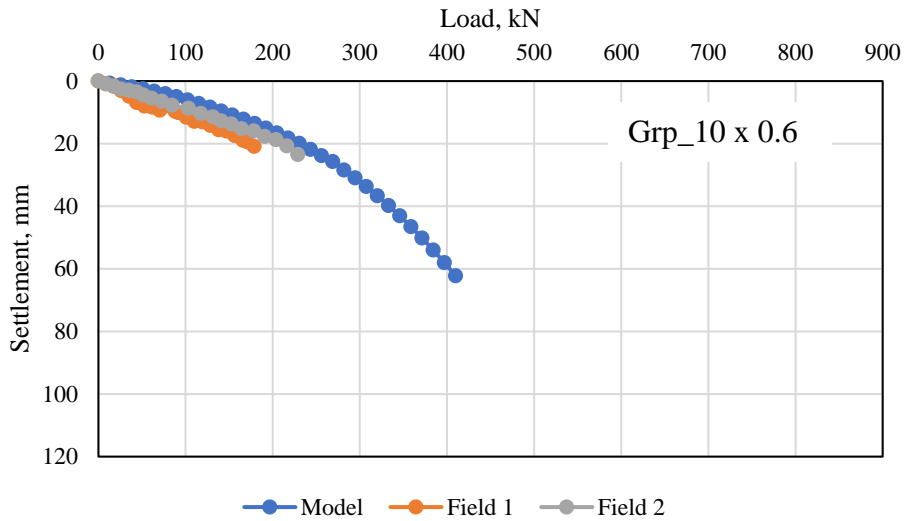
(c)

Figure 4-6 Comparison of Field and Model Settlement of 10 cm x 10 cm Single and Group RPPs

4.3.2 Stress Concentration Ratio (SCR)

The SCR values can be used to quantify the load transfer mechanism. Numerical modeling was used to determine the pressures on the RPP and the nearby soil between RPPs. By dividing the axial force by the RPP's cross-sectional area, the average vertical stress was computed for the RPP. The stress concentration ratio, SCR, can be used to assess the performance of an RPP-supported

25 x 25

embankment (Han and Gabr 2002; Oh and Shin 2007). The stress concentration ratio was computed for various combinations in order to understand the load transfer effectiveness on RPP. The vertical stress measured acting on the top of the RPP (σ_p) divided by the vertical stress acting at the ground surface between the RPPs (σ_s) is known as the SCR. SCR is expressed as:

$$SCR = \frac{\sigma_p}{\sigma_s} \qquad\qquad (4.1)$$

The most efficient load transfer by the RPPs is indicated by the high value of SCR. The stress concentration ratio (SCR) for varied loading, reinforced with 10 cm by 10 cm RPP at 0.9 m spacing, is found to be 4.14 using the numerical modeling data. When the RPPs of the same size were set at 0.6 m apart, this factor rises to 4.35. The stress concentration ratio is 4.86 when 15 cm by 15 cm RPPs are installed at 0.9 m apart, and it rises to 5.81 when they are installed at 0.6 m apart. The SCR determined by the numerical analysis were later contrasted with the results of the field study. Figure 4-7 demonstrates that, the values from the numerical analysis and the values from the field are in good agreement with a maximum difference of 7% in case of 15 cm by 15 cm RPP put at 0.6 m spacing.
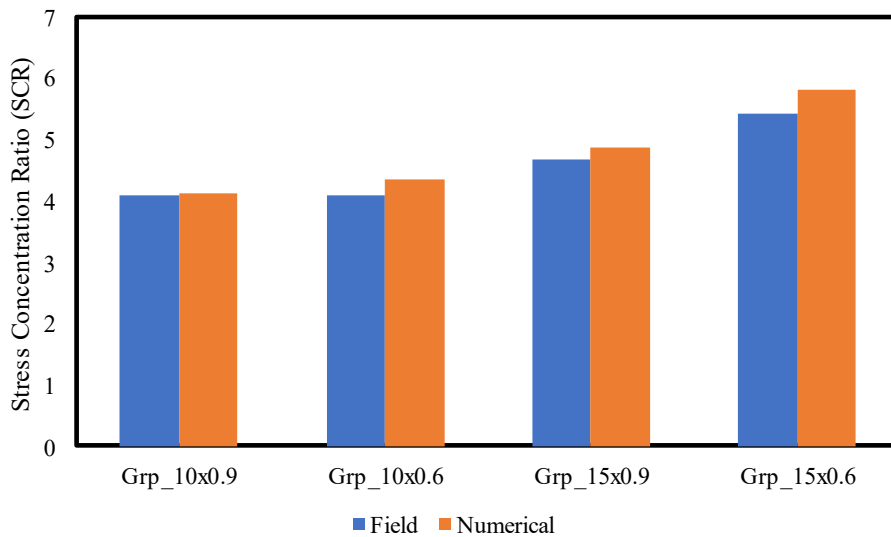

Figure 4-7 Comparison of Stress Concentration Ratio obtained from Field Tests and Numerical Modeling

4.3.3 Stress Reduction Ratio (SRR)

The stress reduction ratio is defined as the ratio between the pressure coming on top of soil in between RPPs and the pressure that was applied to the section. SRR can have values ranging from 0 to 1. The amount of load transfer is reflected by a lower SRR number. Complete soil arching is indicated by an SRR of 0, and there is no soil arching if the ratio is equal to 1. Less pressure on the soil of the reinforced section was indicated by a lower SRR measurement.

The numerical modeling data shows that the stress reduction ratio (SRR) for various loading, reinforced with 10 cm by 10 cm RPP at 0.9 m spacing, is 0.22. This ratio reduces to 0.19 when RPPs of the same size are spaced 0.6 m apart. When 15 cm by 15 cm RPPs are set at a distance of 0.9 m apart, the stress reduction ratio is 0.16; however, at a distance of 0.6 m, it reduces to 0.14. Later, the SRR calculated through numerical analysis was compared to the outcomes of the field investigation. Figure 4-8 shows that the numbers from the numerical modeling and the values from the field are in good agreement with a maximum variation of 15% for 15 cm by 15 cm RPP set at 0.9 m spacing.
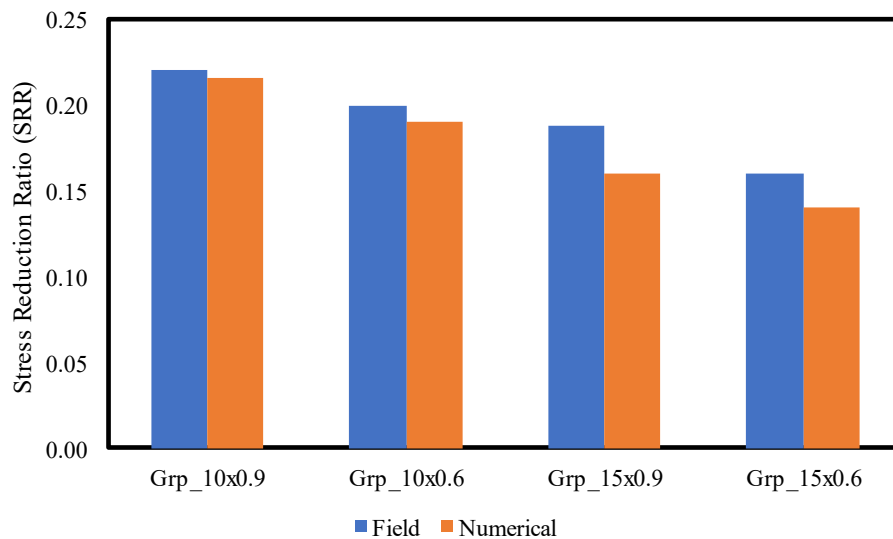

Figure 4-8 Comparison of Stress Reduction Ratio obtained from Field Tests and Numerical Modeling

4.4 Parametric Study

After calibrating the FE model based on field behavior, a parametric analysis was carried out to determine the relationship between various parameters and the load transfer behavior of RPP

reinforced foundation soil. In this study, a parametric study was conducted to investigate the effect of varying soil and RPP parameters on the load settlement and load transfer behavior of the RPPs subjected to vertical load test. The primary objective of the parametric study was to develop a comprehensive dataset to understand the behavior of RPPs subjected to vertical load test. As shown in Figure 4-9, a parametric study matrix was formulated, considering the probable associated parameters. Six different foundation soil conditions were investigated with varying RPP parameters. Soil parameters found from the calibrated model through back analysis were used for the whole set of parametric matrixes with the only exception of the parametric study of soil strength parameters. Based on the intersection of all criteria, there were 144 distinct scenarios. For this study, one parameter was varied at a time keeping the other parameters constant to keep the study in reasonable range.

The RPP cross-sections varied from smaller to larger sizes to assess the variation in performance. Larger size RPPs are difficult to install in field conditions and require bigger equipment, ultimately incurring extra costs. Three RPP center-to-center spacings at 0.3 m increments were chosen. The basis for this was the group action of RPPs. The RPP spacing was limited to a maximum of 1.2 m c/c since a spacing more than this might result in reduced group efficiency.
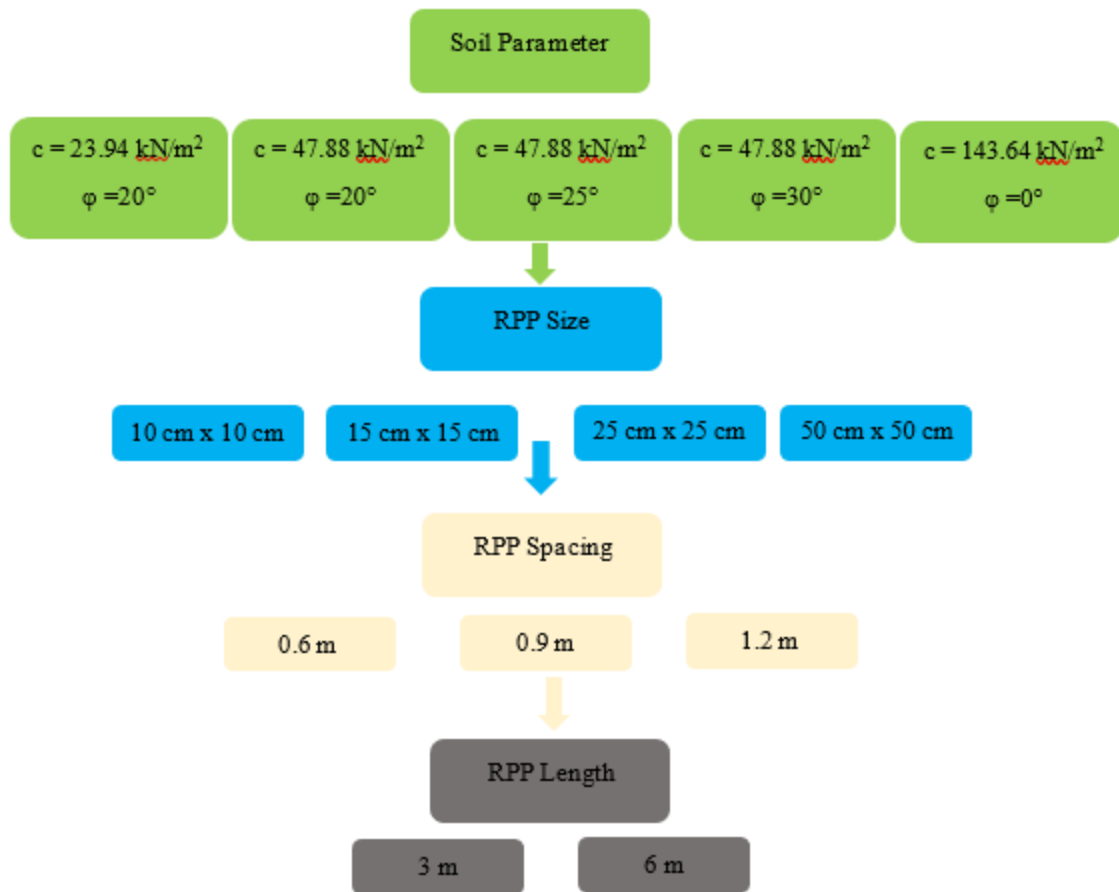
Soil Parameter

| $c = 23.94$ kN/m^2 $\varphi = 20°$ | $c = 47.88$ kN/m^2 $\varphi = 20°$ | $c = 47.88$ kN/m^2 $\varphi = 25°$ | $c = 47.88$ kN/m^2 $\varphi = 30°$ | $c = 143.64$ kN/m^2 $\varphi = 0°$ |

RPP Size

| 10 cm x 10 cm | 15 cm x 15 cm | 25 cm x 25 cm | 50 cm x 50 cm |

RPP Spacing

| 0.6 m | 0.9 m | 1.2 m |

RPP Length

| 3 m | 6 m |

Figure 4-9 Parametric study matrix

4.4.1 Parametric Study for Settlement

10 cm by 10 cm, 15 cm by 15 cm and 25 cm by 25 cm RPPs of 3 m length were used as a load transfer system, as well as to improve the condition of weak foundation soil and reduce the possibility of foundation settlement, during the current field scale investigation. Six distinct cohesion and friction angles, together with four different RPP sizes, three different spacings, two different lengths, were chosen. Settlements were determined for all scenarios.

4.4.1.1 Effect of Foundation Soil Strength

Settlement behavior is directly influenced by soil strength characteristics. Settlement decreases with increasing cohesion and friction, and vice versa. The effect of different foundation soil having three cohesions and three frictions angles was investigated using the calibrated model. These combinations were selected to investigate the effect of decreasing friction angle and increasing

cohesion. For studying the effect of soil strength parameters, all four layers of soil were considered as a single layer and the soil properties were varied according to the matrix for the parametric study. The study was conducted for both 15 cm by 15 cm and 10 cm by 10 cm RPPs. However, the vertical displacement trends were similar. Figure 4-10 compares the settlement behavior of single RPPs of size 15 cm by 15 cm and 10 cm by 10 cm with different foundation soil cohesion. Foundation soils were assumed to have the same friction angle ($\phi = 20°$); however, the cohesion (c) was varied (c = 23.94 kN/m^2, c = 47.88 kN/m^2, and c = 143.64 kN/m^2) to study the effect of only soil cohesion on vertical settlement. An interesting trend was found from the numerical analysis, such that, even though the friction angle was fixed, the increase in cohesion reduced the settlement to some extent.

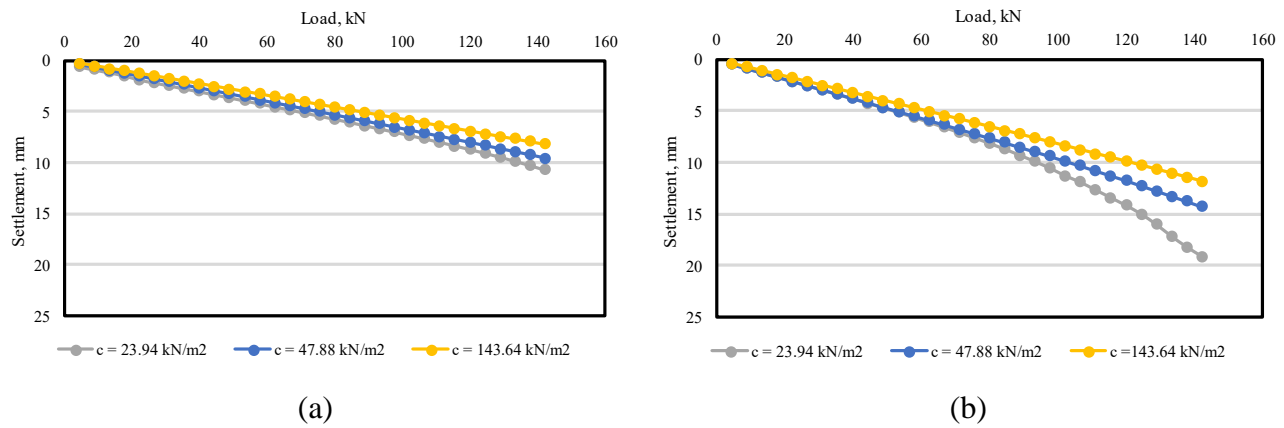(a)   (b)

Figure 4-10 Effect of Foundation Soil Strength (c) on settlement behavior of (a) RPP Size 15 cm by 15 cm (b) RPP Size 10 cm by 10 cm

Figure 4-11 shows vertical displacement of RPP with varying soil friction angles ($\phi = 20°$, $\phi = 25°$ and $\phi = 30°$). The soil cohesion was fixed at 47.88 kN/m^2 for both 15 cm by 15 cm and 10 cm by 10 cm. As expected, the vertical displacement in the case of friction angle 30° was the least for both RPP sizes and was the highest in the case of friction angle 20°. However, the effect of soil friction angle was very subtle for vertical settlement of RPPs, especially in the case of 15 cm by 15 cm RPPs. The displacements were relatively closer for different friction angles. The effect of friction angle might have been very less for resisting the vertical displacement.
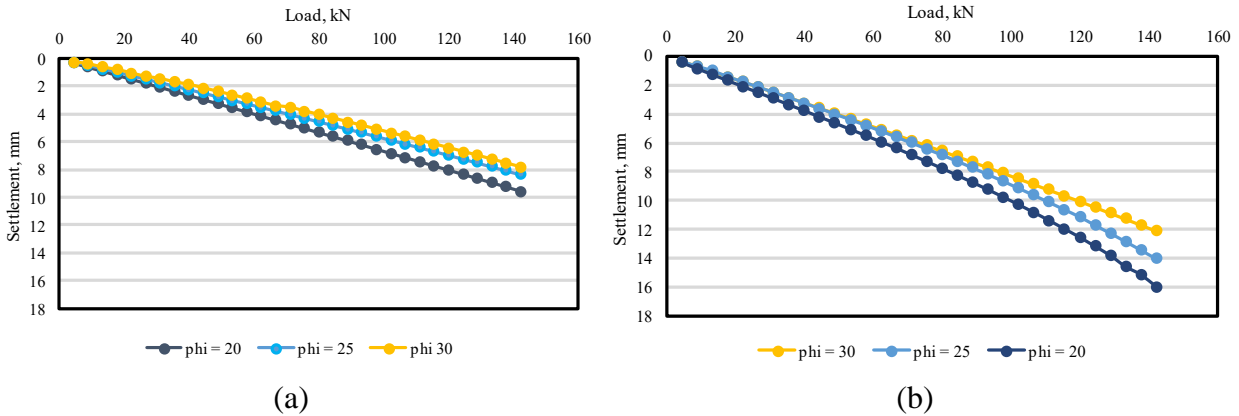
Figure 4-11 Effect of Foundation Soil Friction Angle (ϕ) on Vertical Displacement of (a) RPP Size 15 cm by 15 cm, (b) RPP Size 10 cm by 10 cm

4.4.1.2 Effect of RPP Parameters

The effect of different RPP parameters on the load settlement response can be beneficial in evaluating an appropriate design layout for future use. It is a known fact that larger cross-section and closer spacing of RPPs improves the bearing capacity of the foundation soil (Badhon, 2021). The field results of the current study point towards the same inference. However, it is important to quantify the reduction of vertical settlement to facilitate the design process.

RPP Size

As expected, the higher size RPP reduced the settlement by a greater extent and were able to withstand more load. 10 cm by 10 cm, 15 cm by 15 cm, 20 cm by 20 cm, along with RPP with 50 cm by 50 cm RPP were considered for the comparative study. These sizes were considered based on the availability in the market. Figure 4-12 compares the settlement behavior of RPP at variable size. Increasing the RPP size from 40% to 50% resulted in settlement reduction of about 50% to 80%.
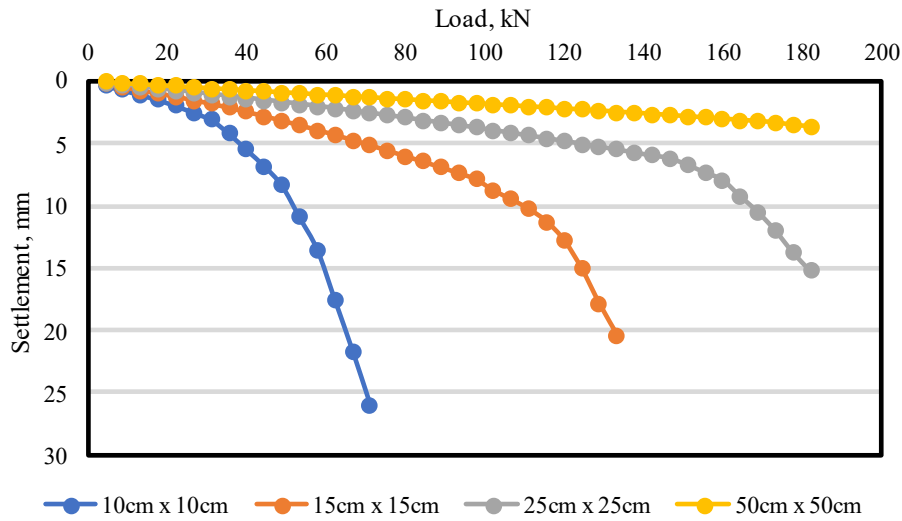
Figure 4-12 Effect of RPP Size on Load Settlement Behavior of RPP

RPP Length

Two different lengths of 3 m and 6 m were considered for the two most used RPP sizes of 15 cm by 15 cm and 10 cm by 10 cm. The failure load shifted to right for longer RPPs, suggesting much higher load capacity. At the failure of 3 m RPPs, longer RPPs showed 47% to 63% less settlement. Figure 4-13 shows the settlement behavior of RPP with variable length.
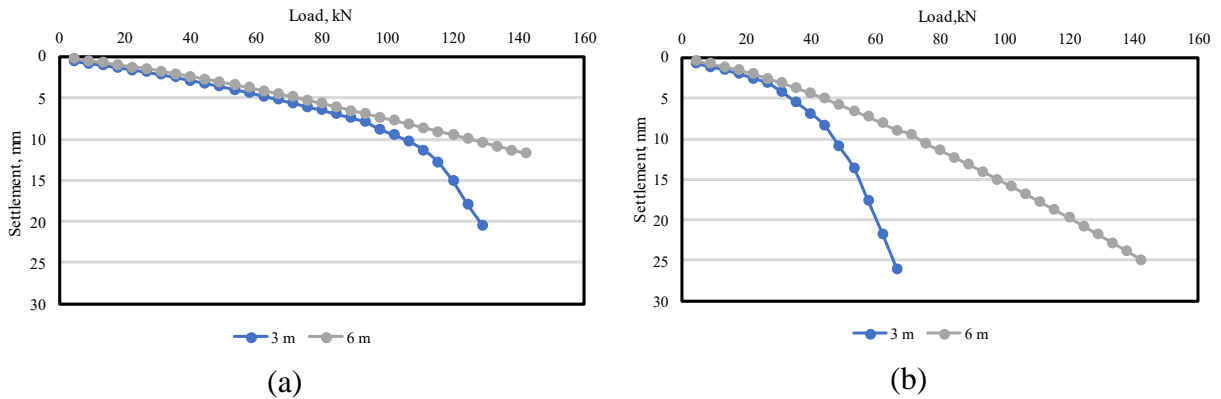

(a)

(b)

Figure 4-13 Effect of RPP Length on Load Settlement Behavior of (a) 15 cm by 15 cm RPP, and (b) 10 cm by 10 cm RPP

RPP Spacing

The effect of RPP spacing on the load settlement behavior was analyzed for different center to center spacing of RPP groups as spacing between RPP has significant effect on settlement. Figure

4-14 shows the variation of vertical settlement and load capacity of RPP groups at different RPP spacings. It can be observed that the closer spacings of RPP largely restrict the vertical settlements. This is mostly because raising the RPP spacing reduces the RPP replacement ratio per area of foundation, which in turn reduces the loads that can be transferred via the RPPs to the stiffer layer. Both 15 cm by 15 cm and 10 cm by 10 cm RPP showed similar patterns of settlement although the 15 cm by 15 cm RPP produced comparatively smaller vertical settlement. The settlement reduced by 34% and 32% when the RPP spacing lowered from 1.2 m to 0.6 m at 300 kN load for RPP size 15 cm by 15 cm and 10 cm by 10 cm, respectively.
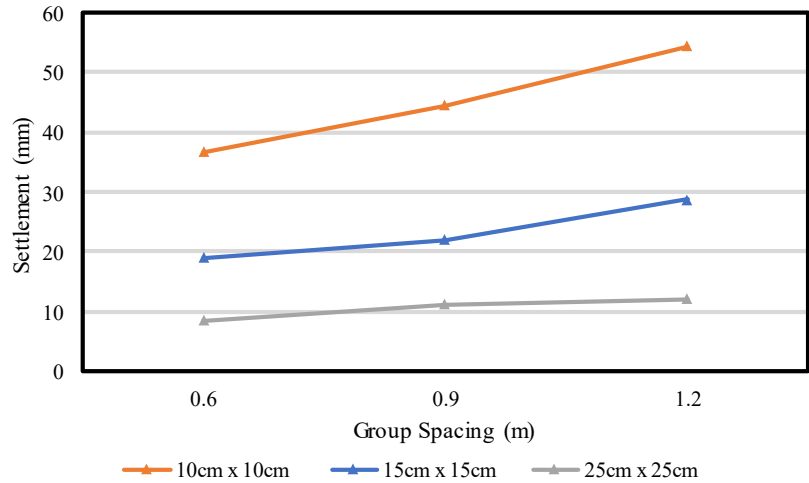
(a)
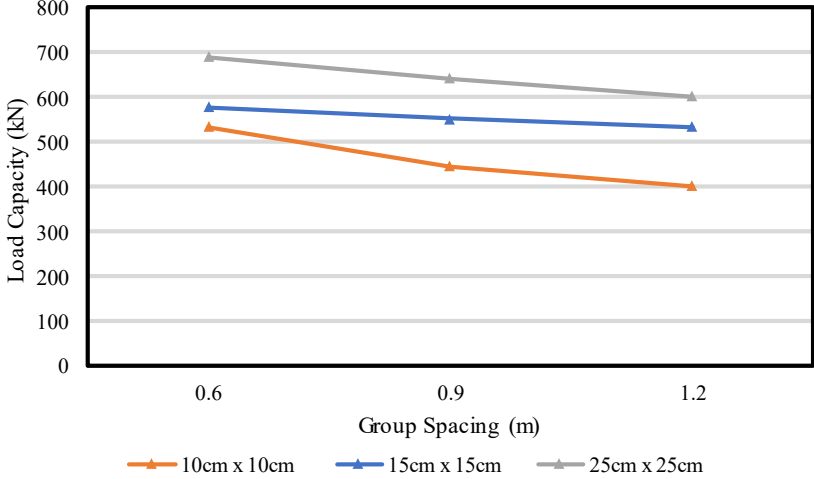
(b)

Figure 4-14 Effect of RPP Spacing on (a) Settlement of RPP (b) Load Capacity of RPP

As the spacing increased for the smaller RPPs, settlement rose, and load capacity declined. Comparing settlement and load capacity findings varying with spacing of 25 cm by 25 cm RPPs, revealed a similar phenomenon. Load capacity of 15 cm by 15 cm RPPs had minimum variation with increasing spacing. Settlement was higher for this larger RPPs at a spacing of 1.2 m, but when the spacing decreased to 0.9 m and then 0.6 m, settlement began to decline. However, as the spacing rose, the load capacity began to fall which is a similar pattern shown for the smaller RPPs.

4.4.1.3 Effect of area replacement ratio

The ratio of the loaded area to the overall area of RPP is known as the area replacement ratio, or A_r. For an efficient and cost-effective design in the improvement of foundation soil, this parameter is crucial. The ratio of the settlement of the control section without any RPP to that of the reinforced section is known as the settlement improvement factor, or n. The association between the settlement improvement factor and the inverse of the area replacement ratio is shown in Figure 4-15.

The settlement improvement factor falls as the area replacement ratio inverse increases. As can be seen from Figure 4-15, the shift in the settlement improvement factor is significant for greater area replacement ratios. When the inverted area ratio is more than 15, the drop in the settlement improvement factor is minimal. Elsawy and El-Garhy (2017) produced similar findings after conducting numerical research on granular pile-improved soft ground beneath raft foundation. They found that the settlement improvement factor diminishes at a slower rate when the inverted area replacement ratio is greater than 10. The tendency of the curves is consistent with the findings of the current investigation.

169
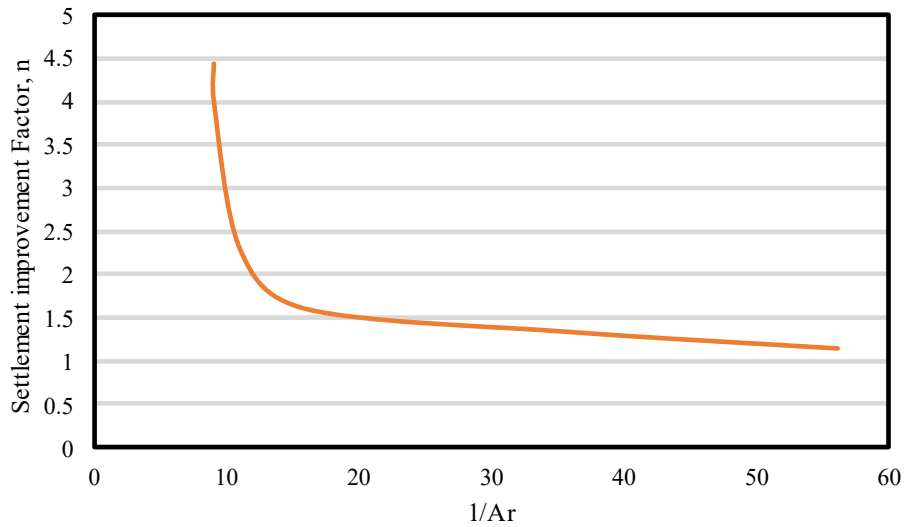
Figure 4-15 Relationship between Settlement Improvement Ratio and the Area Replacement Ratio Inverse

4.4.1.4 Effect of Ground Water Table Fluctuation

For RPPs measuring 15 cm by 15 cm and 10 cm by 10 cm, the impact of water table variation on the load settlement behavior was examined. The results are presented in Figure 4-16. To determine the impact on RPP settlement with the application of load, various depths of the ground water table were taken into consideration. With the application of load, settlement increases as the water table rises. Settlement decreases when the water table is far below.
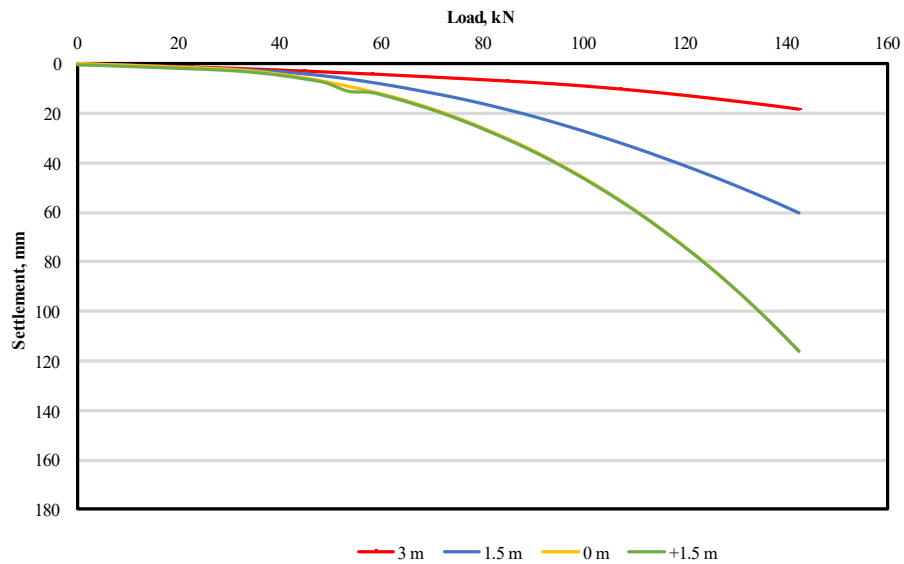
(a)
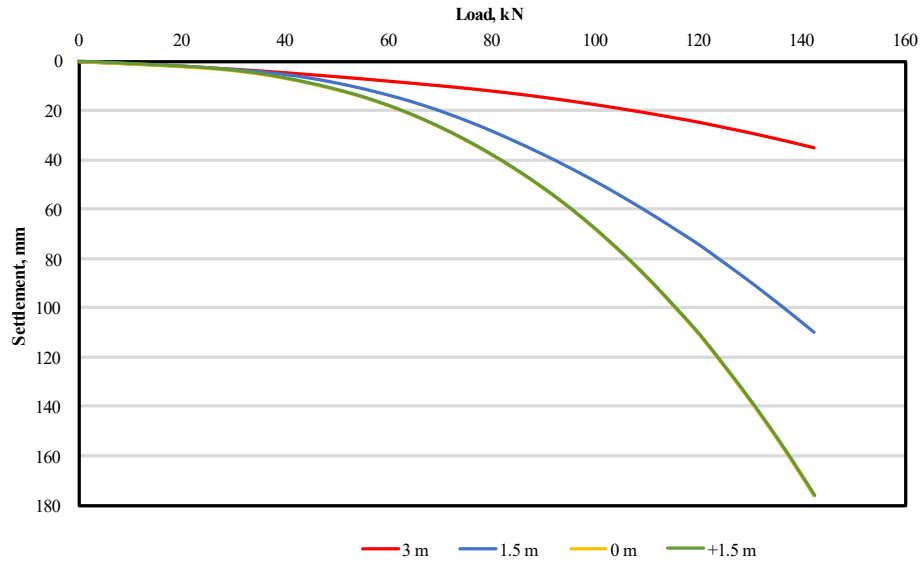
(b)

Figure 4-16 Effect of Ground Water Table Fluctuation of (a) 15 cm by 15 cm RPP, and (b)10 cm by 10 cm RPP

The water table at 1.5 m above ground was also taken into consideration for creating a flooding environment. According to the analysis, putting the water table above ground produces the same outcome as putting it at the ground's surface (overlapping the load settlement curve when water at ground surface). This finding suggests that the behavior of RPP subjected to load depends on the soil's saturation level. The soil is already saturated when water is at the surface, thus it produces the same results. Also, the water table above ground applies additional load to the soil. However, this load only increases the total stress, not effecting the effective stress. As a result, there was no significant change of settlement when water table was put on 1.5 m above the ground level to replicate flooding condition.

4.4.2 Parametric Study for Stress Concentration Ratio (SCR)

The vertical stress at the top of the RPP is compared to the vertical stress at the top of the surrounding soil to get the stress concentration ratio (SCR). A high SCR rating indicates that the RPPs are handling a greater load. The values of SCR are greatly influenced by the unit weight of soil, RPP diameters and spacing.
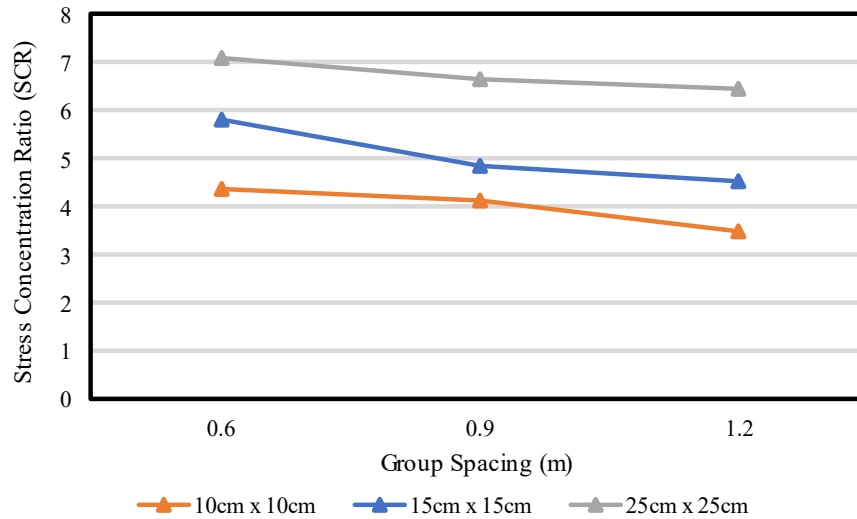
Figure 4-17 Effect of RPP Spacing and Sizes on The Stress Concentration Ratio

The effect of RPP spacing and sizes on the stress concentration ratio is depicted in Figure 4-17. The propensity of SCR to rise with decreasing pile spacing was observed. SCR on RPP is 4.35 when the soil is reinforced with 10 cm by 10 cm RPP spaced at 0.6 m. The SCR decreases and becomes 4.14 when the spacing is extended to 0.9 m. The SCR value approaches 3.5 as the distance between RPPs is increased further. 15 cm by 15 cm and 25 cm by 25 cm RPPs followed a similar pattern with greater SCR at the same spacing. As seen in Figure 4-17, the SCR will increase as the RPP size is raised. RPP size should be enlarged or the distance between RPPs should be reduced if the stress concentration on top of RPPs needs to be increased.

4.4.3 Parametric Study for Stress Reduction Ratio (SRR)

The pressure exerted on the soil's surface can be computed using SRR. Figure 4-18 presents the effect of RPP size and spacing on Stress Reduction Ratio. The soft soil layer between the piles is stiffened by the reinforcement at the foundation, which lowers differences in settlement. Arches are more difficult to develop when differential settlement is lessened. Soil arching is increased as a result, and SRR is decreased. Along with the reduction in RPP spacing, SRR also falls.
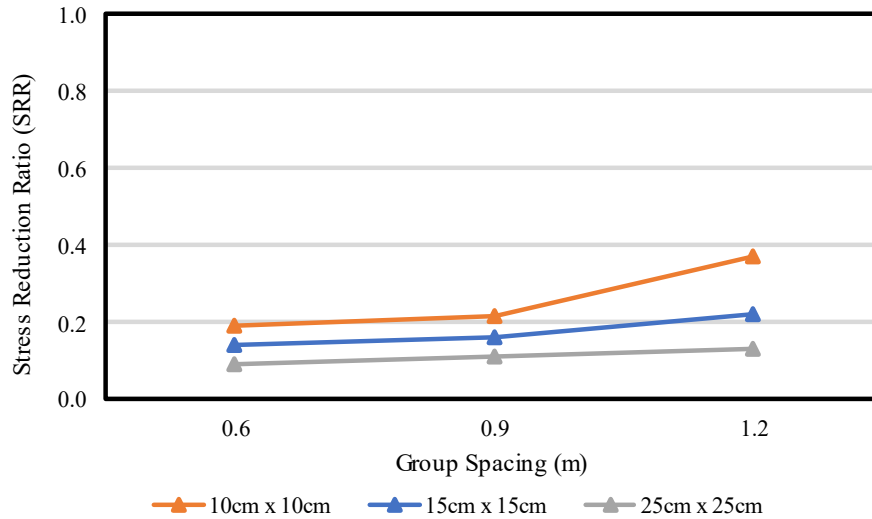
Figure 4-18 Effect of RPP Size and Spacing on Stress Reduction Ratio

The tendency has been consistent across all RPP sizes apart 25 cm x 25 cm RPPs. Greater reinforcement and more loads are handled by the RPP reinforcement when RPP spacing reduces. As a result, the load on the soil between RPPs decreases, which lowers SRR. The same pattern was noted by Roy and Bhasi (2018). The vertical strains on the foundation soil surface were observed to significantly rise in that study as the pile separation increased. This demonstrates that the pile center-to-center spacing is crucial for the load transfer mechanism to properly develop the bearing capacity of foundation systems.

4.5   Conclusion

The current research focuses on developing a numerical model using PLAXIS 3D to find out the vertical load bearing capacity of RPPs. The main results and conclusion can be summarized as follows:

- The numerical model exhibits a high degree of resemblance with the outcomes derived from field tests, indicating a strong correspondence between the predictions and empirical observations in the real-world geotechnical context.
- The measured displacements of single and group RPPs in the field closely matched the predictions from the Finite Element (FE) model, with a maximum variation of just 12.1%.
- The Stress Concentration Ratios by numerical analysis for RPPs of 10 cm x 10 cm at 0.9 m spacing, 10 cm x 10 cm at 0.6 m spacing, 15 cm x 15 cm at 0.9 m spacing and 15 cm x 15 cm

at 0.6 m spacing are 4.14, 4.35, 4.86, 5.81 respectively. The values from the numerical analysis and the values from the field are in good agreement with a maximum difference of 7% in the case of 15 cm by 15 cm RPP put at 0.6 m spacing.

- The Stress Reduction Ratios by numerical analysis for RPPs of 10 cm x 10 cm at 0.9 m spacing, 10 cm x 10 cm at 0.6 m spacing, 15 cm x 15 cm at 0.9 m spacing and 15 cm x 15 cm at 0.6 m spacing are 0.22, 0.19, 0.16, 0.14 respectively. The values from the numerical analysis and the values from the field are in good agreement with a maximum difference of 15% in the case of 15 cm by 15 cm RPP put at 0.9 m spacing.

- From parametric studies:
  - For constant friction angle, with the increase of cohesion, the settlement is reduced.
  - For constant cohesion, with the increase of friction angle, the settlement is reduced.
  - Increasing the RPP size from 40% to 50% resulted in a settlement reduction of about 50% to 80%.
  - When subjected to an equivalent load that caused the 3 m RPPs to fail, longer RPPs exhibited 47% to 63% reduction in settlement.
  - The settlement decreased by 34% and 42% when the spacing between Recycled Plastic Pins (RPPs) was reduced from 1.2 meters to 0.6 meters, under a load of 300 kN, for RPPs of sizes 15 cm x 15 cm and 10 cm x 10 cm, respectively.
  - When using Recycled Plastic Pins (RPPs) that are 25 cm x 25 cm in size, a noticeable pattern emerged. As the spacing between these pins increased up to 0.9 m, the settlement decreased. However, beyond this 0.9 m spacing, the settlement started to increase again. This change in settlement behavior is a result of the overlapping influence areas of the RPPs.
  - The settlement improvement factor decreases as the inverse of the area replacement ratio increases.
  - With the application of load, settlement tends to increase as the water table rises. Conversely, settlement decreases when the water table is significantly lower.
  - The Stress Concentration Ratio (SCR) rises as the Recycled Plastic Pin (RPP) size increases, but it decreases with an increase in RPP spacing.
  - The Settlement Reduction Ratio (SRR) decreases as the Recycled Plastic Pin (RPP) size increases, and it also decreases as the RPP spacing increases.

CHAPTER 5

LATERAL LOAD TEST OF RECYCLED PLASTIC PIN

ABSTRACT

Geo structures, like MSE wall constructed over weak soil are prone to base sliding failure which causes failure in the long run. Recycled Plastic Pins (RPP) can be a viable and sustainable solution for increasing the lateral resistance of the foundation system. The objective of the present study is to evaluate the lateral load capacity of RPPs in terms of load deflection behavior by conducting field load tests using plate load tester. In this study, RPP of three different sizes were driven into high plastic clay at three different embedment depths and were laterally loaded to failure or until excessive deflection occurred. Based on the load deflection behavior obtained by the field load test results, the 10cm x 10cm RPPs, 15 cm x 15 cm and 25 cm x 25 cm RPPs had lateral load bearing capacity ranging from 24 kN to 27 kN, 33 kN to 38 kN and 44 kN to 54 kN respectively. It was observed that lateral load capacity increased 40% to 100% as RPP size increased and deflection increased up to 50% as embedment depth decreased.

Key words: RPP; Lateral Load Capacity; Field Load Test; Load Deflection Behavior.

5.1 Introduction

RPP has proved its ability as a ground improvement technique. Previously, RPP has been used for slope stabilization to increase lateral resistance of slopes (Khan et al., 2014). Islam et al. (2021) investigated the use of RPP in ground settlement reduction of foundation soil and proved the efficiency of RPP by supporting embankment load. Badhon et al., (2021) showed the ability of increasing bearing capacity of foundation soil using different sizes of RPP. Bhandari (2021) also explored the viability of using RPP as shear key against base sliding of MSE wall and established that RPP can increase the shearing resistance of MSE wall base. However, the lateral load carrying capacity of the individual RPP is still unexplored. Hence, field study on the capacity of RPP due to the horizontal loading is now a critical parameter to study.

RPP subjected to lateral loading can be compared to a pile experiencing lateral loading. Piles subjected to lateral loading due to wind, wave, etc. will suffer a horizontal shift in the entire or a portion of the pile, mobilizing the resistance of the surrounding soil. The lateral load is transferred

from the pile to the soil by the soil's lateral resistance, which balances the pile's external horizontal stresses and bending moments. According to Winkler's model (Winkler, 1867), the pile can be viewed as a flexible beam on the ground rotated by 90 degrees, with independent springs along the pile replacing the earth resisting lateral loads. The modulus of subgrade response, or spring stiffness, is defined as follows:

$$E_{py} = \frac{p'}{y} \qquad (5.1)$$

Where, p' is the force per unit length of the pile and y is the pile's deflection.

The partial differential equation for pile deflection under lateral loading can be calculated using the Euler-Bernoulli beam theory on elastic foundations as follows:

$$E_p I_p \frac{d^4y}{dx^4} + P_x \frac{d^2y}{dx^2} + E_{py} y = 0 \qquad (5.2)$$

where E_p and I_p are the elastic modulus and second moment of area of the pile, respectively. P_x represents the axial force, while x represents the depth.

When E_{py} is constant, eq. (5.2) can be solved using the Davisson and Gill (1963) approach. Terzaghi (1955) claimed that the modulus of subgrade reaction increases linearly with depth in the case of sand soils. The solutions for this instance were offered by Matlock and Reese (1960). Elastic solutions can forecast pile deformation, slope, bending moment, and shear. However, the maximum load cannot be determined. The ultimate load approach, introduced by numerous academics including Broms (1966) and Hansen (1961), is another technique for studying the lateral behavior of piles. The ultimate load technique predicts the ultimate lateral resistance of the piles, but it does not forecast the pile response.

The value of E_{py} is not regarded as a constant value in the p-y curve technique established by McClelland and Focht (1958), but rather diminishes progressively as the pile deflection develops. The fluctuating value of E_{py} with deflection, y, can be integrated into eq. (5.2), and the pile response can be solved using finite difference or finite element methods. The p-y curves were created using analytical analysis and full-scale load measurements. Analytical methods for obtaining p-y curves imply numerous simplifications, such as calculations of active and passive forces from Rankin's theory based on wedge geometry for failure near the ground surface and

Rankin active failure condition based on two-dimensional behavior for plane-strain failure at a significant depth below the ground surface (Reese et al. 1984; Zhang et al. 2005). Full-scale pile load tests were performed on a limited number of piles with precise pile diameters and soil types to back compute the p-y curves.

Lateral load test on piles is a type of structural test that is used to determine the capacity and behavior of piles under lateral loads. It is an important aspect of geotechnical engineering and can be used to verify the design assumptions, assess the safety and reliability of the pile foundation, and optimize the foundation design for specific site conditions.

Davisson (1970) stated that shear along the base of the pile can be very effective in resisting lateral load i.e., pile can be used as shear key for resisting lateral earth pressure. Wu et al., (1998) installed strain gauges in the piles to determine the lateral deflections and distribution of moment along the pile. Furthermore, wave equations can be an efficient method for anticipating the excess driving force so that pile installation in the soil does not fail in its capacity (Adib, 2001). Along with the single pile, a pile group should always be incorporated for comparison in the lateral load test (Christensen, 2006).

White et al., (2008) installed the reinforced cementitious grout pile through a shear box and the shear box was loaded by lateral translation in three types of cohesive (loess, glacial till and weathered shale) soil. Shirato et al., (2009) demonstrated 37 field tests to find out the elastic displacement of soil due to lateral loading of reinforced concrete piles and the design horizontal displacement was reported as 2% to 4% of the pile diameter. Ba'ist et al., (2019) also stated that the lateral deflection depends on the soil properties, the type of foundation and the force acting on the pile.

Therefore, studies focused on the lateral capacity of RPP are necessary to be carried out under field condition for facilitating RPP use as load bearing piles. This study presents the lateral load carrying capacity of the RPP and the deformation behavior due to the application of the lateral load. Field load tests were carried out to directly find out the displacement of the pile as result of the applied load. Using the field data, the ultimate lateral load capacity was estimated subsequently using p-y analysis. Furthermore, a parametric study was undertaken to investigate the effect of soil strength parameters, the size and length of RPPs, and their embedment depth in the ground.

5.2 Methodology

5.2.1 Project Background and Site Soil Conditions

A location inside Hunter Ferrell Landfill in the City of Irving, Texas was selected for the study. Geotechnical drilling and resistivity imaging were conducted for the sub-soil investigation. Two locations were selected for soil investigation and drillings were conducted for these locations with a drilling depth of about 6 m to investigate the soil properties.

Figure 5-1 Location of field load testing on RPP in the Hunter Ferrell Landfill Site in Irving

The average blow count of the foundation soil was found to be 5 at a depth of 1.2 m. Disturbed and undisturbed soil samples were collected during boring. A detailed laboratory investigation was carried out to determine the index properties and shear strength parameters of collected soil samples. The results indicated the presence of medium to high plastic clay throughout the borehole depth and classified as Fat clay (CH) according to the Unified Soil Classification System (USCS). No groundwater level was detected during the drilling. The moisture content varied from 10% to 28%. The plasticity index varied from 36 to 48, and the range of liquid limit was between 51 to 66.
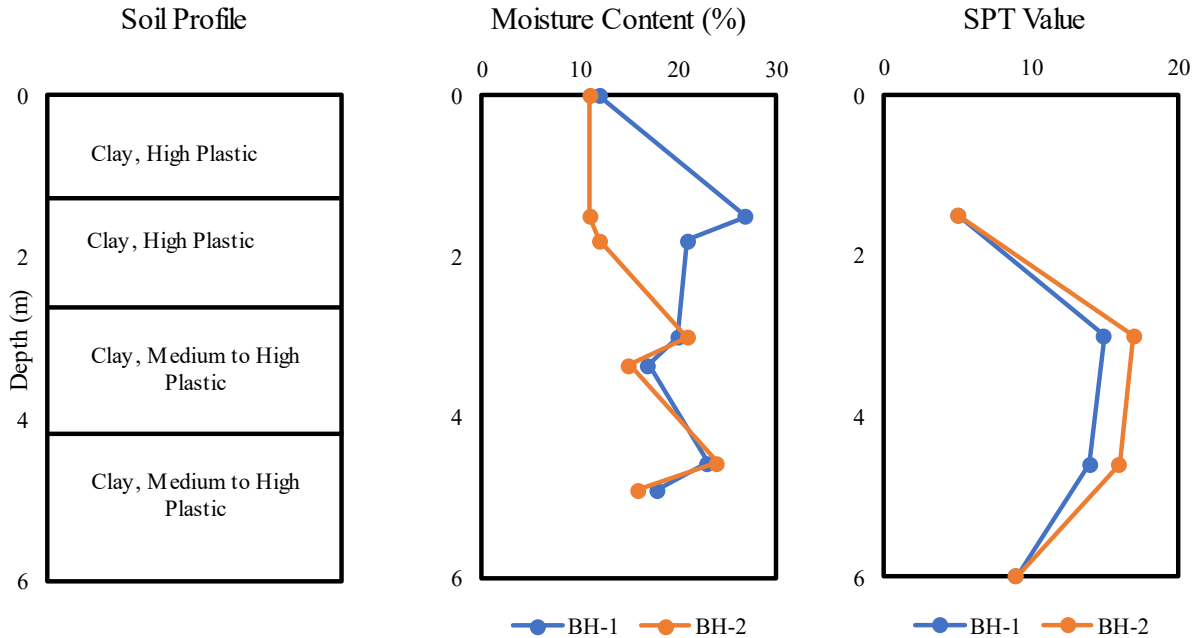
Figure 5-2 Variation of moisture content and SPT value in different layers of soil

UCS tests were conducted on undisturbed soil samples collected in thin-walled Shelby tubes at two different depths of 1.5 m. and 4.6 m. respectively. The undrained shear strength at 1.5 m depth was found to be 6.7 kN/m^2 and the ultimate bearing capacity was calculated to be 34.5 kN/m^2. Based on the field SPT data, N value for the top layer (From BH1_S4) of soil was 5, which indicates that the compressive strength will be in between 23.9 to 47.9 kN/m^2. For the sample collected from 4.6 m depth, undrained shear strength was found as high as 114.9 kN/m^2 and the ultimate bearing capacity was calculated to be 590 kN/m^2, indicating an extremely stiff soil layer. Based on undrained shear strength parameter as well as field SPT value, it was confirmed that topsoil within this zone was weak and thus, was selected for conducting the tests.

5.2.2 Design and Construction Details

The field experiments were designed to incorporate a total of 16 tests for lateral load tests. Finite element modeling was conducted using PLAXIS 2D with the in-situ soil properties. A parametric study was performed with available RPP properties to investigate the effect of different RPP sizes and embedment length. The Mohr-Coulomb soil model with elastic perfectly plastic behavior was used for deformation calculations using 15 node triangular elements. The FEM analysis employed 9 stress points for producing high quality stress results. The FEM analysis was covered in detail

under the study by Zaman (2019). The Engineering properties of RPPs used in this context are listed in Table 5-1.

Table 5-1 Engineering properties of Recycled Plastic Pin (Chen, 2003 and Bowders et al. 2003)

Parameter	Value
Modulus of Elasticity (MPa)	1170
Compressive Strength (kPa)	31,026.4
Tensile Strength (kPa)	24,821.1
Specific Gravity (g/cc)	0.93

Based on the results, embedment depth played a key role in lateral displacement. Lateral displacement was observed to be less with the increase of embedment depth. Based on the finite element modeling results, three different RPP sizes of 10 cm x 10 cm, 15 cm x 15 cm and 25 cm x 25 cm and three different embedment depths of 2.1 m, 2.4 m and 2.7 m were selected. 10 cm x 10 cm and 15 cm x 15 cm RPPs were installed at the three different embedment depths whereas, 25 cm x 25 cm RPPs were installed at embedment depth of 2.4 m and 2.7 m for field load testing. Table 5-2 summarizes the design details of the load tests. The typical plan and layout of the load test is shown in Figure 5-3.

Table 5-2 Summary of design details of Lateral Load Tests

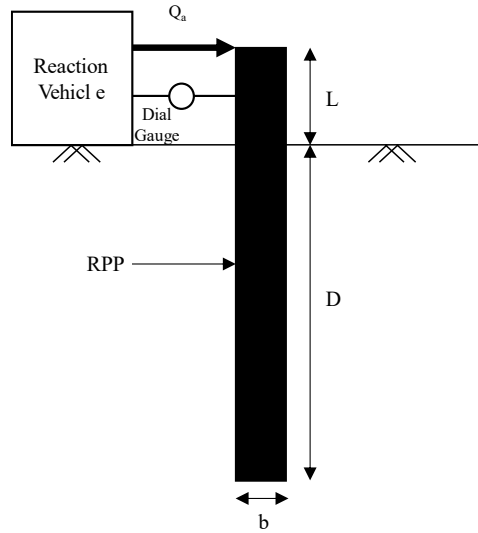| RPP size	Cantilever length, L (m)	Embedment depth, D (m)	Number of tests	Number of RPPs	Instrumented RPPs	Total Number of RPPs
10 cm x 10 cm	0.3	2.7	2	1*2 =2	1	6
	0.6	2.4	2	1*2 =2	1	
	0.9	2.1	2	1*2 =2	1	
15 cm x 15 cm	0.3	2.7	2	1*2 =2	1	6
	0.6	2.4	2	1*2 =2	1	
	0.9	2.1	2	1*2 =2	1	
25 cm x 25 cm	0.6	2.4	2	1*2 =2	1	4
	0.9	2.1	2	1*2 =2	1	

Total Number of Test =   16

Figure 5-3 Schematic diagram of test setup for Lateral Load Test

5.2.3 Instrumentation

The RPPs were instrumented with electrical resistance type strain gauges with a view of obtaining lateral deflection and distribution of moment while conducting the load tests. One out of the two RPPs of each size and arrangement, total 8 RPPs were instrumented to ensure at least one set of all the combination of RPPs were instrumented. All the RPPs were 3 m long and strain gauges were installed in 3 different depths of 0.3 m, 1.5 m and 2.7 m. At each depth 2 strain gauges were installed on opposite sides totaling to 6 strain gauges per RPP. System 8000 data acquisition (DAQ) system with 8 channels was used to collect the data from the strain gauges during load testing. The instrumentation process of RPP is discussed in detail in Chapter 3. Figure 5-4 shows the schematic diagram and instrumented RPP in field.

181

| (a) | (b) |
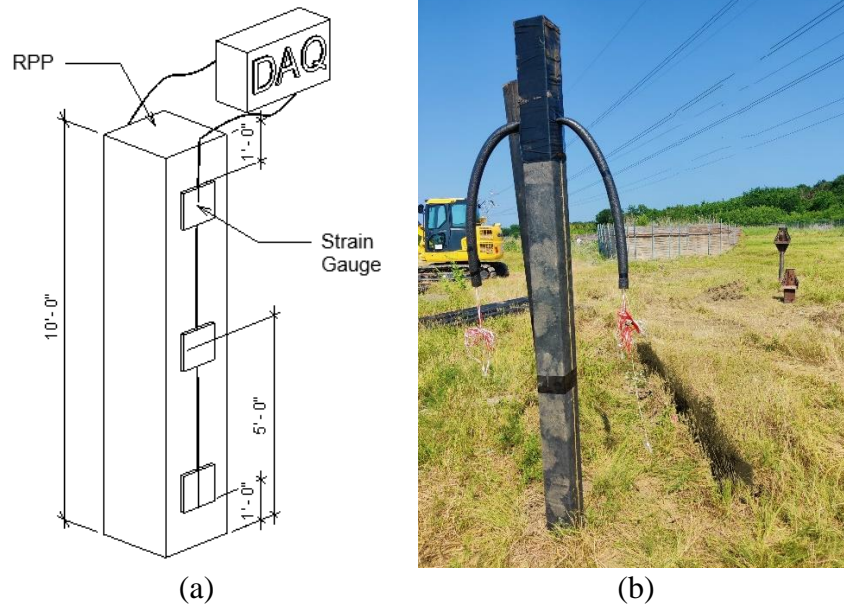
Figure 5-4 (a) Schematic diagram of instrumented RPPs; (b) Instrumented RPP.

5.2.4   Installation of the RPPs

The installation of RPP took place on two phases (May 19, 2022, May 25, 2022; and March 14, 2023). An excavator equipped with a hydraulic breaker hammer was utilized to install the smaller RPPs (10 cm × 10 cm, and 15 cm × 15 cm). Flags were used to mark the locations where the RPPs would be installed. A steel pin was used to create a hole at each marked location and the RPPs were then placed in the holes and driven into the ground with the help of a conventional hydraulic excavator (KOBELCO model: SK210LC), which was equipped with two different Hydraulic Breaker hammers NPK GH-3 and NPK GH-6 for 10 cm × 10 cm, and 15 cm × 15 cm RPPs respectively. Stroimatic Pile Driver was used to install the larger RPPs with the dimensions of 25 cm × 25 cm. A total of 16 RPPs were install with different embedment depth into the ground for lateral load tests as shown in Figure 5-5.
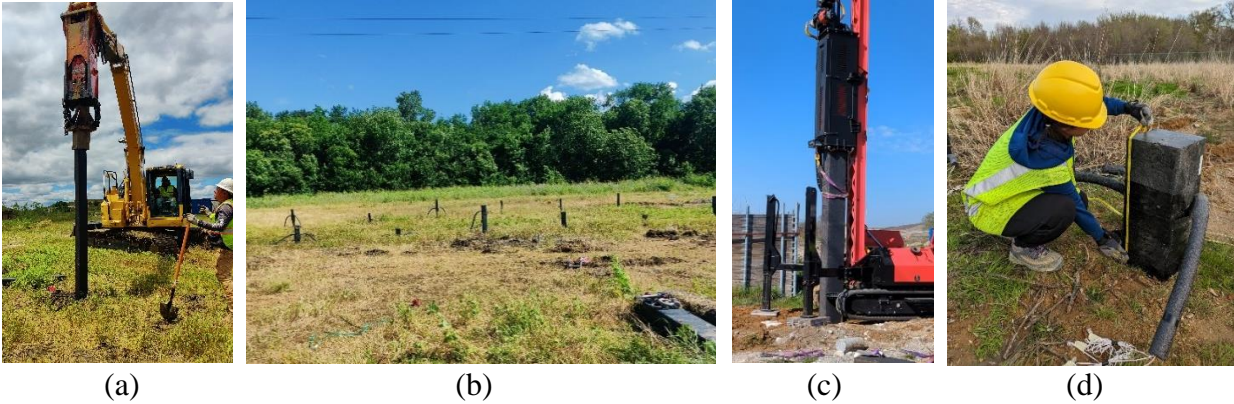
Figure 5-5 (a) RPP installation using hydraulic excavator; (b) 10 cm x 10 cm RPP and 15 cm x 15 cm RPP after installation (c) RPP Installation with Stroimatic Pile Driver; (d) 25 cm x 25 cm RPP after Installation

5.2.5 Load Test on RPP

Lateral Load test was performed according to ASTM- D3966 standard test method. Field load test for lateral load capacity required a total of 16 tests to be performed on individual RPP. As a reaction vehicle, Crawler Dozer from the Irving Landfill was utilized, and the hydraulic jack was placed horizontally against the blade to apply lateral load on the RPPs. Figure 5-6 shows the test set up and reaction vehicle used for lateral load test.

The load was applied laterally with the help of the lever attached to the hydraulic pump and load was applied until ultimate load capacity was reached, or failure has occurred. Displacement resulting from corresponding load application was recorded with the help of dial gauges. Later field data were utilized for analysis. The test results are evaluated to determine if, after applying an appropriate factor of safety, the pile or pile group has an ultimate lateral capacity and a deflection at service load to satisfy specific foundation requirements.

<center>(a)   (b)</center>

Figure 5-6 (a) Field set up for lateral load test; (b) Reaction vehicle used for Lateral Load Test

5.3   Results and Analysis

5.3.1   Load vs deformation

The load test results from the field lateral load tests are presented in this section. Lateral load failure is defined as the sudden occurrence when the RPPs experienced drastic lateral deformation as the result of application of lateral load. Figure 5-7 shows the lateral load test results from the field load test of the RPPs. The load test results revealed one notable observation in the field that RPP displayed a substantial deflection before yielding or demonstrating any plastic deformation. Based on the observations, the application of load was limited to a significant amount of deformation that can be allowed in the design process after factor of safety application. The load was applied in the field until the deflection of RPP reached roughly 20 cm, which is far larger than the deflection that can be allowed in any geotechnical application.

The lateral load versus deformation curve got steeper with increasing embedment depth suggesting improvement of lateral resistance with decreasing cantilever length. The larger sized RPPs excelled the smaller RPPs both in terms of application of maximum lateral load and permanent deformation. 25 cm x 25 cm RPPs had the steepest curve representing better resistance against applied lateral load. At the same deflection 25 cm x 25 cm RPPs were able to sustain 120% to 214% more load than 15 cm x 15 cm and 10 cm x 10 cm RPPs.
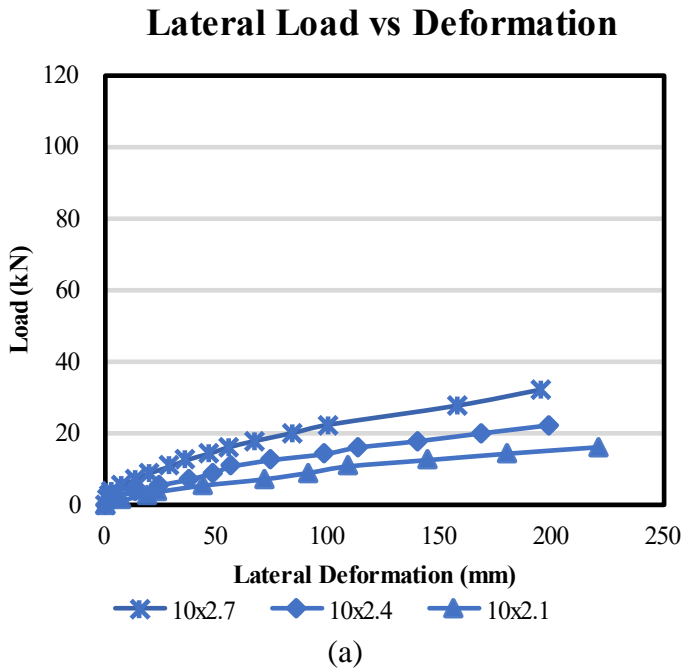
<center>184</center>
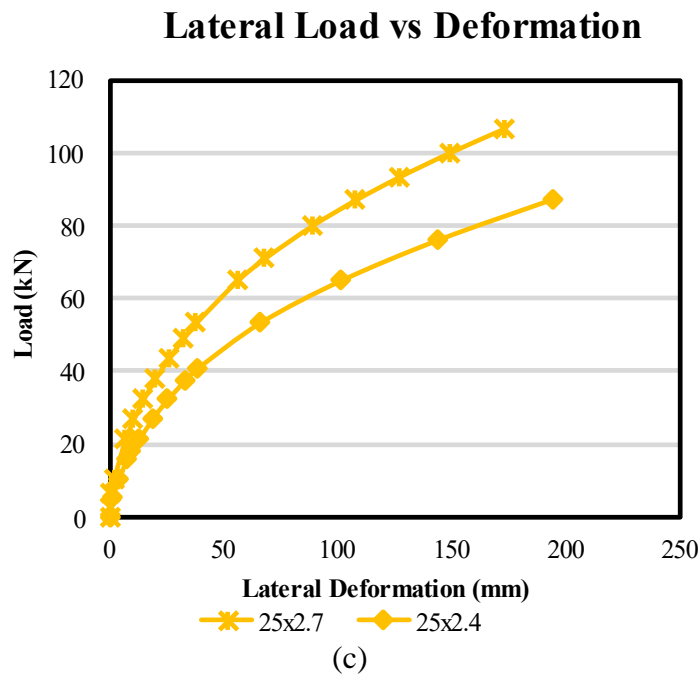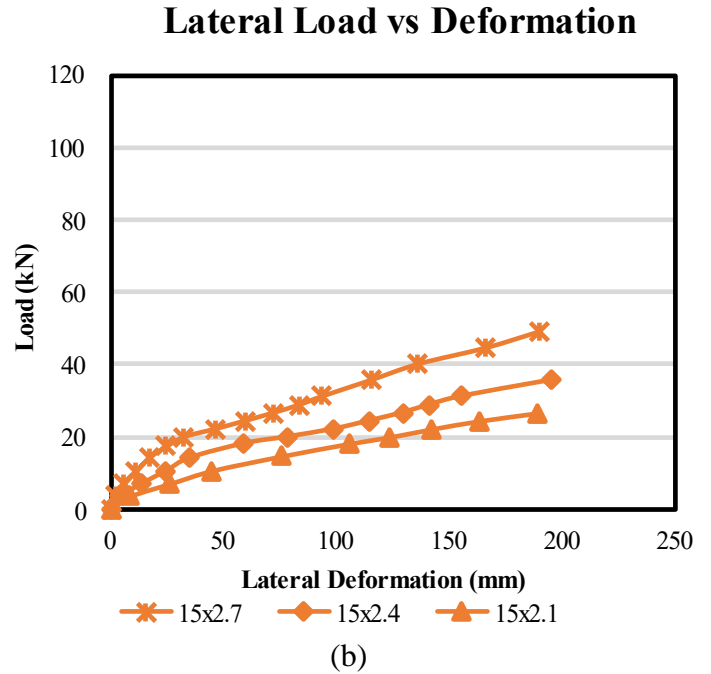
Figure 5-7 Lateral load vs Deflection curve (a) 10 cm x 10 cm RPP at different embedment depth; (b) 15 cm x 15 cm RPP at different embedment depth; (c) 25 cm x 25 cm RPP at different embedment depth

The curve gets flatter as the embedment depth decreases indicating more deflection at lower applied load. With decreasing embedment depth, the RPPs loses support of surrounding soil and thus results in more lateral deflection. A similar trend was observed for all three sizes of RPPs.

However, as the sizes of RPP increased, curves started getting steeper. The results of field load test data were further used towards determining ultimate load capacity of the RPPs subjected to lateral loading.

5.3.2 Strain Gauge Data

The load testing and strain gauge data analysis of various sizes and configurations of RPP reveal significant trends and findings. These investigations help in understanding the behavior of RPPs under lateral loads, providing insights into deflection and moment at different depths.

In this study, the measured moments were calculated from strain gauge measurements of the instrumented piles. The bending moment can be calculated from measurements of strain gauges using the following formula (Reese et al., 1974):

$$M(x) = \frac{E_p I_p (\varepsilon_t - \varepsilon_c) x}{h} \qquad (5.3)$$

Where, E_p is the elastic RPP stiffness; I_p is the section's second moment of area; ε_t and ε_c are the strains at the tension side and compression side, respectively; and h is the horizontal distance between bending the strain gage pair in the pile's section.

The deformation of the RPP were calculated from measurements of strain gauges using the following two formula:

$$P = \bar{\varepsilon} E_p A \qquad (5.4)$$

$$\Delta l = \frac{Pl}{AE} \qquad (5.5)$$

Where, Δl is the deformation of pile at each area; $\bar{\varepsilon}$ is strain gauge reading at each depth and A is the surface area of RPP.

The moment and deformation along the length of the RPP calculated from the strain gauge are measured at the maximum applied load in the field. The results are tabulated in the following Table 5-3 and Table 5-4. For easier presentation, 10 cm x 10 cm RPP with 2.7 m, 2.4 m and 2.1 m were referred to as 10 x 2.7, 10 x 2.4 and 10 x 2.1 respectively. Similarly, 15 cm x 15 cm and, 25 cm x 25 cm RPPs were referred to as 15 x 2.7, 15 x 2.4 and 15 x 2.1; and 25 x 2.7 and 25 x 2.4.

Table 5-3 Summary of distribution of moment along the RPP

RPP	Moment (kN-m)		
	0.3 m	1.5 m	2.7 m
10 x 2.7	-12.36	8.42	0.01
10 x 2.4	-10.82	7.61	0.02
10 x 2.1	-9.71	6.77	0.03
15 x 2.7	-21.34	12.78	0.58
15 x 2.4	-19.41	11.96	0.25
15 x 2.1	-17.99	10.25	0.80
25 x 2.7	-76.75	18.80	6.85
25 x 2.4	-78.10	9.52	6.13

The moment distribution along the length of the RPP revealed that RPPs were able to withstand more moments before failure as their size increased. In other words, larger RPPs exhibited greater moment resistance. Moment resistance capacity rose as embedment depth increased. A negative moment was developed at the RPP head due to the application of lateral load on top. The RPPs encountered positive moments at 1.5 m and 2.7 m depths resulting from soil enclosure. The moment that was at the bottom had a negligible value that was nearly zero. The only exceptions were 25cm x 25cm RPPs that had significant moment development at the bottom. The moment at top drastically increased in comparison to the moments of smaller RPP. This occurrence pointed to 25 cm $\times$ 25 cm RPPs functioning as a short pile.

Table 5-4 Summary of deformation along the RPP

RPP	Deformation (mm)		
	0.3 m	1.5 m	2.7 m
10 x 2.7	134.1	3.82	0.05
10 x 2.4	183.9	14.86	0.07
10 x 2.1	195.9	25.89	0.08
15 x 2.7	169.5	22.3	0.09
15 x 2.4	171.1	27.98	0.41
15 x 2.1	180.86	39.1	0.85
25 x 2.7	167.8	73.98	-6.3
25 x 2.4	188.45	91	-5.85

The deformation along the length of the RPP revealed that due to the application of lateral force on top, deformation was greatest at the top due to the ability to move the head freely. As the embedment depth of RPP decreases, the deformation at all depths increases.The more load was applied, the more was the deformation. Since the maximum load endured by the RPPs was greater for larger RPPs, the deformation was likewise greater for larger RPPs. The RPPs of same size had significantly reduced deformation at 1.5 m and 2.7 m depths due to soil enclosure. The deformation at the bottom was remarkably small practically nil. The lone exception was 25 cm x 25 cm RPPs that developed substantial deformation at the bottom in the opposite direction of load application. This occurrence pointed to 25 cm $\times$ 25 cm RPPs functioning as a short pile.

5.4   Modeling

LPILE 2022 was used for developing a model to simulate the behavior of RPP during lateral load testing. Model calibration was necessary using field measurements from load tests on RPP, to ensure an accurate representation of site-specific conditions. The model underwent refinement and iteration based on results and additional data, and reports summarizing analysis outcomes were generated for the model calibration purposes. LPILE employs the p-y method to model the interaction between piles or shafts and the surrounding soil. This method involves creating p-y curves for the soil-pile interaction along the length of the foundation elements. By integrating these p-y curves, LPILE can calculate the lateral deflections, bending moments, and shear forces for different loading conditions.

Model development in LPILE follows a systematic process that begins with the collection of essential data related to the project, encompassing soil properties, pile dimensions, material specifications, and loading conditions. Accurate data is crucial for a reliable analysis. The next step involves defining the geometry of the pile, specifying its length, diameter, and depth of embedment within the soil. Equally important is defining the geometry of the surrounding soil layers. Soil properties are then input, including layer thickness, soil type, and geotechnical parameters like cohesion, and friction angle. The software uses these properties to calculate the soil response to applied loads.

Once the data is in place, the loads to which the pile will be subjected are defined, including axial loads, lateral loads, and moments. Analysis parameters, such as the chosen method for assessing lateral load-deflection behavior and the number of load cases, are set. The software performs

computations to generate load-displacement curves, revealing the relationship between applied loads and lateral pile deflection at different points along the pile length. Results, including capacity, deflection behavior, and settlement predictions, are reviewed to assess pile performance and safety.

A model has been developed to simulate the lateral load test for field scale study of all three RPP sizes with different embedment depth. The model is calibrated to reflect field scenario using field test results. For variable parameters, the calibrated model is utilized to anticipate the load settlement results of RPP more accurately in the field. Initial properties of the foundation soil were as per the laboratory results. The properties of the structural elements were in accordance with the manufacturer's specification. Figure 5-8 shows the geometry of the developed model in LPILE to simulate the field load test condition.
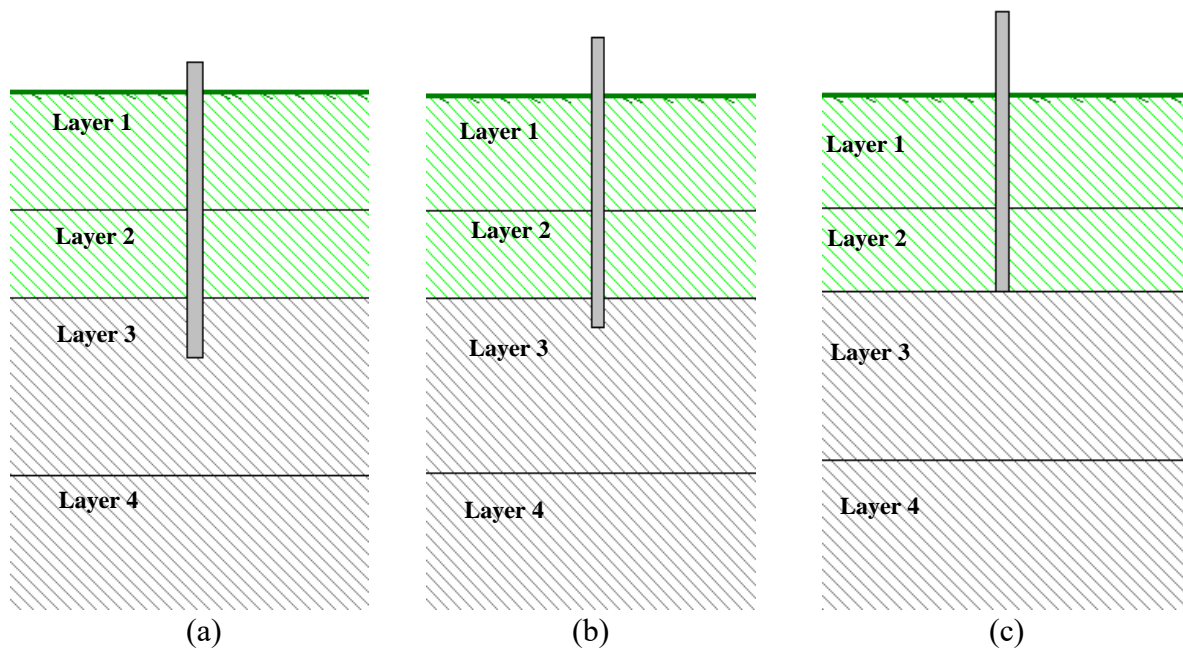
Figure 5-8 Geometry of the field load test section in the LPILE Model for 15 cm x 15 cm RPP at embedment depth of (a) 2.7 m; (b) 2.4 m; and (c) 2.1 m

5.5 Model Calibration and Validation

The deformations as seen in the field during the load tests were used to calibrate the LPILE model. Laboratory test results were employed to establish calibration parameters for soil, which encompass soil unit weights and the strength properties of cohesion and friction angle. The calibration was performed by back analysis of the foundation soil properties. Several iterations

were performed by changing the soil parameters within a certain range as obtained from the laboratory tests. Table 5-5 shows the back-calculated soil properties along with all the soil parameters used in the calibrated the model. Various interface friction angles were chosen for the soil blocks as shown in Table 5-5.

Table 5-5 Properties of the Soil in the FE Model

Pile properties used in LPILE				
RPP	B (m)	L (m)	I (m^4)	E (kN/m^2)
10 cm x 10 cm	0.10	3.0	8.88E^{-6}	2.0xE^6
15 cm x 15 cm	0.15	3.0	4.495E^{-5}	2.0xE^6
25 cm x 25 cm	0.25	3.0	3.5E^{-4}	2.0xE^6

Soil Properties used in LPILE						
P-y model	Depth (m)		γ ' (kN/m^3)	k (kN/m^3)	Su (kN/m^2)	ε_{50}
	Top	Bottom				
Stiff Clay w/o Free Water	0.30	1.52	19.32	-	57.46	0.02
Stiff Clay w/o Free Water	1.52	2.44	19.38	-	71.82	0.02
Modified Stiff Clay w/o Free Water	2.44	4.27	19.63	0	105.34	0.01
Modified Stiff Clay w/o Free Water	4.27	6.40	19.32	0	153.22	0.005

Four layers of native soil profile are used to simulate the model, together with an applied load. The foundation of the soil profile is made up of 2.13 m of modified stiff clay (soil layer 4), which is covered by 1.83 m of modified stiff clay (soil layer 3) ,0.90 m of stiff clay (soil layer 2) and 1.2 m of stiff clay on top (soil layer 1). All the soil layers were modeled without free water as no ground water was encountered during drilling. The calibrated model was reinforced with individual RPPs to match the load settlement results as recorded in the field test. Different sizes and arrangements of RPP reinforced sections were modeled with the respective RPP parameters. The calibrated

model held good for all three sizes of RPPs and different arrangement of embedment of RPPs. The magnitude and resulting settlement of the failure load predicted from LPILE was fairly similar to the actual movement measured during field testing. It is to be noted that the LPILE model could successfully simulate the behavior of RPP reinforced foundation soil.

The load deformation profiles comparing the field and model outputs for the lateral load test are presented in Figure 5-9. The figures also show the comparison between the field and the model results. A very close match between the displacements measured in the field and the model was found with a maximum variation of 12.9%. The charts presented validate the model since the load deformation behavior predicted by the model were very close to the actual measurements recorded in the field. The slight variations encountered can be attributed to the soil heterogeneity in the real field condition. So, the lateral resistance provided by RPPs with varying size and spacing could be effectively simulated by the LPILE model.

(a)   (b)

191
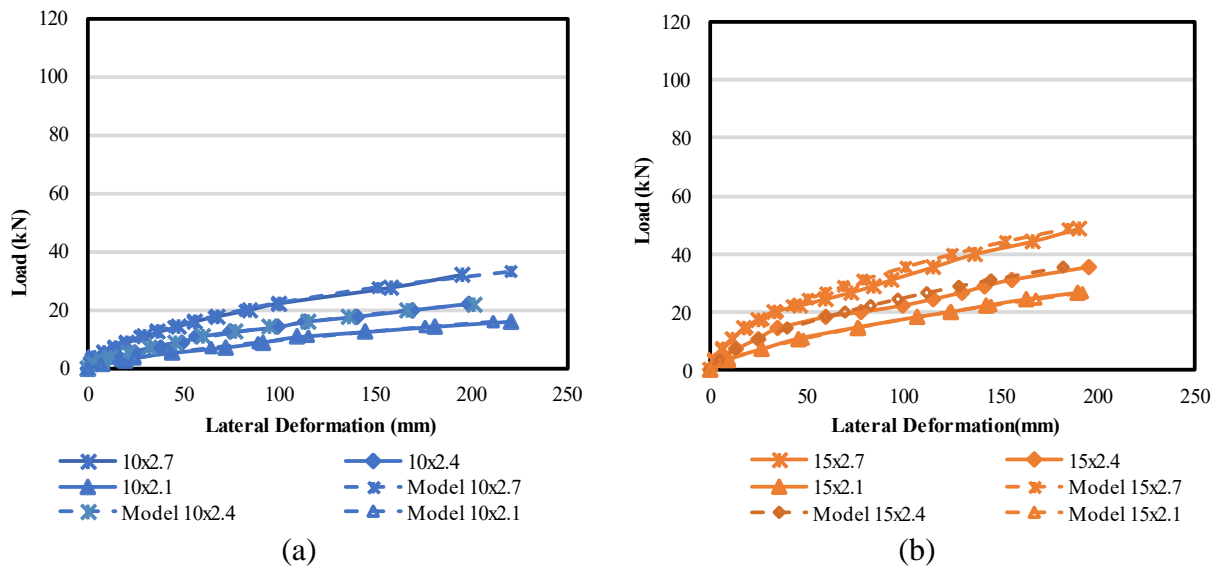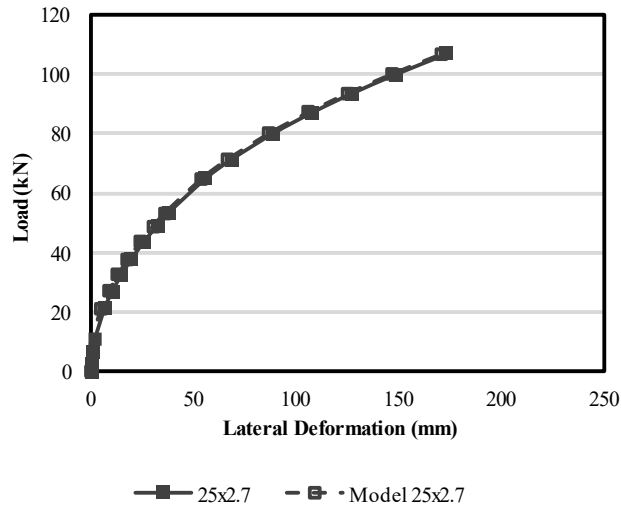
(c)

Figure 5-9 Comparison of Field and Model deformation of (a) 10 cm x 10 cm RPP at different embedment depth; (b) 15 cm x 15 cm RPP at different embedment depth; (c) 25 cm x 25 cm RPP at different embedment depth

The computed deflection and moment distribution for the laterally loaded piles have been compared with the measured deflection and moment distribution. It can be seen from Figure 5-10 that the agreement between the measured and computed lateral deflection and moment distribution for the RPPs are very satisfactory. In general, the computed bending moment a bit more above the ground. The maximum displacement and bending moment for the RPPs are shown in Figure 5-10 (a), (b) and (c). The agreement between measured and computed values is quite acceptable.

(a)

(b)

(c)
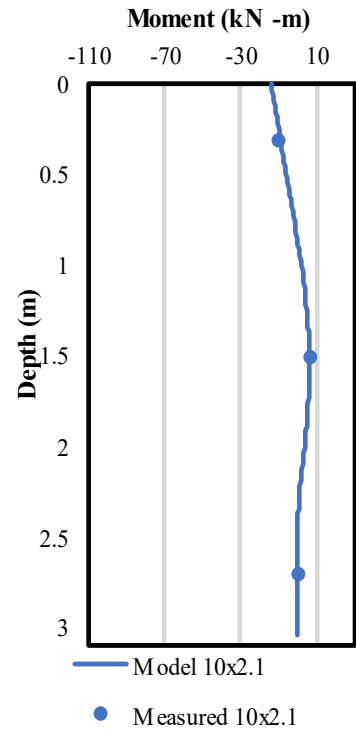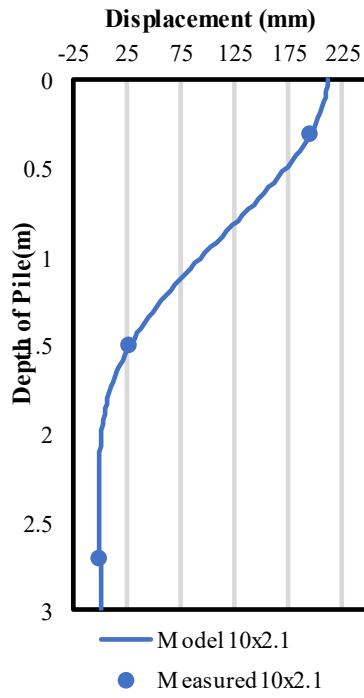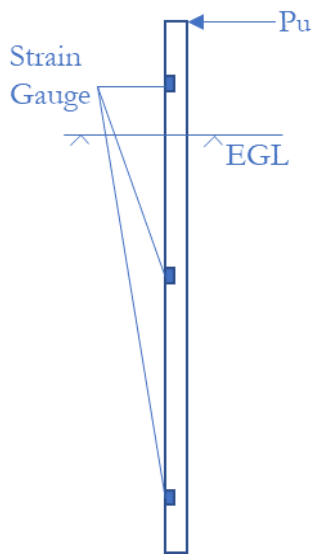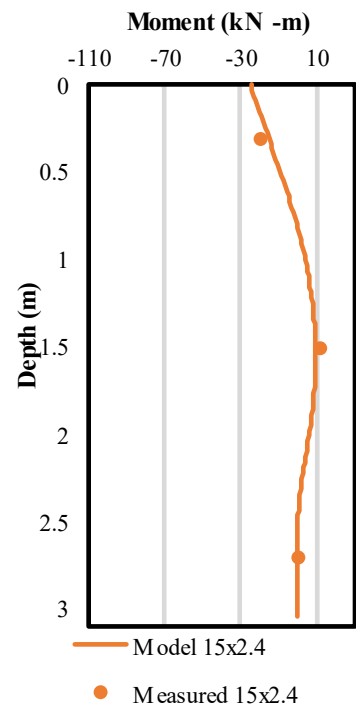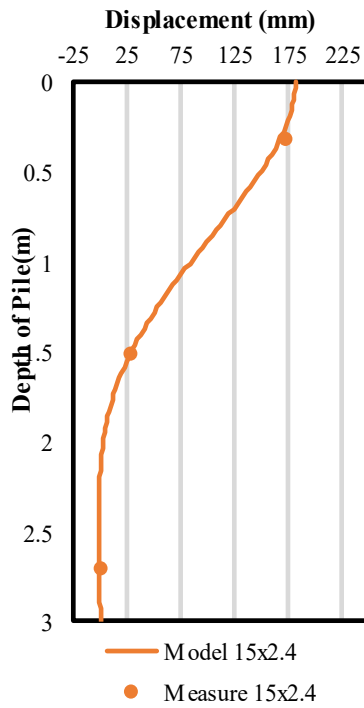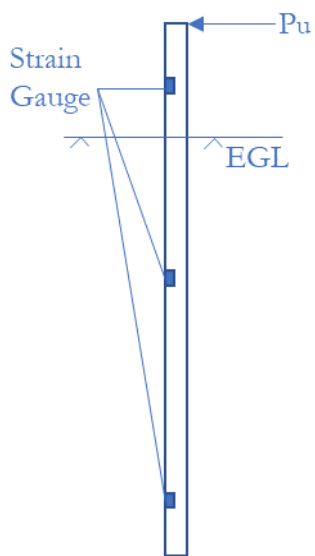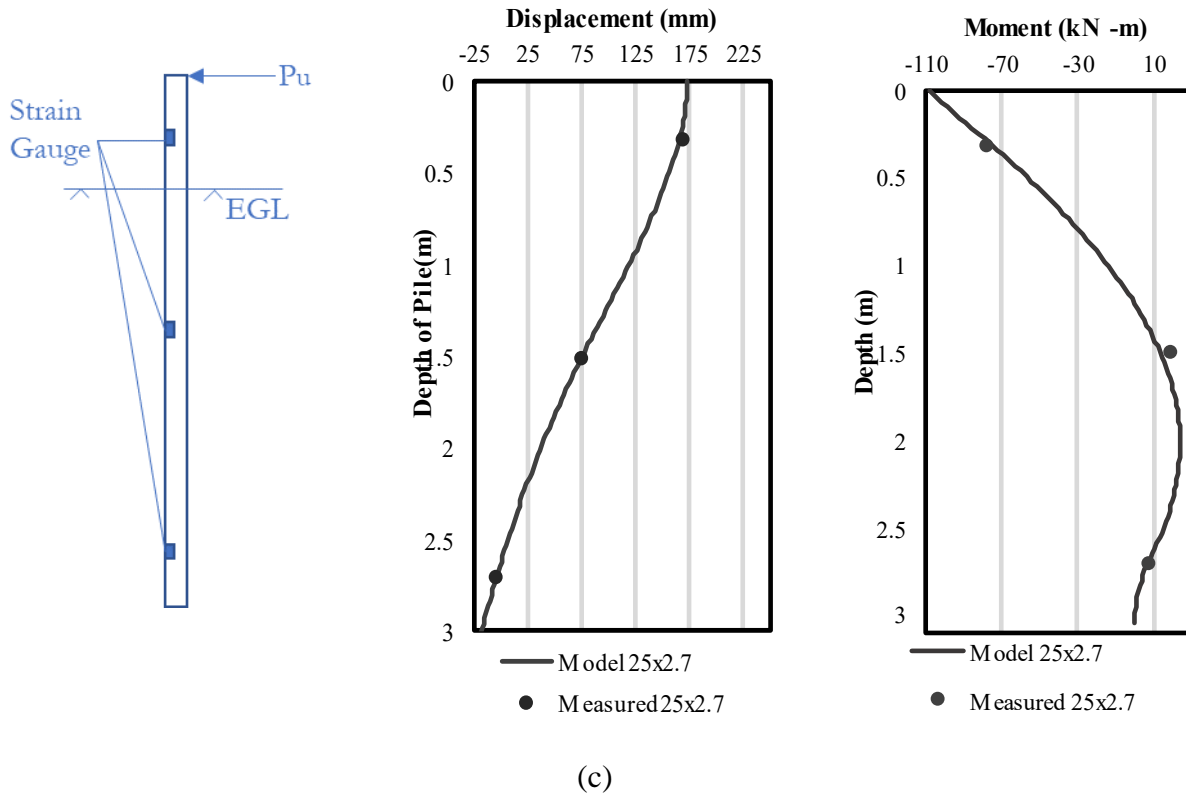
Figure 5-10 Comparisons between measured and computed displacement and moment curves of (a) 10 cm x 10 cm RPP embedded at 2.1 m, (b) 15 cm x 15 cm RPP embedded at 2.4 m, and (c) 25 cm x 25 cm RPP embedded at 2.7 m

5.6 Ultimate Load Capacity

In many of the previous studies, failure has been set as a predefined deflection limit resulting from applied load either based on the dimension of the pile or on the estimated design load of the super structure. RPP, predominantly being a product of plastic and having much less dimension than a regular concrete or steel pile, the aforementioned failure criteria does not suit as a preferrable technic to define the failure. The transmission of lateral loads from deep foundations to the ground is a problem involving soil-structure interaction between foundations and the underlying soil. In other words, whereas the soil resistance depends on the foundation's movements and flexural stresses, the foundation's movements depend on the soil resistance. Therefore, it is not possible to arbitrarily divide the analyses' structural and geotechnical components. Both must be assessed simultaneously.
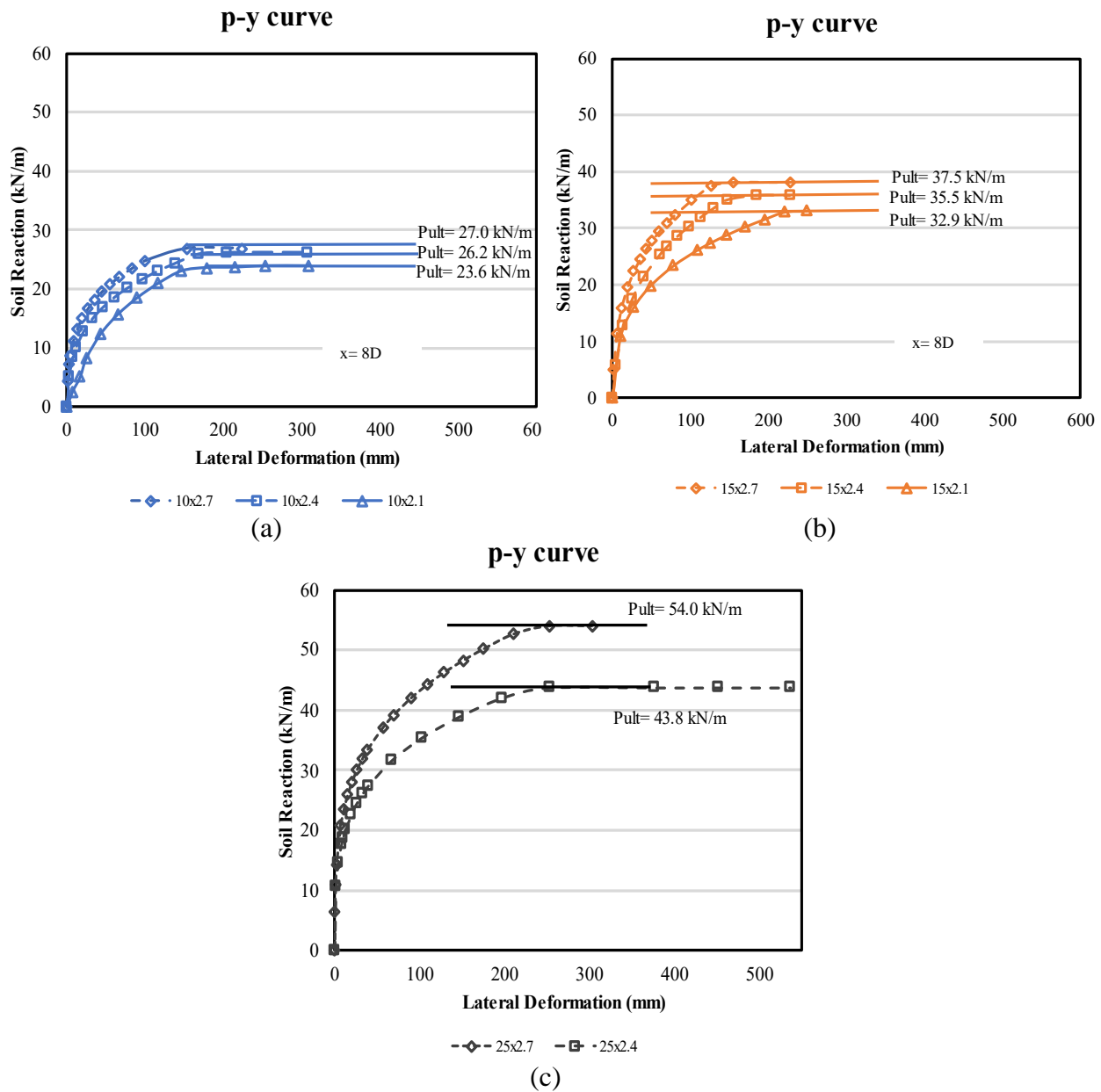
Figure 5-11 p-y curves (a) 10 cm x 10 cm RPP at x = 8D depth; (b) 15 cm x 15 cm RPP at x = 8D; (c) 25 cm x 25 cm RPP at x = 8D

With application of load, RPP showed longer range of elastic deformation before reaching yielding point or plastic deformation. Considering the uniqueness of the study, p-y analysis was employed to determine the ultimate lateral load capacity of the RPPs. As the lateral load capacity of the piles depends extensively on pile soil interaction, it was crucial to determine the load at which the soil surrounding the piles fails to indicate failure of the pile soil combined system. Due to the lack of

a definite threshold point of failure in RPP, it was more critical to examine the p-y curve for estimating the failure of the field lateral load testing.

P-y curve, a vastly used finite difference method in understanding the nonlinear behavior of pile soil interaction was constructed with the help of LPILE after the calibration efforts based on the load test results and subsoil conditions in the field. As shown by Duncan et al. (1994) and Christensen (2006), the lateral behavior of piles is significantly dependent on the properties of soil within a zone varying from ground surface down to 8D to 10D below surface. Therefore, p-y curves for soil to depth, x = 8D were obtained and studied in this research. Figure 5-11 shows the p-y curves for soil at the depth, x = 8D up to the maximum applied load in the field and corresponding ultimate soil resistance, p_{ult}, which is defined as the straight portion of the curve at end of the parabolic section. Figure 5-12 shows the applied lateral load and deformation corresponding to the ultimate load capacity of the soil pile interaction.
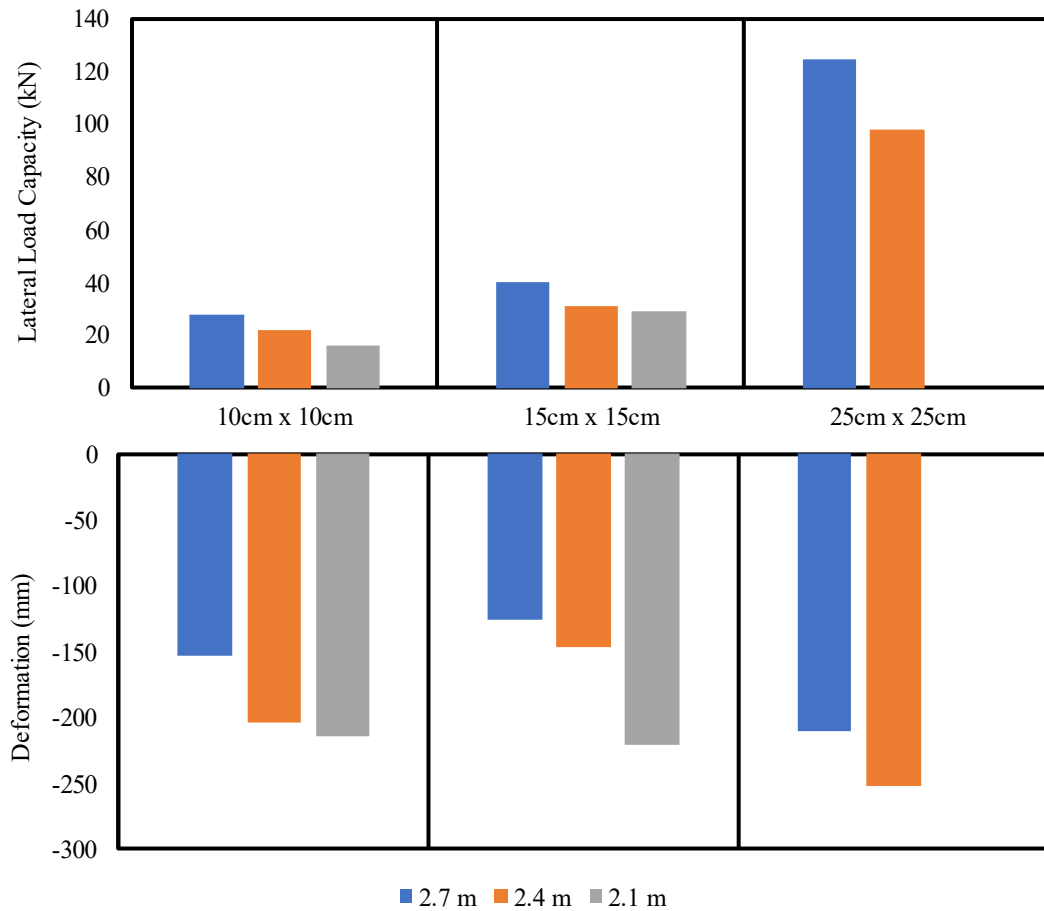
Figure 5-12 Lateral load capacity and deformation of the RPPs at ultimate loading

The RPPs' lateral load carrying capacity increased while their displacement reduced as embedment depth increased. With the same embedment depth, 25cm x 25cm RPP excelled both 15cm by 15cm and 10cm x 10cm RPP in terms of lateral load capacity due to its higher cross-sectional area. 25cm x 25cm RPP had 44% to 100% higher load carrying capacity with 24% to 38% more deformation. The fact that deformation increases with application of significant amount of load and that 25cm x 25cm RPPs were behaving like short piles, the deformation in this case was higher. When the embedment depth was raised by 1 ft, the displacement reduction ranged from 4% to 25% for a 10cm x 10cm RPP, 13% to 33% for a 15cm x 15cm RPP, and about 16% for a 25cm x 25cm RPP. While comparing 10cm x 10cm RPP and 15cm x 15cm RPP with the same embedment depth, RPPs with smaller cross section displaced 21% to 39% more than the RPPs with greater cross sections, and the latter had a 35% to 40% higher capacity for lateral load carrying. The lateral load capacity of 10cm x 10cm RPP rose by 3% to 11% for every 1 ft increase in embedment depth, up to 6% to 8% for 15cm x 15cm RPP, and roughly 23% for 25cm x 25cm RPP.

5.6.1 Pile Characteristics along the RPP

The pile behavior characteristics, moment distribution and displacement along the length of the test RPPs at the ultimate load corresponding to p_{ult}, was determined with the help of LPILE. The load corresponding to the p_{ult} was selected for analysis as this load corresponds to the ultimate soil reaction or ultimate load capacity of pile soil combination. Displacement and moment along the RPP at failure are shown in Figure 5-13.

Displacement was largest at top of the RPPs because of having free head movement at top. The displacement reduced as the movement was restricted by soil enclosure. After reaching a specific depth of 1.5 m to 2 m length, in the case of 10 cm x 10 cm and 15 cm x 15 cm RPP, the displacement ultimately decreased to zero. A different trend was noticed for 25 cm x 25 cm RPP. With depth, the displacement kept growing and turned negative near the bottom. This trend observed from the model was similar to the deformation pattern measured from the strain gauge reading in the field. The displacement reduces as the RPP size goes up. However, in case of 25 cm x 25 cm RPP, the RPP failed after encountering greater load, but with higher deformation. When piles are shallower and have a restricted depth of embedment in the soil, negative displacement development can be more substantial. This means that 25 cm $\times$ 25 cm RPPs were behaving as short piles.
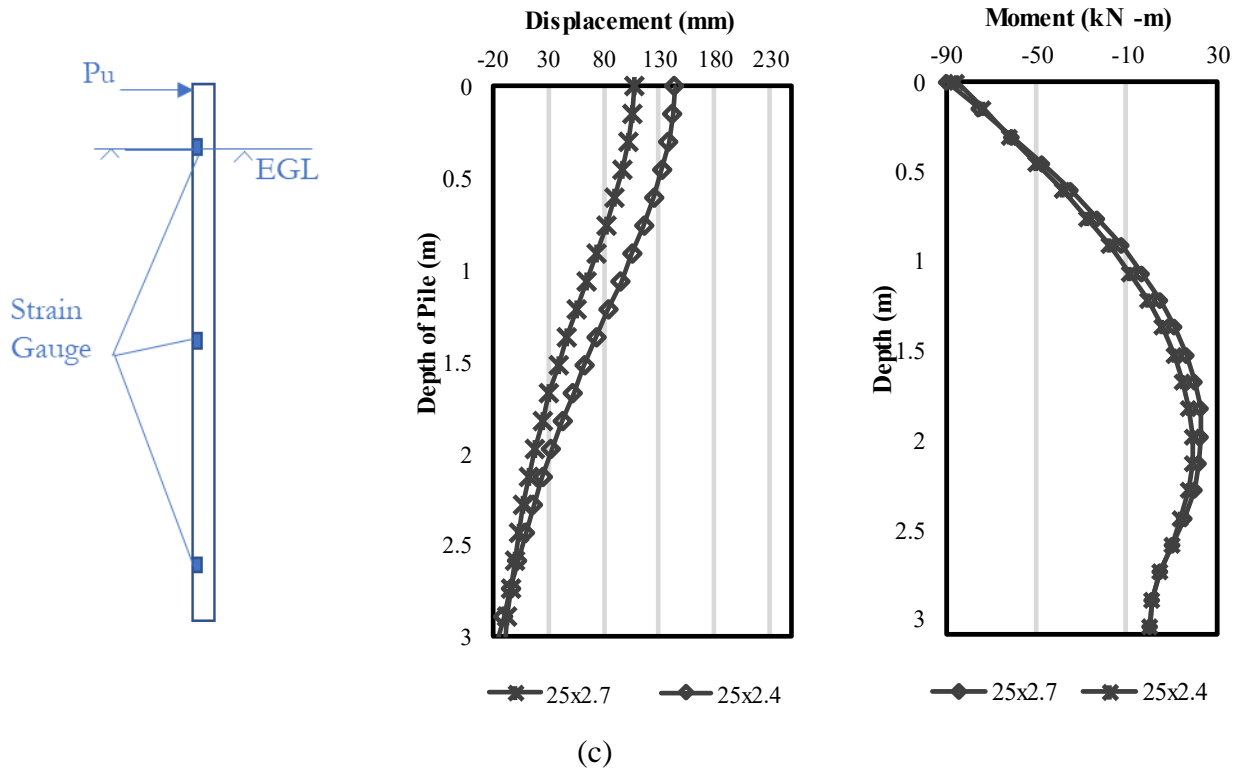
(a)

(b)

198
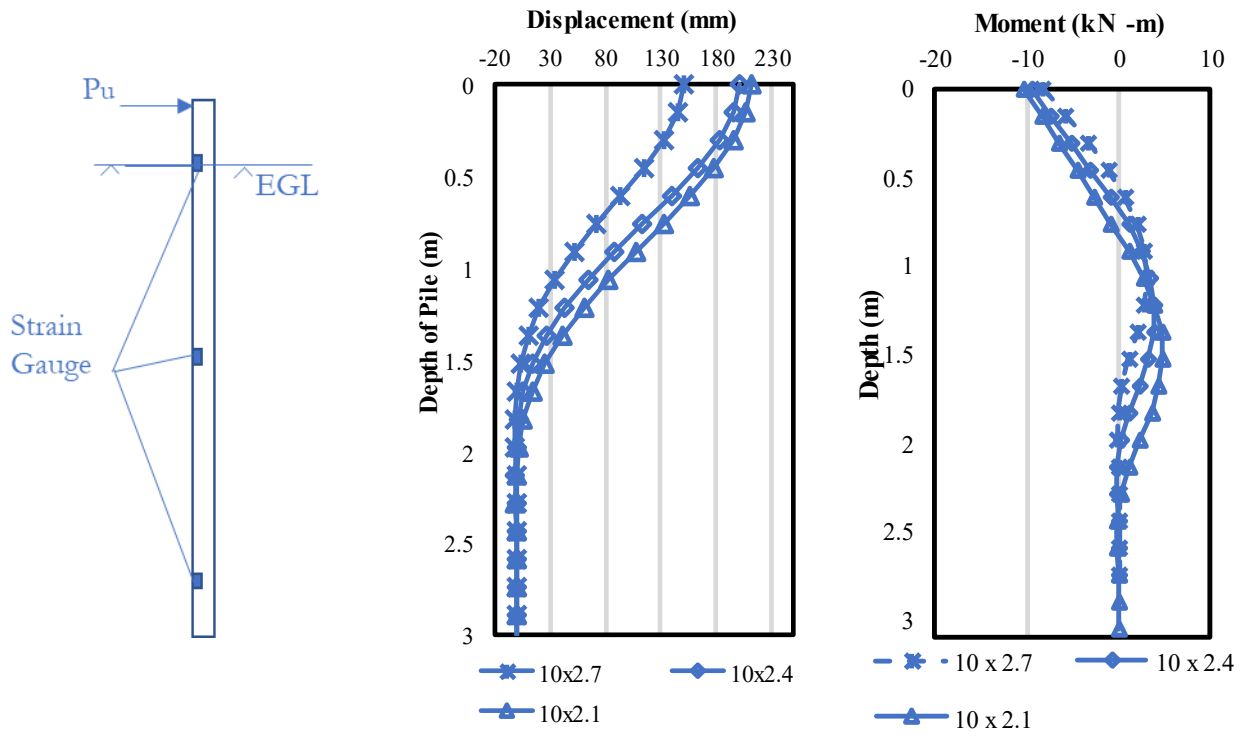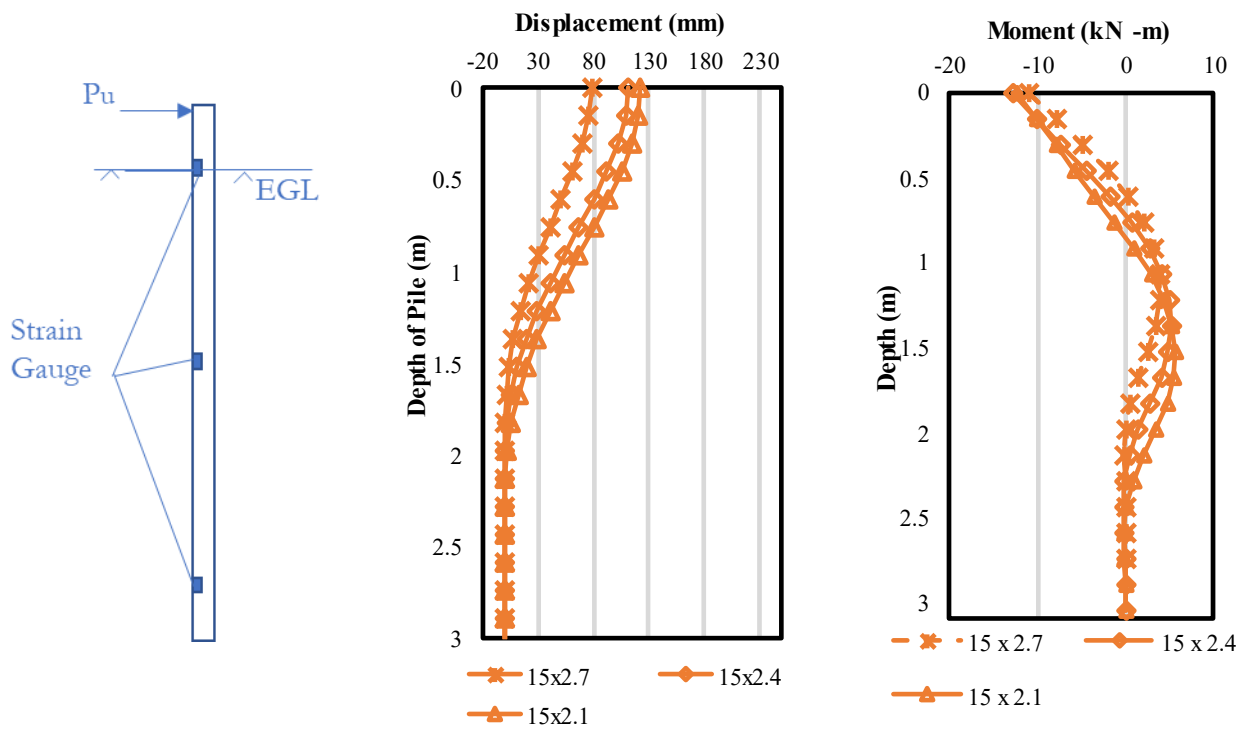
Figure 5-13 Displacement and moment along the RPP at failure of (a) 10 cm x 10 cm RPP (b) 15 cm x 15 cm RPP; and (c) 25 cm x 25 cm RPP

Moment vs depth curve depicts that maximum moment at failure occurs at 0.8 m to 1 m from the ground surface. This is owing to the RPP head's ability to move freely. As the length increases and RPP is surrounded by soil, there develops positive moments which eventually decreases with depth and gets to zero. The maximum moment increases with increasing applied load and the location of the maximum bending moment moved downward when embedment depth decreased. Moment development and displacement increased as the anchorage length of the RPP reduced. Moment tends to decrease as the depth increases after the curve reaches its maximum value. For 10 cm x 10 cm RPP, the maximum moment was discovered at a depth of 9D, for 15 cm x 15 cm RPP at a depth of 6D, and for 25 cm x 25 cm RPP at a depth of 8D. It is safe to remark based on the moment and displacement results along the length of the RPP that the embedment depth is the main governing factor in lateral load behavior of RPP.

5.7   Parametric Study

The primary objective of the parametric study was to develop a comprehensive dataset to understand the load deformation behavior of the RPPs subjected to lateral load test. As shown in Figure 5-14, a parametric study matrix was formulated, considering the probable associated parameters. Four different foundation soil conditions were investigated. For investigating the effect of RPP properties on the load deformation behavior, the soil properties of all four layers were varied for the parametric study.

In the present study, the lateral behavior of piles was examined in relation to various soil and RPP factors. Included are the soil's undrained shear strength (c), angle of internal friction (ϕ), pile length (L) and width (D) and extension length to embedment ratio. Table 5-6 displays the range of values of these variables employed in the parametric investigation.

Table 5-6 Consideration for Design Chart Development of Lateral Load Capacity of RPP

Cohesion (psf)	Friction Angle ϕ	Extension Length to Embedment Ratio	Slenderness Ratio
0	20 30 35	0.11 0.25 0.4	30 20 12 6
100	0	0.11 0.25 0.4	30 20 12 6
500	0	0.11 0.25 0.4	30 20 12 6
1000	0	0.11 0.25 0.4	30 20 12 6

Figure 5-14 Parametric study matrix

5.7.1 Effect of Soil Strength Parameters

Deformation behavior is directly influenced by soil strength characteristics. Deformation decreases with increasing cohesion and friction, and vice versa. The effect of four different foundation soil cohesions and frictions angles were investigated using the calibrated model. These combinations were selected to investigate the effect of decreasing friction angle and increasing cohesion. The study was conducted for 3 m long 15 cm x 15 cm RPP extended 0.6 m above ground.

The range of values of angle of friction, φ for very loose, loose, medium, dense and very dense sands are $< 29°$, $29°$-$30°$, $30°$-$36°$, $36°$-$41°$, and $> 41°$, respectively. Parametric study was conducted to develop load deformation curves for sand soils with $\varphi' = 20°$, $30°$ and $35°$. Figure 5-15 (a) shows lateral deformation with varying soil friction angles ($\phi = 20°$, $\phi = 30°$ and $\phi = 35°$). The soil cohesion was fixed at 0 kN/m^2 for 15 cm x 15 cm RPP. The slender ratio (L/D) and extension length to embedment ratio for this RPP was found to be 20 and 0.25 respectively for 15

cm x 15 cm RPP embedded at 2.4 m. As expected, the lateral deformation in the case of friction angle 35° was the least and was the highest in the case of friction angle 20°.

(a)   (b)
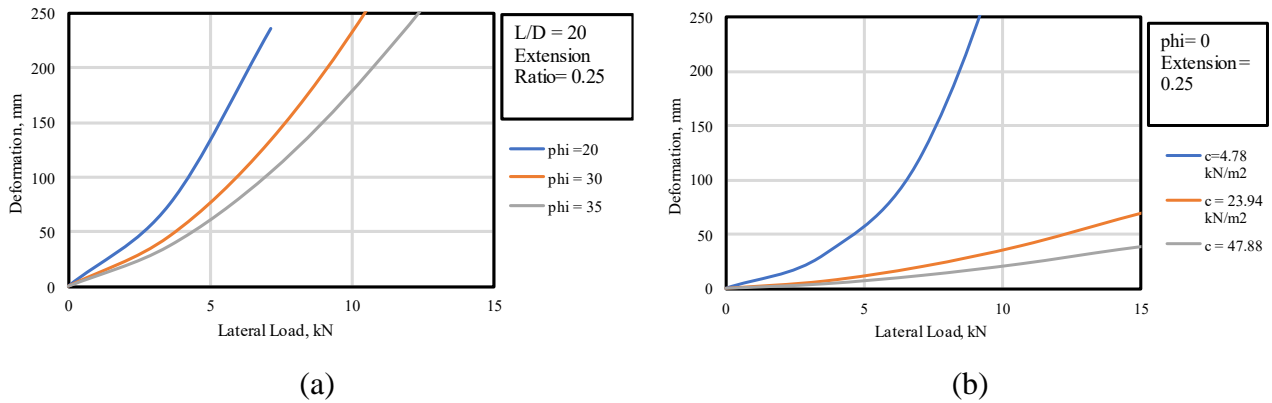
Figure 5-15 Effect of Foundation Soil Strength on deformation behavior of 15 cm x 15 cm RPP extended 0.6 m above ground with (a) varying internal friction angle (ϕ); (b) varying cohesion strength (c)

Figure 5-15 (b) compares the deformation behavior of the same RPPs with different foundation soil cohesion. Foundation soils were assumed to have the same friction angle ($\phi = 0°$); however, the cohesion (c) was varied (c = 4.78 kN/m², c = 23.94 kN/m², and c = 47.88 kN/m²) to study the effect of only soil cohesion on lateral deformation. An interesting trend was found from the numerical analysis, such that, even though the friction angle was fixed, the increase in cohesion reduced the deformation to a significant extent.

5.7.2   Effect of Pile Size

The effect of different RPP parameters on the load deformation response can be beneficial in evaluating an appropriate design layout for future use. It is a known fact that larger cross-section and closer spacing of RPPs improves the performance of RPPs (Bhandari, 2021). The field results of the current study point towards the same inference. The effect of RPP size was studied for soil having cohesion strength, (c = 23.94 kN/m²) and the friction angle ($\phi = 0°$).

In this study, three square RPP with dimensions of 0.10, 0.15, 0.25 and 0.30 m were selected to investigate the effect of RPP sizes on the load deformation behavior. The RPP size effect was investigated in the form of slenderness ratio keeping the length of RPP constant at 3.0 m and

extension length of 0.6 m. From Figure 5-16, it was observed that increasing slenderness ratio of the RPPs leads to significant increase in deformation.
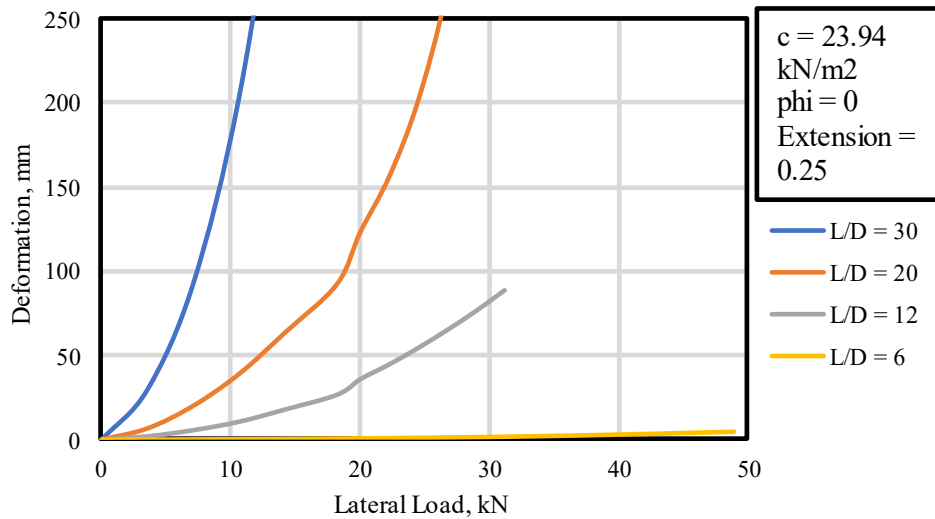
Figure 5-16 Effect of RPP size on load deformation behavior of RPP

5.7.3 Effect of Extension above Ground

Since the extension to embedment length ratio governed the lateral load behavior of RPP, a comparative study was conducted to investigate the effect of varying extension to embedment length ratio on the load deformation behavior of RPP. This study considered different extension to embedment ration of 15 cm x 15 cm RPP into soil having cohesion strength, ($c = 23.94$ kN/m^2) and the friction angle ($\phi = 0°$). In some cases, lateral displacement is taken to be critical design criteria. RPPs with greater size are expected to restrict lateral deformation to a greater extent. Therefore, a comprehensive parametric study was undertaken with calibrated model. Figure 5-17 shows the variation of lateral load – deformation behavior of RPP with varying extension length to embedment depth ratio.
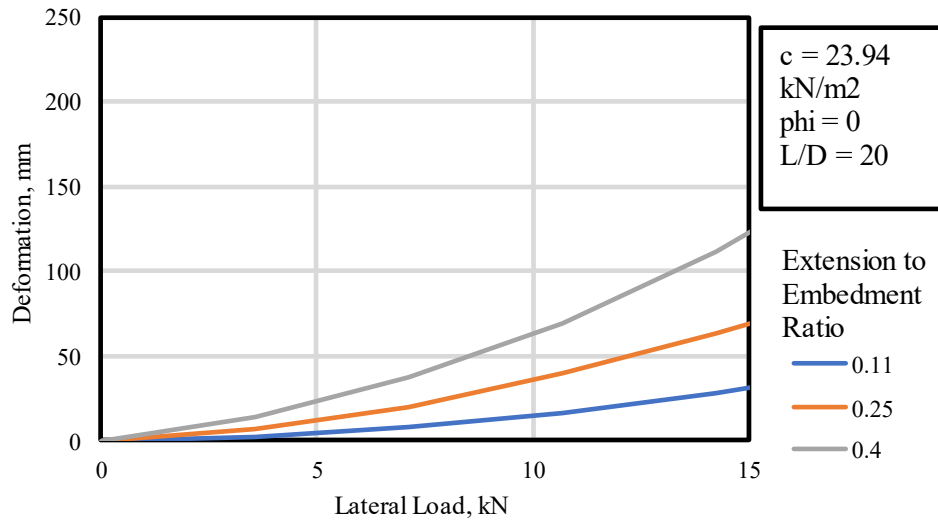
Figure 5-17 Effect of extension length to embedment depth ratio on load deformation behavior of RPP

Figure 5-17 illustrates the variations in lateral displacement with extension length to embedment depth ratio for three different ratios of 0.11, 0.25 and 0.40 for 15 cm x 15 cm RPP. The chart shows the influence of the extended portion to anchorage length, showing that as the ratio rose, lateral displacement increased, and load capacity dramatically fell.

5.8   Comparison with Other Pile Materials

The lateral load behavior of RPP was compared to that of other pile materials. The load deflection behavior of RPP was compared with the LPILE study performed by Briaud and Wang, 2018 using the lateral load test results from New Orleans, LA. This study was chosen because it used three different types of piles embedded in a sand layer in New Orleans. The diameter and length of the timber pile, bored pile, and steel pipe pile are all 0.36 m and 21 m, respectively. Replicating the model, resulting deflection was found to be 88.5 mm, 17 mm., and 37.3 mm at pile top for the maximum applied lateral loads of 127 kN. To compare the results, RPPs of identical dimensions were exposed to lateral load in the soil conditions described in the study. RPP was found to deflect 84 mm when 127 kN was applied. Table 5-7 lists the pile properties and the soil data used in LPILE. Figure 4-8 shows the soil stratigraphy and the field test results.

Table 5-7 Pile and Soil Properties of New Orleans Test

Pile properties used in LPILE					
Pile Type	B (m)	L (m)	t (m)	I (m^4)	E (kN/m^2)
RPP	0.36	21	-	0.000787	12.8xE^6
Timber	0.36	21	-	0.000787	14.0xE^6
Concrete	0.36	21	-	0.000787	2.0xE^8
Steel Pipe Pile	0.36	21	0.01	0.000163	2.7 xE^7
Soil Properties used in LPILE					
P-y model	Depth (m)		γ ' (kN/m^3)	k (kN/m^3)	φ (°)
	Top	Bottom			
Sand	0	25.0	20.0	-	28
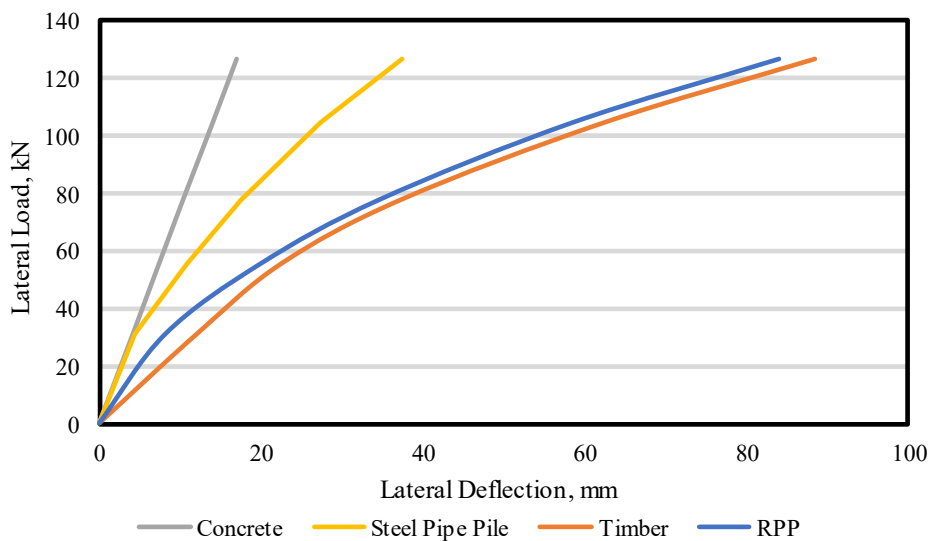
Figure 5-18 Lateral load vs deflection curve for different types of piles

5.9 Conclusion

Field Load Test was performed to find out the lateral load capacity of the Recycled Plastic Pins by means of horizontal loading. A total of 16 RPPs with 3 different cross-sections were installed having embedment depth of 2.1 m, 2.4 m and 2.7 m respectively. The take-away from this study is listed here.

- Larger RPPs demonstrated greater resistance to applied lateral stress. 25 cm x 25 cm RPPs were able to sustain 120% to 214% higher load than 15 cm x 15 cm and 10 cm x 10 cm RPPs at the same deflection.

- Moment calculated during field load test suggested that the application of a lateral load at the top of the RPP resulted in the generation of a negative moment at the head. As the RPPs reached depths of 1.5 meters and 2.7 meters with soil confinement, they experienced positive moments. The moment at the bottom had a minimal value, approaching zero.

- The deformation along the RPP length during field load test showed that, with a lateral force applied at the top, the greatest deformation occurred there because of unrestricted head movement. Deformation increased at all depths as the RPP embedment depth decreased, and it increased with greater applied load. Larger RPPs withstood higher loads and, consequently, exhibited more significant deformation.

- LPILE 2022 was employed to create a model for simulating RPP behavior in lateral load testing. Model calibration based on field measurements obtained from load tests on RPP, was essential to ensure an accurate depiction of site-specific conditions.

- The ultimate lateral load capacity results determined from p-y analysis show that, for the same depth of embedment, larger RPPs had 35% - 100% higher lateral load carrying capacity.

- Deformation increases as the load application increases. For similar load, smaller RPPs displaced 21%-39% more than RPPs with greater cross sections. Although deformation increases fractionally with a considerable increase in load application, this increase is insignificant when compared to the increase in loading. For 40% to 100% more load application, 25 cm x 25 cm RPPs had 24% to 38% more deformation.

- Increasing the embedment depth by 0.3 m resulted in varying degrees of displacement reduction, with a range of 5% to 33%. Conversely, the lateral load capacity showed an increase with the same increase in embedment depth, ranging from 8% to 39%. These findings highlight the significant influence of embedment depth on both displacement and lateral load capacity, with larger RPP sizes generally experiencing greater improvements in load capacity.

- In the cases of the 10 cm x 10 cm and 15 cm x 15 cm RPP, displacement peaked at the top of the RPP and then gradually dropped until it was zero when it reached a predetermined depth of 1.5 m to 2 m along the RPP due to soil anchorage. However, the displacement of 25 cm x 25 cm RPP kept growing and turned negative at the bottom showing short pile failure behavior.

- Moment at failure is maximum at 0.8 m to 1.0 m from ground surface according to the moment vs depth curve. With increasing applied load, the maximum moment increases, and with decreasing embedment depth, the maximum bending moment shifts downward. Moment tends to decrease when the curve reaches its greatest value as the depth rises.

- Using a calibrated model, a parametric investigation was conducted to assess the influence of soil strength parameters, the size and length of RPPs, and their depth in the ground. It was observed that as the values of soil strength parameters and embedment depth increased, and the slenderness of RPPs decreased, an apparent rise in load capacity and a reduction in deformation was observed.

CHAPTER 6

COMPARISON OF LOAD CAPACITY BETWEEN RPP AND TIMBER

ABSTRACT

Timber piles are frequently employed in various geotechnical projects for both vertical and lateral support, despite their degradable nature and role in deforestation. In contrast, Recycled Plastic Pins (RPP) offer a sustainable alternative for such projects by effectively replacing timber piles. The objective of the study is to experimentally investigate the load capacity of RPP in comparison with timber piles. In this paper, field measurements of four vertical load tests and four lateral load tests on RPP and timber of two different embedment depth driven in high plastic clay have been assessed. Six empirical methods were used to evaluate and compare the ultimate vertical load bearing capacity of RPPs and timber piles. Field lateral load tests results were used to calibrate numerical models to simulate the load transfer behavior of the piles. Consequently, the results were compared to assess the viability of RPPs as a substitution of timber piles. In every instance, the load-bearing capacity of RPP piles is nearly equivalent to that of timber piles. Results indicated stress strain behavior dictated by the fiber weaving and orientation exert a significant influence on the pile axial capacity. The lower stiffness of the RPP piles leads to increased pile head displacement under vertical and lateral loading compared to timber piles. In addition, a comprehensive parametric analysis was carried out to determine the impact of the pile extension above ground and size of the piles on the results.

Keywords: Field Load Test, Axial Load Test, Lateral Load Test, Recycled Plastic Pin (RPP), Timber Pile

6.1 Introduction

The drive towards sustainable construction practices has prompted researchers and engineers to explore eco-friendly materials and techniques. Industrialization has led to an increase in the need to install piles in corrosive and contaminated soils. This poses a serious challenge to construction, as concrete, steel, and wood can all deteriorate in these environments. Sulfides and chlorides, in particular, can cause significant damage to piling systems. The United States spends nearly $2 billion per year on repair and replacement of these systems (Iskander and Hassan, 1998). Timber piles have been extensively utilized in geotechnical projects for their effectiveness in providing

208

both vertical and lateral support. However, the environmental concerns associated with the use of timber, such as its degradable nature and contribution to deforestation, have led to the search for more sustainable alternatives (Iskander and Hassan, 1998 and Islam, 2021).

Table 6-1 The mechanical properties of timber and RPP

Properties	Units	Timber (Fengel and Wegener, 2011; Morrell, 2018; and Armstrong, 2013)	RPP (Chen, 2003 and Bowders et al. 2003)
Tensile strength	MPa	70-140	30-50
Compressive strength	MPa	30-60	50-100
Bending strength	MPa	100-180	100-200
Elastic modulus	GPa	10-15	1-2
Shear strength	MPa	5-10	15-30

Recycled Plastic Pins (RPP) can be a promising alternative to timber piles due to their potential to address these environmental issues (Islam et al. 2023 and Badhon et al. 2023). RPPs are primarily made from collected recycled plastics. Some additives are added during the molding process in order to increase the mechanical properties of RPPs. Previous research has explored the mechanical properties, durability, and behavior of RPP in various conditions (Chen, 2003 and Bowders et al. 2003). According to Bowders et al. the tensile strength, compressive strength, and elastic modulus of RPP can vary between 30 to 50 MPa, 50 to 100 MPa, and 1 to 2 GPa, respectively. Researchers from Columbia University, Carroll et al. (2001), discovered that the modulus of plastic lumber is lower than that of wooden lumber regardless of whether the modulus is evaluated in compression, flexure, or tension. It is an unsuitable material when acting as a tensile member since it has a low tensile strength. Plastic lumber is more resilient to shear than timber lumber and is probably less prone to crack and break. Overall, plastic lumber is more

environmentally friendly than timber lumber and has sufficient structural qualities for a wide range of applications. The comparative evaluation of mechanical properties for timber and RPPs is presented in Table 6-1.

For many years, timber has been used for piles to support structures. However, timber is susceptible to decay and insect attack, moisture damage, durability, and biological degradation (Wang et al. 2018). To make timber durable for use as piles in underground applications, it is essential to take specific measures to enhance its resistance to decay, insects, and other environmental factors. Timber can be made more durable for long-term performance underground by pressure treatment, preservative addition, proper dying, and protective barriers (Morrell, 2018; and Armstrong, 2013). However, these techniques are often associated with high cost and time which might not be feasible for some projects. Ahmed (2013) compared RPP, wood, and bamboo piles, finding that wood had the highest compressive and flexural strengths, while RPP allowed for greater soil movement, up to 19%. RPP's adaptability to various chemical and climatic conditions made it the preferred choice, with only an 8% reduction in strength under different climates, compared to approximately 50% for wood and 65% for bamboo. RPP's strength, longevity, and minimal strength reduction in various conditions make it a cost-effective alternative. On the other hand, RPPs are chemically inert, which means they do not react with other chemicals. This makes them very durable and allows them to last for more than 500 years without any degradation (Hossain et al., 2017)

Much research has been done for the determination of timber and RPP properties (Armstrong, 1979; Hossain et al. 2017; and Ahmed, 2013). The use of RPPs in geotechnical applications has been investigated in several studies (Badhon et al., 2023; Islam et al., 2023; Chen, 2003; and Bowders e al,. 2003). RPPs can be used in a variety of applications, including slope stabilization, foundation reinforcement of retaining walls, embankments, and more (Iskander and Hassan, 1998; Hossain et al., 2017; Bhandari et al., 2022). However, the present studies are focused only on the performance of RPPs as a system in different geotechnical structures that has been evaluated by many researchers (Badhon et al., 2023; Islam et al., 2023; and Bhandari et al., 2022). There is limited research on the vertical and lateral load capacity of single RPPs embedded in the ground. Thus, it is necessary to understand the fundamental behavior of individual RPPs under vertical and

lateral load. Furthermore, it is necessary to investigate the load capacity comparison between timber and RPP to explore the possibility of using RPPs as an alternative to timber piles.

The experimental investigation presented in this paper provides valuable insights into the load capacity of Recycled Plastic Pins (RPP) in comparison with traditional timber piles. The research involves field measurements of four vertical load tests and four lateral load tests on RPP and timber piles embedded at two different depths in high plastic clay soil. The inclusion of both vertical and lateral load tests provides a comprehensive assessment of the load-carrying capabilities of the two materials.

6.2   Materials And Method

6.2.1   Test Site and Soil Conditions

A location inside Hunter Ferrell Landfill in the City of Irving, Texas was selected for the study. Geotechnical drilling and resistivity imaging were conducted for the sub-soil investigation. Two locations were selected for soil investigation and drillings were conducted for these locations with a drilling depth of about 6 m to investigate the soil properties.

Figure 6-1 Location of Test Site Installation in The Hunter Ferrell Landfill in Irving, TX

The average blow count of the foundation soil was found to be 5 at a depth of 1.2 m. Disturbed and undisturbed soil samples were collected during boring. A detailed laboratory investigation was carried out to determine the index properties and shear strength parameters of collected soil samples. No groundwater table was detected during the drilling. The moisture content varied from 10% to 28%. The plasticity index varied from 36 to 48, and the range of liquid limit was between

51 to 66. The results indicated the presence of medium to high plastic clay throughout the borehole depth and classified as Fat clay (CH) according to the Unified Soil Classification System (USCS).

UCS tests were conducted on undisturbed soil samples collected in thin-walled Shelby tubes at two different depths of 1.5 m and 4.6 m respectively. The undrained shear strength at 1.5 m depth was found to be 6.7 kN/m^2 and the ultimate bearing capacity was calculated to be 34.5 kN/m^2. Based on the field SPT data, N value for the top layer (From BH1_S4) of soil was 5, which indicates that the compressive strength will be in between 23.9 to 47.9 kN/m^2. For the sample collected from 4.6 m depth, undrained shear strength was found as high as 114.9 kN/m^2 and the ultimate bearing capacity was calculated to be 590 kN/m^2, indicating an extremely stiff soil layer. Based on undrained shear strength parameter as well as field SPT value, it was confirmed that topsoil within this zone was weak and thus, was selected for conducting the tests.

Figure 6-2 Variation of moisture content and SPT value in different layers of soil

6.2.2 Design and Construction Details

The field experiments were designed to incorporate four vertical field load tests and four lateral field load tests. 10 cm × 10 cm RPP and Timber piles of two different lengths of 2.13 m and 1.68 m were selected for vertical load test in field. The RPPs and timbers were embedded full length into the ground for the purpose of conducting vertical load test. For lateral load tests, 10 cm × 10 cm RPP and timber of two different embedment depths of 1.22 m and 1.52 m with an extended

length of 0.46 m and 0.61 m above ground were selected for field installation. Table 6-2 and Table 6-3 summarize the design details of the load tests.

Table 6-2 Summary of design details of vertical load tests

Pile Type	Pile Length (m)	Number of Tests	Number of Piles	Total Number of Tests
10 cm x 10 cm RPP	2.13	1	1	2
	1.68	1	1	
10 cm x 10 cm Timber	2.13	1	1	2
	1.68	1	1	

Table 6-3 Summary of design details of lateral load tests

Pile Type	Cantilever length, L (m)	Embedment depth, D (m)	Number of Tests	Number of Piles	Total Number of Tests
10 cm x 10 cm RPP	0.46	1.22	1	1	2
	0.61	1.52	1	1	
10 cm x 10 cm Timber	0.46	1.22	1	1	2
	0.61	1.52	1	1	

6.2.3 Installation of the RPP and Timber Piles

The installation of RPP took place during March 2023 with the help of Stroimatic Pile Driver. For vertical load tests, the piles were flushed to the ground whereas for lateral load test piles were embedded at 1.22 m and 1.52 m depth into the ground with extended portion of 0.46 m and 0.61 m above the ground.

(a)   (b)   (c)

Figure 6-3 (a) RPP and Timber Pile Installation; (b) RPP and Timber Piles for Vertical Load Test; (c) RPP and Timber Piles for Lateral Load Test

6.3   Load Test on RPP and Timber Piles

The vertical load test was performed according to ASTM- D1143 (Quick test) standard. Field load test for vertical load capacity requires a total of four tests to be performed. Vertical load tests were conducted using a plate bearing load tester. Heavy weight dump truck was used as reaction vehicle and load was applied against the rear axle. Axial compressive load was continuously applied until failure was initiated, that means the test load caused rapid continuing, progressive movement, or the total axial movement exceeds 15 % of the pile diameter or width. The ultimate load capacity of the pile is determined by the point at which either of these phenomena or failure is observed. The axial compressive load was applied parallel to the longitudinal direction of the fibers of timber piles. Once failure occurred, the pile was unloaded from the maximum load in eight steps. Three dial gauges were used to report the settlement resulting from the application of load. Figure 6-4 (a) shows the plate load test equipment. Figure 6-4 (b) and (c) show the reaction vehicle used and the vertical load test set up.

(a)   (b)   (c)

Figure 6-4 (a) Load testing equipment; (b) Reaction vehicle; and (c) Vertical load test set up in field

Lateral load tests were conducted according to ASTM- D3966 using plate load tester. As a reaction vehicle, Crawler Dozer from the Irving Landfill was utilized, and the hydraulic jack was placed horizontally against the blade to apply lateral load on the RPPs. The load was applied laterally with the help of the lever attached to the hydraulic pump and displacement resulting from corresponding load application was recorded with the help of dial gauges. Figure 6-5 (a) and (b) show the field set up for the lateral load test of RPP. Figure 6-5 (c) shows the reaction vehicle used for lateral load test.

(a)   (b)   (c)

Figure 6-5 Field test set up for lateral load of (a) RPP; (b) Timber; (c) Reaction vehicle used for lateral load test

215

6.4 Result Analysis and Discussion

6.4.1 Vertical Load Test

For clarity, 1.63 m long RPP and timber piles were referred to as RPP 1 and Timber 1; and 2.13 m long RPP and timber piles were referred to as RPP 2 and Timber 2, respectively. Based on the field test results, RPP 1 and Timber 1 experienced rapid movement after reaching 16 kN and 15 kN respectively with corresponding settlement of 3.63 mm and 3.45 mm. Permanent settlement was 10.8 mm and 7.3 mm respectively for RPP and timber piles after withdrawal of load. Failure of RPP 2 and Timber 2 occurred at 26 kN and 28 kN, respectively, with settlement of 2.5 mm and 2.3 mm. Following the removal of the load, the permanent settlement for RPP 2 and Timber 2 was 4.5 mm and 3.2 mm, respectively. Regardless of the length of the piles, timber piles settled less than RPP and RPP settlement rate was much higher after reaching failure. However, timber failure happened to occur almost at the same load as RPP.

Timber, being a stiffer material with higher modulus of elasticity (E) in comparison to RPP, showed more resistance to settlement. This phenomenon is evident in the initial portion of the load deflection curve prior to failure where it undergoes elastic deformation. Even after failure the settlement was fairly low with increasing load in comparison with the RPP. Timber settled progressively after the failure with little increase in load indicating failure whereas in case of RPP entered into the plastic zone immediately resulting in large settlement, with application of additional load. This result is heavily influenced by the stress strain property of the two materials. Timber, being a stiffer material with higher E value, were more resistant in settlement. However, in case of RPP the curve behaved more ductile than timber and after failure it showed more settlement with application of load and eventually ended up with large permanent settlement. Figure 6-6 shows one load-displacement graph for each size of the RPP and timber piles tested for vertical load capacity.
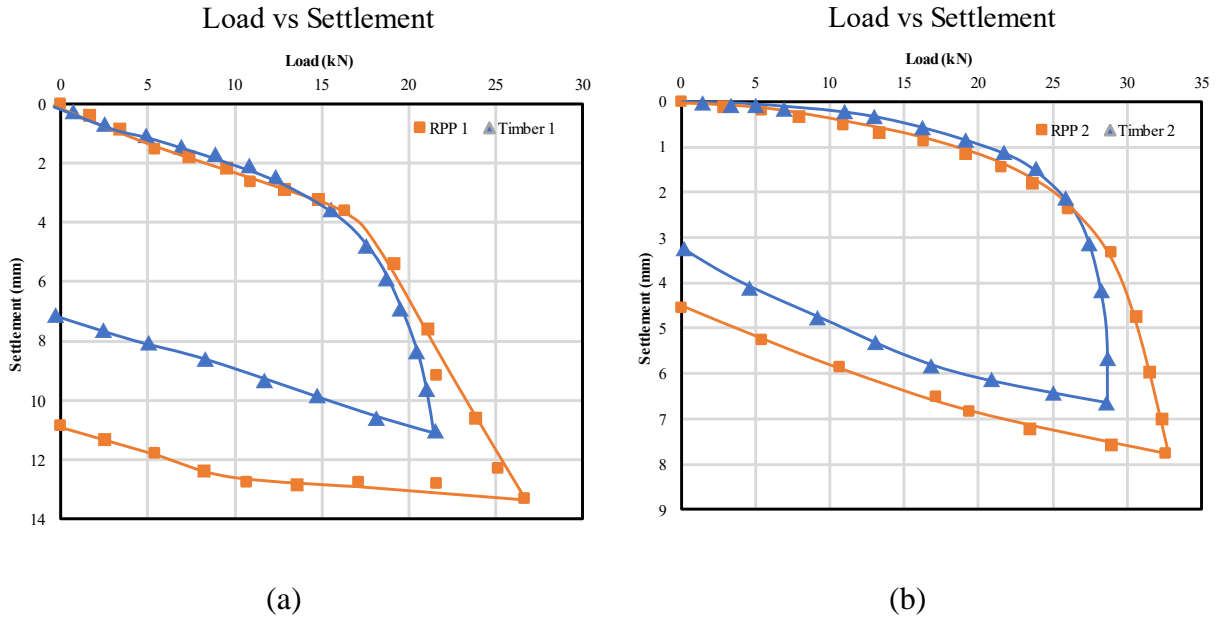
Figure 6-6 Load vs Deformation Curve (a) 1.63 m Long (b) 2.13 m Long RPP and Timber Piles

Six alternative approaches, including the Davisson's Method, Brinch Hansen's 90% Method, Chin's Method, Van Weele's Method, Fuller and Hoy's Method, and Butler and Hoy's Method, were used to analyze the ultimate vertical load capacity for RPP and timber piles. Table 6-4 tabulates the results of evaluating field data to produce the summary of ultimate load and the settlement at the ultimate load.

The maximum ultimate load for RPP 1 and Timber 1 were found 33 kN and 40 kN respectively utilizing Chin's method and the minimum load was found 17 kN and 23 following Van Weele and Butler and Hoy's Method. The RPP 2 and Timber 2 cases also showed the same pattern. Chin's Method yielded maximum ultimate load of 36 and 44 kN, respectively, and minimum ultimate load of 24 kN and 25 kN, respectively, using Butler and Hoy's Method.

Piles with longer length showed higher ultimate load carrying capacity. A 30% increase in pile length increased the ultimate load capacity by 10% (Chin's Method) to 41% (most conservative in Butler and Hoy's Method). The settlement also decreased with the piles reaching deeper depths. Settlement at failure was found to be 66 % to 70% less for both RPP and timber with the deeper piles.

Table 6-4 Ultimate Vertical Load Capacity Result Summary

CODES/ METHODS	RPP 1		Timber 1		RPP 2		Timber 2	
	Ultimate Load (kN)	Settlement at Ultimate Load (mm)	Ultimate Load (kN)	Settlement at Ultimate Load (mm)	Ultimate Load (kN)	Settlement at Ultimate Load (mm)	Ultimate Load (kN)	Settlement at Ultimate Load (mm)
Davisson Method (1972)	23	8.3	21	8	32	7.5	-	-
Brinch Hansen's (1963)	20	6.3	25	4.2	28	3.3	31	3.5
Chin's Method (1971)	33	----	40	----	36	----	44	----
Van Weele (1957)	17	3.8	23	3.8	26	2.3	32	2.5
Fuller and Hoy's (1970)	18	5.3	25	7.8	27	3	34	4.2
Butler and Hoy's Method (1977)	17	3.5	23	3.5	24	1.2	25	1.8

A comparative graphical representation is shown in Figure 6-7. Ultimate vertical load capacity of RPP and timber piles of two different lengths following different methods are presented here. Furthermore, the average load capacity found from the methods are presented with straight lines. Following various approaches, it was found that RPP 1 and Timber 1 had average ultimate load capacities of 21 kN and 27 kN, respectively, whereas RPP 2 and Timber 2 had average ultimate load capacities of 33 kN and 29 kN. Average ultimate load capacities varied by 13% to 22% for RPP and timber.
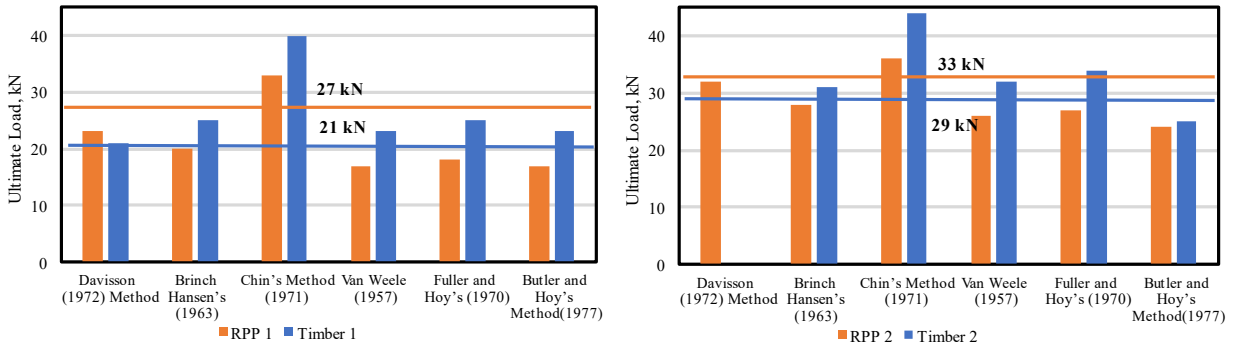
Figure 6-7 Ultimate vertical load capacity of (a) RPP 1 and Timber 1 and (b) RPP 2 and Timber 2 following different methods.

6.4.2 Lateral Load Test

The load test results from the lateral load tests are presented in this section. Lateral load failure is defined as the sudden occurrence when the piles experienced drastic lateral deformation as the result of application of lateral load. Figure 6-8 shows the load vs deformation curves of RPPs and timber piles obtained from the lateral load test results. For the ease of understanding, piles with extension to embedment ratio of 0.38 (0.46 m extension to 1.22 m embedment) are referred to as RPP I and Timber I and piles with extension to embedment ratio of 0.4 (0.61 m extension to 1.52 m embedment) are referred to as RPP II and Timber II. Upon calculating the dimensions and extension lengths, it becomes evident that these piles can be categorized as short piles, given their specific measurements.

The lateral load versus deformation curve is steeper for timber piles signifying more resistance to deflection in response to the application of load. Timber piles excelled RPP both in terms of enduring higher lateral load and less permanent deformation. Increasing embedment depth suggests improvement of lateral resistance with decreasing cantilever length. Ratio of pile extension to embedment depth plays the major role in lateral load response of the piles. As the ratio increases the pile presents more deformation both for RPP and timber piles for having less anchorage. For the same load application, Timber I with extension to embedment ratio of 0.38, displaced 25% less deflection than Timber II with extension to embedment ratio of 0.40. The same phenomenon was seen to occur with RPPs, however with the application of an equal load, RPP I and RPP II displaced 98% and 96% more lateral displacement than the corresponding Timber I and Timber II.
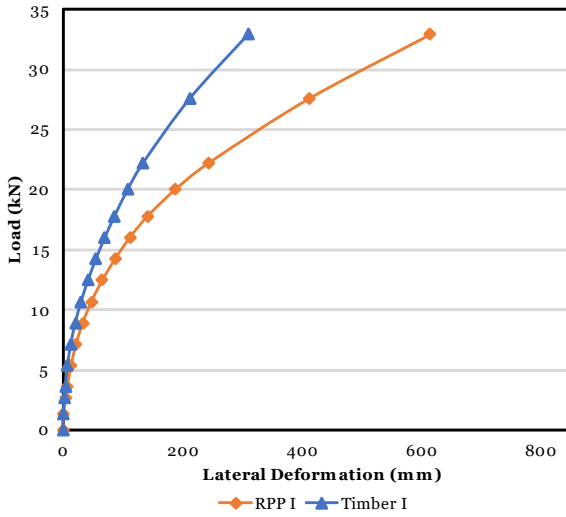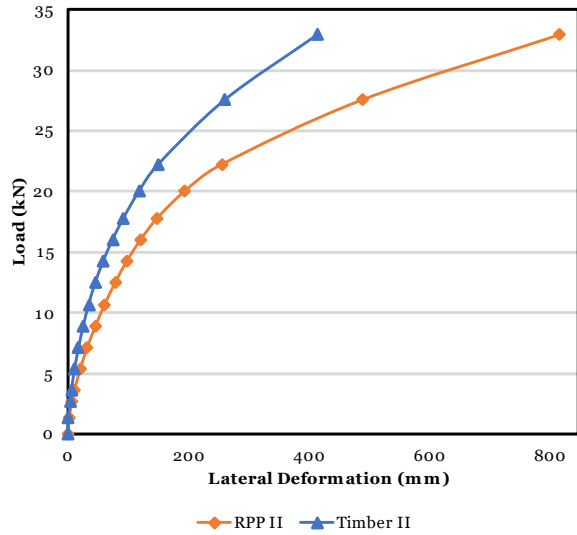
(a)   (b)

Figure 6-8 Lateral load vs Deflection curve (a) RPP I and Timber I; (b) RPP II and Timber II

In order to conduct a more comprehensive analysis of the lateral load-deflection behavior, a model was created to simulate conditions similar to those encountered in field tests. Modeling of the pile under lateral loading was performed using the computer program LPILE 2022. The shear strength of soil at the top 6 m was varied until a reasonable agreement between the measured and calculated behavior was observed. The model was calibrated and validated against the field test results as discussed in detail in the previous section. A review of the pile and soil shear strength data for which the agreement occurred is showed in Table 6-5. These values were taken from the range of the property of each soil type.

Table 6-5 Pile and soil properties used for model

Pile Properties					
Pile type	D(mm)	L(m)	I (m4)		E(kN/m2)
RPP I	101.6	1.6764	8.878E-6		2.0E+6
RPP II	101.6	2.13	8.878E-6		2.0E+6
Timber I	101.6	1.6764	8.878E-6		8.1E+6
Timber II	101.6	2.13	8.878E-6		8.1E+6

Soil Properties used in LPILE						
P-y model	Depth (m)		γ' (kN/m3)	c (kN/m2)	K (kN/m3)	$\varepsilon 50$
	Top	Bottom				
Stiff Clay w/o Free Water (Reese)	0.46	1.68	19.32	57.46	-	0.02
Stiff Clay w/o Free Water (Reese)	1.68	2.59	19.38	71.82	-	0.02
Mod. Stiff Clay w/o Free Water	2.59	4.42	19.64	105.34	0	0.01
Mod. Stiff Clay w/o Free Water	4.42	6.55	19.32	153.22	0	0.005

In many of the previous studies, failure has been set as a predefined deflection limit resulting from applied load either based on the dimension of the pile or on the estimated design load of the super structure. RPP, predominantly being a product of plastic and having much less dimension than a regular concrete or steel pile, the aforementioned failure criteria does not suit as a preferrable technic to define the failure under design standards. Considering the uniqueness of the study, p-y

curve was constructed for estimating the failure of the field lateral load tests. P-y curve which is a vastly used finite difference method in understanding the nonlinear behavior of pile soil interaction was constructed with the help of LPILE after the calibration efforts based on the load test results and subsoil conditions in the field.
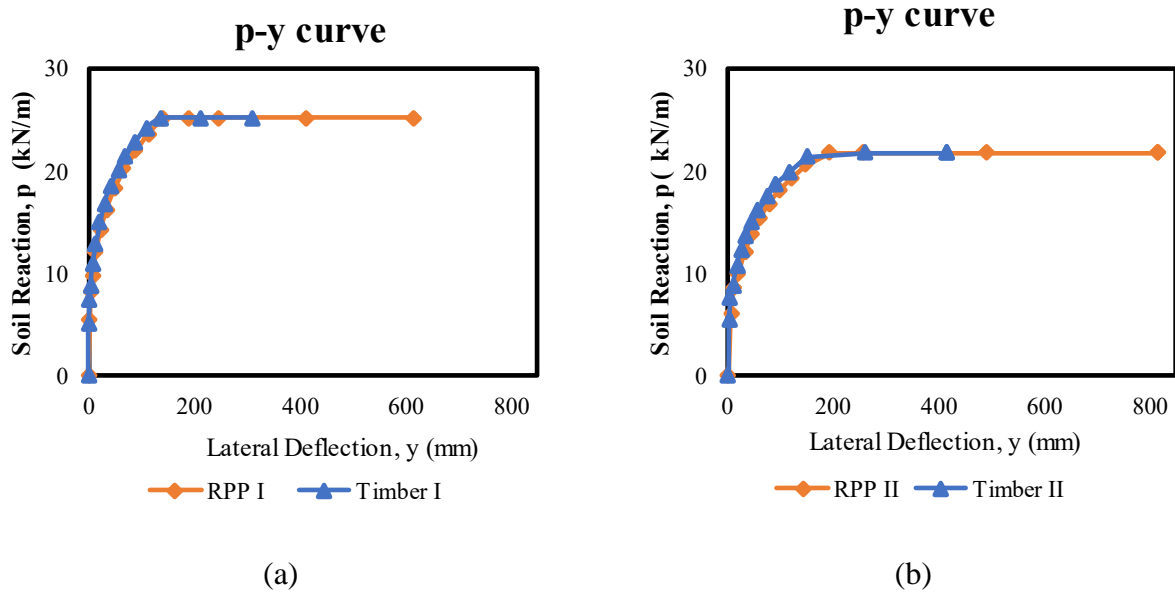
Figure 6-9 p-y Curves (a) RPP I and Timber I; (b) RPP II and Timber II

As shown by Duncan et al. (1994) and Christensen (2006), the lateral behavior of piles is significantly dependent on the properties of soil within a zone varying from ground surface down to 8D to 10D below surface, where D is the dimension of the pile. Therefore, p-y curves for soil to depth, x = 8D were obtained and studied in this research. Figure 6-9 shows the p-y curves for soil at depth, x = 8D at the maximum applied load in the field and corresponding ultimate soil resistance, p_{ult}, which is defined as the straight portion of the curve at end of the parabolic section. Similar extension to embedment ratio of timber piles and RPP showed nearly identical pult, indicating soil fails almost at the same load. As a result, soil response of the piles is more critical than top deflection of the piles. The ultimate load capacity improved by 15% as the extension to embedment ratio increased.

The piles lateral load carrying capacity increased while their displacement reduced as extension to embedment ratio decreased. Considering soil response of the timber piles and RPPs with the same extension to embedment depth had similar lateral load capacity and lateral deflection at top. RPP

I and Timber I had failure occurring at 16 kN showing similar deflection of 109 mm and 113 mm. RPP II and Timber II withheld 149 mm and 151 mm of lateral deflection until failing at 20 kN. Although only considering the load versus deflection curve gave a false impression about the load and deflection behavior of the piles, it became clear that they both displayed identical results while taking into account the actual failure scenario with the aid of the p-y curve. As a result, the large difference in the top deflection of RPPs and timber piles in Figure 6-8 actually depicts the after-failure condition of the piles. The failure occurs at the elastic range of the piles and after the failure of subsoil in the pile soil interface, RPP behaves like a plastic material resulting in large deformation whereas timber having stiffer property shows less deformation.

6.4.3   Pile Characteristics along the Piles

The pile behavior characteristics, moment and displacement along the length of the test piles at the ultimate load corresponding to p_{ult}, was determined with the help of LPILE 2022. The load corresponding to the p_{ult} was selected for analysis as this load corresponds to the ultimate soil resistance. Moment vs depth curve depicts that maximum moment at failure occurs at 0.5 m to 0.8 m from the ground surface. The maximum moment increases with application of load and the location of the maximum bending moment moved downward when extension to embedment ratio increased. Displacement increased as the anchorage length of the plies reduced. It was apparent from the displacement patterns observed in the RPP and timber piles that they were functioning as short piles, exhibiting negative displacement in the opposite direction of the applied load. Displacement and moment along the length of RPP are shown in Figure 6-10. Moment tends to decrease as the depth increases after the curve reaches its maximum value. Maximum moment was found at 5D (RPP I and Timber I) and 8D (RPP II and Timber II) depth from ground surface.

It is safe to remark based on the moment and displacement results along the length of the pile that the anchorage length or extension to embedment ratio is the governing factor in lateral load behavior of RPP. At the same embedment depth top deflection was similar for both RPP and timber piles which agrees with outcome of the previous section.
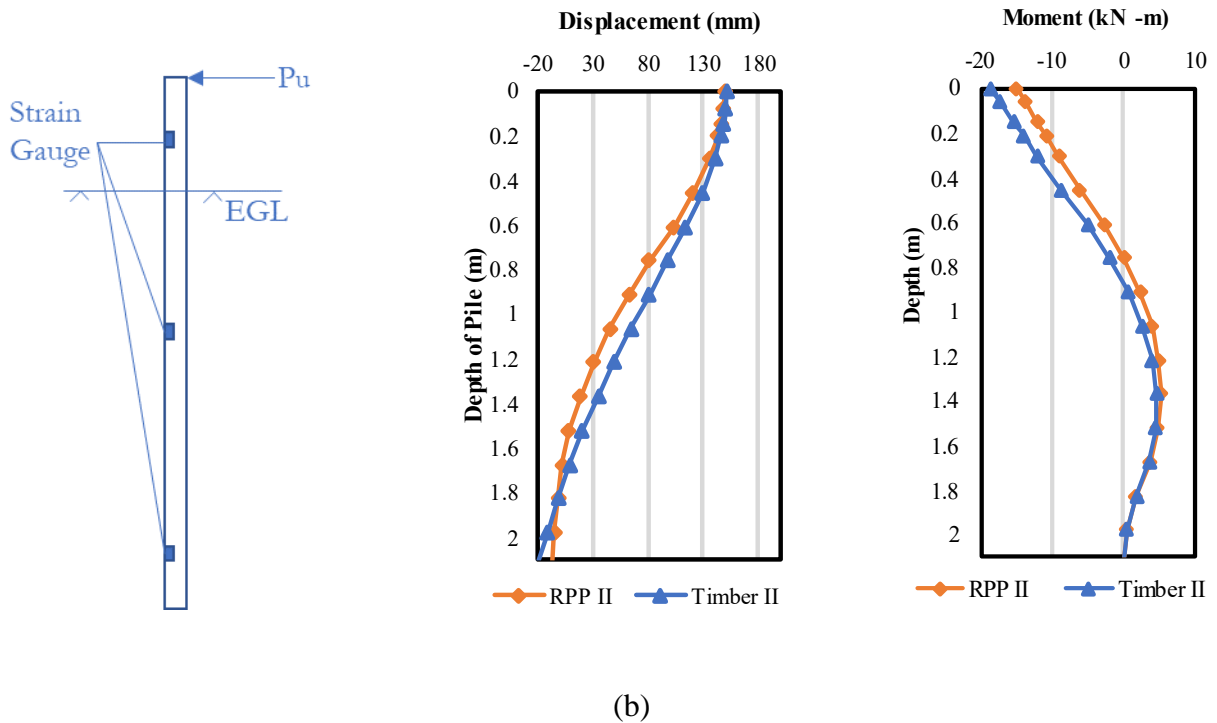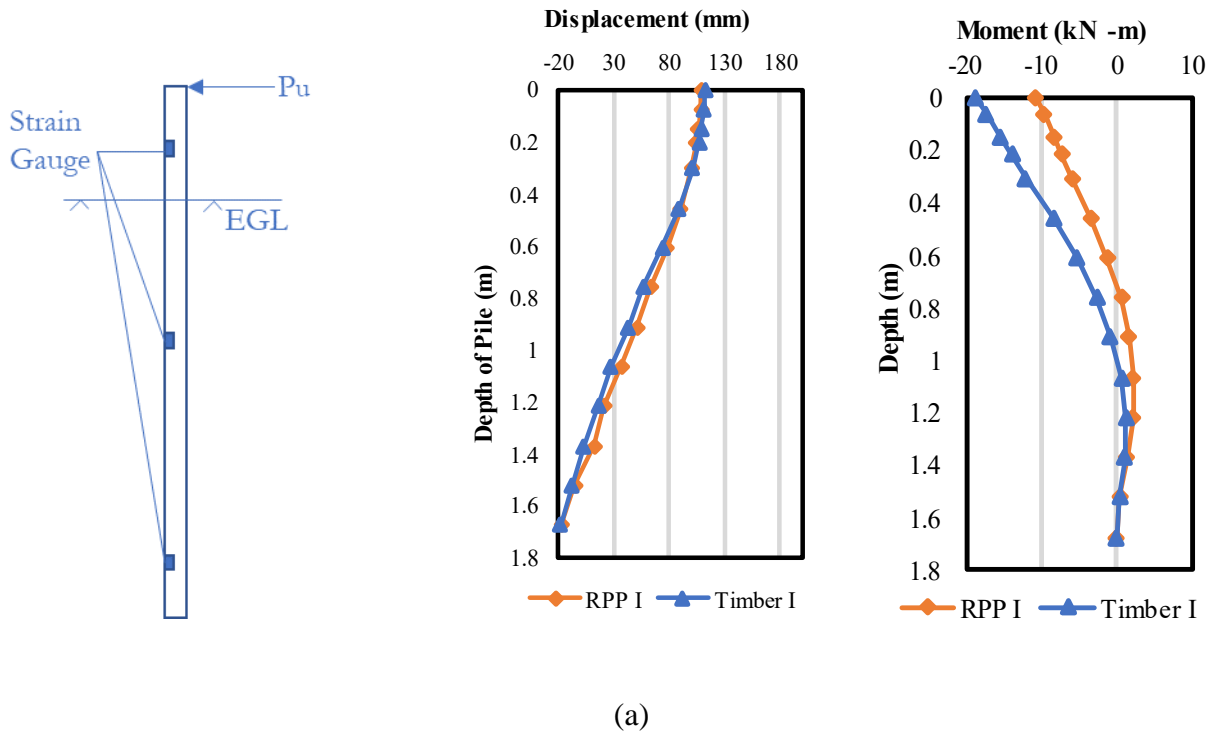
Figure 6-10 Displacement and Moment along the Piles at Failure of (a) RPP I and Timber I; (b) RPP II and Timber II

Negative moments were observed to develop in the overhanging portion above the ground surface of the piles and was observed to be increasing with greater anchorage length. When the section bending moment capacity is mobilized, a long or flexible pile failure mode is seen. In this situation, pile head deflection may be greater than soil surface displacement. Negative bending moments are produced by the negative soil reaction, which occurs when pile deflection exceeds soil displacement, stabilizing piles between the soil. For the same load, negative moment development at the top was observed to be increasing as the extended length of the RPP increased. However, with the reduction of embedment depth, the RPPs failed at smaller moment development. Timber failed at 12% to 41% less positive moments while withstanding at 20% to 43% more negative moments. As the bending stiffness of the pile is reliant on EI, timber piles were more effective in resisting negative moments developed at the top. Timber piles demonstrated more bending moment capacity than RPPs.

6.5   Effect of Varying Extension to Embedment Ratio and Size

Since the extension to embedment length ratio governed the pile lateral load behavior, a comparative study was conducted to investigate the effect of varying pile parameters on the load settlement behavior of RPP and timber piles. This study conducted load tests only on 10 cm x 10 cm RPP and timber piles. In some cases, lateral displacement is taken to be critical design criteria. Piles with greater size are expected to restrict lateral displacement to a greater extent. Therefore, a comprehensive parametric study was undertaken with the calibrated model. Figure 6-11 shows the variation of lateral load – settlement behavior of RPP and timber piles with varying extension length to embedment ration and size.
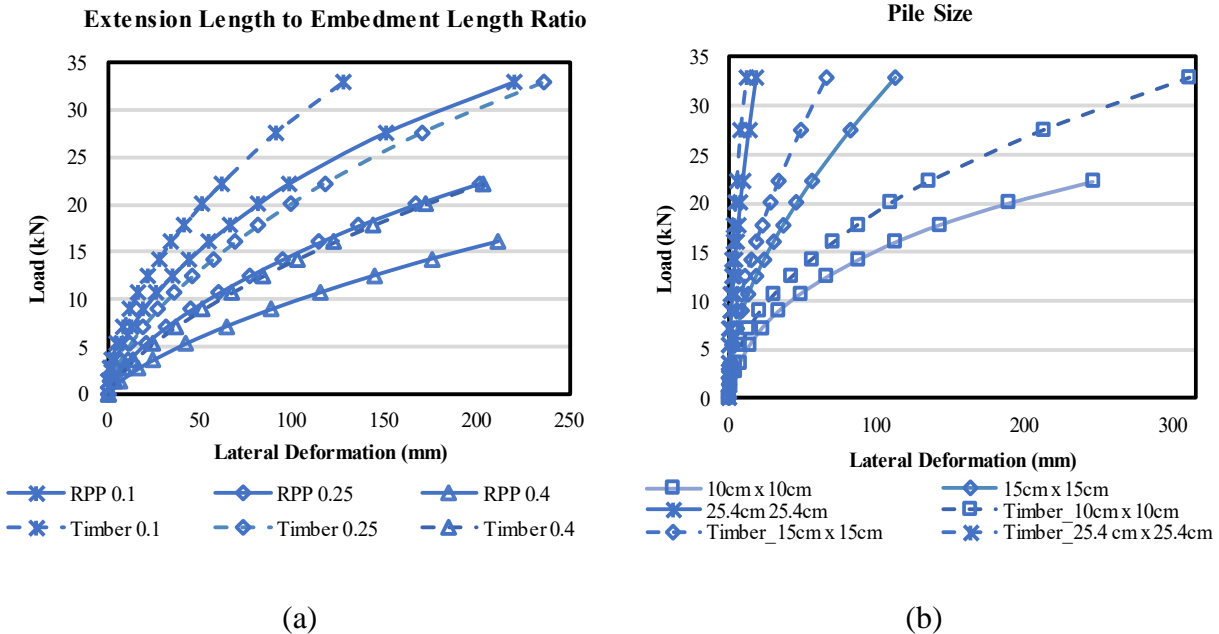
Figure 6-11 Effect of (a) Extension Length to Embedment Depth; and (b) Pile Size

Figure 6-11 (a) illustrates the variations in lateral displacement with extension length to embedment depth ratio for three different ratios of RPP and timber piles. The pile was maintained at a set dimension of 10 cm × 10 cm. The chart shows the influence of the extended portion to anchorage length, showing that as the ratio rose, lateral displacement increased, and load capacity dramatically fell. Timber with a higher E value is more resistant to deflection. RPP deflects 73% more than the timber piles for the same load after passing the elastic portion of the curves.

Figure 6-11 (b) shows the variations of lateral movement for different sizes of the piles. The extension length to embedment depth ratio was kept constant at 0.38 for the RPP and timber piles. The load-deformation curves were found to have steeper slopes for greater sizes of piles, suggesting higher lateral load capacity and lesser deformation. RPP of same size deflected more than the timber piles.

The explanation above is only applicable when the section is subject to external horizontal forces without external shear or axial loads. As with fixed-head piles, where the largest shear and the maximum moment often occur at the top of the pile, the presence of significant shear and moment in the section may impair the pile's capacity for bending moments as well as its ductility. Additionally, the ductility of the pile as well as its permissible bending moment capacity will be impacted by the presence of external axial loads. Therefore, in order to effectively apply the test

226

results presented here, it is crucial to carefully consider a number of factors, such as (1) the type of subsurface conditions, (2) the intensity and type of the external loads (both axial and shear), and (3) the type of loading (cyclic versus static).

6.6 Conclusions

This manuscript presented four vertical pile load tests and four lateral pile load tests on RPPs and timber piles. Efforts were made to experimentally compare the load capacity and deformation behavior of RPPs as an alternative to timber piles based on the field test results. The axial compressive load tests results were analyzed in six methods to evaluate the ultimate load capacity of the piles. Field lateral-load tests were also performed to inspect the lateral capacity of the piles. The computer software LPILE was used to model the lateral-load behavior of the piles subjected to lateral loading after establishing good agreement with the measured behavior. A unique approach was employed to assess the loads at failure from lateral load tests using results from LPILE and the load at which the ultimate resistance of the soil is mobilized (i.e., p_{ult}) from the back analyses of p-y curves. This model was also used towards investigating the load deformation behavior with varying extension to embedment length ratio and pile size of these piles. The summary of the findings of the study are:

1. Field testing revealed that RPP and timber piles had similar axial compressive load carrying capacities and settlement upon failure, with very small differences of 7% to 8% for axial load capacity and 5% to 9% for settlement.

2. Timber, being a stiffer material in comparison to RPP, showed more resistance to settlement in the initial elastic portion of the load vs settlement curve. RPP reached the plastic zone immediately after the failure, displaying considerable settlement, whereas the settlement was still fairly small for timber piles even after failure with the application of additional load. The permanent settlement of RPP was 29% to 33% more than timber after the withdrawal of load.

3. The average ultimate vertical load capacity of RPP and timber found in six empirical methods differed by 13% to 22%. This percentage differed from the field tests because of involvement of the plastic portion of the load settlement curve of RPP in most of the analysis method.

4. For RPP and timber, a 30% increase in pile length led to an increase in ultimate vertical load capacity of 10% to 41% and a decrease in settlement of 66% to 70%, respectively.

227

5. As the extension to embedment ratio dropped, there was a considerable decrease in lateral displacement. When the extension to embedment ratio is reduced from 0.40 to 0.38, with the same load application, the displacement is reduced by 25%.

6. Considering soil response scenario with the aid of the p-y curve it was observed that with the same extension to embedment depth ration, soil failure occurs within the elastic limit at the same load for both the piles with a difference of 1% to 4% in lateral deflection.

7. At failure, the difference between moment capacity of RPP and timber was 12% to 41% for positive moment and 20% to 43% for negative moment.

8. As the extended portion to anchorage length ratio rises, lateral displacement increased, and load capacity dramatically fell.

9. It was discovered that the load-deformation curves had steeper slopes for larger pile sizes, indicating more lateral load capacity and less deformation. Similar-sized RPP deflected more than timber piles after passing the elastic zone.

When the failure occurs within the elastic limit of the piles as a result of application of lateral loading, the load capacity and deformation behavior of RPP and timber are relatively similar. As in the majority of comparable situations, soil failure takes place within the elastic limit of pile failure. When compared to timber piles in situations like this, RPP could be a sustainable alternative to timber piles considering the added environmental benefits.

The study demonstrates that RPPs present a viable and sustainable alternative for geotechnical projects, showing comparable load-carrying capacities when appropriately designed and manufactured. The findings of this study contribute to the ongoing efforts to develop environmentally friendly solutions in construction and support the transition towards more sustainable practices in the field of geotechnical engineering.

CHAPTER 7

DEVELOPMENT OF DESIGN CHART

7.1   Introduction

The current study presented a design methodology for implementing RPPs in improving vertical and lateral capacity of foundation for different site and loading conditions. The performance of RPPs having different sizes, spacing, and embedment under applied vertical and lateral load for different soil conditions were analyzed and a simple easy-to-use design chart was developed. The charts can provide certain combinations of RPP sizes and spacings for given load conditions, which can be evaluated based on the design criteria to estimate the final design parameters. The details of the design approach are presented below.

The objective of the current design approach was to develop design charts to evaluate the load capacity of RPP based on vertical and horizontal displacement. A series of loads were applied over the RPP, and the corresponding vertical and horizontal displacement were determined for each case. The current study considered a wide range of soil strength parameters, fluctuation of ground water table, slenderness ratio width to spacing ratio as well as extension length to embedment ratio of RPP, as presented in the following sections.

7.2   Vertical Load Response

The deformation analysis was performed using PLAXIS 3D. The FEM analysis was performed using the model as presented in Chapter 4. It should be noted that only one layer of soil was considered over the whole depth in the model while developing the design chart. The deformation analysis was conducted by applying uniform load on the RPP and vertical deformation was determined. Based on the applied load, corresponding vertical deformation is summarized for a given soil strength and ground water condition (for example cohesion c = 100 psf and friction angle ϕ =10˚, ground water table at 20 ft from ground surface, detail parameters for FEM analysis are presented in Table 7-1 and RPPs are typically utilized in groups in practice. When building a foundation system, understanding the load capacity and corresponding settlement of a group of RPPs is crucial. Design charts for group RPPs are required when employing a group of RPPs to strengthen foundation soil or when manually estimating the design of a group RPP. To develop the design charts for group RPPs, a wide range of soil strength criteria and different depths of the ground water table were chosen. RPP size and spacing can be decided from the design charts by

determining the width to spacing ratio that meets the design criteria. Engineering judgment-based interpretation or the prediction model discussed in the following section can be used if the site demand a different soil condition. A total of 144 scenarios were considered for the development of the design charts as presented in Table 7-2 and Figure 7-2.

Table 7-2), with varied slenderness ratio and width to spacing ratio.

7.2.1 Single RPP

When using single RPPs to reinforce foundation soil or when manually calculating the design of a group RPP, design charts for single RPPs are necessary. A wide variety of soil strength parameters and various depths of the ground water table were selected for Single RPPs for developing the design chart. RPP size and length can be decided from the design charts by determining the slenderness ratio that meets the design criteria. If the site requirements call for a different soil condition, engineering judgment-based interpretation or the prediction model covered in the following section can be applied.

For the purpose of creating design charts, Table 7-1 displays the parameters utilized for analyzing the settlement with corresponding vertical load application. The flow chart for the development of design chart is presented in Figure 7-1. 240 scenarios in total were considered for the development of the design chart.

Table 7-1 Consideration for Design Chart Development of Vertical Load Capacity of Single RPP

Cohesion (psf)	Friction Angle φ	Water Table below Ground (ft)	Slenderness Ratio (L/D)	Total Model Run
100	10 20 30	0 10 15 20	30 20 12 6	48
200	10 20 30	0 10 15 20	30 20 12 6	48
300	10 20 30	0 10 15 20	30 20 12 6	48
500	10 20	0 10	30 20	48

Cohesion (psf)	Friction Angle φ	Water Table below Ground (ft)	Slenderness Ratio (L/D)	Total Model Run
	30	15	12	
		20	6	
1000	0 10 20	0 10 15 20	30 20 12 6	48

Figure 7-1 Flow Chart for development of design charts for Single RPP

7.2.2 Group RPP

RPPs are typically utilized in groups in practice. When building a foundation system, understanding the load capacity and corresponding settlement of a group of RPPs is crucial. Design charts for group RPPs are required when employing a group of RPPs to strengthen foundation soil or when manually estimating the design of a group RPP. To develop the design charts for group RPPs, a wide range of soil strength criteria and different depths of the ground water table were chosen. RPP size and spacing can be decided from the design charts by determining the width to spacing ratio that meets the design criteria. Engineering judgment-based interpretation or the prediction model discussed in the following section can be used if the site demand a different soil condition. A total of 144 scenarios were considered for the development of the design charts as presented in Table 7-2 and Figure 7-2.

Table 7-2 Consideration for Design Chart Development of Vertical Load Capacity of Group RPP

Cohesion (psf)	Friction Angle φ	Water Table below Ground (ft)	Width to Spacing Ratio	Total Model Run
100	10 20 30	0 10 15 20	0.1 0.2 0.3 0.4	48
500	10 20 30	0 10 15 20	0.1 0.2 0.3 0.4	48
1000	0 10 20	0 10 15 20	0.1 0.2 0.3 0.4	48

Figure 7-2 Flow Chart for development of design charts for Group RPP

7.3 Lateral Load Response

The deformation analysis was performed using LPILE 2022. The numerical analysis was performed using the model as presented in Chapter 5. It should be noted that only one layer of soil was considered throughout the depth in the model while developing the design chart. The deformation analysis was conducted by applying horizontal load on the RPP and resulting deformation was determined. Based on the applied load, corresponding horizontal deformation is summarized for a given soil strength and ground water condition (for example cohesion c = 200 psf and friction angle ϕ =10˚, ground water table at 20 ft from ground surface, detail parameters for numerical analysis are presented in Table 7-3), with varied slenderness ratio, width to spacing ratio and extension length to embedment ratio as presented in Figure 7-3. RPP size and embedment

233

length can be decided from the design charts by determining the extension length to embedment ratio and slenderness ratio that meets the design criteria.

For the creation of the design chart, a total of 156 scenarios were taken into consideration as presented in Table 7-3 and Figure 7-3.

Table 7-3 Consideration for Design Chart Development of Lateral Load Capacity of RPP

Cohesion (psf)	Friction Angle φ	Water Table below Ground (ft)	Extension Length to Embedment Ratio	Slenderness Ratio (L/D)	Total Model Run
0	20 30 35	0	0.11 0.25 0.4	30 20 12 6	36
100	0	0 20	0.11 0.25 0.4	30 20 12 6	24
200	0	0 20	0.11 0.25 0.4	30 20 12 6	24
300	0	0 20	0.11 0.25 0.4	30 20 12 6	24
500	0	0 20	0.11 0.25 0.4	30 20 12 6	24
1000	0	0 20	0.11 0.25 0.4	30 20 12 6	24

Figure 7-3 Flow Chart for development of design charts for Lateral Load capacity of RPP

7.4   Finalizing Design Chart

Based on the considerations made for the study, a series of design charts were developed for vertical and lateral loading condition. The appendix, Appendix C, contains the design charts.

7.5 Limitation of the Design Method

The present study introduced a design chart that accounts for the interaction between RPP and the foundation soil when subjected to applied loading. However, it's worth mentioning that these design charts tend to underestimate the resistance of RPP when it is used in a group installation. It's important to highlight that our current research focused on assessing the capacity of both a single RPP and a group of RPPs, consisting of four individual RPPs. Nevertheless, in practical scenarios, RPPs are typically installed in groups, which results in higher resistance and, consequently, a greater load capacity. Therefore, it is advisable to consider the possibility of conducting future research that incorporates the load resistance resulting from more RPPs in a group in different arrangements into the design methodology.

CHAPTER 8

DEVELOPMENT OF PREDICTION MODEL

8.1 Introduction

To develop the prediction model, the results from field tests and parametric studies were used. The results were used in statistical analysis software MATLAB to develop a model that allows to determine the load capacity of RPPs based on the soil strength parameters, RPP size, length and spacing, and extension length above and below ground for settlement or deflection to reach a certain level.

8.2 Regression Learner App

Regression models, such as linear regression models, regression trees, Gaussian process regression models, support vector machines, kernel approximations, ensembles of regression trees, and neural network regression models, can all be trained using the MATLAB module known as Regression Learner. It can be used to analyze data, choose features, define validation schemes, and assess outcomes in addition to training models. The model can be generated as MATLAB code to learn about programmatic regression or exported to the workspace to use with new data.

Two steps are involved in training a model in Regression Learner:

Validated Model: Train a model using a validation strategy, or validated model. By default, the program uses cross-validation to safeguard against overfitting. Holdout validation is an additional option. The app displays the validated model.

Full Model: Train a model using all available data, except test data. Along with the approved model, the app also trains this model. The whole data model, however, is not accessible in the app. Regression Learner exports the entire model if a regression model is chosen to be exported to the workspace.

The app shows the model's validated results. The findings of the validated model are reflected in diagnostic metrics, such as model accuracy, and graphs, such as a response plot or residuals plot. One or more regression models can be automatically trained, and the optimal model for a given regression problem can be selected by comparing validation results. The app shows the model's validated results. The findings of the validated model are reflected in diagnostic metrics, such as model accuracy, and graphs, such as a response plot or residuals plot. One or more regression

models can be automatically trained, and the optimal model for a given regression problem can be selected by comparing validation results.

8.3   Training Data

8.3.1   Group RPPs Subjected to Vertical Load

The input data for this MATLAB regression learner session included 4717 observations and five predictor variables: the undrained cohesive strength (c), internal friction angle (φ), water table (WT), width to clear spacing ratio (WS), and applied vertical load (VL). The prediction model's objective is to predict the settlement using these 5 predictors.

Five fold cross-validation was utilized during the training procedure to evaluate the model's performance. The dataset is randomly split into five subsets (or "folds") for 5-fold cross-validation. Five times the model will be trained, using four of the folds for training and one for validation each time. This makes it easier to make assured that the model's performance is reliable and unaffected by the particular data split.

The predictors (Undrained cohesive strength (c), internal friction angle (φ), water table (WT), width to spacing ratio (WS) and applied vertical load (VL)) and the response variable (settlement) can be compared using the Regression Learner App in MATLAB. In order to determine the regression model for predicting settlement based on the provided predictors, the software will automatically handle data preparation, algorithm selection, and model evaluation. Various performance indicators derived from the 5-fold cross validation findings can be used to evaluate the model's correctness after the training procedure. 15% of the total dataset was taken into account when testing the data.

The following code was used to train the model.

```
function [trainedModel, validationRMSE] = trainRegressionModel(trainingData)
% [trainedModel, validationRMSE] = trainRegressionModel(trainingData)
% Returns a trained regression model and its RMSE. This code recreates the
% model trained in Regression Learner app. Use the generated code to
% automate training the same model with new data, or to learn how to
% programmatically train models.
%
%  Input:
%      trainingData: A table containing the same predictor and response
%       columns as those imported into the app.
%
%
%  Output:
%      trainedModel: A struct containing the trained regression model. The
```

```
%        struct contains various fields with information about the trained
%        model.
%
%      trainedModel.predictFcn: A function to make predictions on new data.
%
%      validationRMSE: A double representing the validation RMSE. In the
%        app, the Models pane displays the validation RMSE for each model.
%
% Use the code to train the model with new data. To retrain your model,
% call the function from the command line with your original data or new
% data as the input argument trainingData.
%
% For example, to retrain a regression model trained with the original data
% set T, enter:
%   [trainedModel, validationRMSE] = trainRegressionModel(T)
%
% To make predictions with the returned 'trainedModel' on new data T2, use
%   yfit = trainedModel.predictFcn(T2)
%
% T2 must be a table containing at least the same predictor columns as used
% during training. For details, enter:
%   trainedModel.HowToPredict

% Auto-generated by MATLAB on 12-Nov-2023 16:24:56


% Extract predictors and response
% This code processes the data into the right shape for training the
% model.
inputTable = trainingData;
predictorNames = {'c', 'phi', 'WaterTableft', 'WidthToSpaceRatio', 'VerticalLoad'};
predictors = inputTable(:, predictorNames);
response = inputTable.Settlementin;
isCategoricalPredictor = [false, false, false, false, false];

% Train a regression model
% This code specifies all the model options and trains the model.
regressionTree = fitrtree(...
    predictors, ...
    response, ...
    'MinLeafSize', 4, ...
    'Surrogate', 'off');

% Create the result struct with predict function
predictorExtractionFcn = @(t) t(:, predictorNames);
treePredictFcn = @(x) predict(regressionTree, x);
trainedModel.predictFcn = @(x) treePredictFcn(predictorExtractionFcn(x));

% Add additional fields to the result struct
trainedModel.RequiredVariables = {'VerticalLoad', 'WaterTableft',
'WidthToSpaceRatio', 'c', 'phi'};
trainedModel.RegressionTree = regressionTree;
trainedModel.About = 'This struct is a trained model exported from Regression Learner
R2023a.';
```

```
trainedModel.HowToPredict = sprintf('To make predictions on a new table, T, use: \n
yfit = c.predictFcn(T) \nreplacing ''c'' with the name of the variable that is this
struct, e.g. ''trainedModel''. \n \nThe table, T, must contain the variables returned
by: \n  c.RequiredVariables \nVariable formats (e.g. matrix/vector, datatype) must
match the original training data. \nAdditional variables are ignored. \n \nFor more
information, see <a href="matlab:helpview(fullfile(docroot, ''stats'',
''stats.map''), ''appregression_exportmodeltoworkspace'')">How to predict using an
exported model</a>.');

% Extract predictors and response
% This code processes the data into the right shape for training the
% model.
inputTable = trainingData;
predictorNames = {'c', 'phi', 'WaterTableft', 'WidthToSpaceRatio', 'VerticalLoad'};
predictors = inputTable(:, predictorNames);
response = inputTable.Settlementin;
isCategoricalPredictor = [false, false, false, false, false];

% Perform cross-validation
partitionedModel = crossval(trainedModel.RegressionTree, 'KFold', 5);

% Compute validation predictions
validationPredictions = kfoldPredict(partitionedModel);

% Compute validation RMSE
validationRMSE = sqrt(kfoldLoss(partitionedModel, 'LossFun', 'mse'));
```

The independent variables in a regression model should not be correlated with one another; instead, they should be independent of one another. Response plots have been examined to ensure that, and the following figures in Figure 8-1 illustrate the independence of the variables.

The results obtained from the training data are tabulated below:

Table 8-1 Training data results using different algorithms

Model Type	RMSE (Validation)	MSE (Validation)	RSquared (Validation)	MAE (Validation)
Tree	0.337	0.113	0.78	0.168
Linear Regression	0.59	0.348	0.33	0.456
Linear Regression	0.571	0.326	0.37	0.436
Linear Regression	0.597	0.357	0.31	0.441

Model Type	RMSE (Validation)	MSE (Validation)	RSquared (Validation)	MAE (Validation)
Stepwise Linear Regression	0.574	0.33	0.36	0.44
Fine Tree	0.337	0.113	0.78	0.16755
Medium Tree	0.342	0.117	0.77	0.195
Coarse Tree	0.389	0.151	0.71	0.238
Linear SVM	0.613	0.376	0.27	0.437
Quardratic SVM	0.559	0.312	0.4	0.378
Cubic SVM	0.669	0.447	0.13	0.425
Fine Gaussian SVM	0.335	0.112	0.78	0.181
Medium Gaussian SVM	0.424	0.18	0.65	0.2612
Course Gaussian SVM	0.589	0.347	0.33	0.411
Ensemble Boosted Trees	0.313	0.098	0.81	0.184
Ensemble Bagged Trees	0.305	0.093	0.82	0.159
Gaussian Process Regression Squared Exponential GPR	0.311	0.097	0.81	0.168

Model Type	RMSE (Validation)	MSE (Validation)	RSquared (Validation)	MAE (Validation)
Gaussian Process Regression Matern 5/2 GPR	0.309	0.096	0.81	0.162
Gaussian Process Regression Exponential GPR	0.324	0.105	0.8	0.171
Gaussian Process Regression Rational Quadratic GPR	0.31	0.096	0.81	0.159
Narrow Neural Network	0.386	0.149	0.71	0.262
Medium Neural Network	0.323	0.104	0.8	0.195
Wide Neural Network	0.327	0.107	0.79	0.163
Bilayered Neural Network	0.342	0.117	0.77	0.204
Trilayered Neural Network	0.333	0.111	0.79	0.188
SVM Kernel	0.539	0.291	0.44	0.359
Least Squares Regression Kernel	0.494	0.245	0.53	0.348

The table shows the outcomes of multiple machine learning models that were trained to forecast settlement using five predictors: undrained cohesive strength (c), internal friction angle (φ), water table (WT), width to spacing ratio (WS) and applied vertical load (VL). The table's columns include data on the model type, Mean Squared Error (MSE), Root Mean Squared Error (RMSE), R-squared (R^2) value, and Mean Absolute Error (MAE) for each row's corresponding model.

The model with the highest R-squared (R^2) value and the lowest MSE, RMSE, and MAE values among the models yields the best results. These measures show how well the model predicts settlement and how accurate it is. The most pertinent predictors from a broader pool of potential predictor variables are selected using the Stepwise linear regression technique, which was observed to be useful in multiple linear regression. In order to achieve strong predictive performance and prevent overfitting, the model must contain only meaningful predictors.

From the table, it was observed that the Bagged Trees algorithms showed the best result with the following metrics:

• MSE: 0.093

• RMSE: 0.305

• R2: 0.82

• MAE: 0.159

The model's predictions are quite close to the actual settlement values, as seen by the low values of MSE, RMSE, and MAE. The predictor factors may account for about 82% of the variability in the settlements, according to the R-squared value of 0.82, which is a reasonably excellent fit. The very low root mean square value supports the claim. In Figure 8-1 training data's predicted response and actual reaction are compared. Figure 8-1 and Figure 8-2, respectively, display the projected response in comparison to the actual response and the residual plot of the training data.

(a)

(b)

(c)

(d)

245
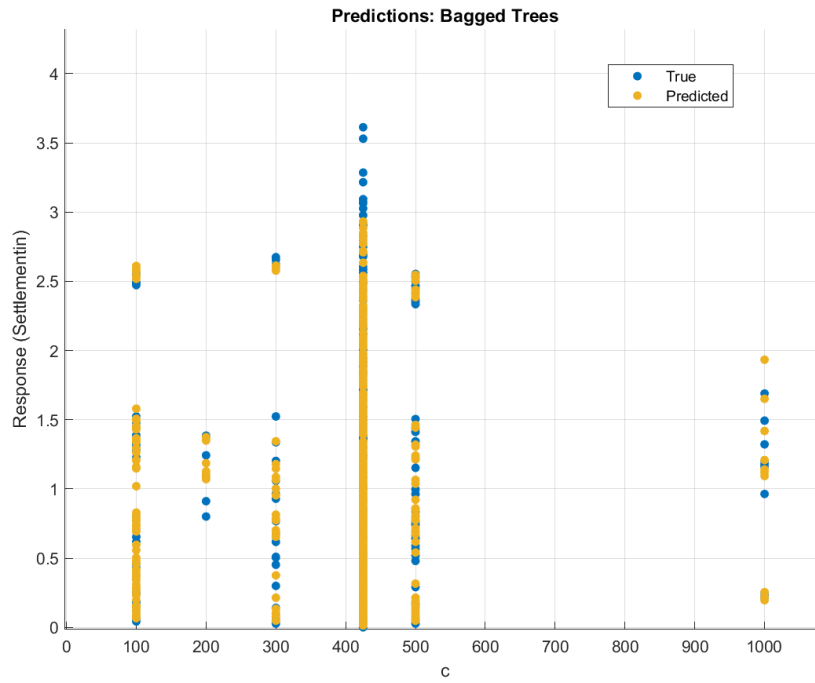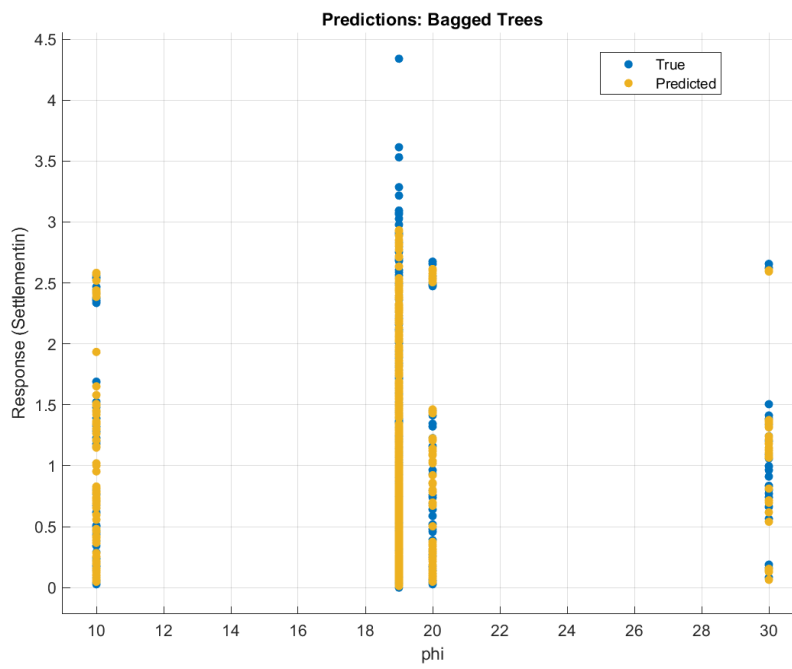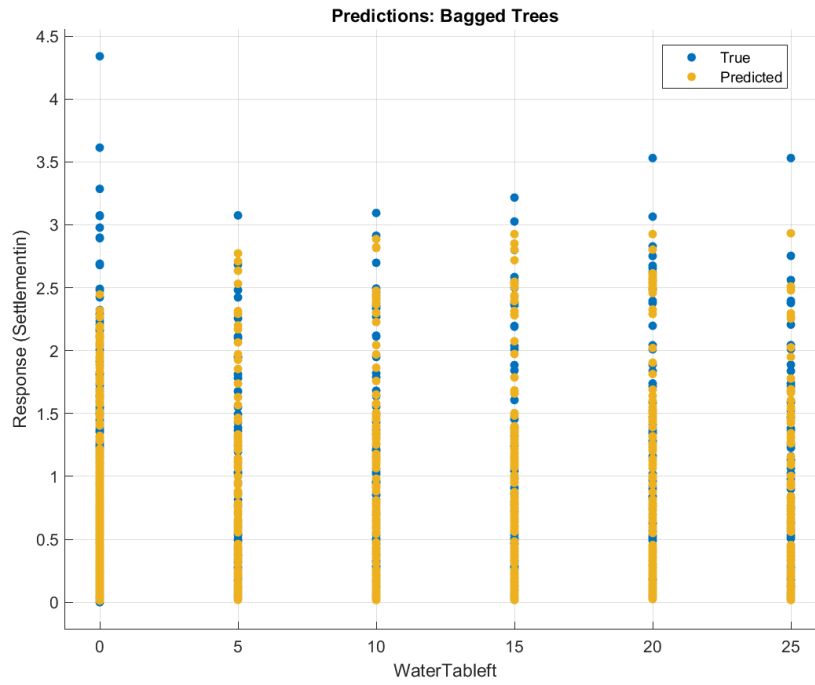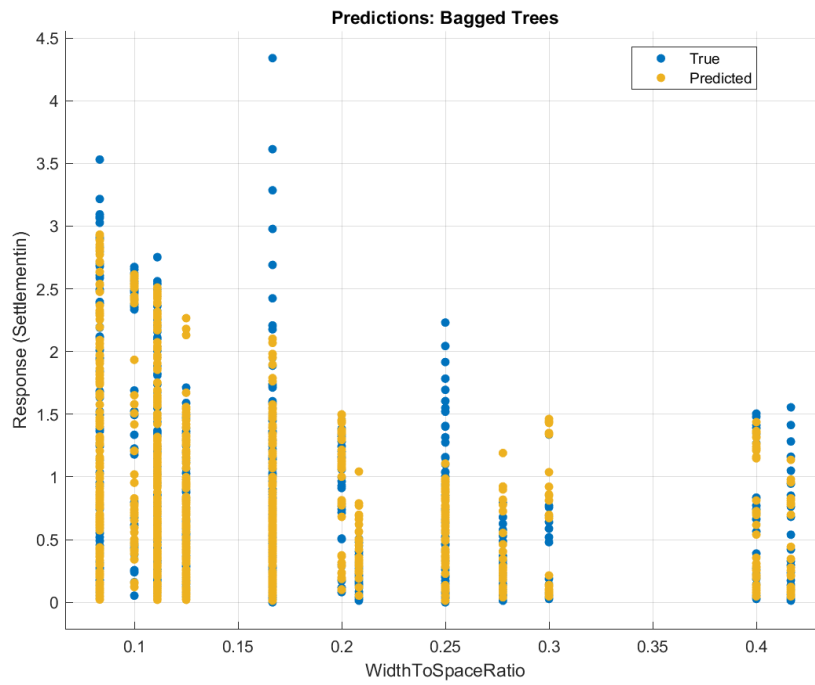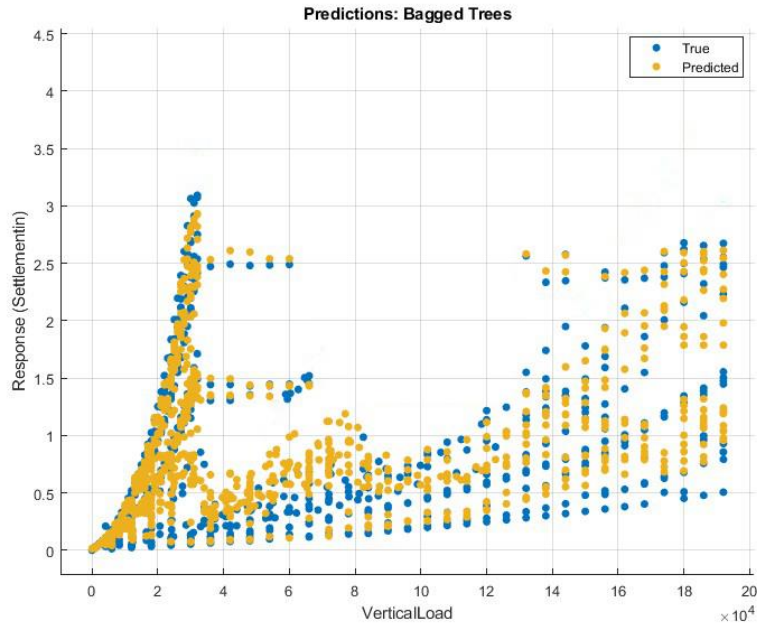
(e)

Figure 8-1 Predictor vs response plot (a) Settlement vs Undrained Shear Strength (b) Settlement vs Internal Friction Angle (c) Settlement vs Water Table (d) Settlement vs Width to Clear Spacing Ratio and (e) Settlement vs Vertical Load

(a)

246
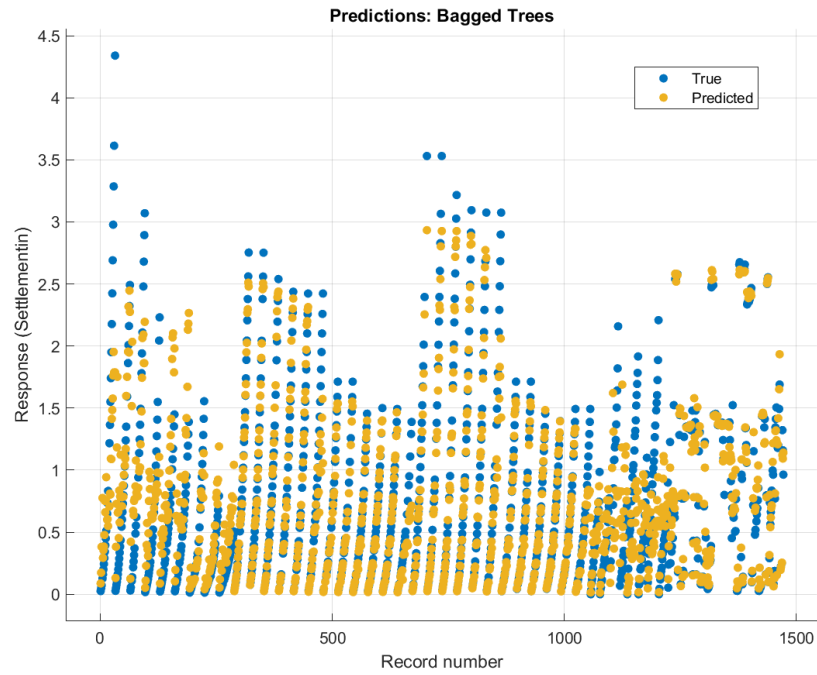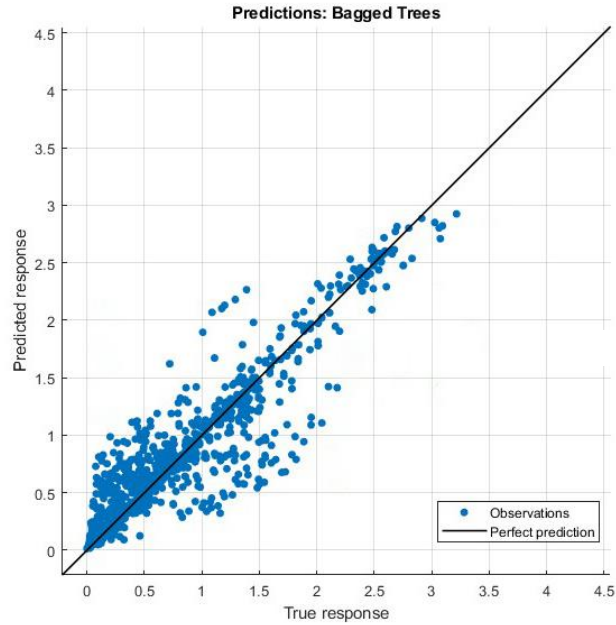
Figure 8-2 Predicted vs true response using Bagged Tree algorithm for training data

The following function can be used in MATLAB to make further predictions using the predictor variables, where T is the new matrix for the predictor variables:

yfit = trainedModel.predictFcn(T)

The remaining 15% of the dataset was utilized to test the model after the data had been used to train it. Figure 8-3 shows a plot of expected vs. actual reaction. For the test data, 0.86 and 0.028 were found to be the R-squared and RMSE values, respectively. It means that 86% of the data can be explained by the model created using the training set of data.
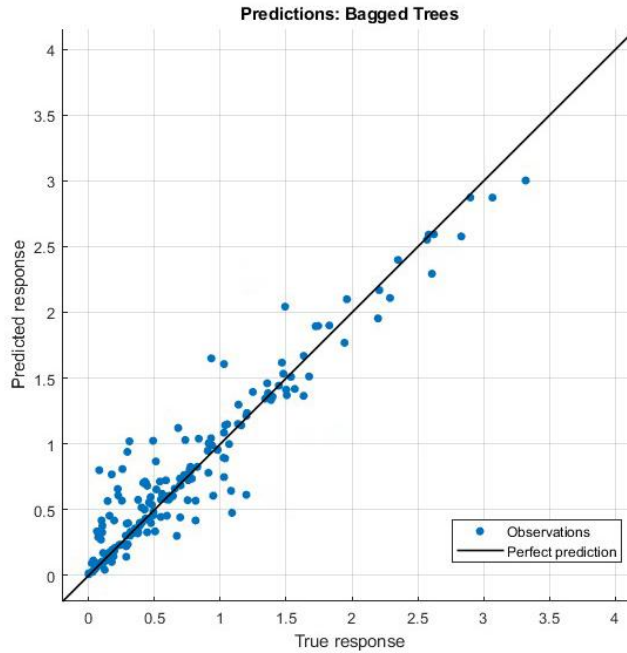
Figure 8-3 Predicted vs true response using Bagged Tree algorithm for test data

According to the results of the F-test, the predictor factors with the highest importance score were those related to applied vertical load and width to spacing ratio. That indicates that the change in these two parameters, as depicted in Figure 8-4, had greater influence on the settlement.
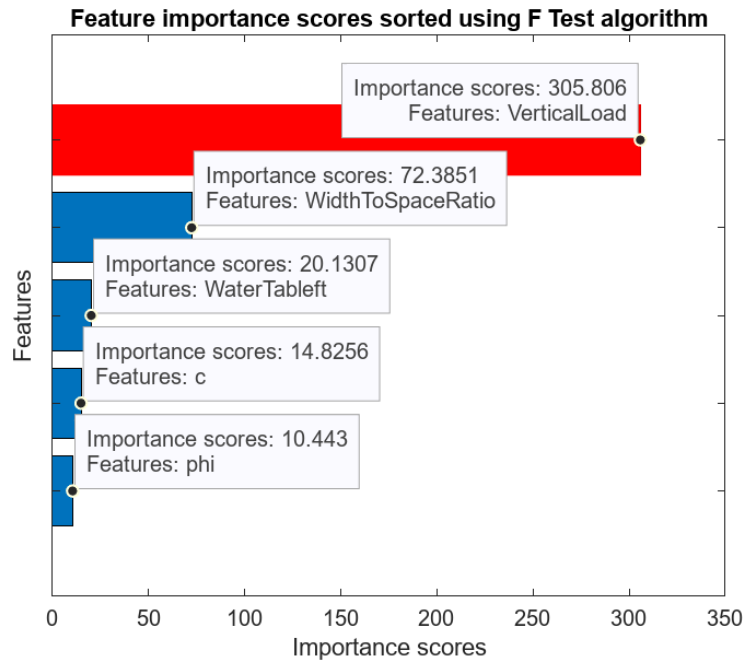
Figure 8-4 Importance scores from F-test

8.3.2 Single RPPs Subjected to Vertical Load

The input data for this MATLAB regression learner session included 10,961 observations and five predictor variables: the undrained cohesive strength (c), internal friction angle (φ), water table (WT), Slenderness ratio (SR), and applied vertical load (VL). The prediction model's objective is to predict the settlement using these 5 predictors.

The following code was used to train the model.

```
function [trainedModel, validationRMSE] = trainRegressionModel(trainingData)
% [trainedModel, validationRMSE] = trainRegressionModel(trainingData)
% Returns a trained regression model and its RMSE. This code recreates the
% model trained in Regression Learner app. Use the generated code to
% automate training the same model with new data, or to learn how to
% programmatically train models.
%
%  Input:
%      trainingData: A table containing the same predictor and response
%       columns as those imported into the app.
%
%
%  Output:
%      trainedModel: A struct containing the trained regression model. The
%       struct contains various fields with information about the trained
%       model.
%
%      trainedModel.predictFcn: A function to make predictions on new data.
%
%      validationRMSE: A double representing the validation RMSE. In the
%       app, the Models pane displays the validation RMSE for each model.
%
% Use the code to train the model with new data. To retrain your model,
% call the function from the command line with your original data or new
% data as the input argument trainingData.
%
% For example, to retrain a regression model trained with the original data
% set T, enter:
%   [trainedModel, validationRMSE] = trainRegressionModel(T)
%
% To make predictions with the returned 'trainedModel' on new data T2, use
%   yfit = trainedModel.predictFcn(T2)
%
% T2 must be a table containing at least the same predictor columns as used
% during training. For details, enter:
%   trainedModel.HowToPredict

% Auto-generated by MATLAB on 12-Nov-2023 16:28:27


% Extract predictors and response
% This code processes the data into the right shape for training the
% model.
inputTable = trainingData;
```

```matlab
predictorNames = {'c', 'phi', 'WaterTableft', 'SlendernessRatio', 'VerticalLoad'};
predictors = inputTable(:, predictorNames);
response = inputTable.Settlementft;
isCategoricalPredictor = [false, false, false, false, false];

% Train a regression model
% This code specifies all the model options and trains the model.
regressionTree = fitrtree(...
    predictors, ...
    response, ...
    'MinLeafSize', 4, ...
    'Surrogate', 'off');

% Create the result struct with predict function
predictorExtractionFcn = @(t) t(:, predictorNames);
treePredictFcn = @(x) predict(regressionTree, x);
trainedModel.predictFcn = @(x) treePredictFcn(predictorExtractionFcn(x));

% Add additional fields to the result struct
trainedModel.RequiredVariables = {'c', 'phi', 'WaterTableft', 'SlendernessRatio',
'VerticalLoad'};
trainedModel.RegressionTree = regressionTree;
trainedModel.About = 'This struct is a trained model exported from Regression Learner
R2023a.';
trainedModel.HowToPredict = sprintf('To make predictions on a new table, T, use: \n
yfit = c.predictFcn(T) \nreplacing ''c'' with the name of the variable that is this
struct, e.g. ''trainedModel''. \n \nThe table, T, must contain the variables returned
by: \n  c.RequiredVariables \nVariable formats (e.g. matrix/vector, datatype) must
match the original training data. \nAdditional variables are ignored. \n \nFor more
information, see <a href="matlab:helpview(fullfile(docroot, ''stats'',
''stats.map''), ''appregression_exportmodeltoworkspace'')">How to predict using an
exported model</a>.');

% Extract predictors and response
% This code processes the data into the right shape for training the
% model.
inputTable = trainingData;
predictorNames = {'c', 'phi', 'WaterTableft', 'SlendernessRatio', 'VerticalLoad'};
predictors = inputTable(:, predictorNames);
response = inputTable.Settlementft;
isCategoricalPredictor = [false, false, false, false, false];

% Perform cross-validation
partitionedModel = crossval(trainedModel.RegressionTree, 'KFold', 5);

% Compute validation predictions
validationPredictions = kfoldPredict(partitionedModel);

% Compute validation RMSE
validationRMSE = sqrt(kfoldLoss(partitionedModel, 'LossFun', 'mse'));
```

Five fold cross-validation was utilized during the training procedure to evaluate the model's performance. The predictors (the undrained cohesive strength (c), internal friction angle (φ), water table (WT), slenderness ratio (SR), and applied vertical load (VL)) and the response variable (settlement) was compared using the Regression Learner App in MATLAB. Various performance indicators derived from the 5-fold cross validation findings were used to evaluate the model's correctness after the training procedure. 15% of the total dataset was considered when testing the data. The same code was used to train the model, only substituting the predictor names and variables. Response plots have been examined to ensure that, and the following figures Figure 8-5 in Figure 8-1 illustrate the independence of the variables.

The results obtained from the training data are tabulated below:

Table 8-2 Training data results using different algorithms

Model Type	RMSE (Validation)	MSE (Validation)	RSquared (Validation)	MAE (Validation)
Tree				
Linear Regression	0.0623	0.004	0.10	0.014
Linear Regression	0.060	0.004	0.16	0.013
Linear Regression	0.064	0.004	0.06	0.011
Stepwise Linear Regression	0.060	0.003	0.16	0.013
Fine Tree	0.056	0.003	0.27	0.004
Medium Tree	0.059	0.003	0.20	0.006
Coarse Tree	0.059	0.003	0.19	0.007
Linear SVM	0.063	0.004	0.07	0.011
Quardratic SVM	0.061	0.0044	0.13	0.007
Cubic SVM	0.058	0.003	0.21	0.005
Fine Gaussian SVM	0.061	0.004	0.14	0.004

Model Type	RMSE (Validation)	MSE (Validation)	RSquared (Validation)	MAE (Validation)
Medium Gaussian SVM	0.060	0.0036	0.16	0.005
Course Gaussian SVM	0.062	0.004	0.10	0.008
Efficient Linear Least Squares	0.066	0.004	0.0	0.025
Efficient Linear SVM	0.064	0.004	0.40	0.016
Ensemble Boosted Trees	0.054	.003	0.61	0.007
Ensemble Bagged Trees	0.056	0.003	0.68	0.004
Gaussian Process Regression Squared Exponential GPR	0.051	0.003	0.70	0.006
Gaussian Process Regression Matern 5/2 GPR	0.052	0.003	0.73	0.004
Gaussian Process Regression Exponential GPR	0.060	0.004	0.071	0.003
Gaussian Process Regression Rational Quadratic GPR	0.052	0.003	0.78	0.006

Model Type	RMSE (Validation)	MSE (Validation)	RSquared (Validation)	MAE (Validation)
Narrow Neural Network	0.050	0.003	0.88	0.006
Medium Neural Network	0.051	0.003	0.78	0.009
Wide Neural Network	0.052	0.003	0.77	0.009
Bilayered Neural Network	0.061	0.004	0.75	0.007
Trilayered Neural Network	0.050	0.003	0.71	0.006
SVM Kernel	0.057	0.003	0.65	0.004
Least Squares Regression Kernel	0.057	0.003	0.65	0.009

The table shows the outcomes of multiple machine learning models that were trained to forecast settlement using five predictors: undrained cohesive strength (c), internal friction angle (φ), water table (WT), Slenderness ratio (L/D) and applied vertical load (VL). The model with the highest R-squared (R2) value and the lowest MSE, RMSE, and MAE values among the models yields the best results. These measures show how well the model predicts settlement and how accurate it is.

From the table, it was observed that the Narrow Neural Network algorithms showed the best result with the following metrics:

• MSE: 0.003

• RMSE: 0.050

• R2: 0.88

• MAE: 0.006

The model's predictions are quite close to the actual settlement values, as seen by the low values of MSE, RMSE, and MAE. The predictor factors may account for about 88% of the variability in the settlements, according to the R-squared value of 0.88, which is a reasonably excellent fit. The very low root mean square value supports the claim. In Figure 8-5 training data's predicted response and actual reaction are compared. Figure 8-5 and Figure 8-6, respectively, display the projected response in comparison to the actual response and the residual plot of the training data.
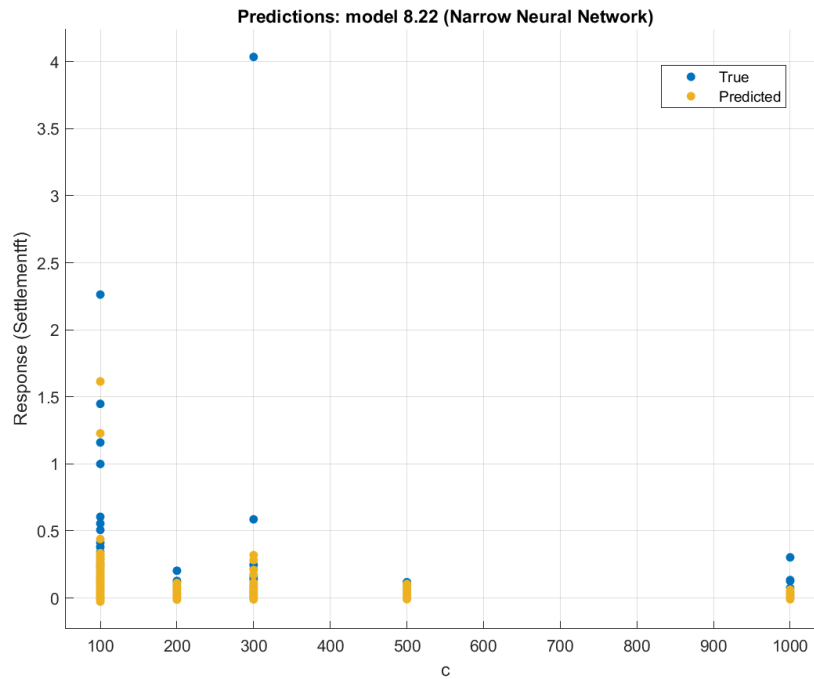
(a)
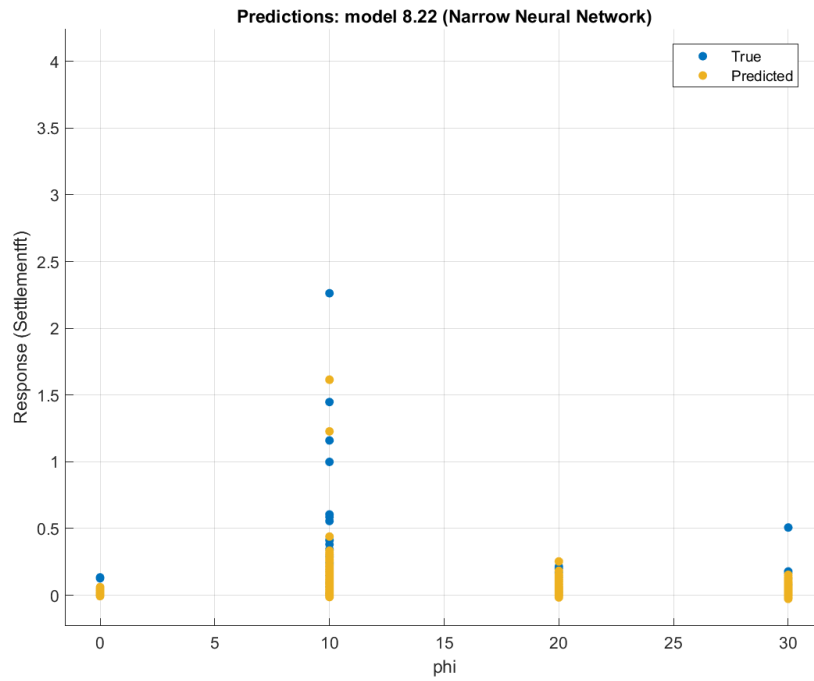
(b)
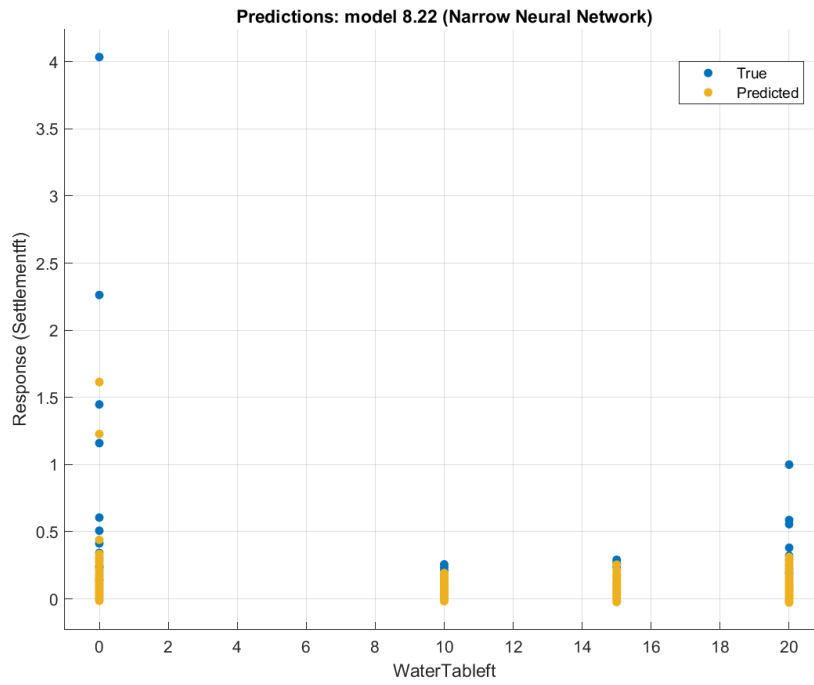
(c)
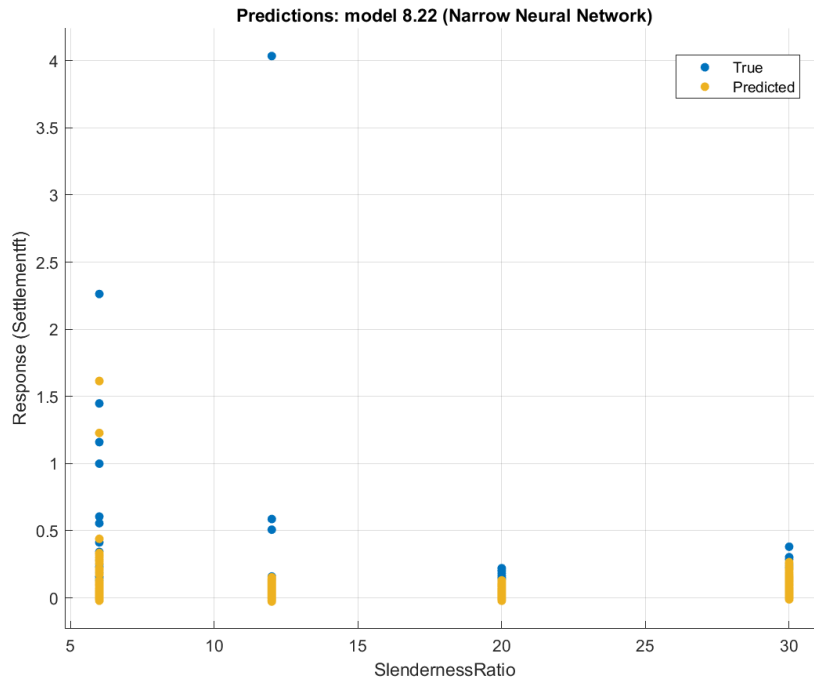
(d)
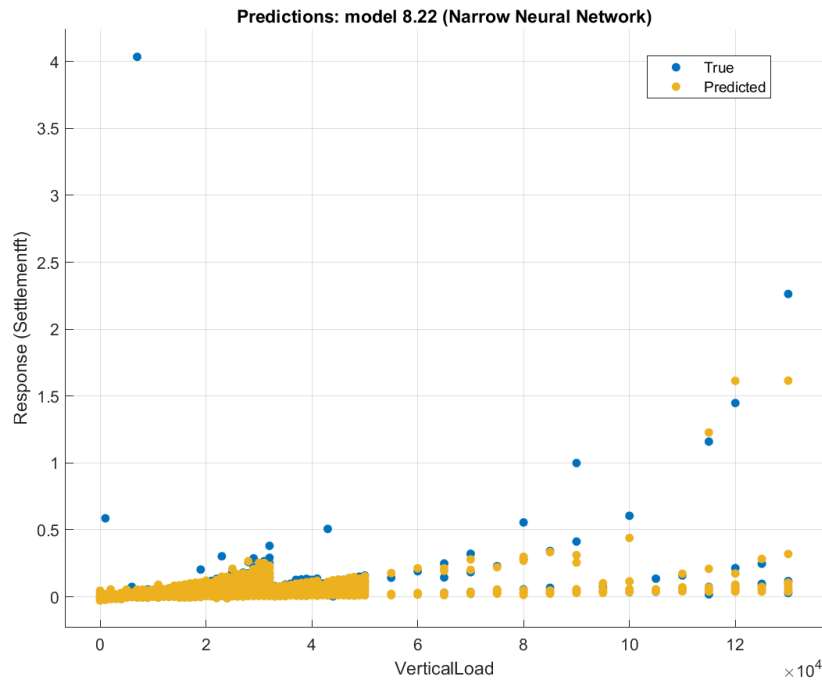
(e)

Figure 8-5 Predictor vs response plot (a) Settlement vs Undrained Shear Strength (b) Settlement vs Internal Friction Angle (c) Settlement vs Water Table (d) Settlement vs Slenderness Ratio and (e) Settlement vs Vertical Load
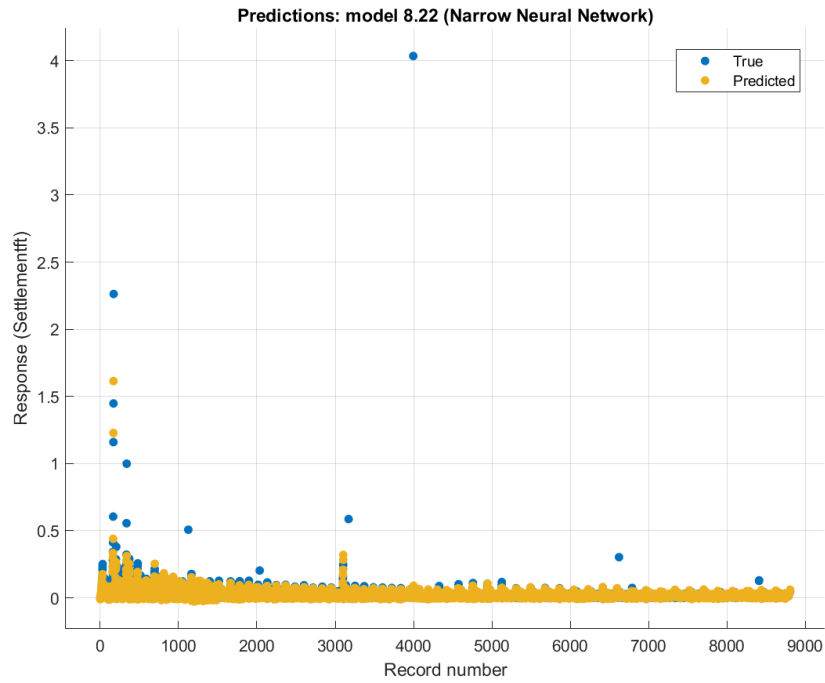
(a)
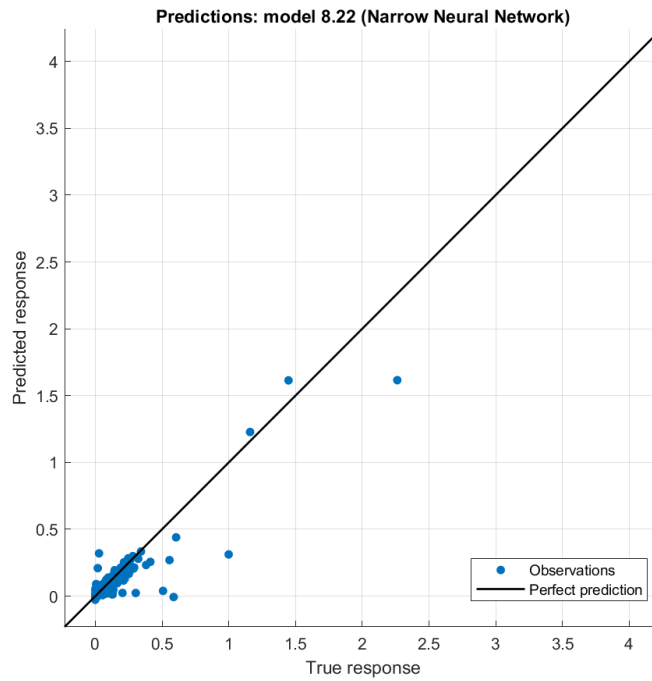
(b)

Figure 8-6 Predicted vs true response using Narrow Neural Network algorithm for training data

The following function can be used in MATLAB to make further predictions using the predictor variables, where T is the new matrix for the predictor variables:

yfit = trainedModel.predictFcn(T)

The remaining 15% of the dataset was utilized to test the model after the data had been used to train it. Figure 8-7 shows a plot of expected vs. actual reaction. For the test data, 0.95 and 0.016 were found to be the R-squared and RMSE values, respectively. It means that 95% of the data can be explained by the model created using the training set of data.

Predictions: Narrow Neural Network
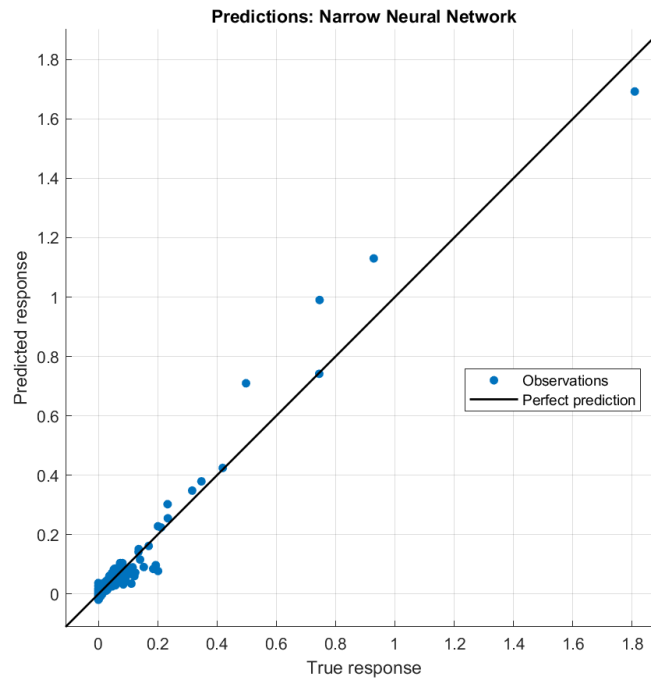
Figure 8-7 Predicted vs true response using Narrow Neural Network algorithm for test data

The F-test findings showed that the applied vertical load and undrained shear strength predictor factors had the greatest importance scores. This suggests that the settlement was more affected by the adjustment in these two factors, as seen in Figure 8-8.
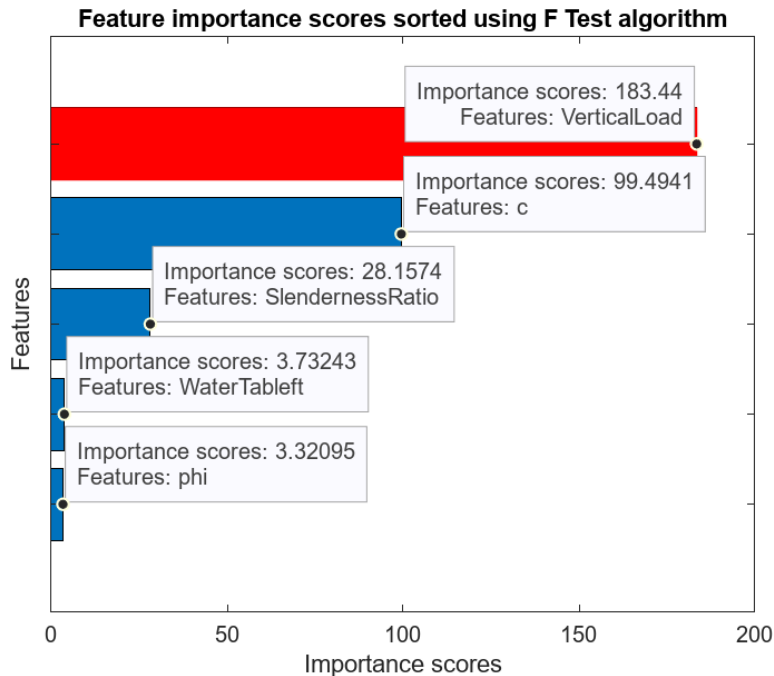
Figure 8-8 Importance scores from F-test

8.3.3 RPPs Subjected to Lateral Load

The data for this MATLAB regression learner session included 2143 observations and six predictor variables: the undrained cohesive strength (c), internal friction angle (φ), water table (WT), slenderness ratio (SR), extension length to embedment ratio (EE) and applied lateral load (LL). The prediction model's objective is to predict the deflection using these 6 predictors.

Five fold cross-validation was utilized during the training procedure to evaluate the model's performance. The predictors (the undrained cohesive strength (c), internal friction angle (φ), water table (WT), slenderness ratio (SR), extension length to embedment ratio (EE) and applied lateral load (LL)) and the response variable (deflection) was compared using the Regression Learner App in MATLAB. Various performance indicators derived from the 5-fold cross validation findings were used to evaluate the model's correctness after the training procedure. 15% of the total dataset was considered when testing the data. The function used to predict:

```
function [trainedModel, validationRMSE] = trainRegressionModel(trainingData)
% [trainedModel, validationRMSE] = trainRegressionModel(trainingData)
% Returns a trained regression model and its RMSE. This code recreates the
% model trained in Regression Learner app. Use the generated code to
% automate training the same model with new data, or to learn how to
% programmatically train models.
%
%  Input:
```

```
%       trainingData: A table containing the same predictor and response
%        columns as those imported into the app.
%
%
%  Output:
%       trainedModel: A struct containing the trained regression model. The
%        struct contains various fields with information about the trained
%        model.
%
%       trainedModel.predictFcn: A function to make predictions on new data.
%
%       validationRMSE: A double representing the validation RMSE. In the
%        app, the Models pane displays the validation RMSE for each model.
%
% Use the code to train the model with new data. To retrain your model,
% call the function from the command line with your original data or new
% data as the input argument trainingData.
%
% For example, to retrain a regression model trained with the original data
% set T, enter:
%   [trainedModel, validationRMSE] = trainRegressionModel(T)
%
% To make predictions with the returned 'trainedModel' on new data T2, use
%   yfit = trainedModel.predictFcn(T2)
%
% T2 must be a table containing at least the same predictor columns as used
% during training. For details, enter:
%   trainedModel.HowToPredict

% Auto-generated by MATLAB on 12-Nov-2023 16:32:15


% Extract predictors and response
% This code processes the data into the right shape for training the
% model.
inputTable = trainingData;
predictorNames = {'c', 'phi', 'WaterTable', 'SlendernessRatio', ...
'ExtensionLengthToEmbedmentRatio', 'LateralLoad'};
predictors = inputTable(:, predictorNames);
response = inputTable.Deflection;
isCategoricalPredictor = [false, false, false, false, false, false];

% Train a regression model
% This code specifies all the model options and trains the model.
regressionTree = fitrtree(...
    predictors, ...
    response, ...
    'MinLeafSize', 4, ...
    'Surrogate', 'off');

% Create the result struct with predict function
predictorExtractionFcn = @(t) t(:, predictorNames);
treePredictFcn = @(x) predict(regressionTree, x);
trainedModel.predictFcn = @(x) treePredictFcn(predictorExtractionFcn(x));
```

```matlab
% Add additional fields to the result struct
trainedModel.RequiredVariables = {'ExtensionLengthToEmbedmentRatio', 'LateralLoad',
'SlendernessRatio', 'WaterTable', 'c', 'phi'};
trainedModel.RegressionTree = regressionTree;
trainedModel.About = 'This struct is a trained model exported from Regression Learner
R2023a.';
trainedModel.HowToPredict = sprintf('To make predictions on a new table, T, use: \n
yfit = c.predictFcn(T) \nreplacing ''c'' with the name of the variable that is this
struct, e.g. ''trainedModel''. \n \nThe table, T, must contain the variables returned
by: \n  c.RequiredVariables \nVariable formats (e.g. matrix/vector, datatype) must
match the original training data. \nAdditional variables are ignored. \n \nFor more
information, see <a href="matlab:helpview(fullfile(docroot, ''stats'',
''stats.map''), ''appregression_exportmodeltoworkspace'')">How to predict using an
exported model</a>.');

% Extract predictors and response
% This code processes the data into the right shape for training the
% model.
inputTable = trainingData;
predictorNames = {'c', 'phi', 'WaterTable', 'SlendernessRatio',
'ExtensionLengthToEmbedmentRatio', 'LateralLoad'};
predictors = inputTable(:, predictorNames);
response = inputTable.Deflection;
isCategoricalPredictor = [false, false, false, false, false, false];

% Perform cross-validation
partitionedModel = crossval(trainedModel.RegressionTree, 'KFold', 5);

% Compute validation predictions
validationPredictions = kfoldPredict(partitionedModel);

% Compute validation RMSE
validationRMSE = sqrt(kfoldLoss(partitionedModel, 'LossFun', 'mse'));
```

The results obtained from the training data are tabulated below:

Table 8-3 Training data results using different algorithms

Model Type	RMSE (Validation)	MSE (Validation)	RSquared (Validation)	MAE (Validation)
Tree	0.784	0.615	0.78	0.355
Linear Regression	0.788	0. 691	0.31	0.898
Linear Regression	0.492	0.809	0.67	6.535
Linear Regression	1.91	285.96	0.03	1.17

Model Type	RMSE (Validation)	MSE (Validation)	RSquared (Validation)	MAE (Validation)
Stepwise Linear Regression	0.507	0.39	0.67	0.550
Fine Tree	0.842	0.492	0.78	0.549
Medium Tree	0.390	0.391	0.75	0.978
Coarse Tree	0.666	0.790	0.59	0.243
Linear SVM	0.868	0.376	0.09	0.998
Quardratic SVM	0.544	0.325	0.52	0.395
Cubic SVM	0.218	0.521	0.81	0.746
Fine Gaussian SVM	0.927	0.250	0.49	0.309
Medium Gaussian SVM	0.795	0.520	0.58	0.495
Course Gaussian SVM	1.518	0.408	0.13	0.585
Ensemble Boosted Trees	0.756	0.504	0.84	0.1726
Ensemble Bagged Trees	0.746	0.504	0.84	0.1726
Gaussian Process Regression Squared Exponential GPR	0.326	0.431	0.97	0.062

Model Type	RMSE (Validation)	MSE (Validation)	RSquared (Validation)	MAE (Validation)
Gaussian Process Regression Matern 5/2 GPR	0.728	0.440	0.97	0.163
Gaussian Process Regression Exponential GPR	0.825	0.628	0.95	0.503
Gaussian Process Regression Rational Quadratic GPR	0.768	0.766	0.97	1.011
Narrow Neural Network	0.356	0.689	0.90	0.421
Medium Neural Network	0.588	0.708	0.94	0.338
Wide Neural Network	0.2894	0.82	0.96	0.863
Bilayered Neural Network	0.64	0. 325	0.95	0.755
Trilayered Neural Network	0.368	0.411	0.97	0.415
SVM Kernel	1.558	1.980	0.05	2.486
Least Squares Regression Kernel	1.016	1.472	0.19	0.841

From the table, it was observed that the Squared Exponential GPR algorithms showed the best result considering R-squared value 0.97 and RMSE value of 0.305. This denoted that 97% data can be explained and predicted using these models. Response plots have been examined to ensure that the independent variables in the regression model should not be correlated with one another. The following figures in Figure 8-9 illustrate the independence of the variables. The true vs predicted response were shown in Figure 8-10.

(a)

264

Predictions: Squared Exponential GPR

(b)

Predictions: Squared Exponential GPR

(c)

265
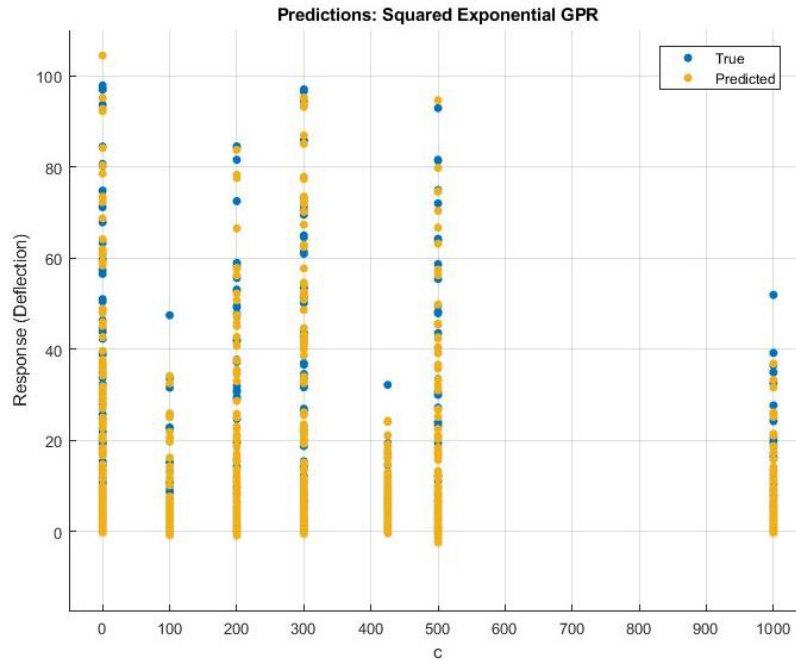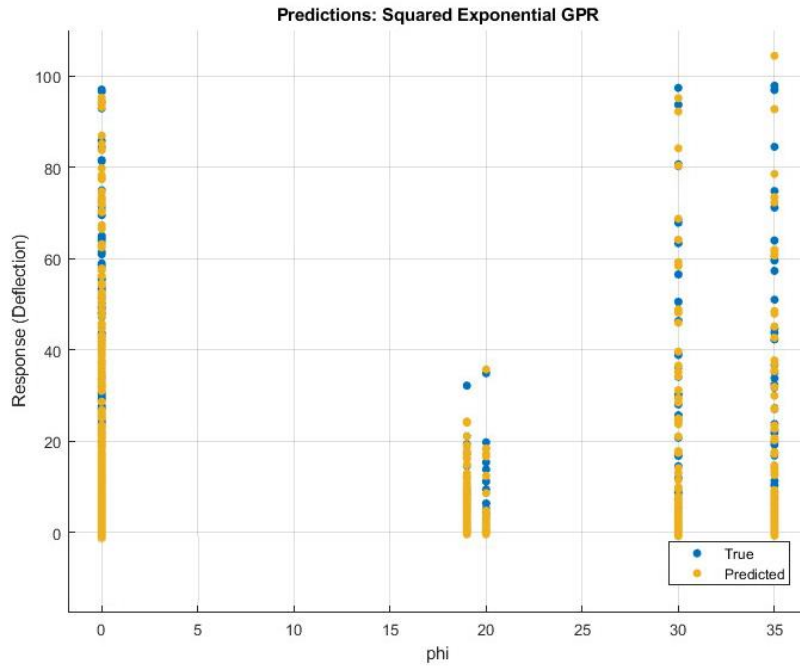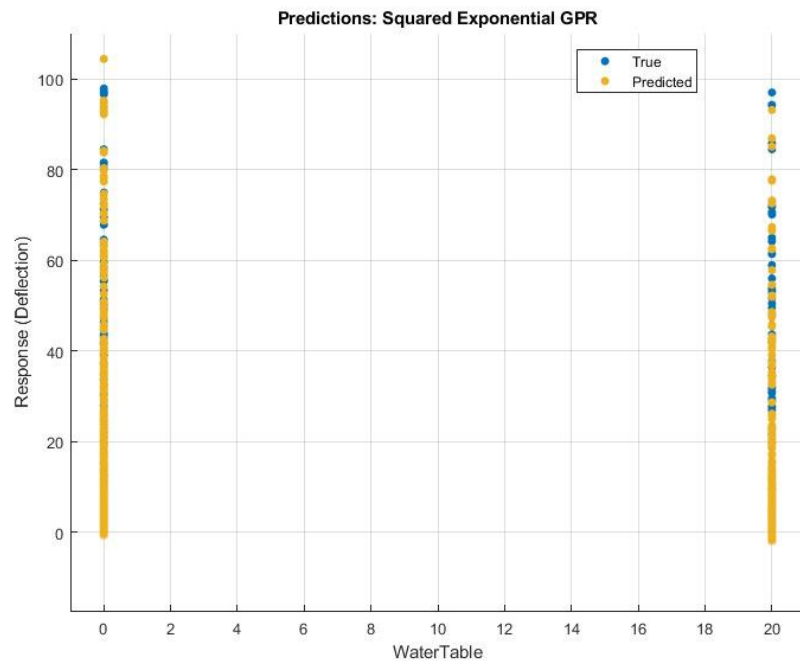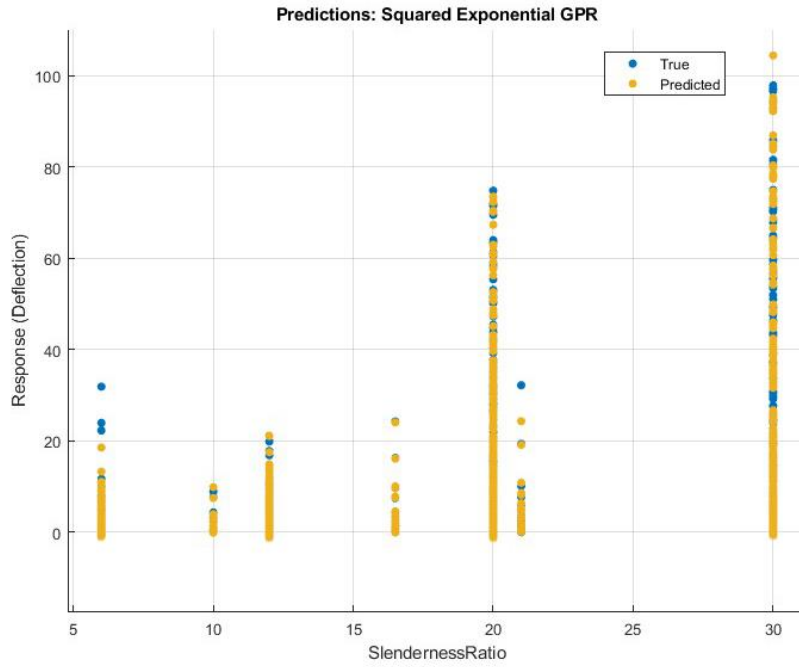
(d)
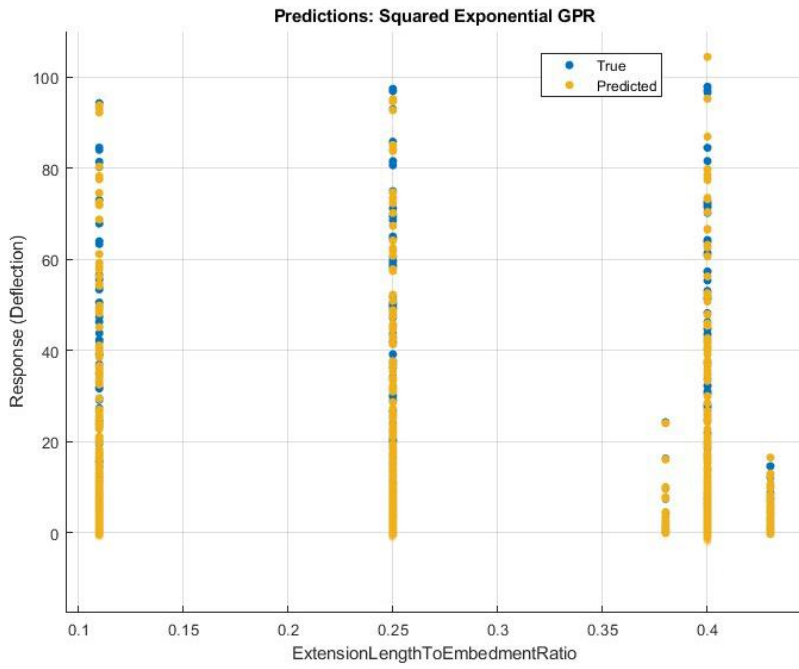
(e)
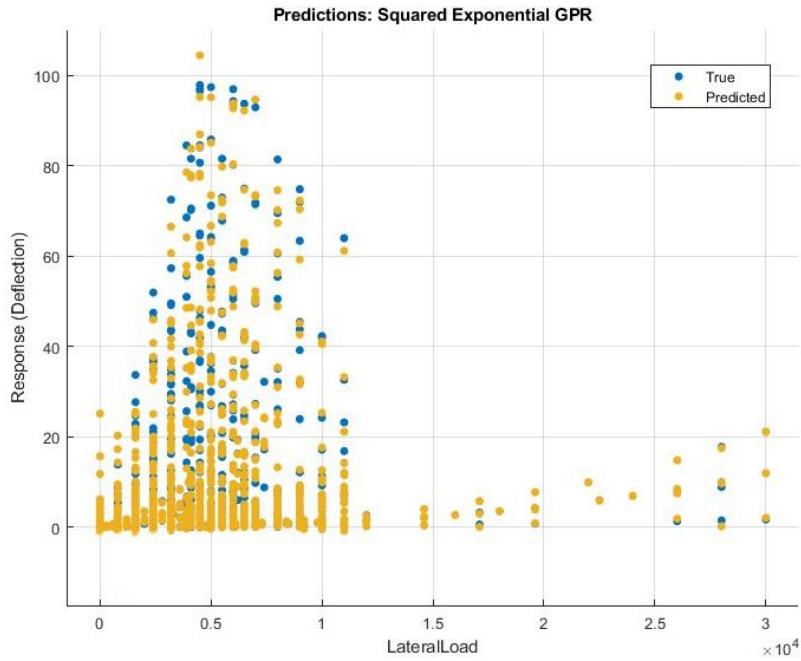
(f)

Figure 8-9 Predictor vs response plot (a) Deflection vs Undrained Shear Strength (b) Deflection vs Internal Friction Angle (c) Settlement vs Water Table (d) Deflection vs Slenderness Ratio (d) Deflection vs Extension Lenth to Embedment Ratio and (e) Deflection vs Lateral Load
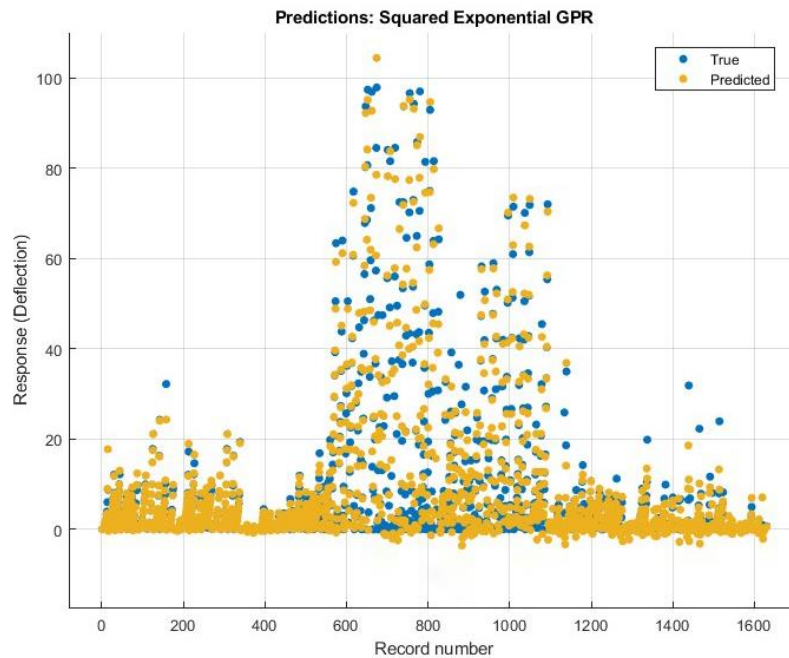
(a)
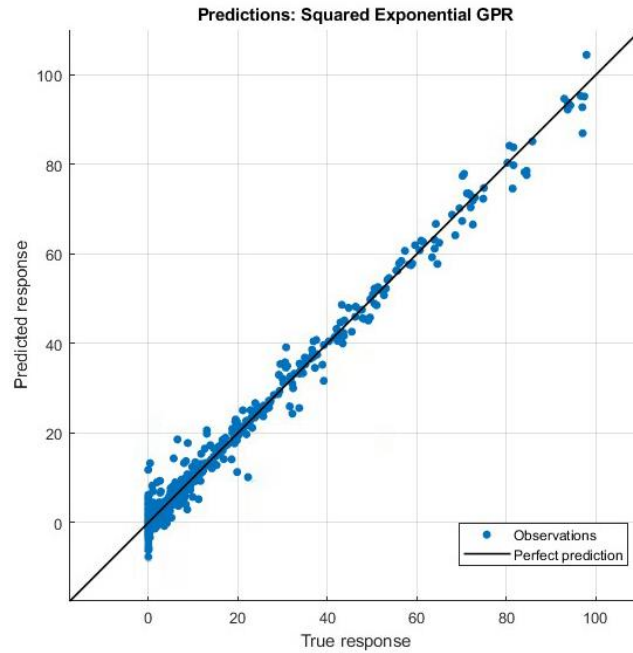
(b)

Figure 8-10 Predicted vs true response using Squared Exponential GPR algorithms for training data.

The following function can be used in MATLAB to make further predictions using the predictor variables, where T is the new matrix for the predictor variables:

yfit = trainedModel.predictFcn(T)

The remaining 15% of the dataset was utilized to test the model after the data had been used to train it. Figure 8-11 shows a plot of expected vs. actual reaction. For the test data, 0.97 and 0.278 were found to be the R-squared and RMSE values, respectively. It means that 97% of the data can be explained by the model created using the training set of data.
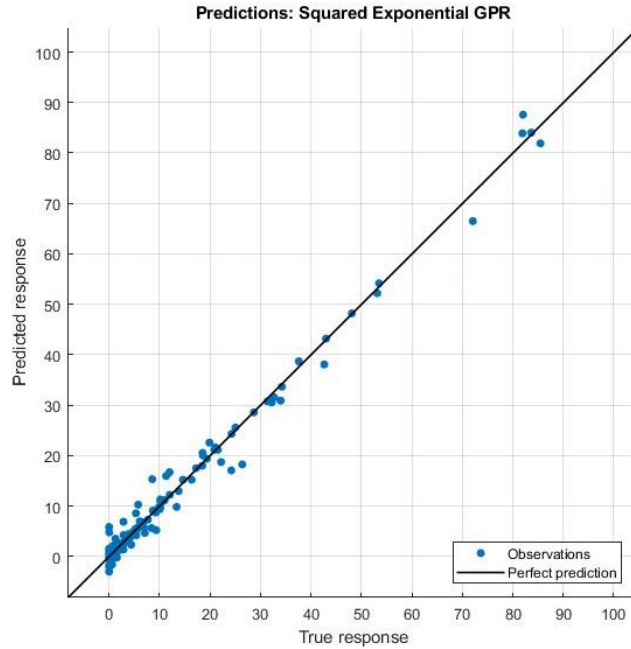
Figure 8-11 Predicted vs true response using Squared Exponential GPR algorithms for test data

According to the results of the F-test, the predictor factors with the highest importance score were those related to slenderness ratio. That indicates that the change in slenderness ratio, as depicted in Figure 8-12, had a greater influence on the deflection.
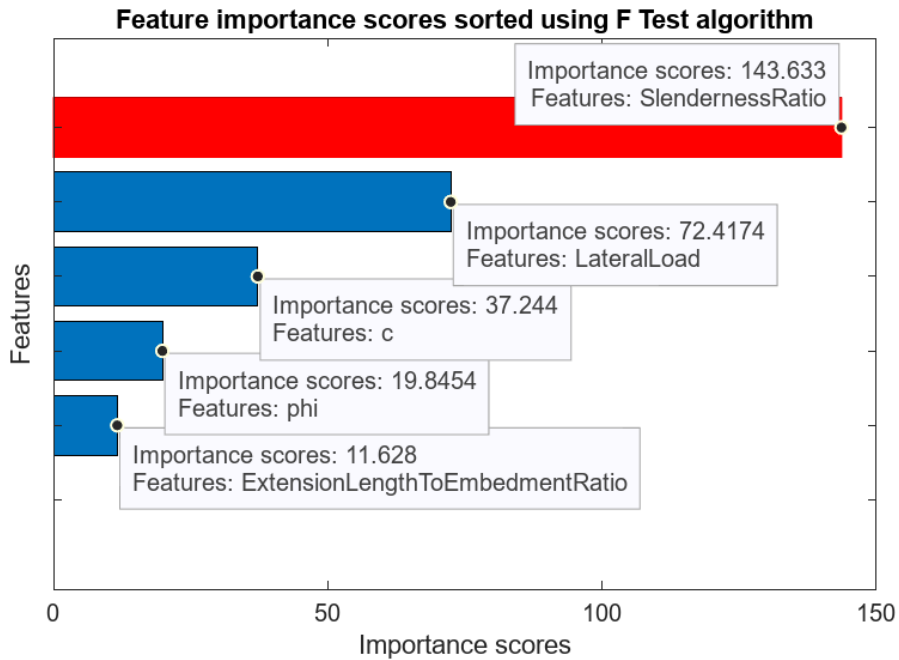
Figure 8-12 Importance scores from F-test

8.4 Data Validation

A set of field data that had not previously been utilized for training was used to validate the data from the prediction model. The corresponding settlement statistics were found using the prediction model. The field test settlement data and the estimated settlement data were compared, and the results are tabulated below:

Table 8-4 Comparison of field test data and the predicted data

Vertical Load Test				Lateral Load Test	
Single RPP		Group RPP			
Field Test Result	Predicted Result	Field Test Result	Predicted Result	Field Test Result	Predicted Result
0.0691	0.0719	0.6672	0.6749	0.0000	0.0311
0.0925	0.1021	0.7248	0.7501	0.1097	0.0669
0.1185	0.1280	0.7655	0.8414	0.2939	0.2490
0.1476	0.1501	0.9225	0.9406	0.4484	0.4106
0.1792	0.2348	0.9939	1.0020	0.8226	0.8137
0.2136	0.2302	1.0489	1.0603	1.1968	1.2169
0.2516	0.3304	1.1662	1.1789	1.2773	1.3034
0.2946	0.3603	1.1834	1.2015	1.8047	1.8603
0.3428	0.3910	1.2948	1.3963	2.4017	2.4719
0.3964	0.4221	1.4352	1.4934	3.2608	3.0912
0.4549	0.4533	1.5876	1.6895	3.9453	3.6567
0.5195	0.4844	1.7520	1.8277	6.0304	5.6739
0.5910	0.5152	1.9224	1.9334	8.8107	9.2788

To interpret the data, linear regression analysis was performed, and the R-squared values were calculated as 0.8929, 0.9421 and 0.9747 for vertical load test data on single and group RPP, and lateral load test data respectively. It can be explained that in 89%, 94% and 97% cases, the data were interpretable as shown in Figure 8-13, Figure 8-14 and Figure 8-15.
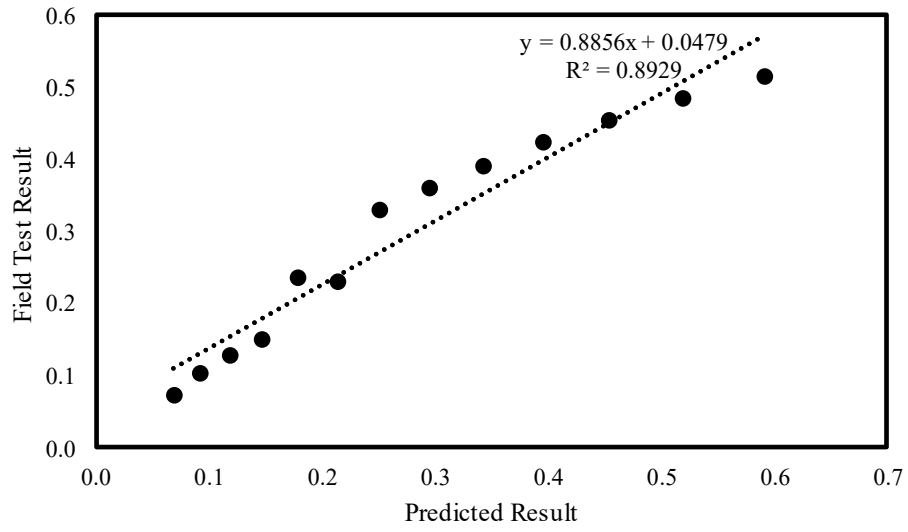
Figure 8-13 Regression analysis for vertical load test data of Single RPP
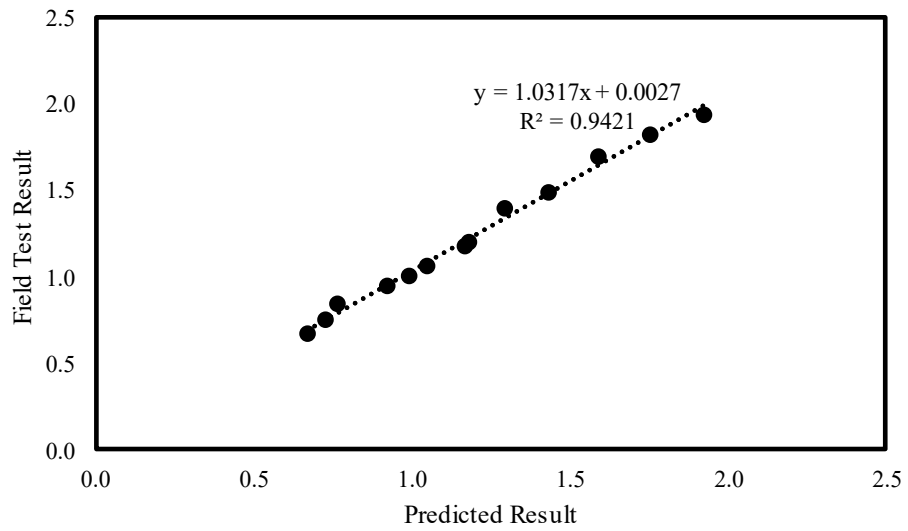
Figure 8-14 Regression analysis for vertical load test data of Group RPP
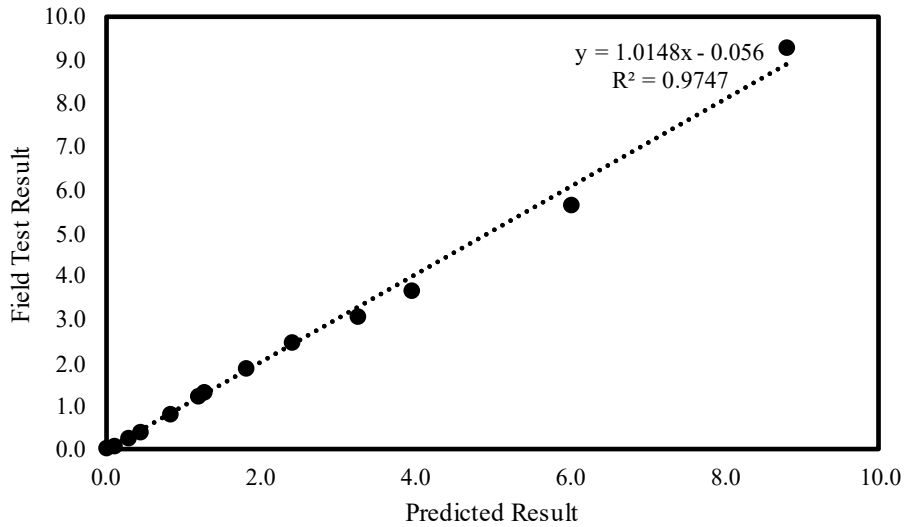
Figure 8-15 Regression analysis for lateral load test data

Additionally, a two-sample independent t-test with unequal variance was performed to determine if there were any statistically significant discrepancies between the actual and predicted outcomes. On the presumption that the two sets of values were independent of one another, it was decided to use an independent test.

In the test, the mean of the observed values was compared to the mean of the predicted values. A significance level of 0.1 was used in the analysis, which was conducted at a 90% confidence level. The significance level was changed from 0.1 to 0.05 because a two-tailed test was used to account for the likelihood of changes in either direction.

There was no statistically significant difference between the means of the expected and observed values of settlement, according to the null hypothesis (H_0) for the two-sample t-test. The alternative hypothesis (H_a) claimed that the two means differed statistically significantly. The t-test was used to determine if the observed variations in the means were most likely the result of random chance or if they had real significance. The following statement sums up the two-sample t-test's main hypothesis:

H_0: $m1-m2 = 0$

H_a: $m1-m2 \neq 0$

where,

$m1$= mean of the actual settlement

$m2$= mean of the predicted settlement

Table 8-5 Summary of two-tailed T- test

		Mean	Std. Dev	Variance	t- value	P- value
Single RPP	Field	0.2824	0.1685	0.0284	-1.3451	0.2035
	Predicted	0.2980	0.1538	0.0237		
Group RPP	Field	1.1896	0.3960	0.1568	-0.2558	0.8003
	Predicted	1.2300	0.4100	0.1681		
Lateral Load Test	Field	2.3386	2.6151	6.8464	0.3902	0.7032
	Predicted	2.3173	2.6644	7.0882		

From Table 8-5, it was observed that the P-value was 0.2035, 0.8003 and 0.7032 for Single, Group and Lateral Load. That explains that P-value is way higher than the significance level (0.05) and it fails to reject the null hypothesis. The p-values for all scenarios are relatively high, indicating that these differences are not statistically significant. Therefore, it appears that the predicted settlement values are reasonably close to the predicted values for these scenarios.

The t-value is additionally employed in hypothesis testing to establish whether there is a statistically significant difference between the two-sample means. The t-value's magnitude and sign (+ or -) show the amount and direction of the difference between the means, respectively.

T-value of -1.3451and -0.2558 suggest that the observed mean is slightly lower than the predicted mean, but the difference is not statistically significant. Again, a negative t-value indicates that the observed mean is lower than the predicted mean. The t-value of 0.3902 indicates that the observed mean for lateral load test in the field is approximately 0.3902 standard errors greater than the predicted mean. In this case, the observed mean is slightly higher than the predicted mean, but the difference is not statistically significant. A positive t-value suggests that the observed mean is higher than the predicted mean.

In all three scenarios, the t-values are relatively close to zero, and their associated p-values are relatively high. This indicates that there is no strong statistical evidence to suggest significant differences between the observed and predicted means for these scenarios. The differences, while present, are not large enough to be considered statistically significant at typical significance levels

(e.g., $p < 0.05$). Therefore, the field test results can be obtained from the predicted value using the following equations as per regression analysis:

Vertical Load Test Datta (Single RPP): Field Test Result (in) = 0.8856*Predicted Result (in) + 0.0479

Vertical Load Test Data (Group RPP): Field Test Result (in) = 1.0317*Predicted Result (in) + 0.0027

Lateral Load Test Data: Field Test Result (in) = 1.0148*Predicted Result (in) -0.056

8.5   Design Methodology

In the current study, a design methodology can be proposed for implementing RPPs to enhance the vertical and lateral load-bearing capacity of foundations under various site and loading conditions. The methodology is centered around assessing settlement resulting from load application and will be instrumental in integrating RPPs into foundation design to improve both vertical and lateral load capacity. This design methodology can be used for estimating settlement or deflection resulting for load application or to determine the suitable RPP parameters for the design. The process will involve combining settlement estimates obtained from design charts and predictive models with other factors, such as soil undrained cohesion, soil friction angle, and the groundwater table level, to make appropriate design decisions. These actions could encompass preliminary assessments or inform foundation design.

Utilizing the framework outlined in Figure 8-16, we can select appropriate RPP size and spacing from design for the anticipated load in foundation. The design procedure begins with a chosen design load and allowable settlement. By applying an appropriate factor of safety, we can determine the ultimate load from the design load and allowable deformation. If the site-specific data aligns with the information in the design charts, we can find the settlement resulting from expected structural loads using the design charts and based on the allowable settlement or deflection RPP size and spacing can be determined. However, if the site conditions do not correspond to any of the soil and groundwater conditions provided in the design charts from Chapter 7, we can determine settlement or deflection using the prediction model described in this chapter. This prediction model is valuable for both calculating settlement due to load application

and creating a comprehensive load-settlement or load-deflection curve. Consequently, we can determine the suitable RPP parameters and spacing for the anticipated design load.
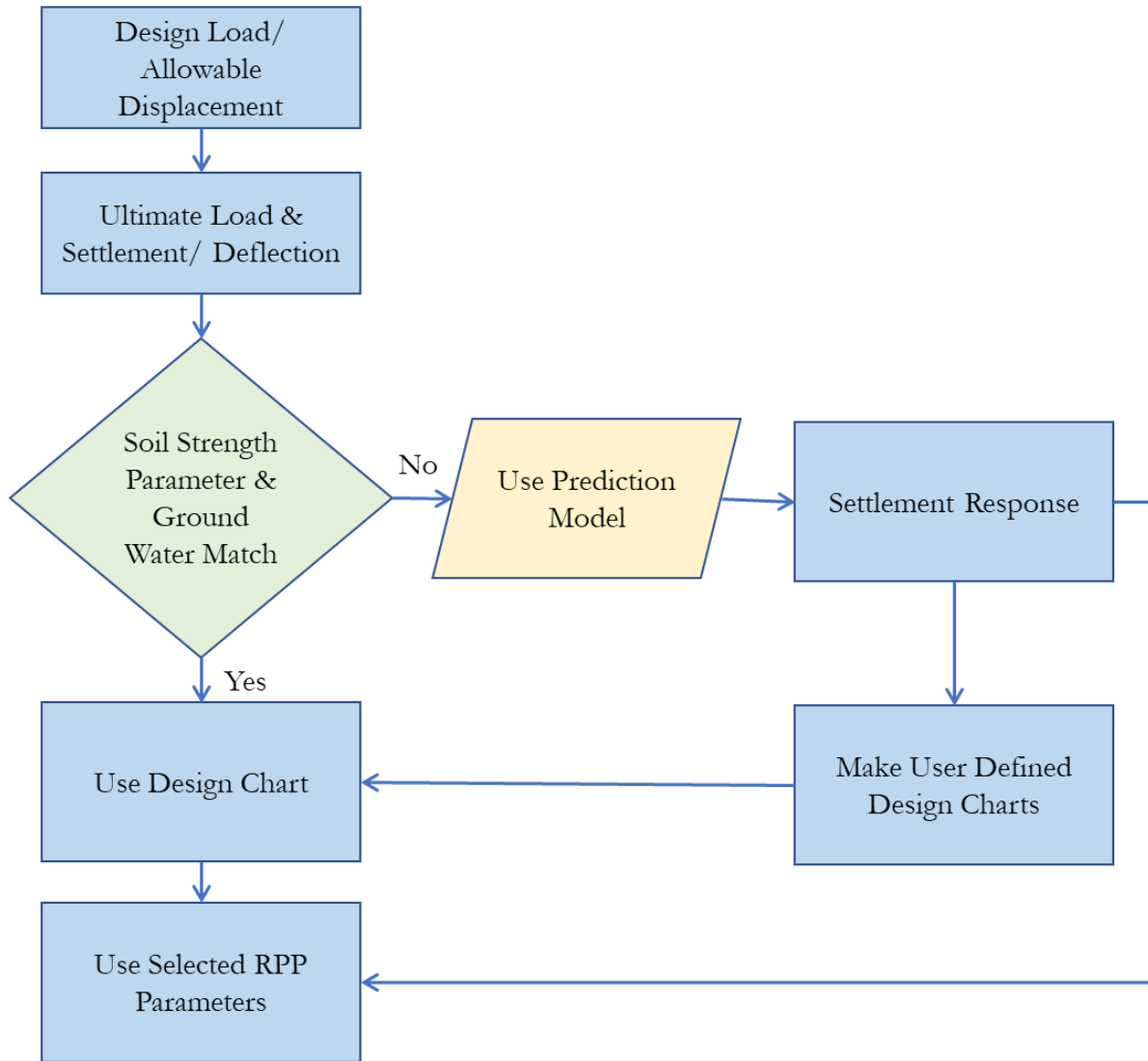
Figure 8-16 Flowchart for selecting RPP parameters for design

CHAPTER 9

SUMMARY AND CONCLUSION

9.1 Summary and Conclusion

RPP has proven itself as a long-term and cost-effective alternative to ground improvement. This study sought to determine the load carrying capability of the RPP in order to develop design charts. RPPs were subjected to field load testing to determine their vertical and lateral load capacities. The load experiments were conducted at Hunter Ferrell Landfill in Irving, Texas, to evaluate the load capacity of RPP in enhancing the load carrying ability of weak foundation soil.

A total of 32 field load tests were conducted, equally divided into 16 for vertical load testing and 16 for lateral load testing. Various RPP sizes (10cm x 10cm, 15cm x 15cm, 25cm x 25cm, and 30cm x 30cm) were installed, with 24 units of the 10cm x 10cm and 15cm x 15cm sizes, 6 units of the 25cm x 25cm size, and 2 units of the 30cm x 30cm size. Reinforced concrete slabs, supported by geogrid, were placed on top of the RPPs to function as load-transferring platforms (LTP). Additionally, geogrid was laid above the RPPs. To assess skin friction and load distribution efficiency, strain gauges and pressure plates were installed on the RPPs and test sections. A total of 20 out of 56 RPPs were instrumented to ensure representation across different RPP combinations.

The vertical load test was carried out in compliance with the ASTM-D1143 (Quick Test) standard. It involved a total of 8 tests on individual RPPs, encompassing four different sizes, as well as 8 tests on grouped RPPs, with two sets involving four distinct combinations of size and spacing. Meanwhile, the lateral load test was conducted following the ASTM-D3966 standard test method, incorporating three different embedment depths of 2.7 m, 2.4 m, and 2.1 m for the three RPP sizes. The results from these field load tests were carefully analyzed to determine the RPPs' ultimate load capacity.

Finite element modeling (FEM) and finite difference methods were utilized to analyze the load behavior of RPP numerically. PLAXIS 3D software was employed for assessing vertical load behavior and settlement, while LPILE software from the Ensoft software package was used to model RPP performance under lateral load conditions. These models were calibrated using field data. The models were utilized to provide valuable insights into RPP deformation and settlement under varying loading conditions, sizes, shapes, and embedment depths. This comprehensive

numerical analysis facilitated the assessment of RPP performance under different vertical and lateral load scenarios, taking into account diverse soil conditions, culminating in the development of a user-friendly design chart. Finally, a prediction model was developed to calculate the extent of settlement or deflection in response to load application on RPPs, considering factors such as soil strength parameters, RPP size, length, spacing, and the extension length both above and below the ground.

The following are the key findings and conclusions based on the current study:

9.1.1 Vertical Load Capacity of RPP

- The ultimate load capacity of single RPPs from the field load test was 45 kN, 116 kN, 155 kN, and 196 kN for 10 cm x 10 cm, 15 cm x 15 cm, 25 cm x 25 cm, and 30 cm x 30 cm RPPs, respectively, with corresponding settlement of 15.45 mm, 12.5 mm, 9.0 mm and 4.0 mm.

- The ultimate load carrying capacity is higher in the RPP with larger cross-section. The increase of load capacity of RPP has an exponential relationship with the increase of RPP size. The relationship can be expressed as y = 19.463e0.0029x providing a significant correlation with the data.

- Average ultimate vertical load capacity of the single RPPs were found to be 50 kN, 119 kN, 162 kN and 207 kN for 10 cm x 10 cm, 15 cm x 15 cm, 25 cm x 25 cm, and 30 cm x 30 cm RPPs, respectively.

- The field load capacity of group RPPs acting as a system was determined to be 203 kN, 235 kN, 525 kN, and 543 kN for 10 x 0.9, 10 x 0.6, 15 x 0.9, and 15 x 0.6 RPP groups, with corresponding settlement of 34 mm, 32 mm, 27.5 mm, and 22.5 mm.

- The average ultimate vertical load capacity of the RPP groups 10 x 0.9, 10 x 0.6, 15 x 0.9, and 15 x 0.6 was determined to be 193 kN, 225 kN, 450 kN, and 477 kN, respectively.

- Chin's Method shows higher ultimate load carrying capacity of the RPPs both in single and group arrangement, however, Butler and Hoy's Method show the most conservative values in both load capacity and settlement criteria.

- The direct relationship between unit skin friction and RPP depth is a consistent trend in all of these RPP studies. Settlement followed the reverse pattern, with the highest settlement at the top and the lowest at the bottom, resulting in a decline of 80% to 92% from top to bottom.

- The ultimate skin resistance and ultimate tip resistance were derived from the field load capacity using the unit skin friction acting on the RPPs measured with the strain gauges.
- According to the pressure plate data, the pressure on the soil at the failure was 75% to 84% lower than that carried by the RPPs. This suggests that the RPPs carried the majority of the applied loads, exposing the weak soil beneath the geogrid to less compressive stress.
- The ultimate load capacity of the RPPs alone in the group arrangement was computed analytically. The study also presented a straightforward analytical method for determining the bearing capacity of an RPP reinforced foundation system. With increasing RPP size, the rate of increase in bearing capacity was observed to rise.

9.1.2   Lateral Load Capacity of RPP

- Moment calculated during field load test suggested that the application of a lateral load at the top of the RPP resulted in the generation of a negative moment at the head. As the RPPs reached depths of 1.5 meters and 2.7 meters with soil confinement, they experienced positive moments. The moment at the bottom had a minimal value, approaching zero.
- The deformation along the RPP length showed that, with a lateral force applied at the top, the greatest deformation occurred there because of unrestricted head movement. Deformation increased at all depths as the RPP embedment depth decreased, and it increased with greater applied load. Larger RPPs withstood higher loads and, consequently, exhibited more significant deformation.
- LPILE 2022 was employed to create a model for simulating RPP behavior in lateral load testing. Model calibration was based on field measurements obtained from load tests on RPP, was essential to ensure an accurate depiction of site-specific conditions.
- The ultimate lateral load capacity results determined from p-y analysis show that, for the same depth of embedment, larger RPPs had 35% - 100% higher lateral load carrying capacity.
- Deformation increases as the load application increases. For similar load, smaller RPPs displaced with smaller cross sections displaced 21%-39% more than RPPs with greater cross sections. Although deformation increases fractionally with a considerable increase in load application, this increase is insignificant when compared to the increase in loading. For 40% to 100% more load application, 25 cm x 25 cm RPPs had 24% to 38% more deformation.

- Increasing the embedment depth by 1 ft resulted in varying degrees of displacement reduction, with a range of 4% to 33%. Conversely, the lateral load capacity showed an increase with the same increase in embedment depth, ranging from 3% to 23%. These findings highlight the significant influence of embedment depth on both displacement and lateral load capacity, with larger RPP sizes generally experiencing greater improvements in load capacity.

- In the cases of the 10 cm x 10 cm and 15 cm x 15 cm RPP, displacement peaked at the top of the RPP and then gradually dropped until it was zero when it reached a predetermined depth of 1.5 m to 2 m along the RPP due to soil anchorage. However, the displacement of 25 cm x 25 cm RPP kept growing and turned negative at the bottom showing short pile failure behavior.

- Moment at failure is maximum at 0.8 m to 1.0 m from ground surface according to the moment vs depth curve. With increasing applied load, the maximum moment increases, and with decreasing embedment depth, the maximum bending moment shifts downward. Moment tends to decrease when the curve reaches its greatest value as the depth rises.

- Using a calibrated model, a parametric investigation was conducted to assess the influence of soil strength parameters, the size and length of RPPs, and their depth in the ground. It was observed that as the values of soil strength parameters and embedment depth increased, and the slenderness of RPPs decreased, there was an apparent rise in load capacity and a reduction in deformation.

9.1.3 Numerical Analysis of Vertical Load Capacity

- The numerical model exhibits a high degree of resemblance with the outcomes derived from field tests, indicating a strong correspondence between the predictions and empirical observations in the real-world geotechnical context.

- The measured displacements of single and group RPPs in the field closely matched the predictions from the Finite Element (FE) model, with a maximum variation of just 12.1%.

- The Stress Concentration Ratios by numerical analysis for RPPs of 10 cm x 10 cm at 0.9 m spacing, 10 cm x 10 cm at 0.6 m spacing, 15 cm x 15 cm at 0.9 m spacing and 15 cm x 15 cm at 0.6 m spacing are 4.14, 4.35, 4.86, 5.81 respectively. The values from the numerical analysis

and the values from the field are in good agreement with a maximum difference of 7% in the case of 15 cm by 15 cm RPP put at 0.6 m spacing.

- The Stress Reduction Ratios by numerical analysis for RPPs of 10 cm x 10 cm at 0.9 m spacing, 10 cm x 10 cm at 0.6 m spacing, 15 cm x 15 cm at 0.9 m spacing and 15 cm x 15 cm at 0.6 m spacing are 0.22, 0.19, 0.16, 0.14 respectively. The values from the numerical analysis and the values from the field are in good agreement with a maximum difference of 15% in the case of 15 cm by 15 cm RPP put at 0.9 m spacing.

- A parametric study was performed on varying soil condition and RPP parameters.

9.1.4 Comparative Study of RPP with Timber piles

- Field testing revealed that RPP and timber piles had similar axial compressive load carrying capacities and settlement upon failure, with very small differences of 7% to 8% for axial load capacity and 5% to 9% for settlement.

- Timber, being a stiffer material in comparison to RPP, showed more resistance to settlement in the initial elastic portion of the load vs settlement curve. RPP reached the plastic zone immediately after the failure, displaying considerable settlement, whereas the settlement was still fairly small for timber piles even after failure with the application of additional load. The permanent settlement of RPP was 29% to 33% more than timber after the withdrawal of load.

- The average ultimate vertical load capacity of RPP and timber found in six empirical methods differed by 13% to 22%. This percentage differed from the field tests because of involvement of the plastic portion of the load settlement curve of RPP in most of the analysis method.

- For RPP and timber, a 30% increase in pile length led to an increase in ultimate vertical load capacity of 10% to 41% and a decrease in settlement of 66% to 70%, respectively.

- As the extension to embedment ratio dropped, there was a considerable decrease in lateral displacement. When the extension to embedment ratio is reduced from 0.40 to 0.38, with the same load application, the displacement is reduced by 25%.

- Considering soil response scenario with the aid of the p-y curve it was observed that with the same extension to embedment depth ratio, soil failure occurs within the elastic limit at the same load for both the piles with a difference of 1% to 4% in lateral deflection.

- At failure, the difference between moment capacity of RPP and timber was 12% to 41% for positive moment and 20% to 43% for negative moment.

- As the extended portion to anchorage length ratio rises, lateral displacement increased, and load capacity dramatically fell.

- It was discovered that the load-deformation curves had steeper slopes for larger pile sizes, indicating more lateral load capacity and less deformation. Similar-sized RPP deflected more than timber piles after passing the elastic zone.

9.1.5 Development of Design Chart

- Employing PLAXIS 3D for settlement analysis subjected to vertical load test, design charts for both single RPPs and group RPPs were created based on a comprehensive set of 384 scenarios, facilitating the selection of RPP size, length, and spacing to meet specific design criteria across a wide range of soil strength parameters and groundwater table depths.

- The design charts illustrating the lateral load deformation behavior of RPP were created through a comprehensive numerical analysis of 276 distinct scenarios, offering guidance for selecting RPP sizes, and embedment lengths to fulfill specific design requirements in varying soil conditions,.

9.1.6 Development of Prediction Model

- The Bagged Trees algorithm demonstrated superior performance for group RPPs, achieving high R-squared values of 0.82 for training data and 0.86 for test data, suggesting a well-fitted model, particularly in cases where the applied vertical load and width-to-spacing ratio were identified as the most influential predictor factors based on F-test results.

- The Narrow Neural Network algorithms performed best for a single RPP subjected to vertical load, with R-squared values of 0.78 and 0.95 for training and test data, respectively, indicating a reasonably good match with highest importance score for he applied vertical load and undrained shear strength predictor factors.

- The Squared Exponential GPR algorithms produced the greatest results for RPPs subjected to lateral load, with R-squared values of 0.97 for training data and 0.86 for test data, yielding slenderness ratio the highest importance score.

9.2 Recommendation for Future Studies

- This study utilized RPP groups with four individual RPPs arranged in a square layout, but the potential for testing and analyzing RPP groups with different orientations and larger numbers of individual RPPs is a promising avenue for future research.

- RPP with just rectangular cross sections was used in the current investigation. Other commercially available shapes (e.g., circular, H-pile, etc.) can be utilized to conduct another study to determine the effect of other RPP shapes.

- The effectiveness of different load transferring systems in transmitting load while performing field load tests on RPP groups should be investigated.

- Future study can employ comparative load test on timber and RPP after immersing them in water for a specific duration. This study is essential to evaluate their structural performance and durability in aquatic environments, aiding in material selection for construction projects.

- The present design models have a limited range of predictor variables. They would be strengthened by further research into a larger variety of foundation soil properties.

- It is advisable to consider the possibility of conducting future research that incorporates the lateral load resistance resulting from more RPPs in a group in different arrangements into the design methodology.

- In this research, a preliminary investigation was conducted to determine the effect of floods. More detailed studies on the effects of climatic or environmental loading, such as rainfall and water pressure, can be carried out.

REFERENCES

Abbas, J. M., Chik, Z. H., & Taha, M. R. (2008). Single pile simulation and analysis subjected to lateral load. Electronic Journal of Geotechnical Engineering, 13(E), 1-15.

Adib, M. E. (2001). Load tests on prestressed precast concrete and timber piles. Journal of geotechnical and geoenvironmental engineering, 127(12), 1043-1050.

Ahmed, F. S. (2013). Engineering Characteristics of Recycled Plastic Pin, Lumber and Bamboo for Soil Slope Stabilization. M. S, Thesis, University of Texas at Arlington, Arlington, TX.

Ahmed, F. S. (2013). Engineering Characteristics of Recyled Plastic Pin, Lumber and Bamboo for Soil Slope Stabilization, Doctoral dissertation, The University of Texas at Arlington.

Ahmed, A., Alam, M. J. B., Madanayake, S., & Gupta, N. (2023). Investigation of Non-Equilibrium and Dynamic Behavior of Soil Water Characteristic Curves through Field Monitoring. Transportation Research Record, 03611981231201109.

AISI (1975), Steel Pile Load TestData, American Iron and Steel Institute, Washington, DC, 84 pp.

Aksoy, H. S., Gör, M., and Inal, E. (2016). A new design chart for estimating friction angle between soil and pile materials. Geomechanics and Engineering, 10(3), 315-324.

AlKhafaji, H., & Imani, M. (2022). Numerical simulation of driven piles under static axial compressive load testing using finite element model. In Geotechnical Engineering and Sustainable Construction: Sustainable Geotechnical Engineering (pp. 305-314). Singapore: Springer Singapore.

Amirmojahedi, M., Abu-Farsakh, M., Voyiadjis, G., & Souri, A. (2022). Development of py Curve Model for Sand Using Finite Element Analysis of Laterally Loaded Piles.

Anagnostopoulos, C., & Georgiadis, M. (1993). Interaction of axial and lateral pile responses. Journal of Geotechnical Engineering, 119(4), 793-798.

Armstrong, R. M. (1979). Structural Properties of Timber Pile. ASTM International.

Ashour, M., & Norris, G. (2000). Modeling lateral soil-pile response based on soil-pile interaction. Journal of Geotechnical and Geoenvironmental Engineering, 126(5), 420-428.

ASTM D 1143 Standard test method for piles under static axial compression load, Designation. ASTM International, West Conshohocken, PA.

ASTM D6109: Standard Test Methods for Flexural Properties of Unreinforced and Reinforced Plastic Lumber. ASTM International, West Conshohocken, PA.

ASTM D796: Standard Practice For Compression Molding Test Specimens of Phenolic Molding Compounds (R 1981) ASTM International, West Conshohocken, PA.

Aurpa, S. S. (2021). Characterization of MSW and Plastic Waste Volume Estimation During Covid-19 Pandemic. M. S, Thesis, University of Texas at Arlington, Arlington, TX.

Aurpa, S. S. (2024), Gupta, N., Ahmed, Z., & Hossain, M. S. Vertical Load Capacity of Recycled Plastic Pin in Clay Subjected to Field Load Test. In Geo-Congress 2024.

Aurpa, S. S. (2024), Gupta, N., Ahmed, Z., & Hossain, M. S. Lateral Load Deflection Behavior of Recycled Plastic Pin Subjected to Field Load Test. In Geo-Congress 2024.

Babu, A., & Nayak, S. (2022). A Review on Methods for Analysis of Laterally Loaded Piles. Sustainable Cities and Resilience: Select Proceedings of VCDRR 2021, 407-418.

Badhon, F. F. (2021). *Performance of Recycled Plastic Pins for Increasing Bearing Capacity of Foundation Soil*. Doctoral dissertation, The University of Texas at Arlington.

Badhon, F. F., Islam, M. A., Bhandari, P., & Hossain, M. S. (2023). Performance of Recycled Plastic Pins for Improving Unsuitable Foundation Soil. Transportation Research Record, 2677(6), 852-865.

Ba'ist, A. J., Upomo, T. C., Apriyatno, H., & Nugroho, U. (2019). Lateral Deflection of Single Pile due to Lateral Loads in Clay Soils based on The PY Curve Method with Finite Difference Solution, ALLPILE Program, and PLAXIS Program. Jurnal Teknik Sipil dan Perencanaan, 21(2), 71-80.

Barchard, J., (1999). Centrifuge Modeling of Piled Embankments on Soft Soils. *Thesis presented to University of New Brunswick, Canada, in partial fulfillment of the requirement of degree of Master of Engineering*.

Basore, C. E., & Boitano, J. D. (1969). Sand densification by piles and vibroflotation. Journal of the Soil Mechanics and Foundations Division, 95(6), 1303-1324.

Bhandari, P. (2021). Evaluation of Recycled Plastic Pins as Shear Keys in MSE Wall Base. Doctoral dissertation, University of Texas at Arlington.

Bhandari, P., Hossain, M. S., Islam, M. A., & Badhon, F. F. (2022). Controlling base movement of MSE walls using recycled plastic pins. Transportation Geotechnics, 32, 100707.

Bhandari, P., Rauss, C., Sapkota, A., and Hossain, M.S. (2020). "Long term performance of shallow slopes stabilized with recycled plastic pins." In Geo-Congress 2020: Engineering, Monitoring, and Management of Geotechnical Infrastructure (pp. 163- 172). Reston, VA: American Society of Civil Engineers.

Bica, A. V., Prezzi, M., Seo, H., Salgado, R., & Kim, D. (2014). Instrumentation and axial load testing of displacement piles. Proceedings of the Institution of Civil Engineers-Geotechnical Engineering, 167(3), 238-252.

Bowders, J., Loehr, J., Salim, H., and Chen, C. W. (2003). Engineering properties of recycled plastic pins for slope stabilization. Transportation Research Record: Journal of the Transportation Research Board, (1849), 39-46.

Bowles, J. E. (1974), Analytical and Computer Methods in Foundation Engineering, McGraw-Hill, New York, 519 pp.

Bowles, J. E. (1988). Foundation analysis and design. McGraw-hill.

Breslin, V. T., Senturk, U., and Berndt, C. C. (1998). Long-term engineering properties of recycled plastic lumber used in pier construction. Resources, Conservation and Recycling, 23(4), 243-258.

Briaud, J. L., & Wang, Y. C. (2018). Synthesis of Load-Deflection Characteristics of Laterally Loaded Large Diameter Drilled Shafts: Technical Report (No. FHWA/TX-18/0-6956-R1). Texas A&M Transportation Institute.

Brinch Hansen, J. (1963). Discussion of Hyperbolic Stress-Strain Response: Cohesive Soil. by Robert L. Kondner. J. Soil Mech., Found. Div., ASCE, 89(4), 241-242.

British Standard, B. S. (1995). 8006 (1995). Code of practice for strengthened/reinforced soils and other fills.

Broms, B.B. 1966. Design of laterally loaded piles. Journal of Soil Mechanics & Foundations Div, 92(Closure).

Broms, Bengt B. (1964a). Lateral Resistance of Piles in Cohesive Soils. ASCE Journal of the Soil Mechanics and Foundations Division, Vo!. 90, No. SM2, p. 27-63

Broms, Bengt B. (1964b). Lateral Resistance of Piles in Cohesion less Soils. ASCE Journal of the Soil Mechanics and Foundations Division, Vol. 90, No. SM3. p. 123-156

Broms, Bengt B. (1965). Design of Laterally Loaded Piles. ASCE Journal of the Soil Mechanics and Foundations Division, Vol. 91, No. SM3, p. 79-99

Burland, J. B. (1973), Shaft Friction Piles in Clay— A Simple Fundamental Approach. Ground Engineering,vol. 6, no. 3, pp. 30-42.

Butler, H. D., & Hoy, H. E. (1976). Users manual for the Texas quick-load method for foundation load testing (No. FHWA-IP-77-8). United States. Federal Highway Administration. Office of Research and Development.

Carroll, D. R., Stone, R. B., Sirignano, A. M., Saindon, R. M., Gose, S. C., and Friedman, M.A. (2001). Structural properties of recycled plastic/sawdust lumber decking planks. Resources, conservation and recycling, 31(3), 241-251.

Chen, C. W. (2003). Engineering Properties of Recycled Plastic Pins for Use in Slope Stablization (Doctoral dissertation, University of Missouri-Columbia).

Chen, C. W., Salim, H., Bowders, J. J., Loehr, J. E., & Owen, J. (2007). Creep behavior of recycled plastic lumber in slope stabilization applications. Journal of materials in civil engineering, 19(2), 130-138.

Chen, R. P., Chen, Y. M., Han, J., and Xu, Z. Z. (2008). A theoretical solution for pile supported embankments on soft soils under one-dimensional compression. Canadian Geotechnical Journal, 45(5), 611-623.

Chen, R. P., Xu, Z. Z., Chen, Y. M., Ling, D. S. and Zhu, B. (2010). Field tests on pilesupported embankments over soft ground. Journal of Geotechnical and Geoenvironmental Engineering, 136(6), 777-785.

Chin, F. K. (1970). Estimation of the ultimate load of piles from tests not carried to failure. In Proc. 2nd Southeast Asian Conference on Soil Engineering, Singapore, 1970.

Chin, F. K. (1971). Pile Tests—Arkansas River Project. Journal of the Soil Mechanics and Foundations Division, 97(6), 930-932.

Christensen, D. S. (2006). Full scale static lateral load test of a 9 pile group in sand. Brigham Young University.

Coduto, D. P., Kitch, W. A., & Yeung, M. C. R. (2001). Foundation design: principles and practices (Vol. 2). Upper Saddle River: Prentice Hall.

Coyle, H. M., & Reese, L. C. (1966). Load transfer for axially loaded piles in clay. Journal of the soil mechanics and foundations division, 92(2), 1-26.

Coyle, H. M., and R. Ungaro (1991), Improved Design Procedures for Vertically Loaded //-Piles in Sand. JGED, ASCE, vol. 117, GT 3, March, pp.507-528., and R. R. Castello (1981). New Design Correlations for Piles in Sand. JGED, ASCE, vol. 107,GT 7, July, pp. 965-986.

Das, B. M. (2011). Principles of geotechnical engineering, 7th Edition. Cengage learning.

Davisson, M. T. (1972). High capacity piles. Proc. Innovations in Found. Const., 52.

Davisson, M., and Gill, H. 1963. Laterally loaded piles in a layered soil system. Journal of the Soil Mechanics and Foundations Division, **89**(3): 63-94.

Davisson, M.T. (1970), Lateral Load Capacity of Piles. Highwav Research Record No. 333, p. 104-112, Highway Research Board, Washington, D.C.

Domenicus. Prague.

Duncan, J. M., Evans Jr, L. T., & Ooi, P. S. (1994). Lateral load analysis of single piles and drilled shafts. Journal of geotechnical engineering, 120(6), 1018-1033.

Elahi, T. E., Islam, M. A., and Islam, M. S. (2019). Effect of vegetation and nailing for prevention of landslides in Rangamati. In Proceedings, international conference on disaster risk mitigation (ICDRM 2019), Dhaka, Bangladesh (pp. 193-197).

Elsawy, M. B., and B. El-Garhy. (2017). Performance of Granular Piles-Improved Soft Ground Under Raft Foundation: A Numerical Study. Int. J. Geosyn. Ground Eng., 3(4), 36. https://doi.org/10.1007/s40891-017-0113-7

Esmaeili, M., Nik, M. G., & Khayyer, F. (2012). Experimental and numerical study of micropiles to reinforce high railway embankments. International Journal of Geomechanics, 13(6), 729-744.

Feagin, L. B. (1937). Lateral pile-loading tests. Transactions of the American Society of Civil Engineers, 102(1), 236-254.

Fellenius, B. H. (1980). The analysis of results from routine pile load tests. Ground Engineering, 13(6), 19-31.

FHWA Publication (1995) - "Geosynthetic Design and Construction Guideline", FHWA Publication Number: FHWA-HI-95-038, Publication Year: 1995, http://isddc.dot.gov/OLPFiles/FHWA/011431.pdf

Flaate, K. (1972), "Effects of Pile Driving in Clays," CGJ,vol. 9, no. 1, Feb, pp. 81-88., and P. Seines (1977), "Side Friction of Piles in Clay," 9th ICSMFE, vol. 1, pp. 517-522.

Fuller, F. M., & Hoy, H. E. (1970). Pile load tests including quick-load test method, conventional methods, and interpretations. Highway Research Record, (333).

Gao, G., Gao, M., Chen, Q., & Yang, J. (2019). Field load testing study of vertical bearing behavior of a large diameter belled cast-in-place pile. KSCE Journal of Civil Engineering, 23, 2009-2016.

Guetif, Z., Bouassida, M., and Debats, J. M. (2007). Improved soft clay characteristics due to stone column installation. Computers and Geotechnics, 34(2), 104-111.

Gupta, N. (2023). Effect of Impurities in Plastic Waste on the Performance of Plastic road. Doctoral dissertation, The University of Texas at Arlington.

Gupta, A., Islam, M. A., & Alam, M. J. B. (2023). Numerical Evaluation of Slope Stability based on Temporal Variation of Hydraulic Conductivity. In E3S Web of Conferences (Vol. 382, p. 24003). EDP Sciences.

Gupta, A. (2023). Developing an Early Warning System of Highway Slope Failure Based on In-Situ Hydraulic Conductivity of Soil (Doctoral dissertation, The University of Texas at Arlington).

Han, J. and Gabr, M. A. (2002). Numerical analysis of geosynthetic-reinforced and pilesupported earth platforms over soft soil. Journal of Geotechnical and Geoenvironmental Engineering, 128(1), 44-53.

Han, J., and Akins, K. (2002). "Use of geogrid-reinforced and pile-supported earth structures." In Deep Foundations 2002: An International Perspective on Theory, Design, Construction, and Performance (pp. 668-679).

Hansen, J.B. 1961. The ultimate resistance of rigid piles against transversal forces. Copenhagen, Denmark.

Hewlett, W.J., and Randolh, M.F. (1988). Analysis of Piled Embankment. International Journal of Rock Mechanics and Mining Sciences and Geomechanics, 25(6), 297-298.

Hong, W. P., Lee, J., and Hong, S. (2014). Full-scale tests on embankments founded on piled beams. Journal of Geotechnical and Geoenvironmental Engineering, 140(12), 04014067.

Hossain, S., Khan, S., and Kibria, G. (2017). Sustainable Slope Stabilisation using Recycled Plastic Pins. CRC Press.

Howe, W. G. (1955). Some contributions to factor analysis (No. ORNL-1919). Oak Ridge National Lab., Tenn.

Iskander, M. G., & Hassan, M. (1998). State of the practice review in FRP composite piling. Journal of Composites for Construction, 2(3), 116-120.

Islam, A. (2021). Effectiveness of Recycled Plastic Pin for Improving Bearing Capacity of Embankment over Soft Soil, Doctoral dissertation, The University of Texas at Arlington.

Islam, M. A., Sara Aurpa, S., Masiyat, M., & Hossain, M. S. Case History of Recycled Plastic Pins Supported Embankment on a Soft Clay Overlying Shale in Texas. In Geo-Congress 2023 (pp. 20-30).

Islam, M.A., Hossain, M.S., Badhon, F.F., and Bhandari, P. (2021). "Performance evaluation of recycled plastic pin supported embankment over soft soil." Journal of Geotechnical and Geoenvironmental Engineering, 147(6), 04021032.

Islam, M. A., Jeet, A. A., Gupta, N., Gupta, A., & Islam, T. (2022). Factors Affecting the Stability and Behavior of an MSE Wall: A Numerical Approach. In Geo-Congress 2022 (pp. 375-385).

Islam, M. A., Gupta, A., Gupta, N., & Islam, T. (2021). Laboratory Investigation of Soil Plugs in Open Ended Model Piles Driven into Sand. In IFCEE 2021 (pp. 108-118).

Islam, M. A., Gupta, A., Gupta, N., Jeet, A. A., & Islam, T. (2022). Soil Plug Response and Load-Settlement Behavior of Open-Ended Model Piles in Sandy Soil. In Geo-Congress 2022 (pp. 207-217).

Jadid, R., Shahriar, A. R., Rahman, M. R., & Imtiaz, T. (2019). Evaluation of theoretical models to predict the pullout capacity of a vertical anchor embedded in cohesionless soil. Geotechnical and Geological Engineering, 37(5), 3567-3586.

Jamaludin, A., and Hussein, A. σ. (1998). The performance of large diameter bored piles used for road project in Malaysia. Proceedings of the 3rd International Geotechnical Seminar on Deep Foundation on Bored and Auger Piles, Ghent, Belgium pp.335-338.

Janbu, N. (1976, March). Static bearing capacity of friction piles. In Sechste Europaeische Konferenz Fuer Bodenmechanik Und Grundbau (Vol. 1).

Jenck, O., Dias, D., & Kastner, R. (2009). Three-dimensional numerical modeling of a piled embankment. International Journal of Geomechanics, 9(3), 102-112.

Jones, C. J. F. P., Lawson, C. R., and Ayres, D. J. (1990). Geotextile reinforced piled embankments. Geotextiles, Geomembranes and Related Products, Den Hoedt (ed.), 155-160.

Jones, C. J. F. P., Lawson, C. R., and Ayres, D. J. (1990). Geotextile reinforced piled embankments. Geotextiles, Geomembranes and Related Products, Den Hoedt (ed.), 155-160.

Kayyal, M. K. and Wright S.G. (1991). Investigation of Long-Term Strength properties of Paris and Beaumont Clays in Earth Embankments. Research Report 1195-2F, Center for Transportation Research, The University of Texas at Austin, November, 1991.

Khan, M. S., Hossain, M. S., Lozano, N., & Kibria, G. (2014). Temporary Lateral Support of a Concrete Retaining Wall Footing using Recycled Plastic Pin. In *Geo-Congress 2014: Geocharacterization and Modeling for Sustainability* (pp. 3851-3860).

Khan, M. S., Hossain, S., & Kibria, G. (2015). Slope stabilization using recycled plastic pins. *Journal of Performance of Constructed Facilities*, *30*(3), 04015054.

Khan, M. S., S. Hossain, and G. Kibria. 2016. Slope stabilization using recycled plastic pins. J. Perfor. Constr. Facil., 30(3): 04015054.

Khan, M.S. (2014). Sustainable Slope Stabilization Using Recycled Plastic Pin in Texas. Doctoral Dissertation, The University of Texas at Arlington.

Kibria, G., Hossain, M. S., & Khan, M. S. (2014). Influence of soil reinforcement on horizontal displacement of MSE wall. International Journal of Geomechanics, 14(1), 130-141.

Lampo, R. G., and Nosker, T. J. (1997). Construction Productivity Advancement Research (CPAR) Program: Development and Testing of Plastic Lumber Materials for Construction Applications (no. Cerl-tr-97/95). Construction engineering research lab (army) champaign il.

Laskar, A. H., and Dey, A. K. (2011). A study on deformation of the interface between sand and steel plate under shearing. In Proceeding of Indian Geotechnical Conference (pp. 895-898).

Leonards, G. A., & Lovell, D. (1979). Interpretation of load tests on high-capacity driven piles (pp. 388-415). ASTM International.

Liu, C. N., Ho, Y. H., and Huang, J. W. (2009). Large scale direct shear tests of soil/PETyarn geogrid interfaces." Geotextiles and Geomembranes, 27(1), 19-30.

Loehr, J. E., and Bowders, J. J. (2007). Slope Stabilization Using Recycled Plastic Pins, Phase III.

Loehr, J. E., Bowders, J. J., Owen, J., Sommers, L., and Liew, W. (2000). Stabilization of slopes using recycled plastic pins. *J. Trans. Res. B.,* 1714, 1-8. National Academy Press. Loehr, J. E., & Bowders, J. J. (2007). Slope Stabilization Using Recycled Plastic Pins – Phase III. In RI98-007D.

Low, B. K., Tang, S. K., and Choa, V. (1994). Arching in piled embankments. Journal of Geotechnical Engineering, 120(11), 1917-1938.

Malcolm, G. M. (1995), Recycled Plastic Lumber and shapes design and specifications, Proc. Structures congress 13, Boston, Massachusetts, April 2-5, 1995.

Matlock, H., & Reese, L. C. (1960). Generalized solutions for laterally loaded piles. Journal of the Soil Mechanics and foundations Division, 86(5), 63-92.

McClelland, B., & Focht Jr, J. A. (1958). Soil modulus for laterally loaded piles. Transactions of the American Society of Civil Engineers, 123(1), 1049-1063.

McClelland, B., and Focht, J.A. 1958. Soil modulus for laterally loaded piles. Transactions of the American Society of Civil Engineers, **123**(1): 1049-1063.

McLaren, M. G. (1995). Recycled plastic lumber and shapes design and specifications." In Restructuring: America and Beyond, 819-833. Boston, MA: ASCE.

McNulty, J. W. (1965). An experimental study of arching in sand. University of Illinois at Urbana-Champaign.

Meyer, C. (1987). Finite Element Idealization for Linear Elastic, Static, and Dynamic Analysis of Structures in Engineering Practice. ASCE.

Meyerhof, G. G. (1956), Penetration Tests and Bearing Capacity of Cohesionless Soils. JSMFD, ASCE, vol. 82, SM l,pp. 1-19.

Meyerhof, G. G. (1976), Bearing Capacity and Settlement of Pile Foundations. JGED, ASCE, vol. 102, GT 3, March, pp. 195-228 (Terzaghi Lecture).

Morrell, J. J. (2018). Protection of wood-based materials. In Handbook of Environmental Degradation of Materials (pp. 343-368). William Andrew Publishing.

Murugesan, S., & Rajagopal, K. (2009). Studies on the behavior of single and group of geosynthetic encased stone columns. Journal of Geotechnical and Geoenvironmental Engineering, 136(1), 129-139.

Nazir, A. K., and Azzam, W. R. (2010). "Improving the bearing capacity of footing on soft clay with sand pile with/without skirts." Alexandria Engineering Journal, 49(4), 371-377.

Nordlund, R. L. (1963). Bearing capacity of piles in cohesionless soils. Journal of the Soil Mechanics and Foundations Division, 89(3), 1-36.

Oh, Y. I., & Shin, E. C. (2007). Reinforcement and arching effect of geogrid-reinforced and pile supported embankment on marine soft ground. Marine Georesources and Geotechnology, 25(2), 97–118. https://doi.org/10.1080/10641190701359591

Ooi, L. H., and Carter, J. P. (1987). A constant normal stiffness direct shear device for static and cyclic loading. Geotechnical Testing Journal, 10(1), 3-12.

Orrje, O., and B. Broms (1967), Effects of Pile Driving on Soil Properties. JSMFD, vol. 93, SM 5, Sept, part 1, pp. 59-74.

Ozdemir, M. A. (2016). Improvement in Bearing Capacity of a Soft Soil by the Addition of Fly Ash. Thesis presented to Middle East Technical University, Turkey, in partial fulfillment of the requirement for the degree of Master of Science in Civil Engineering.

Pando, M. A., Filz, G. M., Dove, J. E., and Hoppe, E. J. (2002). Interface shear tests on FRP composite piles. In Deep Foundations 2002: An International Perspective on Theory, Design, Construction, and Performance (pp. 1486-1500).

Pham, H. T., Suleiman, M. T., and White, D. J. (2004). Numerical analysis of geosyntheticrammed aggregate pier supported embankments. In Geotechnical engineering for transportation projects (pp. 657-664).

Rabbani, S., Gupta, A., & Ahmed, I. (2020). Requirement of expansion joint for temperature load for RCC structures. In IOP Conference Series: Earth and Environmental Science (Vol. 476, No. 1, p. 012054). IOP Publishing.

Rao, K. N. (2006). Numerical modeling and analysis of pile supported embankments (MS Thesis dissertation). University of Texas at Arlington, USA).

Reese, L.C., Cox, W.R., and Koop, F.D. 1974. Analysis of laterally loaded piles in sand. Offshore Technology in Civil Engineering Hall of Fame Papers from the Early Years: 95-105.

Reese, Lymon C. (1984). Handbook on Design of' Piles and Drilled Shafts Under Lateral Load, Report No. FHWA-IP-84-11. Federal Highway Administration

Reese, Lymon C. Andwang, Shin Tower(1986). Method of Analysis of Piles Under Lateral Loading. Marine Geotechnology and NearshorelOffsllOre Structures, ASTM STP 923, R.e.

Reid, W. M., & Buchanan, N. W. (1984). PAPER 21 Bridge approach support piling. In Piling and ground treatment (pp. 267-274). Thomas Telford Publishing

Rogers, L. E. and Wright, S. G. (1986). The Effects of Wetting and Drying on the Long-Term Shear Strength Parameters for Compacted Beaumont Clay. Research Report 436-2F, Center for Transportation Research, the University of Texas at Austin, November 1986.

Roy, R., and Bhasi, A. (2018). Investigation of arching effect in geosynthetic-reinforced piled embankments. Iranian Journal of Science and Technology, Transactions of Civil Engineering, 43(1), 249-262.

Sakr, M., El Naggar, M. H., and Nehdi, M. (2005). Interface characteristics and laboratory constructability tests of novel fiber-reinforced polymer/concrete piles. Journal of Composites for Construction, 9(3), 274-283.

Schmertmann, J. H. (1991). The mechanical aging of soils. Journal of Geotechnical Engineering, 117(9), 1288-1330.

Shioi, Y., and J. Fukui (1982), Application of N-Value to Design of Foundations in Japan, 2nd ESOPT, vol. l,pp. 159-164.

Shirato, M., Kohno, T., & Nakatani, S. (2009). Geotechnical criteria for serviceability limit state of horizontally loaded deep foundations. In Geotechnical Risk and Safety (pp. 133-140). CRC Press.

Sinnreich, J. (2020). Optimizing the arrangement of strain gauges in pile load testing. Geotechnical Testing Journal, 44(5), 1552-1558.

Skempton, A. W. (1951), The Bearing Capacity of Clays, Proc. BuildingResearch Congress, vol. 1, pp. 180-189. (Also in Selected Papers on Soil Mechanics, published by Thomas Telford, Ltd., London.)

Sloan, J., Filz, G., and Collin, J. (2011). A generalized formulation of the adapted Terzaghi method of arching in column-supported embankments. In Geo-Frontiers 2011: Advances in Geotechnical Engineering (pp. 798-805).

Smith, Trevord. (1989). Fact or Fiction: A Review of Soil Response to a Laterally Moving Pile. Foundation Engineering: Current Principles and Practices, Vo!. I, p. 588-598, Fred Kulhawy. Ed., ASCE

Terzaghi, K. (1936). Stress distribution in dry and in saturated sand above a yielding trapdoor.

Terzaghi, K. (1943). Theoratical Soil Mechanics. New York: Wiley.

Terzaghi, K. 1955. Evalution of conefficients of subgrade reaction. Géotechnique, **5**(4): 297-326.

Tex-142-E (1999). Laboratory Classification of Soils For Engineering Purposes. Texas Department of Transportation, Austin, Texas.

Tiwari, B., and Al-Adhadh, A. R. (2014). Influence of relative density on static soil–structure frictional resistance of dry and saturated sand. Geotechnical and Geological Engineering, 32(2), 411-427.

Tomlinson, M. J. (1971), Some Effects of Pile Driving on Skin Friction. Proc.Conference on Behaviour of Piles, ICE, London, pp. 107-114.

Tomlinson. MJ. (1987), Pile Design and Construction Practice, 3rd ed.. Palladian Publications, London

Trow, W. A. (1967). Analysis of pile load test results. Canadian Good Roads Association Proc.

Tuan, P. A. (2016). A simplified formular for analysis group efficiency of piles in granular soil. International Journal of Scientific & Engineering Research, 7(7), 15-21.

Van Weele, A. A. (1957), "A Method of Separating the Bearing Capacity of a Test Pile into Skin-Friction and Point Resistance," 4th ICSMFE, vol. 2, pp.76-80.

Van Weele, A. F. (1957). A method of separating the bearing capacity of a test pile into skin friction and point resistance. In Proceedings of the Fourth International Conference on Soil Mechanics and Foundation Engineering (Vol. 2, pp. 76-80).

Vesić, A. S. (1975). Principles of pile foundation designs. Duke University.

Vijayvergiya, V. N., and J. A. Focht, Jr. (1972), A New Way to Predict Capacity of Piles in Clay, OTC Paper 1718,4th Offshore Technology Conference, Houston, TX.

Wada, A. (2004). Skin Friction and Pile Design.

Wang, G., & Sitar, N. (2006). Nonlinear analysis of a soil-drilled pier system under static and dynamic axial loading. Pacific Earthquake Engineering Research Center, College of Engineering, University of California, Berkeley.

Wang, J. Y., Stirling, R., Morris, P. I., Taylor, A., Lloyed, J., Kirker, G., ... & Mankowski, M. E. (2018). Durability of mass timber structures: A review of the biological risks. Wood and Fiber Science. 50: 110-127., 50, 110-127.

Whitaker, T., and R. W. Cooke (1966), An Investigation of the Shaft and Base Resistances of Large Bored Piles in London Clay. Proc. Conference: Large Bored Piles, ICE, London, pp. 7-49

White, D. J., Thompson, M. J., Suleiman, M. T., & Schaefer, V. R. (2008). Behavior of slender piles subject to free-field lateral soil movement. Journal of Geotechnical and Geoenvironmental Engineering, 134(4), 428-436.

Winkler, E. 1867. Die Lehre von Elastizitat und Festigkeit (The theory of elasticity and stiffness). H. Wright, S. G. (2005). Evaluation of soil shear strengths for slope and retaining wall stability analyses with emphasis on high plasticity clays. *Project No. 5-1874*, *1*.

Wright, S. G., Zornberg, J. G., & Aguettant, J. E. (2007). The fully softened shear strength of high plasticity clays (No. FHWA/TX-07/0-5202-3).

Wu, D., Broms, B. B., & Choa, V. (1998). Design of laterally loaded piles in cohesive soils using py curves. Soils and foundations, 38(2), 17-26.

Wu, X., & Vanapalli, S. K. (2022). Three-dimensional modeling of the mechanical behavior of a single pile in unsaturated expansive soils during infiltration. Computers and Geotechnics, 145, 104696.

Xiang, B., Zhang, L. M., Zhou, L. R., He, Y. Y., & Zhu, L. (2015). Field lateral load tests on slope-stabilization grouted pipe pile groups. Journal of Geotechnical and Geoenvironmental Engineering, 141(4), 04014124.

Yi, Y., Liu, S., Puppala, A. J., & Xi, P. (2017). Vertical bearing capacity behaviour of single T-shaped soil–cement column in soft ground: laboratory modelling, field test, and calculation. Acta Geotechnica, 12, 1077-1088.

Yousif, A. A., & Ali, E. H. (2021). Determination of Piles Bearing Capacity using Empirical Methods and (AllPile 6) Software-Cases studies Portsudan and Khartoum Cities. Int. J. Mat. Math. Sci, 3(5), 113-121.

Zaman, M.N.B. (2019). *Sustainable Ground Improvement Method Using Recycled Plastic Pins*. Doctoral Dissertation, The University of Texas at Arlington.

Zhang, L., Silva, F., and Grismala, R. 2005. Ultimate lateral resistance to piles in cohesionless soils. Journal of Geotechnical and Geoenvironmental Engineering, **131**(1): 78-83.

BORING NUMBER BH1_S4

DATE STARTED 3/8/18   COMPLETED 3/8/18   GROUND ELEVATION 482 ft

DRILLING CONTRACTOR _____   Time: 8:00AM to 11:00 AM

DRILLING METHOD Auger Drilling _____   Hammer Type: Automatic Hammer (140 lbs, 30" drops)

LOGGED BY Md Nur Basit Zaman   CHECKED BY _____

NOTES _____
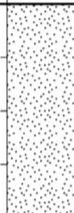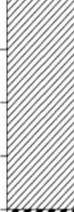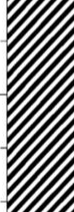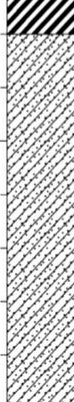
DEPTH (ft)	GRAPHIC LOG	BLOW COUNTS (N VALUE)	Lithology	MOISTURE CONTENT (%)	PLASTICITY INDEX	Remarks
0						
		0-2-3 (5)	Clay, dark grey, high plastic			
5			Clay, dark gray, high plastic			
		4-6-9 (15)				
10			Clay, brown, medium to high plastic			
		4-6-8 (14)				
15			Clay, light brown, medium to high plastic			
		3-4-5 (9)				
20						

Bottom of borehole at 20.0 feet.

Figure A- 1 Log of BH1_S4.

DATE STARTED 3/8/18   COMPLETED 3/8/18   GROUND ELEVATION 482 ft
DRILLING CONTRACTOR _____   **Time: 8:00AM to 11:00 AM**
DRILLING METHOD Auger Drilling _____   **Hammer Type: Automatic Hammer (140 lbs, 30" drops)**
LOGGED BY Md Nur Basit Zaman   CHECKED BY _____
NOTES _____

DEPTH (ft)	GRAPHIC LOG	BLOW COUNTS (N VALUE)	Lithology	MOISTURE CONTENT (%)	PLASTICITY INDEX	Remarks
0						
		0-2-3 (5)	Clay, dark gray, high plastic			
5						
		5-8-9 (17)	Clay, dark gray, high plastic			
10						
		3-7-9 (16)				
15			Clay, light brown, medium to high plastic			
		3-4-5 (9)				
20						

Bottom of borehole at 20.0 feet.

Figure A- 2 Log of BH2_S4

APPENDIX B
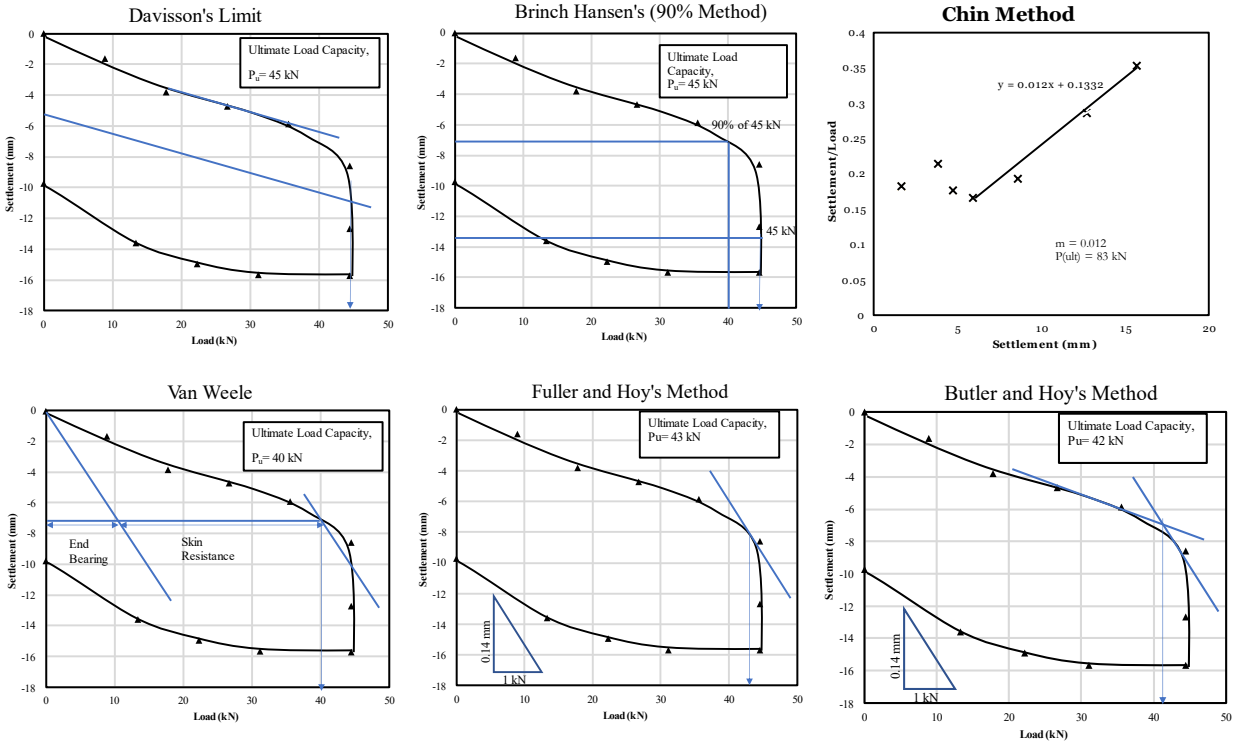
Figure B- 1Ultimate Vertical Load Capacity of 10 cm x 10 cm Single RPP following different method
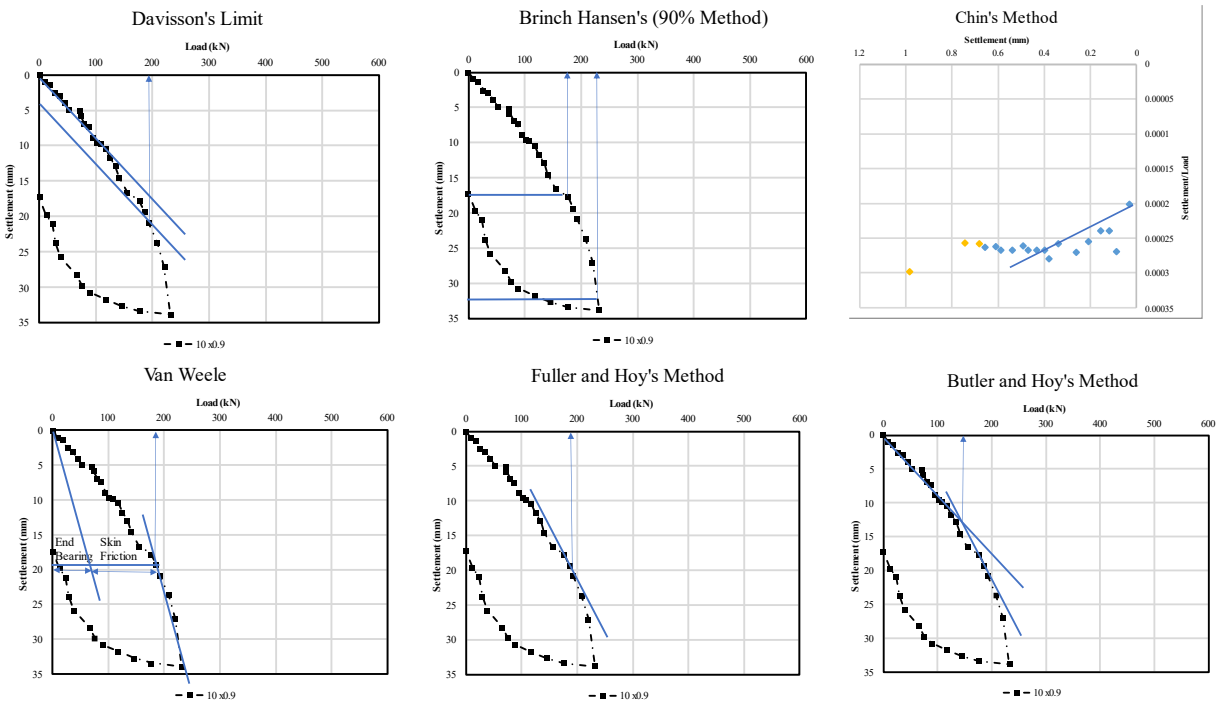
Figure B- 2 Ultimate Vertical Load Capacity of 10 x 0.9 RPP Group following different method
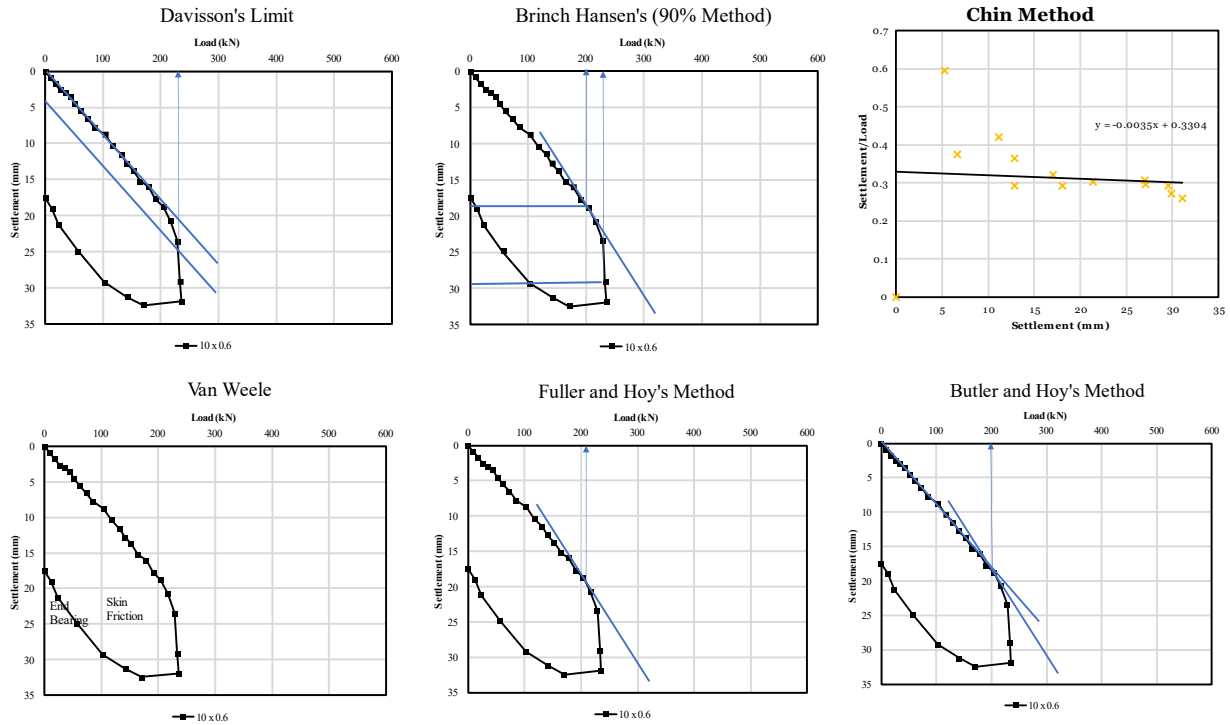
Figure B- 3 Ultimate Vertical Load Capacity of 10 x 0.6 RPP Group following different method
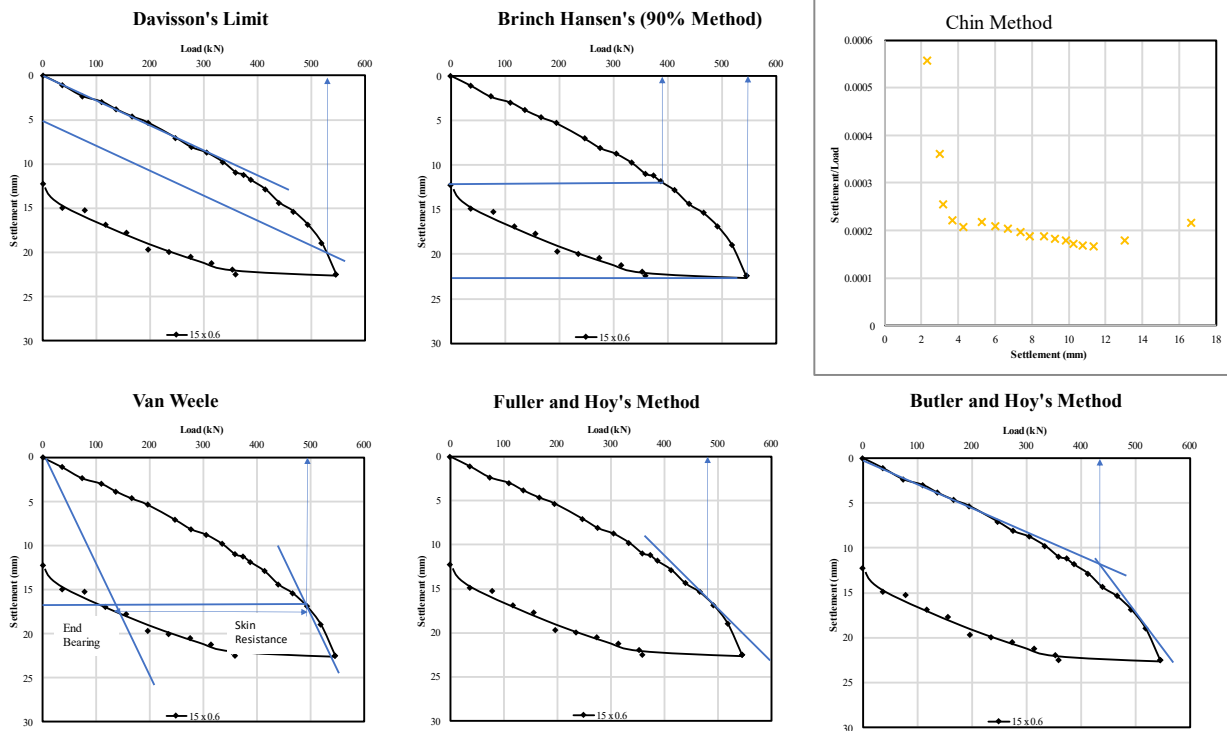
Figure B- 4 Ultimate Vertical Load Capacity of 15 x 0.6 Group RPP following different method

APPENDIX C

Lateral Design Chart (Sand)
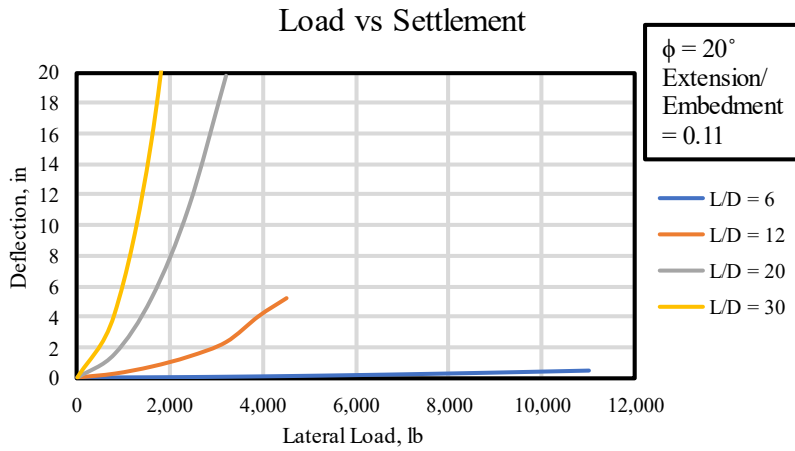
Figure C- 1 Lateral Load vs Horizontal Displacement for c = 0 psf and ϕ = 20˚
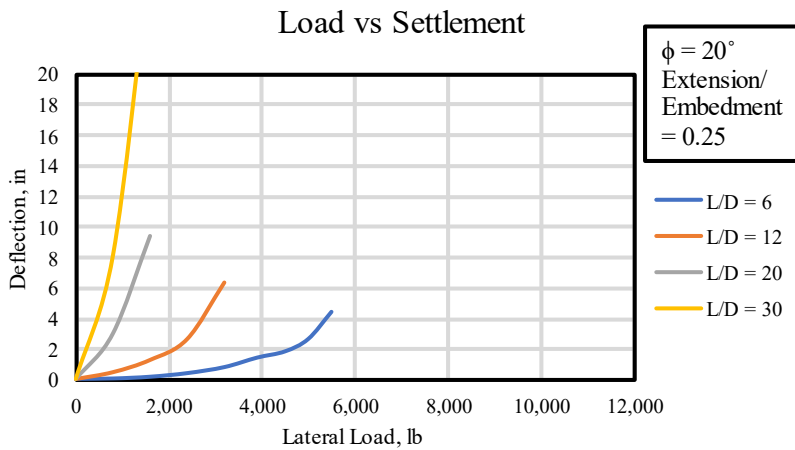
Figure C- 2 Lateral Load vs Horizontal Displacement for c = 0 psf and ϕ = 20˚
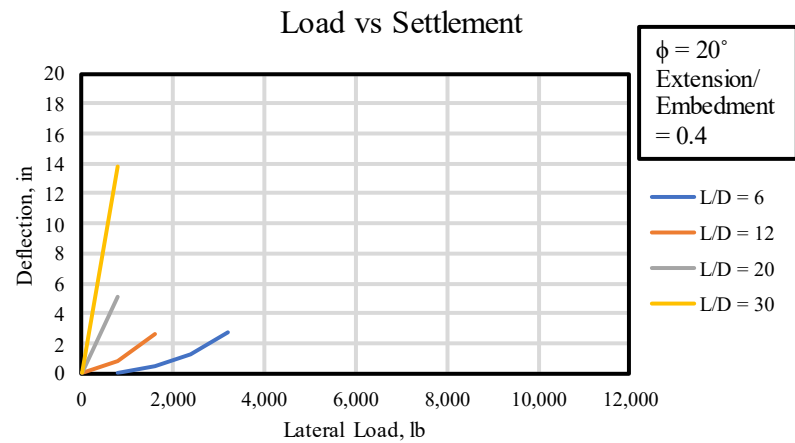
Figure C- 3 Lateral Load vs Horizontal Displacement for c = 0 psf and ϕ = 20˚
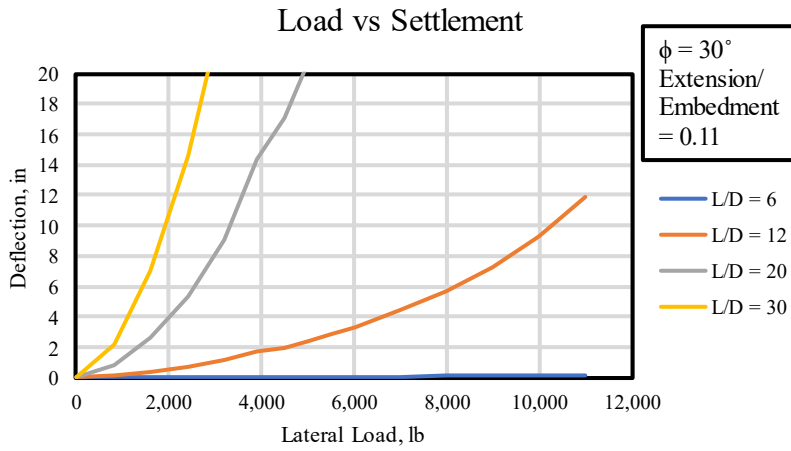
Figure C- 4 Lateral Load vs Horizontal Displacement for c = 0 psf and ϕ = 30˚
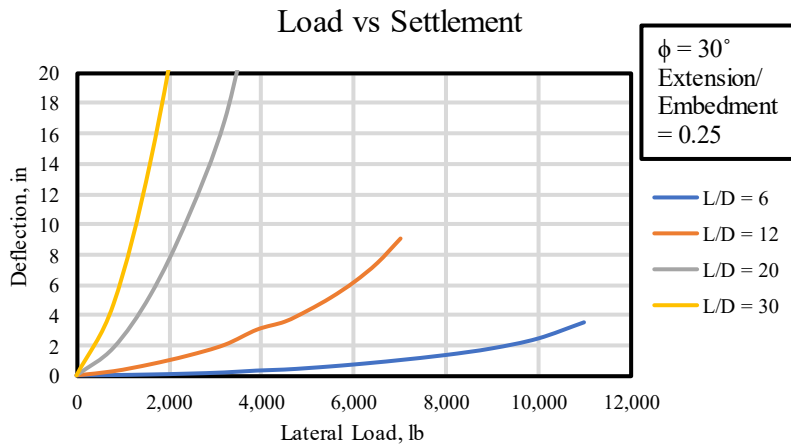
Figure C- 5 Lateral Load vs Horizontal Displacement for c = 0 psf and ϕ = 30˚
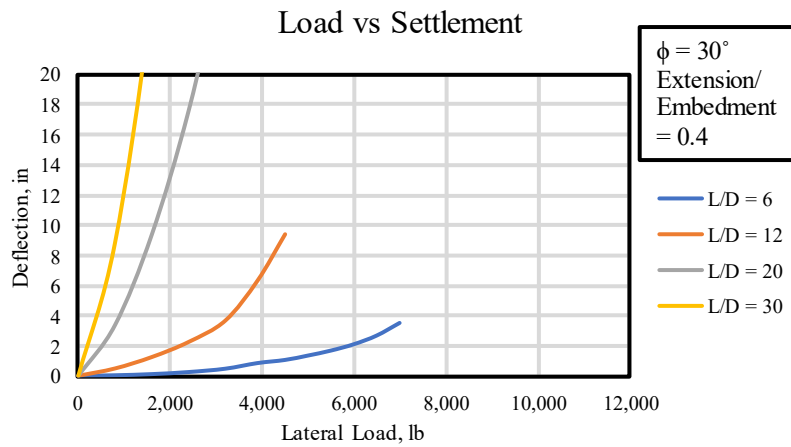
Figure C- 6 Lateral Load vs Horizontal Displacement for c = 0 psf and ϕ = 30˚
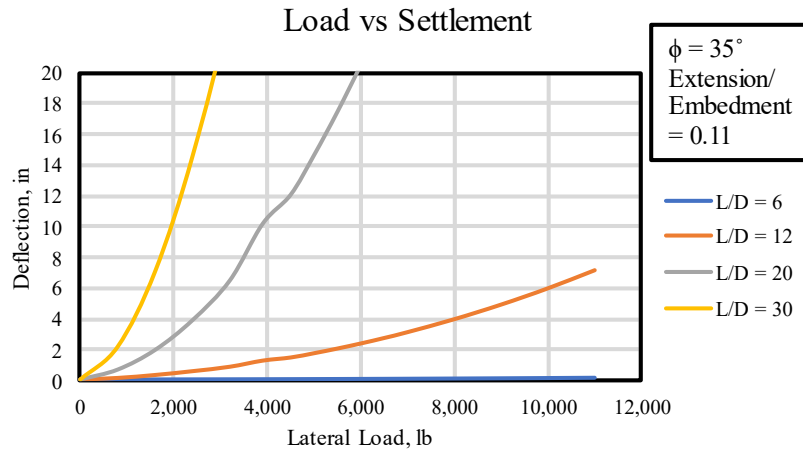
Figure C- 7 Lateral Load vs Horizontal Displacement for c = 0 psf and ϕ = 35˚
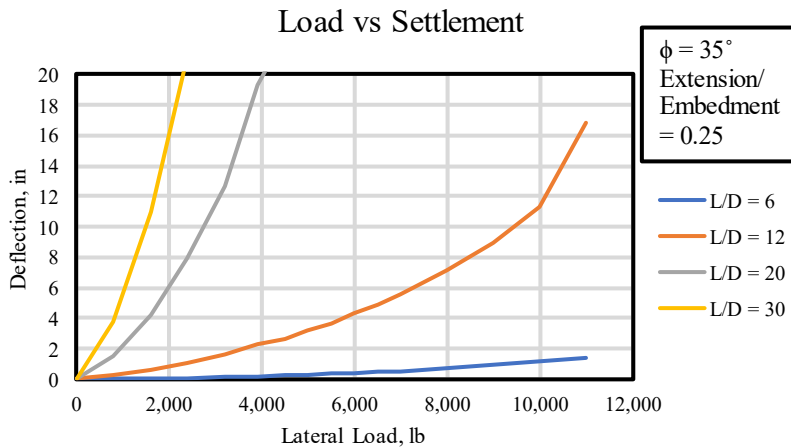
Figure C- 8 Lateral Load vs Horizontal Displacement for c = 0 psf and ϕ = 35˚
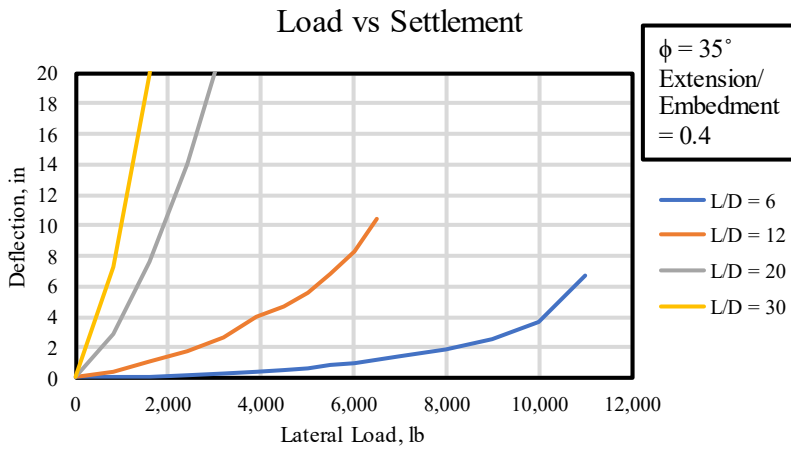
Figure C- 9 Lateral Load vs Horizontal Displacement for c = 0 psf and ϕ = 35˚

Lateral Design Chart (Clay)
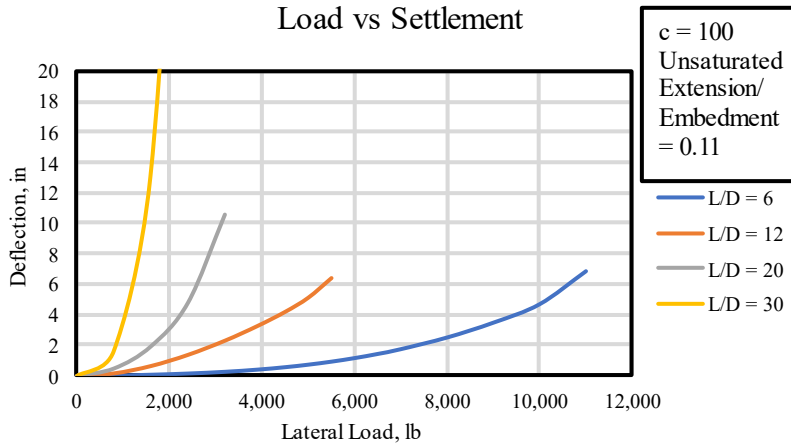
Figure C- 10 Lateral Load vs Horizontal Displacement for c = 100 psf (Unsaturated)
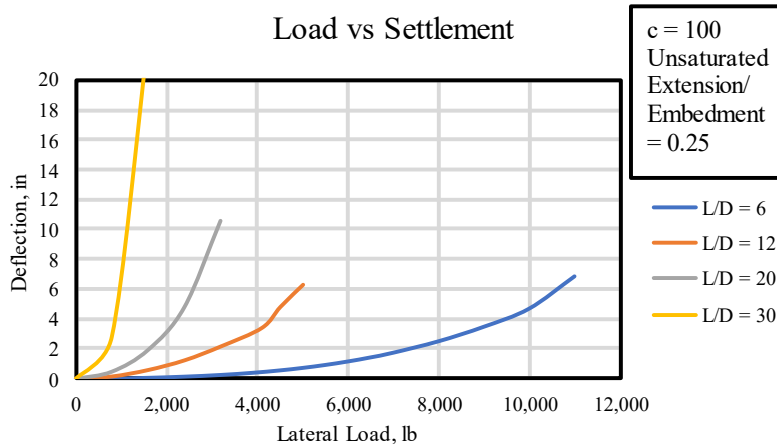
Figure C- 11 Lateral Load vs Horizontal Displacement for c = 100 psf (Unsaturated)
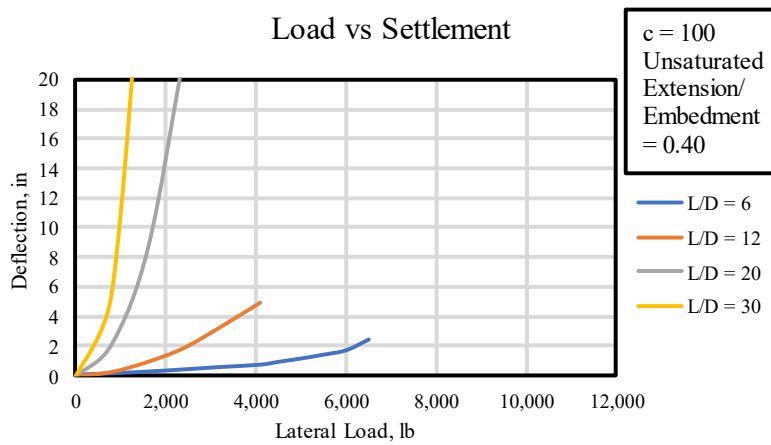
Figure C- 12 Lateral Load vs Horizontal Displacement for c = 100 psf (Unsaturated)
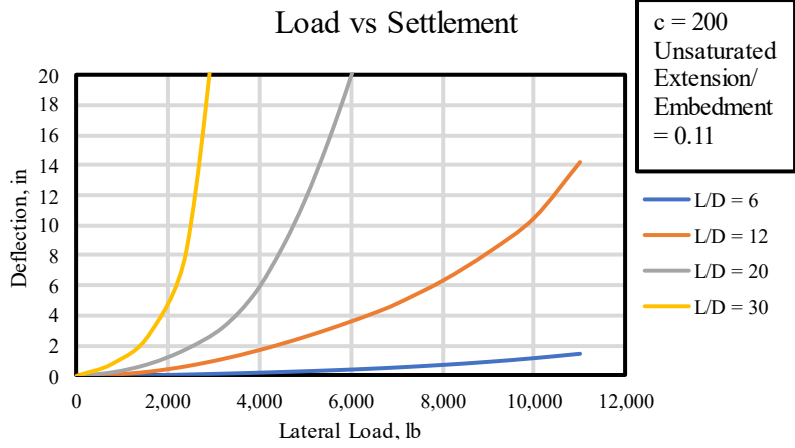
Figure C- 13 Lateral Load vs Horizontal Displacement for c = 200 psf (Unsaturated)
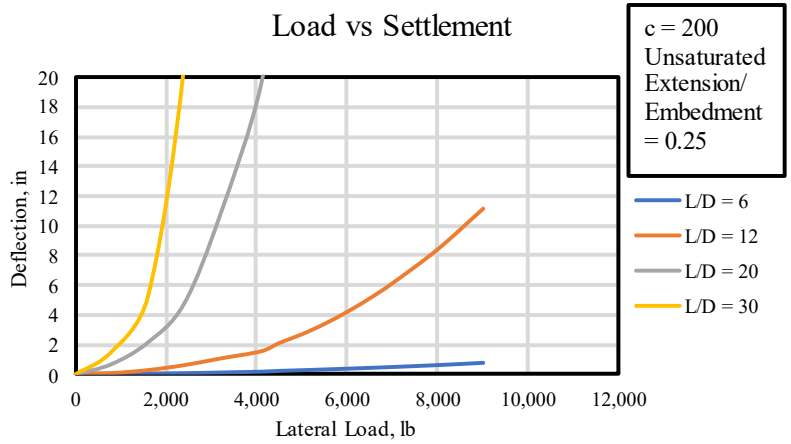
Figure C- 14 Lateral Load vs Horizontal Displacement for c = 200 psf (Unsaturated)
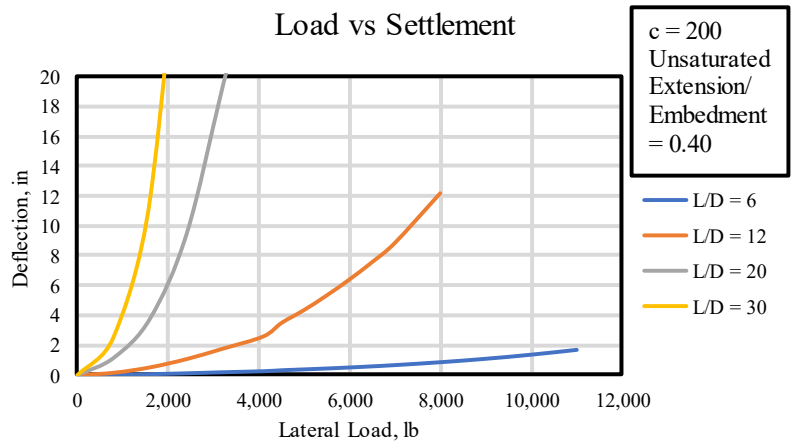
Figure C- 15 Lateral Load vs Horizontal Displacement for c = 200 psf (Unsaturated)
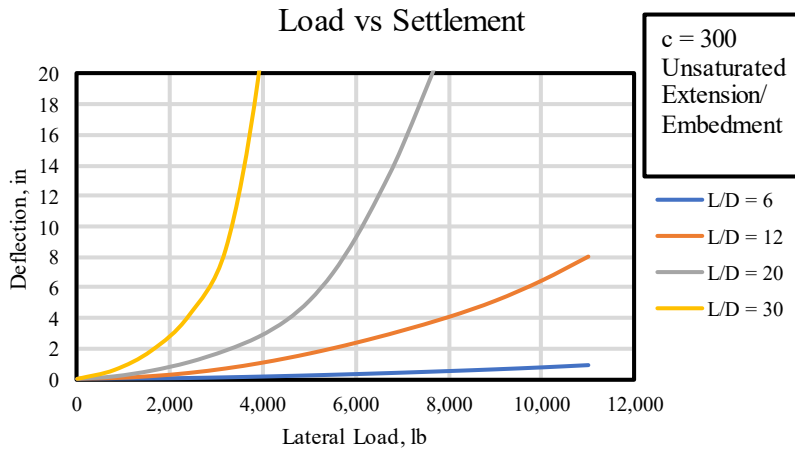
Figure C- 16 Lateral Load vs Horizontal Displacement for c = 300 psf (Unsaturated)
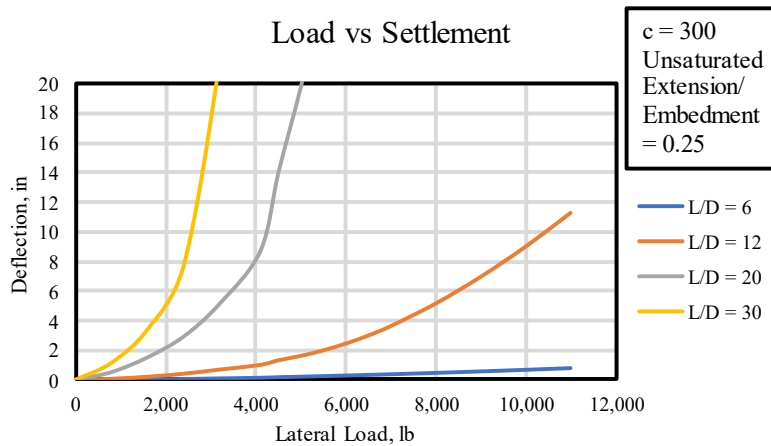
Figure C- 17 Lateral Load vs Horizontal Displacement for c = 300 psf (Unsaturated)
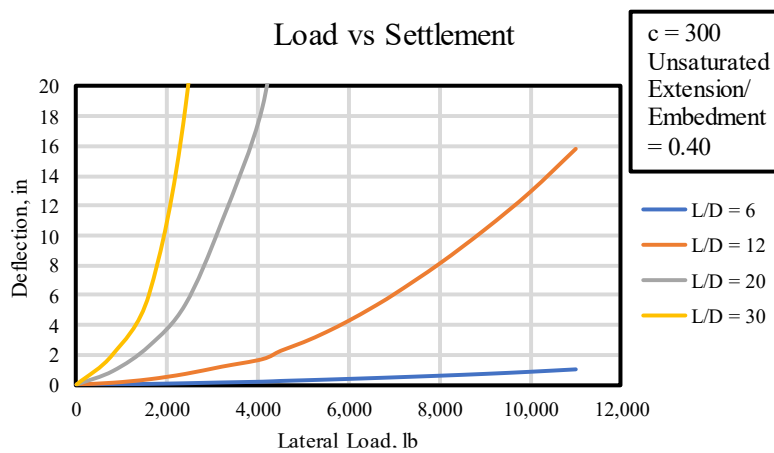
Figure C- 18 Lateral Load vs Horizontal Displacement for c = 300 psf (Unsaturated)
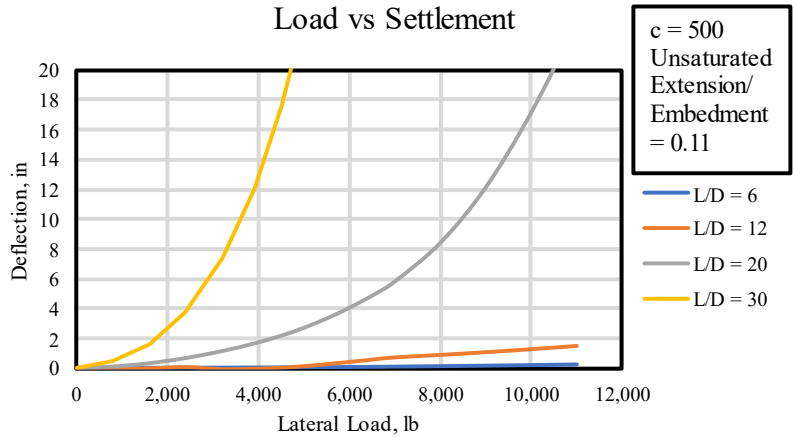
Figure C- 19 Lateral Load vs Horizontal Displacement for c = 500 psf (Unsaturated)
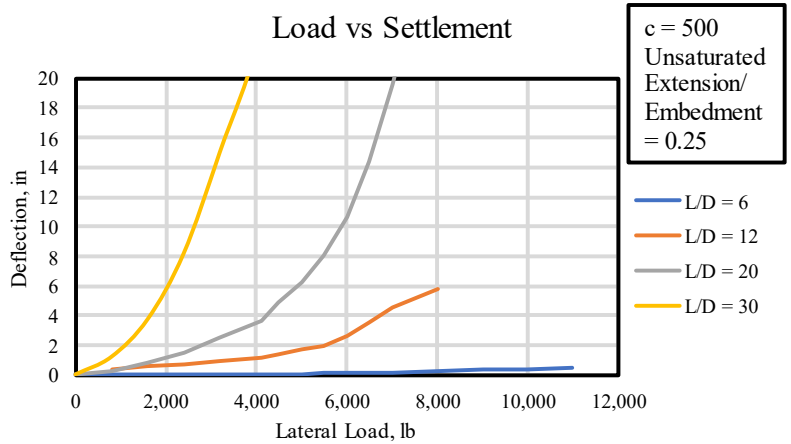
Figure C- 20 Lateral Load vs Horizontal Displacement for c = 500 psf (Unsaturated)
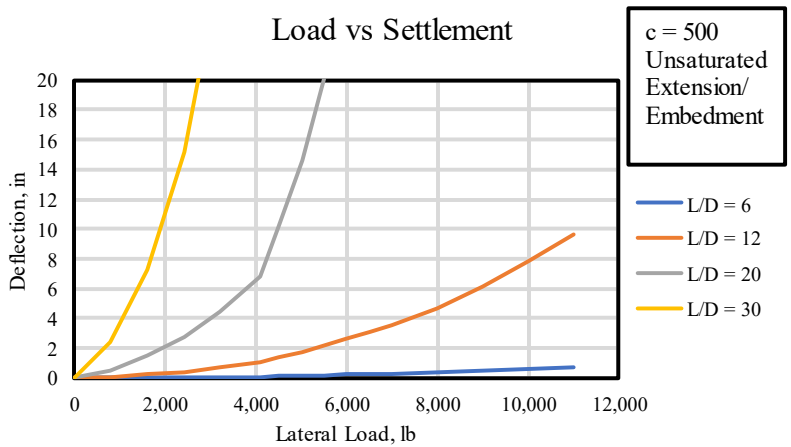
Figure C- 21 Lateral Load vs Horizontal Displacement for c = 500 psf (Unsaturated)

310
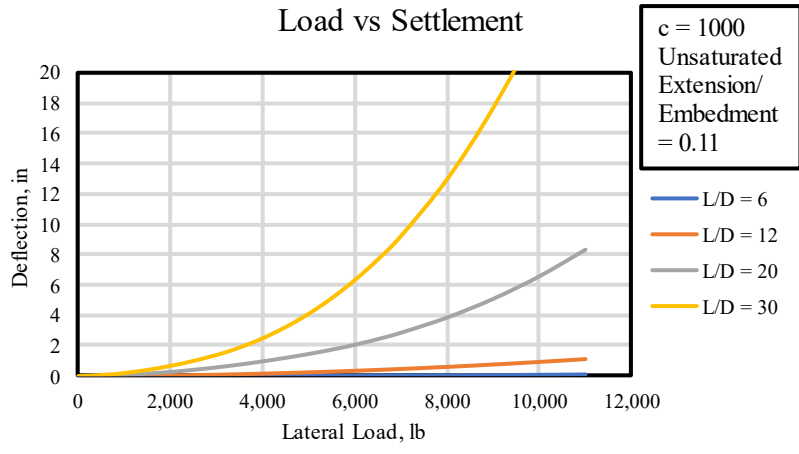
Figure C- 22 Lateral Load vs Horizontal Displacement for c = 1000 psf (Unsaturated)
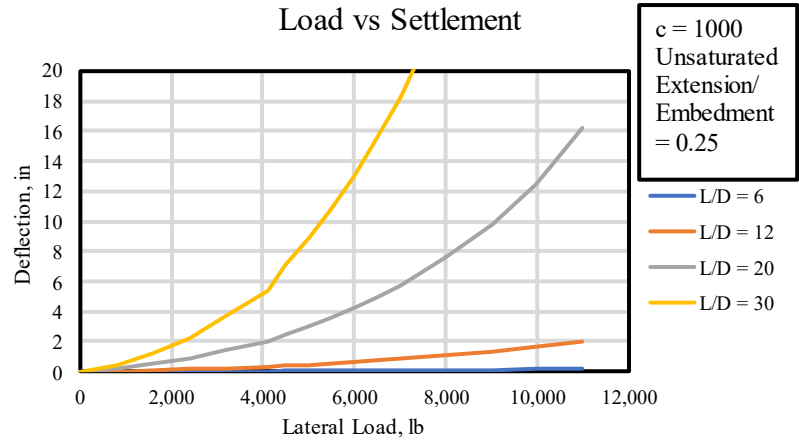
Figure C- 23 Lateral Load vs Horizontal Displacement for c = 1000 psf (Unsaturated)
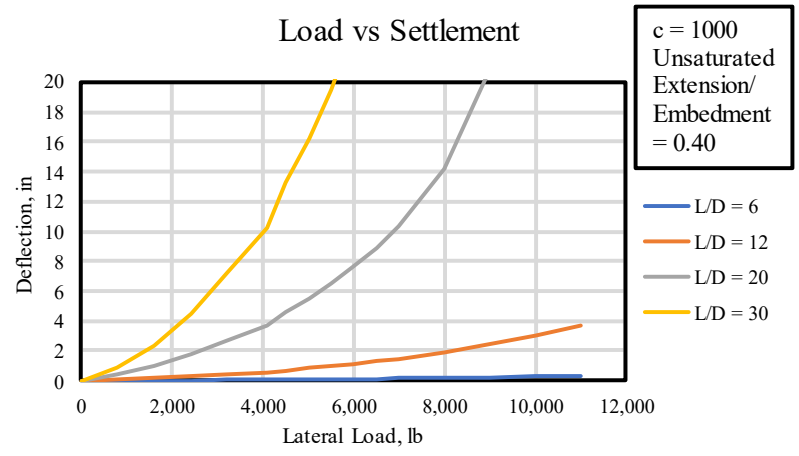
Figure C- 24 Lateral Load vs Horizontal Displacement for c = 1000 psf (Unsaturated)

311
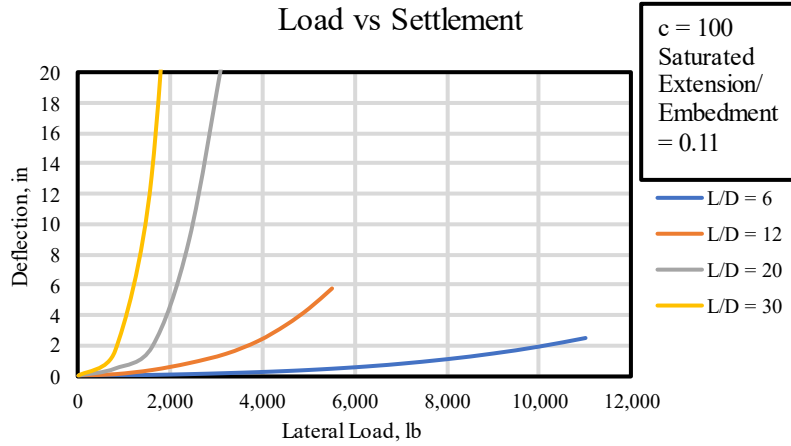
Figure C- 25 Lateral Load vs Horizontal Displacement for c = 100 psf (Saturated)
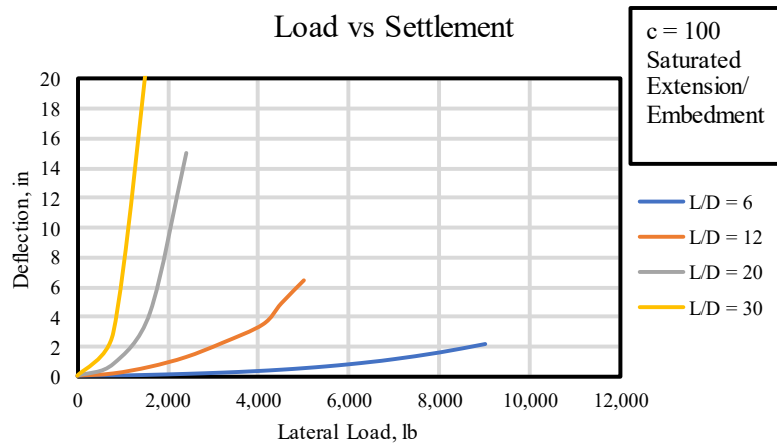
Figure C- 26 Lateral Load vs Horizontal Displacement for c = 100 psf (Saturated)
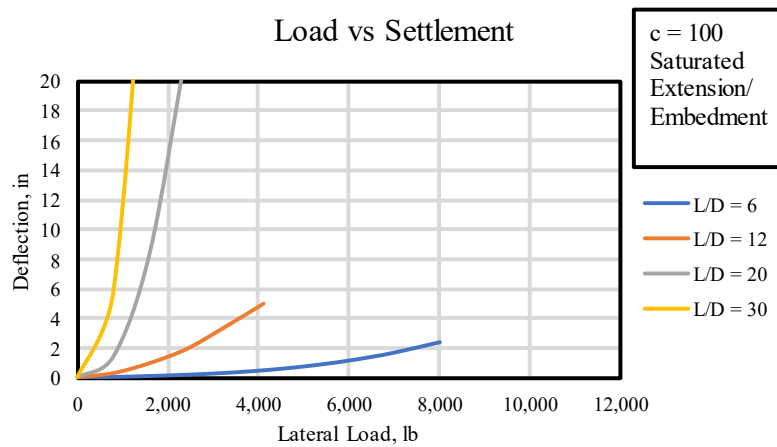
Figure C- 27 Lateral Load vs Horizontal Displacement for c = 100 psf (Saturated)
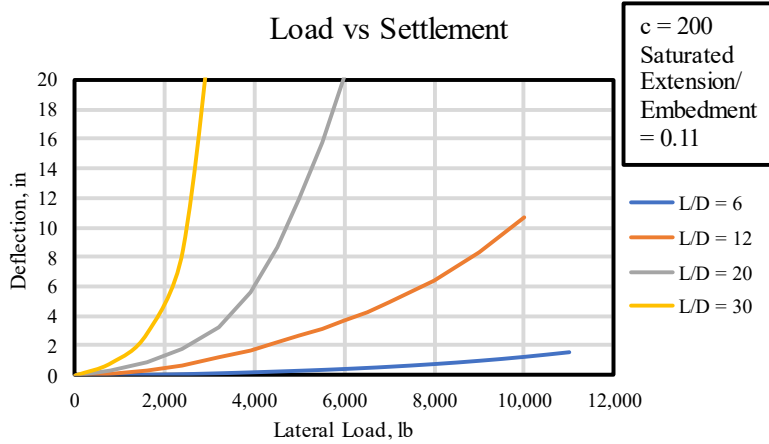
Figure C- 28 Lateral Load vs Horizontal Displacement for c = 200 psf (Saturated)
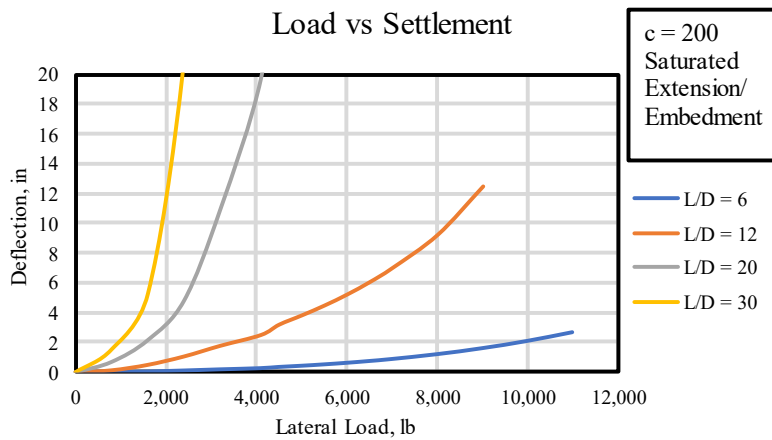
Figure C- 29 Lateral Load vs Horizontal Displacement for c = 200 psf (Saturated)
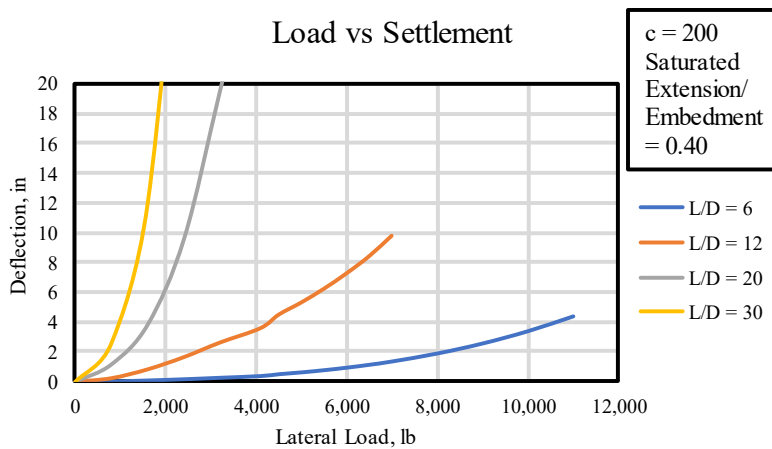
Figure C- 30 Lateral Load vs Horizontal Displacement for c = 100 psf (Saturated)
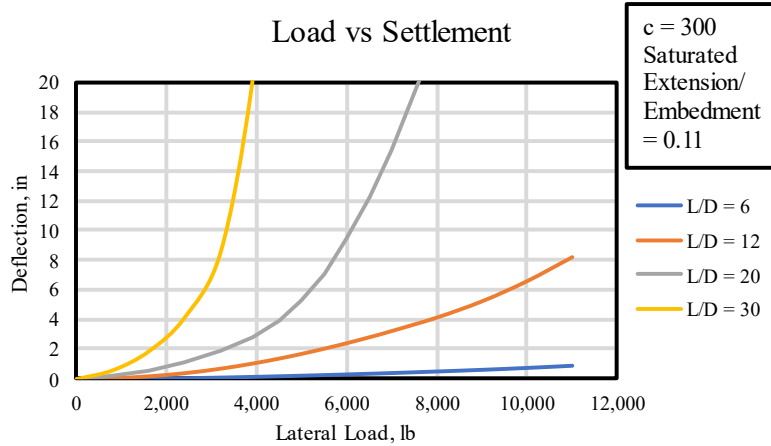
Figure C- 31 Lateral Load vs Horizontal Displacement for c = 300 psf (Saturated)
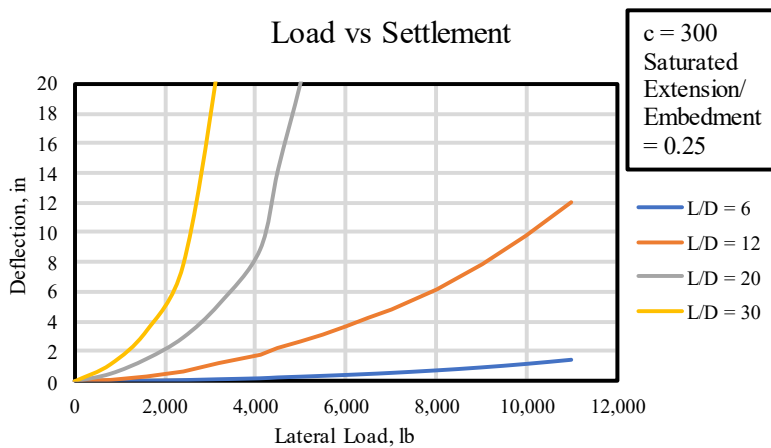
Figure C- 32 Lateral Load vs Horizontal Displacement for c = 300 psf (Saturated)
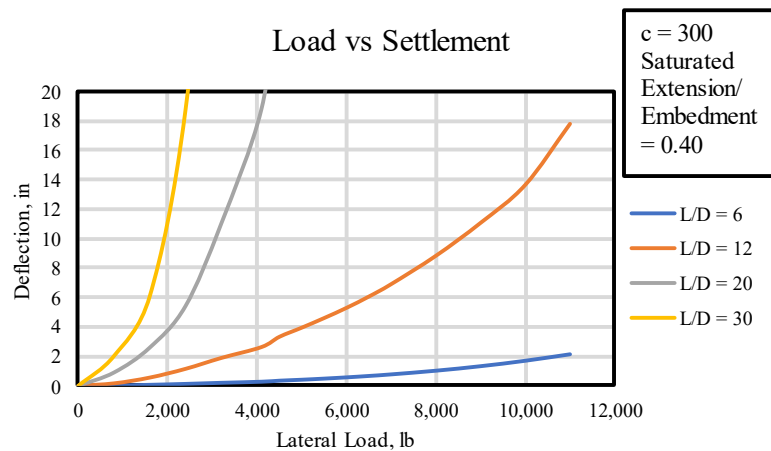
Figure C- 33 Lateral Load vs Horizontal Displacement for c = 300 psf (Saturated)
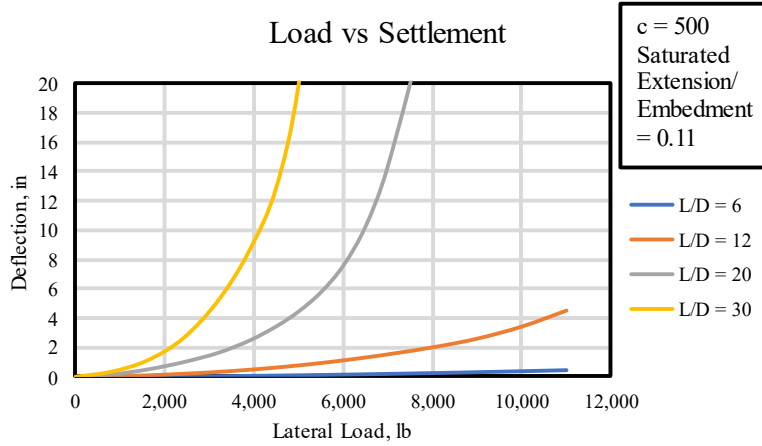
Figure C- 34 Lateral Load vs Horizontal Displacement for c = 500 psf (Saturated)
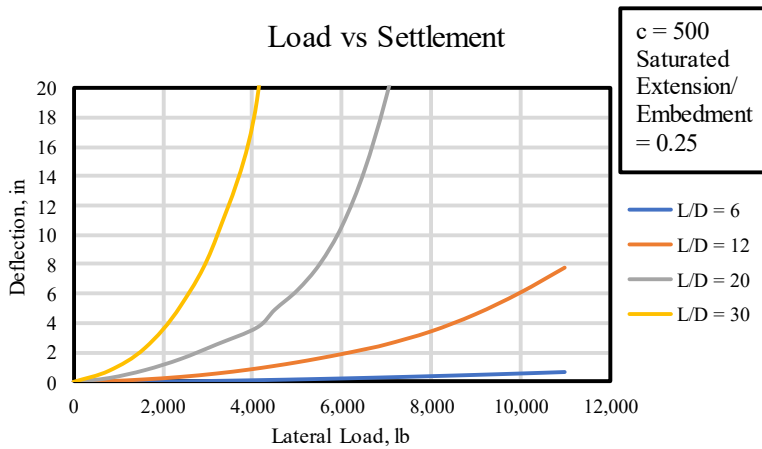
Figure C- 35 Lateral Load vs Horizontal Displacement for c = 500 psf (Saturated)
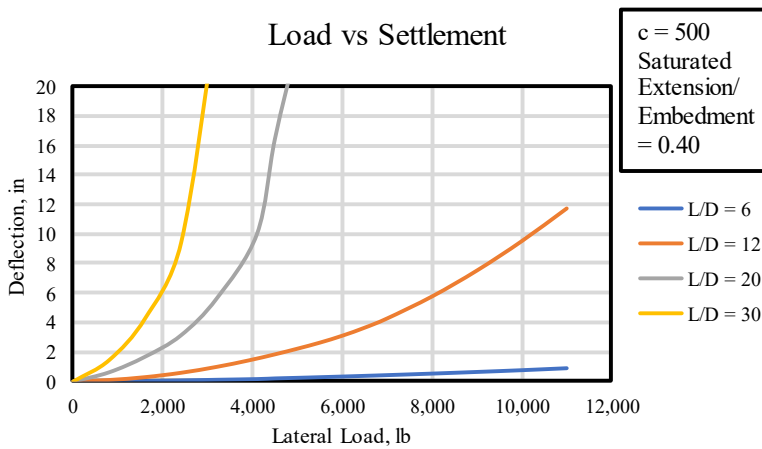
Figure C- 36 Lateral Load vs Horizontal Displacement for c = 500 psf (Saturated)
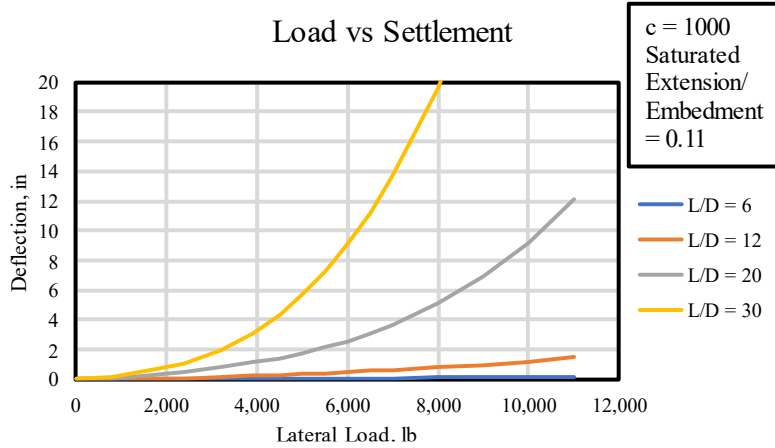
Figure C- 37 Lateral Load vs Horizontal Displacement for c = 1000 psf (Saturated)
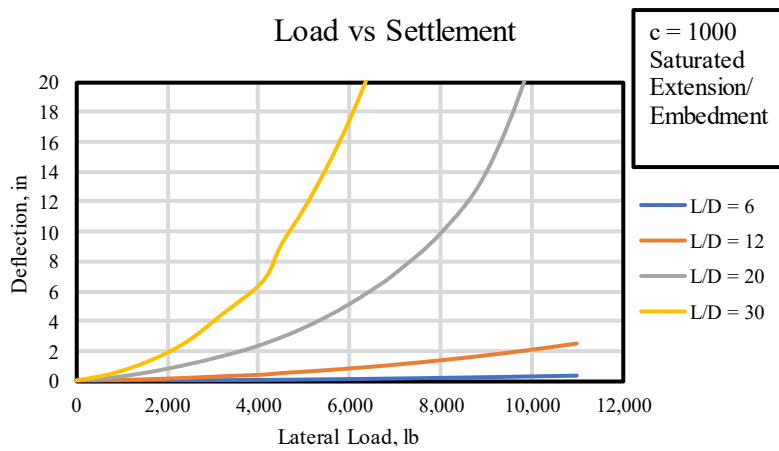
Figure C- 38 Lateral Load vs Horizontal Displacement for c = 1000 psf (Saturated)
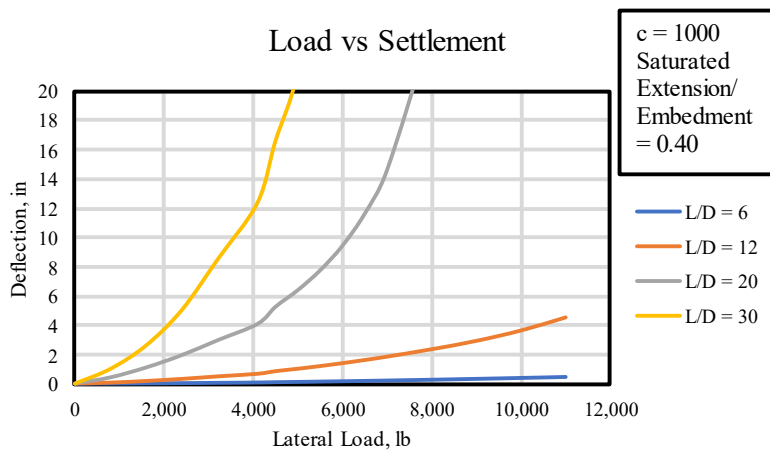
Figure C- 39 Lateral Load vs Horizontal Displacement for c = 1000 psf (Saturated)

Single Design Chart
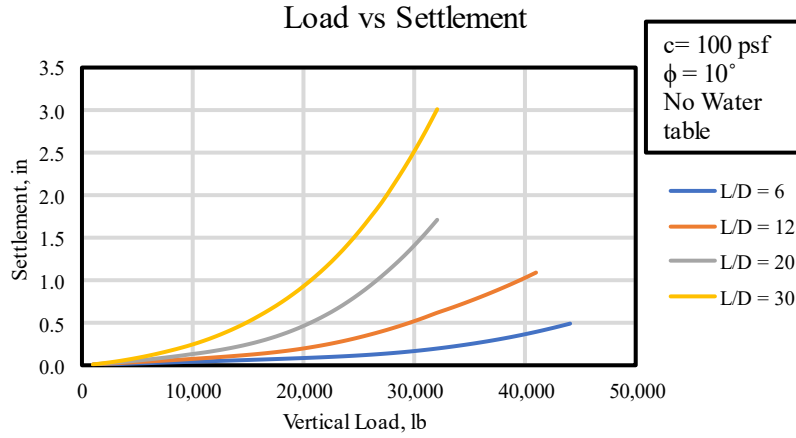
Figure C- 40 Design Chart for c = 100 psf and ϕ = 10˚, with no ground water
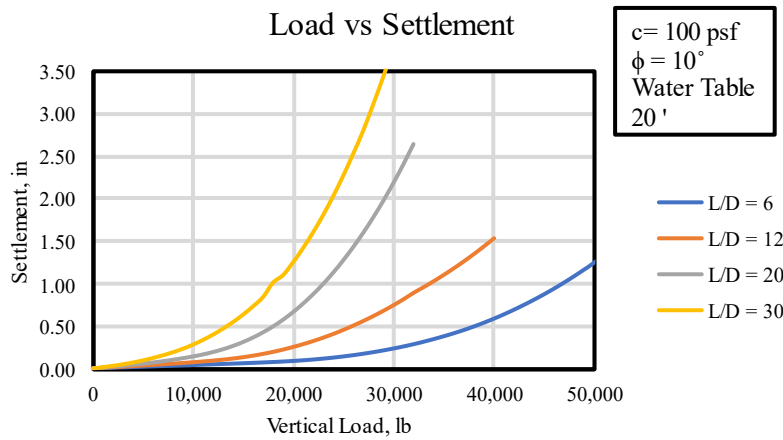
Figure C- 41 Design Chart for c = 100 psf and ϕ = 10˚, with ground water at 20 ft
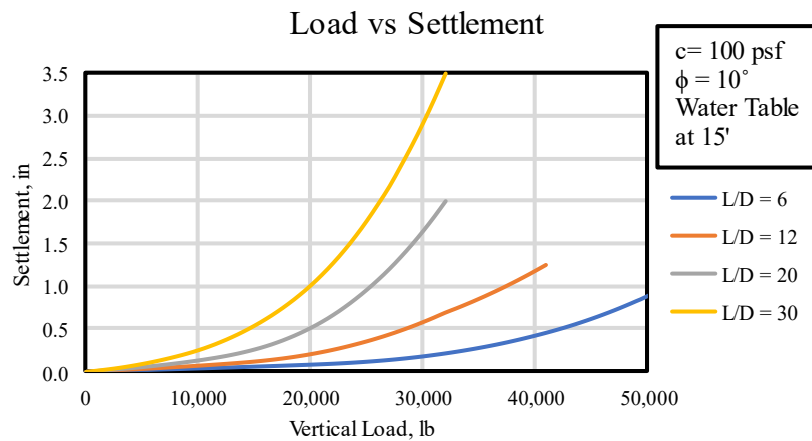
Figure C- 42 Design Chart for c = 100 psf and ϕ = 10˚, with ground water at 15 ft

318
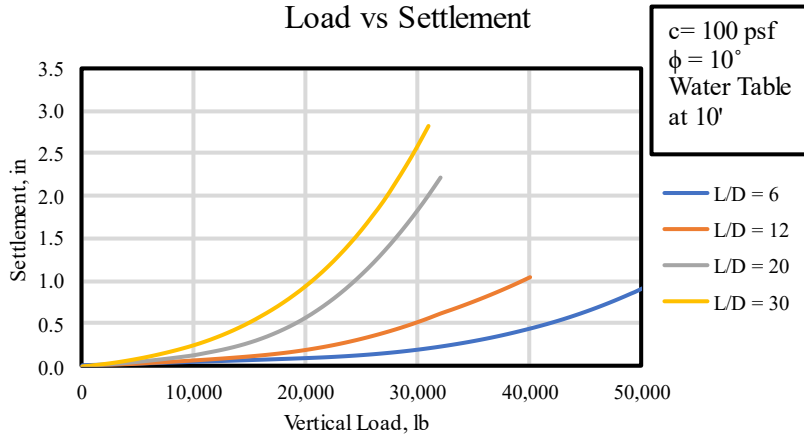
Figure C- 43 Design Chart for c = 100 psf and ϕ = 10˚, with ground water at 10 ft
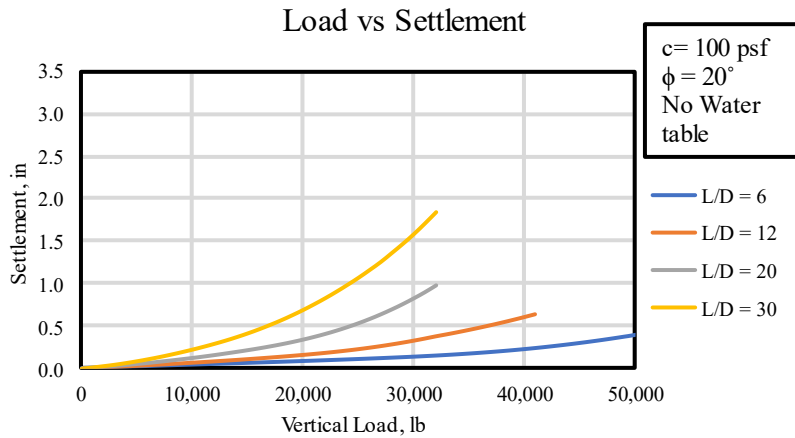
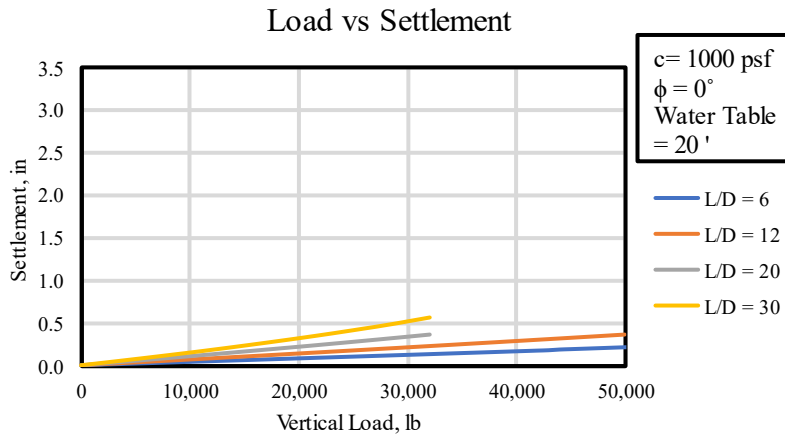Figure C- 44 Design Chart for c = 100 psf and ϕ = 20˚, with no ground water
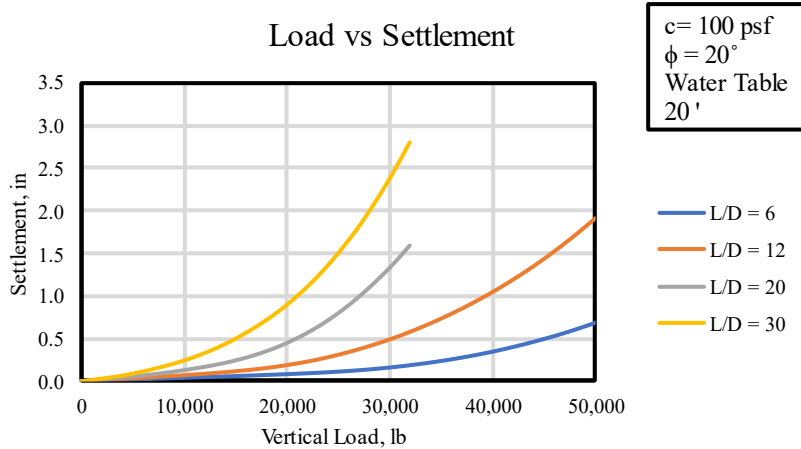
Figure C- 45 Design Chart for c = 100 psf and ϕ = 20˚, with ground water at 20 ft

319

Load vs Settlement
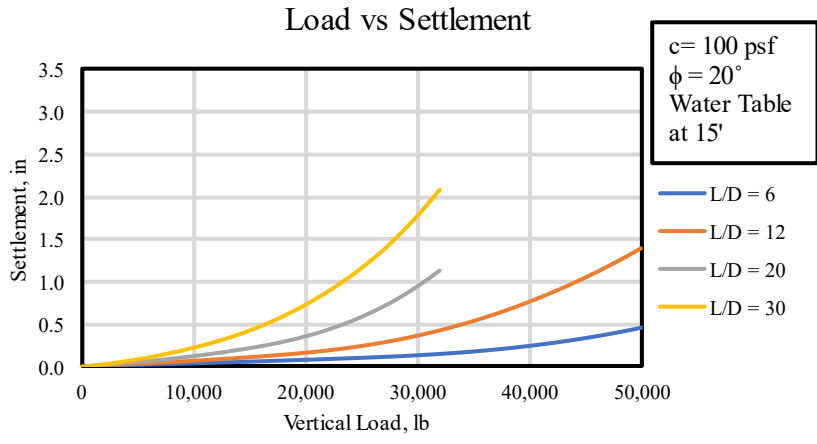
Figure C- 46 Design Chart for c = 100 psf and φ = 20˚, with ground water at 15 ft

Load vs Settlement
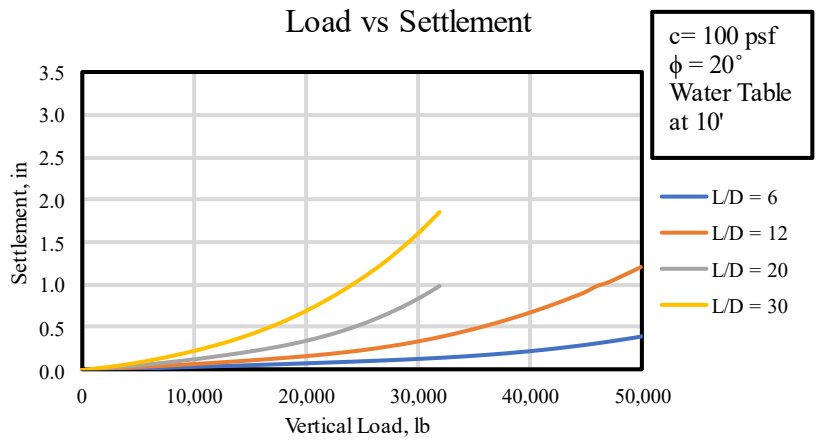
Figure C- 47 Design Chart for c = 100 psf and φ = 20˚, with ground water at 10 ft

Load vs Settlement
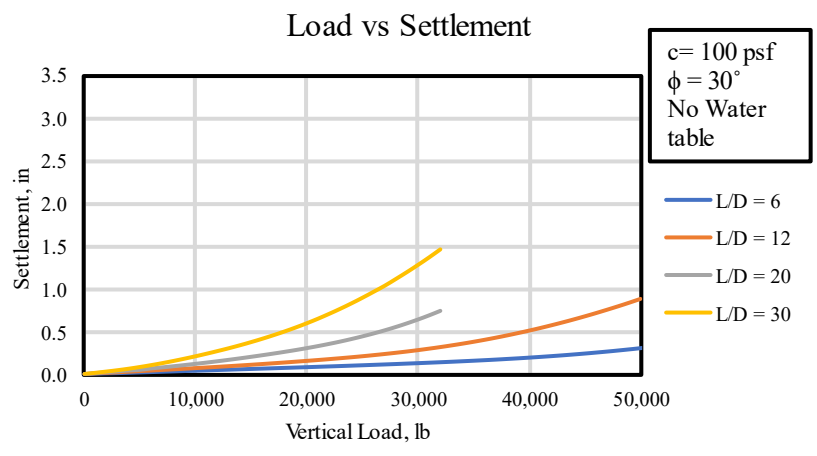
Figure C- 48 Design Chart for c = 100 psf and φ = 30˚, with no ground water
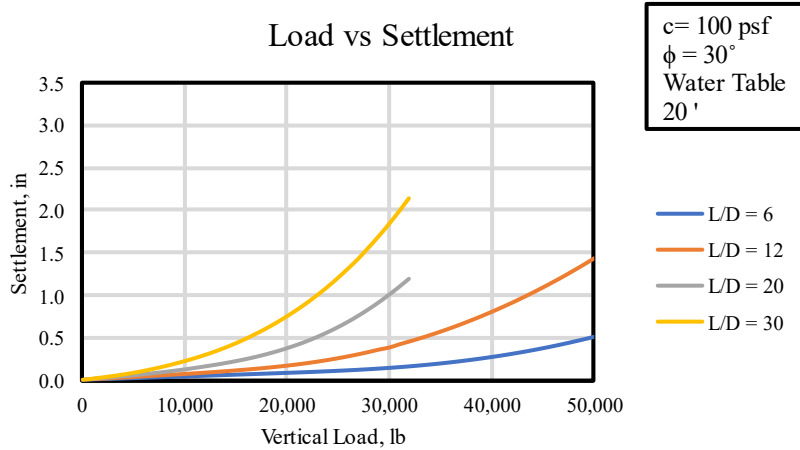
Figure C- 49 Design Chart for c = 100 psf and φ = 30˚, with ground water at 20 ft
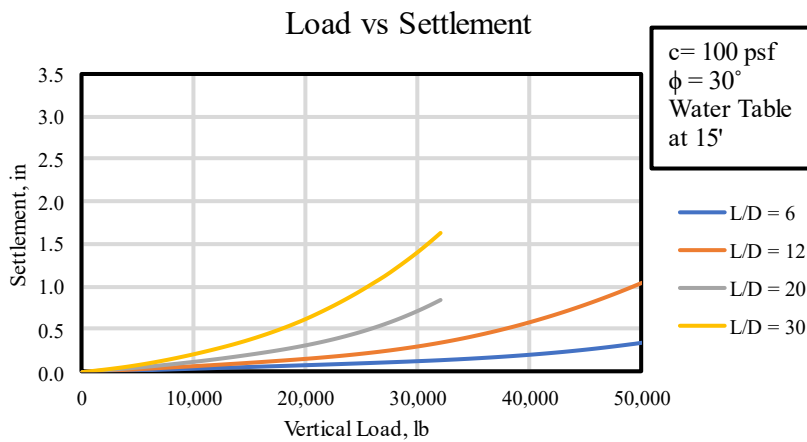
Figure C- 50 Design Chart for c = 100 psf and φ = 30˚, with ground water at 15 ft
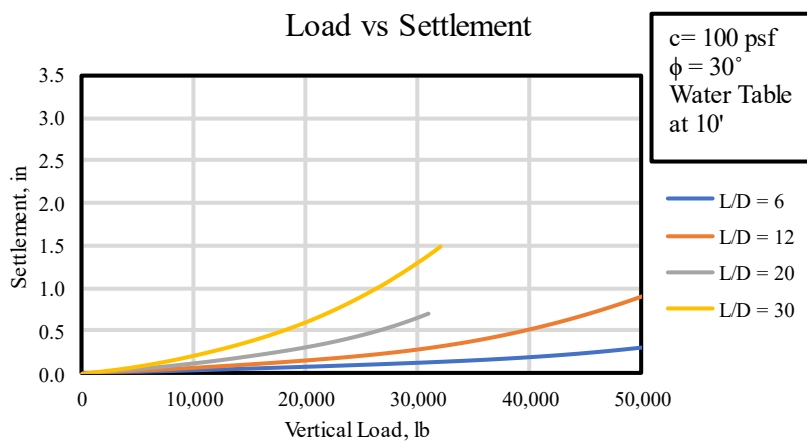
Figure C- 51 Design Chart for c = 100 psf and φ = 30˚, with ground water at 10 ft
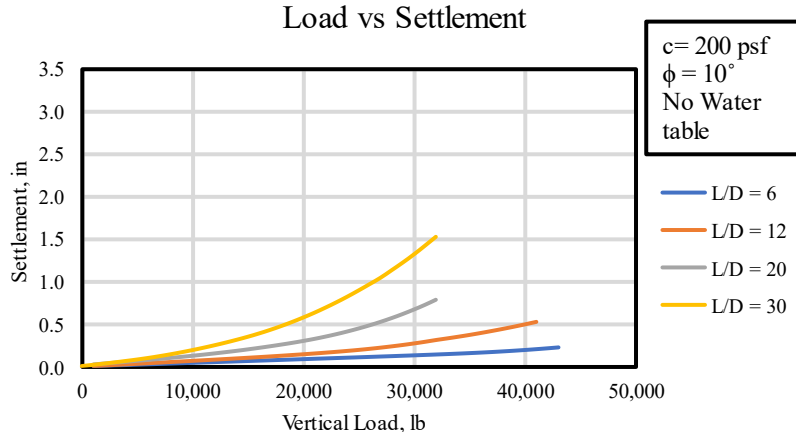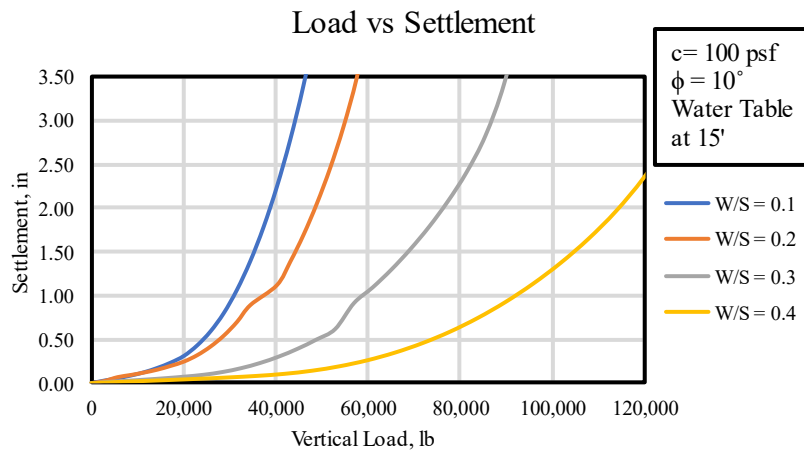
Figure C- 52 Design Chart for c = 200 psf and ϕ = 10˚, with no ground water
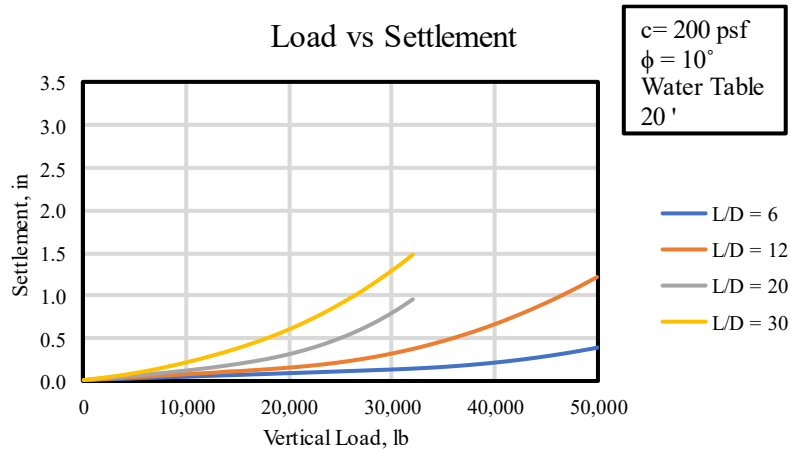
Figure C- 53 Design Chart for c = 200 psf and ϕ = 10˚, with ground water at 20 ft
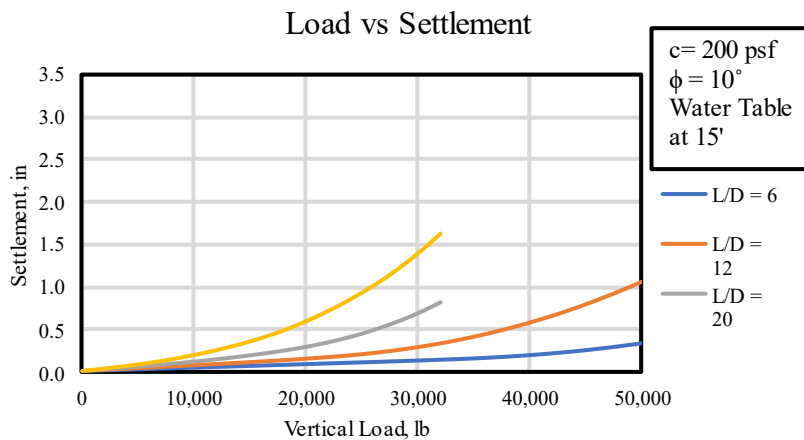
Figure C- 54 Design Chart for c = 200 psf and ϕ = 10˚, with ground water at 15 ft
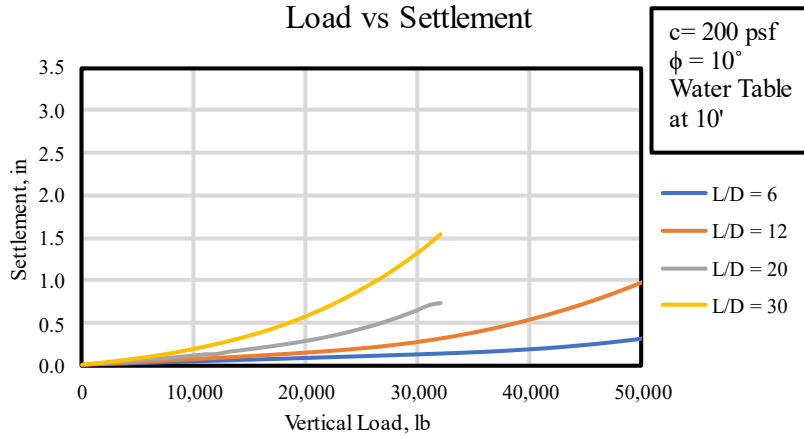
Figure C- 55 Design Chart for c = 200 psf and ϕ = 10˚, with ground water at 10 ft
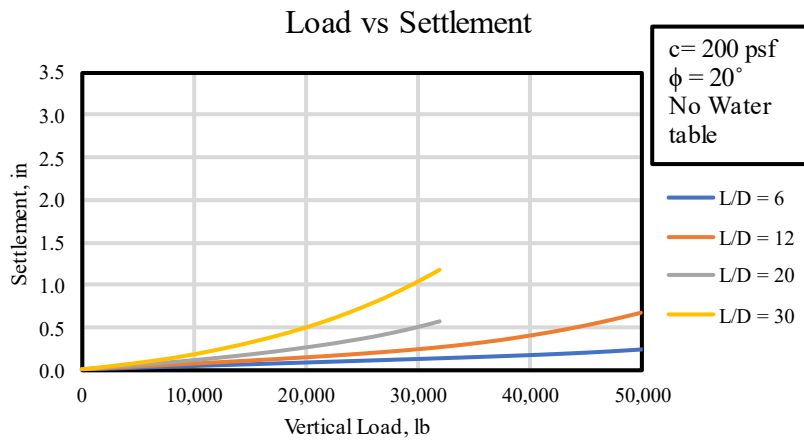
Figure C- 56 Design Chart for c = 200 psf and ϕ = 20˚, with no ground water
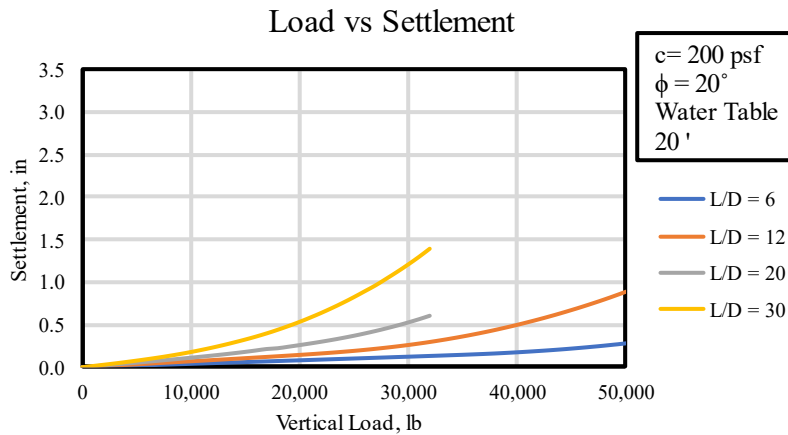
Figure C- 57 Design Chart for c = 200 psf and ϕ = 20˚, with ground water at 20 ft
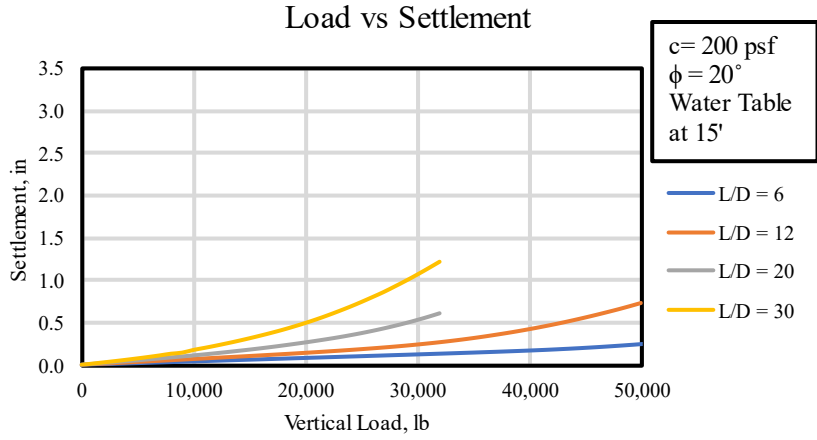
Figure C- 58 Design Chart for c = 200 psf and φ = 20˚, with ground water at 15 ft
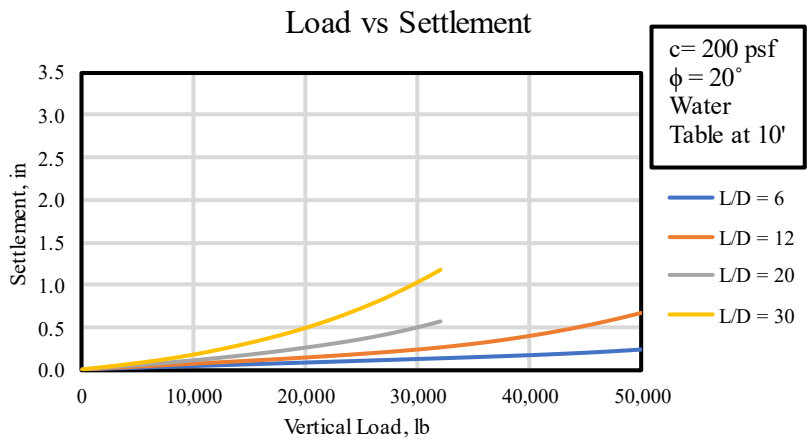
Figure C- 59 Design Chart for c = 200 psf and φ = 20˚, with ground water at 10 ft
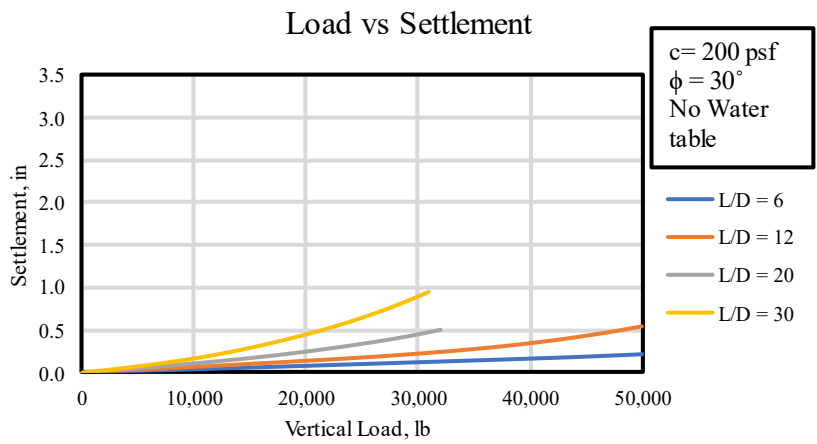
Figure C- 60 Design Chart for c = 200 psf and φ = 30˚, with no ground water

Figure C- 61 Design Chart for c = 200 psf and ϕ = 30˚, with ground water at 20 ft
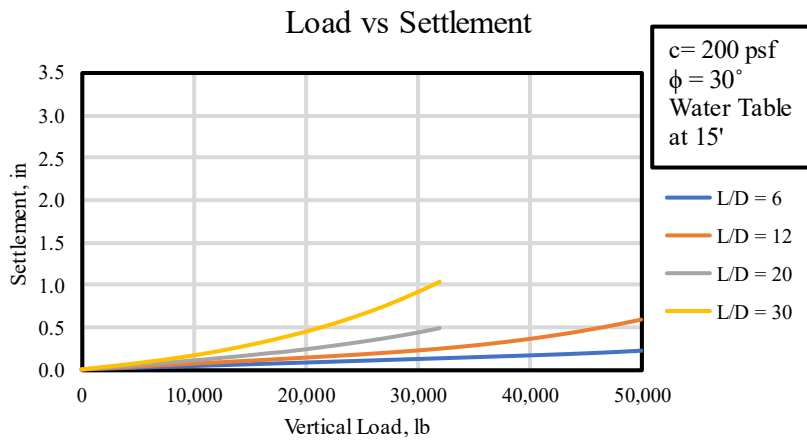
Figure C- 62 Design Chart for c = 200 psf and ϕ = 30˚, with ground water at 15 ft
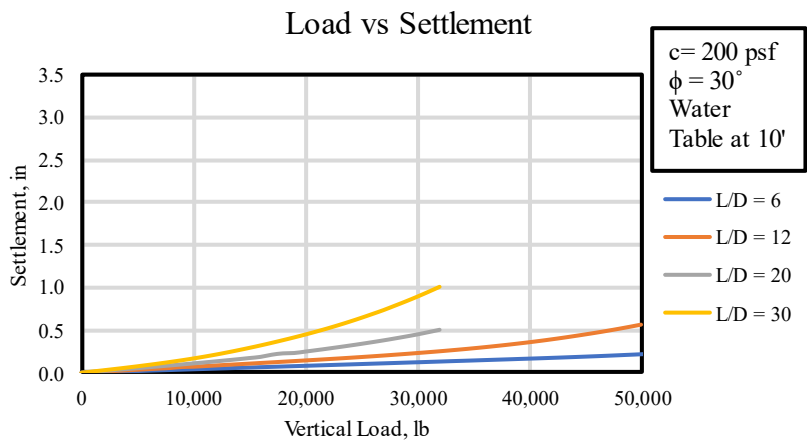
Figure C- 63 Design Chart for c = 200 psf and ϕ = 20˚, with ground water at 10 ft
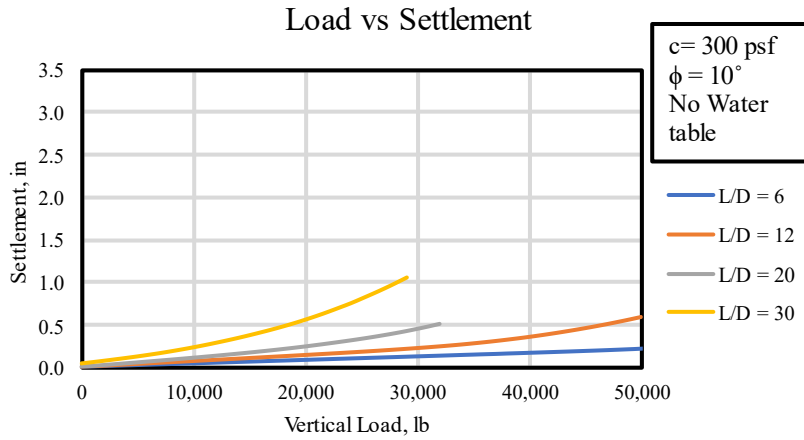
Figure C- 64 Design Chart for c = 300 psf and φ = 10˚, with no ground water
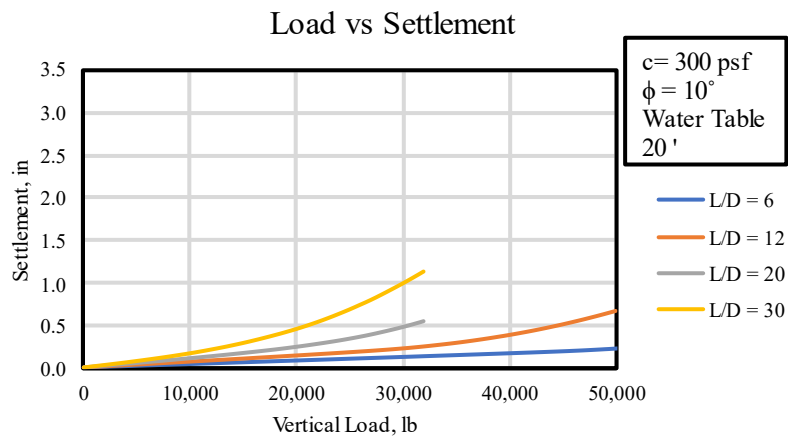
Figure C- 65 Design Chart for c = 300 psf and φ = 10˚, with ground water at 20 ft
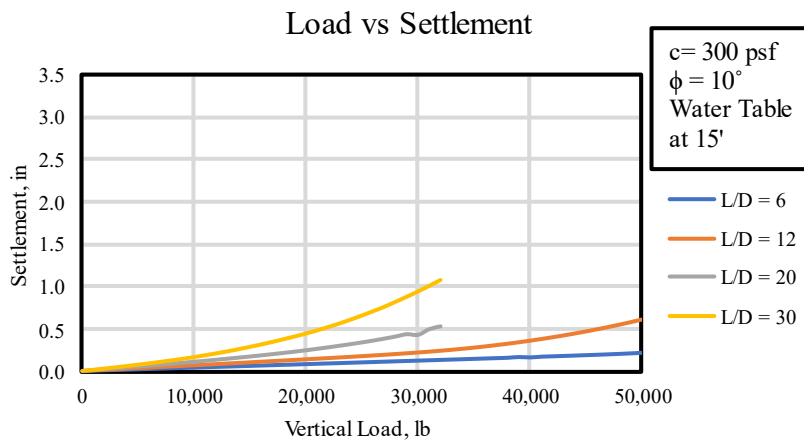
Figure C- 66 Design Chart for c = 300 psf and φ = 10˚, with ground water at 15 ft
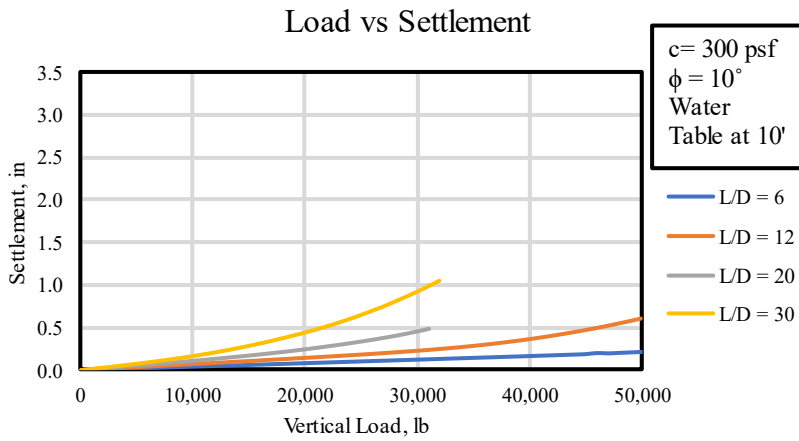
Figure C- 67 Design Chart for c = 300 psf and ϕ = 10˚, with ground water at 10 ft
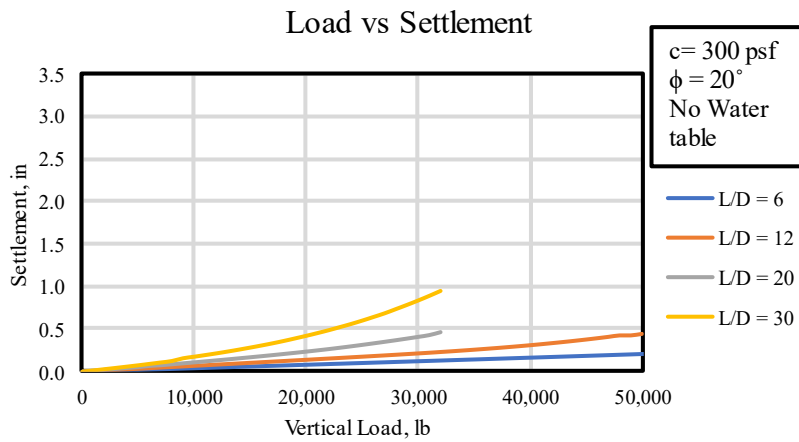
Figure C- 68 Design Chart for c = 300 psf and ϕ = 20˚, with no ground water
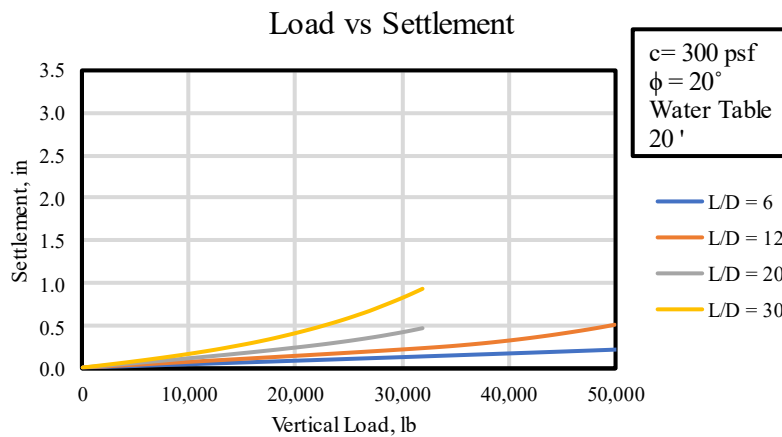
Figure C- 69 Design Chart for c = 300 psf and ϕ = 20˚, with ground water at 20 ft

Load vs Settlement

c= 300 psf
$\phi = 20°$
Water Table
at 15'

— L/D = 6
— L/D = 12
— L/D = 20
— L/D = 30
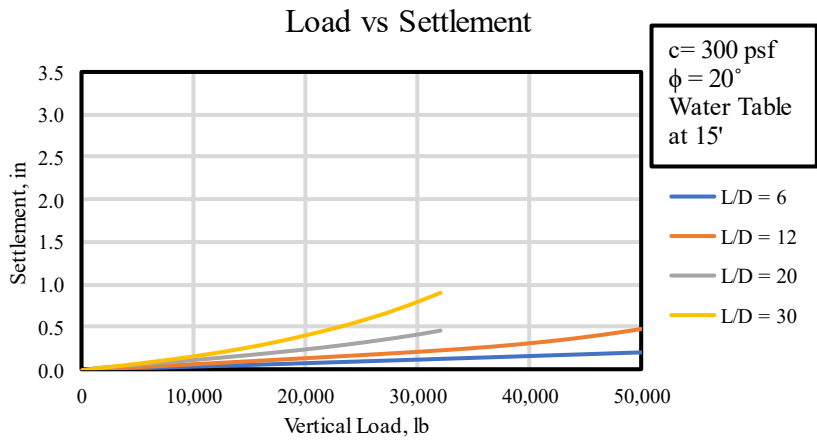
Figure C- 70 Design Chart for c = 300 psf and $\phi = 20°$, with ground water at 15 ft

Load vs Settlement

c= 300 psf
$\phi = 20°$
Water
Table at 10'

— L/D = 6
— L/D = 12
— L/D = 20
— L/D = 30
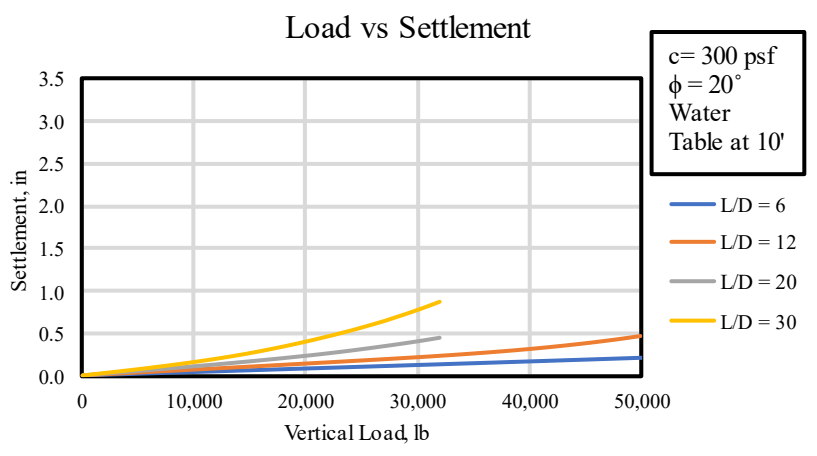
Figure C- 71 Design Chart for c = 300 psf and $\phi = 20°$, with ground water at 10 ft

Load vs Settlement

c= 300 psf
$\phi = 30°$
No Water
table

— L/D = 6
— L/D = 12
— L/D = 20
— L/D = 30
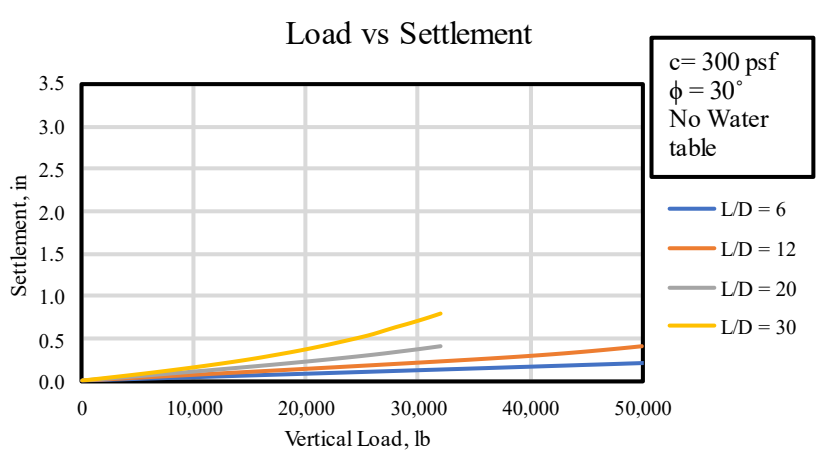
Figure C- 72 Design Chart for c = 300 psf and $\phi = 30°$, with no ground water
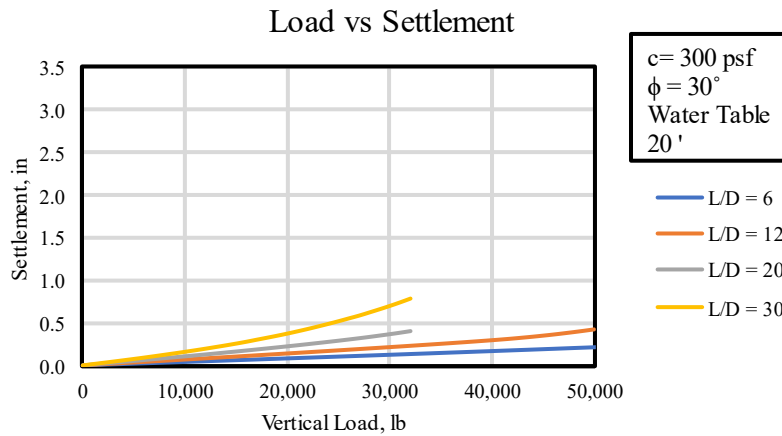
Figure C- 73 Design Chart for c = 300 psf and ϕ = 30˚, with ground water at 20 ft
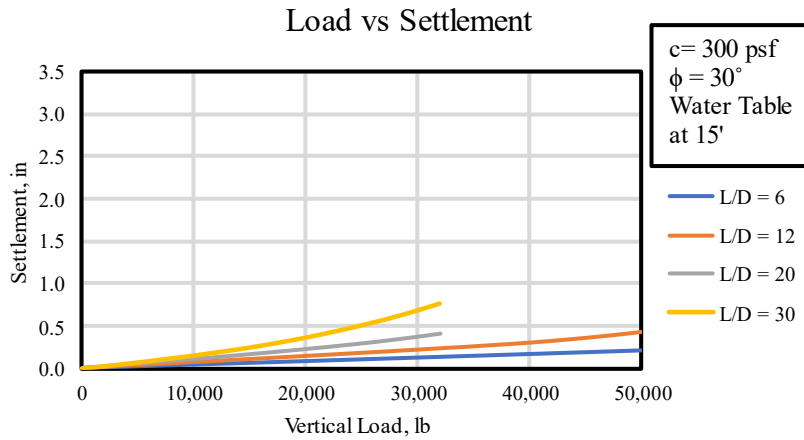
Figure C- 74 Design Chart for c = 300 psf and ϕ = 30˚, with ground water at 15 ft
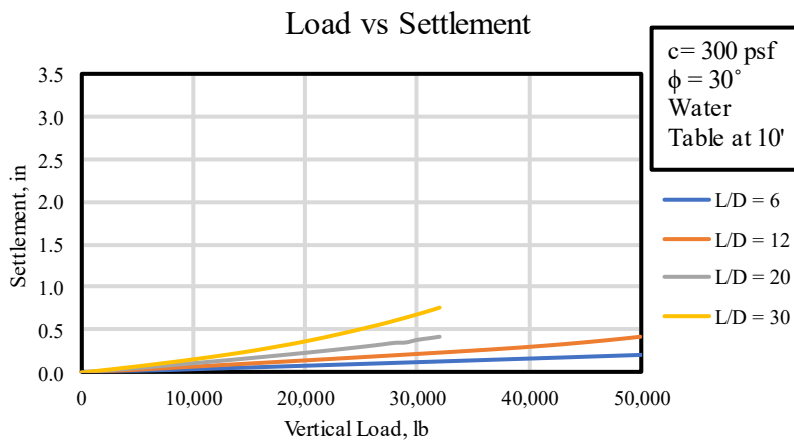
Figure C- 75 Design Chart for c = 300 psf and ϕ = 30˚, with ground water at 10 ft
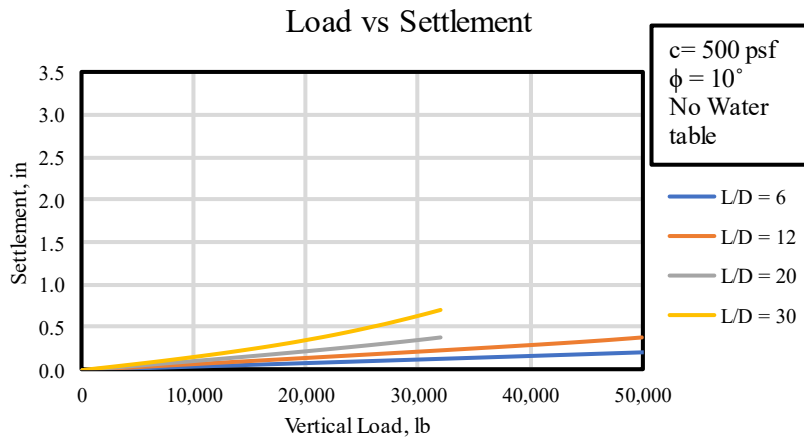
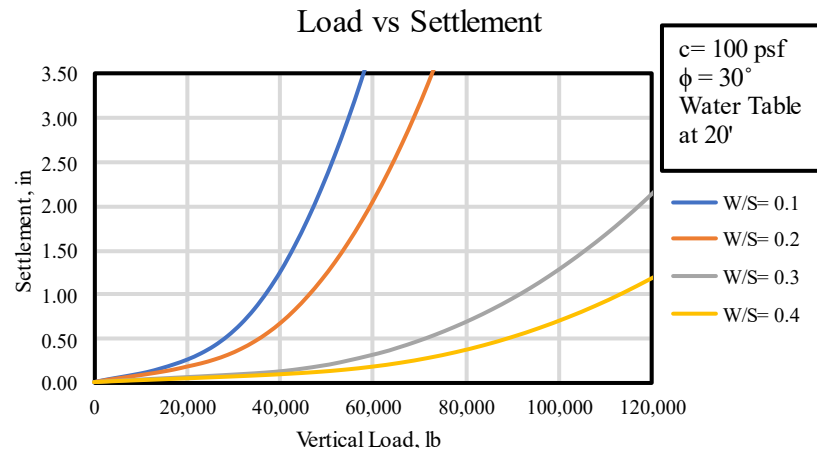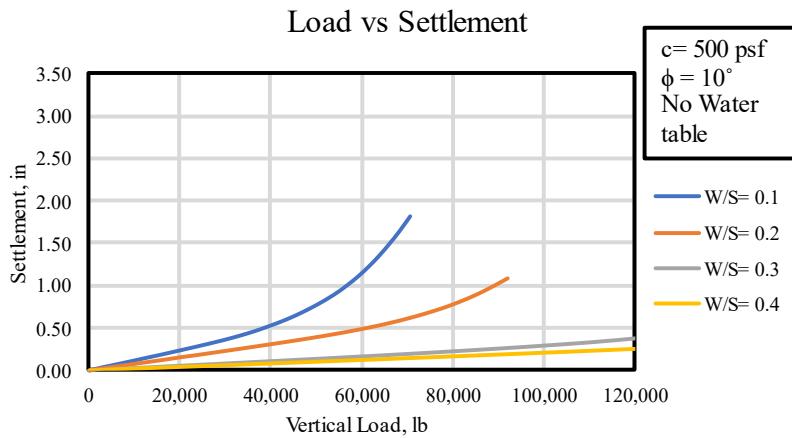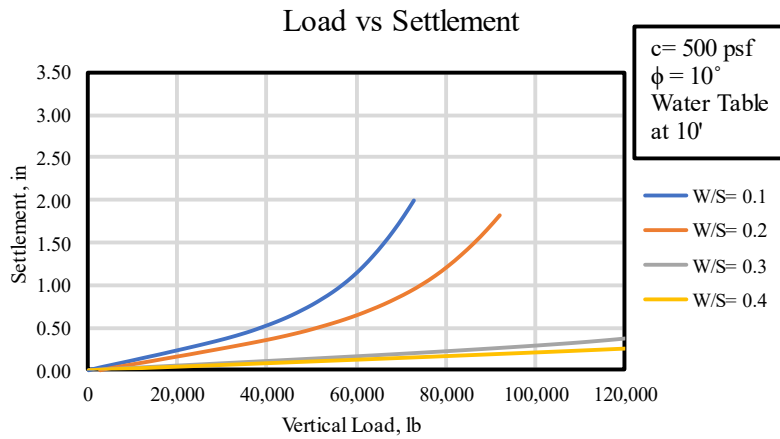Figure C- 76 Design Chart for c = 500 psf and ϕ = 10˚, with no ground water
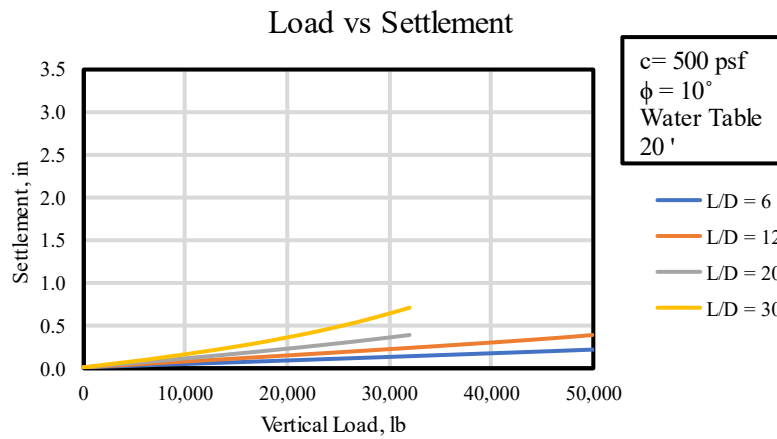
Figure C- 77 Design Chart for c = 500 psf and ϕ = 10˚, with ground water at 20 ft
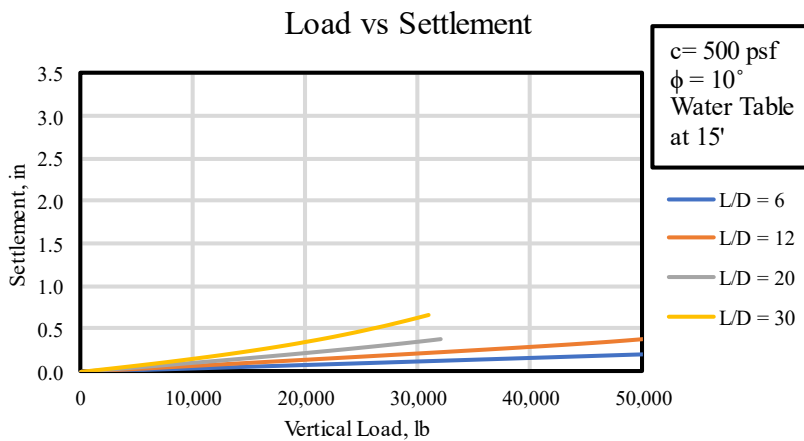
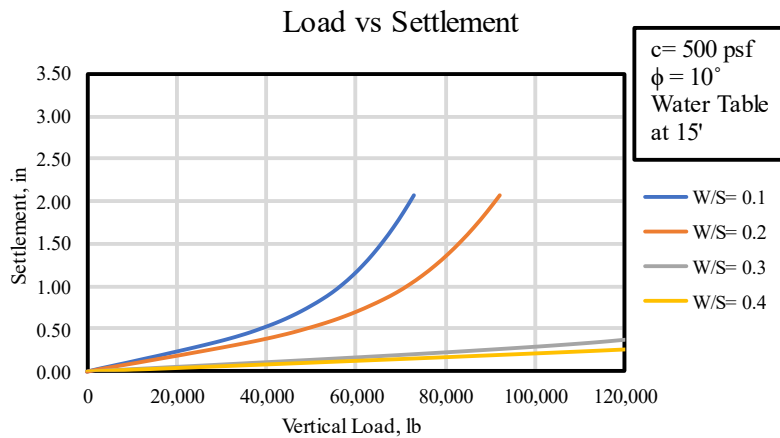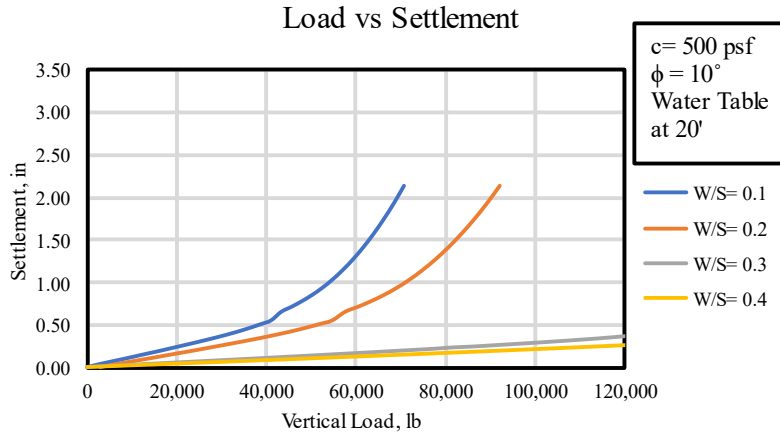Figure C- 78 Design Chart for c = 500 psf and ϕ = 10˚, with ground water at 15 ft

Load vs Settlement

c= 500 psf
φ = 10°
Water Table at 10'

- L/D = 6
- L/D = 12
- L/D = 20
- L/D = 30
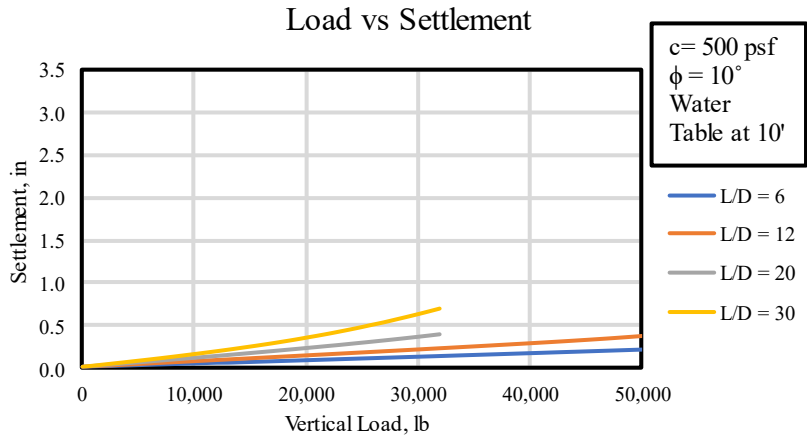
Figure C- 79 Design Chart for c = 500 psf and φ = 10˚, with ground water at 10 ft

Load vs Settlement

c= 500 psf
φ = 20°
No Water table

- L/D = 6
- L/D = 12
- L/D = 20
- L/D = 30
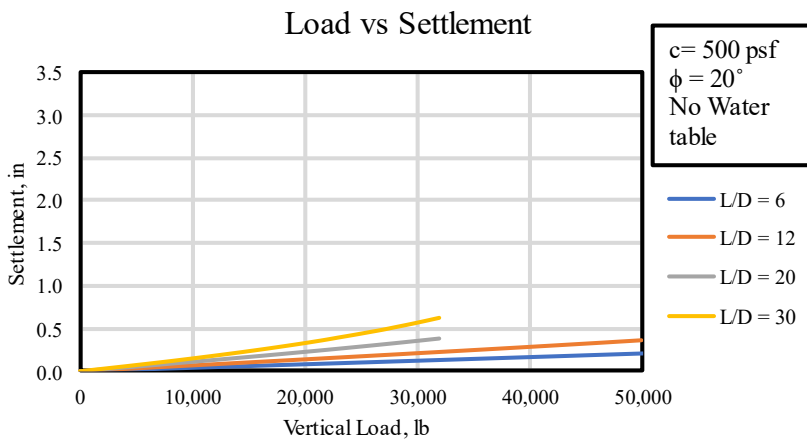
Figure C- 80 Design Chart for c = 500 psf and φ = 20˚, with no ground water

Load vs Settlement

c= 500 psf
φ = 20°
Water Table 20 '

- L/D = 6
- L/D = 12
- L/D = 20
- L/D = 30
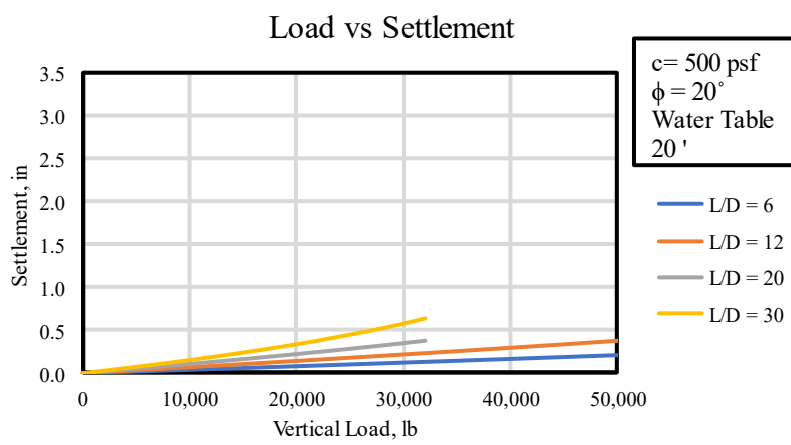
Figure C- 81 Design Chart for c = 500 psf and φ = 20˚, with ground water at 20 ft

331
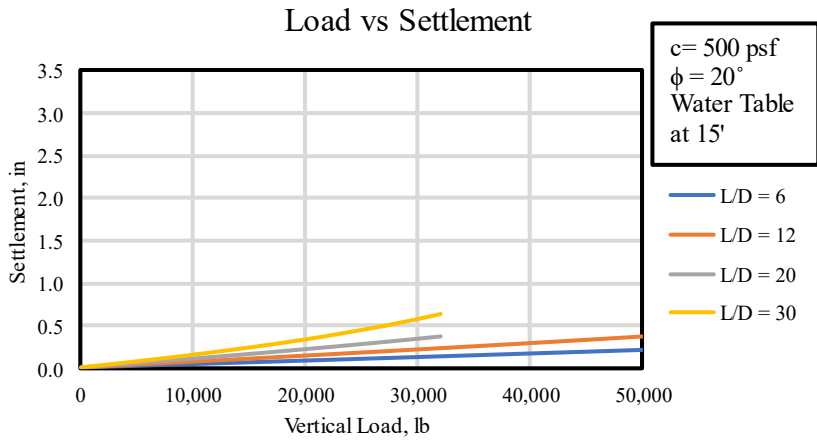
Figure C- 82 Design Chart for c = 500 psf and φ = 20˚, with ground water at 15 ft
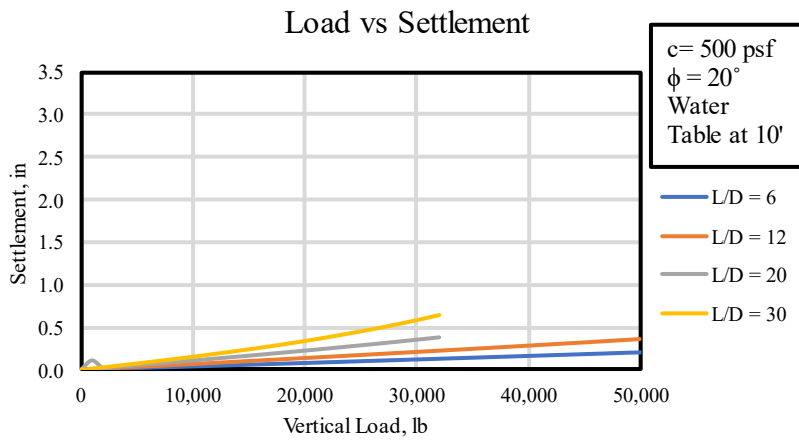
Figure C- 83 Design Chart for c = 500 psf and φ = 20˚, with ground water at 10 ft
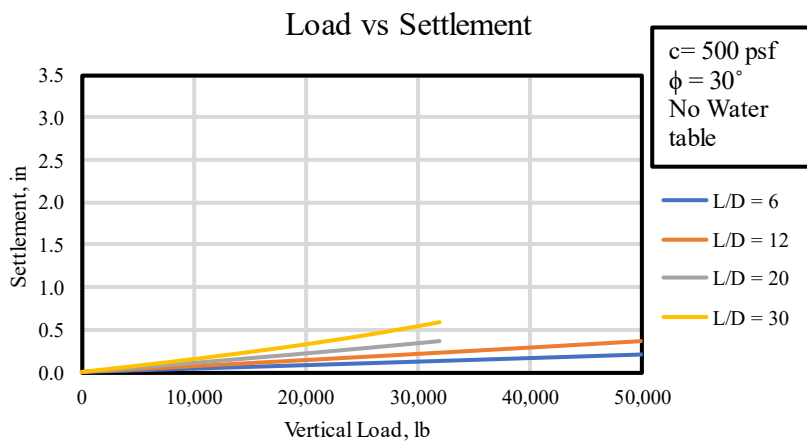
Figure C- 84 Design Chart for c = 500 psf and φ = 30˚, with no ground water

Figure C- 85 Design Chart for c = 500 psf and ϕ = 30˚, with ground water at 20 ft
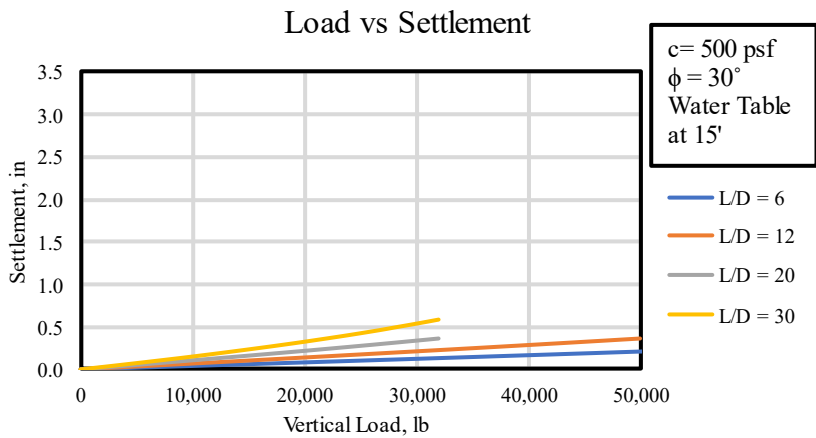
Figure C- 86 Design Chart for c = 500 psf and ϕ = 30˚, with ground water at 15 ft
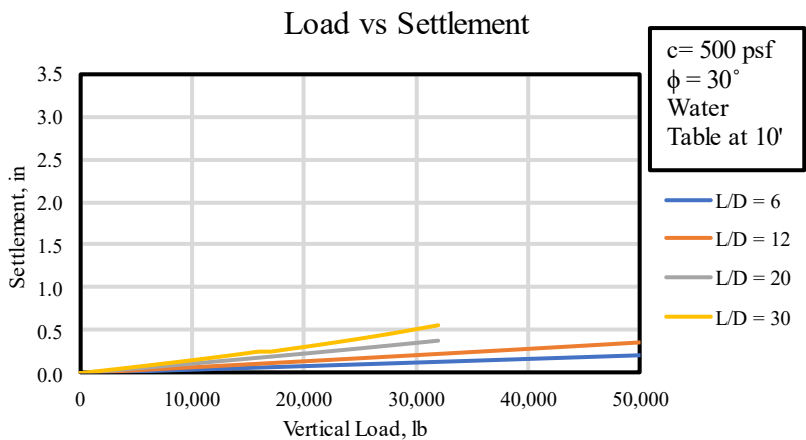
Figure C- 87 Design Chart for c = 500 psf and ϕ = 30˚, with ground water at 10 ft

333
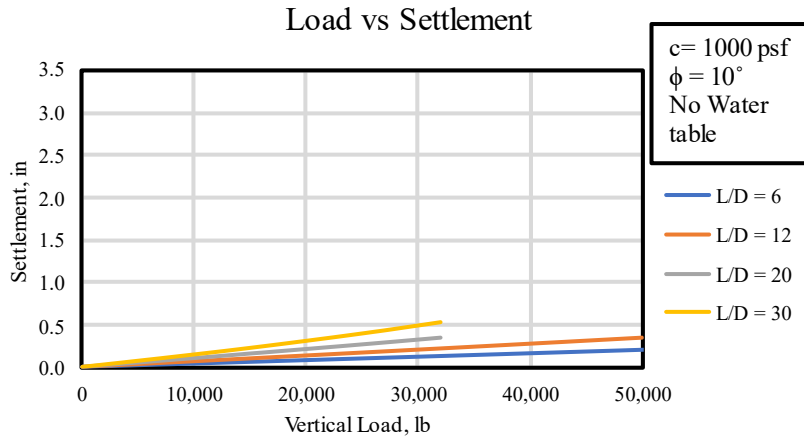
Figure C- 88 Design Chart for c = 1000 psf and φ = 10˚, with no ground water
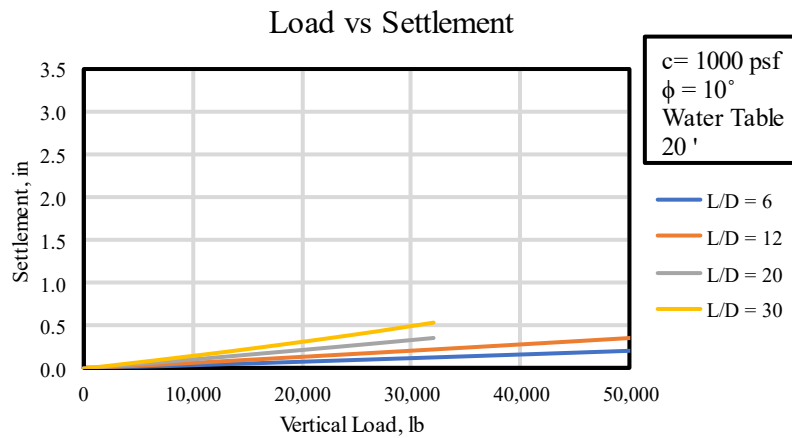
Figure C- 89 Design Chart for c = 1000 psf and φ = 10˚, with ground water at 20 ft
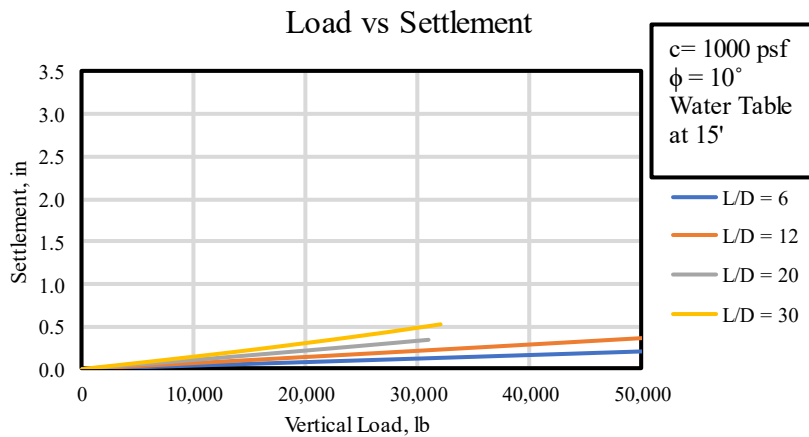
Figure C- 90 Design Chart for c = 1000 psf and φ = 10˚, with ground water at 15 ft
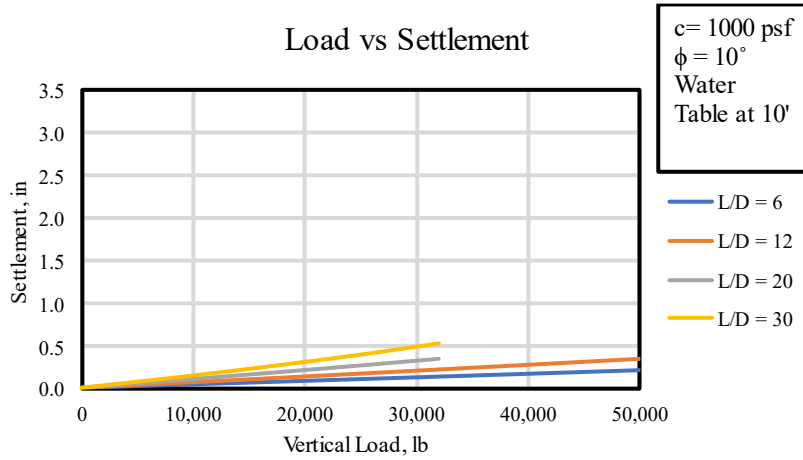
Figure C- 91 Design Chart for c = 1000 psf and φ = 10˚, with ground water at 10 ft
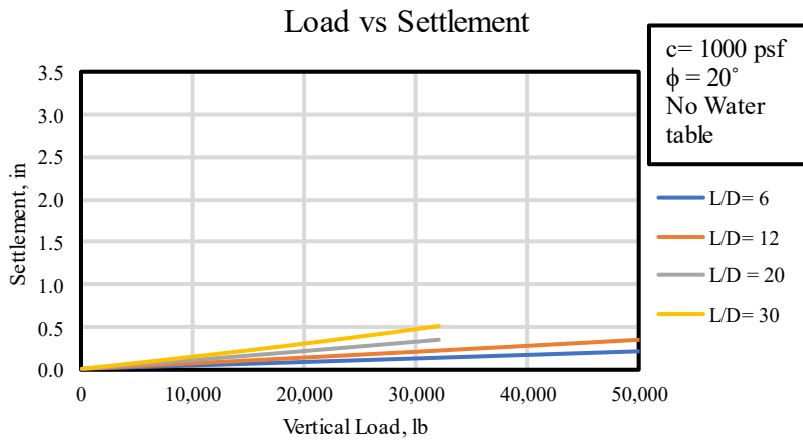
Figure C- 92 Design Chart for c = 1000 psf and φ = 20˚, with no ground water
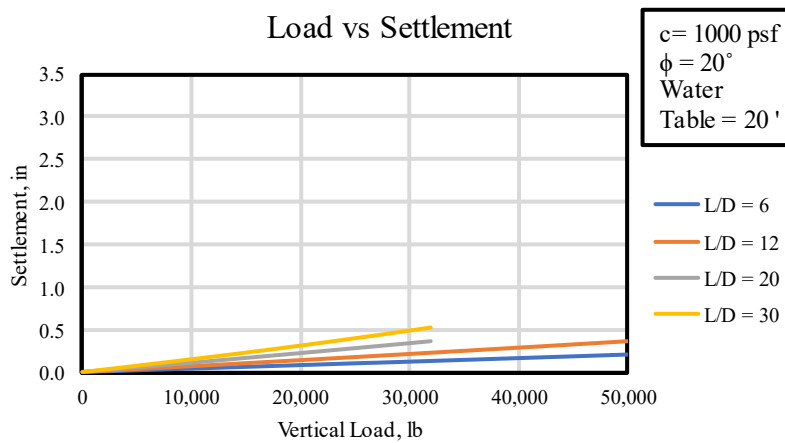
Figure C- 93 Design Chart for c = 1000 psf and φ = 20˚, with ground water at 20 ft
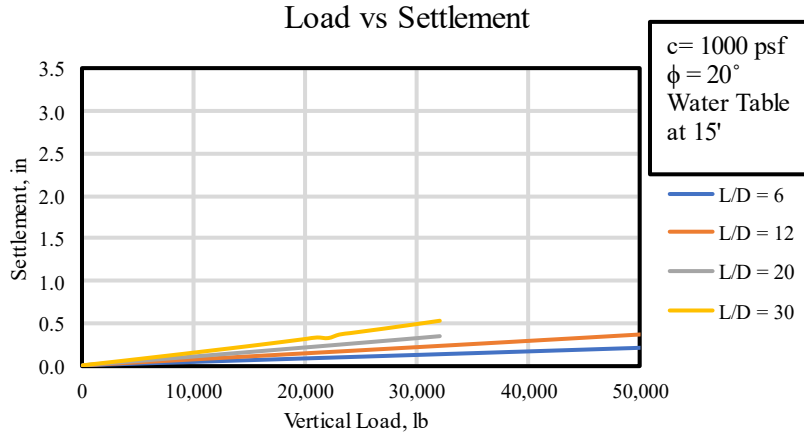
Figure C- 94 Design Chart for c = 1000 psf and ϕ = 20˚, with ground water at 15 ft
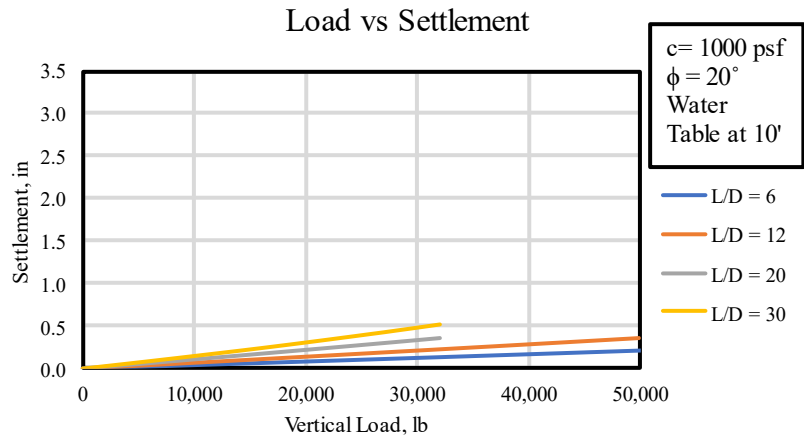
Figure C- 95 Design Chart for c = 1000 psf and ϕ = 20˚, with ground water at 10 ft
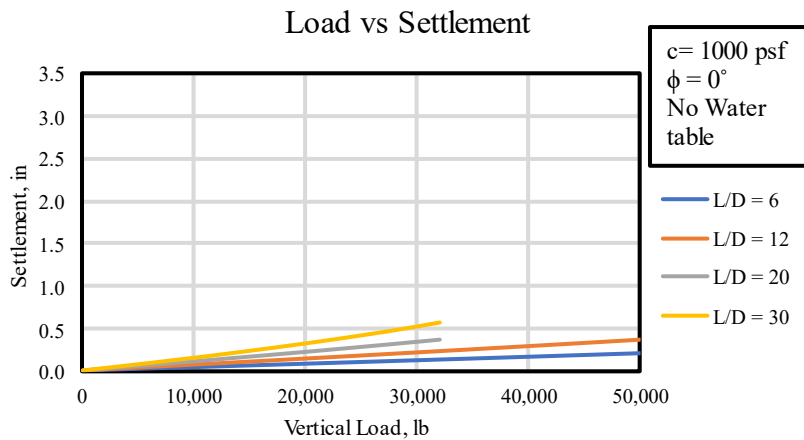
Figure C- 96 Design Chart for c = 1000 psf and ϕ = 0˚, with no ground water

Figure C- 97 Design Chart for c = 1000 psf and ϕ = 0˚, with ground water at 20 ft
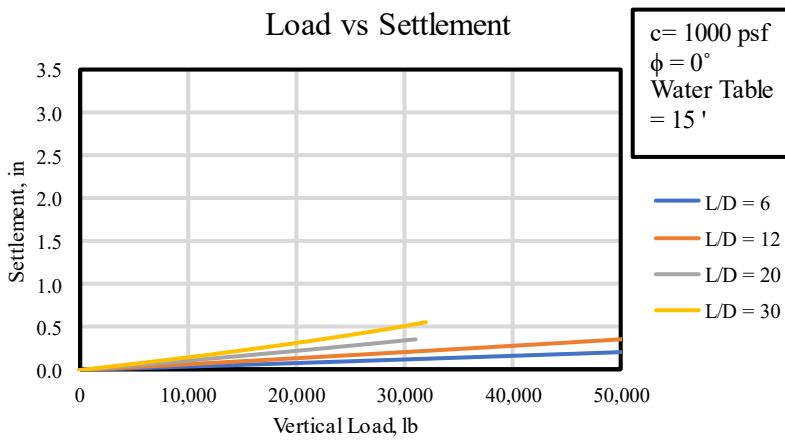
Figure C- 98 Design Chart for c = 1000 psf and ϕ = 0˚, with ground water at 15 ft
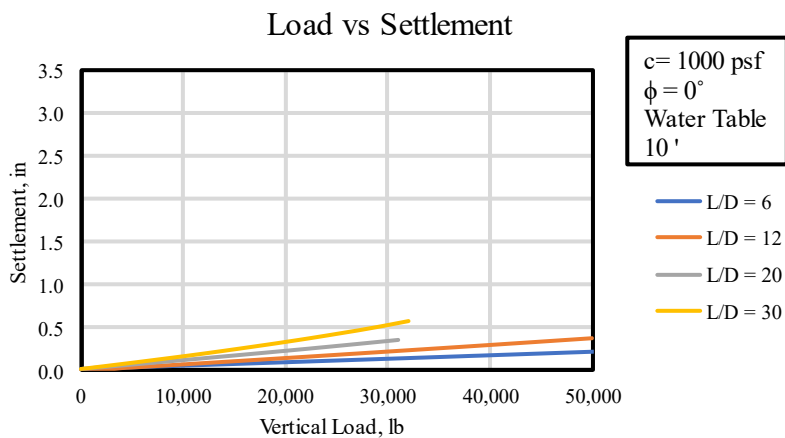
Figure C- 99 Design Chart for c = 1000 psf and ϕ = 0˚, with ground water at 10 ft

Group Design Chart
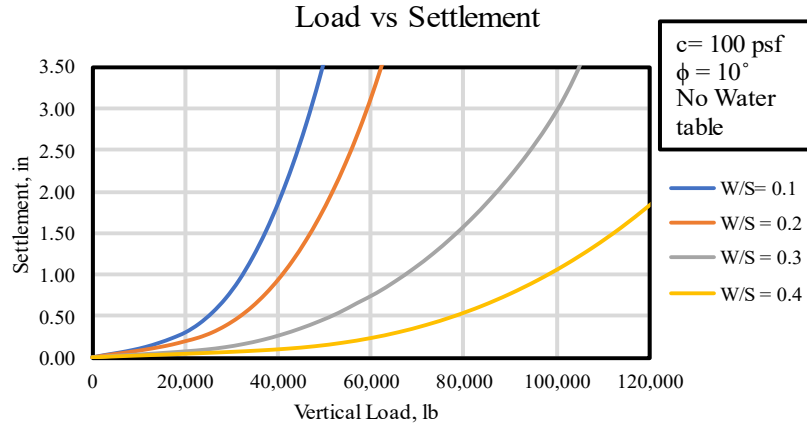
Figure C- 100 Design Chart for c = 100 psf and ϕ = 10˚, with no ground water
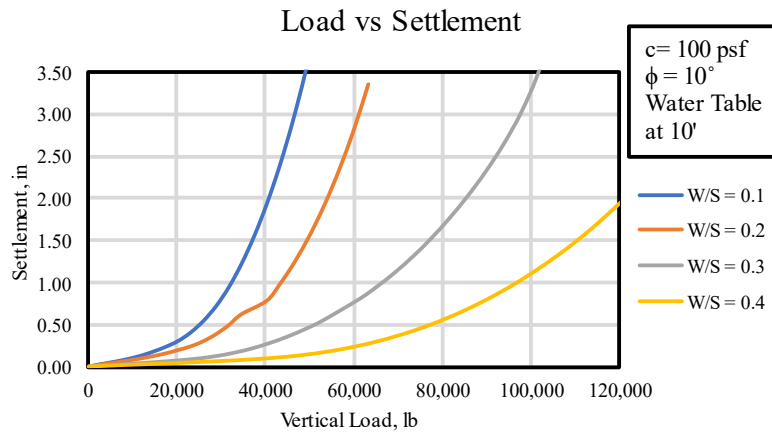
Figure C- 101 Design Chart for c = 100 psf and ϕ = 10˚, with ground water at 10 ft

Figure C- 102 Design Chart for c = 100 psf and ϕ = 10˚, with ground water at 15 ft

339
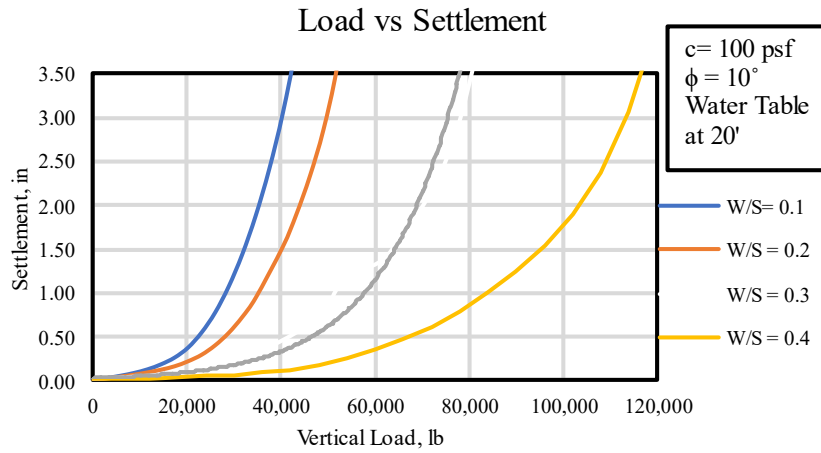
Figure C- 103 Design Chart for c = 100 psf and φ = 10˚, with ground water at 20 ft
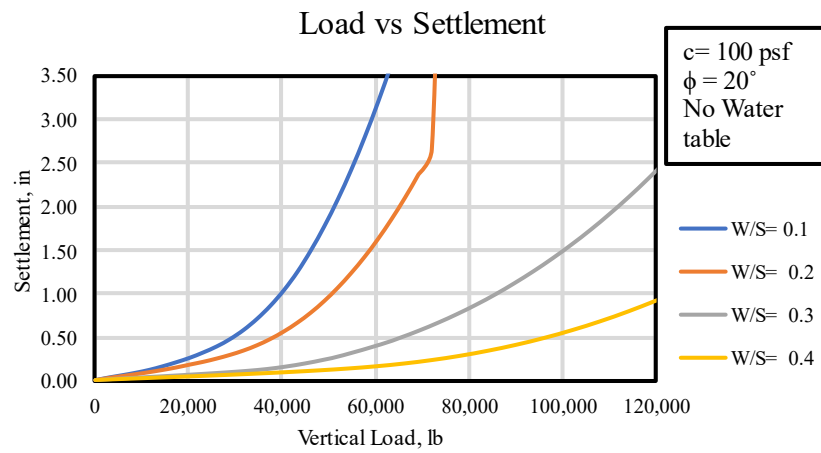
Figure C- 104 Design Chart for c = 100 psf and φ = 20˚, with no ground water
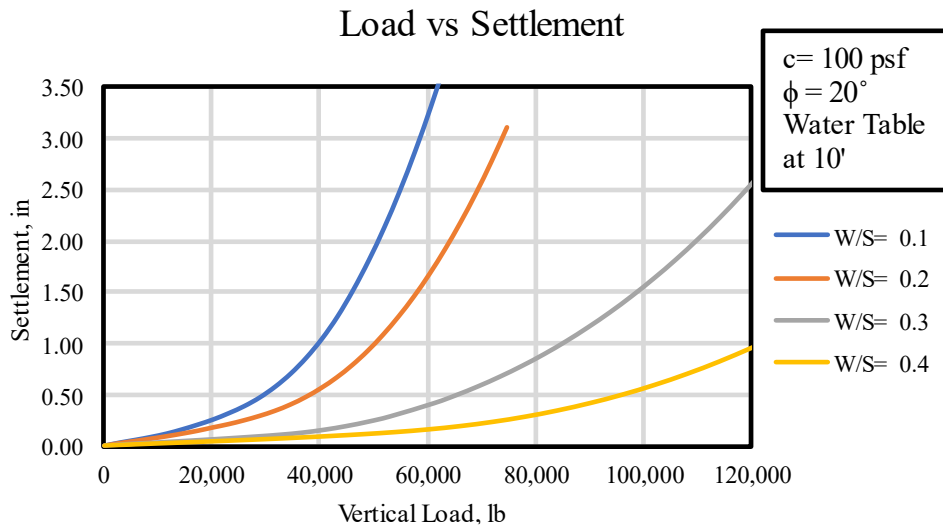
Figure C- 105 Design Chart for c = 100 psf and φ = 20˚, with ground water at 10 ft
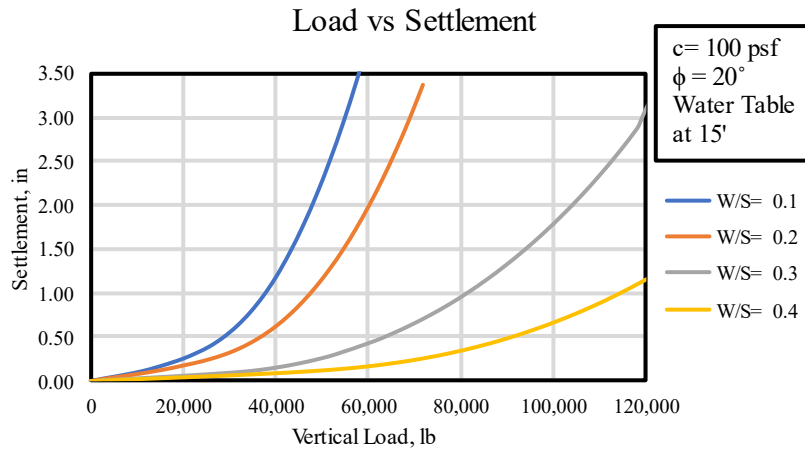
Figure C- 106 Design Chart for c = 100 psf and ϕ = 20˚, with ground water at 15 ft
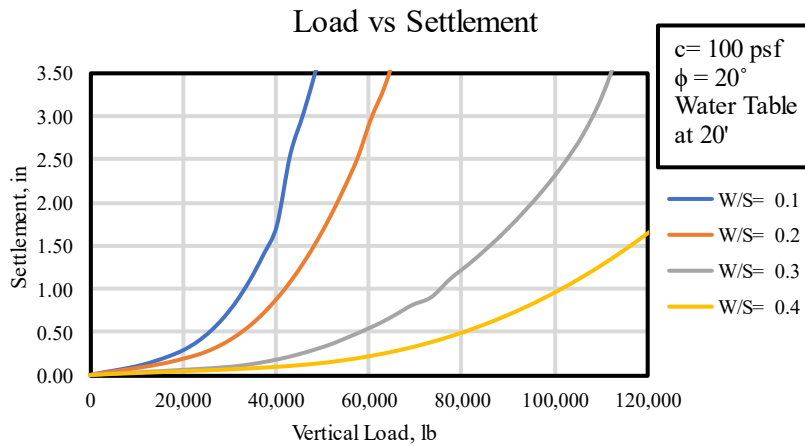
Figure C- 107 Design Chart for c = 100 psf and ϕ = 20˚, with ground water at 20 ft
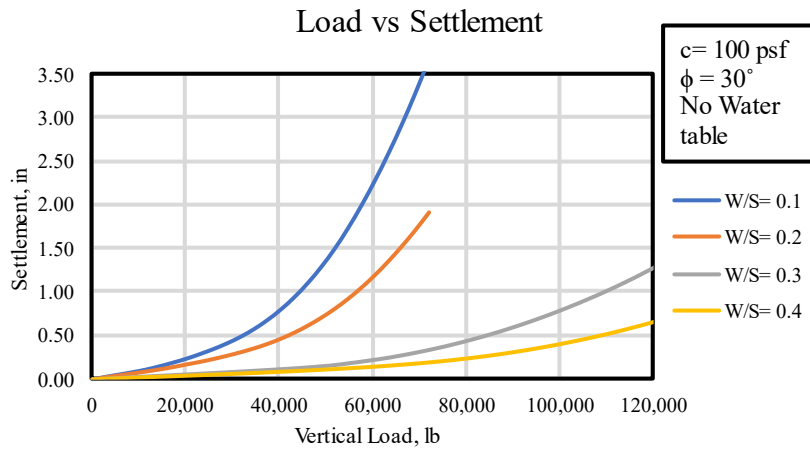
Figure C- 108 Design Chart for c = 100 psf and ϕ = 30˚, with no ground water
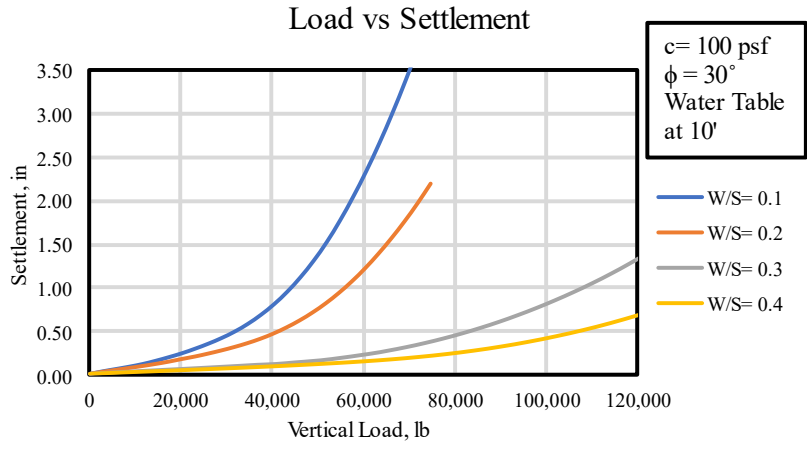
Figure C- 109 Design Chart for c = 100 psf and φ = 30˚, with ground water at 10 ft
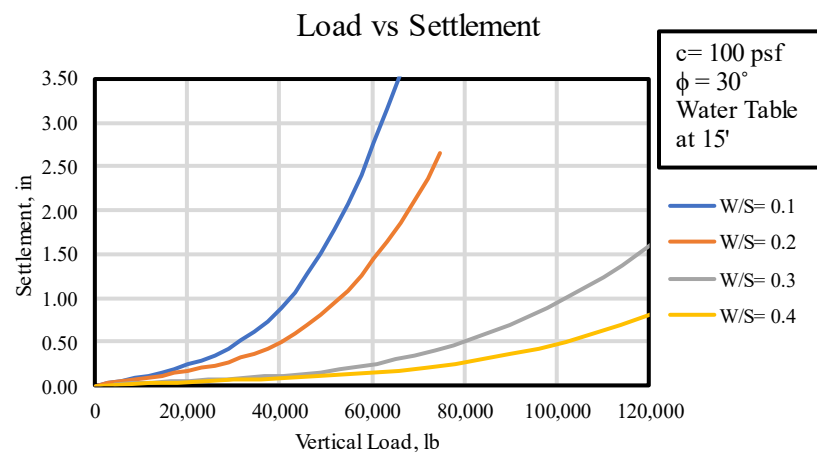
Figure C- 110 Design Chart for c = 100 psf and φ = 30˚, with ground water at 15 ft

Figure C- 111 Design Chart for c = 100 psf and φ = 30˚, with ground water at 20 ft

Figure C- 112 Design Chart for c = 500 psf and φ = 10˚, with no ground water

Figure C- 113 Design Chart for c = 500 psf and φ = 10˚, with ground water at 10 ft

Figure C- 114 Design Chart for c = 500 psf and φ = 10˚, with ground water at 15 ft

343

Figure C- 115 Design Chart for c = 500 psf and ϕ = 10˚, with ground water at 20 ft
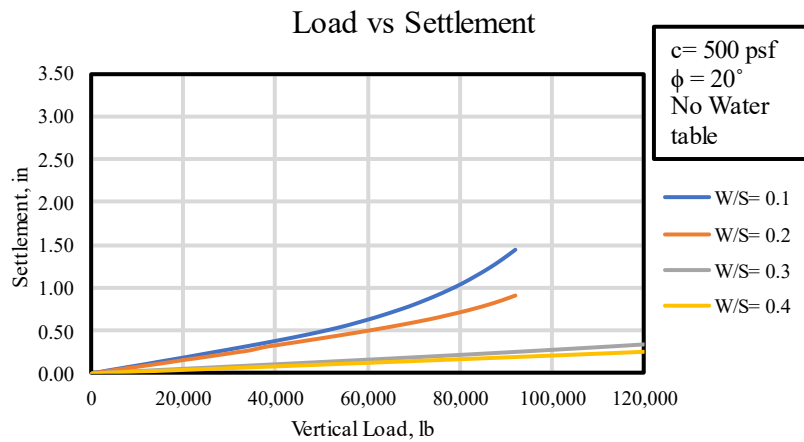
Figure C- 116 Design Chart for c = 500 psf and ϕ = 20˚, with no ground water
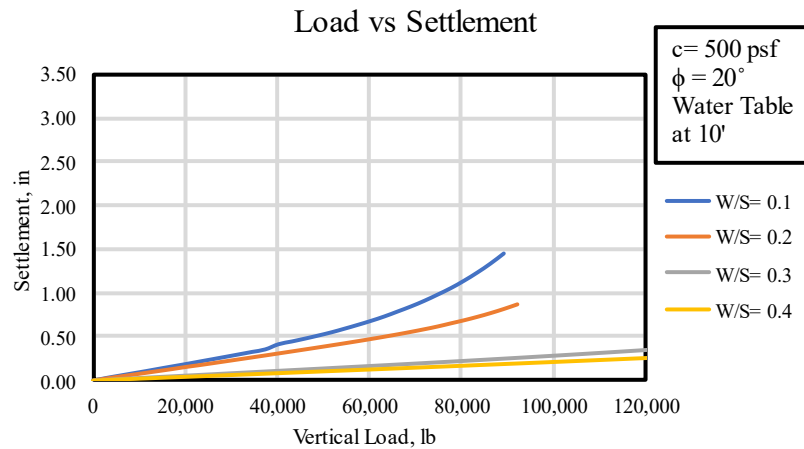
Figure C- 117 Design Chart for c = 500 psf and ϕ = 20˚, with ground water at 10 ft

344
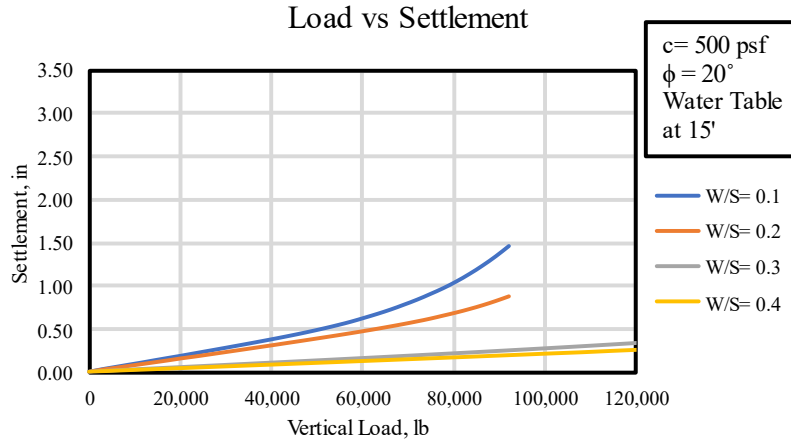
Figure C- 118 Design Chart for c = 500 psf and φ = 20˚, with ground water at 15 ft
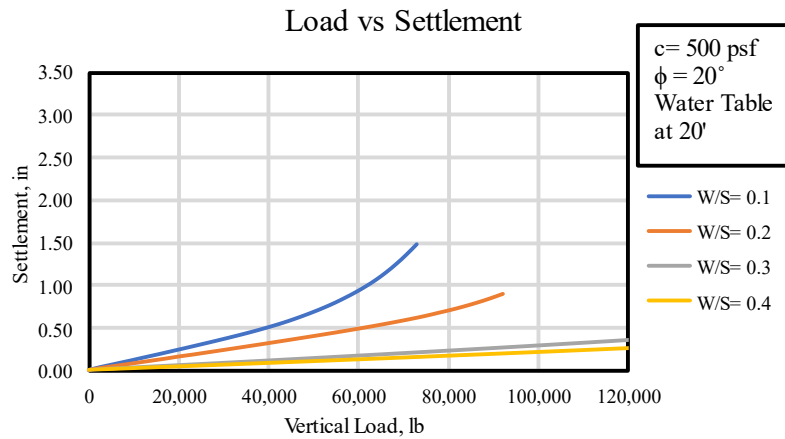
Figure C- 119 Design Chart for c = 500 psf and φ = 20˚, with ground water at 20 ft
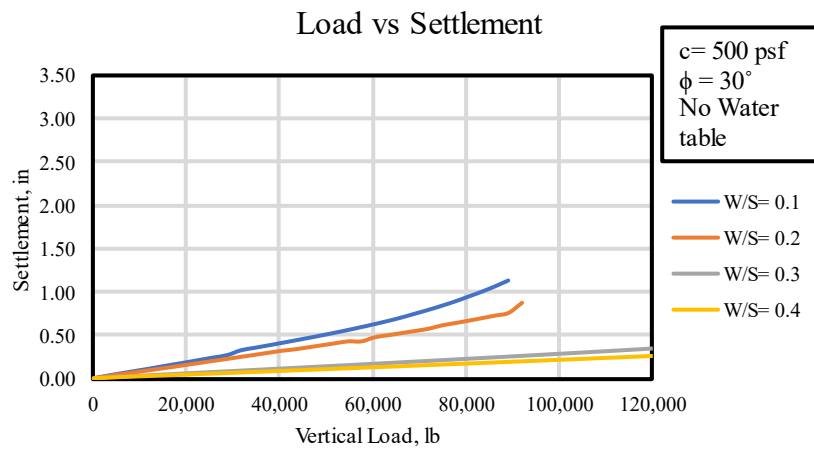
Figure C- 120 Design Chart for c = 500 psf and φ = 30˚, with no ground water

345
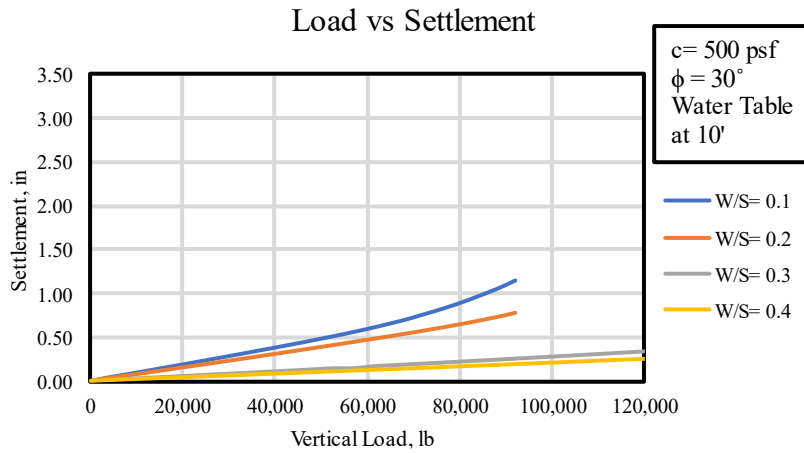
Figure C- 121 Design Chart for c = 500 psf and ϕ = 30˚, with ground water at 10 ft
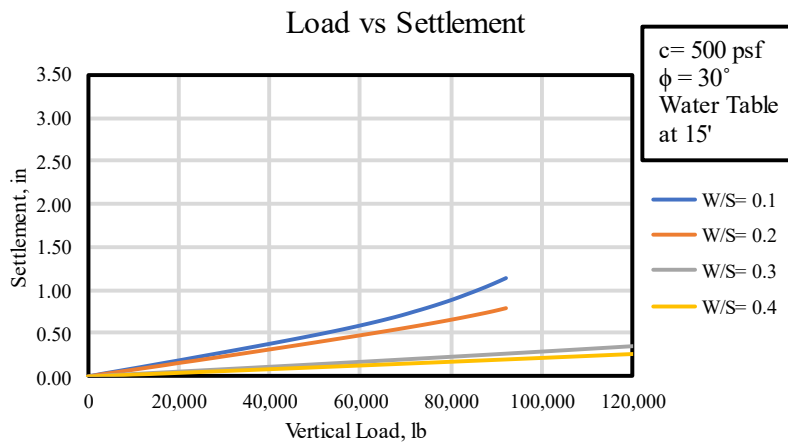
Figure C- 122 Design Chart for c = 500 psf and ϕ = 30˚, with ground water at 15 ft
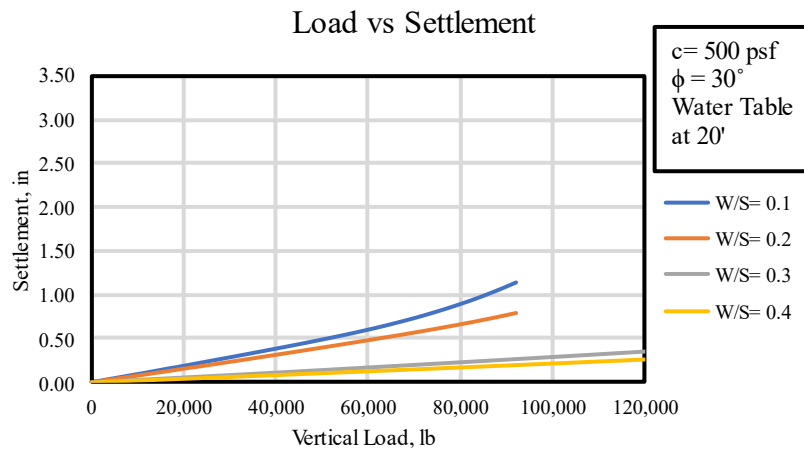
Figure C- 123 Design Chart for c = 500 psf and ϕ = 30˚, with ground water at 20 ft
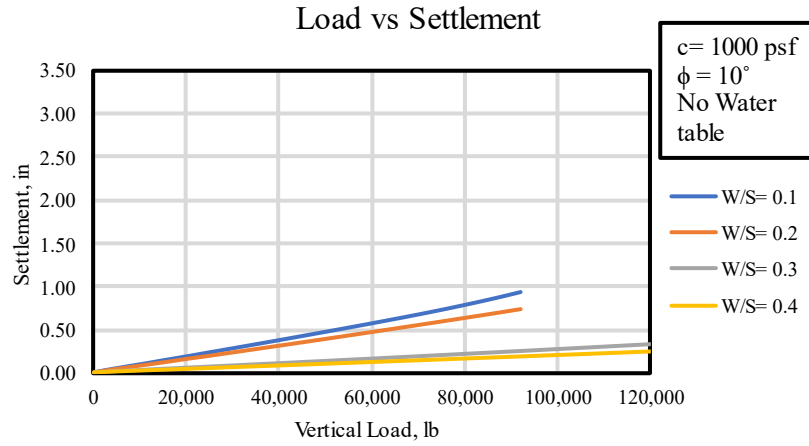
Figure C- 124 Design Chart for c = 1000 psf and φ = 10˚, with no ground water
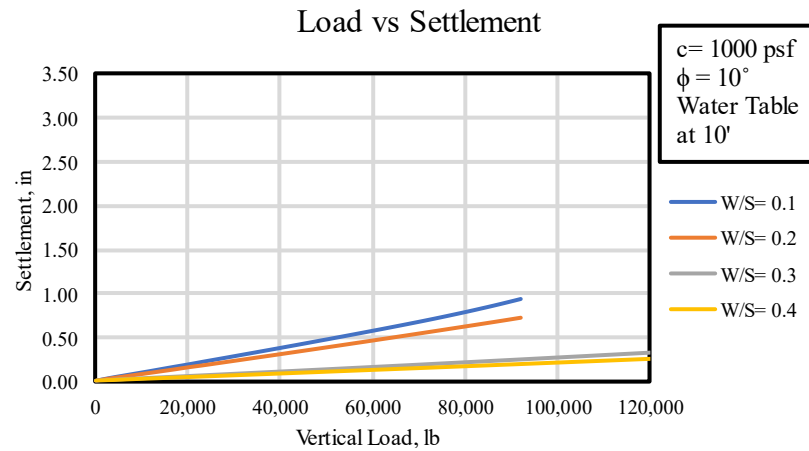
Figure C- 125 Design Chart for c = 1000 psf and φ = 10˚, with ground water at 10 ft
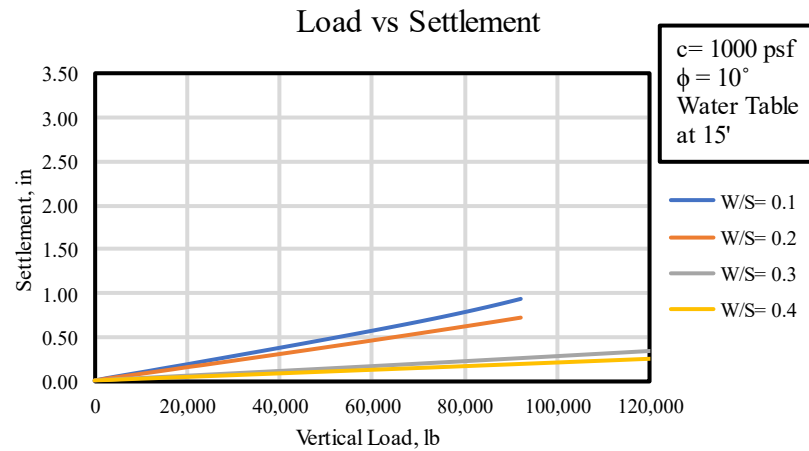
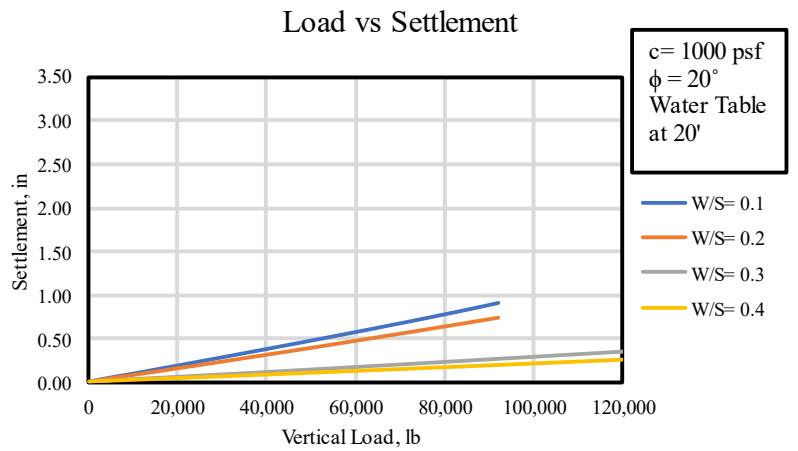Figure C- 126 Design Chart for c = 1000 psf and φ = 10˚, with ground water at 15 ft
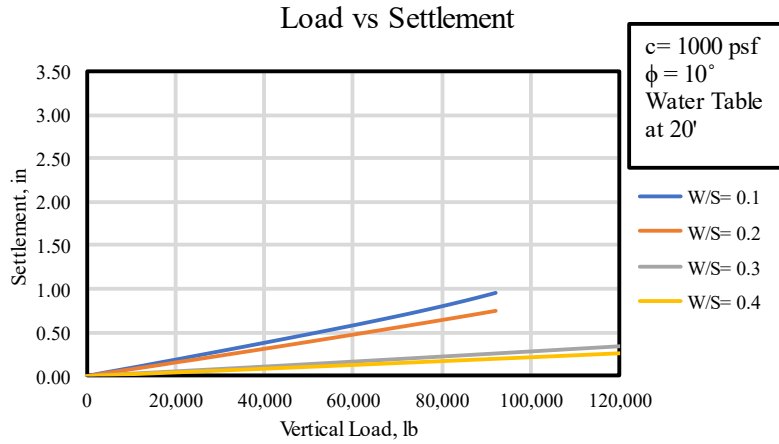
Figure C- 127 Design Chart for c = 1000 psf and φ = 10˚, with ground water at 20 ft
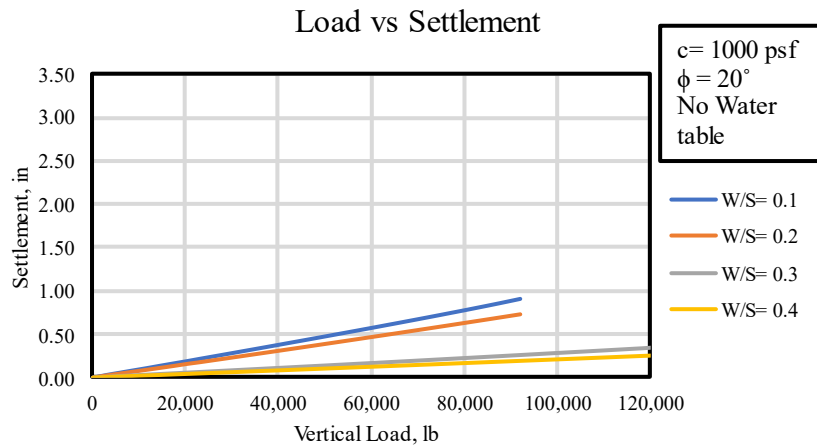
Figure C- 128 Design Chart for c = 1000 psf and φ = 20˚, with no ground water
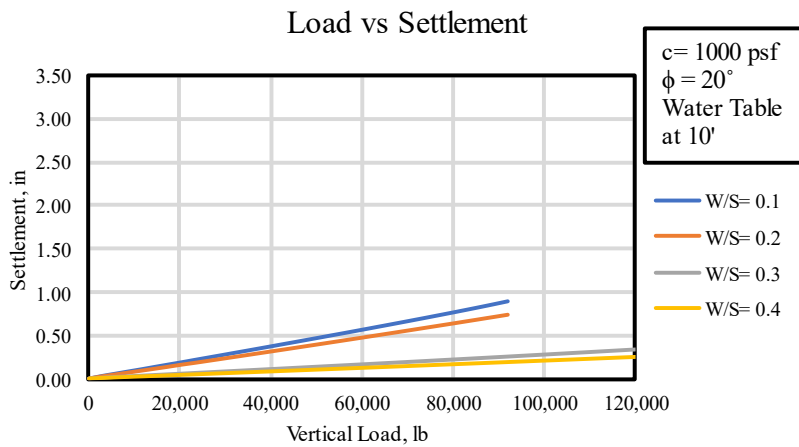
Figure C- 129 Design Chart for c = 1000 psf and φ = 20˚, with ground water at 10 ft

Load vs Settlement

c= 1000 psf
ϕ = 20°
Water Table
at 15'

W/S= 0.1
W/S= 0.2
W/S= 0.3
W/S= 0.4
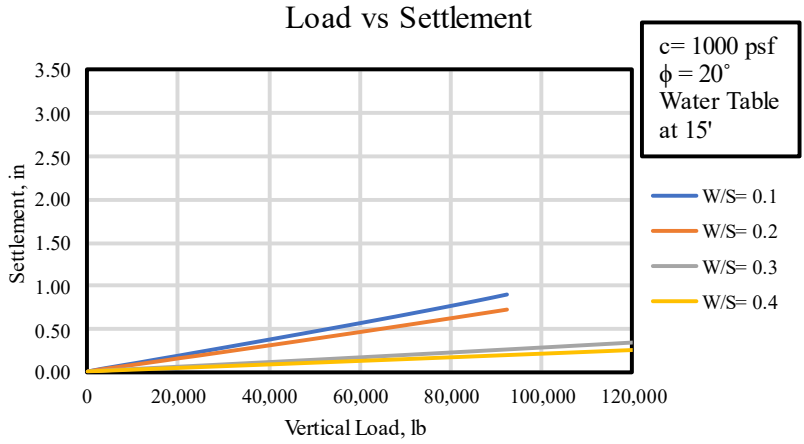
Figure C- 130 Design Chart for c = 1000 psf and ϕ = 20˚, with ground water at 15 ft

Load vs Settlement

c= 1000 psf
ϕ = 20°
Water Table
at 20'

W/S= 0.1
W/S= 0.2
W/S= 0.3
W/S= 0.4

Figure C- 131 Design Chart for c = 1000 psf and ϕ = 20˚, with ground water at 20 ft

Load vs Settlement

c= 1000 psf
ϕ = 0°
No Water
table

W/S= 0.1
W/S= 0.2
W/S= 0.3
W/S= 0.4
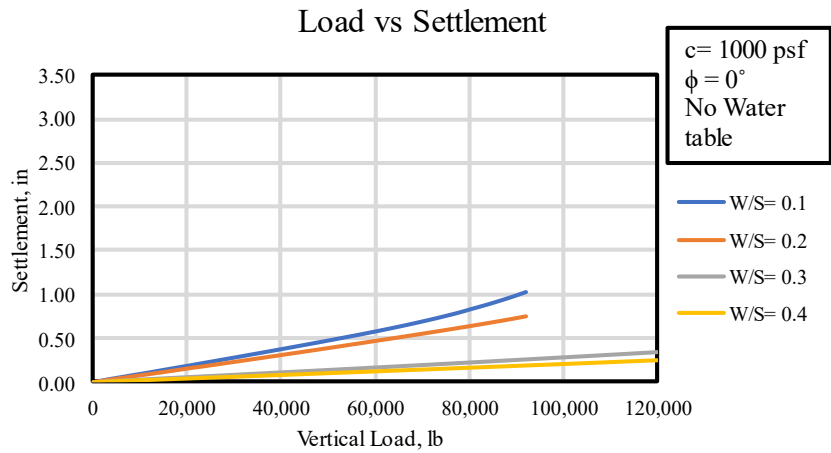
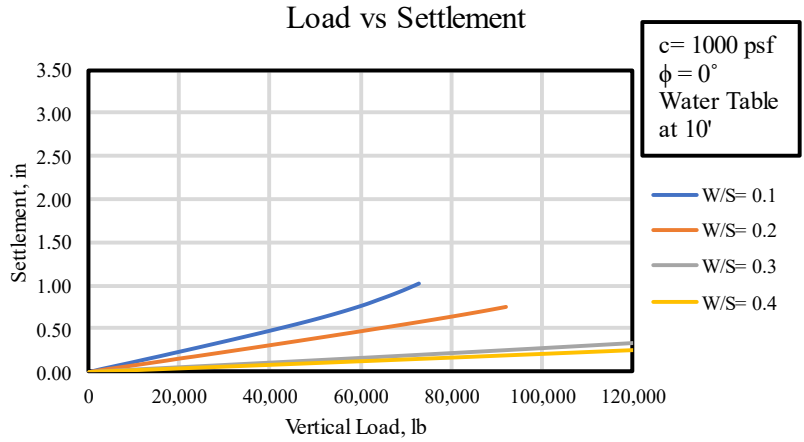Figure C- 132 Design Chart for c = 1000 psf and ϕ = 0˚, with no ground water

349

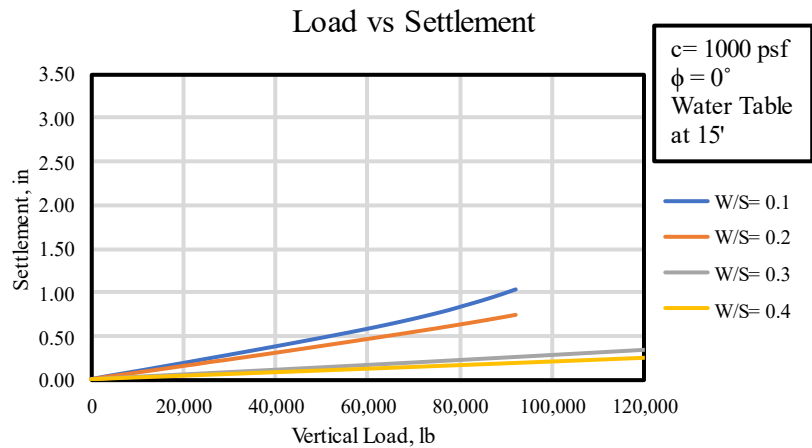Figure C- 133 Design Chart for c = 1000 psf and φ = 0˚, with ground water at 10 ft

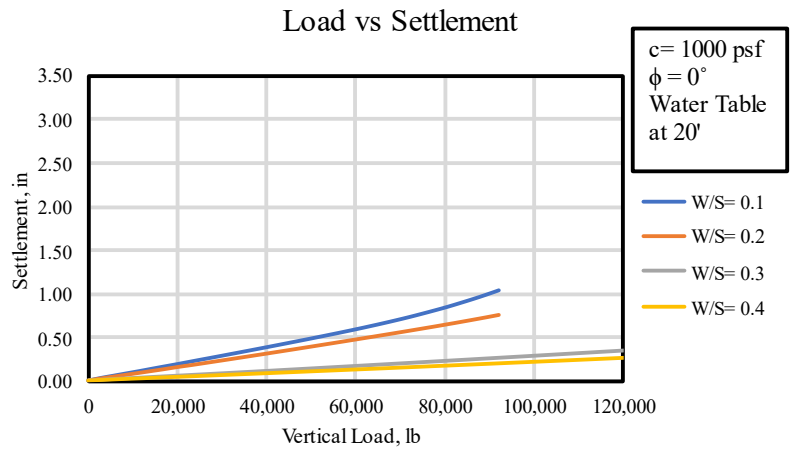Figure C- 134 Design Chart for c = 1000 psf and φ = 0˚, with ground water at 15 ft

Figure C- 135 Design Chart for c = 1000 psf and φ = 0˚, with ground water at 20 ft